CRANFIELD INSTITUTE OF TECHNOLOGY

SCHOOL OF MECHANICAL ENGINEERING

Ph. D. THESIS

Academic Year 1979-80

E.A.SAAD

AN EXPERIMENTAL AND THEORETICAL STUDY OF ---FLOW IN A VORTEX CONTROLLED DIFFUSER

Supervisor: R.J.ADKINS

September, 1980

ACKNOWLEDGEMENT

Now that it is time for me to acknowledge the help and assistance that I have received from various individuals, I find it hard to express how much I am grateful to Mr. R.C.Adkins, my supervisor. At almost every stage of my research activities he was very closely involved, sometimes through direct participation, but mostly in an advisory capacity. His optimistic and encouraging attitude did much to prevent me from being dismayed by the initial difficulties involved. At practically every crossroad, he was able to identify the path that led in the direction of the main goal. At this moment of introspection, I can think of at least few instances when I lost valuable time by either not heeding, or not seeking his advice. If this thesis is still inadequate, as is more than probable, all that I can say is that it would have been much worse but for Adkins' constructive criticism. I cannot truthfully say that I always enjoyed his merciless corrections of my English language but I can definitely say that I always benefited from his criticism: after all, most medicines are bitter to swallow but they do good.

I also owe a lot to Prof. R. Hetherington for his advice on the theoretical aspects of this study.

There are many others to whom my thanks are due. For lack of space, I find myself unable to mention all the individuals by name who have contributed to this thesis in various capacities. But I wish to mention specifically Mr. David Binks and Mrs. Jackie Spendel for correcting most of the typing and spelling mistakes.

I find myself unable to express my feelings in words for the active encouragement and support of my wife Nariman. She spent most of the evenings and nights of the last few weeks patiently typing the thesis. She also provided for me a comfortable and calm house so that I could concentrate on my study. Last but not least, when the family faced financial difficulties, in spite of the Institute's support, she decided to go to work to help in supporting the family. For her I owe so much, God help me to pay her back. For my two beloved sons Wael and Nael I owe an apology for neglecting them during the last two years. I hope one day they can understand that this was unavoidable.

Cranfield, August 1980 E.A.SAAD

SUMMARY

The flow inside a vortex controlled diffuser was studied experimentally and theoretically. The experimental side of the study included the following:

(1) The selection of a suitable laser Doppler velocimeter for the measurement of the mean velocity and the Reynolds' stresses.

(2) An experimental optimisation of the geometry of a diffuser model was conducted. The results were used in the design of the diffuser model which was later used for the measurement with the LDV.

(3) The distribution of the static pressure, the components of the mean velocity and the Reynolds' stresses in the diffuser model were measured. The results were presented and discussed. The analysis of the results established a comprehensive hypothesis about the flow mechanism. This enhanced the present knowledge about the flow behaviour inside this particular diffuser.

(4) Suggestions for further development of the design of the diffuser were proposed.

The theoretical aspects of the study included the following:

(1) A suitable mathematical model of turbulence was selected and incorporated in a well established mathematical approach for the prediction of recirculating flows.

(2) The complete mathematical specification was presented and the finite difference solution procedure was modified to suit this particular case.

(3) A new computer programme was written and developed. The results of the computation proved that the solution was convergent and can be used, after further development, to predict the flow and the performance of this particular type of diffuser. Suggestions for further development of the programme were also proposed.

CONTENTS

LIST OF FIGURES

PAGE

NOTATION

Unless otherwise defined in the text, the notation followed was:

A	Cross-section area.
AR	Area ratio.
B	Bleed rate.
B^*	Minimum bleed requirement.
b	Beam separation.
C	Constant.
C_D	Constant in equation (4-14).
C_L	Total pressure loss coefficient.
C_p	Static pressure rise coefficient.
$C_{p\,i}$	Ideal static pressure rise coefficient.
D	Diameter.
D	Beam separation.
D_1	Primary duct diameter.
D_2	Secondary duct diameter.
$D_{e^{-2}}$	Laser beam diameter before focusing.
D_f	Fence diameter.
d_a	Pinhole diameter.
d_e	Diffuser effective diameter.
$d_{e^{-2}}$	Laser beam diameter after focusing.
d_m	LDV, measuring volume diameter.
E	Bled air flow meter reading.
f	Focal length.
f	Characteristic frequency of the energy-containing eddies.
g	Amplitude of a point on the correlogram.
h	Manometer reading.
I	Horizontal index for computational grid.
i	Horizontal index for experimental grid.

J	Radial index for computational grid.
j	Radial index for experimental grid.
k	Mean value of the kinetic energy of turbulence per unit volume.
k'	Instantaneous kinetic energy of turbulence per unit volume.
L	Vortex chamber length.
l	The average molecular free path length.
l'	Length scale of turbulence.
l	Distance from cross over point of the laser beams.
l_m	LDV, measuring volume length.
l_m	Mixing length.
M	Mach number.
n	Number of fringes.
P	Total pressure.
p	Static pressure.
$\bar{p}$	Mean value of static pressure.
p'	Fluctuating static pressure.
P_1	Inlet static pressure.
P_2	Exit static pressure.
P_c	Vortex chamber static pressure.
P_z	Barometric pressure.
R	Radius.
R	Vortex chamber intermediate radius.
R_1	Primary duct radius.
R_2	Secondary duct radius.
R_3	Primary duct outside radius.
R_e	Reynolds' number.
R_t	Reynolds' number of turbulence.
r	Radial coordinate.

S	Fringe spacing.
S_k	Source term of k.
S_l	Source term of l.
S_ω	Source term of ω.
T	Turbulence intensity.
t	Temperature °C.
t	Time.
U_o	Nominal inlet axial velocity.
$\bar{U}_1$	Axial mean velocity component.
$\bar{U}_2$	Radial mean velocity component.
u	Instantaneous velocity in the x-direction.
$\acute{u}$	Axial fluctuating velocity.
$\acute{u}$	Fluctuating velocity in the x-direction.
$\bar{u}$	Mean velocity in the x-direction.
$\overline{u^2}$	Axial normal Reynolds' stress.
$\overline{\acute{u}\acute{v}}$	Reynolds' shear stress.
V	Molecular velocity.
$\bar{V}$	Mean velocity measured with the LDV.
$\bar{V}$	Radial mean velocity component.
$\bar{v}_1$	Mass flow derived mean inlet velocity.
V_c	Vortex chamber depression parameter.
v_t	Typical velocity scale of the turbulent motion.
v	Instaneous velocity in the y-direction.
$\bar{v}$	Mean velocity in the y-direction.
$\acute{v}$	Fluctuating velocity in the y-direction.
$\acute{v}$	Radial fluctuating velocity.
$\overline{\acute{v}^2}$	Redial normal Reynolds' stress.
$\underline{W}$	Velocity vector.
$\dot{W}_1$	Inlet mass flow rate.

$\dot{W}_B$	Bled air mass flow rate.
w	Instantaneous velocity in the z-direction.
$\overline{w}$	Mean velocity in the z-direction.
$\acute{w}$	Fluctuating velocity in the z-direction.
$\acute{w}$	Tangential fluctuating velocity.
$\overline{\acute{w}^2}$	Normal tangential Reynolds' stress.
x	Fence axial gap.
x	Axial coordinate.
y	Fence radial gap.

Symbols:

α	Kinetic energy flux parameter.
δ	Vortex chamber depth.
ε	Dissipation rate of the kinetic energy of turbulence.
η	Diffuser effectiveness.
θ	Half angle between the two laser beams.
θ	Angle between the axis of symmetry of the transmitting optics and that of the receiving optics.
λ	Wave length of the laser light.
μ	Viscosity.
μ_{eff}	Effective viscosity.
μ_t	Turbulent viscosity.
ν_D	Doppler frequency.
ρ	Density.
σ_k	Prandtl or Schmidt number for k.
σ_l	Prandtl or Schmidt number for l.
τ	Doppler period.
ϕ	Fence angle.
ψ	Stream function.
ω	Vorticity.

Subscripts:

1	Diffuser inlet plane.
2	Diffuser exit plane.
B	Bleed flow.
c	Vortex chamber.
E	East.
ex	Exit condition.
I	Idial case.
N	North.
opt	Optimum value or condition.
P	Condition at grid point P.
S	South.
∞	Wall condition.
W	West.

I INTRODUCTION

INTRODUCTION

Recent developments in aircraft gas turbine engine designs put more emphasis upon stretching the engine components to operate at extreme limits. This led to a considerable increase in both the compressor and turbine exit velocities. Consequently, the engine diffusers, following both the compressor and turbine, need to operate with increased area ratios, Ref.(1). Modern engines also require additional demands from its diffusers, these can be summarized as follows, Ref.(2):

1- Low total pressure loss.
2- High static pressure rise.
3- Uniform outlet velocity profile.
4- Insensitivity to inlet velocity profile.
5- Short length and light weight.

Unfortunately, in spite of the spending of considerable amounts of money, time, and effort, the fact remains that the art of designing a conventional optimum diffuser that would satisfy all these requirements has yet to be mastered.

Back in 1938, G.N.Patterson, Ref.(3), published a review of conical diffuser performance. This review had been accepted as the basic guide to diffuser design for a long time after its publication. Patterson's paper was broad in scope and made clear reference to the effect of parameters which were not fully investigated until much later. More recently, D.J.Cockrell and E.Markland published two valuable articles, Ref.(4) and Ref.(5), in which they reviewed the relevant available experimental data about incompressible fluid flow in conical diffusers. They also presented a new foundation for an improved analytical approach for the treatment of incompressible fluid flow in conventional conical diffusers. The two articles are widely referred to for design purposes, although other reviews have appeared more recently.

Many methods have been suggested and employed to improve the performance of conventional diffusers. Among these methods are:

1- Using forced mixing devices.
2- Using vortex generators.
3- Using moving walls.
4- Boundary layer control by local injection.
5- Boundary layer control by suction.

A detailed review of these methods together with a full discussion of their relative merits can be found in Ref.(6). Although such methods do improve the performance of conventional diffusers, the extent of that improvement still stands short of completely fulfilling the demands of modern aircraft gas turbine engines.

The novel idea of using standing vortices to control the flow in diffusers to improve performance was originally proposed by Ringleb, Ref.(7). The idea was based on observations of mountain ridge vortex flows which cause snow cornice formations. The Ringleb diffuser, Ref.(8), was designed with precisely contoured cusps in the walls intended for vortex trapping. No provision for replenishing vortex energy dissipated by friction was available. As a result, this diffuser achieved only limited success, Ref.(9). Heskestad, Ref.(10), suggested that stabilisation of the vortex might be achieved by the use of suction directly from the vortex, or just downstream of it. A successful short diffuser model producing nearly the ideal static pressure rise coefficient was reported by Heskestad in Ref.(11). R.C.Adkins in Ref.(12), independently, suggested another method to stabilise the controlling vortex. The resulting diffuser is known as the Cranfield diffuser.

During the last twelve years, the Cranfield diffuser has been tested under different operating conditions simulating those which are experienced in gas turbine engines. A brief review of this work is presented in a later part of this thesis. Although the Cranfield diffuser is still in its early development stages, the results of these prove that its performance is superior to that of conventional ones. Further development of such a diffuser to the stage of wide practical applicability would require a huge matrix of research which might be tedious, time consuming, and very costy. It is believed that further understanding of the flow behaviour, and the development of a theoretical approach for the treatment of the flow inside the diffuser, will reduce the required research work quite substantially. The present study was initiated to establish a foundation for a more detailed future study that would satisfy this requirement, hence the exploratory nature of the present study.

There are two aspects of the present study, the first is experimental and the second is theoretical. The objective of the experimental work was to provide detailed experimental data about the parameters of the flow inside

the diffuser. Due to the time and cost limitations which were imposed on the project, it was decided that the flow parameters which were to be measured should be limited to the following:-

1- Static pressure.

2- Time averaged velocity components.

3- Turbulent Reynolds' stresses.

Such experimental information would help to further the present understanding of the flow inside the diffuser. This information is also needed for the theoretical side of the present study. Previous research work, Ref.(1), indicated that the flow inside the diffuser is complicated, particularly near the entrance of the vortex chamber, and at the lee of the fence. In these regions the flow experiences recirculation, steep velocity gradients, and high levels of turbulence intensity, and under such conditions measurement with conventional methods may not be adequate. Thus, the selection of suitable measurement techniques is an essential part of the present study.

The ultimate goal of the theoretical side of this study is to develop a mathematical model which can be used to predict the flow parameters and hence the diffuser performance. Diffusers of this type have usually been developed empirically, with only qualitative guidance from theory. The reason is, that although the relevant processes have long been understood qualitatively, no accurate and economical procedure has been developed for the quantitative prediction of the performance of the Cranfield diffuser. Empirical development of a prediction procedure is expensive and slow, and additionally suffers from the usual deficiencies of limited range of applicability and uncertainty of extrapolation. Thus a generally applicable, theoretically developed prediction procedure would be a considerable aid to the designer of a Cranfiled diffuser. Such a procedure would replace physical experiments by computational research. The development of such a prediction procedure is a major task which is likely to require the effort of several researchers over a long period of time. In this respect, the author of this thesis is deeply conscious of the incompleteness of his work. Nevertheless, it has been presented here because it is useful as a preliminary study for future researchers who might be tempted to make it complete.

This thesis is divided into three parts. Part one was given the title, "Background". As this implies, this part includes basic information about

subjects which were felt essential to follow the discussions presented in the thesis. Part one is further divided into five chapters. Chapter one contains basic information relating to the Cranfield diffuser. Chapter two is a brief historical and literary review of the research work which was conducted at Cranfiled on this type of diffuser. Chapter three is a brief review of the fundamental equations of motion for turbulent flow, and their physical significance. Chapter four is a brief discussion of the widely accepted mathematical models of turbulence. Finally, chapter five contains a short summary of the principles of laser Doppler velocimetry. Readers who are familiar with these subjects are kindly advised to bypass these chapters and to carry on from the next part.

Part two of the present thesis is concerned with the experimental aspects of this study, while part three contains the theoretical study.

II PART ONE

BACKGROUND

CHAPTER ONE

1. THE CRANFIELD DIFFUSER

1.1 Description and definitions:

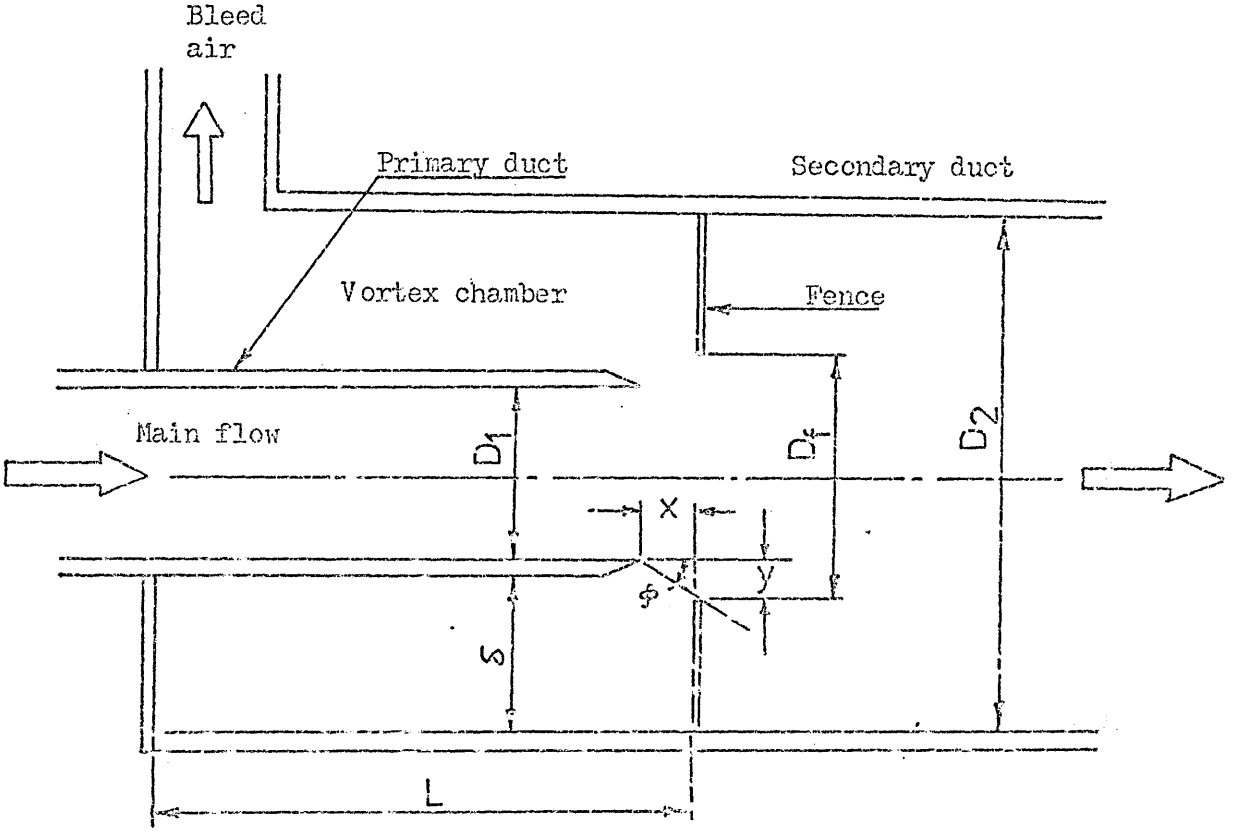

Fig.(1-1): A typical geometric configuration of the Cranfield diffuser.

Fig.(1-1) illustrates diagrammatically a typical geometric configuration of the Cranfield diffuser, which consists of:

1- A straight walled inlet duct called the primary duct, the exit end of which is normally tapered to form a nearly knife edged lip. The inside diameter of the primary duct is denoted, D_1.

2- A coaxial straight walled exit duct called the secondary duct. The inside diameter of the secondary duct is denoted, D_2. The area ratio of the diffuser, AR, is defined as:

$$AR = (D_2/D_1)^2 \qquad (1\text{-}1)$$

3- A thin fence, perpendicular to the diffuser axis of symmetry, located downstream of the primary duct exit lip. The inside diameter of the fence is denoted, D_f . The fence radial gap, y is defined as:

$$y = (D_f - D_1)/2 \qquad (1\text{-}2)$$

The fence angle, ϕ is defined as:

$$\phi = \tan^{-1}(y/x) \qquad (1\text{-}3)$$

where x is the fence axial gap.

4- The vortex chamber in which the controlling vortex is trapped. This is an annular space, bounded on the inside by the primary duct, from the outside by another duct (normally an extension of the secondary duct), and by the fence on the downstream side. The vortex chamber depth is denoted, δ and its length is denoted, L.

1.2 The flow mechanism:

Low energy air is bled off the vortex chamber so that it is replenished by air of a higher energy level from the mainstream. The vortex stability is improved by the presence of the fence. The flow mechanism as suggested by R.C.Adkins in Ref.(1) is best explained with the help of Fig.(1-2):

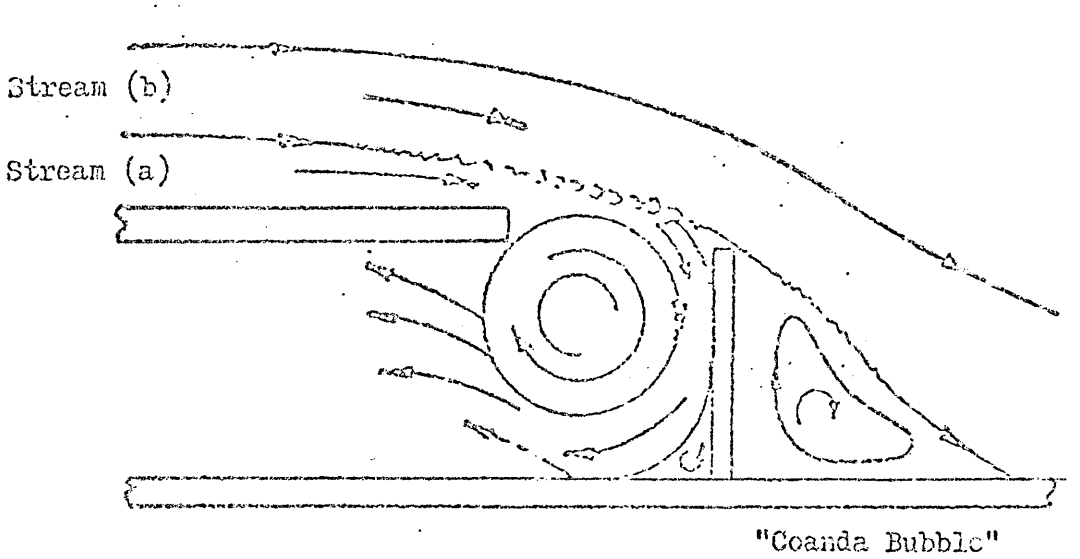

Fig.(1-2): The flow mechanism

1- The stream tube (a) is drawn into the vortex chamber due to the reduced chamber pressure and accelerates as it approaches the entrance.

2- Stream tube (b) continues through the diffuser and decelerates appreciably in the region of the vortex chamber.

3- A turbulent shear action is produced between the two streams which results in an energy transfer from stream (a) to stream(b)

4- Some of the fluid in stream (b) which would otherwise be too energy-deficient for diffusion is then able to flow through the diffuser without stall developing.

5- The mainstream flow is further aided by the formation of a "Coanda Bubble"immediately downstream of the fence which acts in a similar manner to the vortex proposed in Ringleb's diffuser.

This flow mechanism was based on flow visualisation experiments and other limited experimental results that were available at the time. These experimental results lacked the quantitative information on velocity distribution and turbulence structure required to form a more comprehensive picture about the behaviour of the flow inside the diffuser.

1.3 The diffuser performance parameters:

The parameters which are used to evaluate the performance of the Cranfield diffuser are as follows:

1- The static pressure rise coefficient, C_p, which is defined as:

$$C_p = (P_2 - P_1)/(\tfrac{1}{2}\rho \alpha_1 \bar{V}_1^2) \qquad (1\text{-}4)$$

where,

P_1 , is the inlet static pressure measured at a plane at least one hydraulic diameter upstream of primary duct exit lip.

P_2 , is the static pressure measured at an arbitrary plane in the secondary duct.

ρ , is the fluid density.

$\bar{V}_1$, is the mass flow derived mean inlet velocity.

α_1 , is an inlet velocity profile shape factor referred to as the kinetic energy flux parameter, Ref.(1).

2- The bleed rate, B is defined as the ratio of the bled air mass flow rate to the total mass flow rate,

$$B = \dot{W}_B / \dot{W}_1 \qquad (1\text{-}5)$$

3- The diffuser effectiveness, η is the ratio between the measured static pressure rise to the ideal one. The effectiveness can be calculated from the formula, Ref.(1):

$$\eta = (P_2 - P_1) / \tfrac{1}{2} \rho \bar{V}_1^2 \left[\alpha_1 - \left(\frac{1-B}{AR}\right)^2\right] \qquad (1-6)$$

4- The vortex chamber depression parameter, V_c is a measure of the static pressure lost by the bled air. This parameter is defined as:

$$V_c = (P_1 - P_c) / (\tfrac{1}{2} \rho \alpha_1 \bar{V}_1^2) \qquad (1-7)$$

Where p_c is the static pressure of the vortex chamber measured at an arbitrary plane downstream of the vortex.

1.4 The performance characteristics:

A typical performance characteristics of the Cranfield diffuser, as described by R.C.Adkins in Ref.(1), is shown in Fig.(1-3). The figure illustrates the relation between the diffuser effectiveness, η and the bleed rate, B.

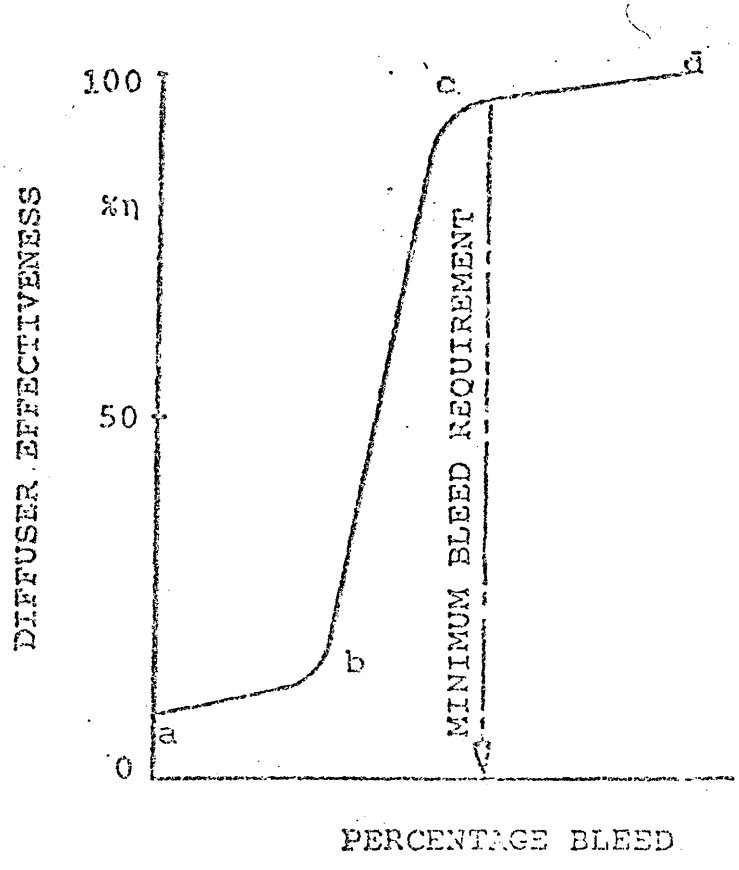

Fig.(1-3): Performance characteristic

Three distinct regions of performance can be readily indentified:

1- Region (a) to (b) is thought to occur when there is insufficient suction to draw fluid directly into the vortex chamber from the upstream region. Instead fluid is drawn from the low velocity in the lee of the fence and this causes a slight increase in pressure recovery as the bleed is increased.

2- Region (b) to (c) is a transition region where the depression in the vortex chamber is sufficient to partially deflect the mainstream flow causing an increase in pressure recovery. The flow continues to enter the vortex chamber from the lee of the fence.

3- Region (c) to (d) describes the performance when a vortex has been established and the mainstream flow, in the positive sense, achieves a stagnation point on the top of the fence. The point (c) relates to a condition which is referred to as the point of "Minimum Bleed Requirement". It may be seen that additional pressure recovery can still be obtained with a further increase in bleed. This increase in pressure recovery is caused by the continued removal of the low energy fluid from the diffuser throat and the intensification of the turbulent energy transfer as previously described.

1.5 The effect of the diffuser geometry on performance:

There are five geometrical parameters which are believed to have strong effects on the performance of a Cranfield diffuser of a certain length and operating with fixed inlet conditions. These parameters are the area ratio (AR) or the expansion ratio(D_2/D_1), the fence radial gap (y), the fence angle (ϕ) or the fence axial gap (x), the vortex chamber depth (δ), and the vortex chamber length (l). The effects of the first three parameters are discussed in detail in Ref.(12), from which the diagrammatic sketches shown in Fig.(1-4) are taken. Fig.(1-4)a shows the effect of AR on the diffuser effectiveness η. Fig.(1-4)b and Fig.(1-4)c illustrate the effect of changing y and ϕ, respectively, on the performance of the diffuser. The graphs are self explanatory. It was concluded in Ref.(12) that most of these effects can be explained in the light of the flow mechanism discussed in section 1-2, but some aspects cannot be explained because of the lack of quantitative information on the behaviour of the flow. It is one of

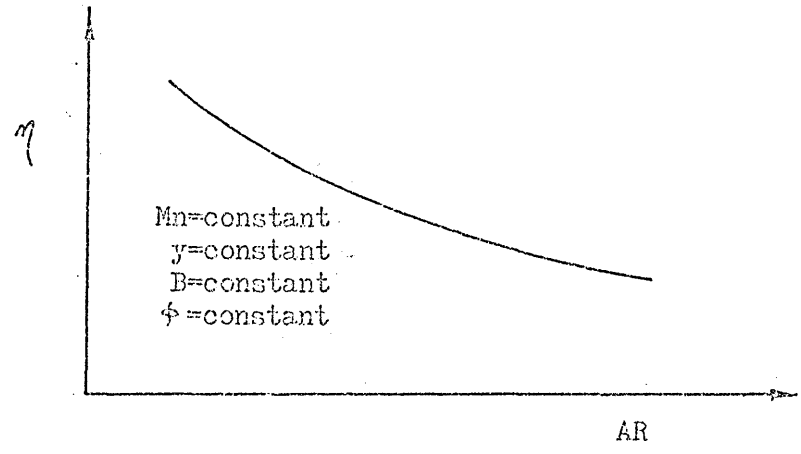

(a)

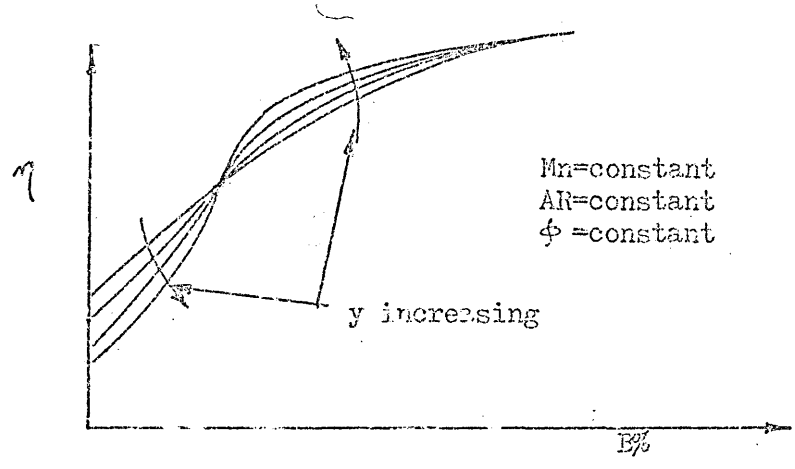

(b)

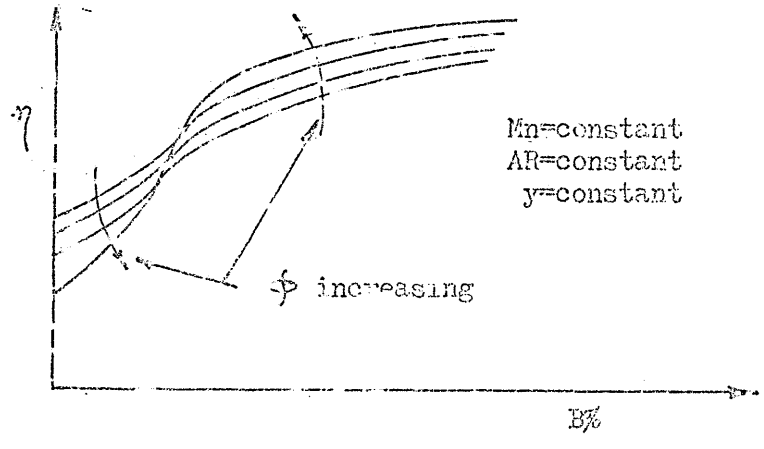

(c)

Fig.(1.4): The effect of the geometric parameters on the performance of the Cranfield diffuser.

the objectives of the present study to overcome this deficiency. To the knowledge of the author of this thesis there is no available information about the effects of the vortex chamber depth or length on the performance of the diffuser.

1.6 The flow characteristics:

From the previous discussions about the flow mechanism and the performance characteristics the flow field, in the case where the bleed rate is higher than the minimum bleed requirement, can be divided into three interactive regions:

1- The main flow which is bound by the physical walls of the primary duct, the shear surface emerging from the vicinity of the primary duct exit lip and impinging on the fence tip, the shear surface emerging from the fence and expanding downstream up to the reattachment plane, and the physical walls of the secondary duct downstream of the reattachment plane.

2- The controlling vortex ring inside the vortex chamber, this is bounded by; the fence from one side, the primary duct and the first shear layer from the inside, and the vortex chamber duct from the outside. The downstream side of the vortex is free, that is the side from which the low energy air is bled.

3- The Coanda Bubble which is a recirculation toroid just downstream of the fence bounded by the second shear layer from the inside, the fence, and the secondary duct.

The mainstream flow will initially be a nearly parallel flow with strong stream line curvature arising in the neighbourhood of the fence. The mainstream flow also faces an adverse pressure gradient all the way downstream from the primary duct exit except perhaps a region near the vortex chamber entrance where the sink effect might offset the adverse pressure gradient effects. In this region the flow is likely to experience a strong radial velocity component for the same reasons. Again, a strong radial velocity component may also be experienced just downstream of the fence. Elsewhere the axial velocity component is predominant. The turbulence intensity is expected to be relatively low in the main stream except near the shear layers and near the walls downstream of the reattachment plane.

The controlling vortex can be considered as a recirculating zone from which low energy air is bled from one side, which for continuity reasons it must be replenished by high energy air from the

mainstream. The flow in this region is expected to experience a rapid change in direction and to recirculate inside the vortex. Little is known about the turbulence structure in this region or about the flow behaviour at the regions where the fluid enters or leaves the recirculation zone. If the conditions in the shear surface between the controlling vortex and the mainstream could be approximated to those conditions which are found in shear surfaces in axisymmetrical sudden expansions, we would expect then, a high intensity of turbulence of highly non-homogeneous and anisotropic nature. We would also expect a very high interdependence with the mean flow. This picture can only be confirmed or denied when a detailed study of the flow and the turbulence structures in this region is available.

The other shear surface, downstream of the fence is expected to be one of intense velocity gradient and shear action. In addition, there is an adverse pressure gradient. These conditions lead to the production of turbulence which in its turn leads to a mixing process causing the quiescent fluid along the surface of separation to be entrained. The entrainment continues as the flow proceeds, but the presence of the solid boundary interferes with the inflow of the fluid required by the entrainment process. For reasons of continuity therefore, return flow is established from downstream, resulting in the formation of a stable zone of back flow. Hence the recirculation zone of the standing eddy which is referred to as the "Coanda Bubble". The formation of the standing eddy, the production of turbulence, and its subsequent convection, diffusion, and decay, have a significant influence on the determination of the entire flow pattern.

Beyond this general qualitative understanding, little is yet known about the details of the fluid motion. Even such knowledge as the velocity and pressure distribution in the early regions of flow, and the energy loss which the separation entails, is not possessed, much less any information regarding the intensity of turbulence or its rate of production or dissipation. An attempt has therefore been made in the present study to quantitatively determine the flow characteristics in the Cranfield diffuser in as much detail as possible.

This qualitative understanding of the flow characteristics helped in selecting the suitable measuring instruments. This is discussed in a later part of the thesis.

CHAPTER TWO

2. HISTORICAL AND LITERATURE REVIEW:

2.1 Introduction

The objective of this chapter is to briefly review how the Cranfield diffuser was historically developed and to highlight some of the results of the research programme that has been conducted at Cranfield on vortex controlled diffusers and other related fluidic devices.

2.2 The evolution of the Cranfield diffuser:

The original idea of the Cranfield diffuser was proposed by R.C.Adkins and first described in a paper present to the Combustion Sub-Comittee of the Gas Turbine Collaberation Commitee in 1969, Ref.(13). The paper was based on flow visualization observation and experimental measurements carried out by M.D.Sims, Ref.(14), on a two dimensional model. The model had a configuration very similar to that shown in Fig.(2-1).

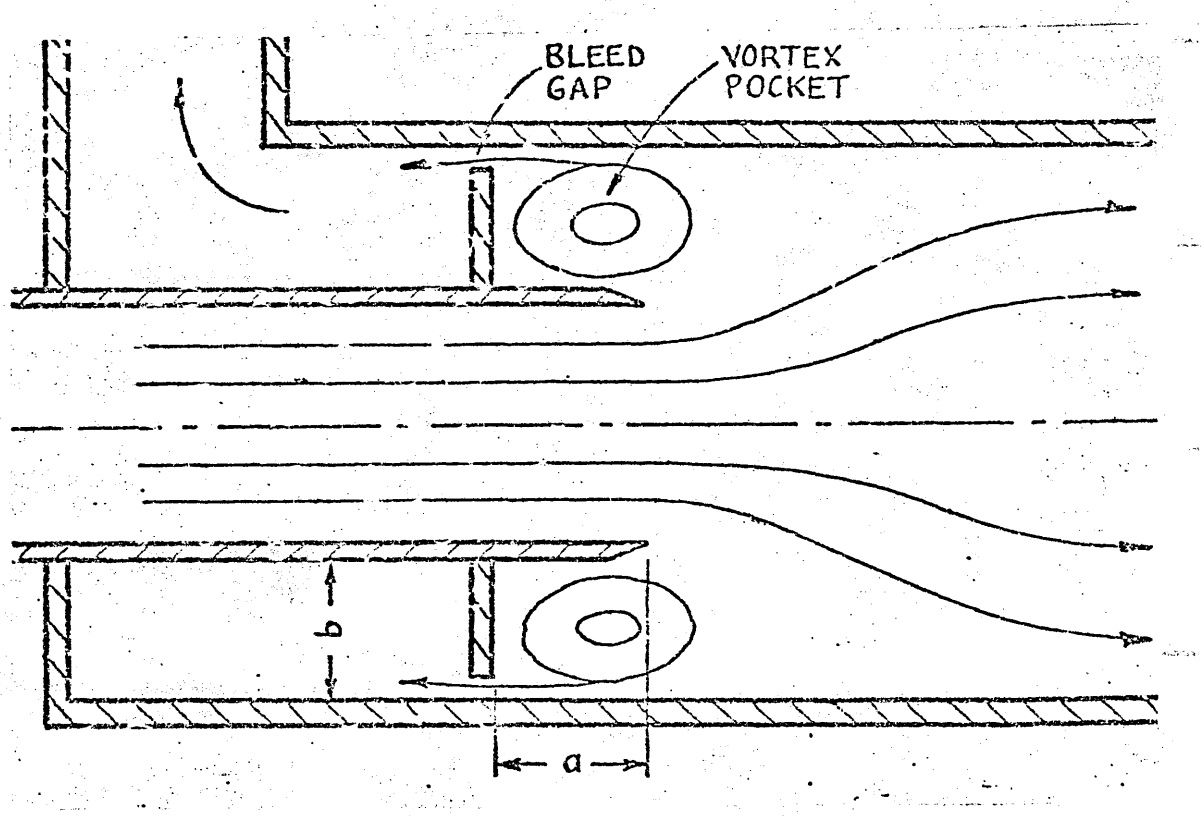

Fig.(2-1): The original configuration of the Cranfield diffuser

The model was considered to roughly represent a section of an annular diffuser. The formation of corner vortices in the model as a result of secondary flows, and their detrimental effect on the diffuser performance, were expected. These were accepted on the basis that performance trends were more important in the early investigation than were absolute test values. Sufficient qualitative results were obtained to indicate that a high level of performance could be expected of the diffuser with further development. The quantitative results showed that substantially high rates were required before the desired vortex mechanism could be stabilised.

The problem was overcome during the work of C.G.Beaty, Ref.(15), who eliminated the end wall effects by using a tubular configuration. A series of flow visualization studies were conducted on a water flow table during which a number of geometrical configuration were used to stabilize the controlling vortex. By careful study of the stream lines the most favourable configuration was determined. This configuration is shown in Fig.(2-2), where a fence was placed downstream of the step.

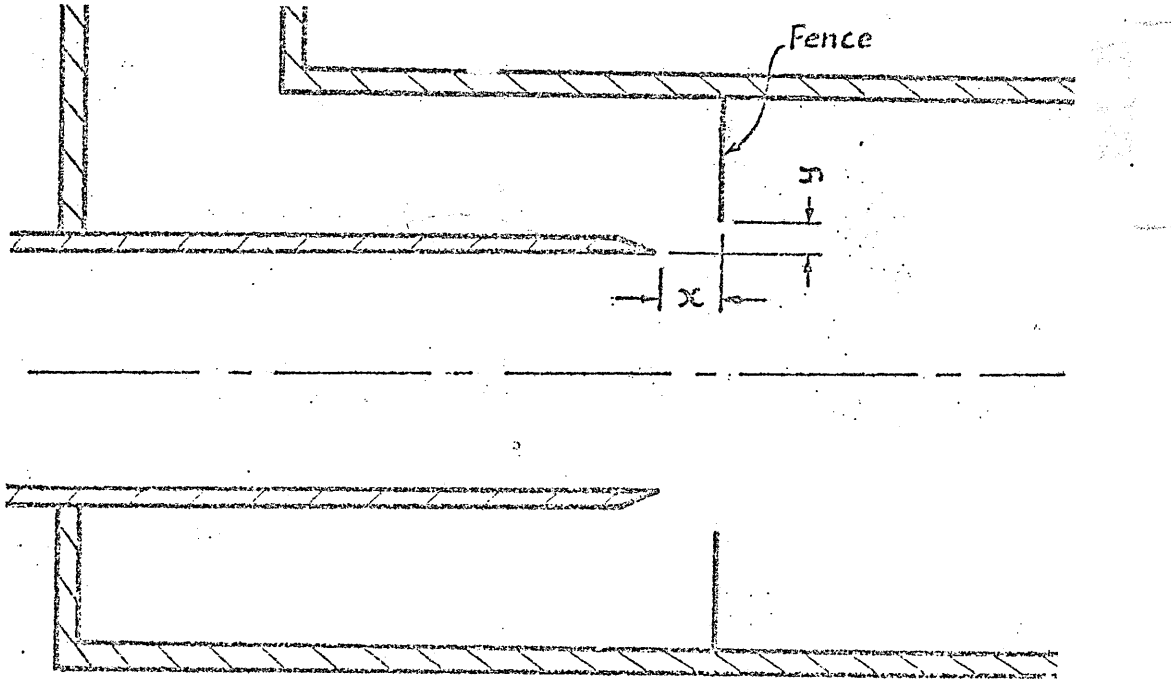

Fig.(2-2): The configuration of the Cranfield diffuser

The fence resulted in an immediate reduction in the bleed rate, and an almost ideal static pressure rise coefficient was obtained from subsequent tests conducted on an air rig. This configuration formed the basic concept of all the vortex controlled diffusers that have been since tested at Cranfield.

Beatty suggested that the radial gap, y and the fence axial gap, x are the most influential geometrical parameters on the performance of a diffuser of constant area ratio. He went on to establish the procedure by which these two parameters should be optimised. Beatty failed to produce a convincing theory of how the diffuser works.

2.3 The Cranfield diffuser as a pre-combustor annular diffuser:

Fenge, Ref.(16), tested an annular model of the Cranfield diffuser, the major geometrical features of which are sketched in Fig.(2-3). The results of Fenge's work, indicated that the annular model was efficient, stable, and had the added advantage of a stable, uniform,

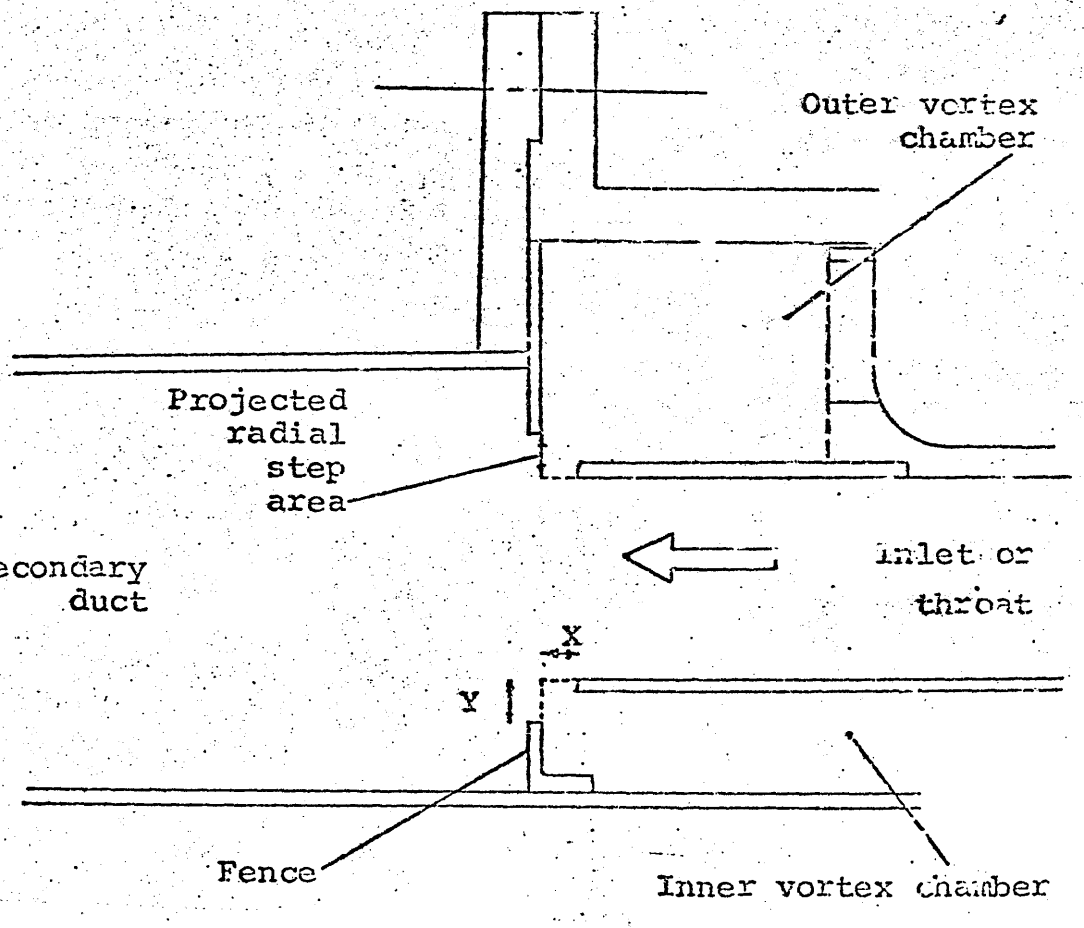

Fig.(2-3): Geometrical configuration of the annular Cranfield diffuser

and controllable, outlet velocity profile. Proffit, Ref.(17), extended Fenge's work by investigating the effect of a distorted peaky inlet velocity profile on the performance of the annular model. Proffit used convergent rings located in the diffuser throat exit to produce the required peaky velocity profiles. The objective was to simulate the conditions experienced by pre-combustor diffusers. There is some doubt about the technique which Proffit used to assess the inlet velocity profile, and hence the performance of the diffuser, because he measured the velocity distribution immediately downstream of the rings, i.e in the wake of the rings. Nevertheless, the results of both Fenge and Proffit indicated that the annular model of the Cranfield diffuser was perfectly suitable for use as a pre-combustor diffuser in that it was both compact and efficient.

2.4 Early investigations of the flow behaviour inside the Cranfield diffuser:

Sutherland, Ref.(18), investigated the flow behaviour inside a two dimensional model of the Cranfield diffuser. He measured the axial velocity distributions and the turbulence level in flow regions where he could probe and traverse physically using a hot wire anemometer. Although, he could not reach a clear theory about the flow mechanism, his experimental results, and some of the conclusions he reached, helped to form part of the basis of the flow mechanism discussed here in chapter one. These conclusions are listed below:

1- The vortex in the vortex chamber is an effect of the phenomenon, but not a cause, although it does increase the effectiveness of the diffuser marginally.

2- The Coanda effect does take place behind the fence once the optimum diffuser bleed rate has been reached.

3- The turbulent shear layer that is formed by the boundary layer separating from the throat plate, forms a turbulent layer, which energises the fluid flowing past it into the secondary duct.

4- A source of turbulence is formed in the vortex chamber and the level of turbulence can be increased by the use of a weir.

5- The shape of the top of the fence has some bearing on the effectiveness, however, the shape of the remainder of the fence had no noticeable effect.

2.5 Design procedure and performance prediction of the Cranfield diffuser:

R.C.Adkins, in his paper to the ASME Symposium on "The Fluid Mechanics

of Combustion", which was held in Montreal, May 1974, Ref.(19), suggested an explanation of the flow behaviour in the Cranfield diffuser. This hypothesis, which was described here in chapter one, has been used by researchers up to this date. In the same paper, Adkins proposed two empirical formulae for the prediction of the performance of the diffuser.

These formulae are as follows:-

1- The optimum area ratio, AR_{opt}, for a Cranfield diffuser, which is equivalent to a conventional one having a total included angle of 30°, is given by:

$$AR_{opt} = 4.23\left[(0.025)^{\sqrt{\alpha_1 - 1}} + 0.236\right] \qquad (2\text{-}1)$$

2- The minimum bleed requirement B^* of an optimized diffuser is given by,

$$B^* = 0.393\,\eta\left[1 - \frac{1}{AR^2}\right]\sqrt{\frac{AR}{d_e}} \qquad (2\text{-}2)$$

Where, η is the diffuser effectiveness.

d_e is the diffuser inlet effective diameter in mm.

Beside these two empirical formulae there are rules of thumb to determine the fence geometry.

1- $\Phi_{opt} \cong 18°$

2- One third of the pressure recovery of the diffuser is gained in the distance between the diffuser throat and the fence. Hence,

$$(C_{pI})_f / C_{pI_\cdot} = 1/3$$

or,

$$3\left(1 - \frac{D_i^4}{D_f^4}\right) = 1 - \frac{1}{AR^2} \qquad (2\text{-}3)$$

From which D_f and hence 'y' can be obtained, Ref.(12).

2.6 The Cranfield diffuser as a tail pipe diffuser:

Hallam, Ref.(20), tested a tubular model of the Cranfield diffuser. He made his tests on the model to find the optimum geometry (without the use of bleed) to generate the vortex. The results achieved with the optimum geometry compared favourably with conventional diffuser of much greater length. Mak, Ref.(21), tested another model under special inlet conditions simulating those conditions which are experienced by turbine exhaust diffuser. He concluded that the Cranfield diffuser was superior to the conventional tail pipe diffuser with a truncated cone configuration in respect of shorter length and higher pressure recovery, even without removing flow from the vortex chamber. A diffuser effectiveness of 95% was achieved with as low a

bleed rate as 1% of the total mass flow. Diacakis, Ref.(22), tested a set of conventional diffusers and compared them with equivalent Cranfield diffusers. The tests were conducted at inlet Mach numbers which varied from 0.1 to 0.525, and with different inlet velocity profiles. The results showed that the Cranfield diffusers were superior to conventional ones, while operating under the same conditions. Diacakis concluded that applying vortex control to a tail pipe diffuser will result in having a diffuser which is much shorter, and far better in terms of performance, than the conventional type.

2.7 Vortex control in radial diffusers:

Allen, Ref.(23), designed and tested a radial out-flow diffuser employing the principle of vortex flow control in the turning of the flow from the axial direction to the radial diffuser channel. The performance of the diffuser was investigated over a range of inlet Mach number from 0.2 to 0.4 and area ratios from 1.5 to 3.0. The optimum vortex corner geometry to produce the maximum static pressure recovery was determined both with and without a small percentage of the mainstream mass flow being bled. As a result, an efficient and compact diffuser was obtained which can have a wide range of practical applications in air flow systems.

2.8 Vortex control as part of a variable geometry combustor:

Rizk, Ref.(24), designed and tested a model of a combustor in which the vortex control principle was used to control the distribution of the inlet air to the combustor zones. The objective was to control the primary zone temperature according to the engine running condition, and hence reduce the pollutants emission level. A diagramatic sketch of the arrangement used is shown in Fig.(2-4). The test results were encouraging, and were reported in Ref.(25), which included additional proposals for further developments. Kwan, Ref.(26), described a simple mathematical model to calculate the air flow distribution in the model. The comparison between his experimental results and the mathematical model was encouraging. El-Saftawy, Ref.(27), modified the experimental rig to make it more practicable, and elaborated the mathematical model. The results of the previously described research work were summarized by Adkins and El-Saftawy, Ref.(28). They concluded that the use of such a technique in

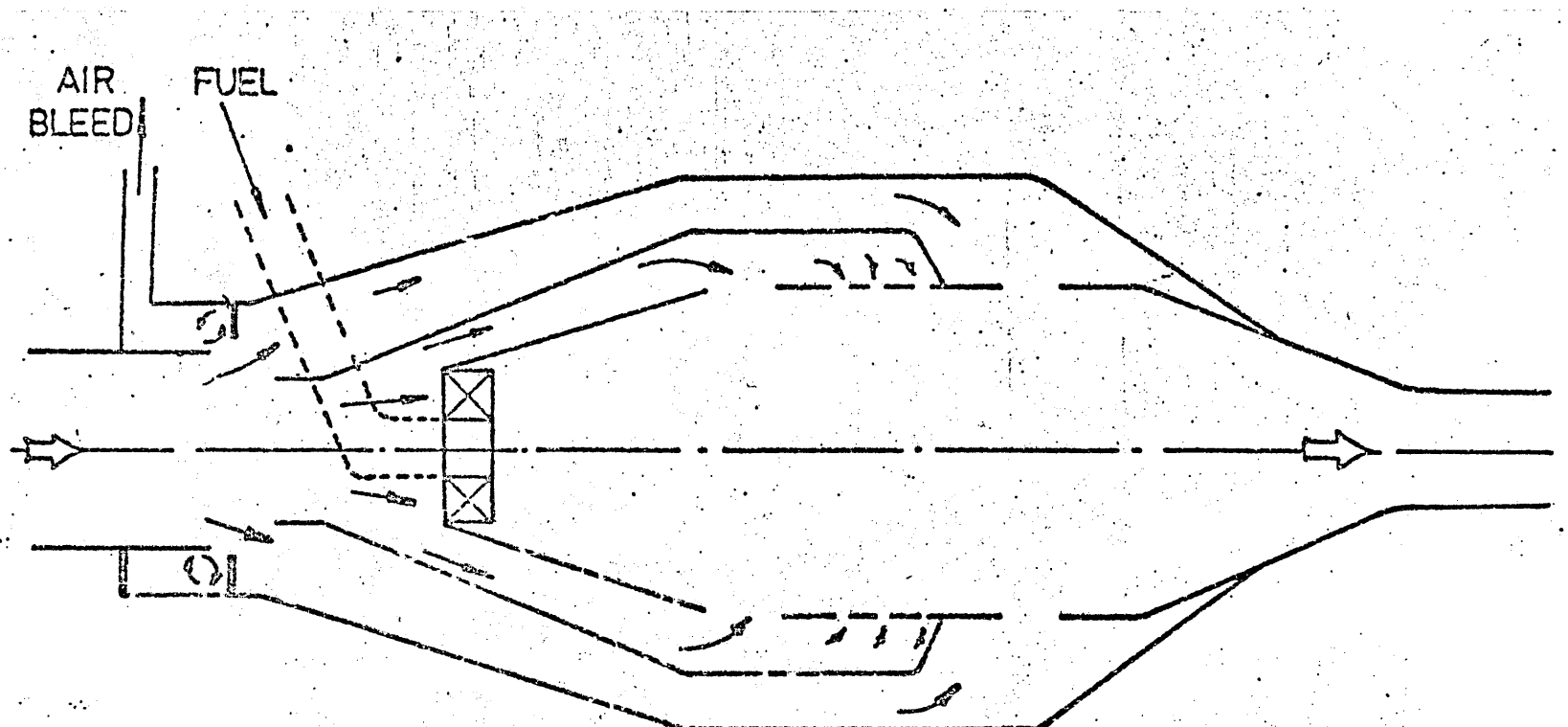

Fig.(2-4): Vortex flow controlled 'variable geometry' combustor.

future combustors is feasable and offers attractive advantages.

2.9 The Cranfield diffuser as a high subsonic inlet Mach number diffuser:

The use of the Cranfield diffuser concept as a high subsonic inlet Mach number diffuser for applications in aircraft intakes was first investigated by Depollas, Ref.(2), and then extended by Saad, Ref.(12). Depollas designed and tested a tubular model suitable for investigating the behaviour of the Cranfield diffuser at high subsonic inlet Mach numbers. Difficulty was experienced in controlling the flow conditions, but in spite of this, the initial results were encouraging. Saad developed the rig, and the technique of controlling the inlet Mach number so that tests could be conducted up to an inlet Mach number of 0.9. The performance of the model was investigated over a range of Mach number from 0.4 to 0.9 and area ratios from 1.5 to 3.0. The results proved that the Cranfield diffuser can perform without stalling, and with a high effectiveness, up to an inlet Mach number of at least 0.9.

2.10 The Cranfield diffuser as part of the hybrid diffuser:

In the Cranfield diffuser, the minimum bleed rate requirement increases rapidly as the area ratio increases, Fig.(2-5).

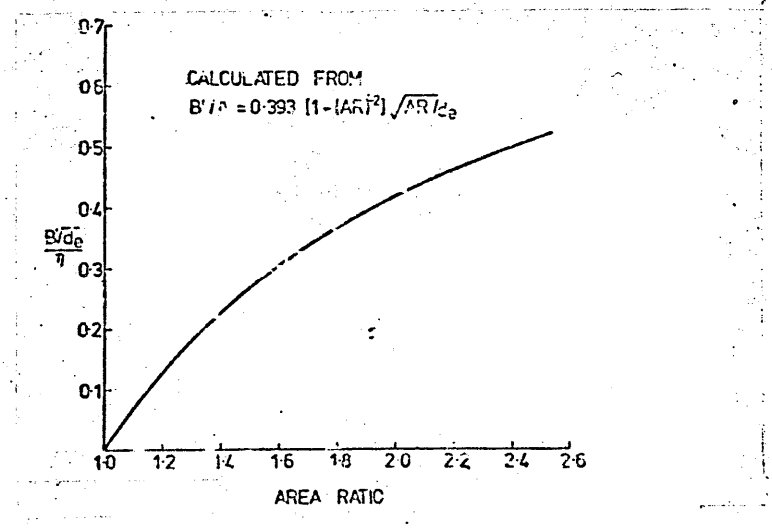

Fig.(2-5): Predicted minimum bleed requirement for vortex controlled diffusers.

The minimum bleed rate requirement also increases very rapidly as the inlet Mach number increases, Ref.(12). Consequently, in some practical applications which require a high area ratio diffuser operating at relatively high subsonic inlet Mach numbers, the minimum bleed rate requirement might not be tolerated. One method

of reducing the quantity of the bleed-off is by combining a low area ratio Cranfield diffuser with a conventional diffuser fitted immediately downstream. This arrangement is referred to as "the hybrid diffuser", and is shown diagrammatically in Fig.(2-6).

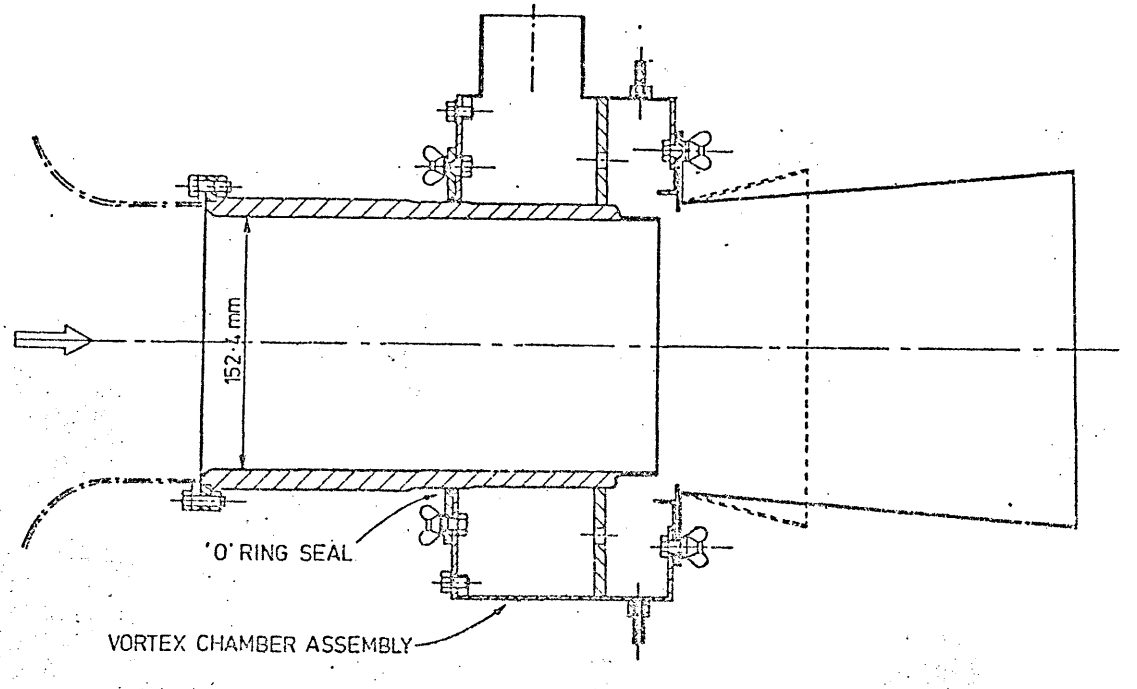

Fig.(2-6): Arrangement of the hybrid diffuser model.

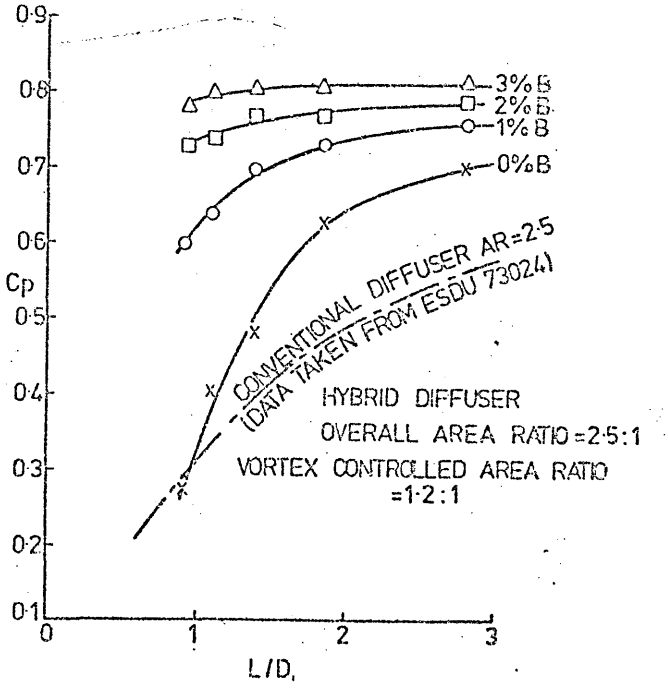

Fig.(2-7): The performance of the hybrid diffuser.

Matharu, Ref.(29), tested a hybrid diffuser model over a range of overall area ratios from 2.0 to 2.5. The results were analysed and reported by Adkins et al in Ref.(30) from which Fig.(2-7) was taken. The figure shows a comparison between the performance of a conventional and hybrid diffuser of the same area ratio for different lengths and bleed rates. Figure(2-7) convincingly proves the superiority of the hybrid diffuser over the conventional one.

2.11 Summary and conclusions:

A considerable amount of research work has been done at Cranfield on the so called Cranfield diffuser and its related fluidic devices. Tubular, annular, two-dimensional, and radial models were tested over a wide range of area ratios, inlet Mach numbers, and inlet velocity distributions. The results of these investigations prove the superiority of the Cranfield diffuser over conventional ones in terms of performance, compactness, stability, and control over the exit velocity profiles. The other related fluidic devices offer attractive advantages over their conventional competitors.

So far, to the knowledge of the author, sections of the gas turbine industry have been reluctant to use the diffuser and its related fluidic devices. The reasons behind this reluctance are likely to be:-

1- Some doubt about the mechanical robustness of the device.

2- The design techniques of the device depends on past experience and some empirical rules and formulae which can only be used for guidance.

3- There is no trustworty method to predict the performance of the diffuser under all the required running conditions. Reliance must therefore be put on extensive experimental work which might be time, effort, and money consumming.

It is believed that further understanding of the flow behaviour inside the diffuser might help in developing a reliable mathematical model which could be used to predict the performance of the diffuser under any running conditions. The mathematical model would help to overcome most of the above mentioned deficiencies, and hence transfer the Cranfield diffuser to an era of practical application. The present project was initiated in an attempt to achieve this target.

CHAPTER THREE

3. THE FUNDAMENTAL EQUATIONS OF MOTION AND THEIR PHYSICAL SIGNIFICANCE:

3.1 The Navier-Stokes' equations:

In the general case of a compressible, viscous, Newtonian fluid, the three dimensional motion of the flow is specified, in the absence of heat transfer, by the following five parameters:-

* The three orthogonal velocity compoments u,v and w.
* The static pressure, .
* The fluid density.

All the five parameters are functions of the coordinates; x, y & z, and the time, t. For the determination of these five quantities, there exist five equations:-

* The continuity equation.
* The three equations of motion.
* The thermodynamic equation of state.

The continuity equation expresses the fact that for a unit volume, there is a balance between the masses entering and leaving per unit time, and the change in density. In the general case of non-steady flow of a compressible fluid. this condition leads to the equation, Ref.(31):

$$\frac{\partial \rho}{\partial t} + \frac{\partial(\rho u)}{\partial x} + \frac{\partial(\rho v)}{\partial y} + \frac{\partial(\rho w)}{\partial z} = 0 \qquad (3-1)$$

The equations of motion are derived from Newtons second law of motion which states that the product of mass and acceleration is equal to the sum of the external forces acting on the body.The equation for an isotropic Newtonian compressible fluid flow can be written in its most general from as, Ref.(31):

$$\rho \frac{Du}{Dt} = X - \frac{\partial p}{\partial x} + \frac{\partial}{\partial x}\left[\mu\left(2\frac{\partial u}{\partial x} - \tfrac{2}{3}\,div\,\underline{W}\right)\right] + \frac{\partial}{\partial y}\left[\mu\left(\frac{\partial u}{\partial y} + \frac{\partial v}{\partial x}\right)\right] + \frac{\partial}{\partial z}\left[\mu\left(\frac{\partial w}{\partial x} + \frac{\partial u}{\partial z}\right)\right] \qquad (3-2)a$$

$$\rho \frac{Dv}{Dt} = Y - \frac{\partial p}{\partial y} + \frac{\partial}{\partial y}\left[\mu\left(2\frac{\partial v}{\partial y} - \tfrac{2}{3}\,div\,\underline{W}\right)\right] + \frac{\partial}{\partial z}\left[\mu\left(\frac{\partial v}{\partial z} + \frac{\partial w}{\partial y}\right)\right] + \frac{\partial}{\partial x}\left[\mu\left(\frac{\partial u}{\partial y} + \frac{\partial v}{\partial x}\right)\right] \qquad (3-2)b$$

$$\rho\frac{Dw}{Dt} = Z - \frac{\partial p}{\partial z} + \frac{\partial}{\partial z}\left[\mu\left(2\frac{\partial w}{\partial z} - \frac{2}{3}\,div\,\underline{W}\right)\right] + \frac{\partial}{\partial x}\left[\mu\left(\frac{\partial w}{\partial x} + \frac{\partial u}{\partial z}\right)\right]$$

$$+\frac{\partial}{\partial y}\left[\mu\left(\frac{\partial v}{\partial z} + \frac{\partial w}{\partial y}\right)\right] \qquad (3\text{-}2)c$$

where:

$$\frac{D}{Dt} \equiv \frac{\partial}{\partial t} + u\frac{\partial}{\partial x} + v\frac{\partial}{\partial y} + w\frac{\partial}{\partial z}$$

$$div\,\underline{W} = \frac{\partial u}{\partial x} + \frac{\partial v}{\partial y} + \frac{\partial w}{\partial z}$$

$\underline{W}$ is the velocity vector defined as:

$$\underline{W} = u\,\underline{i} + v\,\underline{j} + w\,\underline{k}$$

X,Y, and Z are the three orthogonal components of the body force. Equations(3-2) are the very well known partial differential equations usually referred to as the Navier-Stokes' equations. A full derivation of the equations can be found in Ref.(31).

The Navier-Stokes' equations were derived assuming that the normal and shearing stresses are linear functions of the rates of strain in comformity with the older law of friction due to Newton, since the hypothesis of linearity is evidently completely arbitrary, it is not absolutely certain that the equations give a true description of the motion of a fluid. However, known particular solutions of them, such as laminar flow through a circular pipe, agree so well with experiment that the general validity of the Navier-Stokes' equations can hardly be doubted, Ref.(31).

In the case of incompressible flow, we get:-

* ρ = constant, even if the temperature is not constant.
* div $\underline{W}$ = 0, from the continuity equation.
* μ = constant, since the temperature variations are small.

Hence the Navier-Stokes' equations take the simpler form, Ref.(31):

$$\rho\left(\frac{\partial u}{\partial t} + u\frac{\partial u}{\partial x} + v\frac{\partial u}{\partial y} + w\frac{\partial u}{\partial z}\right) = X - \frac{\partial p}{\partial x} + \mu\left(\frac{\partial^2 u}{\partial x^2} + \frac{\partial^2 u}{\partial y^2} + \frac{\partial^2 u}{\partial z^2}\right) \qquad (3\text{-}3)a$$

$$\rho\left(\frac{\partial v}{\partial t} + u\frac{\partial v}{\partial x} + v\frac{\partial v}{\partial y} + w\frac{\partial v}{\partial z}\right) = Y - \frac{\partial p}{\partial y} + \mu\left(\frac{\partial^2 v}{\partial x^2} + \frac{\partial^2 v}{\partial y^2} + \frac{\partial^2 v}{\partial z^2}\right) \qquad (3\text{-}3)b$$

$$\rho\left(\frac{\partial w}{\partial t} + u\frac{\partial w}{\partial x} + v\frac{\partial w}{\partial y} + w\frac{\partial w}{\partial z}\right) = Z - \frac{\partial p}{\partial z} + \mu\left(\frac{\partial^2 w}{\partial x^2} + \frac{\partial^2 w}{\partial y^2} + \frac{\partial^2 w}{\partial z^2}\right) \qquad (3\text{-}3)c$$

and the continuity equation becomes:-

$$\frac{\partial u}{\partial x} + \frac{\partial v}{\partial y} + \frac{\partial w}{\partial z} = 0 \qquad (3-4)$$

The above system of equations becomes further simplified in the case of a steady flow in the absence of body forces. The flow field can now be fully described by the following four equations, Ref.(31):

$$u\frac{\partial u}{\partial x} + v\frac{\partial u}{\partial y} + w\frac{\partial u}{\partial z} = -\frac{1}{\rho}\frac{\partial p}{\partial x} + \nu\left(\frac{\partial^2 u}{\partial x^2} + \frac{\partial^2 u}{\partial y^2} + \frac{\partial^2 u}{\partial z^2}\right) \qquad (3\text{-}5)a$$

$$u\frac{\partial v}{\partial x} + v\frac{\partial v}{\partial y} + w\frac{\partial v}{\partial z} = -\frac{1}{\rho}\frac{\partial p}{\partial y} + \nu\left(\frac{\partial^2 v}{\partial x^2} + \frac{\partial^2 v}{\partial y^2} + \frac{\partial^2 v}{\partial z^2}\right) \qquad (3\text{-}5)b$$

$$u\frac{\partial w}{\partial x} + v\frac{\partial w}{\partial y} + w\frac{\partial w}{\partial z} = -\frac{1}{\rho}\frac{\partial p}{\partial z} + \nu\left(\frac{\partial^2 w}{\partial x^2} + \frac{\partial^2 w}{\partial y^2} + \frac{\partial^2 w}{\partial z^2}\right) \qquad (3\text{-}5)c$$

$$\frac{\partial u}{\partial x} + \frac{\partial v}{\partial y} + \frac{\partial w}{\partial z} = 0 \qquad (3-6)$$

Cylindrical coordinates are the most suitable system for axisymetrical problems, as is the present study. In transferring the Navier-Stokes' equations to cylindrical coordinates, let x,r, and ϕ denote the axial, radial, and azimuthal coordinates respectively, and u,v, and w denote the velocity components in the respective directions. The transformation of variables for the case of incompressible steady fluid flow in the absence of body forces (equations 3-5 and 3-6) leads to the following system of equations, Ref.(31):

$$u\frac{\partial u}{\partial x} + v\frac{\partial u}{\partial r} + \frac{w}{r}\frac{\partial u}{\partial \phi} = -\frac{1}{\rho}\frac{\partial p}{\partial x} + \nu\left(\frac{\partial^2 u}{\partial x^2} + \frac{\partial^2 u}{\partial r^2} + \frac{1}{r}\frac{\partial u}{\partial r} + \frac{1}{r^2}\frac{\partial^2 u}{\partial \phi^2}\right) \qquad (3\text{-}7)a$$

$$u\frac{\partial v}{\partial x} + v\frac{\partial v}{\partial r} + \frac{w}{r}\frac{\partial v}{\partial \phi} - \frac{w^2}{r} = -\frac{1}{\rho}\frac{\partial p}{\partial r} + \nu\left(\frac{\partial^2 v}{\partial x^2} + \frac{\partial^2 v}{\partial r^2} + \frac{1}{r}\frac{\partial v}{\partial r} - \frac{v}{r^2} + \frac{1}{r^2}\frac{\partial^2 v}{\partial \phi^2} - \frac{2}{r^2}\frac{\partial w}{\partial \phi}\right) \qquad (3\text{-}7)b$$

$$u\frac{\partial w}{\partial x} + v\frac{\partial w}{\partial r} + \frac{vw}{r} + \frac{w}{r}\frac{\partial w}{\partial \phi} = -\frac{1}{\rho r}\frac{\partial p}{\partial \phi} + \nu\left(\frac{\partial^2 w}{\partial x^2} + \frac{\partial^2 w}{\partial r^2} + \frac{1}{r}\frac{\partial w}{\partial r} - \frac{w}{r^2} + \frac{1}{r^2}\frac{\partial^2 w}{\partial \phi^2} + \frac{2}{r^2}\frac{\partial v}{\partial \phi}\right) \qquad (3\text{-}7)c$$

$$\frac{\partial u}{\partial x} + \frac{\partial v}{\partial r} + \frac{v}{r} + \frac{1}{r}\frac{\partial w}{\partial \phi} = 0 \qquad (3-8)$$

At present no analytical, general method has become available for the integration of the Navier-Stokes' equations, Ref.(31). Solutions which are valid for all values of viscosity are known only for some particular cases of little practical relevance, as far as aerodynamics

is concerned, such as Poiseuille flow through a circular pipe, or Couette flow between two parallel walls, Ref.(31). Most air flows which occur in practice are turbulent. The most striking feature of turbulent motion is the fact that the velocity and pressure at a fixed point in space do not remain constant with time, but perform very irregular fluctuations of high frequency. A numerical solution of the time dependent Navier-Stokes' equations is beyond the capacity of present-day computers, Ref.(32). Furthermore, it is not possible in the foreseable future, Ref.(32). Reliance must therefore be put on time averaging the time dependent variables to derive the time independent equations of motion applicable to turbulent motion. This is the subject material of the next section.

3.2 The equations of motion for turbulent flow:

Randomness is the essential characteristic of turbulence. Of course, the velocity is still a continous function of space and time, and statistical correlations between the motions at different points can be distinguished, but the probability distribution of the velocity at a given point is nearly the familiar Gaussian distribution. This means that we have to treat turbulence in terms of statistical properties because we cannot cope, either mathematically or experimentally, with the information needed in a full treatment. The simplest statistical property is the average (in this case with respect to time) of the velocity at a point, called the mean velocity. If we could measure only the mean velocity, we should see no qualitative difference between laminar and turbulent flows. The quantitative difference can be seen from the example of a fully developed flow in a pipe. Near the centre of the pipe, the fluctuations of the velocity about the mean value are typically fairly small, say up to ± 10% of the mean velocity. However, the pressure drop down the pipe for a given flow rate may be ten or even a hundred times larger than if the flow could be persuaded to remain laminar. So, in describing a turbulent flow in mathematical terms, it is convenient to separate each parameter into two components; a mean value, and a fluctuation component Denoting the mean value of the component of the velocity, u, by $\bar{u}$, and its fluctuating component by $\acute{u}$, we get:

$$u = \bar{u} + \acute{u} \qquad (3\text{-}9)a$$

Similarly, we can write down the following relationships for the remaining velocity component and the static pressure:

$$v = \bar{v} + v' \qquad (3\text{-}9)b$$

$$w = \bar{w} + w' \qquad (3\text{-}9)c$$

$$p = \bar{p} + p' \qquad (3\text{-}9)d$$

The mean values are taken over sufficiently long intervals of time for them to be completely independent of time. Thus, by definition, the time averages of all quatities describing fluctuation are equal to zero, hence:

$$\bar{u}' = \bar{v}' = \bar{w}' = \bar{p}' = 0 \qquad (3\text{-}10)$$

To derive the equations of motion which must be satisfied by the time-averaged velocity components and static pressure, from the Navier-Stokes' equations for incompressible flow, we substitute for u,v,w and p from equation (3-9) into equations (3-4), and (3-3) and then time averaging, the continuity equation becomes:

$$\frac{\partial \bar{u}}{\partial x} + \frac{\partial \bar{v}}{\partial y} + \frac{\partial \bar{w}}{\partial z} = 0 \qquad (3\text{-}11)$$

Also we get:

$$\frac{\partial u'}{\partial x} + \frac{\partial v'}{\partial y} + \frac{\partial w'}{\partial z} = 0 \qquad (3\text{-}12)$$

It is seen that the time-averaged velocity components and the fluctuating components each satisfy the equation of continuity for incompressible flow.

The Navier-Stokes' equations in the absence of body forces become, Ref.(31):

$$\bar{u}\frac{\partial \bar{u}}{\partial x} + \bar{v}\frac{\partial \bar{u}}{\partial y} + \bar{w}\frac{\partial \bar{u}}{\partial z} = -\frac{1}{\rho}\frac{\partial \bar{p}}{\partial x} + \nu\left(\frac{\partial^2 \bar{u}}{\partial x^2} + \frac{\partial^2 \bar{u}}{\partial y^2} + \frac{\partial^2 \bar{u}}{\partial z^2}\right) - \left(\frac{\partial \overline{u^2}}{\partial x} + \frac{\partial \overline{u'v'}}{\partial y} + \frac{\partial \overline{u'w'}}{\partial z}\right) \qquad (3\text{-}13)a$$

$$\bar{u}\frac{\partial \bar{v}}{\partial x} + \bar{v}\frac{\partial \bar{v}}{\partial y} + \bar{w}\frac{\partial \bar{v}}{\partial z} = -\frac{1}{\rho}\frac{\partial \bar{p}}{\partial y} + \nu\left(\frac{\partial^2 \bar{v}}{\partial x^2} + \frac{\partial^2 \bar{v}}{\partial y^2} + \frac{\partial^2 \bar{v}}{\partial z^2}\right) - \left(\frac{\partial \overline{u'v'}}{\partial x} + \frac{\partial \overline{v^2}}{\partial y} + \frac{\partial \overline{v'w'}}{\partial z}\right) \qquad (3\text{-}13)b$$

$$\bar{u}\frac{\partial \bar{w}}{\partial x} + \bar{v}\frac{\partial \bar{w}}{\partial y} + \bar{w}\frac{\partial \bar{w}}{\partial z} = -\frac{1}{\rho}\frac{\partial \bar{p}}{\partial z} + \nu\left(\frac{\partial^2 \bar{w}}{\partial x^2} + \frac{\partial^2 \bar{w}}{\partial y^2} + \frac{\partial^2 \bar{w}}{\partial z^2}\right) - \left(\frac{\partial \overline{u'w'}}{\partial x} + \frac{\partial \overline{v'w'}}{\partial y} + \frac{\partial \overline{w^2}}{\partial z}\right) \qquad (3\text{-}13)c$$

The quadratic terms of the turbulent velocity components have been transferred to the right hand side because they can be interpreted as the components of an additional stress tensor well known as the Reynolds' stresses. It must be born in mind that such an interpretation does not in itself lead to very much. Equations (3-13), sometimes referred to as Reynolds' equations, constitute the starting point for the mathematical treatment of turbulent flow problems, or, more

precisely for the calculation of the time-averages of the parameters describing the mean flow. However, the equations, as such, cannot be used for rational evaluation of the mean flow as long as the relation between the Reynolds' stresses and the mean velocity components is not known. Such a relationship can only be obtained empirically, and forms the essential contents of all the hypotheses concerning turbulent modelling. In order to assert selection of the most suitable model for the flow under consideration, it is firstly necessary to take a closer look into the Reynolds' stresses and their physical significance.

3.3 The Reynolds' stresses:

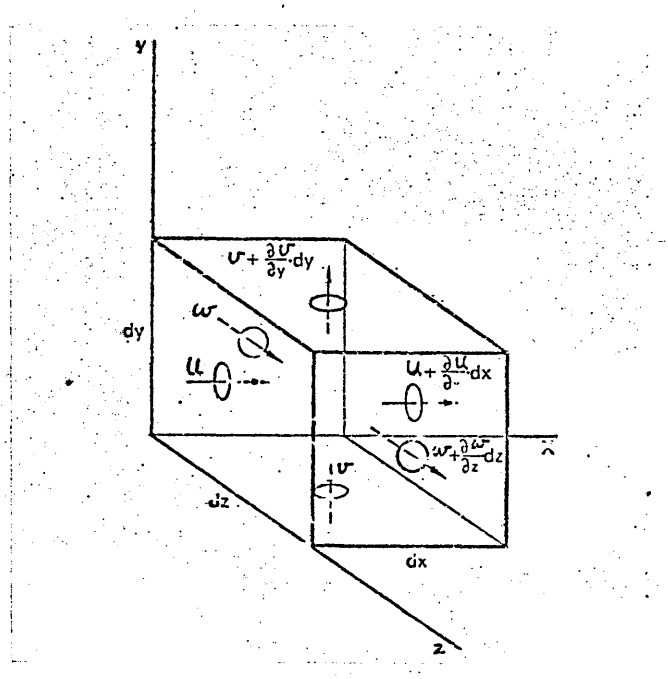

Fig.(3-1): Fixed control volume.

Consider an imaginary fixed infinitesimal control volume with sides dx, dy, and dz in the three coordinate directions, Fig.(3-1). Suppose that in addition to a mean velocity $\bar{u}$, there is a time-dependent (fluctuating) component $\acute{u}$, in the x-direction. The x-component of the momentum flux through the face(dydz) is:

$$\rho(\bar{u}+\acute{u})^2\, dy\, dz$$

time averaging gives:

$$\rho(\bar{u}^2+\overline{\acute{u}^2})\, dy\, dz$$

Therefore, a fluctuation, with zero mean value, superimposed on the mean

velocity produces a mean momentum flux of its own, proportional to the mean square of the fluctuating velocity. This non-linearity of the relationship between velocity and momentum flux appears in the Navier-Stokes' equations and is the basic cause of their mathematical difficulty.

If we measure the mean velocity and pressure in turbulent flow we find that the mean motion is not that which would be produced by viscous forces alone. There is an extra apparent stress, $-\rho\overline{u'^2}$, normal to the face dydz(it is a -ve stress since $\overline{u'^2}$ is positive). The equivalence of stress and momentum flux follows at once from Newton's second law. Similarly, there are extra normal stresses $-\rho\overline{v'^2}$ and $-\rho\overline{w'^2}$ in the y and z directions respectively. Again, the rate at which the x-component of momentum passes through the face dx dz of the control volume is the product of the mass flow in the y-direction, $\rho(\bar{v} + v')\,dx\,dz$, and the velocity in the x-direction, $(\bar{u}+u')$. The mean momentum flux is $\rho(\bar{u}\bar{v}+\overline{u'v'})dxdz$. Hence, $-\rho\overline{u'v'}$, represents an extra shear stress on the face dxdz. Similarly, there are extra shear stresses $-\rho\overline{v'w'}$ and $-\rho\overline{u'w'}$ acting on the faces dxdy and dydz respectively. If we consider the turbulent motion as turbulent eddies superimposed on the main motion. Then, at first sight, the mechanism by which turbulent eddies produce the Reynolds' stresses seems quite similar to that by which random molecular motion produces the viscous stresses. But there is no worth-while analogy between them for two reasons:

1- Turbulent eddies are continuous and contiguous, whereas, gas molecules are discrete and collide only at intervals.

2- Molecular mean free paths are small compared to the dimensions of the mean flow, but turbulent eddies (those which produce the Reynolds' stresses) are not.

It follows that the turbulent transport rates are not determined by the local gradient of the transported quantity as in molecular transport. That is to say that the turbulent transport rates are not usually constants, or even discoverable functions of the local variable, but depend on the previous history of the flow which carries the turbulent eddies. This dependency is one of the crucial factors affecting the selection of a suitable mathematical model of turbulence to treat a certain type of flow.

Since the extra apparent stresses and transport rates are produced by the fluctuating motion itself, it appears that in order to understand them we must at least partly understand the behaviour of the fluctuations. There have been several hypotheses to describe and explain

the behaviour of the turbulent eddies. The work of Batchelor and Townsend in this respect is outstanding. A comprehensive review of which can be found in Ref.(33). But the most appealing is the hypothesis of vortex stretching described by Bradshaw in Ref.(34). This forms the basis of much of the following review.

3.4 Vortex stretching:

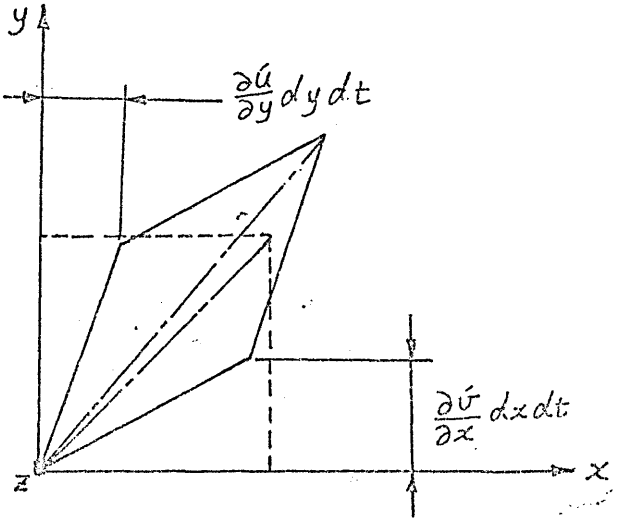

Fig.(3-2): The distinction between vorticity and rate of (shear) strain.

Turbulent eddies have translational and rotational motions. The net rate of rotation(or the average angular velocity), about the z-axis, of the fluid element shown in Fig.(3-2) is given by:

$$\frac{1}{2}\left(\frac{\partial v}{\partial x} - \frac{\partial u}{\partial y}\right)$$

We define the z-component of the vorticity as twice this angular velocity. The vorticity, $\left(\frac{\partial v}{\partial x} - \frac{\partial u}{\partial y}\right)$, is to be distinguished from the rate of shear strain, $\left(\frac{\partial u}{\partial y} + \frac{\partial v}{\partial x}\right)$. The first is a measure of rotation and the second is a measure of deformation. Suppose that in addition to a rotation about the z-axis, the fluid element is under the influence of a rate of linear strain in the z-direction, $\frac{\partial w}{\partial z}$. Then the element will be stretched in the z-direction and its cross-section in the x-y plane will get smaller. The conservation of angular momentum requires the circulation to remain constant in the absence of viscous forces. Circulation is the integral of the tangential component of the

velocity round the perimeter. Consequently, during the stretching process, as the diameter decreases the vorticity increases, and hence the scale of the motion in the x-y plane decreases. Therefore an extension in one direction can decrease the length scales and increase the velocity compoments in the other two directions, which in turn stretch other elements of fluid with vorticity components in these directions increasing and so on. The length scale of the motion, that is augmented, gets smaller at each stage. The well known stretching family tree Fig.(3-3) shows, at least qualitatively that an initial stretching in one direction produces nearly equal amounts of, smaller scale stretching in each of the x, y, and z directions, after a few stages of the process. thus the small-scale eddies in turbulence do not share the preferred orientation of the mean rate of strain. The "Cascade of energy" of the turbulent motion continues to smaller and smaller scales(larger and larger velocity gradients). Indeed, discontinuities of velocity would develop if it were not for the smoothing action of the viscosity. Expressed another way, viscosity finally dissipates (into heat) the energy that is transferred to the smallest eddies, however, viscosity itself does not play any essential part in the stretching process as such.

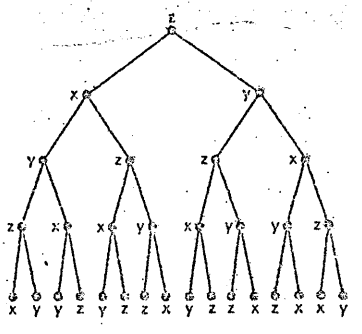

Frequency of symbols at each generation

x	y	z
0	0	1
1	1	0
1	1	2
3	3	2
5	5	6
11	11	10
21	21	22

Fig.(3-3): Family tree, showing how vortex stretching produces small-scale isotropy. The labels are the directions of stretching in each generation.

Turbulence can be thought of as a tangle of vortex lines or partly rolled vortex sheets, stretched in a preferred direction by the mean flow(the mean vortex lines) and in random directions by each other.

Turbulence always occurs in all three directions of motion even if the mean velocity has only one or two components. If the fluctuating velocity component in one direction were everywhere zero, the vortex lines would necessarily all lie in this direction and there would be no vortex stretching, no transfer of fluctuation energy to smaller scales, and the motion would not be what we call turbulence. But for the diffusing effect of viscosity, vortex lines or sheets would move with the fluid. The effect of viscous diffusion is seen in the slow growth of laminar shear layers. In turbulent flow, viscous diffusion of vorticity is negligible except for the smallest eddies (those that dissipate the energy transferred from the larger eddies). Fluid that is initially without vorticity(irrotational) can aquire it only by viscous diffusion,but, once acquired, vorticity can be increased over many orders of magnitude by vortex stretching. Pressure fluctuations do not directly affect vorticity in incompressible flow. The rate of supply of kinetic energy to the turbulence is the rate at which work is done by the mean rate of strain against the Reynolds' stresses in the flow,as it stretches the turbulent vortex lines. The eddies extract energy from the mean flow and retain it for a while before it reaches the stage of the small dissipating eddies. Turbulent kinetic energy per unit volume, k, is introduced into the eddies that contribute to the Reynolds' stresses in direct proportion to their contributions. The stress producing eddies are the larger ones, which are best able to interact with the mean flow. We have already seen that vortex stretching tends to make the smaller eddies lose all sense of direction and become statistically isotropic so that their contribution to the Reynolds'shear stress, $-\rho\overline{u'v'}$ for instance, is zero. The smaller eddies are much weaker than those that produce most of the Reynolds' stresses because most of the energy that reaches them is immediatly passed on to the smallest eddies of all where it is dissipated by viscosity. It is possible to deduce from the Navier-Stokes' equations an exact conservation equation for the kinetic energy of turbulence. This equation is not one of the fundamental equations of motion, but it plays an important role in the subject of turbulence modelling.

3.5 The transport equation of turbulent energy:

The instantaneous kinetic energy per unit volume, k', is defined as:

$$k' = \frac{1}{2}(u'^2 + v'^2 + w'^2)$$

Denoting the time average of $\acute{k}$ by k, we get:

$$k = \tfrac{1}{2}(\overline{\acute{u}^2} + \overline{\acute{v}^2} + \overline{\acute{w}^2}) \qquad (3\text{-}14)$$

For brevity k is sometimes called turbulent energy. The full derivation of the conservation equation for k can be found in Ref.(34). For convenience, the procedure is summarized as follows:-

1- Neglecting body forces, substitute for u,v,w and p from equations (3-9) into equation (3-3).

2- Multiply the momentum equation for each co-ordinate direction by its corresponding fluctuating velocity.

3- Time average, and sum up, the three equations.

It takes only a small amount of patience and manipulative skill to render the resultant equation to the following form:-

$$\bar{u}\frac{\partial}{\partial x}(\rho k) + \bar{v}\frac{\partial}{\partial y}(\rho k) + \bar{w}\frac{\partial}{\partial z}(\rho k) = -\left[\frac{\partial}{\partial x}\overline{\acute{u}(\acute{p}+\rho\acute{k})} + \frac{\partial}{\partial y}\overline{\acute{v}(\acute{p}+\rho\acute{k})} + \frac{\partial}{\partial z}\overline{\acute{w}(\acute{p}+\rho\acute{k})}\right] - \left[\rho\overline{\acute{u}^2}\frac{\partial\bar{u}}{\partial x} + \rho\overline{\acute{v}^2}\frac{\partial\bar{v}}{\partial y} + \rho\overline{\acute{w}^2}\frac{\partial\bar{w}}{\partial z} + \rho\overline{\acute{u}\acute{v}}\left(\frac{\partial\bar{u}}{\partial y}+\frac{\partial\bar{v}}{\partial x}\right) + \rho\overline{\acute{u}\acute{w}}\left(\frac{\partial\bar{u}}{\partial z}+\frac{\partial\bar{w}}{\partial x}\right) + \rho\overline{\acute{v}\acute{w}}\left(\frac{\partial\bar{v}}{\partial z}+\frac{\partial\bar{w}}{\partial y}\right)\right] + \left[\mu\left(\overline{\acute{u}\nabla^2\acute{u}} + \overline{\acute{v}\nabla^2\acute{v}} + \overline{\acute{w}\nabla^2\acute{w}}\right)\right] \qquad (3\text{-}15)$$

$$\nabla^2 \equiv \frac{\partial^2}{\partial x^2} + \frac{\partial^2}{\partial y^2} + \frac{\partial^2}{\partial z^2}$$

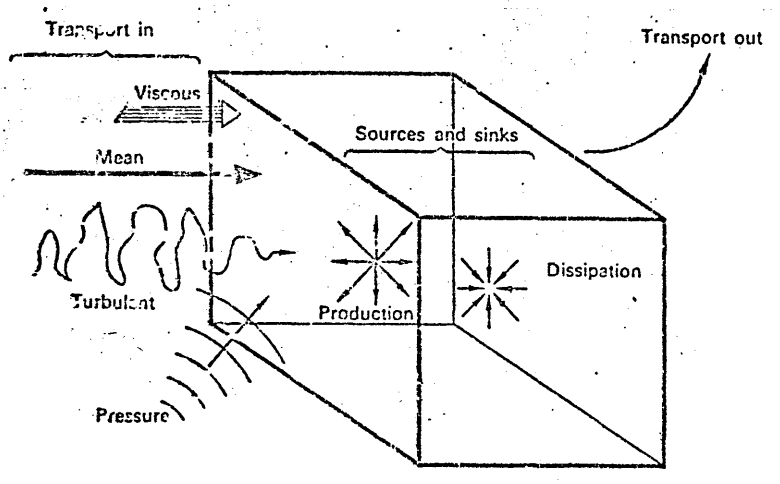

Fig.(3-4): General form of conservation equations-sum of transport terms(spatial gradients of turbulence mean quantities) equals sum of source and sink terms.

The terms of the equation appear in groups of three, one for each coordinate direction. The following discussion identifies the groups of terms with quantities representing sources or sinks of energy, or with transport of energy, in or out of the control volume shown in Fig.(3-4):

1- The physical interpretation of the left hand side of the equation, $[\bar{u}\frac{\partial}{\partial x}(\rho K)+\ldots.]$, is clear enough. It is convective rate of change of kinetic energy along a stream-line. Sometimes it is called the "advection" or "mean energy transport", Ref.(34).

2- The first term on the right hand side, $-[\frac{\partial}{\partial x}\overline{u(p+\rho K)}+\ldots.]$, also represents a net loss of turbulent energy from the control volume via the work done in transporting the fluid through a region of fluctuating pressure and velocity. It is common to regard this as the turbulent energy diffusion, Ref.(32). We can see that it is diffusive in nature if we consider the case of a two-dimensional boundary layer. In this case the term takes the form, $-[\frac{\partial}{\partial y}\overline{v(p+\rho K)}]$. Let us suppose that one edge of the boundary layer is a free stream with zero kinetic energy and that the other boundary is a wall. By integrating this term across the boundary layer, the integral vanishes at both limits. Hence, the term makes no overall contribution to the energy level, but serves merely to re-distribute the energy in space.

3- The second right hand side term, $-[\rho\overline{u^2}\frac{\partial\bar{u}}{\partial x}+\ldots.]$, is a turbulent energy production term. For example $(-\rho\overline{u^2}\frac{\partial\bar{u}}{\partial x}dxdydz)$ represents the rate at which work has to be done against the x-compoment of Reynolds normal stress to stretch an element of fluid (dxdydz) in the x-direction at the rate $\frac{\partial\bar{u}}{\partial x}$. Usually more important in practice are terms like $(-\rho\overline{u'v'}\frac{\partial\bar{u}}{\partial y}dydxdz)$, which represent work done against the shear stress $(-\rho\overline{u'v'})$ to shear an element of fluid at the rate of $(\frac{\partial\bar{u}}{\partial y})$. There is a second term involving $(\overline{u'v'})$, namely $(-\rho\overline{u'v'}\frac{\partial\bar{v}}{\partial x})$ for the other constituent of the rate of strain, $(\frac{\partial\bar{u}}{\partial y}+\frac{\partial\bar{v}}{\partial x})$, so that the sum of the two terms is, $[-\rho\overline{u'v'}(\frac{\partial\bar{u}}{\partial y}+\frac{\partial\bar{v}}{\partial x})]$, which is the product of the Reynolds' shear stress and the rate of strain. From the point of view of the mean motion, these are energy loss terms.

4- The third term on the right side, $\mu(\overline{u'\nabla^2u'}+\ldots.)$, can be reduced to two groups of terms, Ref.(34):

a- A group of terms like, $\mu\overline{(\frac{\partial u'}{\partial y}+\frac{\partial v'}{\partial x})^2}$ and like, $\mu\overline{(2\frac{\partial u'}{\partial x})^2}$. This group of terms represents the rate of viscous dissipation of turbulent energy into thermal internal energy. This is analogous to the dissipation of mean flow kinetic energy into thermal internal

energy. Since the instantaneous velocity gradients in the turbulence are much greater than the mean velocity gradients, except for the region extremely close to a solid surface, then the viscous dissipation of turbulent energy is usually much greater than the dissipation of mean-flow energy.

b- A group of terms contain $(\mu \nabla^2 K)$ and terms like, $(\mu \frac{\partial^2 \overline{u'v'}}{\partial x \partial y})$. This group represent viscous transport of turbulent energy. Like the mean flow energy dissipation by viscosity action, they are negligible execpt near a solid surface and tend to be forgotten altogether in discussions of turbulent energy.

We end this discussion about the energy equation and the physical significance of its terms with some important remarks:-

1- The consideration of the first term on the right hand side as a diffusion term is quite arbitrary. Bradshaw, Ref.(34), considered part of it, namely terms like $-\frac{\partial}{\partial x}(\overline{u'k'})$ as energy transport terms, and the other part, $-\frac{\partial}{\partial x}(\overline{u'p'})$ as an energy loss term via work done in transporting the fluid through a region of changing pressure.

2- It is important to remember that although the separation of the velocity into mean and fluctuating parts is a perfectly legitimate mathematical device, but the instantaneous velocity profile may look very different from the mean profile, and there is no difference in kind between the eddy processes that produce, say, $\overline{u'v'}\frac{\partial \overline{u}}{\partial y}$ and those that produce $\overline{u'v'}\frac{\partial u'}{\partial y}$ which is part of the turbulent energy transport in the y direction.

3- The relative importance of the terms constituting the equation is again quite arbitrary and depends not only on the type of flow being discussed, but also on the region of the flow where the equation is being applied.

CHAPTER FOUR

4. MATHEMATICAL MODELS OF TURBULENCE.

4.1 Introduction:

In the previous chapter it is stated that we cannot cope either mathematically or experimentally with the amount of information needed to fully treat the time dependent turbulent flows. Fortunately, there is no need for an engineer to consider the time dependent details of turbulence. He is usually concerned only with its time averaged effects even when the mean flow is unsteady. If we were given the time-dependent behaviour of a body of fluid, we should do nothing with the data but to integrate them to extract the time-averaged properties. This recognition affords us justification to base predictions of turbulent flows on only the time-averaged properties of turbulence. The process of time-averaging, however, cause statistical correlations involving fluctuating velocities to appear in the equations of motion (equations 3-13). We have no direct way of knowing the magnitudes of these terms. We must therefore approximate or "model" their effect in terms of quantities that we can determine. Thus, by a model of turbulence, we mean a set of equations which, when solved with the equations of motion and the equation of continuity, allows the calculation of the relevant mean flow parameters.

4.2 Types of turbulent models:

There are two types of models. The first employ Boussinesq's suggestion (1877) that the stress-strain law for the time-averaged turbulent flow could be represented in the same form as that for a Newtonian viscous fluid in laminar motion. For example a Reynolds' shear stress, $-\rho\overline{u'v'}$, can be modelled as follows:

$$-\rho\overline{u'v'} = \mu_t \frac{\partial \bar{u}}{\partial y} \qquad (4-1)$$

where,

μ_t is the turbulent-viscosity.

The turbulent-viscosity, unlike the molecular viscosity, is not a property of the fluid. Its value varies from point to point in the flow being largely determined by the structure of the turbulence at the point in question.

This type of model is generally referred to as turbulent-viscosity,

effective-viscosity, or eddy-viscosity models. The other type of model provides differential transport equations for the Reynolds' stresses themselves. The higher order correlations, appearing in the transport equations of Reynolds' stresses are to be approximated in terms of mean-flow parameters. This type of model is generally referred to as a Reynolds' stress model, or sometimes as a multi-equation model. In the next few sections, some of the well established turbulent models are discussed. The emphasis of the discussion is put on the suitability of the model to be used for the prediction of the flow under investigation. It should be mentioned here that the discussions are based on more elaborate reviews, and can be found in Ref.(32) and Ref.(35).

4.3 Prandtl's mixing length model:

This model is based on the well known mixing length hypothesis, MLH, of Prandtl. The hypothesis states that the turbulent viscosity, μ_t, is equal to the local product of the density, the magnitude of the mean rate of strain, and the square of a characteristic length scale of the turbulent motion. The characteristic length scale is referred to as the mixing length. In equation form the model can be expressed as:

$$\mu_t = \rho l_m^2 \left|\frac{\partial \bar{u}}{\partial y}\right| \qquad (4-2)$$

It is widely believed, Ref.(32), that Ludwig Prandtl(1925) invented the MLH as an analogy to the kinetic theory of gases which gives, Ref.(32):

$$\mu = \frac{1}{3} \rho l V \qquad (4-3)$$

where,

μ, the viscosity

ρ, is the density of the fluid.

l, is the average molecular free path length.

V, is the molecular velocity.

Analogous to this, the first part of the MLH gives:

$$\left(-\rho \overline{u'v'}\right) \Big/ \left(\frac{\partial \bar{u}}{\partial y}\right) = \mu_t = \rho l_m V_t \qquad (4-4)$$

where;

l_m, is a typical length scale of the turbulent motion or the mixing length.

V_t, is a typical velocity scale of the turbulent motion.

The second part of the MLH gives:

$$\nu_t = l_m \left|\frac{\partial \bar{u}}{\partial y}\right| \qquad (4\text{-}5)$$

Combining the two parts of the hypothesis gives:

$$-\rho \overline{u'v'} = \rho l_m^2 \left|\frac{\partial \bar{u}}{\partial y}\right| \frac{\partial \bar{u}}{\partial y} \qquad (4\text{-}6)$$

The mixing length, l_m, is still to be prescribed algebraically. Prandtl originally proposed that l_m is proportional to the distance from the nearest wall, that is for boundary layer flows, but researchers have since precribed l_m in many other ways to suit particular flow conditions, Ref.(32). The mixing length model was extensively applied to many types of turbulent flow with different degrees of success. A representative review of such applications can be found in Ref.(32). A conclusion that can be reached is that the model is more successful when applied to near-wall flows than when it is applied to free turbulent flows. There are no reported successful predictions of recirculating flows with the aid of the mixing length model Ref.(32).

This section is concluded with a summary of the advantages and disadvantages of the mixing length model. The advantages include:-

1- It is a simple method requiring no additional differential equations to be solved.
2- Providing that good choice is made for the mixing length distribution, it realistically predicts the behaviour of boundary layer flows.
3- Much experience of using it has been accumulated and made available through publications.

The disadvantages include:

1- There is almost no successful experience of predicting recirculating flows with its aid, for the relationship between the stresses and the velocity gradients is too complicated.
2- Contrary to experimental results, it implies that the turbulent viscosities vanish where the velocity gradients are zero.
3- The model takes no account of processes of convection or diffusion of turbulence.

4.4 The model of Prandtl and Kolmogorov:

This model also employs the eddy viscosity concept, equation (4-4). Kolmogorov (1942) and Prandtl (1945) both, independently, proposed that the square root of the time averaged turbulent kinetic energy was to be used as an appropriate velocity scale of the turbulent motion.

Expressed in an equation form as:

$$V_t \propto \sqrt{k} \qquad (4\text{-}7)$$

where,

$$k = \tfrac{1}{2}\left(\overline{u^2} + \overline{v^2} + \overline{w^2}\right) \qquad (3\text{-}14)$$

This way some of the mixing length disadvantages could be sidestepped. Instead of relating the velocity scale of turbulence, V_t, to a mean velocity gradient, it is related to one of the turbulence properties itself, k. We may expect this method to provide a better formula for determining μ_t. For example, on the centre-line of a pipe, the mean velocity gradient is zero, but the turbulent energy is not.

The formula for μ_t, as suggested by Prandtl is:

$$\mu_t = \rho \sqrt{k}\, l \qquad (4\text{-}8)$$

The formula for μ_t, as suggested by Kolomogorov, is:

$$\mu_t = \rho\, k/f \qquad (4\text{-}9)$$

Where, f, is a characteristic frequency of the energy-containing eddies.

The Prandtl model becomes identical to Kolmogorov's, if we put(from dimensional analysis):

$$l = \sqrt{k}/f \qquad (4\text{-}10)$$

The difference between the two models is that, in the Kolmogorov's model, both(k) and (f) are to be determined from differential transport equations, whereas in the Prandtl's model only (k) is to be determined from a transport equation while (l) is still to be prescribed algebraically. Kolmogorov's choice of (f), as a second parameter to determine the effect of turbulence on the motion, was not quite adequate,Ref.(32). However, this defect scarcely affects the historical importance of Kolmogorov's suggestion that the two parameters should be determined from transport equations.

The transport equation of the turbulent kinetic energy for two dimensional boundary layers at high Reynolds' number takes the form, Ref.(32):

$$\rho \bar{u} \frac{\partial k}{\partial x} + \rho \bar{v} \frac{\partial k}{\partial y} = -\frac{\partial}{\partial y}\left(\rho \overline{v'k'} + \overline{v'p'}\right) - \rho \overline{u'v'} \frac{\partial \bar{u}}{\partial y} - \mu \sum_{ij} \overline{\left(\frac{\partial u_i}{\partial x_j}\right)^2} \qquad (4\text{-}11)$$

Convective flux = diffusion + production - dissipation.

Before equation (4-11) becomes useful , the correlations of the turbulence velocities appearing on its right-hand side are to be approximated in terms of quantities which are either known or can be

determined. The approximation of each term is explained as follows, Ref.(32):

1- The diffusion term:

The diffusion action of turbulence is presumed similar to the molecular diffusion processes. Thus, the rate of transport of turbulence energy by diffusion is taken as the product of the spatial gradient of (k) and the turbulent viscosity divided by a constant. This constant is called the Prandtl number for the diffusion of turbulence energy, σ_K. Thus, the formula takes the form:

$$-(\rho\overline{v'k'} + \overline{p'v'}) = \frac{\mu_t}{\sigma_K}\frac{\partial k}{\partial y} \qquad (4-12)$$

2- The production term:

The turbulence correlation which appears in the production term is just the turbulent shear stress, and this is replaced by the product of μ_t and the mean velocity gradient. Thus, the formula takes the form:

$$-\rho\overline{u'v'} = \mu_t\frac{\partial \bar{u}}{\partial y} \qquad (4-13)$$

3- The dissipation term:

The dissipation of turbulent kinetic energy occurs predominanly in the smallest sizes of eddy. At high Reynolds numbers, these eddies are very much smaller than the energy-containing motions. The dissipation rate is then controlled not by the dissipative motions themselves, but by the processes which transfer energy from larger to successively smaller eddies. This cascading process may be supposed to depend only on ρ, K, and l. Thus for dimensional consistency it follows that:

$$\mu\sum_{i,j}\overline{\left(\frac{\partial u_i}{\partial x_j}\right)^2} = C_D\frac{\rho K^{3/2}}{l} \qquad (4-14)$$

where, C_D is a constant.

Substituting from equations (4-12), (4-13), and (4-14) into equation (4-11) we get the following simulated form of the energy equation:

$$\rho\bar{u}\frac{\partial k}{\partial x} + \rho\bar{v}\frac{\partial k}{\partial y} = \frac{\partial}{\partial y}\left(\frac{\mu_t}{\sigma_K}\frac{\partial k}{\partial y}\right) + \mu_t\left(\frac{\partial \bar{u}}{\partial y}\right)^2 - C_D\frac{\rho K^{3/2}}{l} \qquad (4-15)$$

Equation (11-15), which is appropriate to two-dimensional boundary layer flows, is to be solved simultaneously with a streamwise momentum equation and with equations for such other mean flow parameters as may be of interest. However, before solving the equations, the constants C_D and σ_K must be assigned and the length scale distribution has to be

prescribed. This is done empirically using experimental results and computational optimization.

The model described above is sometimes called the one-equation model since it employs only one additional differential equation to determine the effects of turbulence on the mean motion. The model, in practice, offers only small advantages over the mixing length model. These advantages are summarized as follows:

1- k provides a better measure of V_t than $l_m\left|\frac{\partial \bar{u}}{\partial y}\right|$.

2- The model takes account of transport effects on (k).

However, a sufficiently precise algebraic prescription of (l) can rarely be made for any but boundary layer flows. In more complex flows such as recirculating flows, transport effects on the length scale usually turn out to be very important. Consequently the length scale has to be determined from one more additional transport equation.

4.5 Two-equation models of turbulence:

This type of model employs the same formula for turbulence viscosity as does the one-equation model. The difference in the model is that both (k) and (l) are to be determined by transport equations. The required transport equation for (k) is the same as that for the one-equation model, i.e equation (4-15). We do not actually have to choose the length scale as the dependent variable of the second equation. Any variable, Z, which is made up of some product of (k) and (l) would, in principle, do just as well. Hence, we define a variable, Z so that:

$$Z = k^m l^n$$

Where(m) and (n) are constants.

Many models were developed, each was based on a different form for the second dependent variable, Z . A review of a representative sample of these models can be found in Ref.(32). The following list shows the most important forms of (Z) proposed by different researchers:-

1- Kolmogorov (1942) proposed that:

$$Z = f = k^{\frac{1}{2}}/l$$

2- Chou (1945), Davidov (1961), Harlow-Nakayama (1968), and Jones and Launder (1972) proposed that:

$$Z = \varepsilon = k^{3/2}/l$$

3- Rotta (1951), and Spalding (1967) proposed that:

$$Z = l$$

4- Rotta (1968,1971), Rodi-Spalding (1970), and Ng-Spalding (1972) proposed that:

$$Z = k\,l$$

5- Spalding (1969) proposed that:

$$Z = k/l^2$$

The turbulence energy dissipation rate(ε) has been favoured by more workers than any other variable. The reason for this lies partly in the relative ease with which the exact differential equation of transport for (ε) can be derived, and partly in the fact that (ε) appears directly as an unknown in the exact differential equation of transport for (k), (replacing the dissipation term). Thus, by using (ε) as second veriable there is no need to approximate the dissipation term in the k-equation. Despite the clear visual image which it presents, the length scale (l) has not proved to be a popular second variable. The reason is simply that (l) just does not diffuse at a rate proportional to $(\frac{\partial l}{\partial y})$, Ref.(32). However, if the model is to be used for the prediction of one particular type of flow, such as the flow under investigation, there is a clear advantage in selecting (l) as a second variable. This advantage is that, once the model is adapted and optimized for this particular flow, the solution of the transport equation of (l) could be used as an algebraic prescribed form for the distribution of (l). The model can thus be reduced to a one-equation model that could be used to predict that particular flow type under different conditions. This way the running cost of the model may be reduced considerably.

To derive the equation for (Z), we can proced in precisely the same way as in the derivation of the k-equation (section 3-5). That is, we start off by manipulating the Navier-Stokes' equations to bring the chosen variable into prominence. Then, the various correlations must be represented in terms of calculable flow properties, that is, in terms of k, Z, and mean velocity gradients. The general form of the Z-equation for two dimensional flow taken after Ref.(32) is:

$$\rho\bar{u}\frac{\partial z}{\partial x}+\rho\bar{v}\frac{\partial z}{\partial y}=\frac{\partial}{\partial y}\left(\frac{\mu_t}{\sigma_z}\frac{\partial z}{\partial y}\right)+z\left[C_1\frac{\mu_t}{k}\left(\frac{\partial\bar{u}}{\partial y}\right)^2-C_2\frac{\rho^2k}{\mu_t}\right]+S_z \qquad (4-16)$$

Where, σ_z , C_1 , and C_2 are constants to be determined empirically. S_z represents secondary source terms. In words, the equation expresses the fact that changes in (z) along a streamline arise through the influence of diffusive transport, through interactions of the turbulence with the mean flow, and through self-interactions of the turbulence.

A comprehensive review of the applications of two-equation models can be found in Ref.(32). The final conclusion that can be reached from this review is that two-equation models of turbulence have gone a long way towards taking the guesswork out of the prediction of turbulent flows. With this class of model a single set of empirical constants serves for the prediction of flows, which, with mixing length models, required a large number of rules and constants. But universality at the two-equation level is not complete; even such a superficially simple flow as the axisymmetric round jet cannot be predicted accurately with the set of constants which serves for the plane free shear flows.

4.6 The Reynolds' stress models:

In some types of flows, the shear stress may vanish where the mean velocity gradient is non-zero, and vice versa. This phenomenon, which cannot be predicted when the Boussinesq turbulent-viscosity concept is employed, provides one indication of what is considered to be the more general limitation of all the turbulence models that employ the μ_t concept. This limitation is that, in practice, the turbulent stresses are less directly connected with the mean velocity field than is required by the notion of a turbulent viscosity. This feature is most readily perceived by considering the turbulent normal stress, $\overline{u^2}$ (or energy component). The turbulent-viscosity formula entails that ($\overline{u^2}$) be simulated by ($-2\mu_t\frac{\partial\bar{u}}{\partial x}$). But while the former is essentially a positive quantity, the latter may be variously either positive, negative, or zero, in various regions of the flow. To find a way round this limitation a different path is followed. Instead of employing the turbulent viscosity to correlate the Reynolds' stresses, appearing in the equations of motion, to the mean flow parameters, a set of transport equations for the Reynolds' stresses themselves can be readily derived. Of course, these equations contain unknown correlations

that have to be simulated. Among these correlations are the triple correlations of the fluctuating velocity, e.g $\overline{u'v'^2}$. We can go on and derive a new set of transport equations for the triple correlations, and so on. It is clear that every new set of transport equations introduces greater number of correlations of higher order. At some stage the mere mathematical manipulation has to be stopped, and the correlations appearing in the last set of transport equations have to be approximated in terms of calculable parameters. This is what is called "the closure" of the model. As the level of closure is raised, the number of equations to be solved escalates and the computing time, and hence the cost increases very rapidly. Furthermore as the level of closure is raised the simulation work becomes more and more based on speculations and the amount of guesswork involved increases. Last, and not least, the amount and complexity of the required experimental work increase very rapidly as the level of closure is raised.

Ref.(32) gives a good review of some of the proposed models of this type and compares them with respect to the number of differential equations they require to be solved, and their suitability to be used for the analyses of certain types of flows. Ref.(35) gives full details of two complete Reynolds' stress models and explains in detail the required approximations for the closure of the two models. However Ref.(35) in final assessment of the Reynolds' stress models conclude that some uncertainties exist in the closure approximations even for homogeneous flow conditions. More modelling development and more experimental work still required to improve the approximations involved in Reynolds' stress models.

4.7 The selection of the suitable model:

It is not an objective of this research programme to develop a new mathematical model of turbulence, but one of the objectives is to select an appropriate available model, and to adapt it so that it can be used to predict the parameters of the flow under investigation. A simple process of elimination indicates that the most suitable type of model to the needs of this project is a two-equation turbulent viscosity model. A Reynolds' stress model would not be suitable for the following reasons:-

1- There is still some doubt about the approximations used for the closure of the available models, Ref.(35).

2- For models of this type, there are likely to be nine equations requiring solution. This would raise the computation costs beyond the limitations imposed on this project.

3- The optimization of the empirical constants involved in such a type of model can become a task of major proportions, Ref.(32). Furthermore, the amount of experimental work that would be required to fulfil this task is likely to be far beyond the time limits imposed on this project.

4- Above all, there is no guarantee that such a model would give more accurate results than for example a two-equation turbulent viscosity model. As a matter of fact, recent publications about some of the predictions made by the two types of models, for nearly similar flows to the one under investigation, indicate that the results of turbulent viscosity models are nearer to the experimental results than those obtained by Reynolds' stress models, Ref.(36).

From the above considerations we can conclude that a turbulent viscosity model is more suitable to the needs of this project. The question now is,"What class of turbulent viscosity models is more appropriate?". We can eliminate the mixing length models and the one-equation models for obvious reasons (see discussions in section 4-3 and section 4-4). Consequently, the most suitable type of model to be used to meet the requirement of this project is the two-equation turbulent viscosity model.

Finally, the choice must be made between the various types of the two-equation models. The discussions of section (4-5) indicate that both the (k-l) model and the (k-ε) model are suitable. However, the (k-l) model has a very important advantage over the (k-ε) model, that is it can be reduced at a latter stage to a one-equation model. The final decision is to use a (k-l) model. Gosman et al.offered in Ref.(37) a detailed solution procedure suitable for this type of model. This solution procedure forms the basis of most of the discussions presented in the third part of this thesis, which is concerned with the theoretical aspects of the present study.

CHAPTER FIVE

5. PRINCIPLES OF LASER DOPPLER VELOCIMETRY.

5.1 Introduction:

Laser Doppler velocimetry, LDV, is similar to any other velocity measuring method in that it has its advantages and its limitations. The more conventional methods used to obtain information about the fluid velocity field, such as total pressure probes and hot-wire anemometers, require some form of mechanical probe to reach the point of measurement. These probes disturb the flow in the near vicinity and may influence the overall velocity field. This disadvantage limits the use of such methods to flows of low temperature, low speed, and low turbulence intensity occuring outside regions of recirculation, Ref.(38). Consequently these methods are practically inapplicable in complex flow fields similar to the one under investigation. Laser Doppler velocimetry can overcome all of these limitations by virtue of probing the velocity field only by coherent light beams. LDV does, however, have its own limitations. It is difficult to list exhaustively these limitations because of the wide diversity of the techniques and equiments used in LDV. Nevertheless, the most common and serious limitation of LDV is its poor performance near walls. Such a limitation is particularly restricting in flows bordered by complex solid boundaries, Ref.(39).

5.2 Principle of operation:

A laser-Doppler velocimeter comprises of a laser light source, optical arrangements to transmit and collect light, a photocathode, and signal processing equipment. Fig.(5-1) represents a schematic diagram of a

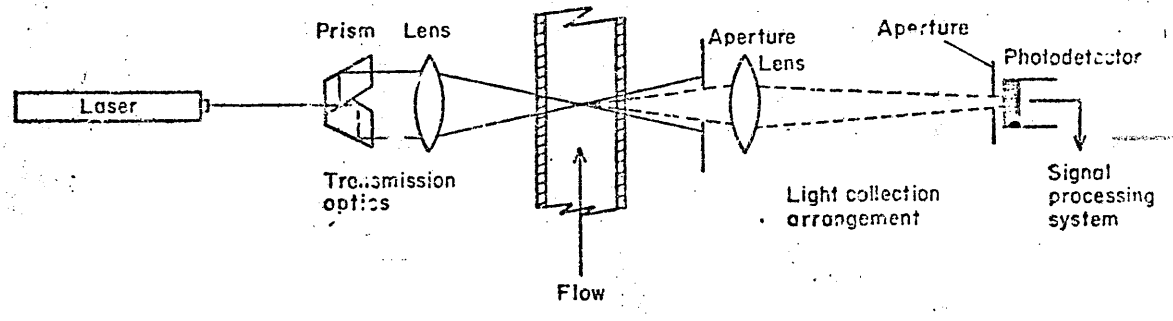

Fig.(5-1): A typical LDV system.

typical LDV system and identifies the various components. The laser beam is split into two separate beams which cross to provide an interference pattern in the local region of the flow where the velocity is to be measured. The interference pattern may be real or virtual depending upon whether incident beams are crossed or scattered light waves are mixed. Moving particles which are carried by the flow will scatter light as they cross the volume of interference. Part of the volume of interference is observed by a light collecting system which then projects the scattered light onto a photodetector. The photodetector converts the optical signal to an electrical one which is then processed by an appropriate signal-processing arrangement to obtain the required velocity information.

5.3 Modes of operation:

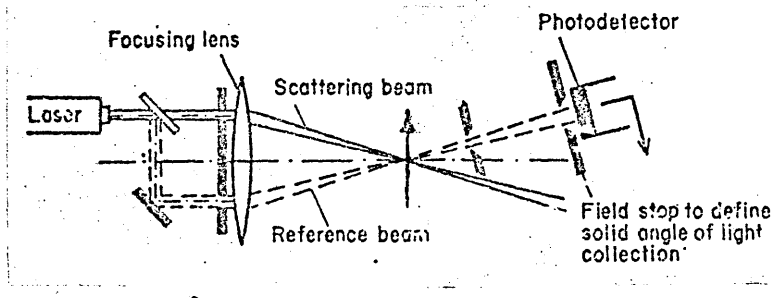

(a) Reference beam mode

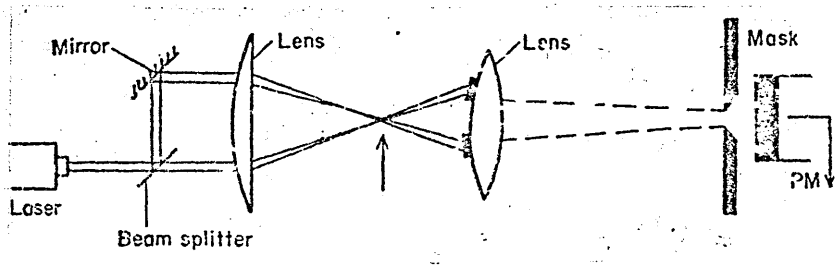

(b) Dual beam mode

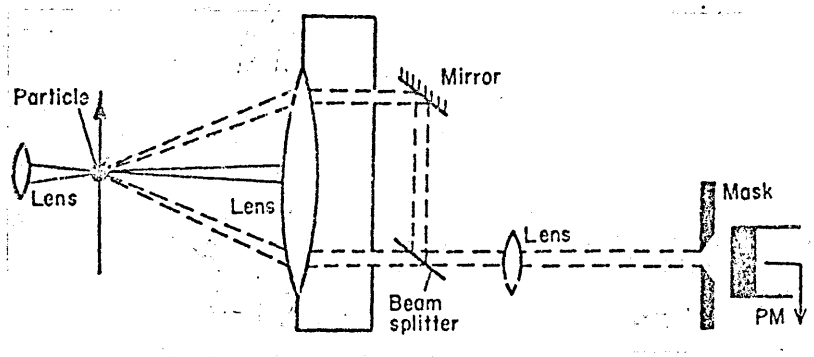

(c) Dual scatter mode

Fig.(5-2): Modes of operation of LDV systems

Light waves scattered from the interference volume by the moving particles experience a Doppler shift relating to the motion of the particles. Analysis of the Doppler shift can then give the relevant information on the velocity. If the Doppler shift is large, as in the case of high speed flow with velocities exceeding 700 m/s, it can be measured spectroscopically using a scanning Fabry-Perot interferometer, Ref.(40). For velocities less than 300 m/s, the Doppler shifts are too small for direct detection. In such a case the preferred technique is that of optical heterodyning by which the Doppler shift is detected as the differrence between the shifted and unshifted light frequencies, Ref.(40). Heterodyne detection is accomplished by mixing the Doppler shifted light wave with another light wave that may or may not be shifted. Heterodyne techniques can be classified into three different modes, Fig.(5-2) namely:-

a- The reference beam mode:
Compares the Doppler shifted frequency of scattered light with the unshifted light of a reference beam.

b- The dual beam mode:
Compares the frequencies of Doppler shifted light waves scattered in the same direction from different illuminating beams.

c- The dual scatter mode:
Compares the Doppler shifted frequencies of two scattered lights in two directions from the same illuminating beam.

In all three modes, the Doppler frequency, ν_D is given by the same formula:-

$$\nu_D = \frac{2U}{\lambda} \sin\theta$$

where,

U , is the flow velocity

λ , is the laser light wave length

θ , is half the angle between the two beams.

All three techniques are satisfactory and can be realized using very similar optical components. Historically, the reference beam mode was the first to be used, but the dual beam mode has become dominant because it is easier to align.

5.4 The effect of the size and concentration of the scattering particles:
It must be always remembered that the measured velocity is the

velocity of the particles carried by the flow and is not the velocity of the flow itself. The relationship between the particle and fluid velocities must be known if the fluid velocity is to be evaluated. However, if the particles are very small so that they can resolve fully the small scale velocity fluctuations in the fluid, then it is reasonable to assume that the measured velocity represents the flow velocity.

In recirculating flows having high turbulence intensities such as the flow under investigation, particle size limitations must be imposed to ensure that the particle velocities agree at any instant with the flow velocity, Ref.(38).A radius of 0.55μm is the upper limit of the particle size that can follow the velocity fluctuations which are experienced by flows of high turbulence intensity, Ref.(41). The light scattered from particles of radius less than 0.1μm will not contribute significantly for LDV, Ref.(41). These limitations can be imposed by filtering the air supply to the test section to eliminate large particles, leaving only small particles so that the diameter of the largest particle still present in the flow after filtration is of the order of, 0.5μm. Filtration also reduces the particle concentration. Experimental evidence indicates that the concentration of the desired particle size in laboratory natural aerosols is likely to be 10 to 100 times too low for laser-Doppler velocimetry using low power lasers, Ref.(38). Such a deficiency would be aggravated by at least one order of magnitude if effecient filtration is used as a size limiting technique. However if lasers of several hundred mW power are used then good results can be obtained from such flows, Ref.(38). Alternatively low power lasers can be used successfully if combined with artificial seeding. Unfortunately, the flow under investigation is very difficult to seed satisfactorilly without causing problems, Ref.(39). The dual-beam mode is the most suitable optical arrangement for measurments in flows of low particle concentrations, Ref.(42), hence it was selected for the present investigation.

5.5 The considerations affecting the selection of the LDV compoments:

Fig.(5-3) shows a typical dual-beam LDV consisting of:

1- Laser.

2- Transmitting optics.

3- Receiving optics.

4- Photodetector.

5- Signal processing system.

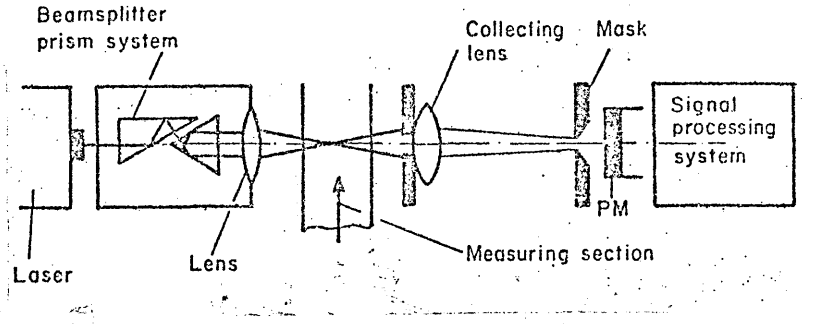

Fig.(5-3): A typical dual-beam LDV arrangement.

The design and development of such a system is a very complicated and specialized subject, Ref.(38), which lies beyond the scope of the present project whose main objective is to investigate the flow mechanism inside the Cranfield diffuser. Reliance was therefore placed on a commercially available LDV system of proven compatibility. The task now is to select a suitable LDV system. The components of the system must be chosen and optimised to suit each other and above all to suit the particuler flow under investigation . In the next few sub-sections the factors affecting the choice of each individual compoment will be discussed.

5.5.1 The laser:

The total number of photons scattered per particle passage is a function of the available laser power, the scattering properties of the particle, the particle size, the fringe spacing (hence the transmitting optics geometry), the particle velocity, and the focusing properties of the transmitting optics, Ref.(38). Only a small proportion of the scattered photons will reach the photodetector due to the finite collection efficiency of the light collecting system. The number of electrons leaving the cathode of the photodetector is given by multiplying the number of collected photons with the quantum efficiecy of the photodetector. There is a minimum flux of electrons required to ensure signal detectalility This number depends very much on the available signal processing system, Ref.(38).

In the case of the flow under investigation, it is unlikely that either the particle scattering properties or the particle size would be under control since no seeding technique is feasible. Consequently, even with the most efficient transmitting and recieving optics, the number of photons reaching the photodetector per particle passage is expected to be comparatively low. This calls for the use of either a high power laser, or an efficient and sensitive signal processing system, or both. Since the cost of lasers increases rapidly with the required power output, they should be carefully selected. For power requirements above approximately 50 mw, however the choice is limited, it involves a cost of approximately eight times that of 5 mw, Ref.(38). The laser light frequency may be important, particularly as it influences fringe spacing, photodetector quantum efficiency, and scattering efficiency of the particles. Also, the laser beam diameter may be inportant if the measuring-volume dimensions are critical. Typical laser-light wave lengths and beam diameters are indicated in the following table.

Laser type	Nominal power	Wave length	Beam diameter
He-Ne	1-15 mW	632.8 nm	0.65 mm
He-Cd	10-50 mW	441.6 nm	0.7-1.5 mm
Argon	1-1000 mW	514.5-488 nm	1.5 mm

Another important effect of the laser power is its influence on the required signal to noise ratio (SNR). The performance of the signal processer depends on the SNR of the electrical signal from the photodetector. The amount of power scattered is important since it defines the signal level and the SNR, but low signal levels can be increased by amplification if the original SNR is high enough. It has been suggested that the SNR depends, among other factors, on the laser power, in fact it is in direct proportionality to it when the other factors are fixed, Ref.(38).

5.5.2 Transmitting optics:

Commercially available transmitting optics are of the type known as "Integrated optical units". The term has two implications. The first is that it should allow operation in more than one of the possible optical modes. The second implication is that the compoments forming the unit should be engineered in such a way that

their alignment can be made optimum and that this condition will survive reasonable laboratory use. Fig.(5-4) shows an integrated optical system which can be used in the reference-beam (a), dual-beam (b), and two-scattered beam (c) modes. The integrated system comprises a lens, mirror, and beam splitter. The last two may be

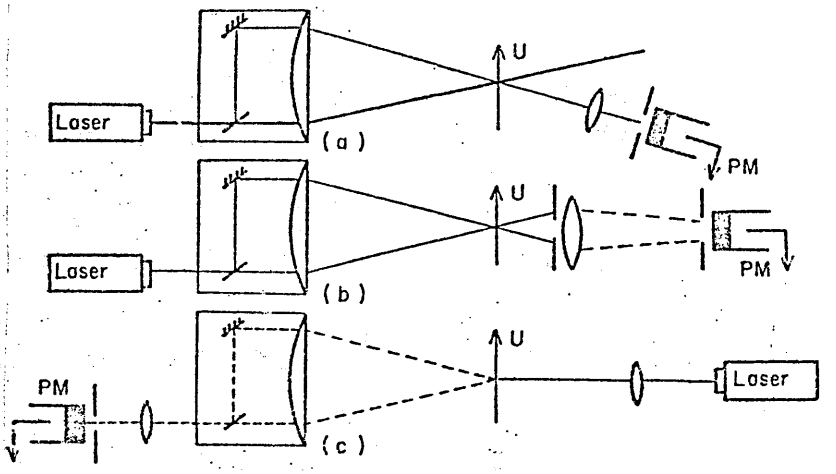

Fig.(5-4): Integrated optical system.

incorporated in a prism. In the reference beam mode, the beam splitter is normally required to transmit more than 95% of the incident light in the scattering beam. In the mode most suitable for the present study, the dual beam mode, the function of the transmitting optics is to produce two beams of equal intensities and path lengths. These are crossed at the required measuring point to form the fringe pattern.

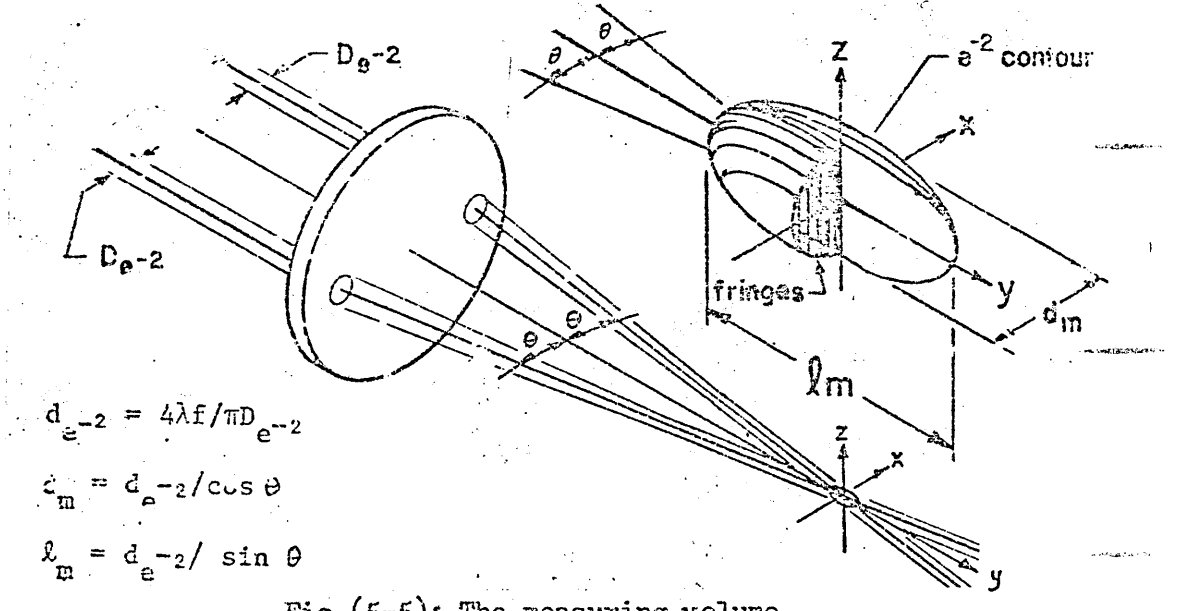

$$d_{e^{-2}} = 4\lambda f/\pi D_{e^{-2}}$$

$$d_m = d_{e^{-2}}/\cos\theta$$

$$\ell_m = d_{e^{-2}}/\sin\theta$$

Fig.(5-5): The measuring volume.

The fringe spacing, S, is given by the equation:

$$S = \frac{l}{b} \cdot \lambda$$

where:

λ, wave length of the laser light.

b, beam separation at an arbitrary point.

l, distance from the crossing point to the arbitrary point at which the beam separation is "b".

The measuring volume and the formulae which are used to calculate its dimensions are shown in Fig.(5-5), which is taken after Ref.(40).

Flow in recirculating regions is characterised by flow reversal and high turbulence intensities. A normal LDV system measures the absolute value of the velocity, and hence, in regions where the flow changes direction, i.e the sign changes, the system does not yield the sense of direction. Furthermore, difficulties arise in measurement in flows of high turbulence intensities, Ref.(43). To obviate these limitations, frequency shifting (sometimes referred to as phase modulation) is used. This is accomplished when the two intersecting light-beams have different frequencies. For convenience, the frequency difference should be variable. The presence of a frequency difference results in the movement of the fringe pattern. If the frequency shifting causes the fringes to move in the direction of the flow, then the apparent velocity will be less than its actual value and vice versa, hence the direction of the flow can be determined.

Frequency shifting can be achieved by the use of one of three methods:-

(a) Using a half-wave rotating grating.

(b) Using Bragg cells.

(c) Using the electro-optic properties peculiar to some types of crystals.

A complete discussion of the principles of operation and the relative merits of these methods can be found in Ref.(38).

5.5.3 Receiving optics:

Fig.(5-3) shows a typical receiving optics arrangement which can be

used in both forward and back scatter modes. The system comprises a large aperture which acts as a stopper for the illuminating beams, a collecting lens, and a small aperture in front of the photodetector. The small aperture in front of the photodetector is chosen so that the number of fringes observed by the photodetector is less than the number of fringes in the measuring volume by about one-fifth, Ref.(38). The choice of the collection lens depends on the spatial ralationship between the photodetector and the measuring volume. Also, it depends on the intensity of the scattered light. The interdependence of the geometrical parameters of both the transmitting optics and the recieving optics emphasises the need to optimize both systems to achieve the best performance.

5.5.4 Photodetectors:

The three types of photodetectors used in laser-Doppler are the photomultiplier, the photodiode, and the avalanche photodiode. Photomultipliers have been used most frequently, as their characteristics are generally the most suitable. The main criteria in the selection of photodetectors for laser-Doppler velocimetry include quantum efficiency, current amplification, frequency response, noise introduced by the detector, and cost, Ref.(38). In general, the quantum efficiency of photomultipliers peaks near 400 nm and is very low at the wavelength of He-Ne lasers (632.8 nm). For photodiodes, the quantum efficiency is maximum in the near infra-red, and hence is higher for a He-Ne laser than for an argon ion laser, Ref.(38).

In a photomultiplier the current amplification is achieved by the secondary emission of electrons in a chain of dynodes. The amount of amplification depends on the number of dynodes and the overall voltage applied across the chain. Tubes with 10 to 12 dynodes give enough amplification for use in LDV, with fast response if suitablly wired and operated. The noise introduced by a photomultiplier is small compared to that from a photodiode. Furthermore a photodiode gives much lower amplification than a photomultiplier, Ref.(38). The output from the photodiode alone is too small for further processing when used at light intensities obtained from LDV, thus a preamplifier is needed. The response time of the photodiode alone can be less than 1 ns, but when the

photodiode output voltage is applied across the input resistance of a preamplifier, the frequency response is then greatly reduced. The resulting compromise limits the use of diodes to situations with strong scattening and low frequency, Ref.(38).

Avalanche photodiodes employ a multiplication effect in which hole-electron pairs, produced by absorbed photons, create additional hole-electron pairs by their collision with atoms. Gains in current in the order of one hundred times are achieved. This provides low noise amplification. Thus the pre-amplifier gain need not be so large as that required for a photodiode, in addition, good frequency response can be attained.

The cost criterion favours the photodiode, but this factor is not too important. The cost of a detector and its power supply is normally a small part of the total cost of the LDV system, so the cost saving obtained with a diode is usually not worth the much reduced performance at low light intensity and high Doppler frequency. For the preceding considerations, it was concluded that the photomultiplier is the most suitable photodetector for the flow conditions likely to be encountered during the present investigation.

5.5.5 Signal-processing systems:

The electrical signal from the photodetector needs to be processed to extract the required velocity information. When the information required consists of the velocity and the turbulence intensity, then there are four possible methods that can be used, Viz.,

(a) Frequency analysis.
(b) Frequency-tracking demodulation.
(c) Counting.
(d) Photon correlation spectroscopy.

The detailed discussion of the principle of operation of each system and their relative merits can be found in reference (38). In flows of low particle concentrations and relatively high Doppler frequencies the photon correlation and the counting techniques are the more suitable, Ref.(40). A brief discussion of the principles of operation of these two systems and their relative merits are given below.

5.5.5.1 Counting techniques:

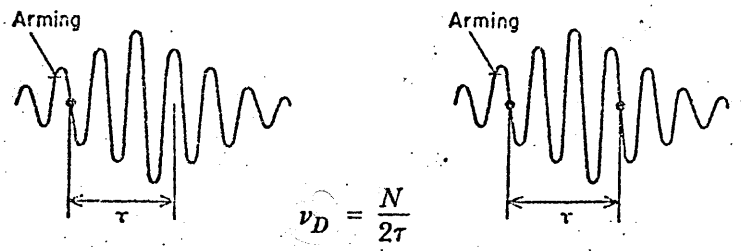

τ = preset time

N = number of zero crossings in time τ

N = preset number of zero crossings

τ = time for N zero crossings

Fig.(5-6): Counting techniques

The principles of operation can be summarized as follows, Ref.(38):

(a) The signal is normally band-pass filtered and possibly mixed with an oscillator signal to provide a convenient frequency.

(b) A counter is armed at a predetermined discrimination level and slope, and begins to count at the next zero crossing.

(c) There are two possible methods for counting, Fig.(5-6).

1- A fixed gate time may be present and the number of zero crossings in this time is measured and the Doppler frequency is determined accordingly.

2- Alternatively, the time taken for a particle to cross a predetermined number of fringes may be measured.

The merits and demerits of the counting techniques can be summarized as follows:-

(a) They can provide digital display of the values of both the mean velocity and turbulence intensity.

(b) Fixed-gate counting is relatively cheap but inherently less precise than preset zero-crossing counting.

(c) Logic circuitry may be required to avoid erroneous counts and sampling errors which may occur.

(d) Preset zero-crossing counting is suited to highly turbulent flows.

(e) Preset counters are suitable for low particle concentration.

5.5.5.2 Photon correlation spectroscopy:

Laser-Doppler signals are made up of contributions from different electron pulses which are each created by a single photoelectron leaving the cathode material. Secondary emission amplification of each electron is achieved in the photomultiplier dynode chain to yield pulses at the anode, Fig.(5-7).

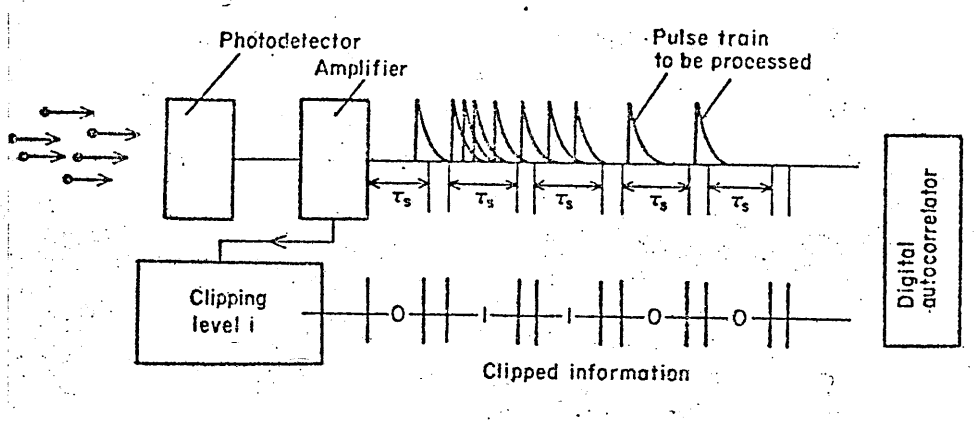

Fig.(5-7): Simulated pulse train.

The average number of these pulses is linearly related to the intensity of the scattered light. If this intensity is low, the average number of photons arriving at the photocathode can be such that single pulses reach the anode at times which are well separated. These pulses show finite durations due to the inherent integration times involved in the amplification processes of the photomultiplier. A statistically viable sample of such signals will show sinusoidal variation in the photon arrival rate due to the light intensity variations across the fringe in the measuring volume, Fig.(5-8).

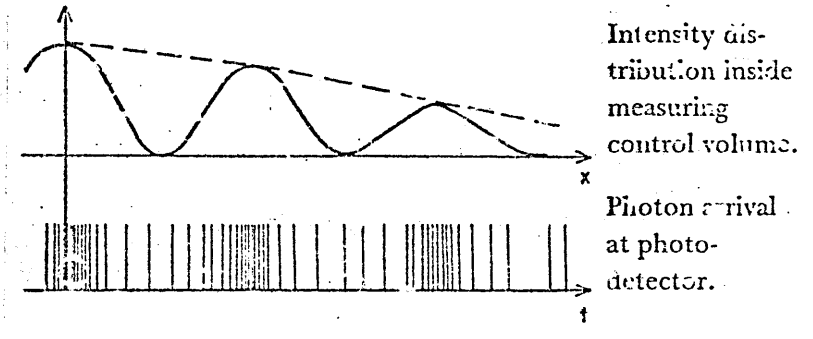

Fig.(5-8): Simulation of the scattered light intensity distribution.

If the light intensity is reduced so that discrete pulses appear at the photomultiplier output then digital autocorrelation may be used. A clipping technique may be used to permit working instruments to be manufactured at an acceptable cost. The technique of clipping, Fig.(5-7), involves the replacement of the signal before autocorrelation by "ones" and "zeros". A "one" is recorded if the signal is above a preset discrimination level and a "zero" if it is not. It can be shown that the loss of statistical significance by clipping prior to autocorrelation is negligible in LDV, and that single-clipping autocorrelation should allow the true autocorrelation function to be recovered, Ref.(41).

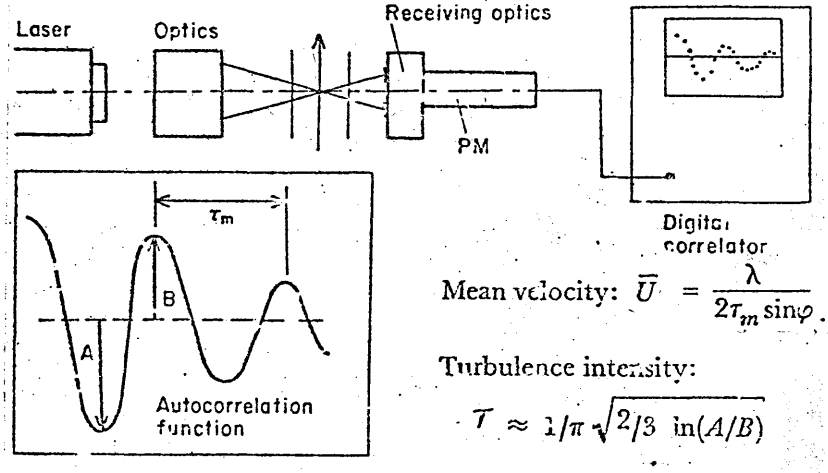

Fig.(5-9): Signal processing by photon correlation.

The recorded autocorrelation function, Fig.(5-9) permits the mean velocity to be calculated over the time period, τ_m, between the two maxima. Also the turbulence intensity can be calculated in terms of the decay of the amplitude of the sinusoidal part of the autocorrelation, Ref.(41).

In circumstances where the intensity of scattered light and the signal-to-noise ratio is very low, photon correlation spectroscopy offers particular advantages. These circumstances may occur when the laser light intensity is low, the particles are of very small diameter, or the particles distribution is very low.

III PART TWO

EXPERIMENTAL INVESTIGATION

INTRODUCTION

The primary task of this section of the study was to obtain experimentally a clear understanding of the velocity distribution and the turbulence structure inside the Cranfield diffuser. It was mentioned in Part One that the flow behaviour and performance are influenced by a large number of parameters which can be divided in two groups:

1- The geometrical parameters including; the area ratio, AR, the fence radial gap, y, the fence angle ϕ , the vortex chamber depth, δ , and the vortex chamber length, L.

2- The inlet flow conditions including the inlet Mach number, Mn, the inlet Reynolds number, Re, and the inlet velocity profile as described by the kinetic energy flux parameter, α_1.

It is obvious that conducting a fully comprehensive programme would be a major task that would definitely exceed the cost and time limitations imposed on this project. Consequently, it was decided to consider the project as an exploratory one and hence, to make a detailed experimental investigation of the flow structure while maintaining all the previously mentioned parameters fixed at certain values. The selection of these values was governed by many factors which are discussed as follows:-

(a)- The values of the parameters should be selected to produce a geometry from which some data, although of a less detailed nature, had already been obtained.

(b)- The values of the parameters should be selected so that the velocity and the turbulence intensities at any point in the flow would be measurable with laser Doppler velocimetry.

(c)- The selection should avoid undue complexities in the theoretical and mathematical part of the study.

(d)- The parameters were to be selected so that the experimental requirements would be within the capacities of certain equipment and measuring instruments available on site.

The selection of the parameters took account of the following points:

1- An inlet Mach number of 0.15 was selected because it enabled the flow to be treated as incompressible and yet gave an inlet mean velocity in the order of 50 m/s which was measureable with commercially available LDV systems.

2- The area ratio, AR, was selected to be in the order of 2.5 so that it would be a representative value of previously tested area ratios. The final selection of the actual value of AR was governed by detailed

design considerations which are discussed in chapter six.

3- From past experience, Ref.(12), the inlet Reynolds' number, Re, based on the mean inlet velocity and the primary duct approach length, was selected to be be in the range from 0.5×10^6 to 1.0×10^6. This was to ensure a turbulent boundary layer flow near the exit of the primary duct.

4- The inlet velocity profile was to be made as flat as possible, thereby producing a value of α_1 close to unity. This was to avoid flow complications which may arise due to a peaky or distorted inlet velocity profile.

5- Since there was no accurate method to provide the optimum values of the other geometrical parameters, namely y, ϕ, δ, and L, they had to be decided by experiments as discussed in chapter six.

This particular part of the thesis is concerned with the experimental aspects of the investigation. It is divided into five chapters. Chapter six describes and discusses the experimental programme for the geometric optimisation. Chapter seven contains a brief description of the selected LDV system and its components, the component specifications, installation procedure, and a brief discussion about the advantages and limitations of the system. Chapter eight discusses the design and development of the LDV test rig. Chapter nine includes a brief description of the experimental procedure and the LDV system method of setting up and adjustment, it also includes a brief discussion of the method of calculation of the results. Finally chapter ten includes the results, discussions, and the conclusions.

CHAPTER SIX

6. GEOMETRIC OPTIMISATION:

6.1 Rig design and instrumentation:

Due to financial constraints, the whole design concept was based on the performance of existing equipment in the allocated site. In particular, attention was given to the performance of an existing supply air fan and of a bleed air suction fan. Furthermore, the cost and manufacture of the various components were also related to the availability of semi-finished commercial products, such as perespex tubes and blanks, and to the available machining facilities.

The experimental programme for geometric optimisation had only one objective, namely to determine the diffuser geometry most suitable for future use on the LDV rig. Clearly requirements of the LDV technique were important factors in the design considerations of the geometric optimisation rig. For example the spatial resolution of the LDV system andthe space required to accommodate the system were factors in deciding the size of the test section. Again, the material from which the test section would be manufactured was selected so that it would be suitable for LDV techniques.

For the purpose of description, the complete rig design can be divided into three distinct components, namely:

(a) The test section.
(b) The supply air pipework.
(c) The bleed air system.

Each with its own requirements, but all interconnected to produce the desired results. Fig.(6-1) is a block diabram illustrating the relationships between the three components.

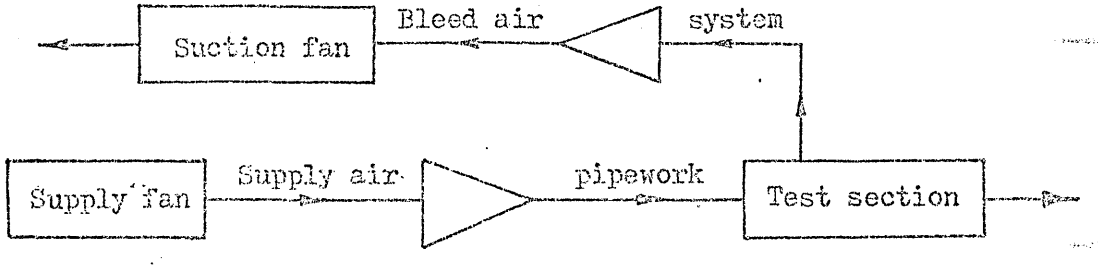

Fig.(6-1) The main components of the test rig.

6.1.1 Specifications:

6.1.1.1 The test section:

It should allow relative axial movement between the primary duct and the fence in order to vary the axial gap, x. It should also allow interchangeability of fences having different internal diameters, so that the radial fence gap, y can be varied. Again it should allow interchangeability of vortex chamber ducts of different lengths and different internal diameters so that the vortex chamber length and depth can be varied. It should facilitate means of measuring the flow parameters required to calculate the diffuser performance parameters namely the effectivencess, η and the vortex chamber depression parameter Vc.

6.1.1.2 Supply air pipe work:

It should provide means of controlling and measuring the supply air mass flow rate. The air should be delivered to the diffuser's primary duct at the required mean velocity and with an acceptable uniform axial velocity profile. Provision must be made for the suppression of any swirl velocity component or excessive turbulence levels. Provision must also be made to filter out large size particles which may be present in the air supply.

6.1.1.3 Bleed air system:

It should provide mean of controlling and accurately measuring the bleed air mass flow rate, $\dot{W}_B$.

6.1.2 Design of the test section:

The test section consisted of four major parts, namely:

1- The primary duct.

2- The secondary duct.

3- The fence.

4- The vortex chamber.

The preliminary design calculations to determine the major dimensions of these components are presented in Appendix A1. The final results are summarized as follows:-

D_1 = 47 mm(1.85 in)

D_2 = 72 mm(2.85 in)

Primary duct length = 245 mm (10.0 in)
Secondary duct length = 152.4 mm (6.0 in)
The predicted optimum vortex chamber depth = 15 mm (0.59 in)
The predicted optimum fence inside diameter = 50.9 mm (2.004 in)
The predicted fence radial gap = 1.95 mm (0.077 in)
The predicted fence axial gap = 6.0 mm (0.236 in)
Provision was made to change, y in the range from 1.016 mm (0.04 in) to 3.048 mm (0.12 in) in five steps by using five fences with different values of D_f . Provision was also made to change ϕ in the range from 10 degrees to 25 degrees for all the fences by mounting the fence on a specially designed fence carrier which enabled it to move coaxially with respect to the primary duct exit lip. The fence carrier also carried interchangeable vortex chamber ducts which enabled the change of its depth, δ in the range from 4.5 mm (0.177 in) to 22.0 mm (0.866 in) and the change of its length, L in the range from 19.05 mm (0.75 in) to 101.6 mm (4.0 in) A precisely contoured inlet nozzle of two smoothly blended circular arcs was designed and manufactured, according to the recommendations of Ref.(44), to ensure a smooth entry of the flow from the supply air pipework to the primary duct. The drawings which were issued for the manufacturing of the components of the test section are presented in appendix A2. Fig.(6-2) is the Assembly drawing of the test section in which the main components and dimensions are shown.

6.1.3 Test section instrumentation:

In order to asses the performance of the diffuser, certain parameters, such as the static pressure rise coefficient C_p , the effectiveness η , and the vortex chamber depression parameter V_c , should be calculated for each particular geometry and bleed rate. This called upon static pressure measurements in the primary and secondary duct as well as the vortex chamber.

1- The primary duct:

To ensure accuracy of measurement, three static pressure tappings at 120° spacing around the circumference were located at a distance equal to 1.5 D_1 upstream of the primary duct exit lip. This distance was chosen , partly to avoid the effect of the streamline curvature and partly because of mechanical constraints. Hypodermic tubes (of 26 gauge)were let into the

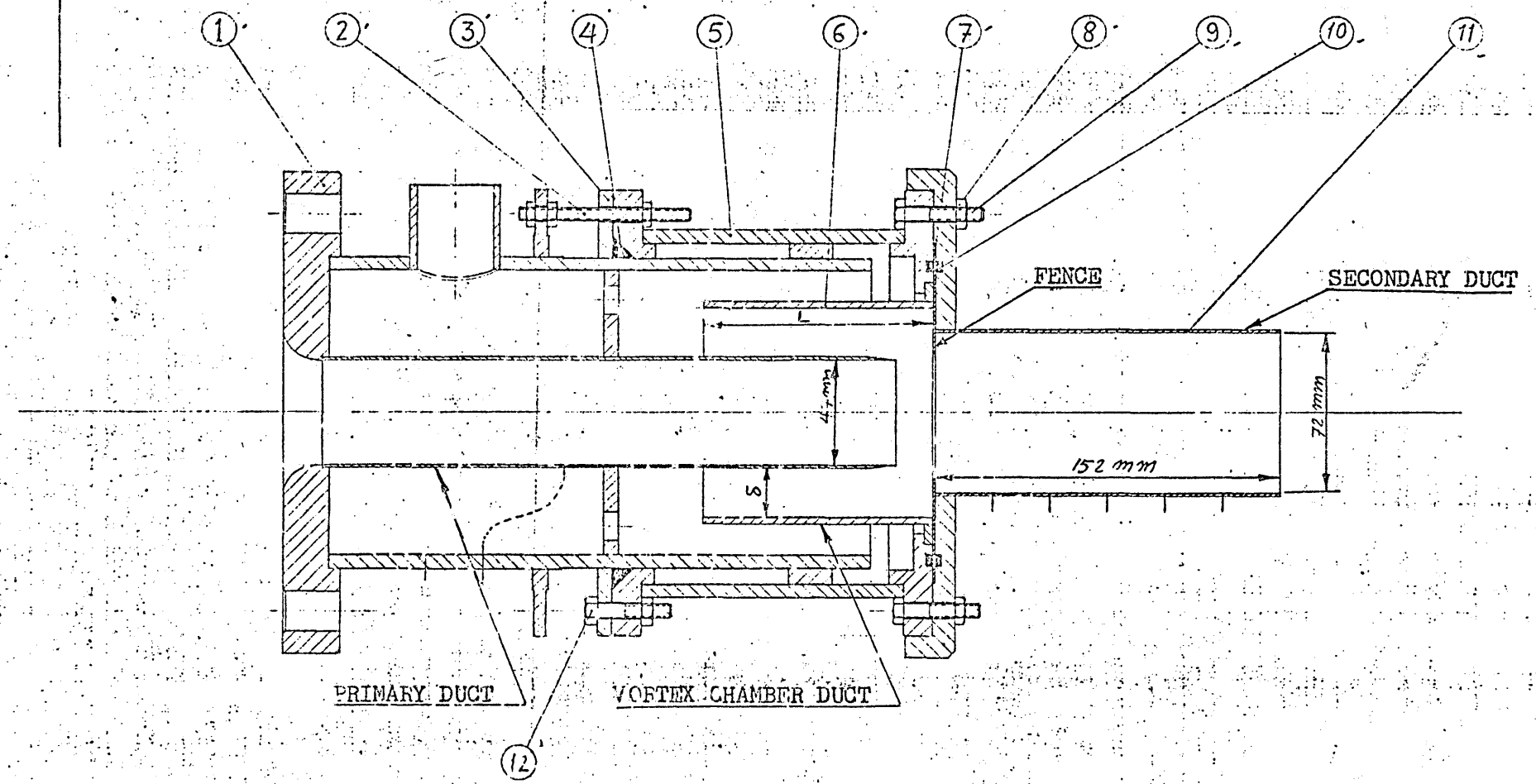

Fig.(6-2) The geometric optimisation test section.

ITEM	PART No.	DESCRIPTION	No. OFF	MATL	SPEC.	REMARKS
12		BOLT	3	M.S		½ BSF LENGTH TO SUIT
11	PC12793	SECONDARY DUCT	1	PERS.		
10		SEAL	2	RUBBER		O RING NO. 25
9		BOLT	4	M.S		½ BSF LENGTH TO SUIT
8		NUT	16	M.S		½ BSF
7	PD12805	FENCE	1	PERS.		
6	PD12804	V.C. DUCT	1	PERS.		
5	PC12800	CARRIER	1	PERS.		
4		SEAL	1	RUBBER		O RING NO. 43
3	PC12799	LOCKING DISK	1	PERS		
2		STUDDING.	3	M.S		½ BSF LENGTH TO SUIT
1	PC12797	MANIFOLD ASS	1	PERS		

THIRD ANGLE PROJECTION

SHEET SIZE A1

GENERAL TOLERANCE ON DIMENSIONS
MACHINED
UNMACHINED
OTHER DIMENSIONS AS STATED
WELD WHERE SHOWN THUS
MACHINE WHERE SHOWN THIS

JOB No. | No. OF SETS REQ'D 1 | USED ON DWG.

SCALE 1:1

FINISH SELF.

DRAWN SRAD 11.79 | CHK'D | APP'D | DATE

TITLE:- OPTIMISATION RIG

ISSUED BY SME

CRANFIELD INSTITUTE OF TECHNOLOGY
CRANFIELD.

DRAWING No. PB12795

SHT. 1 OF 1 SHEETS

pressure tappings. Since the vortex chamber covered the primary duct, and to avoid disturbing the flow in the vortex region, the hypodermic tubes were buried in the primary duct wall. The use of flexible plastic piping enabled the connection of these hypodermic tubes to three tubes passing through the outer wall of the vortex chamber.

2- The secondary duct:

Five equally spaced tappings were provided in order to measure the static pressure along the secondary duct. In this way the static pressure recovery could be monitored down the length of the secondary duct.

3- The vortex chamber:

One pressure tapping was felt to be adequate for measuring the static pressure in the vortex chamber.

All the static pressure tappings on the test section were connected via plastic tubing to a scanning valve which in turn was connected to a Furness micromanometer having a scale of 0 to 1000 mm H_2O .

6.1.4 Design of the supply air pipework:

Provision was made for measuring the air mass flow rate by installing a D , D/2 sharp edged orifice plate according to B.S.1042, Ref.(44). Past experience with the Alcosa fan indicated that the delivered air would have a strong swirl component which would upset the accuracy of the orifice plate. A double Diesel engine air filter was mounted in a special case which was connected to the fan exit port via flexible hose. The delivery side of the case was connected to the supply air pipe work via a transition section. The filter served as an effective device to suppress the swirl component and to reduce the turbulence level in the supply air pipework. It also filtered out dirt and large particles which would otherwise have upset the LDV measurements in a later stage of the investigation. To ensure accurate measurements, a pipe of length equal to over 40 diameters was used upstream of the orifice plate. A suitable length of pipe was placed downstream of the orifice plate which was connected to a larger diameter pipe via a conical transition piece. The larger diameter pipe contained two perforated plates to straighten the flow and thus served as a settling chamber. The settling chamber was connected to the test section with a flange.

The upstream tapping of the orifice plate was connected to a 60 inches water U-tube manometer and the pressure drop across the orifice was measured on another 60 inches water manometer. A dial gauge type of thermometer was inserted in a special pocket, upstream of the orifice plate to measure the temperature of the supply air. The design calculations of the supply air pipework and its details drawings are presented in Appendix A3

6.1.5 Bleed air line:

Appendix A4 shows the calculations made in order to estimate the maximum required bleed air mass flow rate, from which we get, $(\dot{W}_B)_{max} = 0.01$ Kg/s . This is well within the capacity of the bleed air metering system described in Ref.(2) and Ref.(12). Consequently it was decided to use the above mentioned system without any alteration. A single stage centrifugal fan was used as a source of suction downstream of the plenum chamber with a butterfly valve installed so as to control the depression in the plenum chamber.

6.2 Experimental procedure and calculation of results:

Before beginning the geometric optimisation , it was decided to use a static pressure probe and a total pressure probe to examine the symmetry, the steadiness, and the stability of the flow. These tests proved that the flow in the diffuser was axisymmetrical, steady, and stable. However, it was noticed that the readings of the wall static pressure tappings in the primary duct were inconsistent with the readings obtained by the static pressure probe, contrary to the case of the secondary duct tappings. Upon careful inspection of the primary duct tappings, the discrepancy was found to be due to roughness at the opening of the static pressure tapping holes. At this stage the components of the test section had been securely cemented together and so it was practically impossible to correct this manufacturing error without remanufacturing most of the parts of the test section. Therefore, the static pressure was measured at the same plane using the static pressure probe which was located along the axis of symmetry.

The total pressure probe was next used to measure the velocity profile at the plane of measurement of the static pressure in the

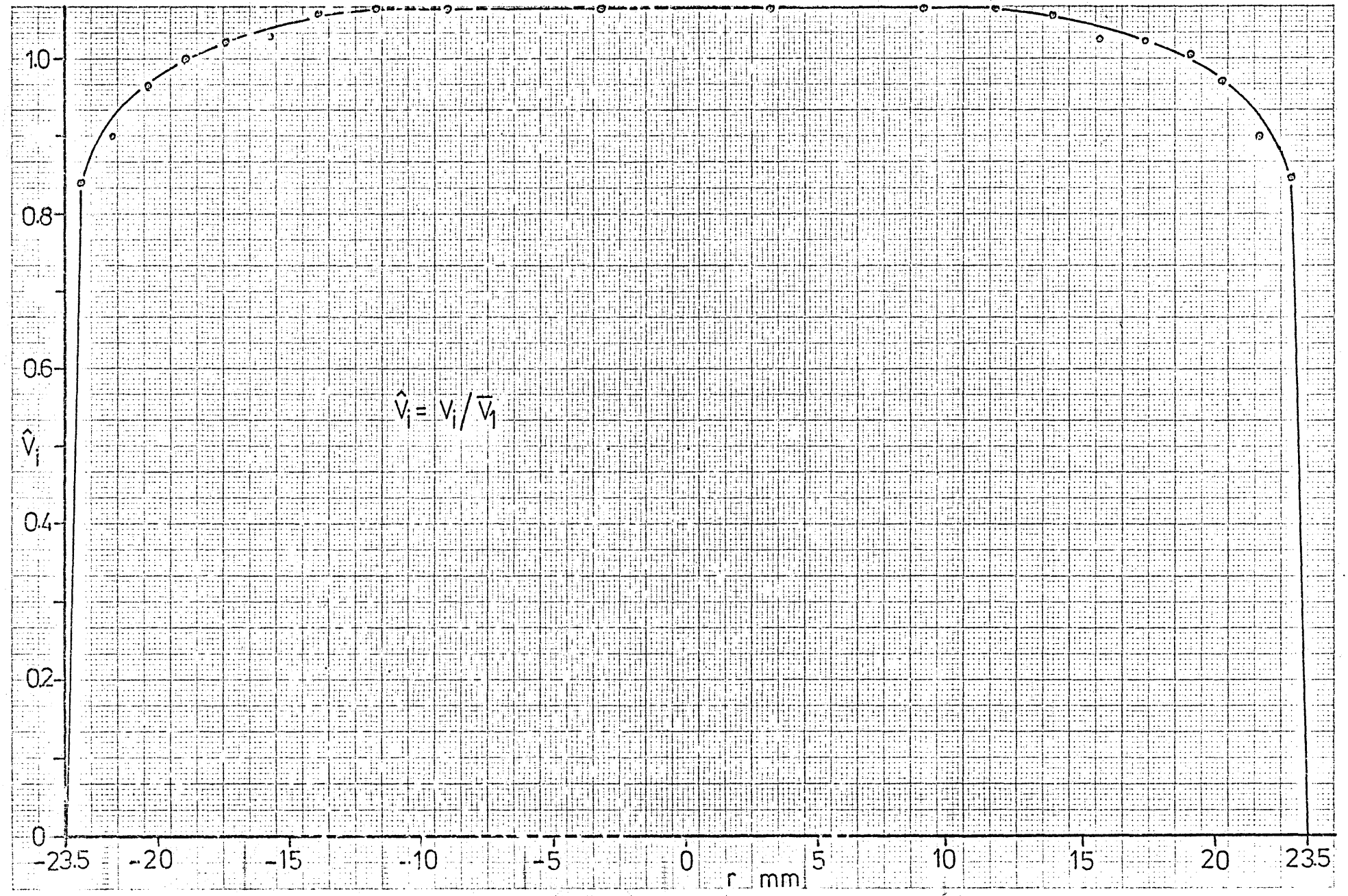

Fig.(6-3): The inlet velocity profile.

primary duct. The result, which is shown in Fig.(6-3), was used to calculate the inlet kinetic energy flux parameter, α_1 . The details of the calculations are shown in Appendix B1 from which $\alpha_1 = 1.011$. This value was assumed to be constant regardless of the running conditions of the diffuser and was used to evaluate the correct inlet dynamic pressure of the diffuser from the mass flow measurement.

The systematic experimental procedure used during the geometric optimisation tests is summarized as follows:-

1- The required fence and vortex chamber duct were assembled into the model.

2- Using a micrometer, the stud and nut mechanisms, Fig.(6-2), were adjusted to give the required value of X in such a manner that coaxiality was maintained and the required value of ϕ was obtained.

3- The air supply was regulated by the control valve to give a predetermined pressure drop across the orifice plate, relating to a mean velocity in the primary duct of 50 m/s.

4- The suction fan was started with the bleed valves closed.

5- The bleed valves were then regulated so that the reading of the flow meters were varied from zero to the maximum possible value.

6- For each setting of the bleed valves, the measured parameters were recorded in a specially prepared result table. Appendix B2 shows the recorded readings of a typical test.

The derivation of the formulae used in the calculation of the results are shown in Appendix B3. For convenience, these formulae are given below in their final form.

1- The absolute static pressure ($p_i$abs) was calculated from the gauge pressure reading (p_i g) using the formula,

$$p_i \text{ abs} = 100p_z + 10p_i \text{ g} \qquad (6\text{-}1)$$

2- The main flow mass flow rate ($\dot{W}_1$) was calculated from the formula,

$$\dot{W}_1 = 0.018535 \frac{\sqrt{h}\sqrt{p}}{\sqrt{t+273.15}} \qquad (6\text{-}2)$$

where,

$$h = h_3 - h_4$$

$$p = 0.4015\, p_z + (h_1 - h_2)$$

3- The bleed air flow rate (W_B) was calculated from the formula:

$$\dot{W}_B = 6.66 \times 10^{-4} \left(E_\beta + 2E_\alpha\right) \frac{\sqrt{10 P_B + P_B}}{\sqrt{t_B + 273.15}} \qquad (6\text{-}3)$$

4- The bleed rate (B) was calculated from the formula:

$$B = \dot{W}_B / \dot{W}_1 \qquad (6\text{-}4)$$

5- The inlet dynamic pressure ($\frac{1}{2}\alpha_1 \rho \bar{V}_1^2$) was calculated from the formula:

$$\frac{1}{2}\alpha_1 \rho \bar{V}_1^2 = \frac{\alpha_1 \dot{W}_1^2 P_1}{0.996(273.15 + t)} \qquad (6\text{-}5)$$

6- The ideal static pressure rise coefficient (C_{pI}) was calculated from the formula:

$$C_{pI} = 1 - \frac{1}{\alpha_1}\left(\frac{1-B}{AR}\right)^2 \qquad (6\text{-}6)$$

7- The actual static pressure rise coefficient (C_p) was calculated from the formula:

$$C_p = \frac{P_2 - P_1}{\frac{1}{2}\alpha_1 \rho \bar{V}_1^2} \qquad (6\text{-}7)$$

8- The effectiveness (η) was calculated from the relation:

$$\eta = C_p / C_{pI} \qquad (6\text{-}8)$$

9- The vortex chamber depression parameter (V_c) was calculated from the formula:

$$V_c = \frac{P_1 - P_c}{\frac{1}{2}\alpha_1 \rho \bar{V}_1^2} \qquad (6\text{-}9)$$

A "Wang 600" programmable calculator was used to calculate the results. A special programme was written and recorded on tape.

6.3 Results and discussions:

The sole purpose of the geometric optimisation was to determine the optimum geometry and running conditions at which the diffuser flow was to be investigated. Hence, it was decided that this should be accomplished by as few tests as was practically possible. The best way to do this was to optimise each geometrical parameter separately in the order of the strength of their influence on the diffuser performance i.e y, ϕ, δ and L respectively. This order was decided upon from past experience, Ref. (12). The test results are presented in Appendix C.

6.3.1 Optimisation of the fence gap, y:

Five fences were tested each of which gave a different value of y. The rest of the geometrical parameters, i.e ϕ , δ, and L, were kept constant at their predicted optimimum values. The results of the tests are shown in figures(c-1), (c-2), (c-3) and (c-4). Fig.(c-1) is a plot of the diffuser effectiveness, η against the percentage bleed rate, B% for the different values of y that were tested. Fig.(c-2) is a plot of the vortex chamber depression parameter, V_c against the same variables. Fig.(c-3) is a cross-plot of Fig.(c-1) showing the variation of η versus y for different values of B%. Fig.(c-4) is a cross-plot of Fig.(3-7) showing the variation of V_c versus y for different values of B%. The graphs show a typical effect of y on the diffuser performance, Ref.(12). For small values of y, e.g.y = 1.02 mm (0.04 in), there is no distinctive bleed rate that can be identified as a minimum bleed rate requirement. For relatively larger values of y, e.g. y = 2.03 mm (0.08 in) or y = 2.54 mm (0.1 in), a minimum bleed rate requirement can be readily identified. At low bleed rates, from 0% to about 2%, higher values of η can be achieved with smaller values of y for the same bleed rate, however higher values of V_c was then required. For values of $y \geqslant 2.03$ mm (0.08 in), the larger the value of y the higher the minimum bleed rate requirement. For the same range of y, once the minimum bleed rate requirement was met, neither y nor B had any significant effect on the diffuser effectiveness. The effect of y and B on V_c can be discussed with the help of fig.(c-2). For low values of y, e.g. y = 1.02 mm (0.04 in) , V_c increases very fast with the increase in B, while for values of $y \geqslant 2.03$ mm (0.08 in) the rate of increase of V_c w.r.t. B is much lower.

From the above discussion it is clear that the selection of the value of the fence radial gap y as being an optimum value is a difficult and arbitrary decision. It depends on the best compromise that can be reached between η and V_c to suit a particular application. For the purpose of the present study, the problem is academic. However, for future use of the results, the selection must be related to the most likely application of the

diffuser, that is in aircraft gas turbine engines. For such an application the reduction of the minimum bleed requirement is of paramount importance because any increase in bleed rate would result in a greater reduction in the overall engine performance. The corresponding value of V_c that could be tolerated depends on the location of the diffuser in the engine and on the planned use of the bleed air. i.e. on the point at which the bleed air is reintroduced into the engine mainflow. Having the above considerations in mind, the optimum value of y was selected to be 2.03 mm (0.08 in) for which a minimum bleed rate requirement of about 3% can be readily recognised from Fig.(c-1). The corresponding values of η and V_c are about 75% and 0.195 respectively.

6.3.2 Optimisation of the fence angle, ϕ :

A series of tests were conducted with the fence radial gap, y, fixed at its selected optimum value, y_{cp} = 2.03 mm (0.08 in). The vortex chamber depth δ and length L were also fixed at their predicted optimum values which were used during the optimisation tests of y. During these series of tests the fence angle ϕ was varied in the range from 12.5 degrees to 22.5 degrees. The results are presented in figures (c-5), (c-6), (c-7) and (c-8). Fig.(c-5) is a plot of η against B% for different values of ϕ. Fig.(c-6) is a plot of V_c against B% for different values of ϕ. Fig.(c-7) is a cross-plot of Fig.(c-5) illustrating the variation of η w.r.t. ϕ for different values of B%. Fig.(c-8) is a cross-plot of Fig.(c-6) illustrating the variation of V_c w.r.t. ϕ for different values of B%. Examination of the graphs reveals that, for y = 2.03 mm (0.08 in) and B = 3%, the optimum value of ϕ is about 18°. The corresponding values of η and V_c are 75.5% and 0.19 respectively. The change in the resulting optimum value of η and V_c are marginal because the predicted optimum value of ϕ (17.5°) at which y was optimised was very near the actual optimum value of ϕ (18°) which was achieved by experimental optimisation.

6.3.3 Optimisation of the vortex chamber geometry:

A third series of tests were conducted in which the fence geometry was kept constant at its previously optimised values of y and ϕ.

The object of this new series of tests was to optimise the vortex chamber geometry that is to find out the values of δ and L that would give the highest possible value of η and the lowest possible value of V_c at the previously determined minimum bleed rate requirement of 3%. In these new tests, twelve different vortex chamber ducts were tested. The results are shown in figures (c-9), (c-10), (c-11) and (c-12). The figures show the variation of η and V_c versus the bleed rate percentage B% for different values of δ and L that were tested. The results show that neither δ nor L are likely to have any significant effect on η. On the other hand, however, both δ and L have some effects on V_c. The effect of the former seems to be the strongest particularely at high bleed rates.

If the diffuser effectiveness η was to be considered the more important performance parameter, then it does not really matter what values of δ and L were to be used since both of them seems to have no significant effect on η. In this case, the requirements of the LDV and the simplicity of its rig are likely to be a more convenient criterion for making such a decision. An extension of the secondary duct beyond the fence and covering the primary duct would render a diffuser of a simple construction in which measurement with LDV is relatively simple. Interpolating the graphs of V_c versus B%, it can be shown that such a model would have a value of V_c of about 0.22 at B = 3% which is still a tolerable level of V_c

6.4 Conclusions:

From the results of the geometric optimisation tests and the associated discussions, it can be concluded that:

1- The optimum fence geometry is given by y_{op} = 2.03 mm (0.08 in) and $\phi_{op} = 18°$.

2- An extension of the secondary duct beyond the fence to cover the primary duct would form a suitable vortex chamber duct.

3- Such a geometry would render a diffuser of a minimum bleed rate requirement of about 3% at which the diffuser performance in given by η = 75.5% and V_c = 0.22.

CHAPTER SEVEN

7. THE LASER DOPPLER VELOCIMETRY SYSTEM

7.1 Selection of the system and its compoments:

The flow under investigation has distinctive characteristics which have been discussed in detail in chapter one. For convenience, they are summarized as follows:-

1- The flow has two regions of recirculation in which it reverses direction.

2- The velocity field has a wide range of velocities. The range in which the magnitudes of the velocity are expected to change is likely to be from over 50m/s for the axial velocity component at the throat of the diffuser to a near zero velocity for the same velocity component at points of flow reversal.

3- There are regions of very high turbulence intensity particularly at and near the shear layers emerging from the primary duct exit lip and from the top of the fence.

4- The light scattering particles naturally present in the flow are small in size and have low concentration.

5- The flow is axisymmetrical of complex solid boundaries.

The implications of these characteristics on the choice of the LDV are:-

1- The flow reversal and the high turbulence intensity necessitate the use of frequency shifting to determine the flow direction and to produce processable signals at regions of high turbulence intensity.

2- The low concentration of small scattering particles necessitate the use of the dual-beam mode as an optical arrangement. Also, it gives only two choices for the signal processing technique, Viz.,
   (a) The counting technique which may require a relatively high power laser of about 50mW or more.
   (b) The photon correlation technique which may require a relatively low power laser of about 5 to 15mW.

3- The wide range of velocities requires a flexible transmitting optics with both the beam separation and the crossing angle as variables. Furthermore, the need to measure in radial traverses, reaching as near possible to the solid boundaries, requires

another form of flexibility from the transmitting optics. This is to facilitate a better control on the size of the measuring volume. Consequently, the receiving optics must be equally flexible because they must be kept in constant match with the transmitting optics.

4- The complex cylindrical solid boundaries are likely to reflect a great deal of light and hence reduce the SNR. This is known as the flare problem. Under such condition, increasing the laser power would give an undesirable effect resulting in a further reduction in the value of SNR. This unfortunate feature favours the use of a photon correlator as a signal processor since it requires minimum laser power.

5- Again, the complex solid boundaries necessitate the measurments, in some regions, to be in the back scatter mode. This calls for the selection of a LDV system where optical components can be arranged in both the forward-scatter and the back-scatter modes. It also necessitates the use of a signal processing system which is capable of processing the relatively poor signal resulting from back-scatter measurements.

The considerations given above lead to two possible systems. The first system is based on the use of a relatively high power laser (about 50mW) together with a signal processor of the counter type. The second system uses a relatively low power laser (5 to 15mW) with the signal processed by a photon correlator. The remainder of the components are similar in both systems.

A number of considerations favoured the adoption of the second system these are as follows:

1- The low power laser was safer to operate.

2- The total cost of the second system is less than that of the first one. Furthermore, a suitable photon correlator was available on site. Use of this correlator reduced the required capital by about one third.

3- The photon correlation technique has been in use at Cranfield for some time and much experience regarding its operation was available. Also a high level of confidence in the accuracy and reliability of the system was established, Ref.(39).

Consequently the decision was made to use the photon correlation technique.

7.2 Description and specification of the LDV system and its components:

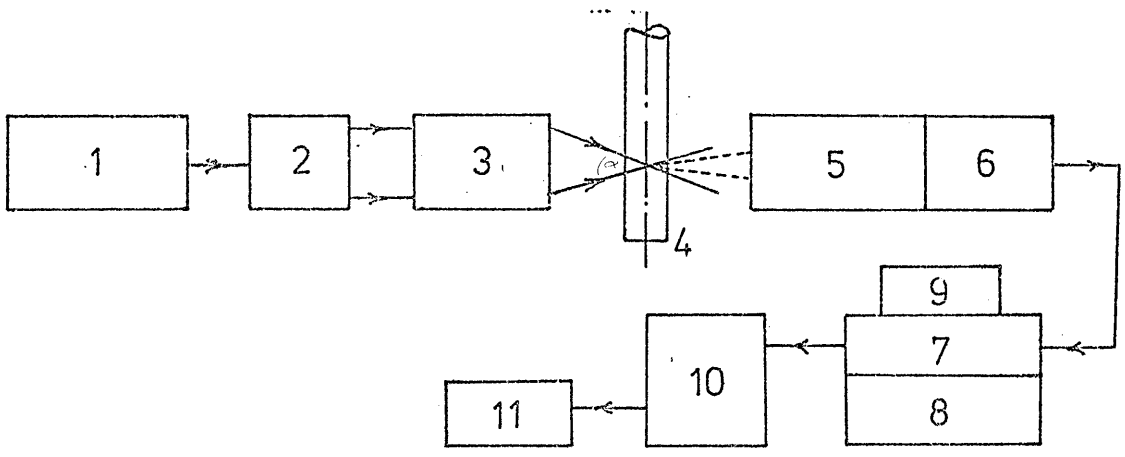

1- The laser.
2- Beam splitter.
3- Phase modulator.
4- Test rig.
5- Receiving optics.
6- Photomultiplier.
7- Photon correlator.
8- Correlator store.
9- Oscilloscope.
10- Data processor.
11- Printer.

Fig.(7-1): Block diagram illustrating the LDV system and its components.

The LDV system, plate (1) and Fig.(7-1), can be divided into three distinctive groups, Viz.,

1- The transmitting optics group, plate (2), consists of the laser, the beam splitter, and the phase modulator.
2- The receiving optics group, plate (3), consists of a viewing telescope, aperture, and a photomultiplier.
3- The signal and data processing group, plate (4), consists of the photon correlator, correlator store, oscilloscope, data processor, and printer.

The detailed description, specifications, and methods of use are given in the manufacturer's catalogues and manuals. For convenience a brief description together with the most relevant specifications for the use of each component are given in the next few sub-sections.

7.2.1 The laser:

The laser was a Spectra-Physics, model 124B, powered by model 255 power supply unit. The relevant specifications are, Ref.(47):

(1) Type: Helium-Neon
(2) Wavelength: 632.8 nm
(3) Output power: 15 mW at 632.8 nm
(4) Beam diameter: 1.1 mm measured at e^{-2} point.
r = 550 μ

7.2.2 The beam splitter:

A Malvern adjustable beam splitter type RF 307 was used. The splitting prism was mounted on a precision, "traverse and rotate", mechanism operated by two controls. These controls provide for the adjustment of beam crossing angle. Provision is also made for the mounting of interchangeable focusing lenses. The beam passes through the focusing lens before meeting the splitting prism. The lens only used in some of the measurements, had a focal length of 200 mm. The focusing lens was removed when the phase modulator was in use. The following is a summary of the relevant specifications, Ref.(48):

1- Minimum fringe spacing is 4 microns.
2- Beam separation is variable from 3mm to 24mm.
3- Beam crossing is variable from convergent at 15cm in front of the beam splitter, through parallel, to divergent at 10° to the optical axis.
4- Polarisation of beams is horizontal with vertically polarised laser.
5- Polarity rotation is 0 to 90°.

7.2.3 The phase modulator:

A Malvern phase modulator type K9023 was used. It is mounted on its special, "tilt and rotate", mount model RR126. The phase of a light beam passing through certain types of electro-optics crystal may be advanced or retarded by the application of a suitable voltage. This principle is used here in the phase modulator which contains two crystals of different cuts, Ref.(49). When a suitable saw-tooth voltage is applied to the crystals, the phase of the outgoing beam from one crystal is advanced, whilst the phase of the other beam is retarded. The two beams then cross to form a fringe pattern which moves linearly in space. The relevant specifications are, Ref.(49):

1- Beam spacing is fixed at 20mm.

2- Beam crossing is variable using lenses of different focal length. The diameter of the focusing lens is 40mm. The lenses used in this project have focal lengths of 50, 25, 20 and 15 centimetres.

3- Switched frequencies are 20, 50, 100, 200, 500 and 1000 kHz.

7.2.4 The receiving optics:

A Malvern RF 313, integrated receiving optics and photomultiplier was used. The function of this unit is to collect the light scattered by the particles in the flow and focus it onto an interchangeable aperture. The aperture served to regulate the diameter of the measuring volume, and also eliminated any scattered light from sources not of interest. Aperture pinhole diameters used in this project are 100, 200 and 400 microns. A suitable viewing telescope is incorporated enabling the focused beam to be accurately directed into the aperture. Coaxially integrated with the unit is a photomultiplier detection unit. This contains a narrow band optical filter, dynode chain, high gain amplifier and discriminater, which amplifies and shapes the pulse signal for direct use by the correlator processor. The detailed specifications of the optical receiving system and the photomultiplier can be found in Ref.(50) and Ref.(51).

7.2.5 The signal processor:

This is the Malvern 50 ns, digital photon correlator type K7023 together with a 96 channel correlator store. The function of the correlator is to process the output pulse train from the photodetector into a correlation function containing the required information on the velocity and turbulence intensity. The following is a summary of the relevant specifications:

1- Temporal resolution ranges from 50 nsec to 1 sec. in steps of 50 n sec.

2- Single or double clipping possible. Single clipping was only used throughout the present programme. Clipping level was selectable in integer steps 0 to 9.

3- There are two input channels, A and B, with 50 n sec pulse per resolution.

4- Sample time was selectable up to 1 sec in multiples of 50 n sec

to two significant figures from an integral crystal controlled clock. The number of samples taken is pre-settable to 10^n where n is an integer value in the range 2 to 9. Total counts are accumulated in monitor channels.

5- Information accumulated in the store channels is duplicated into a dynamic readout system which has an update or hold facility. The main store contents and the accumulating process are undisturbed during the readout process. Throughout the present experimental programme the readout process is controlled by the data processor.

6- The correlator has four channels added to the 96 channels already in the store making a total of 100 channels. The first channel address is (00) and the last channel address is (99).

* Channel (00), records the counts at A input.
* Channel (01), records the number of times the clip level was exceeded.
* Channel (02), records the counts at B input.
* Channel (03), records the number of samples.

More detailed specification can be referred to in Ref.(52).

7.2.6 The Oscilloscope:

The Malvern RR 46 oscilloscope is an OS255, 15MHz, Dual Trace Gould oscilloscope. The detail specifications and instructions for use can be found in Ref.(54). Although just an auxiliary component of the system, the oscilloscope proved to be a very powerful tool for monitoring the correlogram. This enabled judgement to be made on the quality of the correlogram. If this was unsatisfactory, then the experimental parameters could be changed(or other suitable measures taken) to improve the quality of the correlogram.

7.2.7 The Data processor:

This was an improved Commodore 2001-8 PET computer with its memory extended to 32 K bytes. The computer is fitted with an IEEE-488 interface through which it was connected to the correlator by a cable harness. Software subroutines are provided by Malvern Instruments in BASIC language to allow direct control of the correlator and for directly unloading the correlogram into the memory for analysis and data reduction. These programmes are

conversational and were found to be easy to use. A full description of the programmes together with their print-out can be found in Ref(53).The complete specifications and the instructions for use are given in Ref.(53) and Ref.(55). The data processor is also connected to a standared Commodor on-line printer type 3023, Ref.(56), to provide a hard copy of the results togetger with the experimental parameters.The printer is also controlled by the data processor whose software offers the choice between VDU display or the printer hard copy.

7.3 Instalation of the LDV optics:

The transmitting optics and the receiving optics were placed on a specially designed horizental platform. The platform facilitated the arrangement of the optics in full forwared scatter, oblique forward scatter, or oblique backscatter according to the requirement of the measuring conditions. It also facilitated the tilting of the whole system so that the optical axis of the transmiting optics could be made inclined to the axial direction of the flow at any required angle between 45° and 135°. The horizontal platform was fixed rigidly on a Unimatic compound X-Y traversing table. The longitudial traversing direction, which was parallel to the axial direction of the flow, had maximum traverse distance of 410 mm. The cross traversal direction which was parallel to the radial direction of the flow had a maximum traverse distance of 310 mm. The table had indexing dials provided with graduated zeroing devices with 40 divisions each corresponding to one table movement of 0.1 mm. The table had a scale graduated in mm. The traversing table, with the platform fixed on top of it, was carried by a rigid steel frame. The steel frame has an adjusting screw on each of its four supporting legs. The overhanging side of the platform was supported on the steel frame by a screw jack.The adjusting screws and the screw jack were used to ensure a fine adjustment of the correct location of the platform in a horizntal plane at the required level.

Plate (2) illustrates the arrangement of the transmitting optics group. The laser tube was mounted on the Ealing optical bench using two height adjusting brackets. The two brackets also facilitated rotational motion to enable the laser beam to be adjusted in a plane parallel to

the optical bench and offset from it (in the horizontal plane) by any required distance. The beam splitter was fitted directly to the laser tube and locked securely with the locking rings. The tilt and rotate mount of the phase modulator, had a special base enabling it to be fixed on the Ealing optical bench in line with the laser and the beam splitter.

The integrated resieving optics and detector unit was mounted on top of the RF 311 X-Y motion unit. This was fixed on the RF 312 height adjustment unit which in fact, was a part length of an Ealing optical bench carried by four telescopic legs giving a height variation of approximately 4 cm. The whole arrangement facilitated three degrees of freedom with fine adjustment to enable accurate focussing of the scattered light through the aperture pinhole.

7.4 Advantages and limitations of the LDV system:

7.4.1 The advantages of LDV over conventional techniques:

All velocity measuring techniques whether conventional, such as pitot-tubes or hot wire anemometers, or LDV system give similar results when used in low velocity parallel flows with low turbulence intensities. The advantages of LDV over conventional techniques are fully demonstrated when they are used in recirculating regions. Recirculating regions are characterised by having reverse flows and very high turbulence intensities. Conventional instruments are not

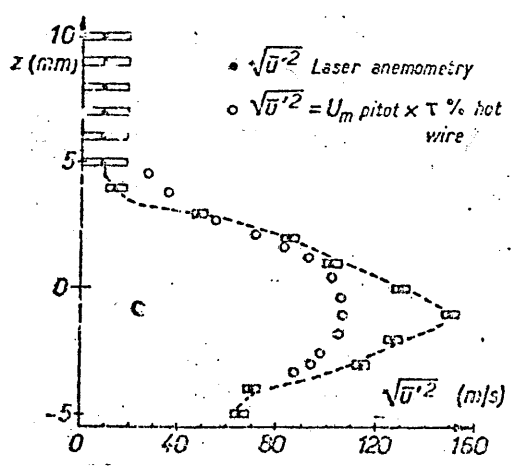

Fig.(7-2): Measurement in a recirculation region.

able to determine the sign of the velocity vector. However, LDV employing frequency shifting can be made to determine the sign of the velocity. At high turbulence levels, exceeding 20%, hot wire measurements of turbulence intensities are misleading, Ref.(57). LDV employing frequency shifting can be operated satisfactorily in regions of very high turbulence intensities even with very low or zero mean velocities ,Ref.(58).

Fig.(7-2) taken after Ref.(42) illustrates the high inaccuracy of the measurement of the turbulence intensity obtained by hot wire anemometer compared with LDV measurements in a mixing region of a high speed flow. Even at moderate and low turbulence intensities, hot wire and hot film measurements tends to underestimate the turbulence intensities. Fig.(7-3) taken after Ref.(59) illustrates this fact.

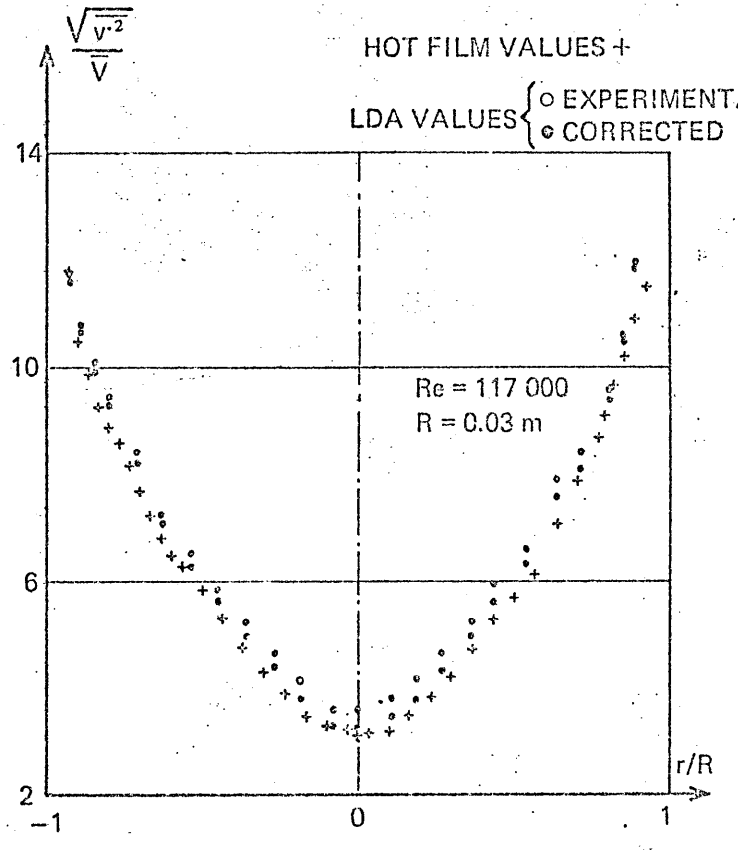

Fig.(7-3): Comparison between measurements with LDA and hot film.

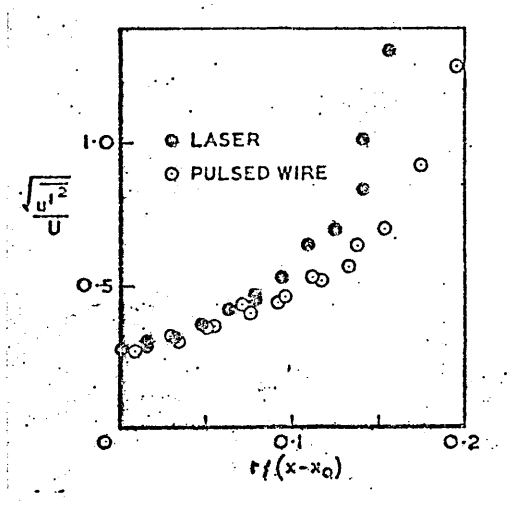

Fig.(7-4): Comparison between measurements with LDA and pulsed wire.

The same tendency to underestimate the turbulence intensities are noticed in pulsed wire measurements, Fig.(7-4) taken after Ref.(43). One more basic attraction of LDV is that it is essentially non-intrusive, it does not disturb the flow being studied.

7.4.2 The advantages of photon correlation over other LDV techniques: Specific advantages of the present LDV are its wide dynamic range, very high spatial resolution, ease of measurements in backscatter without the need to seed the flow, ease of alignment, high collecting efficiency and relative insensitivity to noise and vibration.

E.R. Pike in Ref.(41) argued that accurate measurements can be performed with photon correleter system with the level of the scattered light 1000 times weaker than would have been otherwise required by any other LDV system. He estimated the level of error in measuring the Doppler frequency to be 0.22% when single clipping at "0" clipping level was used. The estimation was made for a correlogram of just over six channels per doppler cycle.

J.B.Abiss, Ref.(60), reported some results obtained at severe measuring conditions with only just over three channels per doppler cycle. A typical result is shown in Fig.(7-5) which demonstrates convincingly the virtually noise-free correlogram which can be obtained with the photon correlator.

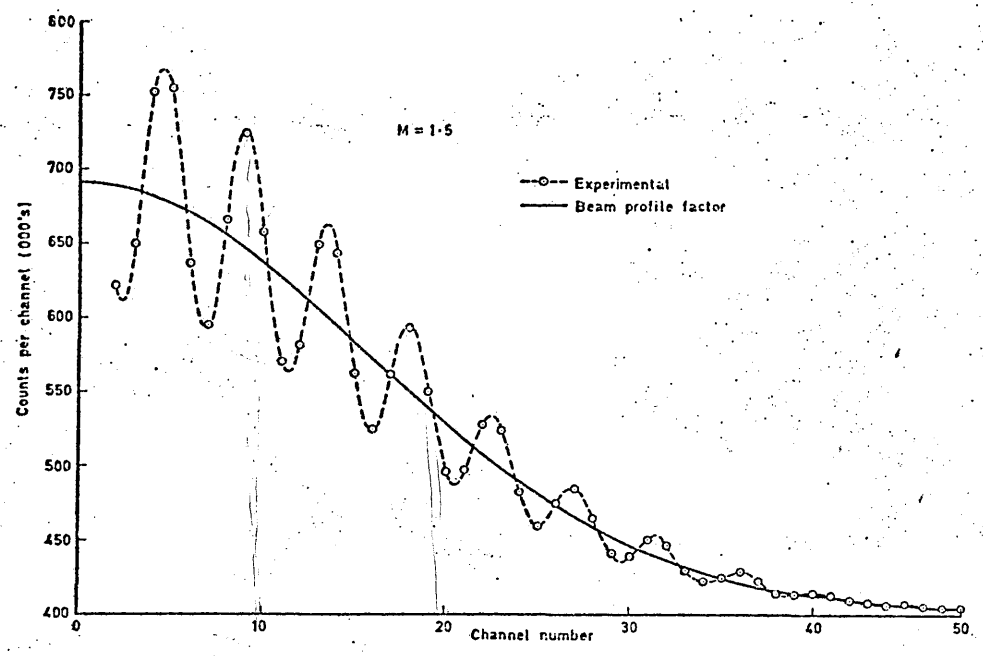

Fig.(7-5): Correlator output in laminar supersonic flow.

Abbis, Ref.(60), also reported test results illustrating the advantages of using frequency shifting when measuring in turbulent flows.

From the above discussions, three conclusions can be reached:-

1- Satisfactory and accurate results can be achieved from measurements with photon correlation LDV systems in flow conditions similar to the one under consideration.

2- During the planned experimental programme, if the number of channels per doppler cycle is kept over six, then better than 1% accuracy can consistantly be achieved.

3- The shape of the correlogram, particularly the level of noise involved i.e. the scatter of the points representing the counts in each channel, can be used as a criterion to determine the adequacy of the correlogram to render accurate results.

7.4.3 Limitations of the LDV system:

In the previous section, it was concluded that, as long as we can get a good, noise-free correlogram of at least six channels per doppler cycle, then we can be sure of an accurate measurement with an error level of less than 1%. To obtain a minimum of six channels in each doppler cycle requires adjustment of either the sample time

or the fringe spacing to match the flow velocity. Adjusting the fringe spacing can be accomplished by changing the separation and/or beam crossing angle. However in the regions of interest, i.e. the two recirculaton zones, the phase modulator is necessary, not only to sense the flow direction,but also to reduce the apparent turbulence intensity, and hence improve the quality of the correlogram. The phase modulator requires that the imput beams are to be parallel with fixed separation. Consequently the only way to control the fringe spacing is by changing the focusing lens located at the exit end of the phase modulator. Each time a lens is changed the whole optical system must be reset and realigned. The need to conduct radial traverses makes the technique very laborious.

Noise-free correlograms can be ensured by careful alignment of the optical system to ensure that the two beams cross at their waists. In addition, suitable apertures must be used to match the measuring control volume and mask light reflections from the solid boundaries of the test rig. This becomes more difficult as the point of measurement comes nearer to the walls. A. Boutier and J. Lefevre reported in Ref.(42) that they could not get satisfactory measurements at distances nearer to the walls than 0.3 mm when the beams were parallel to the wall. The limit was 2.5 mm when the wall was perpendicular to the optical axis. Also E.R. Pike stated in Ref.(40) that, "One of the major experimental problems in LDV, particularly in air-flow measurements, is the suppression of unwanted laser flare from glass windows or other surfaces in the path of the direct beam". Pike suggested that a possible solution of the problem is to use a phase locked laser which produces pulses of less than one n sec duration at each double transit time of the laser cavity. This is combined with fast electronic gating of the detected signal so that only photons originating from a particular point on the path of the laser beam are seen. By this method, windows can be placed in the beam path and are invisible to the detector. Such an instrument would be very expensive and very time consuming. The time and cost limitations imposed on this project would not permit the use of such a technique. Consequently, it was decided to use the present system to make all the possible measurements within its limitations.

CHAPTER EIGHT

8. DESIGN AND DEVELOPMENT OF THE "LDV" RIG:

8.1 Original design of the rig:

The original design of the LDV rig was based on the assumption that cast, clear, acryllic plastic tubes of high diameter-to-thickness ratio would be suitable for measurement with LDV, Ref.(61). Consequently both the primary and the secondary ducts were manufactured from cast clear acryllic plastic tubes of 1.5 mm nominal thickness. The following optimised dimensions resulted from the geometric optimisation tests descussed in chapter six, they are:

$D_1 = 47$ mm.

$D_2 = 72$ mm.

$y = 2.03$ mm.

$\phi = 18^\circ$

Fig.(8-1) illustrates the complete assembly of the test section on which the main dimensions and components are shown. The figure shows that both the primary and the secondary ducts were mounted concentrically on the flange of the inlet nozzle . The primary duct was supported on the inside of the secondary duct by three equi-spaced pins. The inside surface of the pins were finely machined to provide accurate coaxiality of the two ducts. The fence was fixed in position by small pins to avoid interference with the path of the laser beams. The detailed drawings, which were issued for the manufacture of the components of the test section, are presented in Appendix D.

Static pressure tappings were provided to masure the pressure in the primary duct, the secondary duct, and the vortex chamber. The tappings were made from 16 gauge hypodermic tubes. To ensure accuracy of measurement, three tappings were provided in the primary duct. They were located at a plane of 1.51 D_1 distance upstream of the exit lip and were set at 120 degrees spacing around the circumference. Five tappings were provided at equal spacings down the secondary duct in order to monitor the static pressure recovery. Two tappings were provided in the vortex chamber. All the static pressure tappings were connected via flexible plastic tubes through a scanning valve to the

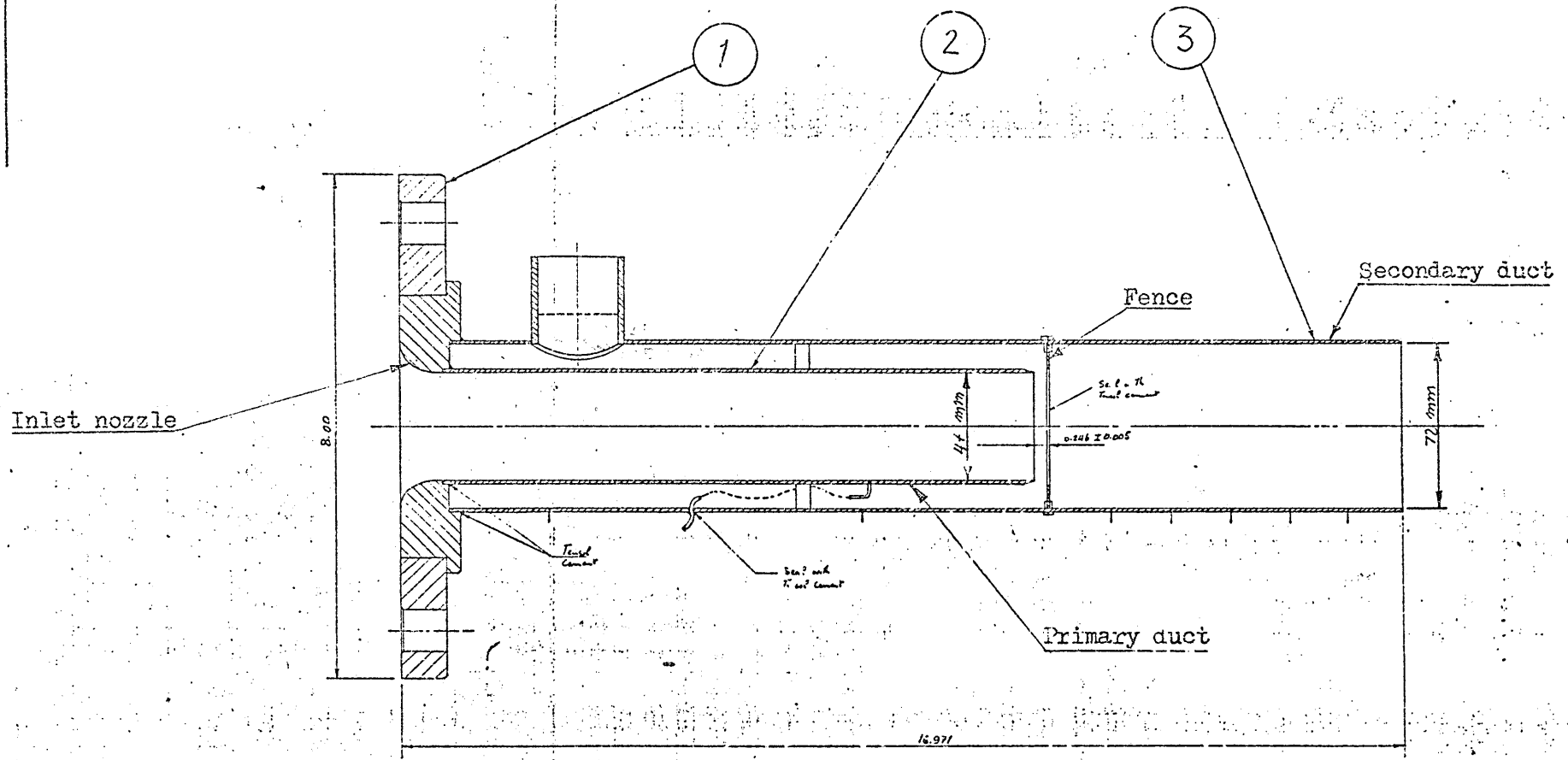

Fig.(8-1): The LDV rig, test section.

ITEM	PART No.	DESCRIPTION	No. OFF	MAT'L	SPEC.	REMARKS
1	PC12827	NOZZLE ASS	1	PERSPEX		
3	PC12820	SECONDARY DUCT	1	PERSPEX		
2	PC12819	PRIMARY DUCT	1	PERSPEX		

THIRD ANGLE PROJECTION

GENERAL TOLERANCE ON DIMENSIONS
MACHINED
UNLESS OTHERWISE STATED

JOB No.

No. OF SHEETS IN JOB: 1

SCALE: 1:1

FINISH: Self

SHEET SIZE: A1

DRAWN: S.A.L. 3.9.79

CHK'D

APPV'D

ISSUED BY: SALE

TITLE:- LDV RIG

CRANFIELD INSTITUTE OF TECHNOLOGY
CRANFIELD.

DRAWING No. PB 12818

SHT. 1 OF 1 SHEETS

micromanometer described in chapter six. The static pressure readings were used to evaluate the performance of the diffuser and also to monitor the diffuser operating conditions. The supply air pipework and bleed air system complete with instrumentation were taken from the previous rig used for geometric optimisation.

8.2 Development of test section:

Early measurements with the LDV, through the clear acryllic plastic walls of the secondary duct, produced very poor quality correlograms which eluded analysis, even at the most favourable location near the tube centre. At first, it was thought that the possible cause of the poor quality signal was the reflected light from the curved surfaces of the tube. Attempts were made to supress this type of reflection. These attenpts included the following:

1- The use of different designs of masks at the source and at the recieving optics.
2- Painting the components of the test section with a non-reflecting black paint except for a narrow slit left for the passage of the laser beams.
3- Exceptionally careful alignment procedures of the optics were followed.
4- The smallest available pinhole was used on the recieving optics which was also placed at a large oblique angle to the axis of symmetry.

All these measures, even when combined, resulted only in marginal improvement in the quality of the correlogram, and so it was concluded that the major cause of the problem was not due to the light reflections on the tube surface.

The major cause of the problem was discovered upon careful observation, using special goggles, of the points of crossing of the laser beams through the tube walls. It was noticed that the light was reflected on a great number of minute cracks in the depth of the tube material. This caused the whole tube to glow as the laser penetrated the tube walls.

The solution was to use optical quality glass windows for the passage

of the beams. Manufacturing cost of elaborate optical windows, similar to these mentioned in Ref.(39), would have been excessive. Furthermore the delivery period of such windows could not be tolerated due to the time restrictions imposed on the project. A simple solution was the use of ordinary microscope slides as windows. The microscope slides by virtue of their function are made of an optical quality glass. Furthermore they had dimensions which were suitable for use on the present rig. An experimental window was mounted in a matching slot in the secondary duct. The result was a dramatic improvement in the quality of the correlogram, plate (5). As a consequence of that success it was decided to adopt this simple solution. Fig.(8-2) is a diagramatic sketch illustrating the dimensions of the windows that was mounted on the secondary duct and extending beyond the fence over the region of interest in the vortex chamber. Two windows were used, one on each side of the duct, to facilitate measurements in both back and forward scatter modes. Two smaller windows were also mounted on the primary duct to enable measurement in the region of interest near the exit of the primary duct. Every possible care was taken to ensure that the windows were parallel and tangential to the surface of tube. Care was also taken to minimize the amount of intrusion by the glass inside the tube to ensure that the flow would not be disturbed by the presence of the windows. Plate (6) shows the final shape of the test section.

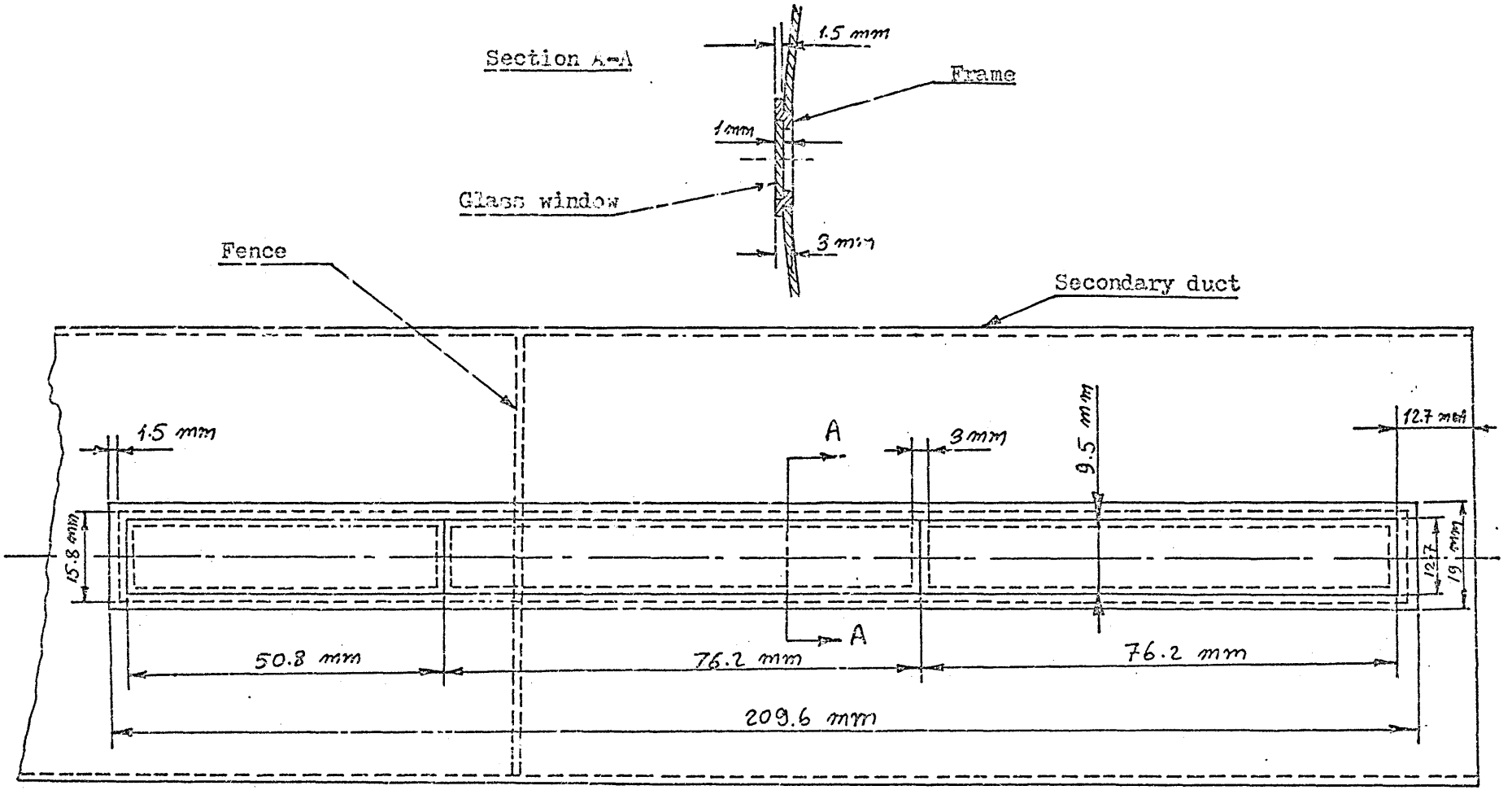

Fig.(8-2): Diagramatic sketch illustrating the glass window mounted on the secondary duct.

CHAPTER NINE

9. THE EXPERIMENTAL PROCEDURE AND CALCULATION OF RESULTS:

9.1 Fluidic tests:

At the beginning of the present experimental programme on the LDV rig, some preliminary fluidic tests were necessary, these can be summarized as follows:-

1- To assess the performance of the LDV diffuser model and to compare it with the performance of the geometric optimisation model as described in chapter six.

2- To assess the steadiness, the stability, and the symmetry of the flow at the precise runing conditions selected for the LDV tests.

3- To investigate, qualitatively, the flow behaviour inside the diffuser, particularly the size of the recirculation zone downstream of the fence.

4- To gain experience in the control of the flow so that its parameters could be fixed over long durations of testing. Accordingly, LDV measurements could be executed at constant flow conditions.

9.1.1 The diffuser performance and the flow control:

Fig.(9-1) shows a typical result taken from the tests conducted to assess the performance of the LDV diffuser model. The figure illustrates a comparison between the performance of the LDV diffuser model and the performance of the geometric optimisation model; the results show a good agreement between the performance of the two models.

The minimum bleed rate requirement operating condition, by definition, is a critical operating condition. A Cranfield diffuser operating at this particular bleed rate is likely to suffer from some instability in its performance as a result of small changes in running conditions. These changes could be due to external disturbances such as a slight reduction in the supply voltage of the suction fan or a slight change in Barometric pressure leading to a reduction in the bleed rate, the consequence of which would be a change in the flow pattern inside the diffuser. Consequently it was

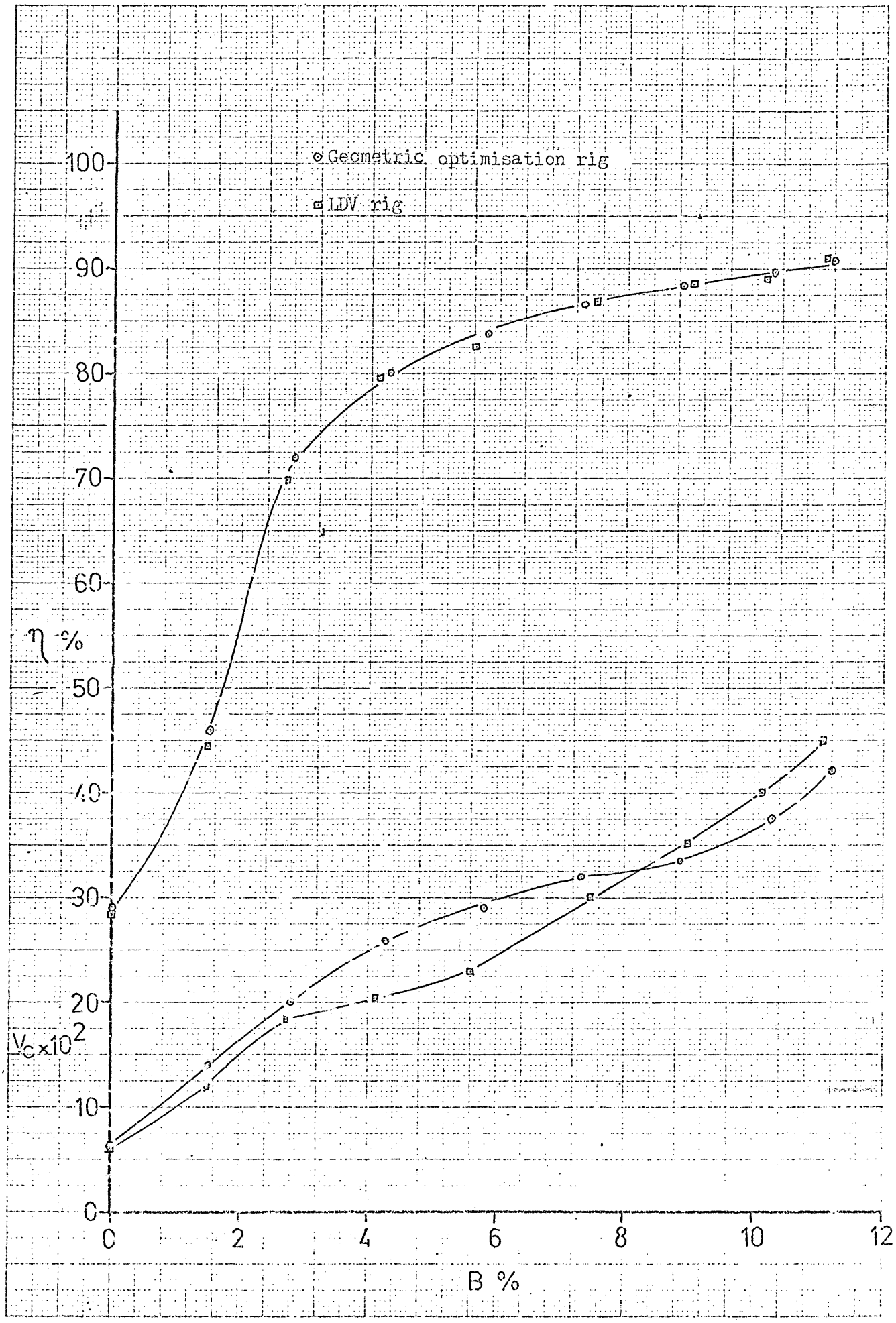

Fig.(9-1). The performance of the LDV model.

decided to conduct the detailed LDV measurement at a bleed rate higher than the minimum bleed rate requirement. A bleed rate of about 5% was felt adequate for this purpose.

Tests were conducted to determine the values of all the measurable fluidic parameters at this bleed rate for future use in setting up and control of the model. These values, table (9-1), were subject to small changes due to slight changes in the barometric pressure or the ambient temperature. To obviate this deficiency a special programme was written for the PET computer to facilitate a quick means of calculating the running conditions and the performance parameters on site. The programme was recorded on tape and was used at the beginning of each testing session to control the operating conditions.

Table (9-1)

The required values of the fluidic parameters.

p_z mbar	h_1 in H_2O	h_2 in H_2O	h_3 in H_2O	h_4 in H_2O	t C	p_B mm H_2O	t_B C	E_α %
1015	40	16	38.25	16.55	19	-759	5	67.5

E_β %	p_c mm H_2O	p_1 mm H_2O	p_2 I mm H_2O	p_2 II mm H_2O	p_2 III mm H_2O	p_2 IV mm H_2O	p_2 V mm H_2O
.0	-137	-104	-28.4	-13.3	-6.2	-2.75	-0.85

The values of the performance parameters of the diffuser when operating at these running condition were as follows:-

$$\eta = 81.2\%$$

$$C_p = 0.68$$

$$V_c = 0.218$$

9.1.2 Qualitative investigation of the flow:

The static pressure and the total pressure probes, described in chapter six, were used to investigate the stability, the steadiness, and the symmetry of the flow. The results showed that the flow

condition was satisfactory. The results of the total pressure probe measurements were also used as estimates for the velocity levels at various regions of the flow. These estimates were of particular importance in the selection of certain components of the transmitting optics. This will be discussed in detail later in this chapter.

A simple wool tuft mounted on a wand was used to estimate the size of the recirculation zone downstream of the fence. The observations showed that it occupied a length of about 25 mm, i.e about $\frac{1}{2}D_1$, downstream of the fence.

9.2 Flow parameters and the experimental grid:

The flow parameters to be measured were:

1- The axial mean velocity components, $\overline{U}_1$.
2- The radial mean velocity components, $\overline{U}_2$.
3- The axial normal Reynolds' stress, $\overline{u^2}$.
4- The radial normal Reynolds' stress, $\overline{v^2}$.
5- The tangential normal Reynolds' stress, $\overline{w^2}$.
6- The Reynolds' shear stress in the x-r plane, $\overline{uv}$.
7- The static pressure, p.

These were to be measured at all the nodes of a two dimensional grid system, referred to as the "experimental grid", covering the flow field, Fig.(9-2). The grid lines are parallel to the x-coordinate and the r-coordinate axis. The first ones were distinguished by the index(j), and the later ones by (i). The index (i) varies from (1) to (43) giving 43 grid lines. The index (j) varies from (1) to (23) giving 23 grid lines. The intersection of the grid lines, i.e. the nodes of the grid, were used as measurement stations. The first i-line was taken at a distance of 47 mm (i.e one primary duct diameter) upstream of the primary duct exit lip. The last i-line was taken at 119.5 mm downstream of the fence that is slightly more than 2.5 D_1. The first j-line was taken to coincide with the axis of symmetry and the last j-line was taken as coinciding with the inner wall of the secondary duct. The grid lines were packed together where the rate of change of the parameters were expected to be highest and vice versa. Table (9-2)a shows the r-coordinates of the j-lines and table (9-2)b shows the x-coordinates of the i-lines. The point of intersection of the first

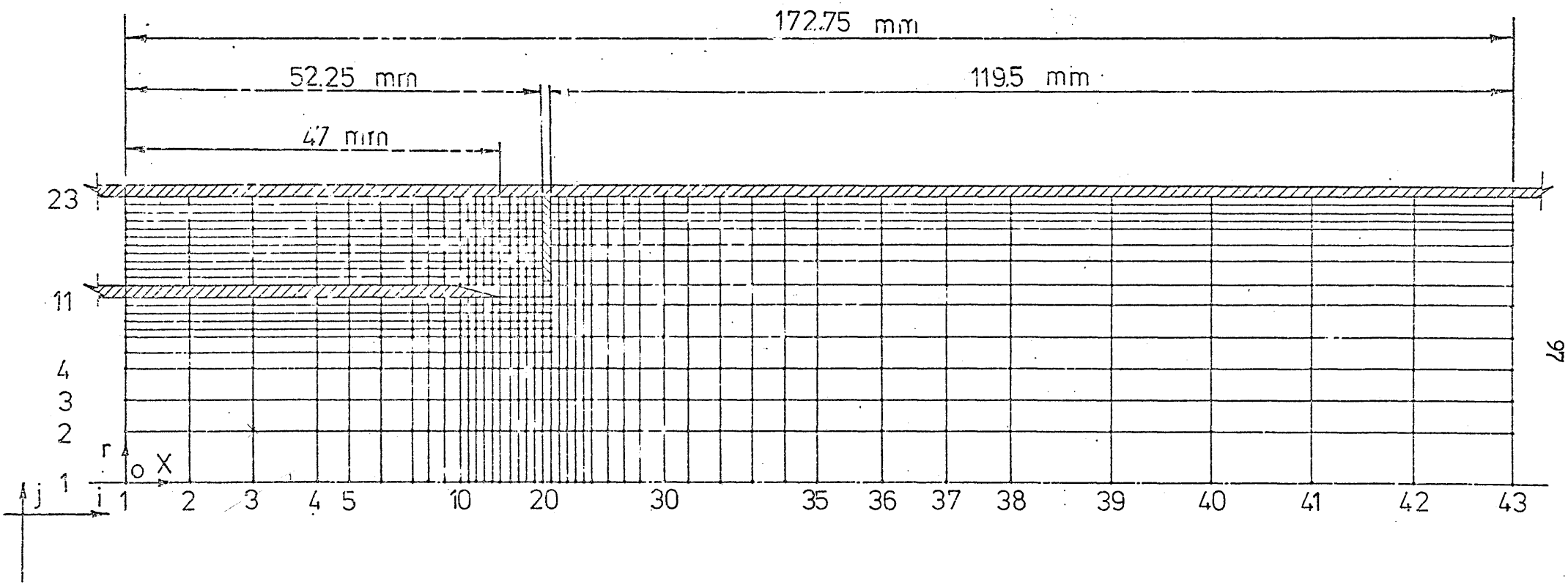

Fig.(9-2): The experimental grid.

j-line and the first i-line was taken as the origin of the coordinate system.

Table (9-2)a

The r-coordinates of the experimental grid j-lines.

j	1	2	3	4	5	6	7	8	9	10	11
r mm	0	6.5	10.5	14.5	16.5	18.5	19.5	20.5	21.5	22.5	23.5

j.	12	13	14	15	16	17	18	19	20	21	22	23
r mm	25	26	27	28	29	30	31	32	33	34	35	36

Table (9-2)b

The x-coordinates of the experimental grid i-lines.

i	1	2	3	4	5	6	7	8	9	10	11	12	13
x mm	0	8	16	24	28	32	36	38	40	42	43	44	45

i	14	15	16	17	18	19	20	21	22	23	24
x mm	46	47	48.25	49.25	50.25	51.25	52.25	53.25	54.25	55.25	56.25

i	25	26	27	28	29	30	31	32	33	34
x mm	57.25	58.25	60.25	62.25	64.25	67.25	70.25	74.25	78.25	82.25

	35	36	37	38	39	40	41	42	43
x mm	86.25	94.25	102.25	110.25	122.75	135.25	147.75	160.25	172.75

The static pressure was measured by the probe described in chapter six. The mean velocity components and the Reynolds' stress were to be calculated from the measurements of the LDV. The LDV measures the mean velocity, $\bar{V}$ and the turbulence intensity, T in the plane of the laser beams in a direction perpendicular to the axis of symmetry of the two beams. Four measurements were to be taken for each grid node. Three of these were to be taken with the two laser beams coinciding with the horizonal plane containing the axis of symmetry of the diffuser model. The axis of symmetry of the beams was set at an angle, θ to the axis of symmetry of the diffuser model. The angle, θ was different for each of the three measurements. From the three measurements the mean velocity components $\bar{U}_1$ and $\bar{U}_2$ and the Reynolds' stresses $\overline{u^2}$, $\overline{v^2}$, and $-\overline{uv}$

were calculated. The method of calculation can be referred to in Appendix E. The tangential normal Reynolds' stress component $\overline{w^2}$ was measured directly with the two beams coinciding with a perpendicular plane to the axis of symmetry of the diffuser model.

9.3 The procedure for setting and adjusting the optics of the LDV system:

9.3.1 Setting and adjusting the transmitting optics:

There are two cases to be considered. The first is when the frequency shifter, or the phase modulater, was not used, and the second case is when it was used.

9.3.1.1 Setting the transmitting optics without the frequency shifter:

An estimation of the level of the mean velocity was required so that the fringe spacing could be calculated and hence the beam separation, and the beam crossing distance could be determined. This is best illustrated by the following example. Supposing that the estimated value of the mean velocity, $\overline{V}$ was of the order of 40 m/s. The data processor requires at least six points per Doppler cycle to be able to analyse the correlegram, Ref.(53). Hence, both the sample time and the fringe spacing should be selected so that the correlogram would have at least six points per Doppler cycle. To accomodate reasonable level of errors in the estimation of the mean velocity, the required number of points per Doppler cycle, n was taken as ten. Operating the correlator at its maximum speed, i.e. the minimum possible sample time of 50 ns, hence the required Doppler period, τ was calculated from the formula, Ref.(52):

$$\tau = n \times (\text{sample time}) \qquad (2-1)$$

Hence,

$$\tau = 10 \times 50 \times 10^{-9} = 5 \times 10^{-7} \text{ s}$$

The fringe spacing, S was calculated from the formula:

$$S = \overline{V} \times \tau \qquad (9-2)$$

Assuming that, $\overline{V} = 40$ m/s

Hence,

$$S = 40 \times 5 \times 10^{-7} = 20 \ \mu\text{m}$$

But,

$$S = \frac{L}{D} \lambda \qquad (9-3)$$

Where,

L, is the beam crossing distance

D, is the beam separation

λ, is the laser light wave length

From equation (9-3)

$$\frac{L}{D} = \frac{S}{\lambda} = 31.6$$

If the beam separation was selected as:

$$D = 10 \text{ mm}$$

Hence, the beam crossing distance was to be set as:

$$L = 31.6 \text{ cm}$$

Selection of the ratio, $\frac{L}{D}$ does not only fix the fringe spacing S, but it also fix the dimensions of the measuring volume, the length, L_m, and the diameter, dm, Fig.(5-5).

The length, lm and the diameter dm were calculated from the formulae, Ref.(40):

$$lm = d_{\bar{e}^2} / \cos\theta \qquad (9\text{-}4)$$

$$dm = d_{\bar{e}^2} / \sin\theta \qquad (9\text{-}5)$$

Where $d_{\bar{e}^2}$ is the diameter of the beam at the focal point of the focusing lens. This can be calculated from the formula:

$$d_{\bar{e}^2} = \frac{4}{\pi} \cdot \frac{\lambda f}{D_{\bar{e}^2}} \qquad (9\text{-}6)$$

where,

f, is the focal length of the focusing lens.

$D_{\bar{e}^2}$, is the beam diameter before the focusing lens, Fig.(5-5).

If no focusing lens was used, then

$$lm = D_{\bar{e}^2} / \cos\theta \qquad (9\text{-}7)$$

$$dm = D_{\bar{e}^2} / \sin\theta \qquad (9\text{-}8)$$

To ensure a uniform spacing of the fringes, the two beams must cross at their waists, i.e at the focus of the focusing lens. This requirement impose a limitation on the selection of the crossing distance, L.

The conclusion is that both the beam separation, D and the beam crossing distance, L must be selected to give the best compromise between the fringe spacing and the size of the measuring volume.

Once, D and L were selected, the procedure for setting the transmitting optics was simple and is summarized as follows:

1- The rear knob, on the beam splitter, was manipulated so that the beam separation was fixed at the required value.

2- The front knob was adjusted so that the two beams crossed at the required distance.

3- The height of the carrying brackets were then adjusted so that the plane of the two beams coinsided with the horizontal plane containing the axis of symmetry of the diffuser model.

4- The optical bench, carrying the transmitting optics, was them tilted so that the axis of symmetry of the two beams intersected the axis of symmetry of the diffuser model at the required angle, .

5- The traverse table was then moved in the radial direction until the crossing point of the two beams fell on the inside face of the far window of the model. The traverse table scale reading was them taken and recorded. The traverse table was then moved radially backwards until the crossing point fell on the inside face of the near window of the model. The traverse table scale reading was then taken and recorded. The traverse table was then moved forward by a distance equal to half the difference between the two recorded readings.

6- The traverse table was then moved axially, then radially, for pre-determined distances so that the beam crossing point coincided with the required node on the experimental grid.

9.3.1.2 Setting the transmitting optics including the frequency shifter:

In the case of using the frequency shifter, no focusing lens was used prior to the beam splitter. For focusing the beams, in this case, reliance was put on the focusing lens placed after the frequency shifter. The selection of the ratio L/D, in this case, was governed by the same factors discussed in section 9.3.1.1. The only difference, however was that the frequency shifter required a constant beam separation of 20 mm, Ref.(49). Consequently, controlling the fringe spacing and the measuring volume size could only be achieved by changing the lens itself. The alignment of the transmitting optics, in this case, required

patience, skill, and experience. The procedure can be summarized as follows:-

1- The laser and the beam splitter were set so that the plane of the beams coincided with the horizontal plane containing the axis of symmetry of the diffuser model.

2- The front knob was then adjusted so that the beam separation was set at 20 mm.

3- The rear knob was then manipulated so that the two beams were parallel. This was achieved by measuring the distance between the beams at a far distance and ensuring that it was 20 mm.

4- The carrying brackets were then manipulated so that the two beams were parallel to the optical bench and their axis of symmetry was offset from it to the right (looking from the back) by 2.5 mm.

5- The vertically polarized light emerging from the beam splitter was rotated by 90° using the polarization rotator.

6- The frequency shifter, without the focusing lens, was then mounted on the optical bench. The height of the frequency shifter was adjusted by manipulating the three carrying screws and spring mechanisms. The adjustment was made so that the crystal was horizontal and the beams hits the input side of the frequency shifter at the middle of the crystal face.

7- A ray diagram of the required frequency shifter setting is given in Ref.(49). The output beams were centred about the optical bench axis 10 mm either side of it in the horizontal plane.

8- The previously selected focusing lens was then mounted in its special holder which was then mounted on the output end of the frequency shifter.

9- The correct voltage was then set by the "Adjust 2π" control on the control panel of the drive unit of the frequency shifter. The method which was used, Ref.(49), was to place a very short focal length lens at the beam crossing point. A screen was then placed at a suitable distance behind the lens so that the fringes were clearly seen. The "Adjust 2π" was manipulated until the fringes disappeared completly, i.e. a condition of zero fringe visibility was reached.

The remainder of the procedure was similar to that described in section 9.3.1.1.

9.3.2 Setting and adjusting the receiving optics:

A ray diagram for the aligmment of the receiving optics is given in Ref.(50). The parameters which were to be determined before the aligmment of the receiving optics are, Fig.(9-3):

1- The effective or reduced measuring volume length, l'_m.
2- The distance from the focusing lens to the measuring volume, f.
3- The angle between the optical axis of the receiving optics and the axis of symmetry of the two beams, θ.
4- The distance between the focusing lens and the pinhole, f_a.
5- The diameter of the pinhole, d_a.

The relation between these five parameters was given by the formula, Ref.(40):

$$l'_m = d_a \frac{f}{f_a \sin\theta} \qquad (9\text{-}4)$$

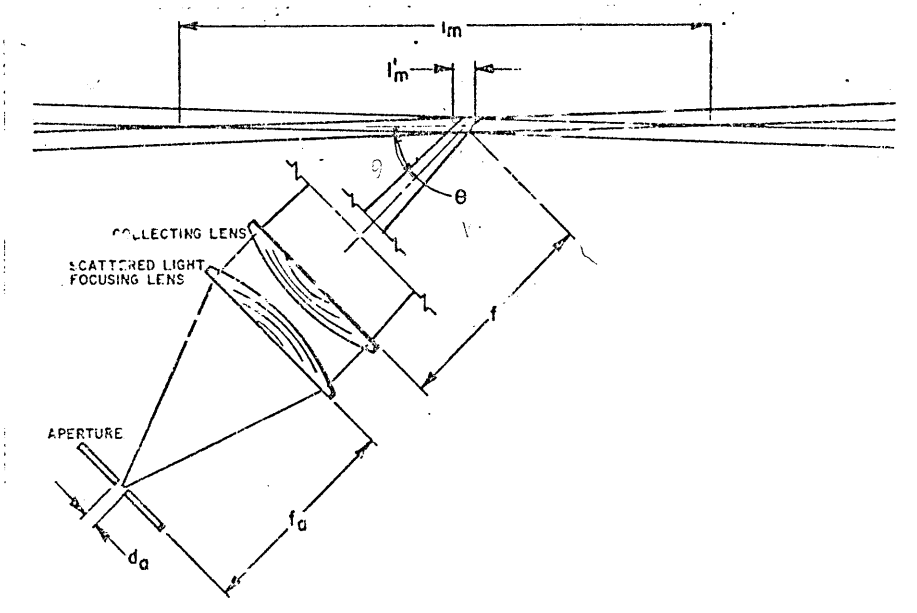

Fig.(9-3): Reducing the effective length l_m.

The required reduced measuring volume length, l'_m was selected according to the conditions of measurement. A typical value of l'_m was 2 mm. The receiving optics was fitted with a focusing lens of the telephoto type. Consequently, both f and f_a were not required to

be selected or set acurately. However, estimates of their values were required to establish a relation between d_a and $\sin\theta$ from equation (9-9). The value of f was selected according to the available space for the movement of the receiving optics assembly. The value of f_a was selected according to the length of the available spacer pieces. There were two spacer pieces available of length 2.5 cm and 6.5 cm respectively.
spacer piece of 9 cm length. Once lm, f, and f_a were selected, a relation between d_a and $\sin\theta$ was established. The value of the angle, θ was also selected according to the available space for the movement of the receiving optics. Finally the diameter of the pinhole d_a was calculated from equation (9-9). The nearest available pinhole was used. The diameters of the available pinholes were 100 μm, 200 μm, and 400 μm. Once the values of the previously discussed parameters were determined, the procedure for the setting and adjustement of the receiving optics was simple, and can be summarized as follows:

1- The suitable pinhole and spacers were mounted on the receiving optics assembly.
2- The receiving optics assembly was placed at the required distance f and angle, θ.
3- The "X10 eyepiece" was removed and the receiving optics was aimed towards the measuring volume. The telephoto lens was then manipulated to give a focused image of the measuring volume as near as possible to the pinhole.
4- The "X10 eyepiece" was then placed in its position. Looking through the "X10 eyepiece", both the Y-control and the x-control knobs were manipulated so that the image of the measuring volume was focused exactly onto the pinhole.
5- The reflex mirror was then rotated so that an image of the cross over area was seen on the cross wire eyepiece. The centre of the measuring volume was then checked to coincide with the cross wires, otherwise further adjustment was made to place it in this position.

9.4 The overall experimental procedure:

A systematic procedure was followed for the conduction of the LDV

experiments, this can be summarized as follows:

1- The transmitting optics was set and adjusted following the procedure described in section (9.3.1).

2- The receiving optics was then set and adjusted following the procedure described in section (9.3.2).

3- With the laser switched off, both the supply fan and the suction fan were started following the manufacturer's instructions.

4- The inlet flow control valve and the suction fan throttle valve were set at a pre-determined positions. The flow was then left to settle down for about twenty minutes.

5- The PET computer was switched on and the flow control programme, was loaded. The flow parameters were read and directly fed into the computer. The inlet flow control valve and the flow meter valves were manipulated until the required flow conditions, as described in section (9.1.1), were achieved and stabilized.

6- The laser was then switched on and the data-processor was switched off.

7- The frequency shifter was then switched on. With the drive selector on the neutral position, the frequency selector was set to the pre-determined value of the shifted frequency. The drive selector was then set to the required position, either drive or reverse.

8- The correlator store, the correlator, the oscilloscope, the data processor, and the printer were switched on in the order of mentioning.

9- The data processor programme was then loaded, consequently, the correlator was under the control of the data processor. The experiment execution programme of the data processor was executed.

10- Once the programme was fully executed, the results were printed out and hence the experiment was completed.

11- The traverse table was moved so that the measuring volume coincided with the next required experimental grid node and then the next measurement was taken.

12- At the end of the testing session a switching-off procedure was followed. This was exactly the reverse of the switching on procedure.

Throughout the present experimental programme, the data processor was used to control the correlator and to calculate the results. The

processor computer programme required to accomplish this was supplied by Malvern Instruments. A print-out of the programme togther with its description can be found in Ref.(53).

9.5 The algorithm used by the data processor to calculate the results:

This section is provided as a guide to the formulae used in the processor programme to calculate the mean velocity, $\bar{V}$ and the turbulence intensity, T from the correlogram data. It is not intended as a theoretical derivation, this is not of interest in the present thesis and can be referred to in Ref.(53), Ref.(41), and Ref.(60).

The measurement with the photon correlator yields a correlogram, plate (5), giving information about the probability distribution of velocities that occurred in the measuring volume during the measurement. A typical correlogram is shown diagramatically in Fig. (9-4). The most striking feature of the correlogram is its cosinusoid shape which is due to the intensity fluctuations caused by the scattering particles crossing the fringes and modulating the scattered light. A first estimate of the mean velocity may be obtained by measuring the period of this cosinusoid, i.e. measuring the rate of fringe crossing. However, this mean velocity estimate would be subject to a systematic error due to the effects of both turbulence and finite beamwidth, Ref.(53).

The data processor programme uses the first turning points p_1, p_2, and p_3 of the correlogram, Fig.(9-4), for the calculation of the mean velocity, $\bar{V}$ and the turbulence intensity, T. The amplitudes of the turning points; g_1, g_2, and g_3 and the delay times at which they occur, t_1, t_2, and t_3 respectively, are all the data required of the correlogram to produce the mean velocity, $\bar{V}$ and the turbulence intensity, T. The processor programme must therefore locate the amplitude, g and the delay time, t of each of the three turning points. This is achieved by differentiation of the correlogram, and locating the zero crossings of the resultant function. The differentiation is performed by subtraction of adjacent channels. For channels h and $(h + 1)$ this gives an estimate for the delay time $(h + \frac{1}{2})$ This procedure locates each turning point to within one channel resolution of the correlator. The exact turning point is located using a parabolic

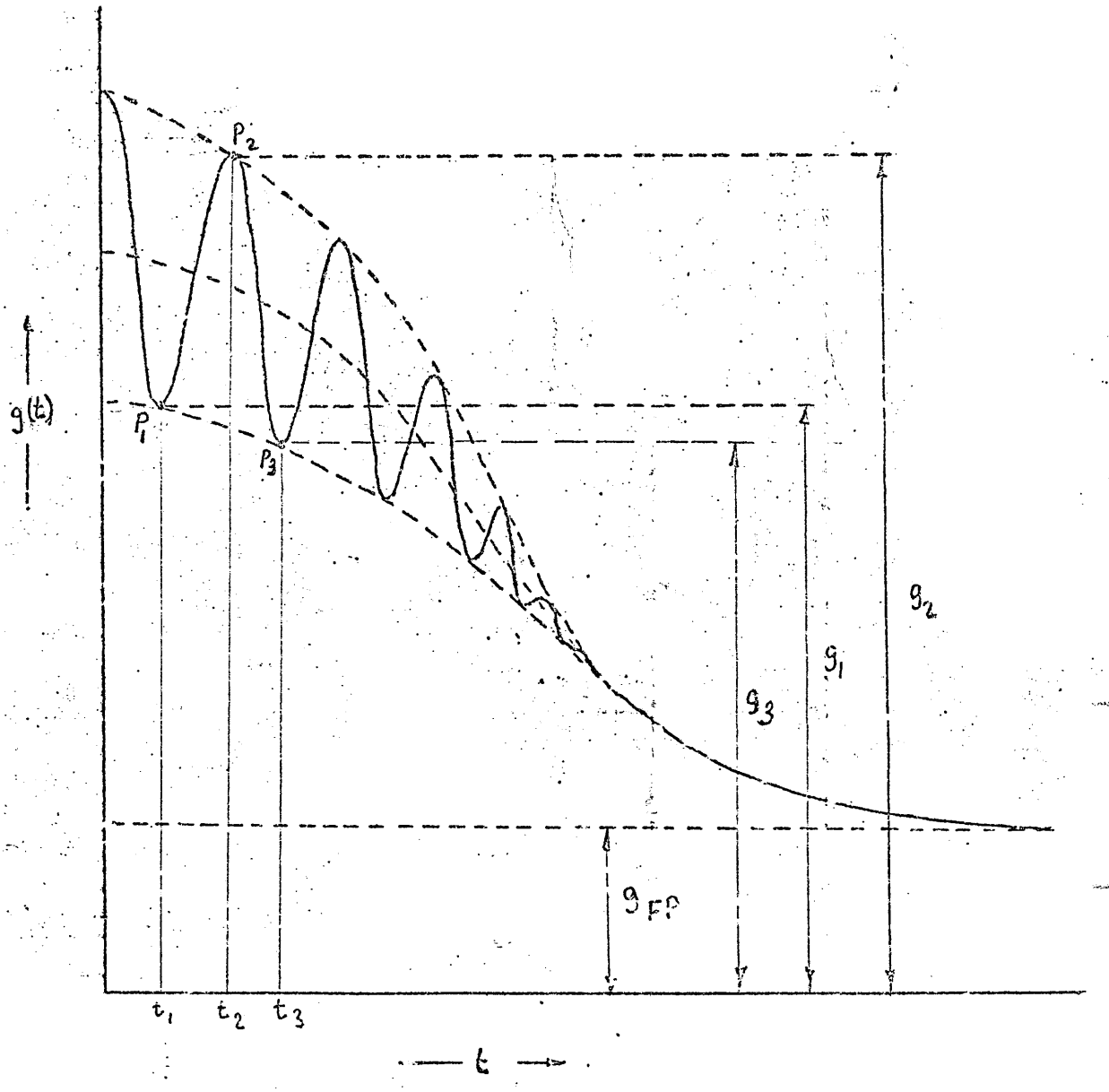

Fig.(9-4): Diagrammatic representation of a typical correlogram.

interpolation over the three points that bracket it. This is fully explained in Ref.(53).

Having calculated g_1, g_2, g_3 and t_1, t_2, t_3 the programme proceeds as follows:

1- The far point amplitude, g_{FP} is calculated from the formula:

$$g_{FP} = \frac{AU \cdot AC}{TS} \qquad (9\text{-}10)$$

where,

AU, Unclipped channel

AC, clipped channel

TS, total samples.

2- The number of fringes in the beam radius, r, denoted by n, is determined from:

$$n = \frac{r}{S} \qquad (9\text{-}11)$$

Where S is the fringe spacing as calculated from equation (9-3).

3- The measured turbulence intensity, T_m is calculated from the formula:

$$T_m = \frac{1}{n}\sqrt{\frac{1}{2}(R-1) + \frac{1}{8n^2}} \qquad (9\text{-}12)$$

Where, the ratio R is calculated from the formula:

$$R = \frac{g_2 - g_1}{g_2 - g_3} \qquad (9\text{-}13)$$

4- The effective fringe visibility, m is empirically determined from, Ref.(53):

$$m = \frac{2(g_2 - g_1)}{(g_2 + g_1 - 2g_{FP})} \qquad (9\text{-}14)$$

5- The average delay time, t_{av} is calculated from the formula:

$$t_{av} = \frac{1}{3}(t_1 + t_2 + t_3) \qquad (9\text{-}15)$$

6- The observed mean velocity, $\bar{V}_o$ is determined from the formula:

$$\bar{V}_o = \frac{S}{\tau \cdot t_{av}} \qquad (9\text{-}16)$$

where, τ is the sample time.

7- The measured mean velocity, $\bar{V}_m$ is calculated from the formula, Ref.(53):

$$\bar{V}_m = \bar{V}_o \left[1 - T_m^2 - \frac{1}{m^2 n^2 \pi^2}\left(1 + \frac{m^2}{2}\right)\right] \qquad (9\text{-}17)$$

If the frequency shifter was used, both the mean velocity and the turbulence intensity were to be corrected for the effect of the shifted frequency. The formula which were used for the corrections were:-

$$\overline{V_t} = \overline{V_m} \pm S/f_s \qquad (9\text{-}18)$$

$$\overline{T_t} = \overline{T_m}\,(V_m/V_t) \qquad (9\text{-}19)$$

where,

V_t is the true mean velocity.
V_m is the measured mean velocity.
S is the fringe spacing.
f_s is the shifted frequency.
T_t is the true turbulence intensity.
T_m is the measured turbulence intensity.

CHAPTER TEN

10. RESULTS AND DISCUSSIONS:

10.1 Introduction:

It may be recalled that the prime object of the present part of this study was to obtain enough information about the velocity distribution and the turbulence structure so that the flow behaviour inside the Cranfield diffuser could be understood. The information were obtained from a long and laborious experimental programme. This chapter was intended to present and discuss these experimental results.

10.2 Method of presentation of the results:

The results of the static pressure measurements are presented in Appendix F1, which contains eight figures numbered from Fig.(F1-1) to Fig.(F1-8). In each figure the local static pressure recovery parameter, $(p-p_o)/\frac{1}{2}\rho U_o^2$, was plotted versus the radius, r, for different axial distances, X, as indicated on the figures. The reference static pressure, p_o, was the area averaged static pressure at the datum plane, X = 0. The reference velocity, U_o, was the nominal inlet axial velocity which, in this case was 50m/s.

The distribution of the non-dimensional axial component of the mean velocity, $\overline{U}/U_o$, is shown in Appendix F2, which contains eleven figures numbered from Fig.(F2-1) to Fig.(F2-11). Each figure consists of a number of velocity profiles measured at different axial distances, X, as indicated on the figures. Similarly, the non-dimensional radial component of the mean velocity, $\overline{V}/U_o$, is presented in Appendix F3 which contains eight figures with numbers from Fig.(F3-1) to Fig.(F3-8).

The flow was treated as being incompressible, i.e the density, ρ, was considered constant. Therefore, $\overline{u'^2}$, $\overline{v'^2}$, $-\overline{u'v'}$, and $\overline{w'^2}$. were proportional to the Reynolds' stresses, $\rho\overline{u'^2}$, $\rho\overline{v'^2}$, $\rho\overline{u'v'}$ and $\rho\overline{w'^2}$ respectively. Those were non-dimensionalized by dividing them by U_o^2. The distributions of the non-dimensional Reynolds' stresses, $\overline{u'^2}/U_o^2$, $\overline{v'^2}/U_o^2$, $-\overline{u'v'}/U_o^2$ and $\overline{w'^2}/U_o^2$ were presented in the Appendices F4, F5, F6 and F7 respectively.

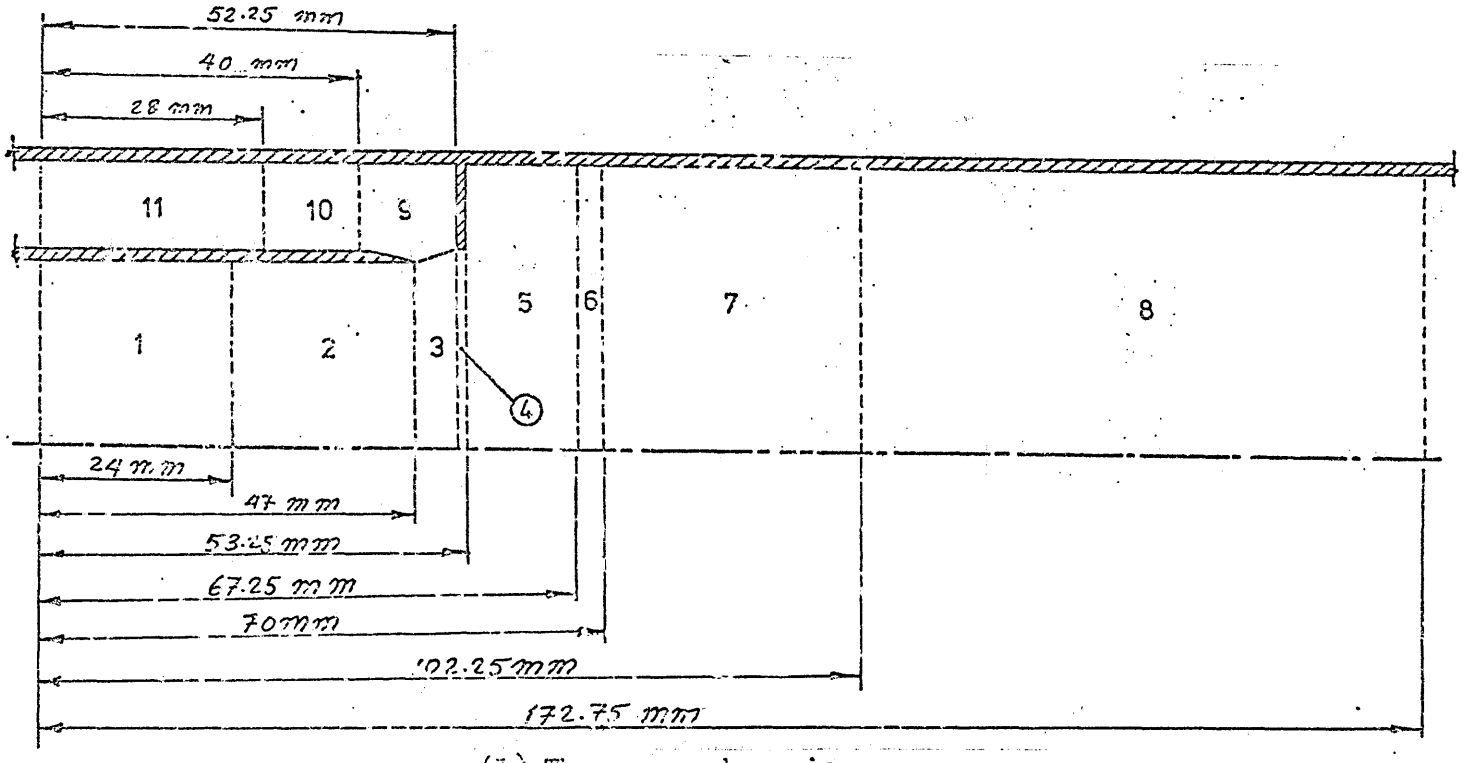

(1) The approach region.
(2) The region of the sink effect.
(3) The separation region.
(4) The fence region.
(5) The recirculation region.
(6) The reattachment region.
(7) The recovery region.
(8) The settling region.
(9) The vortex region.
(10) The bled air diffusion region.
(11) The bled air settling region.

Fig.(10-1): The flow regions.

The profiles showing the distribution of the non-dimensional kinetic energy of turbulence, k/U_o^2 , were presented in Appendix F8, which contains eleven figures numbered from Fig.(F8-1) to Fig.(F8-11). In each figure, k/U_o^2 was plotted against the radius, r, for different axial distances, X, as indicated.

10.3 Discussion:

For the purpose of the discussion, the flow field was divided into eleven regions each having its own distinctive characteristics. Fig.(10-1) is a diagrammatic sketch showing the position and dimensions of these regions. The results obtained from each region are discussed in a separate section. In each section the order of discussion is as follows:

(a) The static pressure distribution.
(b) The distribution of the mean velocity.
(c) The distribution of the Reynolds' stresses.
(d) The distribution of the kinetic energy of turbulence.

This is followed, at the end of each section, by a general discussion about the behaviour of the flow in that particular region.

10.3.1 Region (1), "approach region".

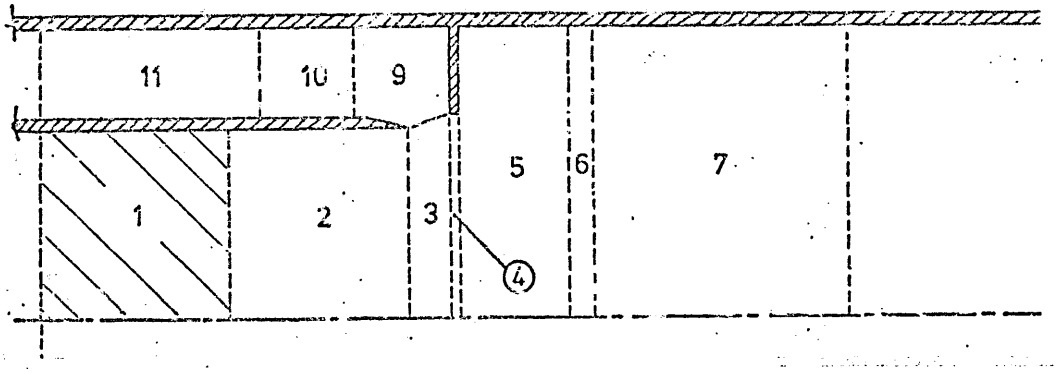

10.3.1.1 The static pressure distribution:

This region is characterized by a general slight decrease in the level of the static pressure as the flow progresses downstream. The profiles, Fig.(F1-1), also show a small increase in the measured static pressure near the wall. This is probably due to the effect of the higher level of turbulence in the neighbourhood of the wall. As the flow reachs the downstream boundary of this

region, X = 24mm, the static pressure near the centre of the flow stops decreasing.

Another interesting feature of the static pressure distribution at this plane is the appearance of a slight dip in the profile at a radius of about 18.5 mm, i.e at a distance of about 5mm from the wall.

10.3.1.2 The mean velocity distribution:

The profiles of the axial component of the mean velocity, Fig.(F2-1), are characterized by a progressive increase in the value of $\overline{U}/U_o$ at the core of the flow, as the flow proceeds downstream. For continuity reasons, this is accompanied by a progressive decrease in $\overline{U}/U_o$ in the region adjacent to the wall.

The mean velocity in this region had no radial component indicating that the flow was axial and parallel.

10.3.1.3 The Reynolds' stresses distribution:

The profiles showing the distribution of the normal Reynolds' stresses $\overline{u'^2}/U_o^2$ and $\overline{v'^2}/U_o^2$, Fig.(F4-1) and Fig.(F5-1), are quite similar particularly at the core of the flow. Their values are relatively low, of the order of 1.0×10^{-3}, and are nearly uniform up to a radius of about 16mm. This indicates that the turbulence in this region is fairly isotropic and homogeneous. Nearer to the wall, $\overline{u'^2}/U_o^2$ increases with a higher rate than does $\overline{v'^2}/U_o^2$. At the radial position of their peaks, which is the same for both of them and is at r = 21.25mm, there is a significant difference between their magnitudes. This difference increases progressively as the flow approaches the downstream boundary of this region.

As expected the Reynolds' shear stress $\overline{u'v'}/U_o^2$ has a negative value Fig.(F6-1), because the measurements were taken at the far side of the duct. The values of $-\overline{u'v'}/U^2$ are of the same order of magnitude of both $\overline{u'^2}/U_o^2$ and $\overline{v'^2}/U_o^2$. The radial position at which $-\overline{u'v'}/U_o^2$ reaches its peak value is also the same as that of both

10.5

$\overline{u^2}/U_o^2$ and $\overline{v^2}/U_o^2$ which is r = 21.25mm. At the exit boundary of this region the peak values of $\overline{u^2}/U_o^2$, $\overline{v^2}/U_o^2$ and $-\overline{uv}/U_o^2$ are 4.1×10^{-3}, 2.5×10^{-3} and 4.2×10^{-3} respectively.

It was not possible to measure $\overline{w^2}/U_o^2$ in this region. It is believed that the reason for this is that the value of $\overline{w^2}/U_o^2$ in this region was too low to be detected by the LDV which was used.

10.3.1.4 The distribution of the kinetic energy of turbulence:

The profiles of the kinetic energy of turbulence, Fig.(F8-1), also indicate that turbulence levels at the core of the flow are fairly weak but that it is both isotropic and homogeneous. Near to the wall the value of k/U_o^2 increases until it reaches its maximum value at about 2 mm away from the wall. The profiles maintain these features except for a continuous increase in the peak value as the flow progresses downstream. The peak value of k/U_o^2 at the downstream boundary of this region is about 3.2×10^{-3}.

10.3.1.5 The flow behaviour in the approach region:

From the above discussions it can be concluded that the flow in the approach region behaves in a similar manner as turbulent flows in the approach length at the entrance of a pipe. The reason behind the relatively low values of the Reynolds' stresses and the kinetic energy of turbulence is believed to be the effect of the carefully contoured inlet nozzle. At the downstream boundary of this region, X = 24 mm, the flow does not reach the condition of a fully developed pipe flow, i.e the boundary layer does not grow to physically fill the whole cross section of the primary duct. At this plane the sink effect, resulting from the suction at the entrance of the vortex chamber, begins to be noticeable.

10.3.2 Region(2), "the region of the sink effect":

10.3.2.1 The static pressure distribution:

The distribution of the static pressure in this region, Fig.(F1-2), is characterized by a continuous increase in the

static pressure at the core of the flow as it progresses downstream. It can also be seen from the profiles that the cross-section of this core is expanding as the flow progresses downstream. A more striking feature of the profiles is that the dip, which was first noticed at the plane X = 24 mm, is not only becoming deeper but also moves towards the wall as the flow proceeds downstream.

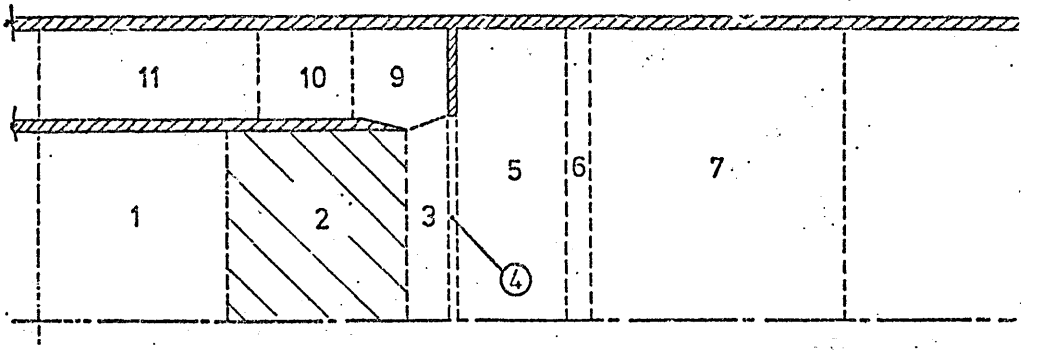

10.3.2.2 The distribution of the mean velocity:

The profiles of the axial component of the mean velocity, Fig.(F2-2), indicate that the fluid at the core of the flow decelerates progressively as the flow approaches the exit lip. Furthermore, the cross-sectional area of this core expands as the flow progresses downstream.

Closer to the wall there is a region of progressively increasing velocity, the result is a progressively steeper velocity gradient in the immediate vicinity of the wall as the flow proceeds downstream. The combination of the decelerating flow, near the centre of the diffuser, and the accelerating one in the neighbourhood of the wall has the effect of moving the position of the peak of the velocity profile from the centre of the flow nearer to the wall, as the flow progresses downstream. Near the exit lip, the velocity profiles have a distictive hate shape.

In this region, the flow does not posses a significant radial velocity component, Fig.(F3-1), until further downstream i.e at X = 40 mm.

At this plane, the flow in the neighbourhood of the wall which is accelerating in the axial direction has negative values of $\overline{V}/U_o^2$.

This decreases progressively as the flow proceeds further downstream towards the primary duct exit lip.

At the exit boundary of this region, X = 47 mm, the radial component of the mean velocity nearly vanishes. This means that the flow in the neighbourhood of the wall regains its axial motion at the plane of the primary duct exit lip.

10.3.2.3 The distribution of the Reynolds' stresses:

The profiles of the axial normal Reynolds' stress, Fig.(F4-2), show that $\overline{u^2}/U_o^2$ increases very rapidly as the flow proceeds downstream. The rate of increase is maximum at the position of profile peak, r = 21.25 mm. At the exit boundary of this region, X = 47 mm, the value of $\overline{u^2}/U_o^2$ at the centre of the flow was 6.2×10^{-3}, this is 4.4 times its value at the inlet boundary, of this region. The value of $\overline{u^2}/U_o^2$ at the peak of the profile at the exit boundary was 21.6×10^{-3}, which is 4.7 times its value at the inlet boundary.

The distribution of the radial normal Reynolds' stress, Fig.(F5-2), shows that $\overline{v^2}/U_o^2$ has the same tendency to increase rapidly as the flow proceeds downstream except that the ratio between the rate of increase at the position of the peak value and that at the centre of the flow is much higher in this case.

At the centre of the flow $\overline{v^2}/U_o^2$ takes the values 0.9×10^{-3} and 1.9×10^{-3} at the inlet and exit boundaries of this region respectively. This gives a ratio of about 2.1:1 which is less than half that of $\overline{u^2}/U_o^2$. At r = 21.25, which is the position of the peak of the profiles, $\overline{v^2}/U_o^2$ takes the values 2.9×10^{-3} and 19×10^{-3} at the inlet and exit boundaries of this region respectively. This gives a ratio of about 6.6:1 which is about 1.4 times that of $\overline{u^2}/U_o^2$.

The above mentioned changes of $\overline{u^2}/U_o^2$ and $\overline{v^2}/U_o^2$ can be partially explained at least qualitatively by relating the local values of these two parameters and also their local rates of change to the corresponding velocity gradients. This is an over-simplification

of the problem but it does explain the high rate of change of $\overline{v'^2}/U_o^2$ in the neighbourhood of the wall since $\overline{V}$ is equally dramatically changing in this region. The exact relationship between the normal Reynolds' stresses and the magnitudes and gradients of their corresponding mean velocity components is very complex and is sufficiently important to merit a separate study limited to this one phenomenon.

The distribution of the Reynolds' shear stress, Fig.(F6-2), is more complex than that of $\overline{u'^2}/U_o^2$ or $\overline{v'^2}/U_o^2$. Near the inlet boundary of this region the profile of $-\overline{u'v'}/U_o^2$ is similar to those of $\overline{u'^2}/U_o^2$ and $\overline{v'^2}/U_o^2$. Downstream of that boundary the value of $-\overline{u'v'}/U_o^2$ decreases very rapidly over the whole cross-section of the flow. The decrease continues until the shear stress reverses its sign. At X = 44 mm the shear stress has its minimum value of about -6×10^{-4} at r = 15.4 mm aproximately. Downstream of this plane the dip in the profile of $-\overline{u'v'}/U_o^2$ moves towards the wall and the profile becomes flatter.

The reversal of the sign of the Reynolds' shear stress coincides with a reversal of the sign of the gradient of the axial component of the mean velocity. This indicates that energy is fed from the flow region which are accelerating under the influence of the sink into the boundary layer.

The tangential normal Reynolds' stress, $\overline{w'^2}/U_o^2$, was only measurable at and downstream of the plane X = 40 mm. The values of $\overline{w'^2}/U_o^2$ in this region are so small that they can be neglected compared to $\overline{u'^2}/U_o^2$ or $\overline{v'^2}/U_o^2$.

10.3.2.4 The distribution of the kinetic energy of turbulence:

The profiles of the kinetic energy of turbulence in this sink region, Fig.(F8-2), show that the value of k/U_o^2 increases progressively over the whole cross-section of flow as it proceeds downstream. The rate of increase at the core of the flow is very low compared with that in the neighbourhood of the wall where the peaks of the profiles are located. The result is that the profiles tend to be more peaky as the flow proceeds downstream. The peak

value of k/U_s^2 at the plane of the exit lip is about 20.7×10^{-3} and the corresponding value at the centre of the flow is about 4.2×10^{-3}.

10.3.2.5 The flow behaviour in the sink region:

From the above discussion, the main features of the flow in the sink region can be summarized as follows:

1- The sink effect resulting from the suction at the vortex chamber entrance penetrates upstream to a distance of about $\frac{1}{2} D_1$. The result is a drop in the static pressure accompanied by a progressive acceleration of the fluid in the region adjacent to the boundary layer.

2- In the early part of the sink region, the accelerating layer possesses, for continuity reasons, a negative radial mean velocity component. This radial component is lost very rapidly in the later part of this region and the accelerating layer regains its axiality at the plane of the exit lip.

3- The accelerated stream tube is also accompanied by, for continuity reasons, the deceleration of the core of the flow. This confirmed by the static pressure measurements which indicated that the pressure is progressively increasing at the core of the flow as it proceeds towards the primary duct exit lip.

4- The combination of the decelerating flow core and the accelerating layer in the neighbourhood of the wall has the effect of producing a distinctive hat shape velocity profile. This is charactarised by a reversal in the sign of the velocity gradient and consequently on the reversal of the shear stress. The velocity profile also has a steeper velocity gradient in the near vicinity of the wall. These two features have the effect of promoting the transfer of energy from the accelerating layer to the boundary layer and hence offsetting the effect of the adverse pressure gradient that would have otherwise been experienced by the boundary layer without the presence of the sink effect.

5- The increase in the normal Reynolds' stresses indicates that the turbulence intensity is also increasing very rapidly in the layer adjacent to the wall. This has the effect of increasing the mixing between the accelerating layer and the boundary

layer and hence promoting the energy transfer process.

10.3.3 Region (3), "the separation region":

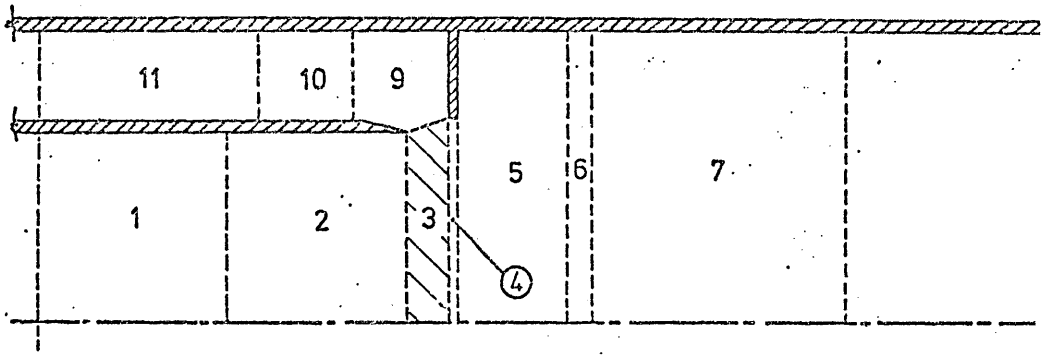

10.3.3.1 The static pressure distribution:

The static pressure profiles, in this region, indicate that the static pressure at the core of the flow continues to rise as the flow proceeds from the plane of the primary duct exit lip towards the fence, Fig.(F1-3) and Fig.(F1-4). The results also indicate that the depression in the profiles continue to get deeper immediatly downstream of the lip. Further downstream the depression gets shallower and closer to the flow centre as the flow proceeds towards the fence. There are two likely reasons for this, the first is the progressive deceleration of the stream tube coinciding with the depression, and the second is the strong effect of the growing shear layer which tends to increase the apparent static pressure due to the effect of strong turbulence in the shear layer. It is very difficult to differentiate between the two effects because the extent of the influence of the second one is not known, but it is expected to be a strong one, Ref.(33),(62) and (63).

10.3.3.2 The distribution of the mean velocity:

The profiles of the axial velocity component of the flow, Fig.(F2-3), indicate that the fluid, over the whole cross-section of the main flow, decelerates as it proceeds towards the fence. The deceleration is minimum at the centre of the flow. This trend is reversed for the outer stream tubes, i.e the rate of reduction of the axial component of the mean velocity increases w.r.t r and X. For continuity reasons therefore, this is accompanied by a

rapid increase in the radial velocity component, Fig.(F3-2).

10.3.3.3 The distribution of the Reynolds' stresses:

The distribution of the Reynolds' stresses indicates the formation of a strong shear layer as the flow separates from the exit lip of the primary duct. This is indicated by sudden increase in the peak values of the stresses in a very short axial distance. At the lip plane the peak value of $\overline{u^2}/U_o^2$ was 21.6 x 10^{-3} while only 1.25 mm downstream of the lip this value jumps to 34.5 x 10^{-3} Fig.(F4-3). The corresponding values for $\overline{v^2}/U_o^2$, Fig.(F5-3), are 19 x 10^{-3} and 29.2 x 10^{-3} respectively. A much higher rate of increase is noticed for $-\overline{uv}/U_o^2$, Fig.(F6-3), which had the peak value of about 3.2 x 10^{-4} at the plane of the lip jumping to 24.5 x 10^{-3} at the plane of 1.25 mm downstream, an increase of nearly one order of magnitude in a distance of about 1.25 mm.

At the time of measurement, these unusually high rate of increase in the level of the Reynolds' stresses was thought to include a high level of error. Consequently the results were checked and rechecked. The final results confirmed the previously mentioned values. There are two likely explanations for this phenomenon. The first is that it is a genuine phenomenon uniquely characterising this particular type of flow. The second, which is more likely, is that the reported values as being the peak values of the Reynolds' stresses at the plane of the lip are not real peak values and that the Reynolds' stresses continue to increase to reach higher peak values closer to the wall. This is supported by the presence of a thin boundary layer at the plane of the lip. This could not be detected because the nearest distance to the wall at which measurement was possible with the LDV was 2 mm. The author of this thesis is more inclined to accept the second explanation.

Nevertheless, the fact remains that a strong shear layer is formed as a result of the separation from the lip of the primary duct.

Further downstream, the shear layer expands radially as the flow

proceeds. This indicated by the change in the shape of there profiles in which the peaks shift to larger radii.

10.3.3.4 The distribution of the kinetic energy of turbulence:

The profiles of the kinetic energy of turbulence, Fig.(F8-3) confirms the existance of the expanding shear layer.

10.3.3.5 The flow behaviour in the separation region:

The above observations were used to build up the following understanding of the flow structure:

1- The expanding flow emerging from the primary duct exit is further helped by the presence of the suction at the entrance of the vortex chamber.

2- The expansion of the flow is accompanied by a general decrease in the axial component of the mean velocity and hence a static pressure recovery.

3- The stream tube which was originally in the imediate vicinity of the primary duct wall decelerate more dramatically as it enters the vortex chamber. The next stream tube decelerate less dramatically and possesses a strong radial velocity component as it approaches the fence. The result is a further increase in the velocity gradient between the two strear tubes This helps to create turbulence of high intensity and consequantly the shear layer resulting from the separation from the lip is further strengthened as the flow proceeds downstream.

10.3.4 Region (4), "the fence region":

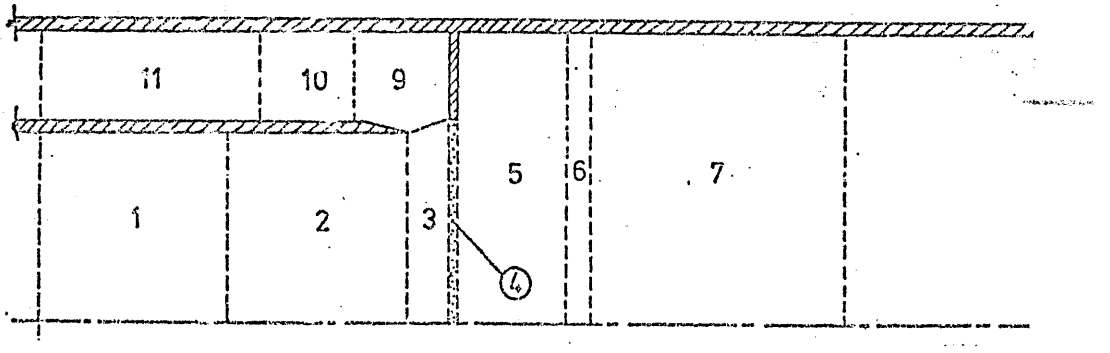

10.3.4.1 The static pressure distribution:

The static pressure profile at the plane of the downstream face of the fence, Fig.(F1-4), show no presence of the dip. This indicates that the sink effect does not influence the region downstream of the fence. On the contrary the profile shows a sharp increase in the static pressure in the vicinity of the fence top. This probably due to the effect of the high turbulence level in this region, or the formation of a stagnation point on the top of the fence.

10.3.4.2 The distribution of the mean velocity:

The profiles of the axial component of the mean velocity, Fig.(F2-4) show that the flow accelerates near the centre of the diffuser as the flow passes through the fence. The radius of the accelerating region is about 12 mm. The flow outside this region, decelerates considerably particularly in the near vicinity of the fence top as it passes through the fence.

The profiles of the radial component of the mean velocity, Fig.(F3-3), show a slight increase in $\overline{V}$ over the whole cross-section of the flow passing through the fence except near the top of the fence where the gradient of the radial component of the velocity is very steep.

10.3.4.3 The distribution of the Reynolds' stresses:

The distribution profiles of the Reynolds' stresses show that a good part of the shear layer, which was originally developed in the separation region, passes through the fence. The peak value of $\overline{u^2}/U_o^2$, Fig.(F4-5), increases sharply from about 20.3×10^{-3} at the plane of the upstream face of the fence to about 28.9×10^{-3} at the plane of the downstream face of the fence.

The peak values of $\overline{v^2}/U_o^2$, Fig.(F5-5), and $-\overline{uv}/U_o^2$, Fig.(F6-4), which are originally higher than that of $\overline{u^2}/U_o^2$ increase less dramatically from 29.6×10^{-3} and 27.6×10^{-3} to 32.4×10^{-3} and 29.6×10^{-3} respectively.

Although $\overline{w^2}/U_o^2$, Fig.(F7-4), shows a considerable increase in its

peak values but this values are still one order of magnitude lower than the other Reynolds' stresses. The peak value of $\overline{w^2}/U_o^2$ increases from 3.1×10^{-4} to 4×10^{-4}.

10.3.4.4 The distribution of the kinetic energy of turbulence:

The profiles of the kinetic energy of turbulence, Fig.(F3-4), show a sudden increase in the peak value of k/U_o^2 in the neighbourhood of the fence top. This indicates the creation of high intensity turbulence.

10.3.4.5 The flow behaviour in the fence region:

This can be summarized, with the help of the above discussion, as follows:-

1- The flow meets the upstream face of the fence with a relatively high velocity, compared to a zero velocity that would have otherwise existed in the case of a sudden enlargement Ref.(36). The velocity of the flow in the immediate vicinity of the fence drops very sharply, due to the non-slip condition at the top surface of the fence, causing a very severe velocity gradient. In other words the relatively high velocity fluid scrubs against the sharp edge of the fence creating a new and strong shear layer.

2- The deceleration of the fluid in the neighbourhood of the fence causes, for continuity reasons, the formation of a local jet at the core of the flow. This should cause a drop in the static pressure at the core of flow, however, no such drop has been noticed from the static pressure measurements. It is believed that the reason for this is likely to be due to the presence of local pressure fluctuations and high turbulence intensity affecting the static pressure measurements.

3- The flow still maintains a relatively high level of radial mean velocity component. This is particularly true in the neighbourhood of the fence. This is expected to help the flow to diffuse very rapidly in the next region.

10.3.5 Region (5) "the recirculating region":

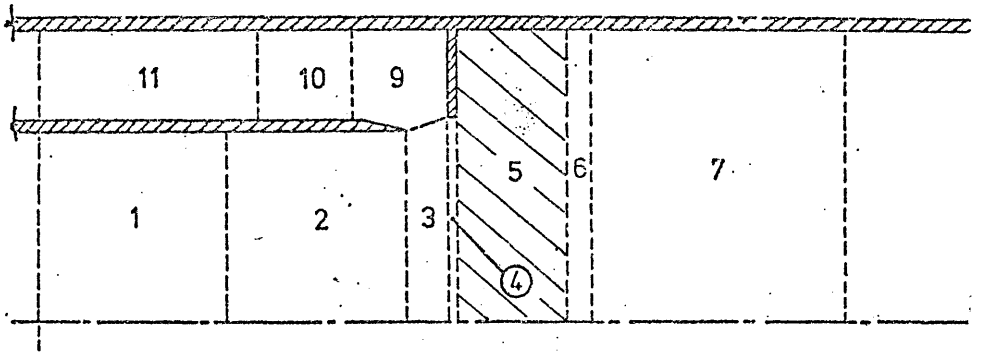

10.3.5.1 The static pressure distribution:

The static pressure continues to increase over the whole cross-section of the main flow, Fig.(F1-5). The shear layer separating the mainflow and the recirculating zone is strongly influencing the static pressure measurements. This is indicated by sharp increases in the measured values of the pressure in the region of this shear layer. The recirculating zone was not accessible for static pressure measurement.

10.3.5.2 The distribution of the mean velocity:

The profiles of the axial component of the mean velocity indicate that the local jet core, which was created due to the presence of the fence in the path of the main flow, continues to exist downstream of the fence for a short distance and with continuously decreasing cross-section, Fig.(F2-5). The velocity difference between this jet core and the surrounding lower velocity air, which decelerates very rapidly as the flow separates from the fence edge, cause a shear action which together with the effect of the adverse pressure gradient decelerates the fluid in the jet core more rapidly than the surrounding air. The result is more uniform velocity profiles over the whole cross-section of the core of the flow as it progresses.

The streamline curvature is more intense near the fence. This causes the flow in this region to be able to negate the effect of the general adverse pressure gradient and hence decelerate less rapidly immediatly downstream of the fence. This is indicated by the presence of decreasing peak values in the velocity profiles which is followed by steep velocity gradients. The steep velocity

gradients lead to a very high rate of turbulence production which causes an intense mixing process between the main flow and the adjacent quiescent air along the surface of separation. This causes the quiescent air to be entrained into the main flow. The demand for entrainment continues as the flow proceeds, but the presence of the solid boundary interferes with the inflow of the air required by the entrainment process. For reasons of continuity, therefore, return flow is established from downstream resulting in the formation of a stable zone of recirculation, which was previously referred to as the "Coanda Bubble".

The originaly high level of radial component of the mean velocity as possessed by the main flow in the neighbourhood of the shear layer, Fig.(F3-4), helps the mainflow to spread or diffuse, rapidly in the radial direction. The result is a continuous reduction in the size of the recirculation zone and an equal increase in the cross-section area of the mainflow. This causes, for continuity reasons, a general reduction in the level of both the axial and radial components of the mean velocity. The diffusion process was greatly helped by the intense mixing in the shear layer separating the mainflow from the recirculating region.

10.3.5.3 The distribution of the Reynolds' stresses:

The development of the shear layer in the recirculation region can be described with the help of the Reynolds' stress profiles, Fig.(F4-5), Fig.(F5-5), Fig.(F6-5) and Fig.(F7-4). As the flow separates from the fence edge a strong shear layer develops and is joined shortly downstream by the original shear layer, which is travelling with the mainflow from the "separation region", through the fence. The production of turbulence continues on the separation surface as a result of the very steep velocity gradients at the separation surface. This causes further strengthening of the combined shear layers as the flow proceeds downstream.

The growing strength of the shear layer continues for a short axial distance of about 3 mm downstream of the fence. This is indicated by the increase in the peak values of the Reynolds'

stresses particularly $\overline{u^2}/U_o^2$ and $\overline{v^2}/U_o^2$.

Downstream of this short axial region, the shear layer grows in size and also moves towards the wall but with rapidly decreasing levels of Reynolds' stresses. The thickening layer grows in the outside direction faster than it does in the inside direction. This is indicated by the shift of the peaks of the profiles towards a larger radii as the flow proceeds downstream. The Reynolds' stresses at the core of the mainflow increase but with very low rates.

10.3.5.4 The distribution of the kinetic energy of turbulence:

The distribution profiles of the kinetic energy of turbulence, Fig.(F8-5), indicate that the peak value of k/U_o^2 increases from about 31.7×10^{-3} at the plane of the downstream face of the fence to about 60×10^{-3} at a plane only one millimetre downstream of the fence. The increase in the kinetic energy of turbulence is extracted from the mean flow.

Downstream of this plane, the peak value of the kinetic energy decreases very rapidly but the level of k/U_o^2 at the core of the flow is increasing slowly as the flow proceeds downstream. It is believed that most of the kinetic energy of turbulence lost by the shear layer is not dissipated into heat but is regained by the mainflow. It is here that the hypothesis of vortex stretching and energy cascading, previously discussed in chapter three, is violated. Ref.(34) suggested that this is feasible, even in straight pipe flows, in the case of non-homogenious anisotropic turbulence. This is very much the case of the present flow.

10.3.5.5 The flow behaviour in the recirculation region:

It is believed that the above discussion gives a comprehensive explanation for the flow behaviour in this region. There is nothing new to add here but to emphasize that it is for the strong mixing action, resulting from the presence of the shear layer that the dramatic rearrangement of the velocity field in this region is attributed. The diffusion processes is further

aided by the presence of the strong radial velocity component possessed by the flow as it enters the secondary duct.

10.3.6 Region (6), "the reattachment region":

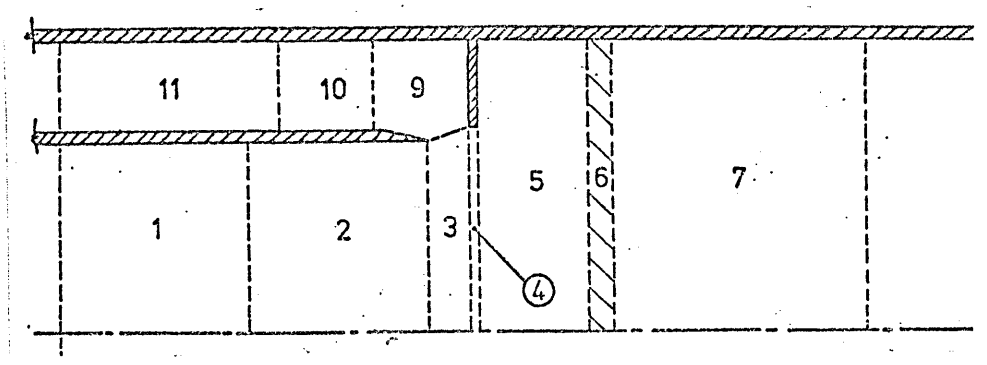

At the downstream end of the recirculation zone the shear layer, which is expanding in width and diminishing in strength, reattaches to the wall of the secondary ducts. The shear layer still has enough strength, Fig.(F4-6), Fig.(F5-6), Fig.(F6-6), Fig.(F7-5) and Fig.(F8-6), to produce a smooth reattachment. Since, the present LDV system did not allow measurement closer than 2 mm to the wall, it was not possible to determine the exact axial position of the reattachment plane. An estimation, based on a study of the velocity profiles in this region, Fig.(F2-6) and Fig.(F3-5), located this position at between X = 67.25 mm and X = 70.25 mm. According to this estimation the length of the recirculation zone is about 17 mm, about $\frac{1}{3} D_1$, or about $1\frac{1}{3}$ the expansion step height [the expansion step height is defined as $(D_2-D_1)/2$] . The recirculation zone is very short compared to that of sudden expansion without suction, in circular pipes where there is a recirculation zone in the order of 10 to 15 step heights, Ref.(33), Ref.(36), and Ref.(64). The reduction in the length of the recirculating zone in the present flow is believed to be due to a much higher rate of mixing. This results from the existence of a much stronger and thicker shear layer and also from the fact that the flow enters the secondary duct possessing a high level of radial velocity component which promotes its ability to diverge more quickly.

10.3.7 Region (7), "the recovery region":

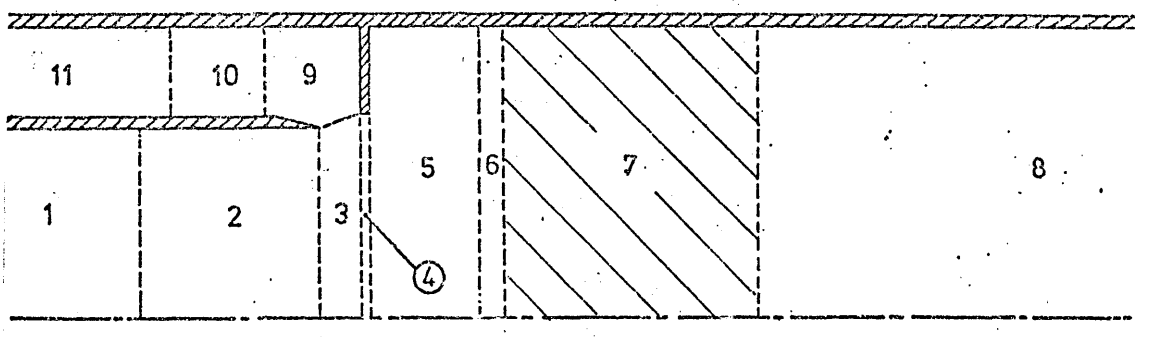

10.3.7.1 The static pressure distribution:

The static pressure in the recovery region continues to increase, over the whole cross-section of the secondary duct, as the flow progresses downstream, Fig.(F1-7). It can also be noticed that the rate of increase is slowing down as the flow proceeds.

10.3.7.2 The distribution of the mean velocity:

The profiles of the axial component of the mean velocity, Fig.(F2-7), indicate that the fluid at the core of the flow is decelerating while the fluid in the outer annulus is accelerating progressively as the flow proceeds downstream.

The profiles of the radial component of mean velocity, Fig.(F3-6) indicate that the flow has a radial velocity component, but this is diminishing very rapidly and the flow recovers its axiality before the end of this region.

10.3.7.3 The distribution of the Reynolds' stresses:

The Reynolds' stress distribution in this region, Fig.(F4-7), (F5-7), Fig.(F7-6) and Fig.(F8-7), indicate that the shear layer which is now smoothly attatched to the wall is still active in promoting mixing and rearrangement of the velocity field. The profiles show that the normal Reynolds' stresses are decreasing over the whole cross-section of the flow and particularly near the wall. The peak shear stress profiles become close to the wall indicating the development of a boundary layer.

10.3.7.4 The distribution of the kinetic energy of turbulence:

The profiles of the kinetic energy of turbulence, Fig.(F8-7), indicate that k/U_o^2 is decreasing very rapidly in the neighbourhood of the wall.

10.3.7.5 The flow behaviour in the recovery region:

It is believed that the originally strong turbulence at the beginning of this region loses much of its energy to the main flow as it proceeds downstream. This is probably the mechanism behind the rearrangement of the flow field in this region.

10.3.8 Region (8), "the settling region":

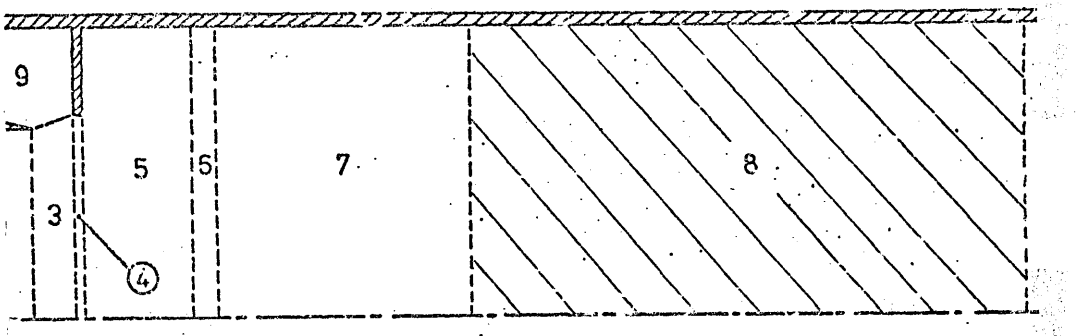

10.3.8.1 The static pressure distribution:

The static pressure in the settling region continues to increase over the whole cross-section of the flow. The profiles, Fig.(F1-8), are also becoming more uniform as the flow proceeds downstream.

10.3.8.2 The mean velocity distribution:

The measurements of the mean velocity indicate that the flow maintains being axial and parallel. The velocity profiles, Fig.(F2-8), show that the core of the flow continues to decelerate and the velocity level in the stream tubes in the neighbourhood of the duct wall continues to increase. The result is that the velocity profiles become more uniform as the flow proceeds towards the downstream end of this region.

10.3.8.3 The distribution of the Reynolds' stresses:

The Reynolds' stress profiles in this region, Fig.(F4-8), Fig.(F5-8), Fig.(F6-8) and Fig.(F7-7), show that there are some irregularities in the pattern of change in the Reynolds' stresses. Some of these irregularities can be attributed to the boundary layer growth on the duct wall. This is particularly true for $-\overline{uv}/U_o^2$ and $\overline{v^2}/U_o^2$ because their peak values are increasing in the neighbourhood of the wall as the flow proceeds downstream. Other changes are probably due to the effect of mixing or the diffusion of energy from the weakening shear layer to the mean motion. This applies for $\overline{u^2}/U_o^2$ and $\overline{w^2}/U_o^2$.

10.3.8.4 The distribution of the kinetic energy of turbulence

The profiles of the kinetic energy of turbulence, Fig.(F8-8), indicate that there is a general trend for the kinetic energy to increase slightly as the flow proceeds downstream. This is particularly noticeable in regions outside the core of the flow.

10.3.9 Region (9), "the vortex region":

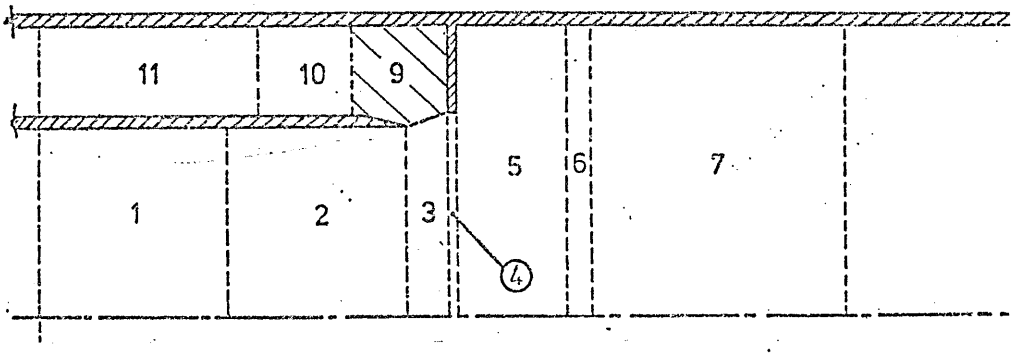

The vortex chamber was not accessible for measurement by the static pressure probe. Consequently, the pressure distribution in the three regions of the vortex chamber is not known. Discussion will be, therefore, limited to the distribution of the mean velocity, the Reynolds' stresses and the kinetic energy of turbulence.

10.3.9.1 The distribution of the mean velocity:

As the flow separates from the primary duct exit lip, the stream tube which was originally closest to the wall enters the vortex chamber. The incoming flow adjusts itself very rapidly to rotate

in an anticlockwise direction around the vortex. This is due to the effect of the suction and the presence of the fence. The result is that the flow loses its axial component of the mean velocity very ralidly, Fig.(F2-9). Due to the rotational motion the radial component of the mean velocity increases, Fig.(F3-7), but not to the extent that would compensate for the reduction in the axial component. The net result is a continuous reduction in the total velocity i.e the flow is decelerating as it flows round the vortex. In other words the flow is diffusing as it moves round the vortex and loses much of its kinetic energy.

The vortex motion entrains the fluid which loses too much of its kinetic energy so that it cannot continue to flow round the vortex. This is recirculated in the vortex and re-energized when comes into contact with the fresh incoming flow. A shear layer is created between the incoming flow and the standing vortex due to the velocity differential between them. The velocity profiles indicate that the vortex rotates as a solid body driven by the incoming flow, contrary to the previously held view that the vortex is of the free type and that it is doing the driving.

Some of the fluid which does not lose too much of its kinetic energy continues to proceed round the vortex and then escapes from it near the top left corner to proceed through the next flow region.

10.3.9.2 The distribution of the Reynolds' stresses:

The Reynolds' stress distribution inside the vortex chamber, Fig.(F4-9), Fig.(F5-9), Fig.(F6-9), and Fig.(F7-8), is complicated and very difficult to analyse. The reason for the difficulty is that in this region there is likely to be a very strong interaction between many sources of turbulence. These sources are; the shear layer at the entrance of the vortex chamber, the boundary layer which is building up on the upstream face of the fence, the boundary layer which is building up on the outer wall of the vortex chamber, the boundary layer which is building up on the inner wall of the vortex chamber, and last but not least the shear action inside the vortex itself and between

the vortex and the entrained incoming flow and the escaping flow.

The profiles of the normal Reynolds' stresses in the region of the standing vortex indicate that the turbulence is a minimum near the vortex eye and increases radially outward in the direction of the previously mentioned sources of turbulence. This can be explained by reference to what was previously noticed from the velocity profiles that the vortex is showing similar characteristics to a solid body rotation. In this case the normal Reynolds' stresses are expected to be a minimum at the eye of the vortex and to increase at its edge.

10.3.9.3 The distribution of the kinetic energy of turbulence:

The profiles of the kinetic energy of turbulence, Fig.(F8-9), indicate that part of the shear layer, originally created by the separation of the flow from the primary duct exit lip is entering the vortex chamber. The profiles also show that the turbulence produced by this shear layer is losing much of its kinetic energy as the flow moves round the vortex. The growth of boundary layer in the outer wall is indicated by the increasing level of turbulence energy at the position of the peaks in the neighbourhood of this wall.

10.3.10 Region (10), "the bled air diffusion region":

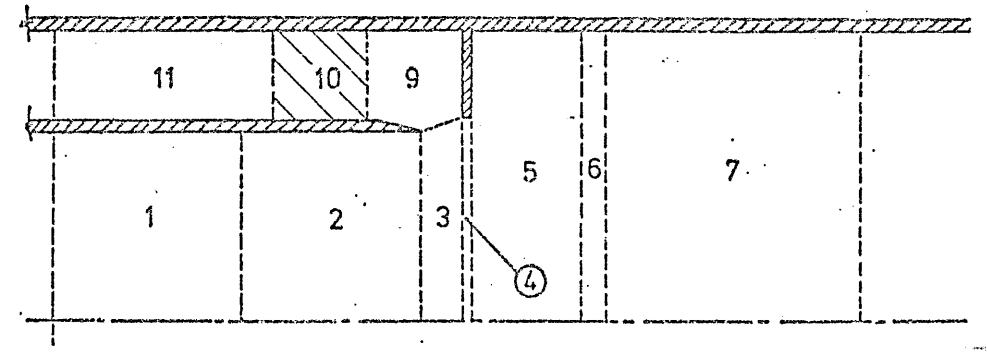

10.3.10.1 The distribution of the mean velocity:

The velocity profiles in this region, Fig.(F2-10) and Fig.(F3-8), indicate that the fluid leaving the vortex region continues to decelerate as it proceeds through the diffusion region. In this region the flow expands very rapidly to fill the whole depth of the vortex chamber. In doing so, the fluid which flows nearer to

inside wall of the vortex chamber decelerates more quickly than that which flows nearer to the outer wall.The former loses a great deal of kinetic energy and hence some of this fluid is entrained by the vortex to be recirculated. The escaping air continues to flow down in the vortex chamber through the settling region.

10.3.10.2 The distribution of the Reynolds' stresses:

The profiles of the normal Reynolds' stresses, Fig.(F4-10) and Fig.(F5-10), indicate the presence of a strong shear layer separating the vortex and the diffusing bled air.

These profiles together with the profiles of the Reynolds' shear stress, Fig.(F6-10), also indicate the presence of a thick boundary layer on the outer wall of the vortex chamber.

10.3.10.3 The distribution of the kinetic energy of turbulence:

The profiles of the kinetic energy of turbulence, Fig.(F8-10), show that the overall level of k/U_o^2 is increasing rapidly, particularly in the neighbourhood of the outer wall of the vortex chamber. This increase in k/U_o^2 is at the expense of the kinetic energy of the mean flow. It is believed that the bled air looses much of its kinetic energy in this severe diffusion process and does not recover enough static pressure to compensate for this loss.

10.3.11 Region (11), "the bled air settling region":

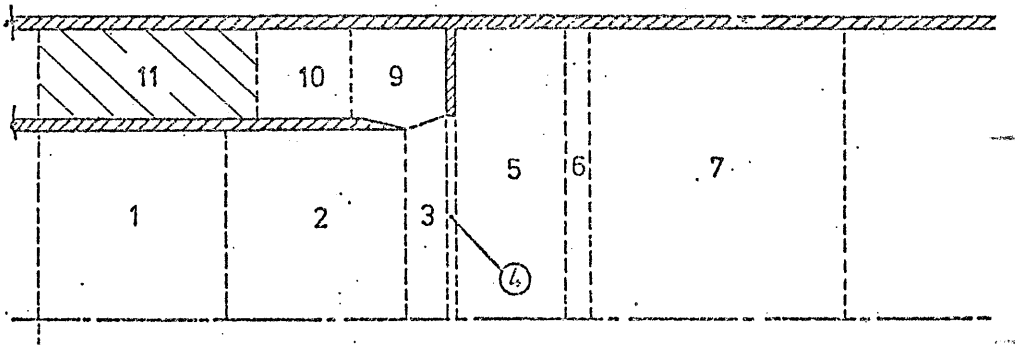

The velocity profiles, Fig.(F2-11), indicate that the flow in this

region is axial and parallel (in the reverse direction to the main diffuser flow). The velocity profiles also become progressively uniform as the flow proceeds towards the downstream boundary of this region.

The Reynolds' stress profiles, Fig.(F4-11), Fig.(F5-11) and Fig.(F6-11), and the profiles of the kinetic energy of turbulence Fig.(F8-11), indicate that the turbulence at the centre of the flow decays as the flow proceeds. They also show that the turbulence distribution is becoming more symmetrical with the development of the boundary layers on the two walls as the flow proceeds towards the downstream boundary of this region.

10.4 The overall flow mechanism:

The overall flow mechanism is described here with the help of Fig.(F10-2) which is a vector representation of the velocity field. The vectors represent the magnitude and direction of the total mean velocity at the mid point of each vector.

1- The precisely contoured nozzle provides a smooth entry to the primary duct. The flow, therefore, has a uniform velocity and relatively low turbulence intensity at the entrance of the primary duct. The length of the primary duct was carefully selected to ensure a turbulent boundary layer flow further downstream, but not to allow the flow to reach the state of a fully developed flow. Therefore, the flow approaches the region where the sink effect is influential having a turbulent boundary layer but still with an acceptably uniform velocity profile.

2- The sink effect, resulting from the suction at the entrance of the vortex chamber, penetrates to a distance of about $\frac{1}{2}D_1$ upstream of the primary duct exit lip. The stream tube, next to the growing boundary layer, accelerates under the influence of the sink effect. Consequently, the growth of the boundary layer on the wall of the primary duct is counteracted and the velocity gradient increases.

3- As the flow separates from the lip of the primary duct a strong shear layer springs off the lip. The boundary layer, which is too energy deficient to follow the main flow, enters the vortex chamber under the influence of the suction and decelerates as it flows

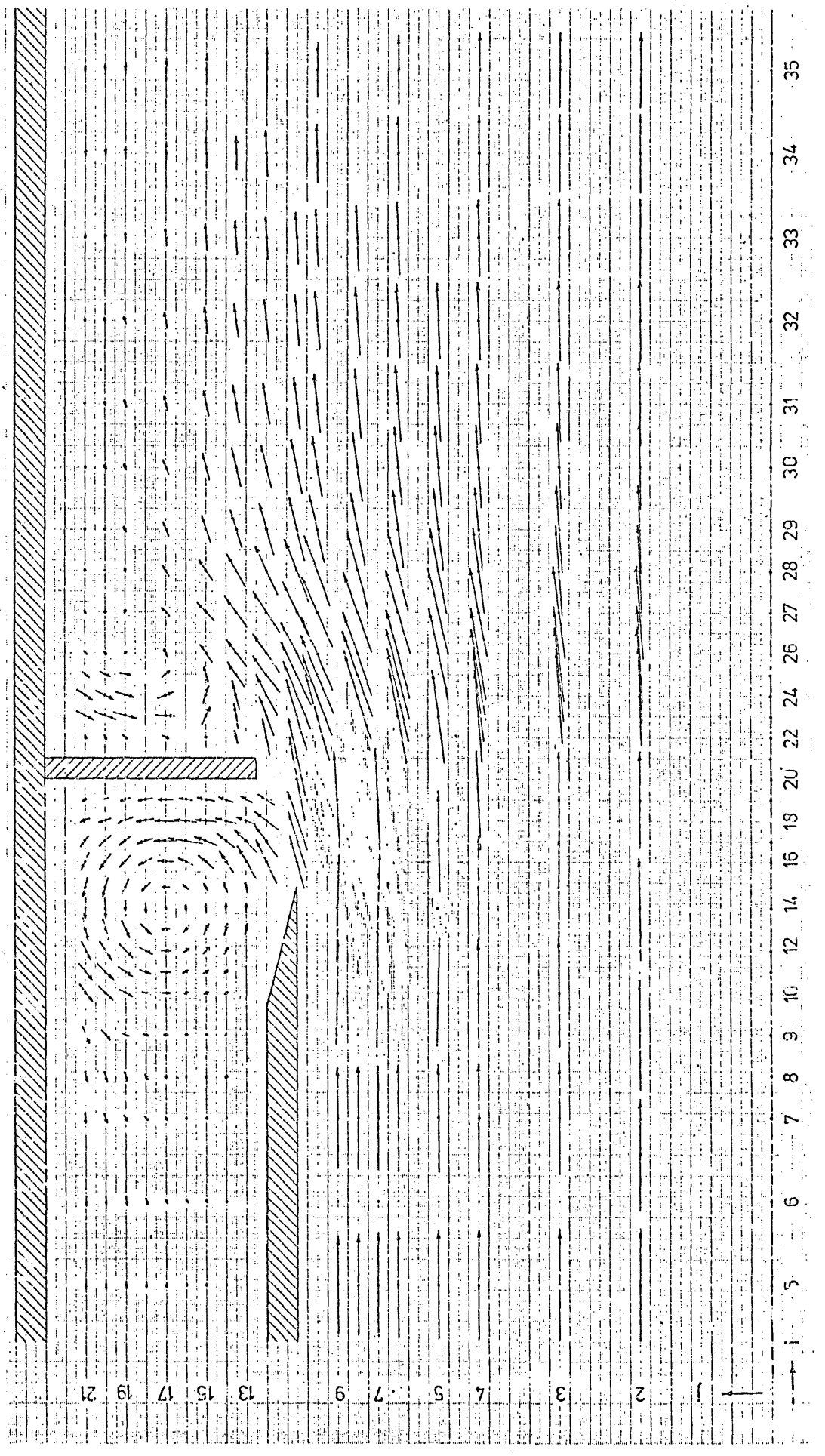

Fig.(10-2): Vector representation of the velocity field.

round the standing vortex. The early separation and the effect of the suction help the main flow to diverge rapidly as it proceeds towards the fence. The divergence is accompanied by, for continuity reasons, deceleration and hence static pressure recovery and also the possession of a high level of a radial velocity component.

4- The main flow reaches the fence having a relatively high velocity in the immediate vicinity of the fence top. This drops to zero value, to fulfil the non-slip requirement at the surface of the fence top, in a very short distance and hence results in a very steep velocity gradient. The result is the creation of a very strong shear layer downstream of the fence. The new shear layer joins the original one flowing through the fence to form an even stronger and broader shear layer which continues to gain more strength for a short distance downstream of the fence. The shear layer has a very intense turbulence level of a highly anisotropic and non-homogeneous nature.

5- The radial velocity component originally possessed by the main flow helps it to diverge very rapidly to fill the whole cross-section of the secondary duct in a very short axial distance, estimated here from the experimental results as about $\frac{1}{3} D_1$. The strong mixing action, created by the shear layer on the separation surface, helps to promote the divergence process. The turbulence in the shear layer can be looked at as an efficient agent which is transporting kinetic energy from the core of the flow to the energy deficient regions in the neighbourhood of the surface of separation and later in the neighbourhood of the duct wall. The result is the redistribution of the kinetic energy and hence a progressive static pressure recovery without significant losses in the total pressure.

6- The efficient mixing process also helps the flow to reattach smoothly to the secondary duct wall and consequently the flow continues to gain static pressure as it proceeds along the diffuser short length.

7- The relatively energy deficient air entering the vortex chamber decelerates as it flows round the standing vortex. The air which is too energy deficient to escape is entrained by the vortex to be

recirculated and hence re-energized by the fresh incoming flow. The present experimental results indicate that the vortex has no significant effect on the main flow and hence on the performance of the diffuser. The energy required to drive the vortex is obtained from the bled air which also loses too much energy during the severe diffusion process following its escape from the vortex.

10.5 Concluding remarks:

1- It is believed that the design of the bled air passage can be developed to provide a smoother diffusion process and the bled air would recover more static pressure efficiently. In this respect it is suggested that the early separation of the main flow from the primary duct exit lip must be maintained, but the vortex motion should be eliminated. This should lead to a reduction in V_c and may also help to reduce the bleed requirement.

2- The detailed experimental results provided quatitative information about the flow parameters and therefore led to a better understanding of the flow behaviour inside the Cranfield diffuser. This understanding can be further enhanced if more quatitative information about some of the flow parameters, such as the Reynolds' stresses and the kinetic energy of turbulence could have been provided. It has been mentioned before, see chapters three and four, that the kinetic energy of turbulence as well as the Reynolds' stresses should not be treated as being local properties of the flow because their local values are the resultant of the balance of their rates of convection, production and dissipation. This balance depends on the whole history of the flow, both upstream and downstream of the particular point at which the local value is considered. To provide such quantitative information about the rates of convection, production, and dissipation of the Reynolds' stresses and the kinetic energy of turbulence, the transport equations of these parameters must be solved so that the terms representing the previously mentioned rates could be calculated. Unfortunately, such solutions are not available for this particular flow. It is hoped that the theoretical study presented in the third part of this thesis, although incomplete, would be a useful step towards the provision of this information.

IV PART THREE

THEORETICAL INVESTIGAION

INTRODUCTION

For many years the science of "Theoretical Hydrodynamics" handled only the non-existent inviscid fluids. In the case of the two most important fluids, water and air, the viscosity is very small. Consequently, the forces due to viscous friction are generally speaking very small compared with the remaining forces (gravitational, inertia, and pressure forces). For this reason it was difficult to accept that frictional forces, omitted from the classical theory of hydrodynamics, influenced the motion of a fluid to so large an extent. Due to the fact that this theory neglected fluid friction, it stood unable to explain or to predict most or all the practically important phenomena such as; drag, flow separation, and pressure losses in pipes.

A complete description of motion for viscous fluid flows has been known for a long time in the form of the Navier-Stokes equations. They are the basis of the modern science of fluid mechanics and form the starting point of any rational attempt to treat real flows mathematically. Unfortunately, until the present day, no analytical solution of these equations was known but satisfactory predictions of real turbulent flows have been achieved numerically. The process starts by considering that real turbulent motion consists of two parts one is the mean motion and the other is the super-imposed fluctuating motion. This leads to the Reynolds' equations of motion derived from the original Navier-Stokes' equations. Next, the turbulent correlations known as the Reynolds' stresses are to be approximated empirically in terms of the mean flow parameters. This process forms the basis of the subject known as "the mathematical modelling of turbulence". Finally, the approximated equations of motion, together with any other fundamental or auxiliary equations, are to be solved numerically.

The mathematical modelling of turbulence was discussed in chapter four, where the object of the discussion was to select the most suitable model to be applied to the flow under investigation. The conclusion was that an effective-viscosity model is likely to be the most suitable type. It was also concluded that in this case, the k-l model has particular advantages. Therefore, the flow is treated as being a steady laminar flow with an effective-viscosity which is calculated from the selected k-l model.

The present part of the thesis, which is concerned with the theoretical

study of the flow under investigation, consists of three chapters. Chapter eleven includes the mathematical formulation of the fundamental and auxiliary equations in the required form for solution. Chapter twelve is then assigned to the development of the solution procedure, while chapter thirteen includes the description and analysis of the computer programme.

CHAPTER ELEVEN

11. THE MATHEMATICAL FORMULATION OF THE PROBLEM:

11.1 Introduction:

The present chapter has two purposes, the first is to present a complete mathematical specification of the problem including the differential equations describing the flow and the second is to provide clear statements of these differential equations in a general form which is common to all of them. This common form is so selected to make the derivation of the finite difference solution more easy. The derivations of the differential equations are not presented, however, the derivation procedures are outlined. The detailed derivations of the more general equations can be referred to in Ref.(37).

11.2 The required mathematical specifications:

The problem can be solved numerically if the following are specified:-

1- The coordinate system and the dependent variables.
2- The continuity equation and the equations of motion.
3- The mathematical model of turbulence.
4- The transport equations of (k) and (l).
5- The domain of the required solution and its grid system.
6- The boundary conditions.
7- The initial conditions.
8- The assigned values of the constants.

Each of these is specified in the following sections respectively.

11.3 The coordinate system and the dependent variables:

The x,r and θ cylindrical coordinate system is the most suitable coordinate system to be used for axisymmetrical problems, Ref.(31). The experimental results show that not only was the mean motion steady, but it also had no swirl component. This means that the flow can be treated as a two-dimensional one, with x and r, Fig.(11-1) as its two independent spatial parameters. In this case the mean velocity field can be described using only two velocity components, $\bar{U}$ and $\bar{V}$, in the x and r coordinate directions respectively. The mean value of the static pressure, $\bar{P}$, is the third dependent parameter required to make the

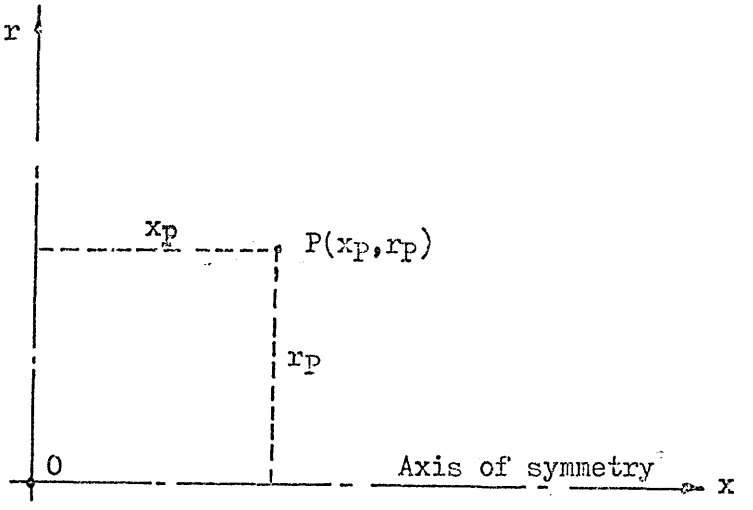

Fig.(11-1): The co-ordinate system

flow field a mathematically determinate one. Using an effective-viscosity turbulent model allows the flow to be treated as though it is a steady laminar one having an effective viscosity which varies in magnitude from place to place. This means, in mathematical terms, that μ_{eff} is a function of x and r.

Since the flow under investigation has two recirculating regions, then the two equations of motion are expected to be of the elliptic type. There are two methods by which the problem can be treated. The first is to solve the mathematically determinate system of three equations, namely the two equations of motion and the continuity equation, in terms of the three dependent variables $\overline{U},\overline{V}$ and $\overline{p}$, Ref.(65). The second method is to mathematically manipulate both the equations and the dependent variables in a process leading to another mathematically determinate system of two equations in only two dependent variables, namely the stream function, ψ, and the vorticity, ω, Ref.(37). The second method, beside being more economical to solve, has the advantage of being more suitable to the solution procedure which is being followed, Ref.(37).

To summarize this section, it is concluded that:

1- The coordinate system is a two-dimensional cylindrical one, with x and r as its spatial independent variables.

2- The dependent variables are the stream function, ψ, and the

vorticity, ω.

11.4 The continuity equation and the two equations of motion:

11.4.1 The continuity equation:

The conservation of mass principle states that, in a steady flow process, the net rate of flow of mass into any control volume is zero. The mathematical statement of the mass-conservation principle for two dimensional axisymmetrical flow in cylindrical coordinates is thus;

$$\frac{\partial \bar{U}}{\partial x} + \frac{\bar{V}}{r} + \frac{\partial \bar{V}}{\partial r} = 0 \qquad (11\text{-}1)$$

The stream function is defined as:

$$\bar{U} = \frac{1}{\rho r}\frac{\partial \psi}{\partial r} \qquad (11\text{-}2)a$$

$$\bar{V} = -\frac{1}{\rho r}\frac{\partial \psi}{\partial x} \qquad (11\text{-}2)b$$

Substituting from (11-2) into (11-1) we get:

$$\frac{\partial}{\partial x}\left(\frac{\partial \psi}{\partial r}\right) - \frac{\partial}{\partial r}\left(\frac{\partial \psi}{\partial x}\right) = 0 \qquad (11\text{-}3)$$

Equation (11-3) is precisely the equation which (ψ) must satisfy if it is to be single-valued in (x) and (r) alone. Thus, the treament of the stream function (ψ) as such a function is made legitimate by the validity of the mass-conservation principle.

11.4.2 The two equations of motion:

Newton's second law of motion, applied to a steady flow through a control volume, states that the net inflow of momentum flux into a control volume is equal to the net force which is exerted on this control volume by its surroundings. Alternatively, it is the moment of these momentum fluxes and forces about a fixed axis that is zero. Applying the alternative statment leads to the following two equations of motion, Ref.(37):

$$\frac{\partial}{\partial x}(\rho \bar{U}^2) + \frac{1}{r}\rho \bar{U}\bar{V} + \frac{\partial}{\partial r}(\rho \bar{U}\bar{V}) - \frac{\partial}{\partial x}\left[\mu_{eff}\left(2\frac{\partial \bar{U}}{\partial x}\right)\right] - \frac{1}{r}\mu_{eff}\left(\frac{\partial \bar{U}}{\partial r} + \frac{\partial \bar{V}}{\partial x}\right)$$

$$- \frac{\partial}{\partial r}\left[\mu_{eff}\left(\frac{\partial \bar{U}}{\partial r} + \frac{\partial \bar{V}}{\partial x}\right)\right] + \frac{\partial \bar{P}}{\partial x} = 0 \qquad (11\text{-}4)a$$

$$\frac{\partial}{\partial r}(\rho\bar{V}^2)+\frac{\rho\bar{V}^2}{r}+\frac{\partial}{\partial x}(\rho\bar{U}\bar{V})-\frac{\partial}{\partial r}\left[\mu_{eff}\left(2\frac{\partial\bar{V}}{\partial r}\right)\right]-\frac{1}{r}\mu_{eff}\left(2\frac{\partial\bar{V}}{\partial r}\right)$$

$$+\frac{1}{r}\mu_{eff}\left(\frac{2\bar{V}}{r}\right)-\frac{\partial}{\partial x}\left[\mu_{eff}\left(\frac{\partial\bar{U}}{\partial r}+\frac{\partial\bar{V}}{\partial x}\right)\right]+\frac{\partial\bar{P}}{\partial r}=0 \qquad (11\text{-}4)b$$

11.4.3 The equation of the stream function:

The vorticity is the measure of the amount of anti-clockwise rotation which the fluid possesses. For two-dimensional axisymmetrical flow, the vorticity (ω) is defined as, Ref.(37):

$$\omega=\frac{\partial\bar{V}}{\partial x}-\frac{\partial\bar{U}}{\partial r} \qquad (11\text{-}5)$$

Substituting for $\bar{U}$ and $\bar{V}$ from (11-2) into (11-5), we get:

$$\omega=-\left[\frac{\partial}{\partial x}\left(\frac{1}{\rho r}\frac{\partial\psi}{\partial x}\right)+\frac{\partial}{\partial r}\left(\frac{1}{\rho r}\frac{\partial\psi}{\partial r}\right)\right] \qquad (11\text{-}6)$$

Equation (11-6) is referred to as the equation of the stream function since it states the relationship between the vorticity, (ω), which is the principle dependent variable, and the stream function (ψ) which is the second dependent variable.

11.4.4 The equation of the vorticity, ω:

The derivation of the vorticity equation from the two equations of motion can be referred to in Ref.(37). The procedure of the derivation is summarized as follows:-

1- Equations (11-4)a and (11-4)b were differentiated with respect to (r) and (x) respectively.

2- The resulting two equations were subtracted from each other to eliminate the static pressure derivatives.

3- Expressions for the mean velocity components $\bar{U}$ and $\bar{V}$ were substituted from equation (11-2).

4- Using equations (11-3) and (11-6) it was possible to reach the final form of the vorticity equation which is stated as follows:-

$$r^2\left\{\frac{\partial}{\partial x}\left(\frac{\omega}{r}\frac{\partial\psi}{\partial r}\right)-\frac{\partial}{\partial r}\left(\frac{\omega}{r}\frac{\partial\psi}{\partial x}\right)\right\}-\frac{\partial}{\partial x}\left\{r^3\frac{\partial}{\partial x}\left(\mu_{eff}\frac{\omega}{r}\right)\right\}-\frac{\partial}{\partial r}\left\{r^3\frac{\partial}{\partial r}\left(\mu_{eff}\frac{\omega}{r}\right)\right\}$$

$$-2r^2\left[\frac{\partial^2\mu_{eff}}{\partial x^2}\left\{\frac{\partial}{\partial r}\left(\frac{1}{\rho r}\frac{\partial\psi}{\partial r}\right)\right\}+\frac{\partial^2\mu_{eff}}{\partial r^2}\left\{\frac{\partial}{\partial x}\left(\frac{1}{\rho r}\frac{\partial\psi}{\partial x}\right)\right\}-\frac{\partial^2\mu_{eff}}{\partial r\partial x}\left\{\frac{\partial}{\partial r}\left(\frac{1}{\rho r}\frac{\partial\psi}{\partial x}\right)\right.\right.$$

$$\left.\left.+\frac{\partial}{\partial x}\left(\frac{1}{\rho r}\frac{\partial\psi}{\partial r}\right)\right\}\right]=0 \qquad (11\text{-}7)$$

11.4.5 The standard formulation of the differential equations:

The equation of the vorticity, equation (11-7), is an elliptic one.

The transport equations of (k) and(l) are also expected to be of an elliptic form. The economy of the solution can be maximized if a standard formulation can be found so that it is common to them all, except only for a few terms which are peculiar to the physical properties which the equations represent. Following the procedure explained in Ref.(37), the following standard formula can be reached:

$$a\left\{\frac{\partial}{\partial x}\left(\phi\frac{\partial\psi}{\partial r}\right)-\frac{\partial}{\partial r}\left(\phi\frac{\partial\psi}{\partial x}\right)\right\}-\frac{\partial}{\partial x}\left\{b_1\frac{\partial}{\partial x}(c\phi)\right\}-\frac{\partial}{\partial r}\left\{b_2\frac{\partial}{\partial r}(c\phi)\right\}+d=0 \quad (11\text{-}8)$$

where:

ϕ, is the dependent variable ψ or $\frac{\omega}{r}$

a, b_1, b_2, c and d are functions given by table (11-1).

Table(11-1)

The functions a, b_1, b_2, c and d associated with equation (11-8)

ϕ	a	b_1	b_2	c	d
ψ	0	$\frac{1}{\varrho r}$	$\frac{1}{\varrho r}$	1	$-\omega$
$\frac{\omega}{r}$	r^2	r^3	r^3	μ_{eff}	$-r^3 S_\omega$

The source term, S_ω, is given by:

$$S_\omega=\frac{1}{\varrho r}\left[\frac{\partial^2\mu_{eff}}{\partial x^2}\left\{\frac{\partial}{\partial r}\left(\frac{1}{r}\frac{\partial\psi}{\partial r}\right)\right\}+\frac{\partial^2\mu_{eff}}{\partial r^2}\left\{\frac{\partial}{\partial x}\left(\frac{1}{r}\frac{\partial\psi}{\partial x}\right)\right\}-\frac{\partial^2\mu_{eff}}{\partial r\partial x}\left\{\frac{\partial}{\partial r}\left(\frac{1}{r}\frac{\partial\psi}{\partial x}\right)+\frac{\partial}{\partial x}\left(\frac{1}{r}\frac{\partial\psi}{\partial r}\right)\right\}\right] \quad (11\text{-}9)$$

11.5 The mathematical model of turbulence:

A two-equation turbulent viscosity model is used with the kinetic energy of turbulence (k) and the length scale (l) as the two characteristic parameters of turbulence. In mathematical form the model is as follows:

$$\mu_{eff}=\varrho k^{\frac{1}{2}} l\, C_\mu \quad (11\text{-}10)$$

where C_μ is a function of the Reynolds' number of turbulence, Rt, which is expressed as:

$$R_t=\frac{\varrho k^{\frac{1}{2}} l}{\mu}$$

At high values of Rt, C_μ tends to reach an asymptotic constant value, Ref.(37).

11.6 The transport equations of (k) and (l):

The transport equation of (k) was discussed in chapter three, equation (3-15), and chapter four, equation (4-11). The equation is an elliptic one, containing convective, diffusion, and source terms. Gosman et al reported, Ref.(37), a similar equation for (k) adapted to the general form, equation (11-8). This is the form which was used in the present solution. Also, reported in the same reference a transport equation for the length scale (l) in the same form. Table (11-2) shows the values of the functions a, b_1, b_2, c and d associated with equation (11-8), corresponding to the equations of (k) and (l).

Table (11-2)

The functions a, b_1, b_2, c and d associated with equation (11-8).

ϕ	a	b_1	b_2	c	d
k	1	$r\mu_{eff}/\sigma_k$	$r\mu_{eff}/\sigma_k$	1	$-rS_k$
l	1	$r\mu_{eff}/\sigma_l$	$r\mu_{eff}/\sigma_l$	1	$-rS_l$

In table (11-2), σ_k and σ_l are Prandtl or Schmidt numbers for k and l respectively, their values are of the order of unity, Ref.(37).
The source terms are given by the following expressions:

$$S_k = W_{Skt} - \frac{\rho K^{3/2}}{l} C_D \qquad (11\text{-}11)$$

$$S_l = \rho k^{\frac{1}{2}} C_S - \frac{l}{k} W_{Skt} C_B \qquad (11\text{-}12)$$

where; C_D, C_S, and C_B are functions of the Reynolds' number of turbulence, R_t. At high values of, R_t, they behave similar to C_μ. In other words they assume constant asymptotic values as R_t becomes large. From Ref.(37), we also get.

$$\frac{W_{Skt}}{(\mu_{eff}-\mu)} = 2\left\{\left[\frac{\partial}{\partial x}\left(\frac{1}{\rho r}\frac{\partial \psi}{\partial r}\right)\right]^2 + \left[\frac{\partial}{\partial r}\left(-\frac{1}{\rho r}\frac{\partial \psi}{\partial x}\right)\right]^2\right\} + \left\{\frac{\partial}{\partial r}\left(\frac{1}{\rho r}\frac{\partial \psi}{\partial r}\right) + \frac{\partial}{\partial x}\left(-\frac{1}{\rho r}\frac{\partial \psi}{\partial x}\right)\right\}^2 \qquad (11\text{-}13)$$

11.7 The domain of the solution and its grid system:

Fig.(11-2) illustrates the domain of the integration and the grid system. The grid lines are lines parallel to the x-coordinate and the

length scale. The formula is thus:

$$l = R_2 C_1 - \frac{C_2 r^2}{R_2} - \frac{(C_1 - C_2) r^4}{R_2^3} \qquad (11\text{-}16)$$

where,

R_2 is the radius of the secondary duct.

C_1 and C_2 are constants to be evaluated by computational trial and error.

For fully developed pipe flow, Ref.(37) gives the values of C_1 and C_2 as 0.14 and 0.08 respectively.

Examination of equation (11-16) reveals that l is zero at the wall and increases as (r) decreases to reach its maximum value of (R_2 C_1) at the axis of symmetry.

11.8.2 The boundary conditions at the inlet plane:

1- The inlet boundary conditions for ψ and $(\frac{\omega}{r})$:

The inlet boundary of the solution domain is selected to be 23 mm upstream of the primary duct lip. The bleed air is considered to be a parallel inflow with negative inlet velocity. The experimental results show that, at the selected inlet boundary, the velocity vectors in both the primary duct and vortex chamber are parallel to the axis of symmetry. The values of the axial velocity component at the grid nodes of the inlet plane were also taken from the experimental results, from which the boundary conditions of both ψ and $\frac{\omega}{r}$ can be calculated as follows:

(a) Inlet conditions for, ψ:

Similar to the exit boundary conditions of ψ, equation (11-14) can be used to calculate the inlet boundary conditions of ψ using the values of $\bar{U}$ given by the experimental results.

(b) Inlet conditions for, $\frac{\omega}{r}$:

Similar to the exit boundary conditions of $\frac{\omega}{r}$, equation (11-15) can be used to calculate the inlet boundary conditions of $\frac{\omega}{r}$ using the values of ψ at the nodes of the inlet plane.

2- Inlet conditions for, k:

Similar to the exit conditions for (k), the inlet conditions for k are of the specified type, and were taken from the experimental results.

3- Inlet conditions for, l:

A formula similar to equation (11-16) can be used to calculate the values of l at the nodes of the primary duct inlet plane, thus:

$$l = R_1 C_3 - \frac{C_4 r^2}{R_1} - \frac{(C_3 - C_4) r^4}{R_1^3} \qquad (11\text{-}17)$$

where,

R_1 is the radius of the primary duct.

C_3 and C_4 are constants to be evaluated by computational trial and error.

Similarly a modified form of equation (12-17) can be used to calculate the inlet boundary conditions of, l in the vortex chamber. Denoting the radius at which $\bar{U}$ is a maximum by R, and the primary duct outer radius by R_3, then for $r \leqslant R$

$$l = (R - R_3) C_5 - \frac{C_6 (R-r)^2}{R - R_3} - \frac{(C_5 - C_6)(R-r)^4}{(R - R_3)^3} \qquad (11\text{-}18)a$$

and, for $r \geqslant R$

$$l = (R_2 - R) C_5 - \frac{C_6 (r-R)^2}{(R_2 - R)} - \frac{(C_5 - C_6)(r-R)^4}{(R_2 - R)^3} \qquad (11\text{-}18)b$$

where,

C_5 and C_6 are constants to be evaluated by computational trial and error.

The experimental results show that, R = 33 mm.

Equations (11-17) and (11-18) can be used to calculate the values of l at the nodes of the inlet boundary.

11.8.3 The boundary conditions at the axis of symmetry:

(a) The stream function, ψ:

Along the axis of symmetry, the stream function must have a constant value, Ref.(37). It is convenient to take this value as zero.

(b) The vorticity function, $\frac{\omega}{r}$:

The vorticity (ω) on the axis of symmetry is zero, Ref.(37). However, since (r) is also zero on the symmetry axis then the dependent variable ($\frac{\omega}{r}$) may take a finite value. These finite values are calculated from values of ψ at interior nodes which are once and twice removed on the normal to the symmetry axis. The ψ-r distribution, in the immediate vicinity of the axis of

symmetry, is parabolic, Ref.(37) thus.

$$\psi = \psi_o + a r^2 + b r^4 \qquad (11\text{-}19)$$

where,

ψ_o is the stream function at the axis of symmetry, a and b are constants for fixed (x).

Substituting for ψ from equation (11-19) into equation (11-6) we get:

$$\omega = - \frac{8 r b}{e}$$

or,

$$\frac{\omega}{r} = - \frac{8 b}{e} \qquad (11\text{-}20)$$

The values of the constants a and b in equations (11-19) and (11-20) can be determined by applying equation (11-19) successively to the next row and then to the row of nodes next to that and solving the resulting two equations in a and b simultaneously.

(c) The kinetic energy of turbulence, k:

The values of k at the nodes of the axis of symmetry were also taken from the experimental results.

(d) The length scale, l:

The length scale (l) is assumed to change linearly along the axis of symmetry, thus:

$$l = R_1 C_3 + \frac{x (R_2 C_1 - R_1 C_3)}{70.25} \qquad (11\text{-}21)$$

Equation (11-21) is used to calculate the value of l at each node on the axis of symmetry.

11.8.4 The boundary conditions at walls:

(a) The stream function, ψ:

The walls are impermeable to matter. The stream function (ψ), in this case, must have constant values along each wall.

(b) The vorticity function, $\frac{\omega}{r}$:

The vorticity boundary conditions at a wall is derived from the no-slip principle which assumes that there is no relative velocity between the wall and the fluid adjacent to it. Near a wall, gradients in the direction parallel to the wall are much smaller than those in the direction normal to it, they may therefore be neglected, Ref.(37). The variation in the

coordinate normal to the wall, within the thin layer adjacent to wall, may also be neglected. In the case of a wall parallel to the axis of symmetry, and assuming uniform viscosity near the wall, equation (11-7) reduces to:

$$-r\mu_{eff}\frac{\partial^2\omega}{\partial r^2} = 0$$

or,

$$r\mu_{eff}\frac{\partial^2\omega}{\partial n^2} = 0$$

where (n) is the normal to the wall measured from the wall. Integrating twice w.r.t. (n), we get:

$$\omega = \frac{An+B}{r\mu_{eff}} \qquad (12\text{-}22)$$

where;

$$A = r\mu_{eff}\left(\frac{\partial\omega}{\partial n}\right)_s$$

$$B = r\mu_{eff}\,\omega_s$$

The subscript (s) denotes the conditions at the wall.
Also, in this case, from equation (11-16), we get:

$$\omega = -\frac{1}{r}\frac{\partial\psi}{\partial r} \qquad (12\text{-}23)$$

Eliminating (ω) from equation (11-22) and (11-23, we get:

$$-\frac{1}{r}\frac{\partial\psi}{\partial r} = n\left(\frac{\partial\omega}{\partial n}\right)_s + \omega_s \qquad (12\text{-}24)$$

Equation (11-24) binds together (ω_s) and $\left(\frac{\partial\omega}{\partial n}\right)_s$ with the stream function and thus, constitutes a satisfactory boundary condition.

(c) The turbulent kinetic energy, k:

By definition, k at all points on a wall is zero.

(d) The length scale, l :

Similar to (k), the value of (l) at all points on a wall is zero.

11.9 The initial conditions:

The solution procedure, discribed in chapter twelve, is a successive iterative one. Such a method requires the prescription of initial guesses of the values of each variable at each internal node of the grid. It is obvious that the closer the initial guesses to the final solution, the fewer will be the iterations required to reach the solution. To make the solution most economic the experimental results

discussed in chapter ten were used to determine the initial conditions The initial conditions of (ψ) and ($\frac{\omega}{r}$) can be calculated from equation (11-2)a and (11-5) respectively, using the values of $\bar{U}$ and $\bar{V}$ as given by the experimental results. The initial condition of (k) is taken directly from the experimental results.

The initial conditions for (l) require more assumptions, since, as discussed in section (11-8), the experimental results do not allow it to be calculated. The domain of integration is divided into five regions, Fig.(11-3). For each region a suitable assumption is made.

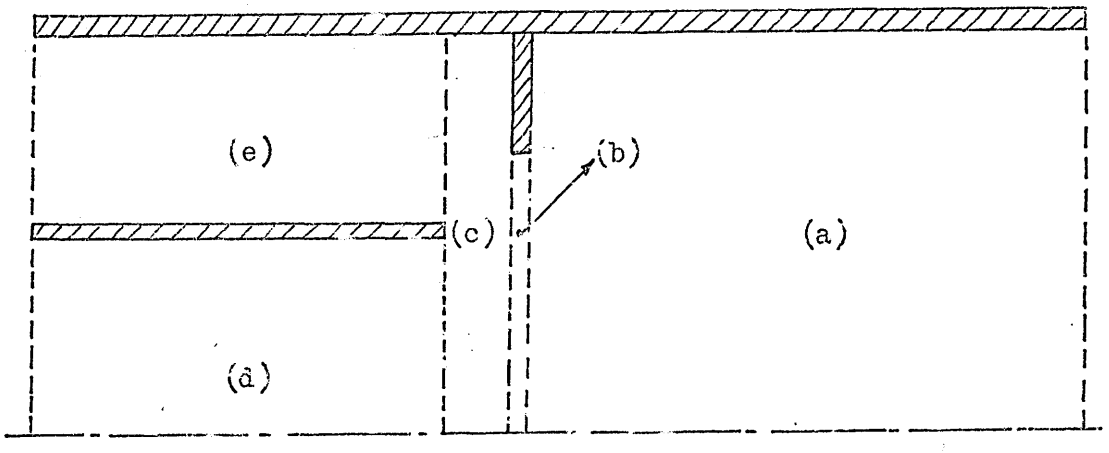

Fig.(11-3): Division of the flow field into five regions, each with suitable assumption for the initial conditions of l.

1- Region (a) is bounded by the down stream face of the fence, the axis of symmetry, the exit boundary and the secondary duct pipe. for this region, (l) is assumed to obey the formula:

$$l = l_o - \frac{C_2 r^2}{R_2} - \frac{(C_1 - C_2) r^4}{R_2^2} \qquad (11\text{-}25)$$

where,

l_o is the length scale at the axis of symmetry as given by the boundary conditions.

R_2, C_1, C_2 are as defined in equation (11-16).

2- Region (b) is bounded by the downstream and the upstream faces of the fence, the fence inward facing surface and the axis of symmetry. For this region, (l) is assumed to obey the formula

$$l = l_o - \frac{C_2 r^2}{R_f} - \frac{(C_1 - C_2) r^4}{R_f^3} \qquad (11\text{-}26)$$

where,

R_f is the fence radius

l_o, C_1 and C_2 are as defined in equation (11-25)

3- Region (c) is bounded by; the upstream face of the fence, the plane of the lip of the primary duct, the vortex chamber duct, and the axis of symmetry. For this region, l is assumed to obey equation (11-25).

4- Region (d) is bounded by; the primary duct pipe inside surface, the plane of primary duct lip, the inlet boundary, and the axis of symmetry. For this region, (l) is assumed to obey the formula:

$$l = l_o - \frac{C_2 r^2}{R_1} - \frac{(C_1 - C_2) r^4}{R_1^3} \qquad (11\text{-}27)$$

where,

l_o is as defined in equation (11-25)

R_1, C_1, C_2 are as defined in equation (11-17)

5- Region (e) is bounded by the primary duct outer surface, the vortex chamber duct inner surface, the plane of the primary duct lip and the inlet boundary. For this region, (l) is assumed to obey equation (11-8).

The values of (l) on the boundaries between the regions may be matched by assuming a linear rate of change in the direction normal to the boundary.

11.10 The initial values to be assigned to the constants:

The optimisation of the solution includes the determination of the final values of the constants. However the solution requires initial guesses to start with. It is obvious that the closer the intial guesses are to the final values, then the fewer will be the trials and the more economical will be the optimisation process. Table (11-4) shows the initial guesses of the values of the constants. The values of C_μ, σ_k and C_D are taken after Ref.(66). The value of σ_l is reccmmended by, Ref.(32). The values of C_1, C_2, C_3, C_4, C_5 and C_6 are also taken after Ref.(32). While the values of C_S and C_B are mere guesses, because to the knowledge of the author, no information is available about them.

Table (11-4)

The initial values assigned to the constants.

Constant	C_μ	σ_k	σ_1	C_D	C_s	C_B	C_1	C_2	C_3	C_4	C_5	C_6
Value	0.2	1.53	1.0	0.313	0.5	0.313	0.14	0.08	0.14	0.08	0.14	0.08

CHAPTER TWELVE

12. THE SOLUTION PROCEDURE:

12.1 Introduction:

The purpose of the present chapter was to apply a modified version of the general solution procedure proposed by Gosman et al in Ref.(37), to the present mathematical problem which was fully specified in chapter eleven. The procedure was based on a finite difference solution of the general differential equation and its auxiliary relations. The main elements of the derivation of the solution procedure were:-

1- The reduction of the differential equations to a set of simultaneous, algebraic, finite-difference equations which relate the values of the dependent variable at each node to the values which prevail at nearby nodes.

2- The recasting of the equations into a suitable form for solution by an iterative method.

3- The outline of the iterative solution procedure.

The following few sections discuss the details of these elements.

12.2 The reformulation of the differential equations:

The differential equations presented in chapter eleven must be recasted in a more convenient form before the finite difference solution could be derived, Ref.(37). This form is presented as follows:

$$a_\phi\left\{\frac{\partial}{\partial x}\left(\phi\frac{\partial\psi}{\partial r}\right)-\frac{\partial}{\partial r}\left(\phi\frac{\partial\psi}{\partial x}\right)\right\}-\frac{\partial}{\partial x}\left\{b_\phi r\frac{\partial}{\partial x}\left(c_\phi\phi\right)\right\}$$

$$-\frac{\partial}{\partial r}\left\{b_\phi r\frac{\partial}{\partial r}\left(c_\phi\phi\right)\right\}+r\,d_\phi=0 \qquad (12\text{-}1)$$

The functions a_ϕ, b_ϕ, c_ϕ and d_ϕ, corresponding to the differential equations of: $\frac{\omega}{r}$, ψ, k and l are presented in table (12-1).

Table (12-1)

The functions a_ϕ, b_ϕ, c_ϕ, and d_ϕ.

ϕ	a_ϕ	b_ϕ	c_ϕ	d_ϕ
$\frac{\omega}{r}$	r^2	r^2	μ_{eff}	$-r^2S$
ψ	0	$\frac{1}{\rho r^2}$	1	$-\frac{\omega}{r}$
k	1	μ_{eff}/σ_k	1	$-S_k$
l	1	μ_{eff}/σ_l	1	$-S_l$

The source terms S_ω, S_k, and S_l were given by equations; (11-9), (11-11), and (11-12) respectively.

12.3 The derivation of the finite-difference equations:

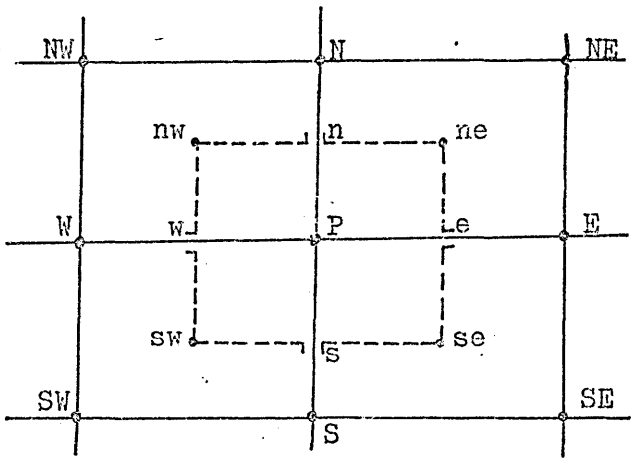

Fig.(12-1): An illustration of the finite-difference grid.

For the purpose of the derivation of the finite-difference equations, the field of interest, generally referred to as the domain of the solution, was covered by the grid network shown in Fig.(11-2). Fig.(12-1) displays a part of this grid. The figure shows a typical node (P), and its surrounding nodes. The integration of the differential equations is performed over the area enclosed by the dotted lines forming the smaller rectangle which encloses the point(P) The sides of this rectangle are supposed to lie midway between the neighbouring grid lines.

Integration of equation (12-1) over the above described area of integration gives:

$$\int_{r_s}^{r_n}\int_{x_w}^{x_e} a_\phi \left\{\frac{\partial}{\partial x}\left(\phi\frac{\partial\psi}{\partial r}\right)-\frac{\partial}{\partial r}\left(\phi\frac{\partial\psi}{\partial x}\right)\right\}dx\,dr-\int_{r_s}^{r_n}\int_{x_w}^{x_e}\frac{\partial}{\partial x}\left\{b_\phi r\frac{\partial}{\partial x}(c_\phi\phi)\right\}dx\,dr$$

$$-\int_{r_s}^{r_n}\int_{x_w}^{x_e}\frac{\partial}{\partial r}\left\{b_\phi r\frac{\partial}{\partial r}(c_\phi\phi)\right\}dx\,dr+\int_{r_s}^{r_n}\int_{x_w}^{x_e}(r\,d\phi)\,dx\,dr=0 \qquad (12\text{-}2)$$

The integration limits of equation (12-2) are the coordinates of the sides of the small rectangle. The first term is a convective term, the second and the third are diffusion terms, and the fourth is a source term. Denoting the convective term by I_c, and the diffusion terms by

I_d, and the source term by I_s, we get:

$$I_c - I_d + I_s = 0 \qquad (12\text{-}3)$$

where,

$$I_c = \int_{r_s}^{r_n}\int_{x_w}^{x_e} a_\phi \left\{ \frac{\partial}{\partial x}\left(\phi \frac{\partial \psi}{\partial r}\right) - \frac{\partial}{\partial r}\left(\phi \frac{\partial \psi}{\partial x}\right)\right\} dx\, dr \qquad (12\text{-}3)a$$

$$I_d = \int_{r_s}^{r_n}\int_{x_w}^{x_e} \left[\frac{\partial}{\partial x}\left\{ b_\phi r \frac{\partial}{\partial x}(c_\phi \phi)\right\} + \frac{\partial}{\partial r}\left\{ b_\phi r \frac{\partial}{\partial r}(c_\phi \phi)\right\}\right] dx\, dr \qquad (12\text{-}3)b$$

$$I_s = \int_{r_s}^{r_n}\int_{x_w}^{x_e} (r d_\phi)\, dx\, dr \qquad (12\text{-}3)c$$

Each of these integrals is to be evaluated separately because they require different assumptions.

12.3.1 Evalution of the convection term:

Inspection of equation (12-3)a reveals that each of its two terms could be formally integrated once (either w.r.t x or r) if a_ϕ was a constant. Table (12-1) shows that a_ϕ is indeed a constant for all the dependent variables except $(\frac{\omega}{r})$ for which it takes on the value (r^2). For this particular case it is assumed that the value of (r^2) over the integration area can be represented by a suitable mean value at the node point, P. Therefore we have for the special case of the vorticity equation:

$$(a_\phi)_P = (r^2)_{mean} = r_P^2 = \text{constant}$$

Hence, the formal integration can be completed, thus:

$$I_c = a_{\phi_P}\left[\int_{r_s}^{r_n} \left\{ \phi_e \left(\frac{\partial \psi}{\partial r}\right)_e - \phi_w \left(\frac{\partial \psi}{\partial r}\right)_w \right\} dr - \int_{x_w}^{x_e} \left\{ \phi_n \left(\frac{\partial \psi}{\partial x}\right)_n - \phi_s \left(\frac{\partial \psi}{\partial x}\right)_s \right\} dx \right]$$

or,

$$I_c = a\phi_P \int_{r_s}^{r_n} \phi_e \left(\frac{\partial \psi}{\partial r}\right)_e dr - a\phi_P \int_{r_s}^{r_n} \phi_w \left(\frac{\partial \psi}{\partial r}\right)_w dr - a_{\phi_P} \int_{x_w}^{x_e} \phi_n \left(\frac{\partial \psi}{\partial x}\right)_n dx + a_{\phi_P} \int_{x_w}^{x_e} \phi_s \left(\frac{\partial \psi}{\partial x}\right)_s dx$$

or,

$$I_c = I_{c1} + I_{c2} + I_{c3} + I_{c4}$$

Considering the first integral I_{c1},

$$I_{c1} = a\phi_P \int_{r_s}^{r_n} \phi_e \left(\frac{\partial \psi}{\partial r}\right)_e dr$$

Assuming that there exists an average value of ϕ_e denoted by $\bar{\phi}_e$ so that;

$$\bar{\phi}_e = \frac{\int_{r_s}^{r_n} \phi_e \left(\frac{\partial \psi}{\partial r}\right)_e dr}{\int_{r_s}^{r_n} \left(\frac{\partial \psi}{\partial r}\right)_e dr} = \frac{I_{c1}}{a\phi_P (\psi_{ne} - \psi_{se})}$$

thus,

$$I_{c1} = a\phi_P \bar{\Phi}_e (\psi_{ne} - \psi_{se}) \qquad (12\text{-}4)$$

One more assumption is introduced here to evaluate I_{c1} from equation (12-4), that is $\bar{\Phi}_e$ takes on the ϕ-value possessed by the fluid upstream of the e-face of the rectangle. This assumption means that if the flow is from E to P then, $\bar{\Phi}_e = \Phi_E$. Alternatively, if the flow is from P to E, then $\bar{\Phi}_e = \Phi_P$. Introducing the mathematical equivalence of the above argument into equation (12-4) we get:

$$I_{c1} = a\phi_P \left[\Phi_E \left\{ \frac{(\psi_{ne} - \psi_{se}) - |\psi_{ne} - \psi_{se}|}{2} \right\} + \Phi_P \left\{ \frac{(\psi_{ne} - \psi_{se}) + |\psi_{ne} - \psi_{se}|}{2} \right\} \right] \qquad (12\text{-}5)$$

The presence of the ψ-difference in equation (12-5), first within brackets and then within a modulus sign, ensures that one of the terms in the curly brackets in the equation will be zero. The term which remains will be that which represents the contribution from the node upstream of the e-fence of the rectangle. This is known as the "upwind differences" technique. The "upwind differences" is introduced to increase the stability of the solution, Ref.(37).

The integrals I_{c2}, I_{c3}, and I_{c4} can be expressed in similar forms, hence:

$$I_c = A_E (\Phi_P - \Phi_E) + A_W (\Phi_P - \Phi_W) + A_N (\Phi_P - \Phi_N) + A_S (\Phi_P - \Phi_S) \qquad (12\text{-}6)$$

where,

$$A_E = (a\Phi_P/2)\left[(\psi_{se} - \psi_{ne}) + |\psi_{se} - \psi_{ne}| \right] \qquad (12\text{-}7)a$$

$$A_W = (a\Phi_P/2)\left[(\psi_{nw} - \psi_{sw}) + |\psi_{nw} - \psi_{sw}| \right] \qquad (12\text{-}7)b$$

$$A_N = (a\Phi_P/2)\left[(\psi_{ne} - \psi_{nw}) + |\psi_{ne} - \psi_{nw}| \right] \qquad (12\text{-}7)c$$

$$A_S = (a\Phi_P/2)\left[(\psi_{sw} - \psi_{se}) + |\psi_{sw} - \psi_{se}| \right] \qquad (12\text{-}7)d$$

To evaluate ψ_{ne}, ψ_{se}, ψ_{nw} and ψ_{sw} in equations(12-7) it is assumed that the value of ψ at each corner of the rectangle is equal to the average of its values at the four neighbouring nodes, thus:

$$\psi_{se} = \frac{1}{4}(\psi_P + \psi_E + \psi_{SE} + \psi_S) \qquad (12\text{-}8)a$$

$$\psi_{ne} = \frac{1}{4}(\psi_P + \psi_E + \psi_{NE} + \psi_N) \qquad (12\text{-}8)b$$

$$\psi_{nw} = \frac{1}{4}(\psi_P + \psi_N + \psi_{NW} + \psi_W) \qquad (12\text{-}8)c$$

$$\psi_{sw} = \frac{1}{4}(\psi_P + \psi_W + \psi_{SW} + \psi_S) \qquad (12\text{-}8)d$$

12.3.2 Evaluation of the diffusion terms:

Inspection of equation (12-3)b, reveals that each of its terms can formally be integrated once, thus:

$$I_d = \int_{r_s}^{r_n} \{(b_\phi r)_e [\frac{\partial}{\partial x}(c_\phi \phi)]_e\} dr - \int_{r_s}^{r_n} \{(b_\phi r)_w [\frac{\partial}{\partial x}(c_\phi \phi)]_w\} dr$$

$$+ \int_{x_w}^{x_e} \{(b_\phi r)_n [\frac{\partial}{\partial r}(c_\phi \phi)]_n\} dx - \int_{x_w}^{x_e} \{(b_\phi r)_s [\frac{\partial}{\partial r}(c_\phi \phi)]_s\} dx$$

or,

$$I_d = I_{d1} - I_{d2} + I_{d3} - I_{d4}$$

Considering the first integral, I_{d1} ,

$$I_{d1} = \int_{r_s}^{r_n} (b_\phi r)_e [\frac{\partial}{\partial x}(c_\phi \phi)]_e \, dr$$

To evaluate I_{d1}, three assumptions are introduced;

$$r_e = (r_E + r_P)/2$$

$$b\phi_e = (b\phi_E + b\phi_P)/2$$

$$[\frac{\partial}{\partial x}(c_\phi \phi)]_e = \frac{(c_{\phi E}\, \phi_E - c_{\phi P}\, \phi_P)}{(x_E - x_P)}$$

Hence,

$$I_{d1} = \frac{(b_{\phi E} + b_{\phi P})}{2} \cdot \frac{(r_E + r_P)}{2} \cdot \frac{(c_{\phi E}\, \phi_E - c_{\phi P}\, \phi_P)}{(x_E - x_P)} \cdot \frac{(r_N - r_S)}{2}$$

I_{d2}, I_{d3}, and I_{d4} may be evaluated by similar arguments.

Summing up the expressions for I_{d1}, I_{d2}, I_{d3} and I_{d4}, we get:

$$I_d = B_E (c_{\phi_E} \phi_E - c_{\phi P} \phi_P) + B_W (c_{\phi_W} \phi_W - c_{\phi P} \phi_P)$$

$$+ B_N (c_{\phi_N} \phi_N - c_{\phi P} \phi_P) + B_S (c_{\phi_S} \phi_S - c_{\phi P} \phi_P) \qquad (12\text{-}9)$$

where,

$$B_E = \left(\frac{b_{\phi E} + b_{\phi P}}{8}\right) \cdot \left(\frac{r_N - r_S}{x_E - x_P}\right) \cdot (r_E + r_P) \qquad (12\text{-}10)a$$

$$B_W = \left(\frac{b_{\phi W} + b_{\phi P}}{8}\right) \cdot \left(\frac{r_N - r_S}{x_P - x_W}\right) \cdot (r_W + r_P) \qquad (12\text{-}10)b$$

$$B_N = \left(\frac{b_{\phi N} + b_{\phi P}}{8}\right) \cdot \left(\frac{x_E - x_W}{r_N - r_P}\right) \cdot (r_N + r_P) \qquad (12\text{-}10)c$$

$$B_S = \left(\frac{b_{\phi S} + b_{\phi P}}{8}\right) \cdot \left(\frac{x_E - x_W}{r_P - r_S}\right) \cdot (r_S + r_P) \qquad (12\text{-}10)d$$

12.3.3 Evaluation of the source term:

$$I_S = \int_{r_s}^{r_n} \int_{x_w}^{x_e} (r \, d\phi) \, dx \, dr \qquad (12\text{-}3)c$$

Assuming that $d\phi$ is uniform over the area of intergration and takes on the value at point P, furthermore, assuming that r_P is a close approximation of the area-average of r, thus:

$$I_s = d\phi_P \cdot V_P \tag{12-11}$$

where,

$$V_P = r_P \left(\frac{x_E - x_W}{2}\right)\left(\frac{r_N - r_S}{2}\right) \tag{12-12}$$

12.3.4 The complete finite-difference equation:

Assembling equations (12-6),(12-9) and (12-11), the resulting complete finite-difference equation is thus:

$$A_E(\phi_P - \phi_E) + A_W(\phi_P - \phi_W) + A_N(\phi_P - \phi_N) + A_S(\phi_P - \phi_S)$$
$$-B_E(c_{\phi_E}\phi_E - c_{\phi_P}\phi_P) - B_W(c_{\phi_W}\phi_W - c_{\phi P}\phi_P) - B_N(c_{\phi_N}\phi_N - c_{\phi P}\phi_P)$$
$$-B_S(c_{\phi S}\phi_S - c_{\phi_P}\phi_P) + d\phi_P V_P = 0 \tag{12-13}$$

where,

The A's are given by equation (12-7),

The B's are given by equation (12-10),

and V_P is given by equation (12-12).

Equation (12-13) must be reformed as a successive-substitution formula, that is by removing ϕ_P to the left-hand side, thus:

$$\phi_P = C_E\phi_E + C_W\phi_W + C_N\phi_N + C_S\phi_S + D \tag{12-14}$$

where,

$$C_E = (A_E + B_E c_{\phi_E})/\sum_{AB} \tag{12-15a}$$
$$C_W = (A_W + B_W c_{\phi_W})/\sum_{AB} \tag{12-15b}$$
$$C_N = (A_N + B_N c_{\phi_N})/\sum_{AB} \tag{12-15c}$$
$$C_S = (A_S + B_S c_{\phi_S})/\sum_{AB} \tag{12-15d}$$
$$D = -d\phi_P V_P/\sum_{AB} \tag{12-15e}$$
$$\sum_{AB} = A_E + A_W + A_N + A_S + c_{\phi P}(B_E + B_W + B_N + B_S) \tag{12-15f}$$

Also we have from equation (12-7) and equation(12-8)

$$A_E = (a_{\phi P}/8)\{(\psi_{SE} + \psi_S - \psi_{NE} - \psi_N) + |\psi_{SE} + \psi_S - \psi_{NE} - \psi_N|\} \tag{12-16a}$$
$$A_W = (a_{\phi P}/8)\{(\psi_{NW} + \psi_N - \psi_{SW} - \psi_S) + |\psi_{NW} + \psi_N - \psi_{SW} - \psi_S|\} \tag{12-16b}$$

$$A_N=(a_{\phi P}/8)\{(\psi_{NE}+\psi_E-\psi_{NW}-\psi_W)+|\psi_{NE}+\psi_E-\psi_{NW}-\psi_W|\} \quad (12\text{-}16)c$$

$$A_S=(a_{\phi P}/8)\{(\psi_{SW}+\psi_W-\psi_{SE}-\psi_E)+|\psi_{SW}+\psi_W-\psi_{SE}-\psi_E|\} \quad (12\text{-}16)d$$

The B's are given by equation (12-10) and V_P is given by equation (12-12).

12.3.5 The substitution formulae for the source terms:

There are four $d\phi$'s, one for each dependent variable. The substitution formula for each is derived separately because there is nothing in common between them.

12.3.5.1 The source term of the vorticity equation, $d\omega$:

From table (12-1) we get:

$$d\omega = -r^2 S_\omega$$

substituting for S_ω from equation (11-9), we get:

$$d\omega = -\frac{2r}{\rho}\left[\frac{\partial^2\mu}{\partial x^2}\left\{\frac{\partial}{\partial r}\left(\frac{1}{r}\frac{\partial\psi}{\partial r}\right)\right\}+\frac{\partial^2\mu}{\partial r^2}\left\{\frac{\partial}{\partial x}\left(\frac{1}{r}\frac{\partial\psi}{\partial x}\right)\right\}-\frac{\partial^2\mu}{\partial r\partial x}\left\{\frac{\partial}{\partial r}\left(\frac{1}{r}\frac{\partial\psi}{\partial x}\right)+\frac{\partial}{\partial x}\left(\frac{1}{r}\frac{\partial\psi}{\partial r}\right)\right\}\right]$$

where μ_{eff} was replaced, for brevity, by μ. Hence,

$$(d\omega)_P = -\frac{2r_P}{\rho}\left[\left(\frac{\partial^2\mu}{\partial x^2}\right)_P\left\{\frac{\partial}{\partial r}\left(\frac{1}{r}\frac{\partial\psi}{\partial r}\right)\right\}_P+\left(\frac{\partial^2\mu}{\partial r^2}\right)_P\left\{\frac{\partial}{\partial x}\left(\frac{1}{r}\frac{\partial\psi}{\partial x}\right)\right\}_P - \left(\frac{\partial^2\mu}{\partial r\partial x}\right)_P\left\{\frac{\partial}{\partial r}\left(\frac{1}{r}\frac{\partial\psi}{\partial x}\right)+\frac{\partial}{\partial x}\left(\frac{1}{r}\frac{\partial\psi}{\partial r}\right)\right\}_P\right].$$

or,

$$(d\omega)_P = -\frac{2}{\rho}r_P\left[D_1E_1+D_2E_2-D_3(E_3+E_4)\right] \quad (12\text{-}17)$$

Expressions for the constituents of equation (12-17) can be obtained on the basis of assumptions similar to those presented in sections 12.3.1 and 12.3.2, thus:

$$D_1=\left(\frac{\partial^2\mu}{\partial x^2}\right)_P=\frac{2}{(x_E-x_W)}\left\{\frac{(\mu_E-\mu_P)}{(x_E-x_P)}-\frac{(\mu_P-\mu_W)}{(x_P-x_W)}\right\} \quad (12\text{-}18)a$$

$$D_2=\left(\frac{\partial^2\mu}{\partial r^2}\right)_P=\frac{2}{(r_N-r_S)}\left\{\frac{(\mu_N-\mu_P)}{(r_N-r_P)}\cdot\frac{(\mu_P-\mu_S)}{(r_P-r_S)}\right\} \quad (12\text{-}18)b$$

$$D_3=\left(\frac{\partial^2\mu}{\partial x\partial r}\right)_P=\frac{1}{(x_E-x_W)(r_N-r_S)}\left(\mu_{NE}+\mu_{SW}-\mu_{SE}-\mu_{NW}\right) \quad (12\text{-}18)c$$

$$E_1=\left\{\frac{\partial}{\partial r}\left(\frac{1}{r}\frac{\partial\psi}{\partial r}\right)\right\}_P=\frac{2}{r_P(r_N-r_S)}\left(\frac{\psi_N-\psi_P}{r_N-r_P}-\frac{\psi_P-\psi_S}{r_P-r_S}\right) \quad (12\text{-}18)d$$

$$E_2=\left\{\frac{\partial}{\partial x}\left(\frac{1}{r}\frac{\partial\psi}{\partial x}\right)\right\}_P=\frac{2}{r_P(x_E-x_W)}\left(\frac{\psi_E-\psi_P}{x_E-x_P}-\frac{\psi_P-\psi_W}{x_P-x_W}\right) \quad (12\text{-}18)e$$

$$E_3=\left\{\frac{\partial}{\partial r}\left(\frac{1}{r}\frac{\partial\psi}{\partial x}\right)\right\}_P=\frac{1}{r_P(x_E-x_W)(r_N-r_S)}\left(\psi_{NE}-\psi_{SE}+\psi_{SW}-\psi_{NW}\right) \quad (12\text{-}18)f$$

$$E_4=\left\{\frac{\partial}{\partial x}\left(\frac{1}{r}\frac{\partial\psi}{\partial r}\right)\right\}_P=E_3 \quad (12\text{-}18)g$$

Therefore,

$$(d_\omega)_P = -\frac{2rp}{\rho}\left[D_1E_1 + D_2E_2 - 2D_3E_3\right] \qquad (12\text{-}19)$$

where,

D_1, D_2, D_3, E_1, E_2 and E_3 were given by equations (13-18)

12.3.5.2 The source term of the stream function equation, d_ψ:

From table (12-1), we get:

$$d_\psi = -\frac{\omega}{r}$$

hence,

$$(d_\omega)_P = -\left(\frac{\omega}{r}\right)_P \qquad (12\text{-}20)$$

12.3.5.3 The source term of the turbulent energy equation, d_K :

From table (12-1), we get:

$$d_K = -S_K$$

hence,

$$(d_k)_P = -(S_k)_P = \rho C_D \frac{(k_p)^{3/2}}{l_p} - (W_{skt})_P \qquad (12\text{-}21)$$

but,

$$(W_{skt})_P = \frac{2(\mu_{eff}-\mu)_P}{\rho^2}\left\{\left[\frac{\partial}{\partial x}\left(\frac{1}{r}\frac{\partial\psi}{\partial r}\right)\right]_P^2 + \left[\frac{\partial}{\partial r}\left(\frac{1}{r}\frac{\partial\psi}{\partial x}\right)\right]_P^2\right\}$$

$$+ \frac{(\mu_{eff}-\mu)_P}{\rho^2}\left\{\left[\frac{\partial}{\partial r}\left(\frac{1}{r}\frac{\partial\psi}{\partial r}\right)\right]_P - \left[\frac{\partial}{\partial x}\left(\frac{1}{r}\frac{\partial\psi}{\partial x}\right)\right]_P\right\}^2$$

or,

$$(W_{skt})_P = \frac{2(\mu_{eff}-\mu)_P}{\rho^2}\left\{F_1^2 + F_2^2\right\} + \frac{(\mu_{eff}-\mu)_P}{\rho^2}\left\{G_1 - G_2\right\}^2 \qquad (12\text{-}22)$$

where,

$$F_1 = \left[\frac{\partial}{\partial x}\left(\frac{1}{r}\frac{\partial\psi}{\partial r}\right)\right]_P = \frac{(\psi_{NE}+\psi_{SW}-\psi_{NW}-\psi_{SE})}{r_P(r_N-r_S)(x_E-x_W)} \qquad (12\text{-}23)a$$

$$F_2 = \left[\frac{\partial}{\partial r}\left(\frac{1}{r}\frac{\partial\psi}{\partial x}\right)\right]_P = \frac{(\psi_{NE}+\psi_{SW}-\psi_{NW}-\psi_{SE})}{r_P(r_N-r_S)(x_E-x_W)} \qquad (12\text{-}23)b$$

$$G_1 = \left[\frac{\partial}{\partial r}\left(\frac{1}{r}\frac{\partial\psi}{\partial r}\right)\right]_P = \frac{2}{r_P(r_N-r_S)}\left[\frac{\psi_N-\psi_P}{r_N-r_P} - \frac{\psi_P-\psi_S}{r_P-r_S}\right] \qquad (12\text{-}23)c$$

$$G_2 = \left[\frac{\partial}{\partial x}\left(\frac{1}{r}\frac{\partial\psi}{\partial x}\right)\right]_P = \frac{2}{r_P(x_E-x_W)}\left[\frac{\psi_E-\psi_P}{x_E-x_P} - \frac{\psi_P-\psi_W}{x_P-x_W}\right] \qquad (12\text{-}23)d$$

Thus,

$$(W_{skt})_P = \frac{(\mu_{eff}-\mu)_P}{\rho^2}\left\{4F_1^2 + (G_1-G_2)^2\right\} \qquad (12\text{-}24)$$

Where F_1, G_1 and G_2 were given by equations (12-23)a, (12-23)c and (12-23)d respectively.

12.3.5.4 The source term of the length scale equation, d_l:

From table (12-1), we get:

$d_l = -S_l$

or,

$$(d_l)_P = -(S_l)_P = C_B \frac{l_P}{k_P} (W_{skt})_P - C_s \varrho k_P^{\frac{1}{2}} \qquad (12\text{-}25)$$

where (W_{skt}) was given by equation (12-24).

12.3.6 The substitution formulae for the boundary conditions:

12.3.6.1 The stream function, ψ:

Equation (11-14) describes the boundary conditions of (ψ) at both the inlet and exit boundaries. Referring to Fig.(12-1), the equation can be integrated, thus:

$$\psi_P = \psi_S + \left(\frac{\bar{U}_{rs} + \bar{U}_{Prp}}{2}\right)(r_P - r_S) \qquad (12\text{-}26)$$

12.3.6.2 The vorticity function, $\frac{\omega}{r}$:

(a) Exit and inlet boundary conditions:

Equation (11-15) describes the boundary conditions of $(\frac{\omega}{r})$ at both the exit and inlet boundaries except those nodes lying on the walls or the axis of symmetry. Referring to Fig.(12-1), the equation can be solved, thus:

$$\left(\frac{\omega}{r}\right)_P = -\frac{4}{\varrho r_P (r_N - r_S)}\left[\left(\frac{\psi_N - \psi_P}{r_N^2 - r_P^2}\right) - \left(\frac{\psi_P - \psi_S}{r_P^2 - r_S^2}\right)\right] \qquad (12\text{-}27)$$

(b) The axis of symmetry boundary conditions:

The values of $(\frac{\omega}{r})$ at the nodes of the symmetry axis, unlike the inlet and exit conditions, cannot be calculated once and for all, because they depend on the values of (ψ) at the nodes of the next and the second next rows which are subject to changes during the iteration process. Therefore, the calculation of the axis of symmetry boundary conditions of $(\frac{\omega}{r})$ must be included in the iteration process. From equations (11-19) and (11-20) the substitution formula for the boundary condition of $(\frac{\omega}{r})$ on the axis of symmetry can be written, Ref.(37), as:

$$\left(\frac{\omega}{r}\right)_P = \frac{8}{e\left(r_{NP}^2 - r_{NPI}^2\right)}\left[\frac{\left(\psi_{NPI} - \psi_P\right)}{r_{NPI}^2} - \frac{\left(\psi_{NP} - \psi_P\right)}{r_{NP}^2}\right] \qquad (12\text{-}28)$$

where the subscripts; P, NP and NPI denote the points; on the axis of symmetry, on the next row, and on the second next row, Fig.(12-2).

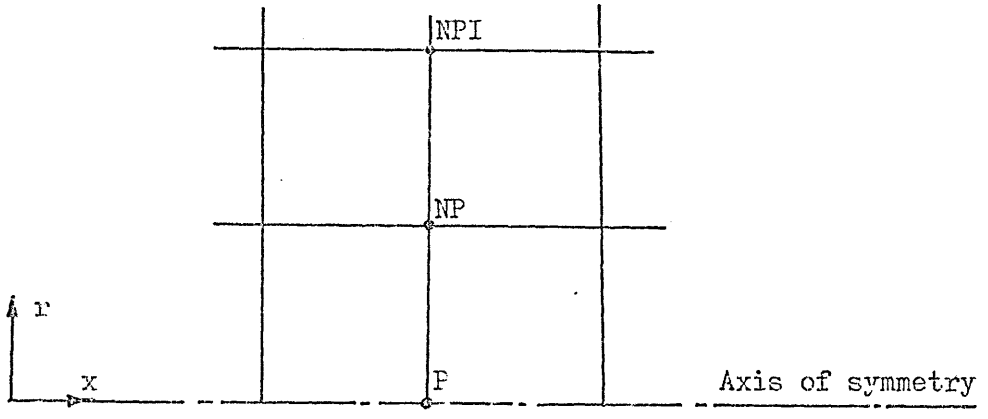

Fig.(12-2): Part of the grid in the neighbourhood of the axis of symmetry.

(c) The boundary conditions at the walls:

Equation (11-24) reveals that the value of $(\frac{\omega}{r})$ at a node on a wall depends on the values of ψ and $\frac{\omega}{r}$ at a node lying on the neighbouring grid line. Hence, the calculation of $(\frac{\omega}{r})$ must be included in the iteration process. According to the geometry of the domain of the solution, two substitution formulae are needed. The first is for nodes lying on walls which are parallel to the axis of symmetry, i.e constant-r walls, and the second for constant-x walls. The formulae written below were taken after Ref.(37):

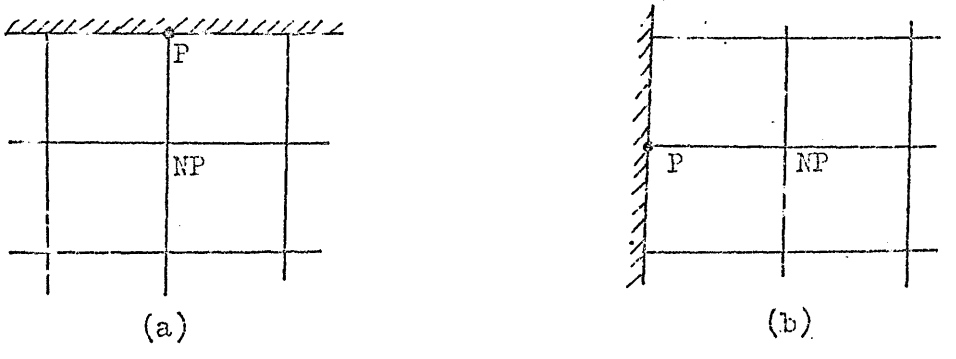

Fig.(12-3): Part of the grid in the neighbourhood of walls.

1- Constant-r walls:

$$\left(\frac{\omega}{r}\right)_P = \frac{24}{\varrho r_P (13 r_P - 5 r_{NP})}\left[\frac{\psi_P - \psi_{NP}}{(r_P - r_{NP})^2} - \frac{\varrho}{24}(2r_P - r_{NP})(7r_P - 3r_{NP})\left(\frac{\omega}{r}\right)_{NP}\right] \qquad (12\text{-}29)$$

Where the subscripts P and NP denote points on the wall and on the next row to the wall respectively, Fig.(12-3)a.

2- Constant-x walls:

$$\left(\frac{\omega}{r}\right)_P = \frac{3(\psi_P - \psi_{NP})}{\varrho r_P^2 (x_{NP} - x_P)^2} - \frac{1}{2}\left(\frac{\omega}{r}\right)_{NP} \qquad (12\text{-}30)$$

Where the subscripts P and NP denote points on the wall and on the next grid line to the wall respectively, Fig.(12-3)b.

12.3.7 The substitution formulae for the initial conditions:

12.3.7.1 The stream function, ψ:

Equation (12-26) was used to calculate the initial values of (ψ) at each internal node using the initial values of $\bar{U}$ given by the experimental results.

12.3.7.2 The vorticity function, $(\frac{\omega}{r})$:

Equation (11-5) describes the initial conditions of $(\frac{\omega}{r})$ at the internal nodes. Referring to Fig.(12-1), the equation can be solved, thus:

$$\left(\frac{\omega}{r}\right)_P = \frac{1}{r_P}\left[\left(\frac{\bar{V}_E - \bar{V}_W}{x_E - x_W}\right) - \left(\frac{\bar{U}_N - \bar{U}_S}{r_N - r_S}\right)\right] \qquad (12\text{-}31)$$

Equation (12-31) was used to obtain the initial values of $(\frac{\omega}{r})$ at each internal node, using the values of $\bar{U}$ and $\bar{V}$ as given by the experimental results.

12.3.8 The recovery of the mean velocity compoments:

At the end of the iteration process both the axial and the radial components of the mean velocity are to be calculated from the final values of the stream function. Equation (11-2)b described the relation between ψ and $\bar{U}$ and $\bar{V}$ respectively. A finite-difference solutions of these two equations are given below. The solutions are based on a three-point quadratic approximation , Ref.(37).

$$(\bar{U})_P = \frac{1}{\varrho r_P}\left[\frac{\{(r_N - r_P)^2 - (r_P - r_S)^2\}\psi_P + (r_P - r_S)^2 \psi_N - (r_N - r_P)^2 \psi_S}{(r_N - r_P)(r_P - r_S)(r_N - r_S)}\right] \qquad (12\text{-}32)a$$

$$(\bar{V})_P = -\frac{1}{\rho r_P}\left[\frac{\{(x_E-x_P)^2-(x_P-x_W)^2\}\psi_P+(x_P-x_W)^2\psi_E-(x_E-x_P)^2\psi_W}{(x_E-x_P)(x_P-x_W)(x_E-x_W)}\right] \qquad (12\text{-}32)b$$

12.3.9 The recovery of the static pressure:

The gradients of the static pressure p w.r.t.x and r can be calculated from equations (11-4)a and (11-4)b respectively. The equations contained derivatives of the mean velocity compoments and their correlations w.r.t.x and r. These can be calculated from a three-point quadratic approximation, according to which the expression for the first derivative of a general dummy function (B) at a node (P) w.r.t.x can be written as:

$$\left(\frac{\partial B}{\partial x}\right)_P = \left[\frac{\{(x_E-x_P)^2-(x_P-x_W)^2\}B_P+(x_P-x_W)^2B_E-(x_E-x_P)^2B_W}{(x_E-x_P)(x_P-x_W)(x_E-x_W)}\right] \qquad (12\text{-}33)a$$

Similarly, the first drivative of (B) at a node (P) w.r.t. r can be written as:

$$\left(\frac{\partial B}{\partial r}\right)_P = \left[\frac{\{(r_N-r_P)^2-(r_P-r_S)^2\}B_P+(r_P-r_S)^2B_N-(r_N-r_P)^2B_S}{(r_N-r_P)(r_P-r_S)(r_N-r_S)}\right] \qquad (12\text{-}33)b$$

Equations (12-33)a and (12-33)b were used to calculate the derivatives in equations (11-4)a and (11-4)b, hence $\left(\frac{\partial p}{\partial x}\right)_P$ or $\left(\frac{\partial p}{\partial r}\right)_P$ was estimated. As soon as the values of $\left(\frac{\partial p}{\partial x}\right)_P$ or $\left(\frac{\partial p}{\partial x}\right)_P$ had been available, the static pressure, p, was obtained from one of the following simple integration formulae.

$$p_P = p_W + \frac{1}{2}\left[\left(\frac{\partial p}{\partial x}\right)_W + \left(\frac{\partial p}{\partial x}\right)_E\right](x_E-x_W) \qquad (12\text{-}34)a$$

or,

$$p_P = p_S + \frac{1}{2}\left[\left(\frac{\partial p}{\partial r}\right)_S + \left(\frac{\partial p}{\partial r}\right)_N\right](r_N-r_S) \qquad (12\text{-}34)b$$

12.3.10 The calculation of additional flow parameters:

Two more flow parameters are relevant to diffuser work, the static pressure rise coefficient at point P, $(C_p)_P$, and the total pressure loss coefficient at point P, $(C_L)_P$. The two parameters are defined as follow:

$$(C_p)_P = \frac{p_P - p_o}{\frac{1}{2}\rho\alpha_o V_o^2} \qquad (12\text{-}35)$$

$$(C_L)_P = \frac{(p_o + \frac{1}{2}\rho\alpha_o V_o^2) - (p_P + \frac{1}{2}\rho V_P^2)}{p_o + \frac{1}{2}\rho\alpha_o V_o^2} \qquad (12\text{-}36)$$

Where:

p_P is the static pressure at point (P)

p_o is the area weighed mean static pressure across the inlet boundary of the main flow.

α_o is the velocity profile shape factor (defined in chapter one) at the inlet boundary of the main flow.

V_o is the area weighed mean axial valocity at the inlet boundary of the main flow.

V_P is the absolute value of the mean velocity at point (P),

$$V_P = (\bar{U}_P^2 + \bar{V}_P^2)^{\frac{1}{2}}$$

12.3.11 The calculation of the diffuser performance parameters:

The diffuser static pressure rise coefficient C_p and the total pressure loss coefficient C_L were calculated from the following two formulae.

$$C_P = \frac{p_{ex} - p_o}{\frac{1}{2}\rho\alpha_o V_o^2} \qquad (12\text{-}37)$$

$$C_L = \frac{(p_o + \frac{1}{2}\rho\alpha_o V_o^2) - (p_{ex} + \frac{1}{2}\rho\alpha_{ex} V_{ex}^2)}{(p_o + \frac{1}{2}\rho\alpha_o V_o^2)} \qquad (12\text{-}38)$$

Where,

p_o, α_o and V_o are as defined in equation (12-36)

p_{ex} is the area weighed mean static pressure at the exit boundary

α_{ex} is the velocity profile shape factor at the exit boundary.

V_{ex} is the area weighed mean axial velocity at the exit boundary

12.4 The outline of the solution procedure:

In chapter eleven the mathematical problem was posed and a full mathematical specifications were presented. In the previous few sections of this chapter, a finite difference solution of the general differential equation was presented together with other substitution formulae required for the solution. The general substitution formula and the associated auxiliary substitution formulae form a set of simultaneous algebraic equations. The present task is to outline a method of solution for this set of algebraic equations.

It has already been stated that the method of solution is an iterative one. Iterative methods for solving simultaneous algebraic equations

CHAPTER THIRTEEN

13. THE COMPUTER PROGRAMME:

13.1 Introduction:

The purpose of the present chapter is to provide the necessary link between the formal description of the solution procedure in terms of symbols, chapter twelve, and the practically useful solution in terms of numbers. This link is of course a computer programme, which translates the procedure into the series of instructions which the digital computer requires in order to carry out the computation.

The programme was written in FORTRAN IV computer language. The computer which was used to develop the programme was an ICL 1903 T machine at the Computer Centre of the Cranfield Institute. During the development of the programme some modifications on the solution procedure, chapter twelve, were found necessary to maximize the stability of the solution. These modifications will be mentioned during the description of the programme.

13.2 Organization and special features:

The programme was divided into a number of subroutines. Unique registers were allocated to the more important variables or quantities This made it possible to use standard COMMON statements to link the various subroutines and hence to reduce the store requirement to a minimum. The numerical input data were specified in the BLOCK DATA and no READ statements were used.

13.3 Description of the programme:

Fig.(13-1) shows the flow diagram of the programme. The diagram indicates the sequence of operations, the inter-connections of the various parts of the programme and their function in brief. A complete listing of the programme is provided in appendix G. Table (13-1) shows a list of the important FORTRAN symbols used in the programme and, wherever possible, their algebraic equivalents. The remainder of the symbols in the programme do not require much explanation.

Fig.(13-1): Flow diagram of the programme

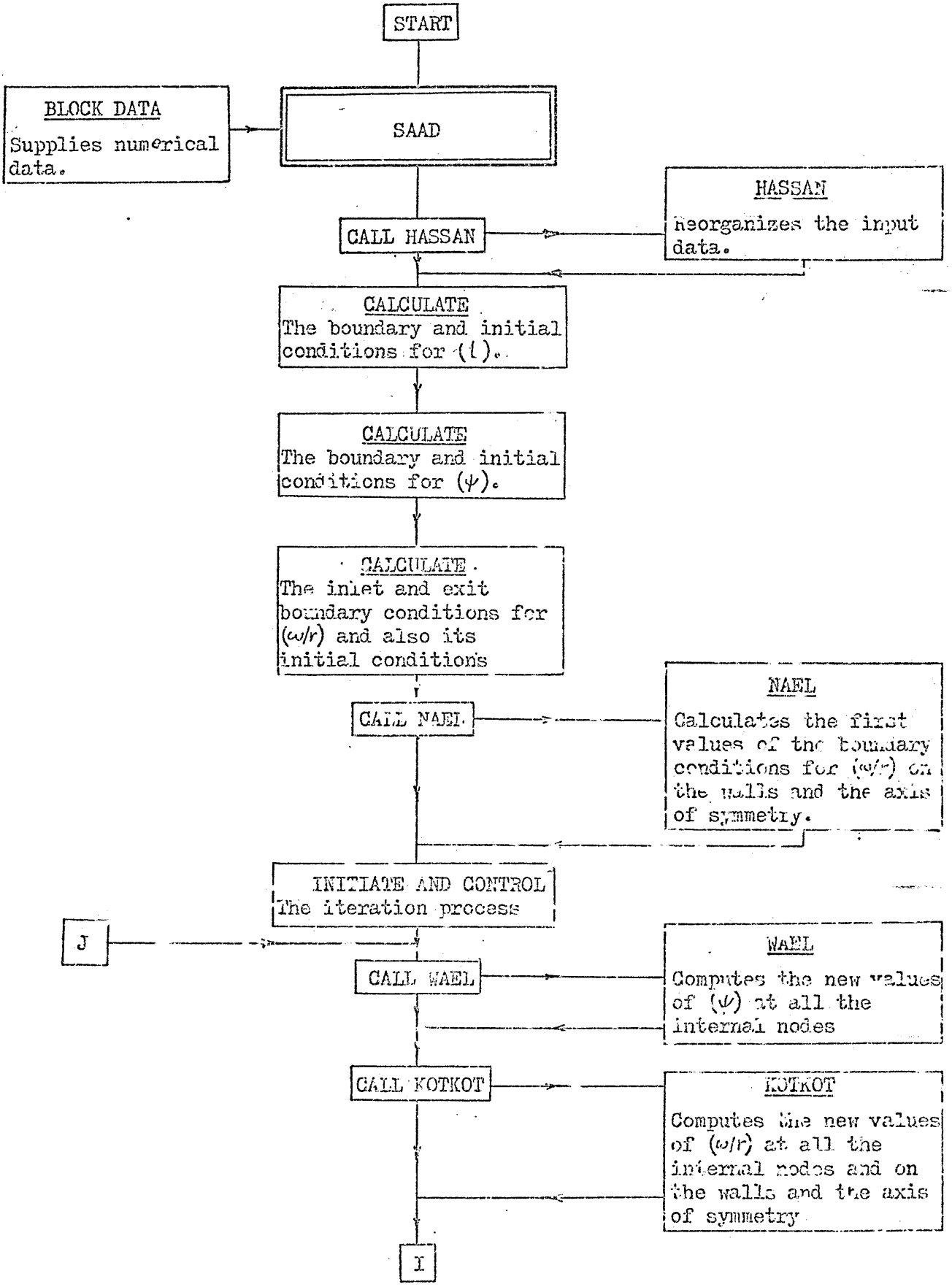

Cont. Fig.(13-1) Flow diagram of the programme

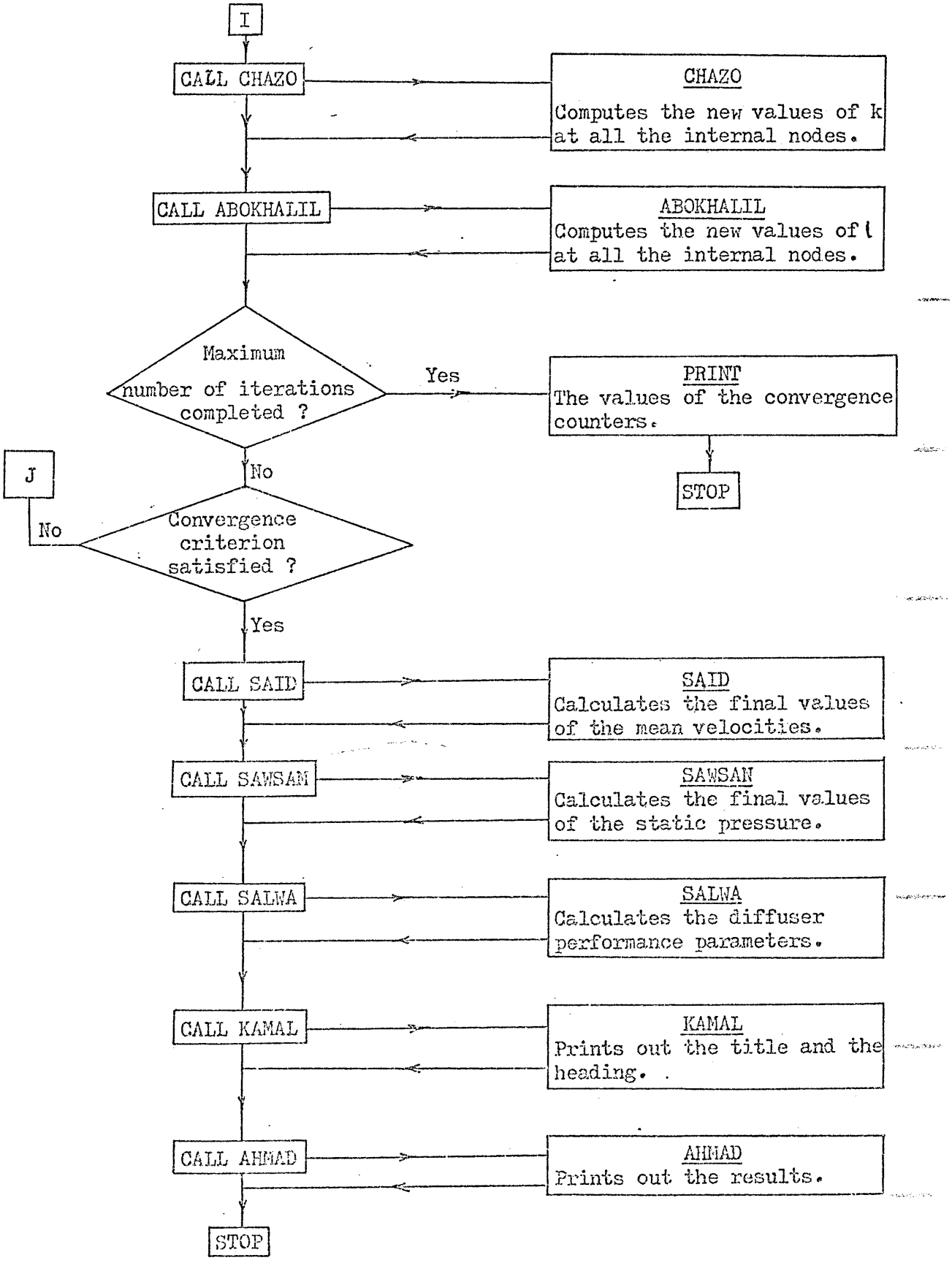

Table (13-1)

List of the used FORTRAN symbols.

FORTRAN symbols	Meaning
R(J), X (I)	Radial and axial coordinate of the node P(J,I) respectively.
UO (J,I), VO (J,I)	Initial values of $\bar{U}_P$ and $\bar{V}_P$ respectively
TO (J,I)	Initial values of k_P.
SP (J,I)	p_P
CON, CTO, CTR	C_1, C_2, C_3
CFO, CFV, CSX	C_4, C_5, C_6
RP, RS, RF	R_1, R_2, R_f
RPO, RIC	Outside radius of the primary duct and the mean radius of the vortex chamber respectively.
ROH, MU	ϱ, μ
CD, SEGK	C_D, σ_k
CA, CB, SEGL	C_s, C_B, σ_l
AL (J,I)	Values of l_P computed from the iteration cycle number N-1
ALR (J,I)	Values of l_P computed from the next iteration cycle number N.
EPSI (J,I)	Values of ψ_P computed from the (N-1)th cycle.
EPSIR (J,I)	Values of ψ_P computed from the Nth cycle.
OMEGA (J,I)	Values of $(\omega/r)_P$ computed from the (N-1)th cycle.
OMEGAR (J,I)	Values of $(\omega/r)_P$ computed from the Nth cycle.
T (J,I)	Values of k_P computed from the (N-1)th cycle.
TR (J,I)	Values of k_P computed from the Nth cycle.
U (J,I), V (J,I)	The final values of $\bar{U}_P$ and $\bar{V}_P$ respectively.
CP (J,I), CL (J,I)	$(C_p)_P$ C_L
SPOT, ALPHO, VOI	p_o, α_o, V_o

Cont. Table (13-1)

List of the used FORTRAN symbols.

FORTRAN symbols	Meaning
SPET, ALPHE, VE	P_{ex}, α_{ex}, V_{ex}
CPT, CLT	C_P, C_L
K	Iteration counter
MEPSI, MOMEGA	Convergence counters for ψ and ω/r respectively.
MT, MAL	Convergence counters for k and λ respectively.
AE, AW, AN, AS	The A'S of equation (12-7)
BE, BW, BN, BS	The B'S of equation (12-10)
CE, CW, CN, CS	The C'S of equation (12-14)
D (J,I)	$(D)_P$
DON, DTO, DTR	D_1, D_2, D_3
EON, ETO, ETR	E_1, E_2, E_3
DOMEGA (J,I)	$(d_\omega)_P$
FON, GON, GTO	F_1, G_1, G_2
WSKT (J,I)	$(W_{skt})_P$
SEGAB (J,I)	$(\Sigma_{AB})_P$
DK (J,I)	$(d_k)_P$
DL (J,I)	$(d_l)_P$

In the next few subsections a complete, though necessarily brief, description of the various parts of the programme is presented:

13.3.1 The main programme, "MASTER SAAD":

Because of the subdivision of the computation into various subroutines, the main programme has been assigned a relatively light duties which can be summarized as follows:

1- It calculates the boundary and the initial conditions of the length scale (l) using the equations (11-16), (11-17), (11-18), (11-21), (11-25), (11-26) and (11-27).

2- It calculates the boundary and the initial conditions of the stream function (ψ) using equation (12-26).

3- It calculates the exit and inlet boundary conditions of the vorticity function (ω) using equation (12-27). It also calculates the initial conditions of (ω) using equation (12-31)

4- When all these have been done the main computations are started by calling the relevant subroutines.

In the subsequent iteration process the field of integration is confined entirely to the area enclosed by the grid-lines one mesh distance from the boundaries, except the vorticity function for which some of its boundary conditions are calculated during the iteration process. Thus, known boundary values can be conveniently specified as they will be safe from any later interference. An example is the set of boundary values of (k), these are zero on all boundaries except those on the inlet, exit and the axis of symmetry boundaries.

13.3.2 BLOCK DATA:

All the numerical data are specified here. This includes the boundary and the initial values of $\bar{U}$, $\bar{V}$ and k. It also includes the fluid properties, the grid dimensions and the values assigned to the various constants required for the solution.

13.3.3 Subroutine "HASSAN":

Some of the numerical data specified in the BLOCK DATA were introduced in an unsuitable order for use by the programme. Consequently, this subroutine was provided to reorganize these data.

13.3.4 Subroutine "NAEL":

This subroutine calculates the first set of values of $(\frac{\omega}{r})$ at the nodes of the wall and the axis of symmetry boundaries using equations (12-28), (12-29) and (12-30). It is called into action only once and is not part of the iteration process.

13.3.5 Subroutine "WAEL":

Computes the new values of (ψ) as part of the iteration process using the general substitution formula, equation (12-14), and its associated equations given in section 12.3.4. The method of calculation of the B's included in the general substitution formula had to be modified. This was because $b_\psi = 1/\varrho r^2$, hence the calculation of the B's at the nodes of the grid line next to the axis of symmetry involved the division by a zero which for obvious reasons caused serious computational problems. The modified formulae for the B's in this particular case is given as follows:-

$$B_E = \frac{(r_N - r_S)}{2\varrho r_P (x_E - x_P)} \qquad (13\text{-}1)a$$

$$B_W = \frac{(r_N - r_S)}{2\varrho r_P (x_P - x_W)} \qquad (13\text{-}1)b$$

$$B_N = \frac{x_E - x_W}{\varrho (r_N + r_P)(r_N - r_P)} \qquad (13\text{-}1)c$$

$$B_S = \frac{x_E - x_W}{\varrho (r_P + r_S)(r_P - r_S)} \qquad (13\text{-}1)d$$

Equations (13-1) were derived assuming similar assumptions to those introduced in chapter twelve.

13.3.6 Subroutine "KOTKOT":

Computes the new values of $(\frac{\omega}{r})$ as part of the iteration process using the general substitution formula, equation (12-14), and its associated equations. This is for all the internal nodes except those nodes on the grid-lines one mesh distance from wall boundaries. The $(\frac{\omega}{r})$ values at these nodes were calculated from implicit formulae in which the value of $(\frac{\omega}{r})$ at the wall node does not appear explicitly. An example is the case where the node "P" is on a grid-line one mesh distance north of a wall. The implicit

formula in this case is as follows:

$$\left(\frac{\omega}{r}\right)_P = \frac{C_E(\omega/r)_E + C_W(\omega/r)_W + C_N(\omega/r)_N - 3C_S(\psi_P-\psi_S)/\rho r_S^2(r_P-r_S)^2 + D}{1+C_S/2} \qquad (13\text{-}2)$$

Here, $(\omega/r)_S$ does not appear explicitly for it has been eliminated by the use of equation (12-30). This method was used to eliminate divergence which would have otherwise been experienced due to the use of non-uniform spacing between the grid-lines, Ref.(37).

The calculation of the values of $(\frac{\omega}{r})$ at the wall and axis of symmetry boundaries was also included in this subroutine. Equations (12-28), (12-29), and (12-30) were used for this purpose.

13.3.7 Subroutine "CHAZO":

This subroutine computes the new values of (k) at all the interanal nodes as part of the iteration process.

At the early stages of development of this programme, divergence occurred when(k) was calculated using the general substitution formula. It is believed that the reason for this was that large variations in the C's and D of equation (12-14) were experienced. This impaired convergence and sometimes led to instability. Two remedies were found to be successful for this source of divergence. Both of them were suggested in Ref.(37) and are described below.

The first remedy was specifically devised to reduce variations in the source term D. From table (12-1) and equations (12-14), (12-15)e and (12-21) it may be shown that the formula for k_P is:

$$(k)_P = C_E k_E + C_W k_W + C_N k_N + C_S k_S + V_P(W_{int} - D_K)_P / \sum_{nb} \qquad (13\text{-}3)$$

where,

$$(D_k)_P = \left(C_D \rho k^{3/2}/l\right)_P \qquad (13\text{-}4)$$

Here, k_P appears to the power 3/2 in equation (13-4). It might therefore be anticipated that $(D_K)_P$ could vary so widely as to provoke divergence. In fact the results obtained during the early stages of development of the programme showed that this was the case. The problem was solved by the re-arrangement of equation

(13-3) so that it takes the following form:

$$(k)_p = \frac{[C_E k_E + C_W k_W + C_N k_N + C_S k_S + V_P (W_{SK})_P / \Sigma_{AB}]}{(1 + V_P (D'_K)_P / \Sigma_{AB})} \qquad (13\text{-}5)$$

where,

$$(D'_K)_P = (C_D \rho k^{\frac{1}{2}} / \ell)_P \qquad (13\text{-}6)$$

The point about equations (13-5) and (13-6) is that the variation in the modified source term can be expected to be much less than those of the original one.

The second remedy is a commonly-employed one, which is known as under-relaxation. For this, the value of k which was computed in the (N-1) iteration cycle is denoted by $k^{(N-1)}$ and the value of k being computed in the current iteration cycle number N is denoted $k^{(N)}$. Then the value which is actually used in the next iteration cycle number N+1 and is used for calculating the value of k at the adjacent nodes in the current iteration cycle is computed from

$$k = \gamma\, k^{(N)} + (1-\gamma)\, k^{(N-1)} \qquad (13\text{-}7)$$

Here, the coefficient γ, which is often termed the "under-relaxation parameter" was assigned the value 0.5.

13.3.8 Subroutine "ABOKHALIL":

This subroutine computes the new values of (ℓ) at all the internal nodes as part of the iteration process. The general substitution formula was used in this subroutine. Similar to the case of (k), the results obtained from the early stages of development proved that the solution for (ℓ) was divergent. The use of an under-relaxation parameter having the value of 0.5 solved the problem.

13.3.9 Subroutine "SAID":

Once the convergence criterion was satisfied, this subroutine would be used to calculate the final values of the components of the mean velocity at all the internal nodes using equations (12-32).

13.3.10 Subroutine "DAWSAN":

This subroutine may be used to calculate the values of the static

pressure at all the nodes of the grid using the method described in section 12.3.9.

13.3.11 Subroutine "SALWA":

This subroutine may be used to calculate the static pressure rise coefficient, equation (12-35), and the total pressure loss coefficient, equation (12-36), at all the nodes of the grid. It may also be used to calculate the performance of the diffuser as described in section 12.3.10.

13.3.12 Subroutine "KAMAL":

This subroutine prints out the title and the heading of the output results.

13.3.13 Subroutine "AHMAD":

This subroutine prints out the output results.

13.4 The development of the computer programme:

The early attempts to run the programme proved that the solution was divergent. The introduction of the modifications which were mentioned in the previous section solved the problem and hence the programme became convergent. However, the rate of convergence was slow and no satisfactory results were achieved within the allocated computational time. It is believed that the problem is not a mathematical but a computational one which can be solved by further development of the programme. Due to the cost and time limitations imposed on the present study, it was not possible to develop the programme any further. Suggestions for future development are as follows:

1- Divergence can be enhanced by changing the order of scanning the solution domain so that it may approximately follow the flow inside the diffuser.

2- It is believed that the major cause of the problem is the unsatisfactory assumptions about the boundary and initial conditions of the length scale (l). An improvement in this area may increase the rate of convergence. The only problem is that, to the knowledge of the author, there is no available information about the distribution of the length scale in similar flows. One way around the problem is to calculate the length scale ...

distribution from the turbulence spatial correlations or autocorrelations which can be measured experimentally.

3. If the previous suggestions proved successful and a reasonable rate of convergence was achieved, then this can be enhanced by computational optimisation in which the best values of the constants introduced in the solution, particularly C_S, C_B and σ_l, are selected by trial and error.

V CONCLUSIONS AND RECOMMENDATIONS

CONCLUSIONS

The flow in a vortex controlled diffuser was studied experimentally and theoretically. The experimental aspects of the study included the following:-

(1) The selection of a suitable laser Doppler velocimeter for the measurement of the mean velocity and the Reynolds' stresses. It was concluded that the most suitable LDV was the type which uses photon correlation for the analysis of the signal.

(2) An experimental optimisation of the geometry of a diffuser model was conducted. The results were used in the design of the diffuser model which was later used for the measurement with the LDV.

(3) The distribution of the static pressure, the components of mean velocity and the Reynolds' stresses were measured. The results were presented and discussed. A comprehensive hypothesis describing the flow behaviour in the diffuser was established. This can be summarized as follows:-

a- The precisely contoured nozzle provides a smooth entry to the primary duct. The flow, therefore, has a uniform velocity and relatively low turbulence intensity at the entrance of the primary duct. The length of the primary duct was carefully selected to ensure a turbulent boundary layer flow further downstream, but not to allow the flow to reach the state of a fully developed flow. Therefore, the flow approaches the region where the sink effect is influential having a turbulent boundary layer but still with an accertably uniform velocity profile.

b- The sink effect, resulting from the suction at the entrance of the vortex chamber, penetrates to a distance of about $\frac{1}{2}D_1$ upstream of the primary duct exit lip. The stream tube, next to the growing boundary layer, accelerates under the influence of the sink effect. Consequently, the growth of the boundary layer on the wall of the primary duct is counteracted and the velocity gradient increases.

c- As the flow separates from the lip of the primary duct a strong shear layer springs off the lip. The boundary layer, which is too energy deficient to follow the main flow, enters the vortex chamber under the influence of the suction and decelerates as it flows round the standing vortex. The early separation and the effect of the suction help the main flow to diverge rapidly as it proceeds towards the fence. The divergence is accompanied by, for continuity

reasons, deceleration and hence static pressure recovery and the possession of a high level of a radial velocity component.

d- The main flow reaches the fence having a relatively high velocity in the immediate vicinity of the fence top. This drops to zero value, to fulfill the non-slip requirement at the surface of the fence top, in a very short distance and hence results in a very steep velocity gradient. The result is the creation of a very strong shear layer downstream of the fence. The new shear layer joins the original one flowing through the fence to form an even stronger and broader shear layer which continues to gain more strength for a short distance downstream of the fence. The shear layer has a very intense turbulence level of a highly anisotropic and non-homogeneous nature.

e- The radial velocity component originally possessed by the main flow helps it to diverge very rapidly to fill the whole cross-section of the secondary duct in a very short axial distance, estimated here from the experimental results as about $\frac{1}{3}D_1$. The strong mixing action, created by the shear layer on the separation surface, helps to promote the divergence process. The turbulence in the shear layer can be looked at as an efficient agent which is transporting kinetic energy from the core of the flow to the energy deficient regions in the neighbourhood of the surface of separation and later in the neighbourhood of the duct wall. The result is the redistribution of the kinetic energy and hence a progressive static pressure recovery without significant losses in the total pressure.

f- The efficient mixing process also helps the flow to reattach smoothly to the secondary duct wall and consequently the flow continues to gain static pressure as it proceeds along the diffuser short length.

g- The relatively energy deficient air entering the vortex chamber decelerates as it flows round the standing vortex. The air which is too energy deficient to escape is entrained by the vortex to be recirculated and hence re-energized by the fresh incoming flow. The present experimental results indicate that the vortex has no significant effect on the main flow and hence on the performance of the diffuser. The energy required to drive the vortex is obtained from the bled air which also loses too much energy during the severe diffusion process following its escape from the vortex.

(4) Recommendations for the development of the design of this particular type of diffuser were also presented.

The theoretical aspects of the study included the following:-

(1) A suitable mathematical model of turbulence was selected. This was a k-l effective-viscosity model. The model was incorporated in a previously established mathematical approach which is usually used for the prediction of recirculating flows.

(2) The approach was modified to suit the flow conditions in this paticular diffuser. The mathematical problem was completely specified and hence the finite difference solution procedure was developed to suit this particular case.

(3) A new computer programme was written and developed. The results of the computation proved that the solution was convergent and can be used, after further development, to predict the flow and the performance of this particular type of diffuser. Suggestions for further development of the programme were also proposed.

RECOMMENDATIONS FOR FURTHER RESEARCH:

As a closure of this study it may be appropriate to venture into that area which is the privilege of every research worker, that is the suggestions for further research.

Undoubtedly, further research on the turbulence structure inside this type of diffuser must form the focus of immediate attention. Extensive measurements must be made and carefully scrutinized to test and improve the present knowledge about the turbulence structure inside the diffuser, particularly in the vicinity of solid walls. Another area of interest is the measurement of the spatial and autocorrelations of turbulence and also their frequency spectra. This would lead to a better understanding of the distribution of the length scale.

On the theoretical side, more development of the proposed computer programme is required. Detailed suggestions for the development of the programme have already been put forward.

VI REFERENCES

REFERENCES

(1) Adkins, R.C. "A short diffuser with low pressure loss." Journal of fluids engineering. September 75.

(2) Depollas, H.E. "The effect of Mach number on vortex controlled diffusers." C.I.T. M.Sc. Thesis, October 1977.

(3) Patterson, G.N. "Modern diffuser design." Aircraft Engineering, Vol. 10, p.267, September 1938.

(4) Cockrell, D.J. and Markland, E. "A review of incompressibel diffuser flow." Aircraft Engineering, October1963, p.286.

(5) Cockrell, D.J. and Markland, E. "The effects of inlet conditions on incompressible fluid flow through conical diffusers." J.Roy.Aero.Soc., Vol. 66. No. 613, January 1962.

(6) Adkins, R.C. "Diffusers and their performance improvement by means of boundary layer control." Lecture supplement, Von Karman Institute. March 1977.

(7) Ringleb, F.O. "Flow control by generation of standing vortices and the cusp effect." Rep. 317, Princeton University July 1955.

(8) Ringleb, F.O. "Separation control by trapped vortices" Published in, "Boundary layer and flow control. "Edited by Lachman. Published by Pergamon Press, 1961.

(9) Juhasz, A.J. and Smith, J.M. "Performance characteristics of two annular dump diffusers using suction-stablized vortex flow control." Paper presented to the joint symposium on the design and operation of fluid machinary. ASCE-IAHR-AIHR-ASME. Ft. Collins-Colorodo, USA,1978.

(10) Heskestad, G. "Remarks on snow cornice theory and related experiments with sink flows." Journal of Basic engineering. June 1966, pp. 539-549.

(11) Heskestad, G — "Further experiments with suction at a sudden enlargement in a pipe." Journal of Basic engineering. September 1970, pp. 437-449.

(12) Saad, E.A. — "High subsonic Mach number behaviour of vortex controlled diffuser." C.I.T. M.Sc. thesis, Semptember 1978.

(13) Adkins, R.C. — "Preliminary investigation of a vortex controlled diffuser." Paper presented to the combustion Sub-Committee of the Gas Turbine Collaboration Committee, 69.

(14) Sims, M.D. — "Diffuser flow control using trapped vortices." C.I.T. M.Sc. thesis, June 1969.

(15) Beatty, C.G. — "Diffuser control by trapped vortices." C.I.T. M.Sc. thesis, September 1970.

(16) Fenge, B.B. — "Some optimisation studies on vortex controlled diffusers." C.I.T. M.Sc. thesis September 1971.

(17) Proffit, P.J.G. — "Optimisation and investigation of a vortex controlled annular diffuser." C.I.T. M.Sc. thesis September 1972.

(18) Sutherland, G.D. — "An investigation into the flow of vortex diffusers." C.I.T. M.Sc. thesis, September 1972.

(19) Adkins, R.C. — "A short diffuser with low pressure loss." Paper presented to the ASME symposium on "The fluid mechanics of combustion." Montreal, May 1974.

(20) Mallam, A — "Vortex Diffuser Without Bleed." C.I.T. M.Sc. thesis, September 1974.

(21) Mak, K.H. — "Application of vortex flow control to turbine exhaust diffusers." C.I.T. M.Sc. thesis, September 1974.

(22) Diacakis. — "Tail pipe diffusers." C.I.T. M.Sc. thesis, September 1975.

(23) Allen, J.E. — "A vortex controlled radial diffuser." C.I.T. M.Sc. thesis, September 1975.

(24) Rizk, N.K. "The Application of fluidics to the control of pollutant emission from gas turbine combustion." C.I.T. M.Sc. thesis, 1974.

(25) Fletcher, R.S. Adkins, R.C. "The variable geometry combustor." Proc. AGARD conference, Variable Geometry and Multi-cycle Engines(48 PEP Meeting), Paris September 1976.

(26) Kwan, W.C.T. "The use of vortex flow control in variable geometry combustion." C.I.T. thesis, 1976.

(27) Elsaftawy, A.S. "A double acting variable geometry combustor." C.I.T. M.Sc. thesis, September 1978.

(28) Adkins, R.C. Elsaftawy, A.S. "A double acting variable geometry combustor." An ASME paper 79-GT-197, presented to the Gas turbine conference, San Diego Calif. March 79.

(29) Matharu, D.S. "An investigation of a hybrid diffuser." C.I.T. M.Sc. thesis, September 1978.

(30) Adkins, R.C. Matharu, D.S. Yost, J.O. "The Hybrid diffuser." An ASME publication 80-GT-136, presented to the Gas turbine conference, New Orleans, March 1980.

(31) Schlichting, H. "Boundary layer theory." Six edition published by McGraw-hill, 1968.

(32) Launder, B.E. and Spalding, D.B. "Mathematical models of turbulence." Academic press, 1972.

(33) Chaturvedi, M.C. "Flow characteristics at abrupt axisymmetric expansions." Ph.D. dissertation, Iowa State University, 62

(34) Bradshaw, P. "An introduction to turbulence and its measurement." Pergamon press, 1971.

(35) Gibson, M.M., McGuirk, J.J., Jones, W.P., Whitelaw, J.H. "Mathematical modelling of turbulent flows." Outline notes for ashort post-experience course held at the Imperial College, London, 1979.

(36) Ha Minh, H. and Chassaing, P. "Perturbations of turbulent pipe flow." A paper presented to the First International Symposium on Turbulent Shear Flows, the Pennsylevania state University, USA, April 1977.

(37) Gosman, A.D. et al "Heat and mass transfer in recirculating flows." Academic press, 1969.

(38) Durst.F. et al "Principles and practice of laser Doppler anemonetry." Academic press, 1976.

(39) Elder, R.L. "The Application of laser Doppler velocimetry to the measurement of the flow exhausting from a high speed centrifugal impeller." Paper prepared for the Photon Correlation Techniques In Fluid Mechanics, Stockholm, Sweden, June, 1978.

(40) Adrian, R.J. and Fingerson, L.M. "laser Anemometry, theory, Application, and techniques." Course suplement, Manchester University, 1979.

(41) Pike, E.R. "Photon correlation velocimetry." Published in "Photon correlation spectroscopy and velocimetry." Edited by H.Z. Cummins and E.R.Pike. NATO advanced study institutes series,series B: Physics, volume 23.

(42) Boutier, A. and Lefevre, J. "Some applications of laser anemometry in wind-tunnels." Proceedings of the LDA-Symposium, Copenhagen, 1975.

(43) Abbiss, J.B. and Wright,M.P. "Measurements on an axi-symmetric jet using a photon correlator." Proceeding of the LDA-Symposium, Copenhagen, 1975.

(44) B.S. 1042 "Methods for the measurement of fluid flow in pipes." Part 1,1964.

(45) Adkins, R.C. "Diffuser performance-parameters and techniques." C.I.T. lecture note, SME/1734/RCA/DC.

(46) B.S.1042 "Methods for the measurement of fluid flow in pipes." Part 2A,1973.

(47) Spectra-Physics "Model 124B Helium-Neon Laser, instruction Manual.

(48) Malvern Instruments Adjustable beam splitter and polarisation unit type RF 307, catalogue.

(49) Malvern Instruments K9023 phase modulator, handbook.

(50) Malvern Instruments RF 313 Anemometer optical reflex system, instruction manual.

(51) EMI, E lectron tube division Photomltiplier power supply, type PM 28B, operation notes.

(52) Malvern Instruments Malvern digital correlator type K 7023, operating and installation manual.

(53) Malvern Instruments Malvern computing data processor MDP 7023, instruction manual.

(54) Gould Advance OS255 15 MHz, Dual trace oscilloscope, instruction manual.

(55) Commodor Business Machines PET personal computer, user manual.

(56) Commodor Business Machines Printer user manual.

(57) Adrian, R.S. et al "Preliminary studies using photon correlation velocimetry in turbomachinary and combustion system." Physica scripta(Sweden) 19, p.p.441-446, 1979.

(58) Freeman, A.E. "Laser anemometer measurements in the recirculating region downstream of a sudden pipe expantion." Proceedings of the LDA-Symposium, Copenhagen. 1975.

(59) Masberant, L. et al — "Turbulent velocity measurements in a stratified co-current two-phase flow." Proceedings of the LDA-Symposium, Copenhagen, 1975.

(60) Abbiss, J.B. — "Photon correlation velocimetry in aerodynamics." NATO advanced study institutes series, series B: physics, volume 23.

(61) Thew, M.T. and Bedi, P.S. — "A technique of laser Doppler anemometry applied to confined swirling water flow." One-day symposium at Borough Polytechnic June 1970.

(62) Walshe, D.E. and Garner, H.C. — "Usefulness of various pressure probes in fluctuating low-speed flow." Aeronoutical Research council, London, FM 2917, 1960.

(63) Toomre, A. — "The effect of turbulence on static pressure measurements." Aeronautical Research Council, London, FM 2972, 1960.

(64) Moon, L.F. and Rudinger, G. — "Velocity distribution in an abruptly expanding circular duct." Journal of fluids Engineering, March 1977, pp. 226, 230.

(65) Patankar, S.V. and Spalding, D.B. — "Numerical prediction or three-dimensional flows." Imperial College, Report EF/TN/A/46, June, 1972.

(66) Runchal, A.K. — "Transfer processes in steady two-dimensional separated flows." Imperial College Ph.D. thesis. Imperial College Report EF/R/G/1, 1968.

VII APPENDICES

Appendix A1

The design calculations of the geometric optimisation test section:

1- Estimation of the supply air mass flow rate, $\dot{W}_1$

Assuming; an area ratio AR = 2.5, a minimum bleed requirement B* = 3%, and an inlet kinetic energy flux parameter $\alpha_1 = 1.01$, the ideal static pressure rise coefficient C_{pI} can be calculated from equation (6-6), thus:

$$C_{p\,I} = 1 - \frac{1}{\alpha_1} \cdot \left(\frac{1-B^*}{AR}\right)^2$$

hence

$$C_{p_I} = 0.851$$

Assuming a diffuser effectiveness $\eta = 0.75$, then the actual static pressure rise coefficient, C_p can be evaluated from equation (6-8), thus:

$$C_p = C_{p_I} \times \eta = 0.638$$

From equation (6-7), we get:

$$C_p = \frac{p_2 - p_1}{\frac{1}{2}\alpha_1 \rho \bar{V}_1^2} \qquad (-7)$$

Also we have,

$$\rho = \frac{p}{RT} \qquad (-10)$$

Since the diffuser will exhaust to atmospheric pressure, hence, $p_2 = 101325\ N/m^2$.

Assuming T = 300° K and $\bar{V}_1 = 50$ m/sec, substituting in equation (6-7), we get:

$$p_1 = 100386\ N/m^2$$

Substituting in equation (3-10), we get:

$$\rho = 1.166\ kg/m^3$$

But,

$$\dot{W}_1 = \rho A_1 \bar{V}_1 = \rho \pi R_1^2 \bar{V}_1 = 183\ R_1^2\ \ kg/s$$

For a primary duct diameter D_1 of 50 mm, the required inlet mass flow rate would be:

$$\dot{W}_1 = 0.114\ kg/s.$$

The manufacturer's specification of the ALCOSA FAN in the ALLIS CHALMERS TEST HOUSE, which had been allocated to this project for use as an inlet delivery fan, states that the fan is capable of delivering 975 ft^3/min of air at 32" H_2O gauge pressure. Hence, the required mass flow rate was well within the capacity of the ALCOSA FAN.

For AR = 2.5 and D_1 = 50 mm, D_2 = 79 mm. The nearest commercially available cast perspex tubes(i.e clear acryllic) were found to have internal diameters of 47 mm and 72 mm.

Hence,

D_1 = 47 mm

D_2 = 72 mm

AR = 2.347

For $\bar{V}_1$ = 50 m/s and ρ = 1.166 Kg/m^3, then

$\dot{W}_1$ = 0.101 Kg/s.

2- Estimation of the primary duct length:

From past experience, Ref.(12), the inlet flow Reynolds' number, Re based on the primary duct length (approach length) and the mean inlet velocity was selected to be in excess of 5×10^5. This would ensure a turbulent boundary layer flow at the exit of the primary duct.

$$Re = \frac{\rho \bar{V}_1 l_1}{\mu}$$

Taking Re = 5×10^5, $\bar{V}_1$ = 50 m/s, and $\mu = 1.808 \times 10^{-5}$ N/m^2 gives a value of l_1 = 152 mm.

Taking the primary duct length to be 254 mm (10 in) would give an inlet Reynolds' number,

Re = 8.2×10^5

This would ensure a turbulent BL flow in the primary duct hence, the primary duct was taken to be of 254 mm length.

3- Estimation of the secondary duct length:

Neglecting the fence axial gap x, and assuming a total included angle of 30°, Ref. (1) , the required minimum length of the secondary duct can be estimated, thus,

$$l_2 = \left(\frac{D_2 - D_1}{2}\right) \tan 15^\circ = 46.5 \text{ mm}$$

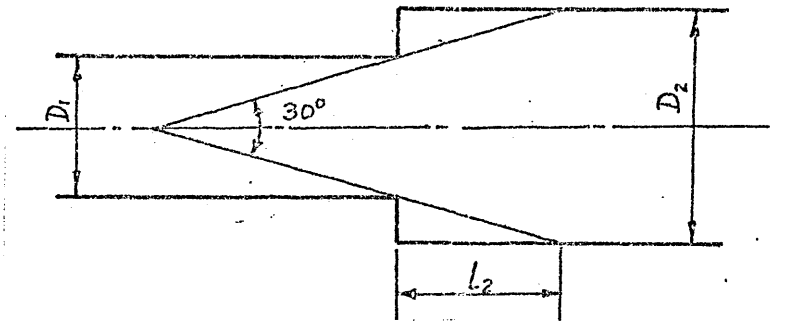

This represent the minimum length of the diffuser to produce the required static pressure recovery. Accordingly, the secondary duct length was taken as 6" or about 152 mm, to enable monitoring the static pressure recovery produced by longer diffusers.

4- Estimation of the optimum fence diameter:

From equation (2-3), D_f can be astimated, thus:

$$3\left(1-\frac{D_1^4}{D_f^4}\right) = 1-\frac{1}{AR^2}$$

From which, $D_f = 50.9$ mm

Hence the estimated optimum radial fence gap is:

$$Y_{cp} = (D_f - D_1)/2 = 1.95 \text{ mm}$$

5- Estimation of the optimum fence axial gap, x:

From equation (1-3), and assuming ϕ_{op} to be 18° (see chapter two), x_{op} can be estimated, thus:

$$x_{cp} = Y_{op}/\tan 18 = 6 \text{ mm}$$

6- Estimation of the optimum vcortex chamber depth, δ_{op} and the length, L_{op}

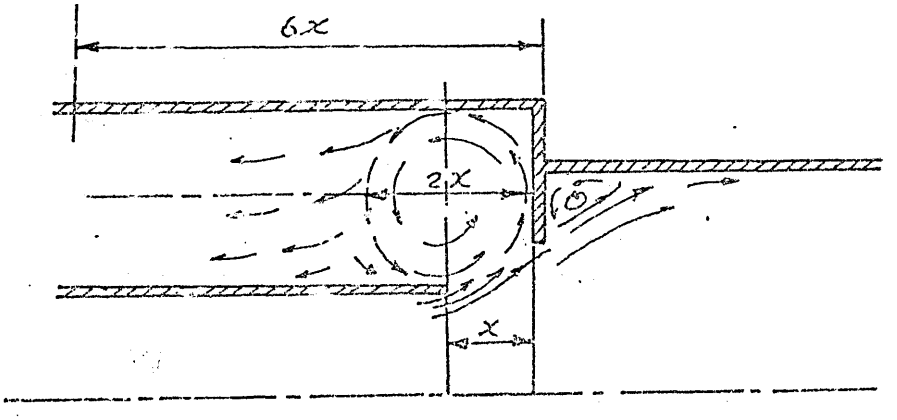

Assuming that the vortex would assume a circular section, then, from the figure:

$$\delta_{op} = 2x_{op} = 12 \text{ mm}$$

Allowing two vortex diameters for the bleed air to settle down, hence:

$$L_{op} = 6x_{op} = 36 \text{ mm}$$

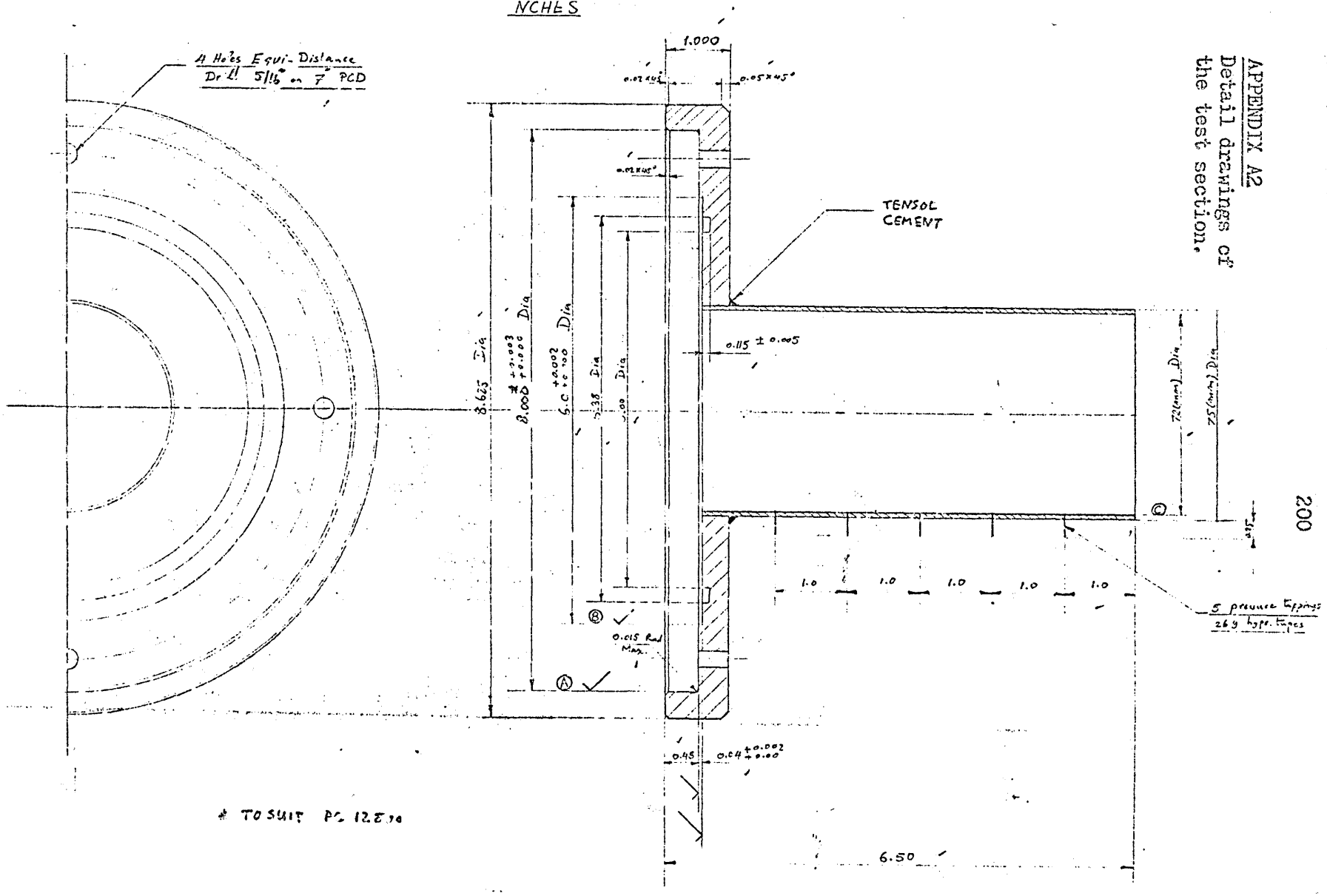

Machining:
All machined surfaces marked (✓) are to be machined after the two parts are assembled with dimension (A), (B) & (C) Concentric.

Fig.(A2-1): Secondary duct.

1	PC12798	SECONDARY DUCT.	1	Perspex				
ITEM	PART No.	DESCRIPTION	No. OFF	MAT'L	SPEC.	REMARKS		

THIRD ANGLE PROJECTION

SHEET SIZE A 2

GENERAL TOLERANCE ON DIMENSIONS
MACHINED ±·005"
UNMACHINED
OTHER DIMENSIONS AS STATED
WELD WHERE SHOWN THUS
MACHINE WHERE SHOWN THUS ✓

JOB No. | No. OF SETS REQ'D: 1 | USED ON DRG. PC12795

SCALE 1:1

FINISH SELF

DRAWN	CHK'D	APPV'D	STRESS APPV'L
SAAD			
	13.79		

TITLE:- SECONDARY DUCT

ISSUED BY SME.

CRANFIELD INSTITUTE OF TECHNOLOGY
CRANFIELD.

DRAWING No. PC12798

SHT. 1 OF 1 SHEETS

ISSUE	MODIFICATION
A	—

ISSUE	MODIFICATION
A	—

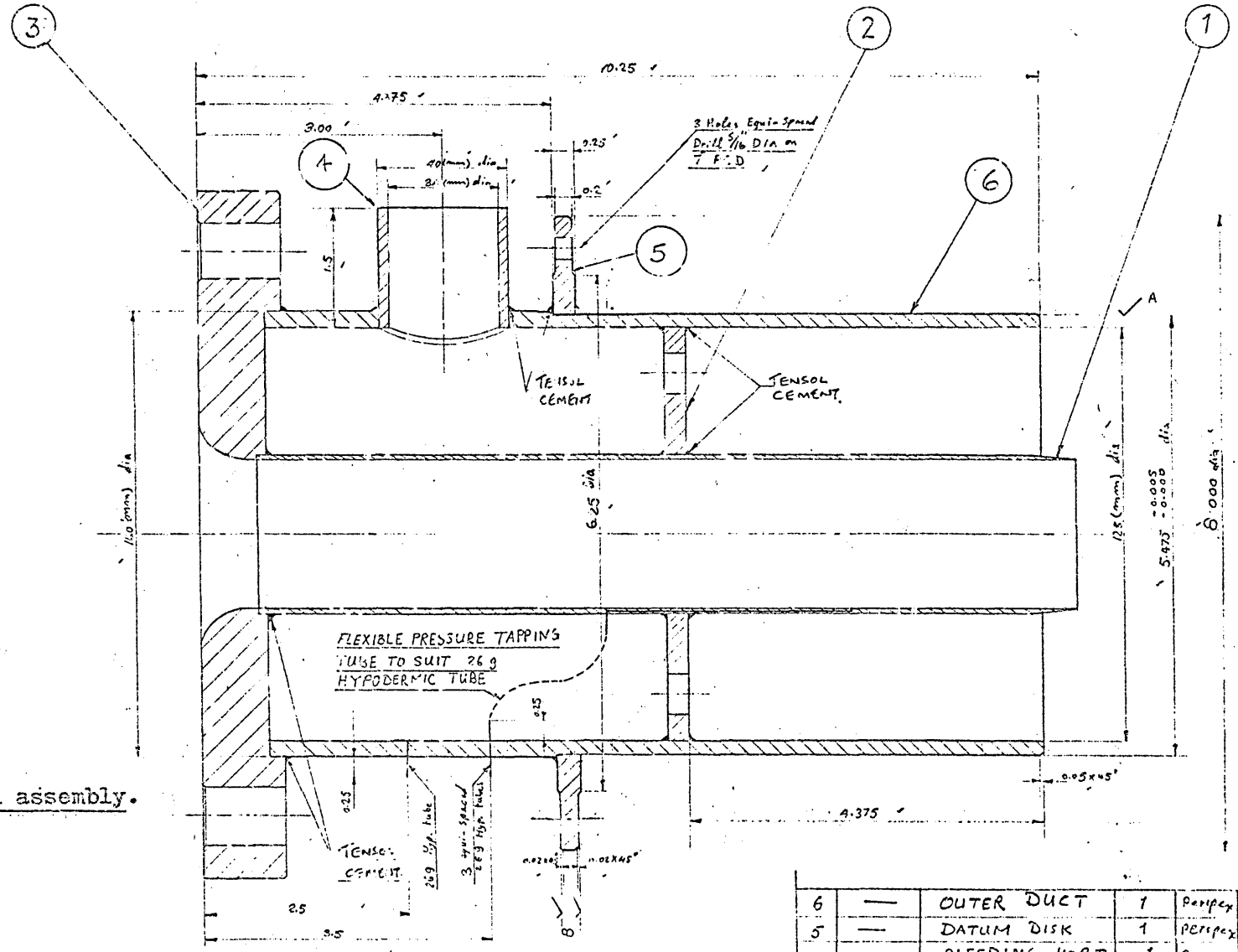

MACHINING:

① Surfaces A & B are to be machined after all the parts are assembled.

② Surface A is to be machined concentric with inner surface of part No. ①

Fig.(A2-2): Manifold assembly.

ITEM	PART No.	DESCRIPTION	No. OFF	MATL	SPEC.	REMARKS
6	—	OUTER DUCT	1	Perspex		140mm × 128mm × 10"
5	—	DATUM DISK	1	Perspex		8" DIA × 1/4 THK.
4	—	BLEEDING PORT	1	Perspex		
3	PC12796	NOZZLE FLANGE	1	Perspex		
2	PD12806	SUPPORTING DISK	1	Perspex		
1	PC12803	PRIM. DUCT	1	Perspex		

THIRD ANGLE PROJECTION

SHEET SIZE A2

GENERAL TOLERANCE ON DIMENSIONS
MACHINED ±·010"
UNMACHINED
OTHER DIMENSIONS AS STATED
WELD WHERE SHOWN THUS ⌒
MACHINE WHERE SHOWN THUS ✓

JOB No. | No. OF SETS REQD | USED ON DRG. P 312795

SCALE 1:1

FINISH SELF.

DRAWN	CHKD	APPVD	STRESS APPVD.
SAAD			
1·3·79			

TITLE:- MANIFOLD ASS.

ISSUED BY S M E

CRANFIELD INSTITUTE OF TECHNOLOGY
CRANFIELD.

DRAWING No. PC12797

SHT. 1 OF 1 SHEETS

ISSUE	MODIFICATION
A	—

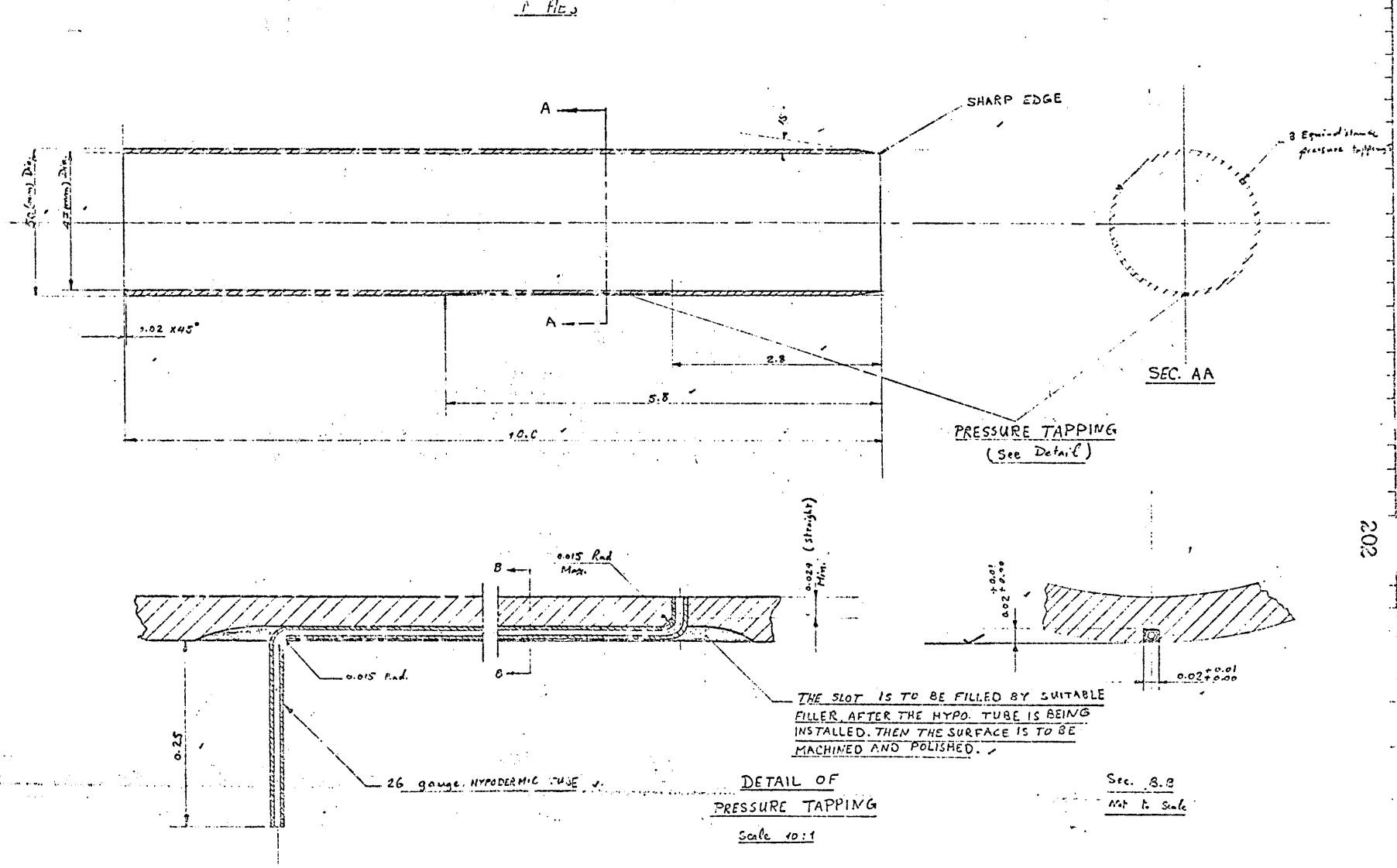

Fig.(A2-3): Primary duct.

THIRD ANGLE PROJECTION			SHEET SIZE A2	1	PC12803	Primary Duct	1	Perspex		50 mm OD Cast tube 42 mm ID
				ITEM	PART No.	DESCRIPTION	No. OFF	MAT'L	SPEC.	REMARKS
GENERAL TOLERANCE ON DIMENSIONS MACHINED ± .005" UNMACHINED OTHER DIMENSIONS AS STATED	JOB No.	No. OF SETS REQ'D 1	SCALE 1:1	DRAWN SAND 11	CHK'D 13.7.72	APP'D	STRESS APP'D	TITLE:- PRIMARY DUCT		
WELD WHERE SHOWN THUS ⌒			FINISH SELF	ISSUED BY S M E.				DRAWING No. PC 12803		
MACHINE WHERE SHOWN THUS ✓	USED ON DRG. P.- 12797			CRANFIELD INSTITUTE OF TECHNOLOGY CRANFIELD.				SHT. 1 OF 1 SHEETS		

ISSUE	MODIFICATION
A	—

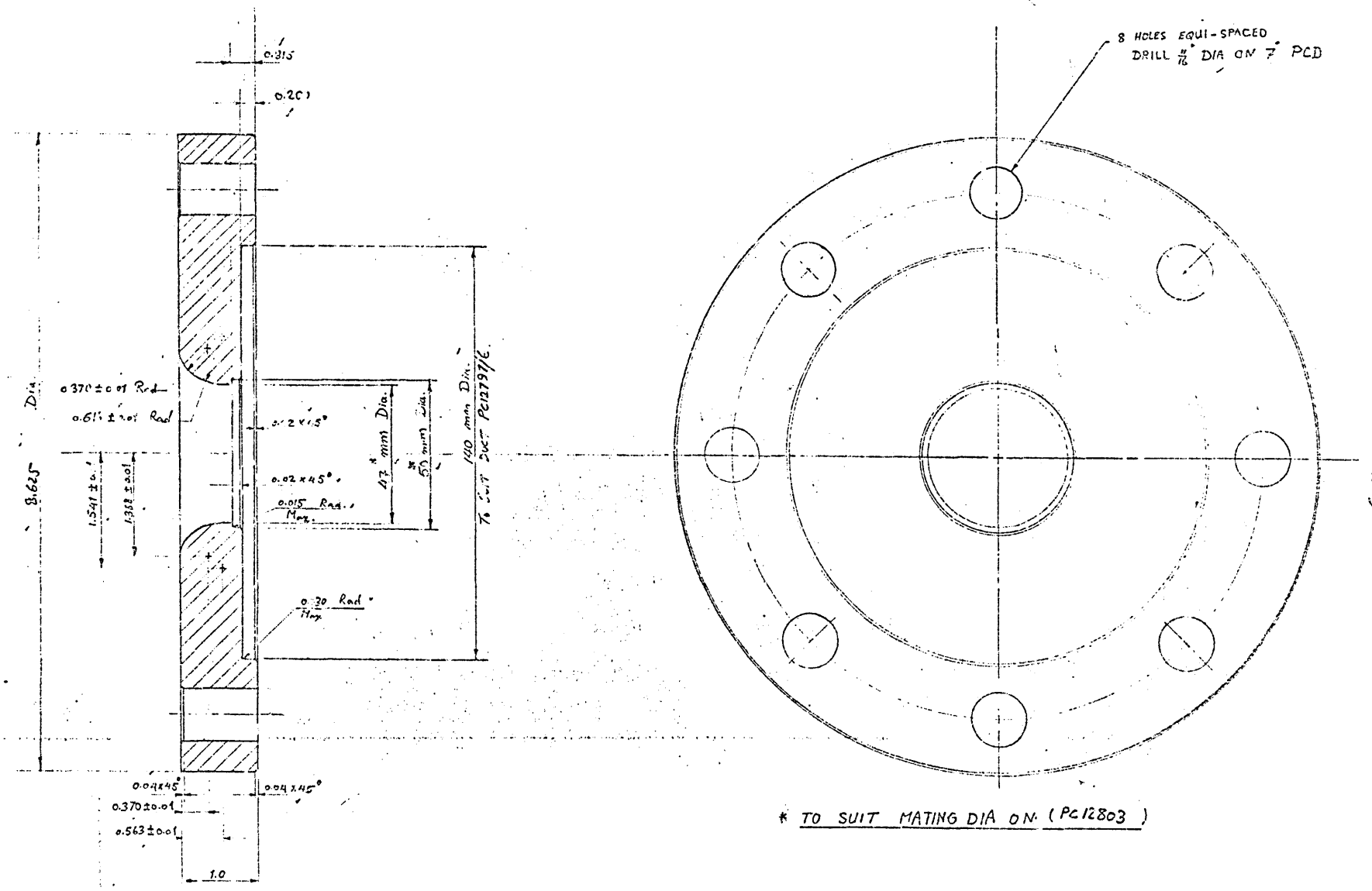

Fig.(A2-4): Inlet nozzle flange.

THIRD ANGLE PROJECTION			SHEET SIZE	ITEM	PART No.	DESCRIPTION	No. OFF	MATL	SPEC.	REMARKS
			A 2	1	Pc12796	FLANGE.	1	Perspex		1" Blank
GENERAL TOLERANCE ON DIMENSIONS MACHINED ± .005" UNMACHINED OTHER DIMENSIONS AS STATED WELD WHERE SHOWN THUS ⌒ MACHINE WHERE SHOWN THUS ✓	JOB No.	No. OF SETS REQ'D 1 USED ON DRG. Pc12797	SCALE 1:1 FINISH Self	DRAWN SAAD 1.3.79	CHK'D	APPV'D	ITPESS APPVD.	TITLE:- NOZZEL FLANGE		
				ISSUED BY S M E CRANFIELD INSTITUTE OF TECHNOLOGY CRANFIELD.				DRAWING No. Pc12796 SHT. 1 OF 1 SHEETS		

ISSUE	MODIFICATION
A	—

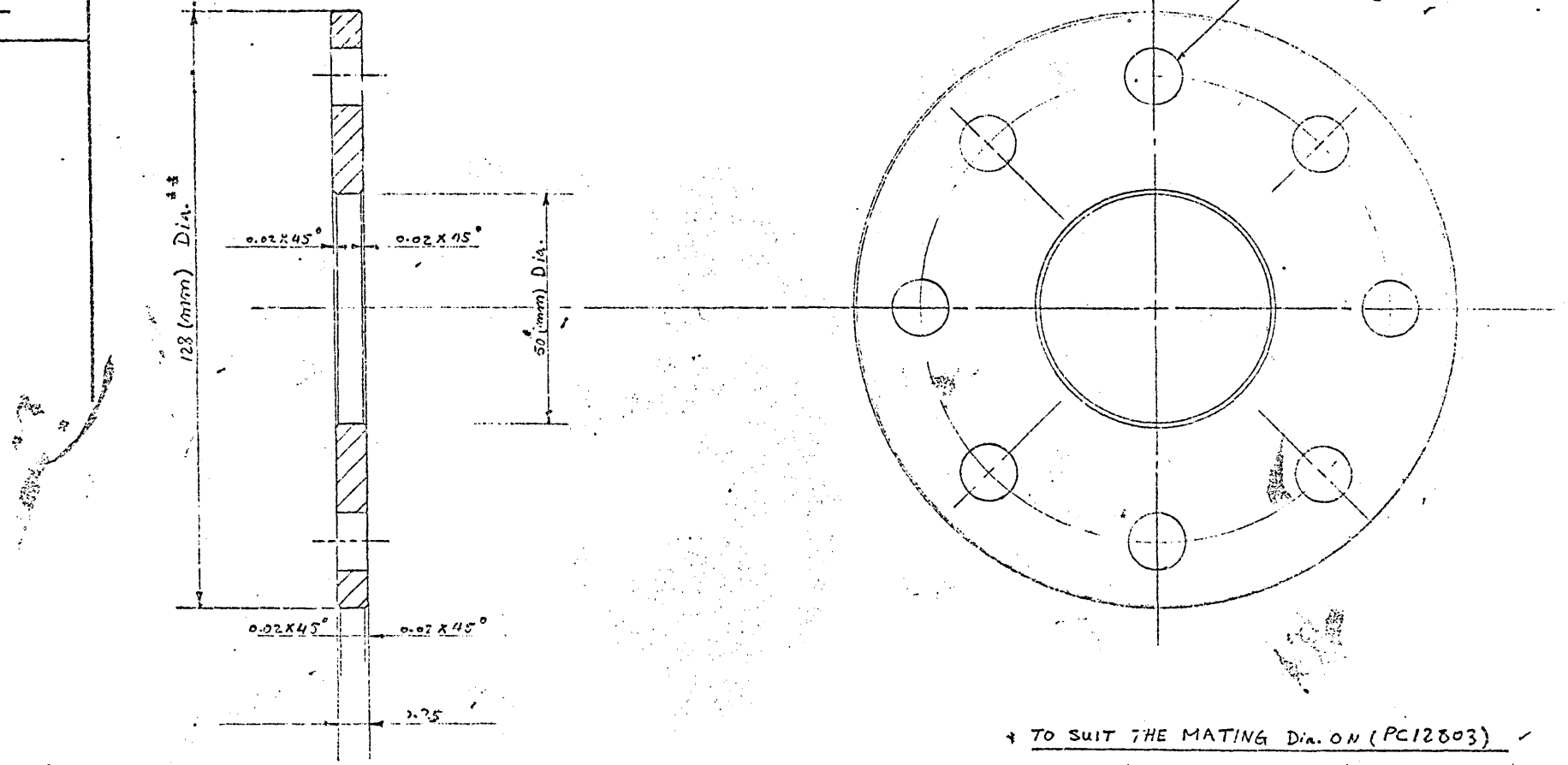

Fig.(A2-5): Supporting disk.

* TO SUIT THE MATING Dia. ON (PC12803)

** TO SUIT THE MATING Dia. ON (PC12797)/6

THIRD ANGLE PROJECTION	SHEET SIZE A3	1	PD12806	DISK.	3	Perspex.		¼" Blank
		ITEM	PART No.	DESCRIPTION	No. OFF	MAT'L	SPEC.	REMARKS

GENERAL TOLERANCE ON DIMENSIONS MACHINED ±·005" UNMACHINED OTHER DIMENSIONS AS STATED	JOB No.	No. OF SETS REQ'D	SCALE 1:1	DRAWN	CHK'D	APPV'D	STRESS A.P.V.D.
		1		SAAD			
					1·5·79		

TITLE:- SUPPORTING DISK

WELD WHERE SHOWN THUS		FINISH SCF	ISSUED BY SME
MACHINE WHERE SHOWN THUS	USED ON DRG. PC12797		CRANFIELD INSTITUTE OF TECHNOLOGY CRANFIELD.

DRAWING No. PD12806

SHT. 1 OF 1 SHEETS

ISSUE	MODIFICATION
A	—
B	NOTE ADDED ⚠ 15-3-79

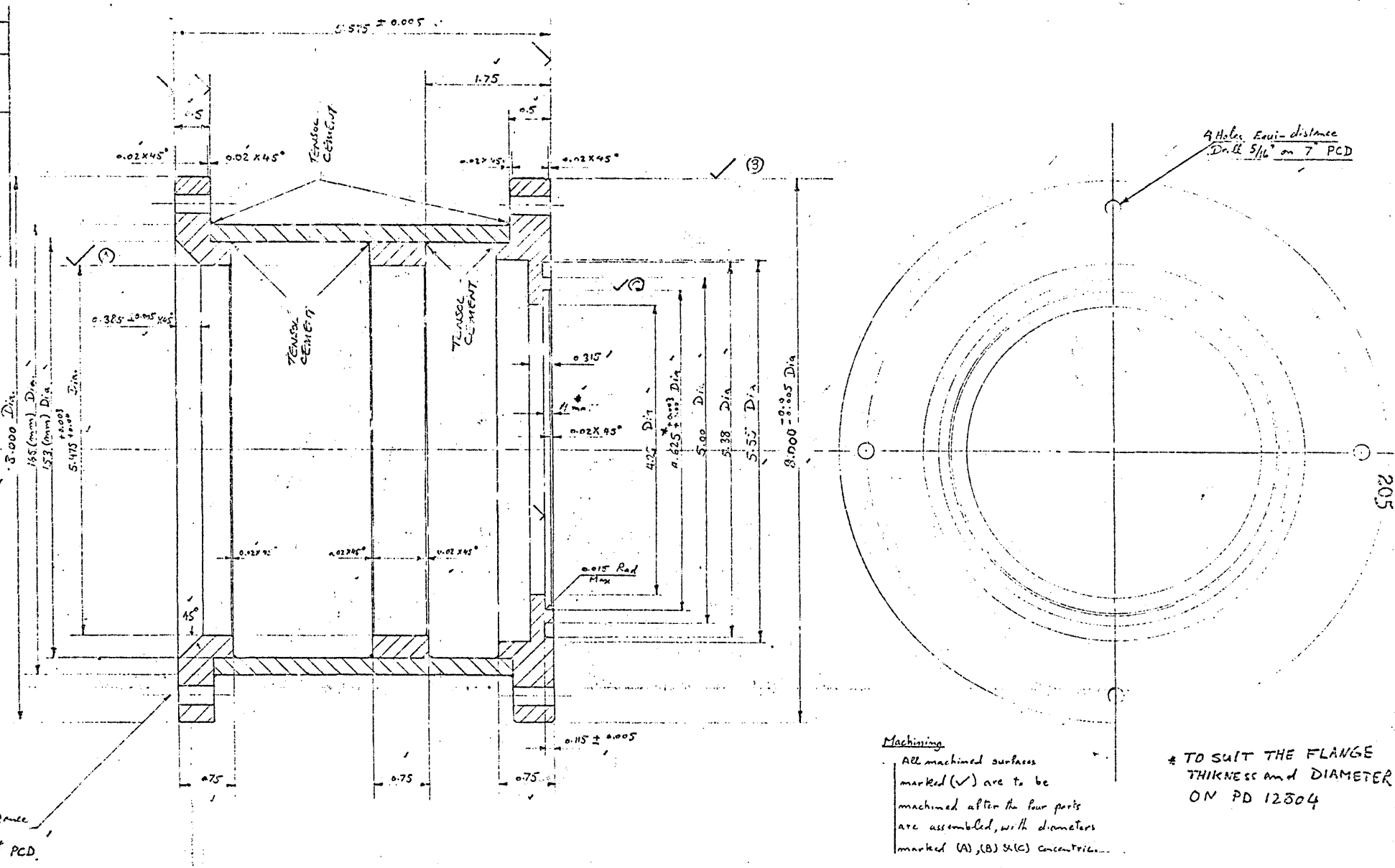

⚠ NOTE:- TUBE TO BE ROLLED BY PROTO PLASTICS LTD O/DIA AND I/DIA ARE NOMINAL. DIMENSIONS.

Machining
All machined surfaces marked (✓) are to be machined after the four parts are assembled, with diameters marked (A), (B) & (C) concentric.

* TO SUIT THE FLANGE THICKNESS and DIAMETER ON PD 12804

Fig. (A2-6) Carrier.

ITEM	PART No.	DESCRIPTION	No. OFF	MAT'L	SPEC.	REMARKS
1	PC12800	CARRIER	1	Perspex		

THIRD ANGLE PROJECTION

SHEET SIZE A2

GENERAL TOLERANCE ON DIMENSIONS
MACHINED ± '005
UNMACHINED
OTHER DIMENSIONS AS STATED
WELD WHERE SHOWN THUS ~~~
MACHINE WHERE SHOWN THUS ✓

JOB No.

No. OF SETS REQ'D 1

USED ON DRG. # 12795

SCALE 1/1

FINISH SELF

DRAWN	CHK'D	APPV'D	STRESS APPV'D.
SAAD			
	1-3-79		

TITLE:- CARRIER

ISSUED BY SME

CRANFIELD INSTITUTE OF TECHNOLOGY
CRANFIELD.

DRAWING No. PC12800

SHT. 1 OF 1 SHEETS

ISSUE	MODIFICATION
A	—

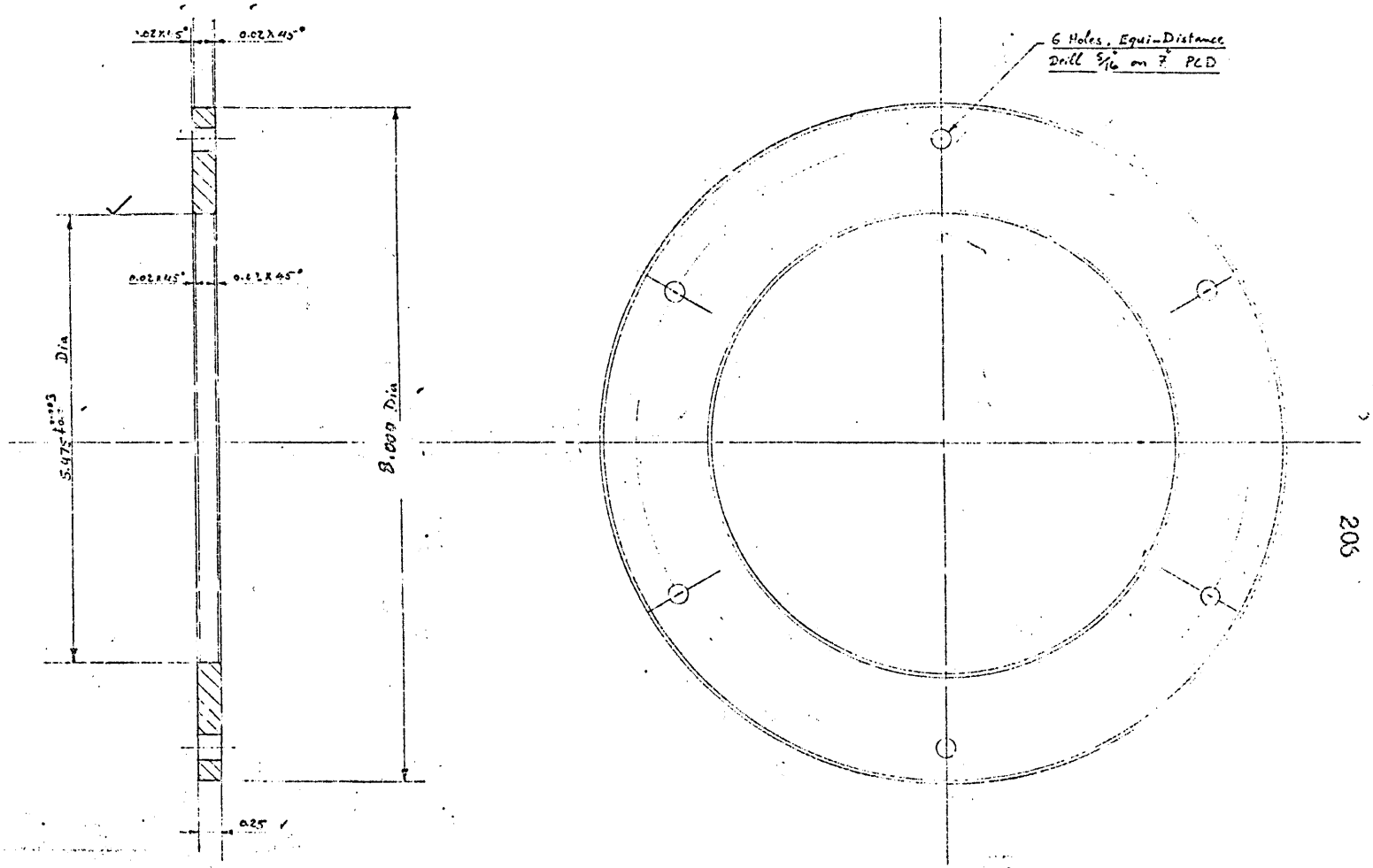

Fig.(A2-7): Locking disk.

	PC12799	Locking Disk.	1	Perspex		½" Blank
ITEM	PART No.	DESCRIPTION	No. OFF	MATL	SPEC.	REMARKS

THIRD ANGLE PROJECTION

GENERAL TOLERANCE ON DIMENSIONS
MACHINED ±.005"
UNMACHINED
OTHER DIMENSIONS AS STATED
WELD WHERE SHOWN THUS
MACHINE WHERE SHOWN THUS

JOB No.

No. OF SETS REQD 1

USED ON DRG. P & 12795

SHEET SIZE A2

SCALE 1:1

FINISH SELF

DRAWN	CHKD	APPVD	STRESS APPVD
SAAD			
	1.3.79		

TITLE:- LOCKING DISK

ISSUED BY SME

CRANFIELD INSTITUTE OF TECHNOLOGY
CRANFIELD.

DRAWING No. PC12799

SHT. 1 OF 1 SHEETS

PD1230.

INCHES

ISSUE	MODIFICATION
A	—

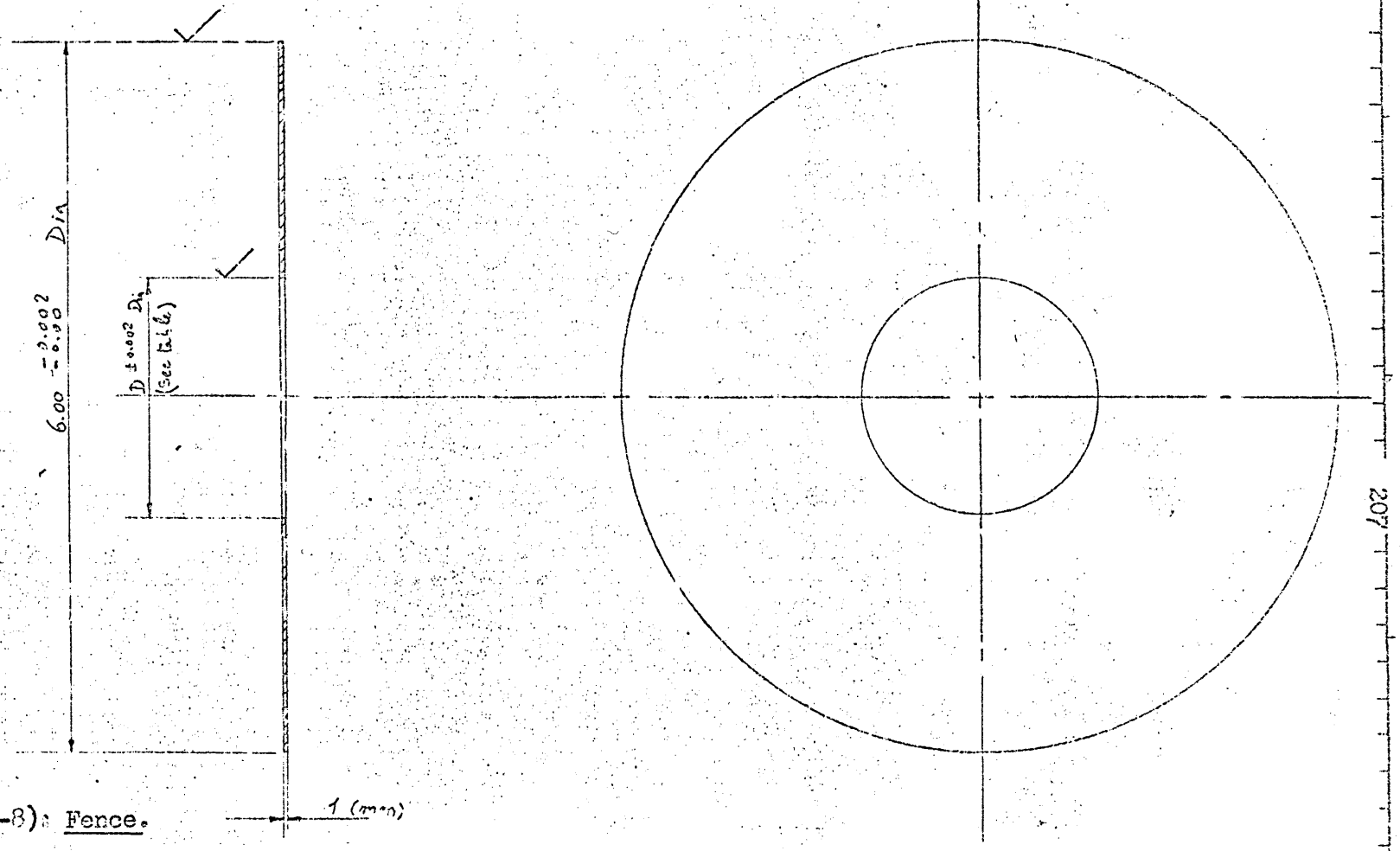

Fence No	D (in)
1	1.89
2	1.93
3	1.97
4	2.01
5	2.05
6	2.09

Fig.(A2-8): Fence.

ITEM	PART No.	DESCRIPTION	No. OFF	MATL	SPEC.	REMARKS
1	PD12805	FENCE.	6	perspex		

THIRD ANGLE PROJECTION

SHEET SIZE A3

GENERAL TOLERANCE ON DIMENSIONS
MACHINED ±.005"
UNMACHINED
OTHER DIMENSIONS AS STATED
WELD WHERE SHOWN THUS
MACHINE WHERE SHOWN THUS ✓

JOB No. | No. OF SETS REQD 1 | USED ON DRG. PD12795

SCALE 1.1

FINISH SELF

DRAWN	CHKD	APPVD	STRESS APPVD.
SAAD			
	13.9.79		

ISSUED BY SME

TITLE: FENCE

CRANFIELD INSTITUTE OF TECHNOLOGY
CRANFIELD.

DRAWING No. PD12805

SHT. 1 OF 1 SHEETS

PD12804

ISSUE	MODIFICATION
A	——
B	ITEMS 7, 8 and 9 DIM^{N} CHANGED FROM 80 x 74 mm 15-3-79 (1)

INCHES

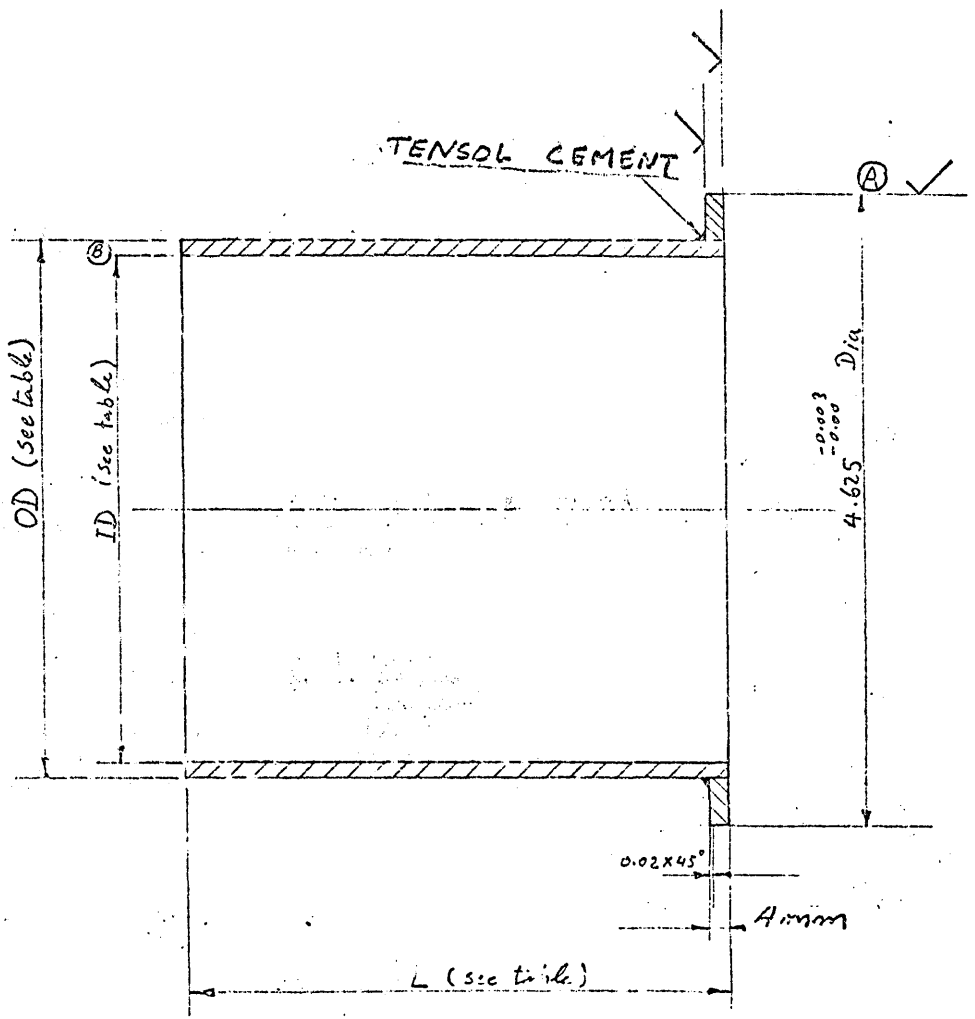

№	ID (mm)	OD (mm)	L (Inches)
1	59	65	0.75
2	59	65	1.5
3	59	65	2.25
4	69	75	0.75
5	69	75	2.0
6	69	75	4.0
(1) 7	78	90	1.0
(1) 8	78	90	2.0
(1) 9	78	90	4.0
10	94	100	1.0
11	94	100	2.0
12	94	100	4.0

Machining-
All surfaces marked (✓) are to be machined after the two parts are assembled with diameters (A) & (B) concentric.

Fig.(A2-9): Vortex chamber duct.

THIRD ANGLE PROJECTION

SHEET SIZE A3

ITEM	PART No.	DESCRIPTION	No. OFF	MATL	SPEC.	REMARKS
			12	perspex		

GENERAL TOLERANCE ON DIMENSIONS
MACHINED ±·005"
UNMACHINED
OTHER DIMENSIONS AS STATED
WELD WHERE SHOWN THUS ⌐⌐⌐
MACHINE WHERE SHOWN THUS —✓—

JOB No.
No. OF SETS REQ^{D} 1
USED ON DRG. PB12795

SCALE 1:1
FINISH SELF

DRAWN	CHK^{D}	APPV^{D}	STRESS APPVD.
SAAD			
"	1·3·79		

TITLE:- VORTEX CHAMBER DUCT

ISSUED BY SME
CRANFIELD INSTITUTE OF TECHNOLOGY
CRANFIELD.

DRAWING No. PD12804
SHT. 1 OF 1 SHEETS

Appendix A3

The design calculations for the supply air pipework:

1- Calculation of the supply pipe diameter, Ds:

From Appendix A1, we have:

$\dot{W}_1 = 0.101$ Kg/s

$p_1 = 100386$ N/m^2

$\bar{V}_1 = 50$ m/s

$\rho = 1.166$ Kg/m^3

Assuming that there is no total pressure loss along the supply air pipework,

hence

$$P = p_1 + \tfrac{1}{2}\rho\bar{V}_1^2 = 100386 + \tfrac{1}{2}\times 1.166 \times (50)^2$$

$$= 101242 \text{ N/m}^2$$

Using compressible flow tables for $\gamma = 1.4$ and assuming that $M_n = 0.05$ Ref.(12), we get

$$\frac{1000\dot{W}_1\sqrt{T}}{A_s P} = 3.487, \text{and} \qquad \frac{T}{t} = 1.0005$$

From which we get

$A_s = 5.565 \times 10^{-3}$ m^2

or

$D_s = 84.2$ mm (3.314 in)

The nearest standard PVC pipe has an internal diameter of $D_s = 3.355$ in which is adequate.

2- Calculation of the orifice plate internal diameter, D_{or}:

Knowing;

$\dot{W}_1 = 0.101$ Kg/s $= 0.247$ lb/s

$\rho = 1.166$ Kg/m^3 $= 0.0727$ lb/ft^3

$D_s = 3.355$ in

$p_1 = 100386$ N/m^2 $= 14.6$ lbf/in^2

From eq^n . (10) page 25 Ref.(44), we have

$$N = \frac{\dot{W}_1}{359.2\, D_s^2 \sqrt{h\rho}}$$

Assuming H = 30 in, hence

$N = 0.15$

But,

$N = m \mathcal{E} E C Z$

Assuming Z and $\mathcal{E}$ to be unity, hence

$m E C = 0.15$

From Fig.(3) page 27 Ref.(44), we get

$m = 0124$

or, $\left(\frac{D_{or}}{D_c}\right)^2 = 0.24$

From which

$D_{or} = 1.644$ in

*17	—	GASKET	1	RUBBER		4" ND Cat No. 410
*16	—	FLANGE/FITTING	1	PVC		4" ND Cat No. 318
15	—	PERFORATED PLATE	1	M.S		PATTERN No. To Suit
14	—	PIPE	1	PVC	3' LONG	4" ND Cat No. 511
*13	—	EXPANDER	1	PVC		3/4" Cat No. 414

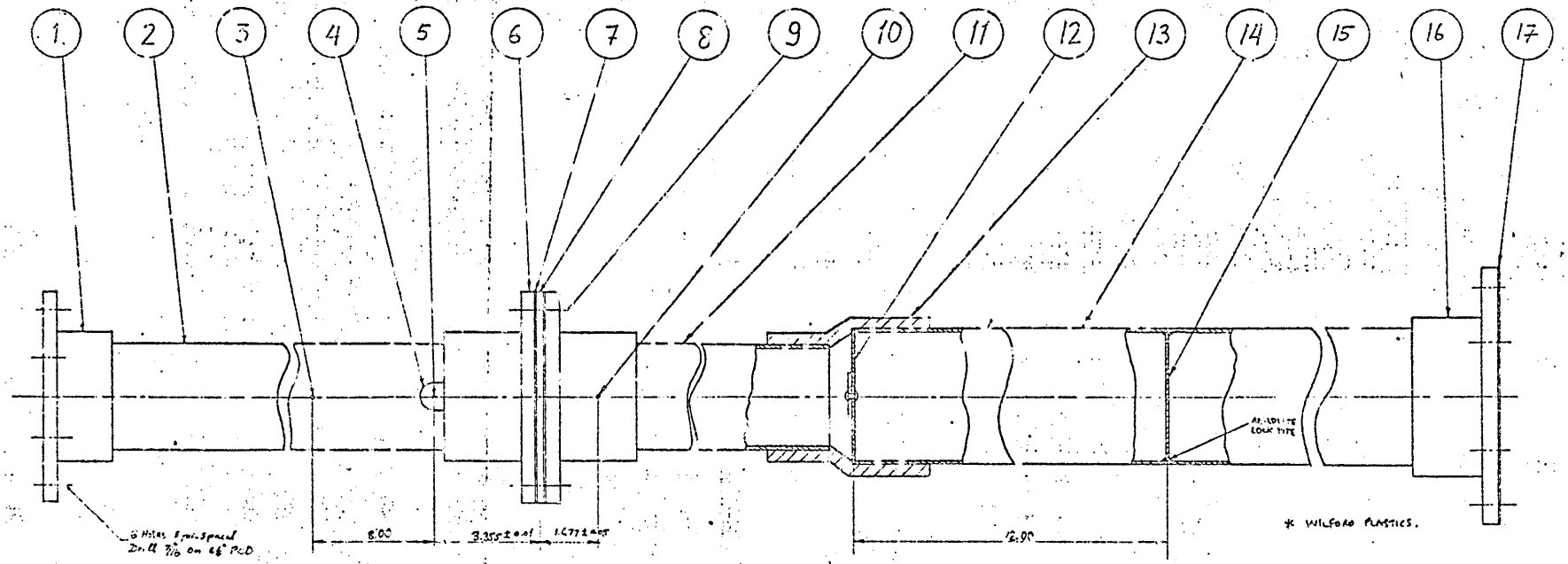

Fig.(A3-1): Supply air pipework.

ITEM	PART No.	DESCRIPTION	No. OFF	MAT'L	SPEC.	REMARKS
12	PD12308	FLOW STABILIZER	1	M.S.		
*11	—	PIPE	1	PVC	2' LONG	3" ND Cat No. 511
10	—	2½" PRESS. TAPPING	1			DRILL TO B.S 10
9	—	BOLT + NUT + 2 WASHERS	12	M.S		5/8" BSF x LENGTH
8	PD12309	ORIFICE PLATE	1	M.S		
*7	—	GASKET	2	RUBBER		3" ND Cat No. 410
*6	—	FLANGE/FITTING	2	PVC		3" ND Cat No. 318
5	—	2" PRESS. TAPPING	1			DRILL TO B.S.1004
4	—	BOSS	1	PVC		
3	—	THERMOMETER	1			-3° TO +65°C
*2	—	PIPE	1	PVC	12" Long	3" ND Cat No. 511
*1	—	FLANGE/FITTING	1	PVC	PLAIN	3" ND Cat No. 139

THIRD ANGLE PROJECTION

SHEET SIZE A1

GENERAL TOLERANCE ON DIMENSIONS
MACHINED
UNMACHINED
OTHER DIMENSIONS AS STATED
WELD WHERE SHOWN THUS
MACHINE WHERE SHOWN THUS

JOB No. | No. OF SETS REQ'D 1 | USED ON L.R.G.

SCALE 1:2

FINISH SELF

DRAWN | CHK'D | APPR'D | DATE ISSUED

TITLE:- INLET DUCT SYSTEM

ISSUED BY S.A.E.

CRANFIELD INSTITUTE OF TECHNOLOGY
CRANFIELD.

DRAWING No. PB 12807

SHT. 1 OF 1 SHEETS

ISSUE	MODIFICATION
A	—

INCHES

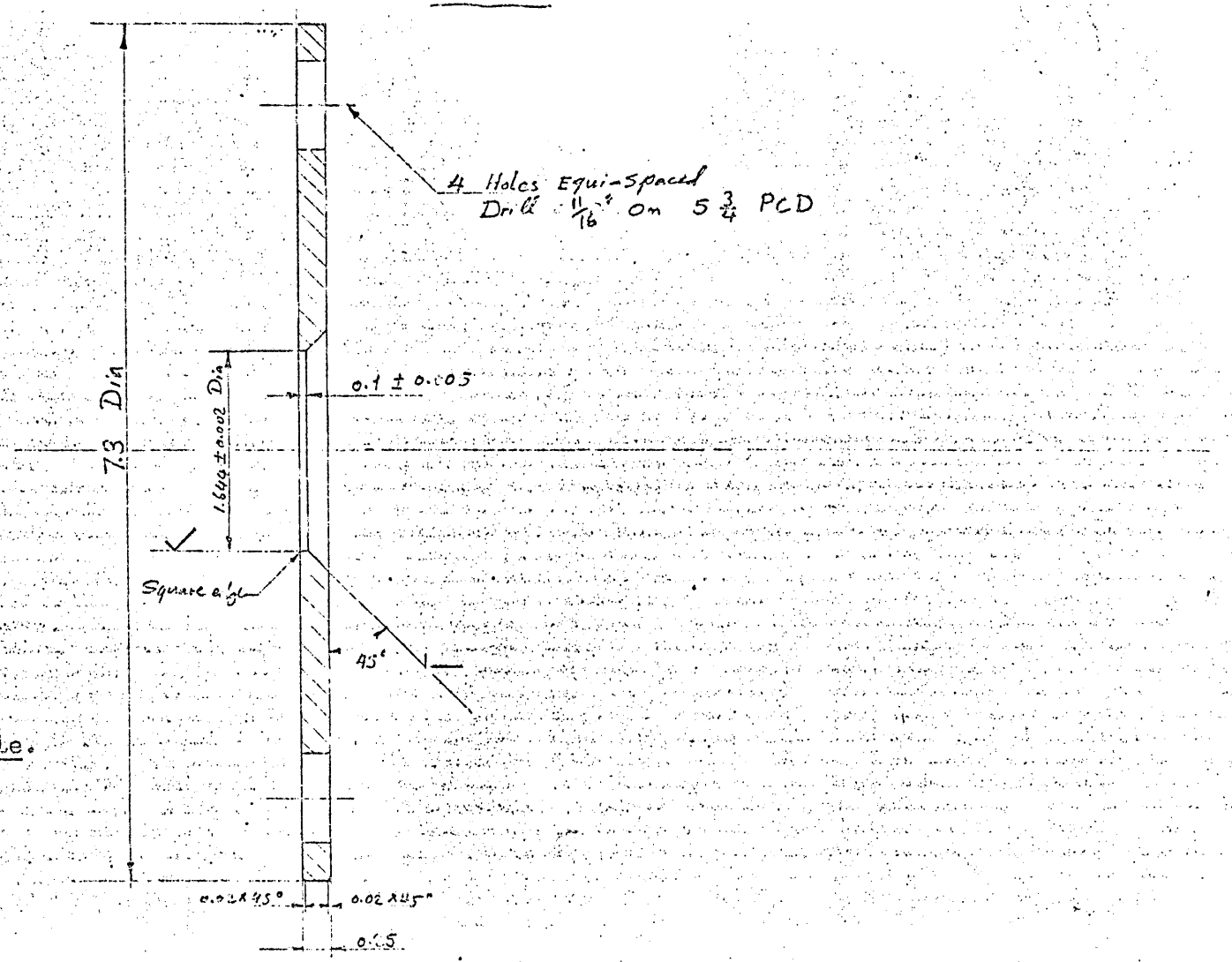

Fig.(A3-2): Orifice plate.

ITEM	PART No.	DESCRIPTION	No. OFF	MAT'L	SPEC.	REMARKS
			1	M.S		

THIRD ANGLE PROJECTION

SHEET SIZE: A3

GENERAL TOLERANCE ON DIMENSIONS
MACHINED ± .010"
UNMACHINED
OTHER DIMENSIONS AS STATED
WELD WHERE SHOWN THUS
MACHINE WHERE SHOWN THUS

JOB No.

No. OF SETS REQ'D: 1

USED ON DRG. PB12807

SCALE: 1:1

FINISH: SELF.

DRAWN	CHK'D	APPV'D	STRESS APPVD.
SAAD			
	21-3-79		

TITLE:- ORIFICE PLATE

ISSUED BY S M E

CRANFIELD INSTITUTE OF TECHNOLOGY
CRANFIELD.

DRAWING No. PD12809

SHT. | OF | SHEETS

ISSUE	MODIFICATION
A	—

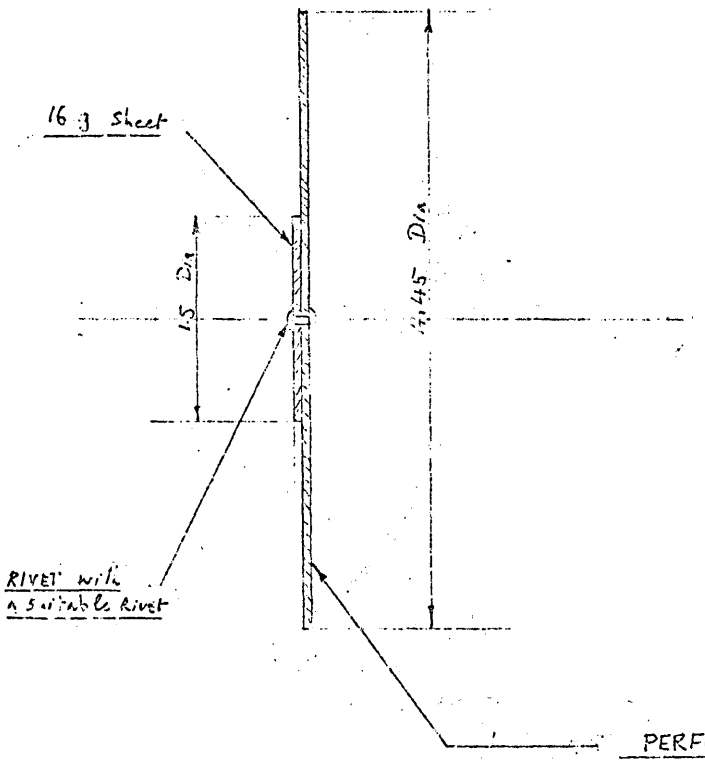

Fig.(A3-3): Flow stabilizer.

THIRD ANGLE PROJECTION	SHEET SIZE A3	ITEM	PART No.	DESCRIPTION	No. OFF	MATL	SPEC.	REMARKS
					1	M.S		

GENERAL TOLERANCE ON DIMENSIONS MACHINED ±.010" UNMACHINED OTHER DIMENSIONS AS STATED	JOB No.	No. OF SETS REQD	SCALE 1:1	DRAWN	CHKD	APPVD	STRESS APPVD.	TITLE:- FLOW STABILIZER
		1		SAAD				
					21.5.79			
WELD WHERE SHOWN THUS ⌒ L			FINISH	ISSUED BY SME				DRAWING No. PD 12808
MACHINE WHERE SHOWN THUS ✓	USED ON DRG. PB12807		Saf	CRANFIELD INSTITUTE OF TECHNOLOGY CRANFIELD.				SHT. 1 OF · SHEETS

1 2 3 4 5 6 7 8

Appendix A4

Estimation of the maximum required bleed air flow rate:

From equation (2-2), we have

$$B^* = 0.393\,\eta\left[1 - \frac{1}{AR^2}\right]\sqrt{\frac{AR}{de}}$$

From Appendix A1, we have

$$AR = 2.347$$

$$d_e = 47 \text{ mm}$$

For $\eta = 0.75$, thus

$$B^* = 0.054$$

Allowing B to vary during the tests from 0 to 10%, hence the maximum required bleed air mass flow, $(\dot{W}_B)_{max}$ is given by:

$$(\dot{W}_B)_{max} = B_{max} \times \dot{W}_1 = 0.1 \times 0.101$$

$$= 0.01 \text{ Kg/s.}$$

Appendix B1:

Calculation of the inlet kinetic energy flux parameter, α_1:

Following the method described in Ref.(45), the area of the primary duct was divided into twenty equal areas, thus:

$$A_1 = \frac{\pi D_1^2}{4} = 1735 \times 10^{-6} \quad m^2$$

$$\Delta A_1 = A_1/20 = 8.675 \quad 10^{-5} \quad m^2$$

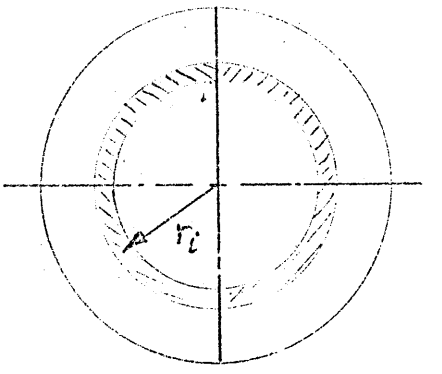

The twenty equal areas forms two symmetrical sets of concentric semi-circular rings.
Table (3-1) shows the radius of the area bisectors of these rings.

Table (6-1)

Radius of the area bisector of the rings

i	1	2	3	4	5	6	7	8	9	10
r_i mm	3.2	9	11.7	13.9	15.7	17.4	18.9	20.3	21.7	22.9

A special total pressure probe was designed and manufactured according to the recommendations of Ref.(46). The probe was used to measure the total pressure at the mean radius of each semi-circular ring on both sides of the axis of symmetry. The readings was take on a micromanometer and are given in table (6-2).

Table (6-2)

The gauge total pressures in mm H_2O

i	1	2	3	4	5	6	7	8	9	10
hi mmH_2O	167	167	167	165	156	155	149	139	121	107

i	11	12	13	14	15	16	17	18	19	20
hi mmH_2O	168	167	167	166	157	155	150	141	120	108

At the day of the test $p_z = 101500$ N/m^2

And, $h_{st} = 6.5$ mm H_2O (gauge pressure)

Also, $t = 24^\circ C$

hence;

$$\rho = \frac{P_{st}}{RT} = \frac{10\times 6.5 + 101500}{287(273.15+24)} = 1.175 \quad Kg/m^3$$

From, Ref.(46),

$$V_i = \sqrt{\frac{2\Delta P_i}{\rho C}}$$

Taking C = 1.0

Hence

$$V_i = \sqrt{\frac{2\Delta P_i}{\rho}} = \sqrt{\frac{2g(h_i - h_{st})}{\rho}} \qquad (6-11)$$

Equation (6-11) was used to calculate the absolute velocity distribution. The results in given in table (6-3)

Table (6-3)

Inlet velocity distribution

i	1	2	3	4	5	6	7	8	9	10
V_i m/s	52.3	52.3	52.3	51.9	50.4	50.3	49.2	47.5	44.2	41.4

i	11	12	13	14	15	16	17	18	19	20
V_i m/s	52.4	52.3	52.3	52.1	50.6	50.3	49.4	47.8	44.0	41.7

The results show a high degree of symmetry within the expected level of error.

The area weighted mean velocity was given by:

$$\bar{V}_i = \frac{1}{20}\sum_{i=1}^{20} V_i = 49.2 \quad m/s$$

The relative velocity distribution was calculated from the formula

$$\hat{V}_i = V_i / \bar{V}_i \qquad (6-12)$$

The results are given in table (6-4).

Table (6-4)

The relative velocity distribution

i	1	2	3	4	5	6	7	8	9	10
$\hat{V}_i$	1.062	1.062	1.062	1.055	1.024	1.022	1.0	0.965	0.898	0.841

i	11	12	13	14	15	16	17	18	19	20
$\hat{V}_i$	1.065	1.062	1.062	1.059	1.028	1.022	1.004	0.972	0.894	0.848

From Ref.(45), α_1 is given by:

$$\alpha_1 = \frac{n^2 \sum_{i=1}^{n} (q_i)^{1.5}}{\left(\sum_{i=1}^{n} \sqrt{q_i}\right)^3} \qquad (6-13)$$

or

$$\alpha_1 = \frac{n^2 \sum_{i=1}^{n} V_i^3}{\left(\sum_{i=1}^{n} V_i\right)^3} \qquad (6-14)$$

From which,

$$\alpha_1 = 1.011$$

Appendix B2:

Typical test Results.

RUN №	64	DATE	20.9.79	P_z m bar	1003
FENCE	3	Y in	0.08	X in	1.374
VOR. CH.	12	L in	4	δ in	0.866

TEST №	1	2	3	4	5	6	7	8	9
h_1 in H_2O	40.95	40.67	40.25	40.2	40.05	40	39.75	39.7	39.7
h_2 in H_2O	15.25	15.65	16.05	16.1	16.25	16.3	16.6	16.6	16.65
h_3 in H_2O	38.75	38.75	38.75	38.8	38.8	38.83	38.7	38.7	38.75
h_4 in H_2O	16.85	16.85	16.9	16.8	16.8	16.8	16.95	17	16.95
t °C	24	26	26	27	27	27	27	27	27
p_B mm H_2O	-823	-794	-780	-768	-762	-753	-748	-741	-733
t_B °C	15	15	15	15	15	15	16	16	16
E_α %	0	25.5	48.5	67.5	85	82.5	82.5	81	100
E_β %	0	0	0	0	0	35	65	92	100
p_c mm H_2O	-62.3	-86.3	-123	-143	-158	-173	-179	-188	-203
p_1 "	-53.3	-70.6	-92.3	-101	-106	-110	-110	-113	-117
$p_{2\,I}$ "	-52.6	-49	-40	-36	-32.8	-30.8	-28.4	-27	-24.8
$p_{2\,II}$ "	-52.4	-45.6	-29.8	-23.6	-19	-16	-13.6	-12.2	-10.2
$p_{2\,III}$ "	-38.2	-27.7	-14	-10.5	-7.9	-6.5	-5.2	-4.5	-3.5
$p_{2\,IV}$ "	-21	-13.2	-5.9	-4.3	-3.3	-2.7	-2.1	-1.7	-1.5
$p_{2\,V}$ "	-8	-4.7	-1.8	-1.2	-0.8	-0.65	-0.45	-0.4	-0.3

Appendix B3

Formulae derived for geometric optimisation.

1- Calculation of the absolute pressures, p_i abs:

p_i g, was measured in mm H_2O, and p_z was measured in mbar. Hence,

$$p_i \text{ abs} = a\, p_z + b\, p_i\ g \qquad (6\text{-}15)$$

Where;

a, is the conversion factor from the barometric scale (mbar) to N/m^2 (a = 100).

b, is the conversion factor mm H_2O to N/m^2, substituting in (6-15), we get:

$$p_i \text{ abs} = 100\, p_z + 10\, (p_i\ g) \qquad (6\text{-}1)$$

2- Calculation of the mainflow mass flow rate, $\dot{W}_1$:

From Ref.(44), we get:

$$\dot{W}_1 = 0.0125\, CZ\varepsilon E D_{or}^2 \sqrt{\rho h}$$

Where;

$\dot{W}_1 \equiv$ Kg/hr

$D_{or} \equiv$ mm

$\rho \equiv Kg/m^3$

$h \equiv$ mm H_2O

or,

$$\dot{W}_1 = 1.633 \times 10^{-5}\ CZ\varepsilon E D_{or}^2\ \frac{\sqrt{h}\sqrt{p}}{\sqrt{t+237.15}} \qquad (6\text{-}16)$$

Where;

$\dot{W}_1 \equiv$ Kg/s

$D_{or} \equiv$ mm

$h \equiv$ in H_2O

$p \equiv$ in H_2O

$t \equiv$ °C

From Appendix A2, we get:

$$D_{or} = 1.644 \text{ in} = 41.76 \text{ mm} \qquad (6\text{-}17)a$$

$$D_s = 3.355 \text{ in}$$

Hence,

$$m = \left(D_{or}/D_s\right)^2 = 0.24 \qquad (6\text{-}17)b$$

and

$$E = \frac{1}{1-m^2} = 1.061 \qquad (6\text{-}17)c$$

From Ref.(44), we get:

$C = 0.6066$

$Z = 1.001$

And for $\frac{h}{p} = 2$

$\varepsilon = 0.98$

Substituting from (6-17) into (6-16), we get:

$$\dot{W}_1 = 0.018535 \frac{\sqrt{h}\sqrt{p}}{\sqrt{t+273.15}} \qquad (6\text{-}2)$$

Where:

$h = h_3 - h_4$

and

$p = 0.4015\, p_z + (h_1 - h_2)$

3- Calculation of the bleed air mass flow rate, $\dot{W}_B$:

The bleed air mass flow rate $\dot{W}_B$ in Kg/s can be calculated from the fomula, Ref. (12):

$$\dot{W}_B = 2.5344 \times 10^{-3} \sqrt{p_o/T_o} \times E \times V \qquad (3\text{-}18)$$

p_o = bleed air pressure at the meter outlet in lbf/in^2 abs

T_o = gas temp at the meter outlet in degree°K.

E = reading of the meter.

V = max flow rate for tube and float.

But,

$$p_o = 0.00145\,(10 p_z + p_B) \qquad (6\text{-}19)a$$

$$T_o = t_B + 273.15 \qquad (6\text{-}19)b$$

$$V_B = 6.9\ ft^3/min \qquad (6\text{-}19)c$$

$$V_\alpha = 13.8\ ft^3/min \qquad (6\text{-}19)d$$

Substituting from (6-19) into (6-18), we get:

$$\dot{W}_B = 6.66 \times 10^{-4} (E_B + 2E) \frac{\sqrt{10 p_z + p_B}}{\sqrt{t_B + 273.15}} \qquad (6\text{-}3)$$

4- Calculation of the bleed rate, B%:

By definition,

$$B\% = \dot{W}_B / \dot{W}_1 \times 100 \qquad (6\text{-}4)$$

5- Calculation of the dynamic pressure,

$$\bar{V}_1 = \frac{\dot{W}_1}{\rho A_1}$$

Hence:

$$\frac{1}{2}\rho\alpha_1 \bar{V}_1 = \frac{1}{2}\alpha_1 \dot{W}_1^2 / \rho A_1^2 \qquad (6\text{-}19)$$

but,

$$\rho = P/RT \qquad (6\text{-}10)$$

Substituting from (6-10) into (6-19), we get:

$$\frac{1}{2}\rho\alpha_1 \bar{V}_1^2 = \frac{\alpha_1 \dot{W}_1^2 P_1}{0.996(273.15+t)} \qquad (6\text{-}5)$$

6- Calculation of the ideal static pressure rise coefficient C_{p_I}:

From Bernoullis equation, we have:

$$P_2 + \frac{1}{2}\alpha_2 \rho \bar{V}_2^2 = P_1 + \frac{1}{2}\alpha_1 \rho \bar{V}_1^2 \qquad (6\text{-}20)$$

By difinition,

$$C_{p\,I} = \frac{P_2 - P_1}{\frac{1}{2}\alpha_1 \rho \bar{V}_1^2} \qquad (3\text{-}21)$$

From (6-20) and (6-21), we get:

$$C_{p_I} = 1 - \frac{\alpha_2}{\alpha_1} \cdot \frac{\bar{V}_2^2}{\bar{V}_1^2} \qquad (6\text{-}22)$$

From the continuity equation, we get:

$$(1 - B)\rho A_1 \bar{V}_1 = A_2 \bar{V}_2 \rho$$

or,

$$\frac{\bar{V}_2}{\bar{V}_1} = (1-B) \cdot \frac{A_1}{A_2} = \frac{1-B}{AR} \qquad (6\text{-}23)$$

From (6-22) and (6-23), we get:

$$C_{p_I} = 1 - \frac{\alpha_2}{\alpha_1}\left(\frac{1-B}{AR}\right)^2$$

Assuming $\alpha_2 = 1.0$ (After all it is an ideal case)

Hence,

$$C_{p_I} = 1 - \frac{1}{\alpha_1}\left(\frac{1-B}{AR}\right)^2 \qquad (6\text{-}6)$$

7- Calculation of the actual static pressure rise coefficient, C_p:

By definition,

$$C_p = \frac{p_2 - p_1}{\frac{1}{2}\rho \overline{V}_1^2 \alpha_1} \qquad (6\text{-}7)$$

8- Calculation of the diffuser effectiveness, η:

By definition,

$$\eta = C_p / C_{pI} \qquad (6\text{-}8)$$

9- Calculation of the vortex chamber depression parameter, V_c:

By difinition,

$$V_c = \frac{p_1 - p_c}{\frac{1}{2}\rho \overline{V}_1^2 \alpha_1} \qquad (6\text{-}9)$$

APPENDIX C:

The results of the geometric optimisation tests.

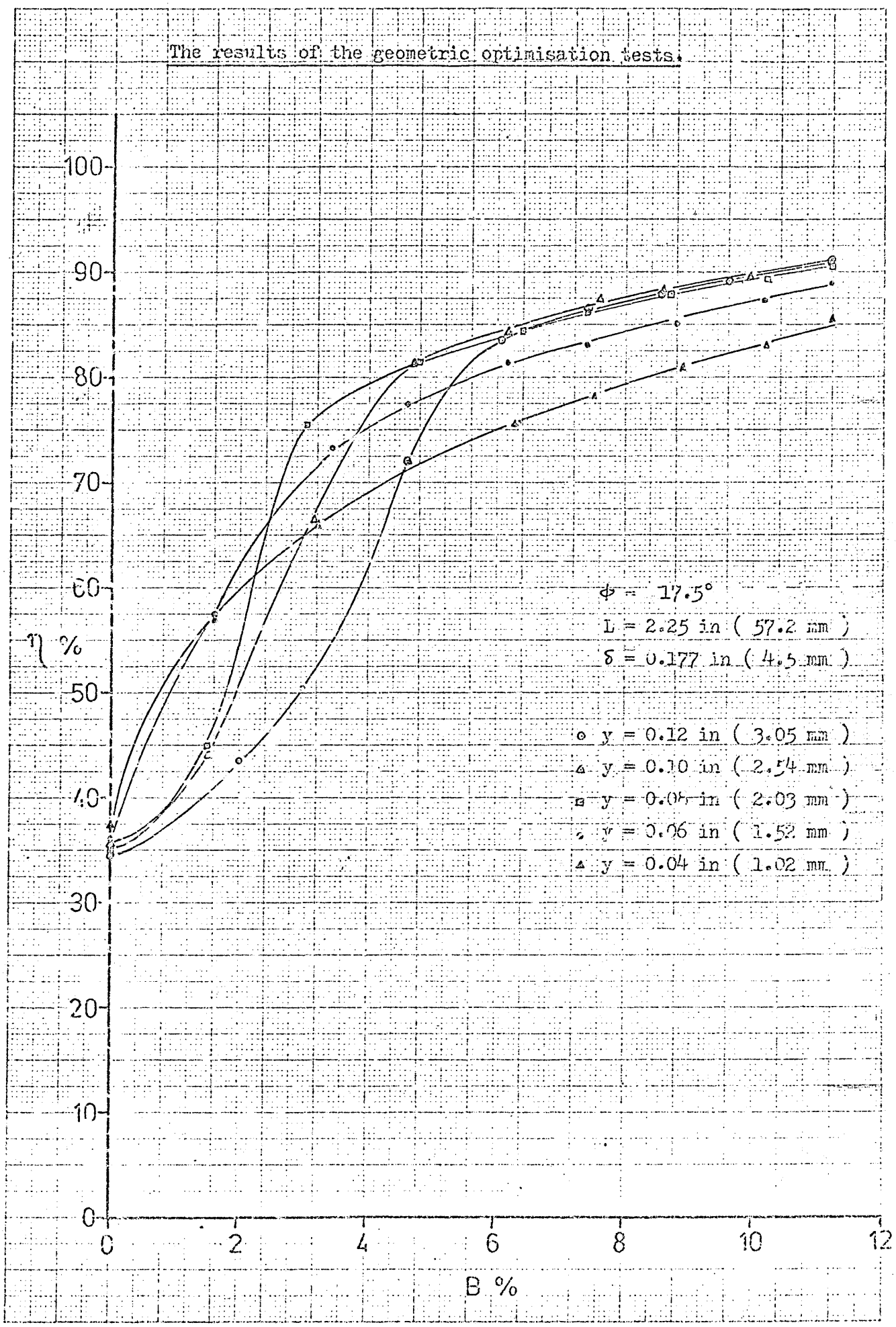

Fig.(c-1): The effect of B% on η for different values of y.

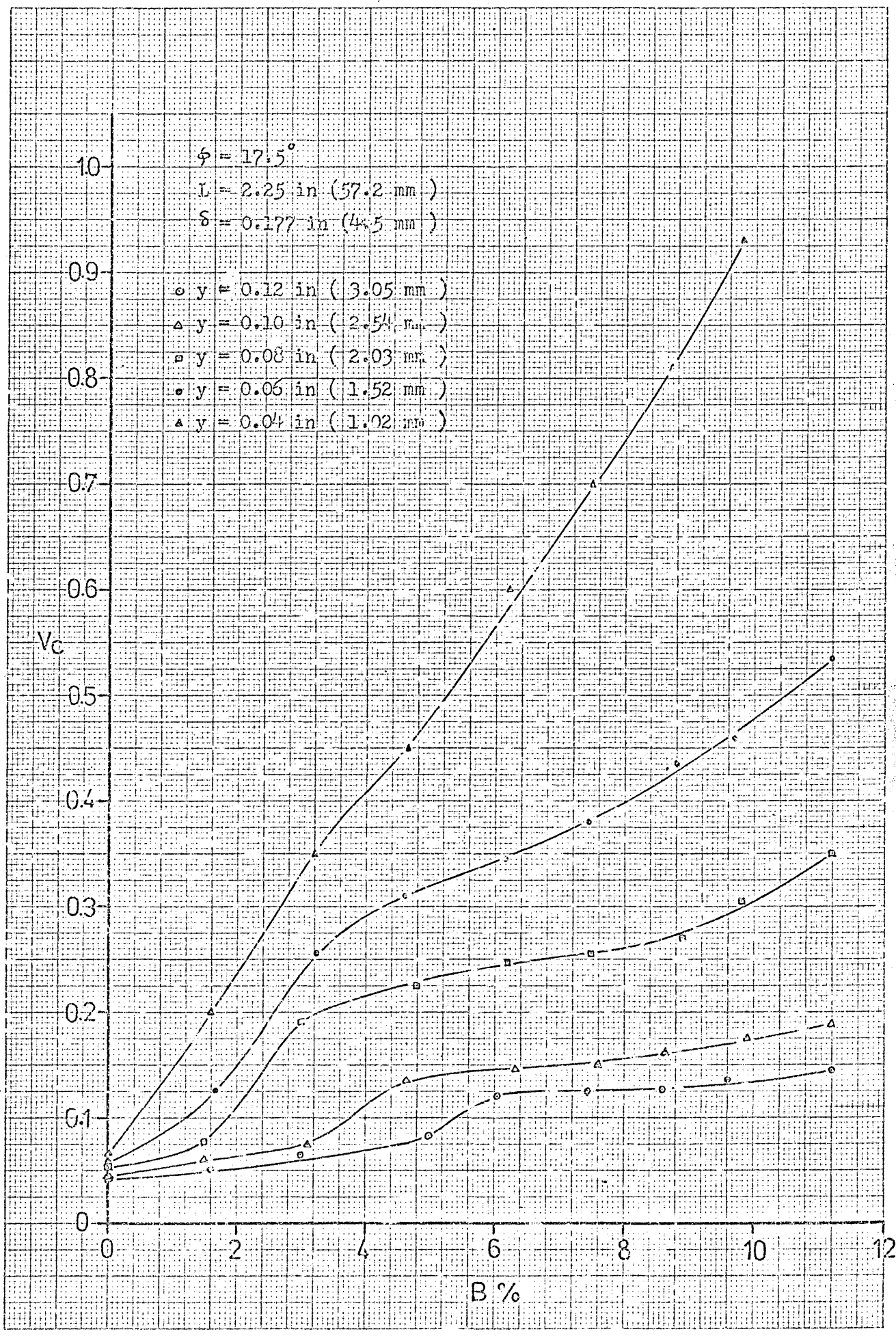

Fig.(c-2): The effect of B% on V_c for different values of y.

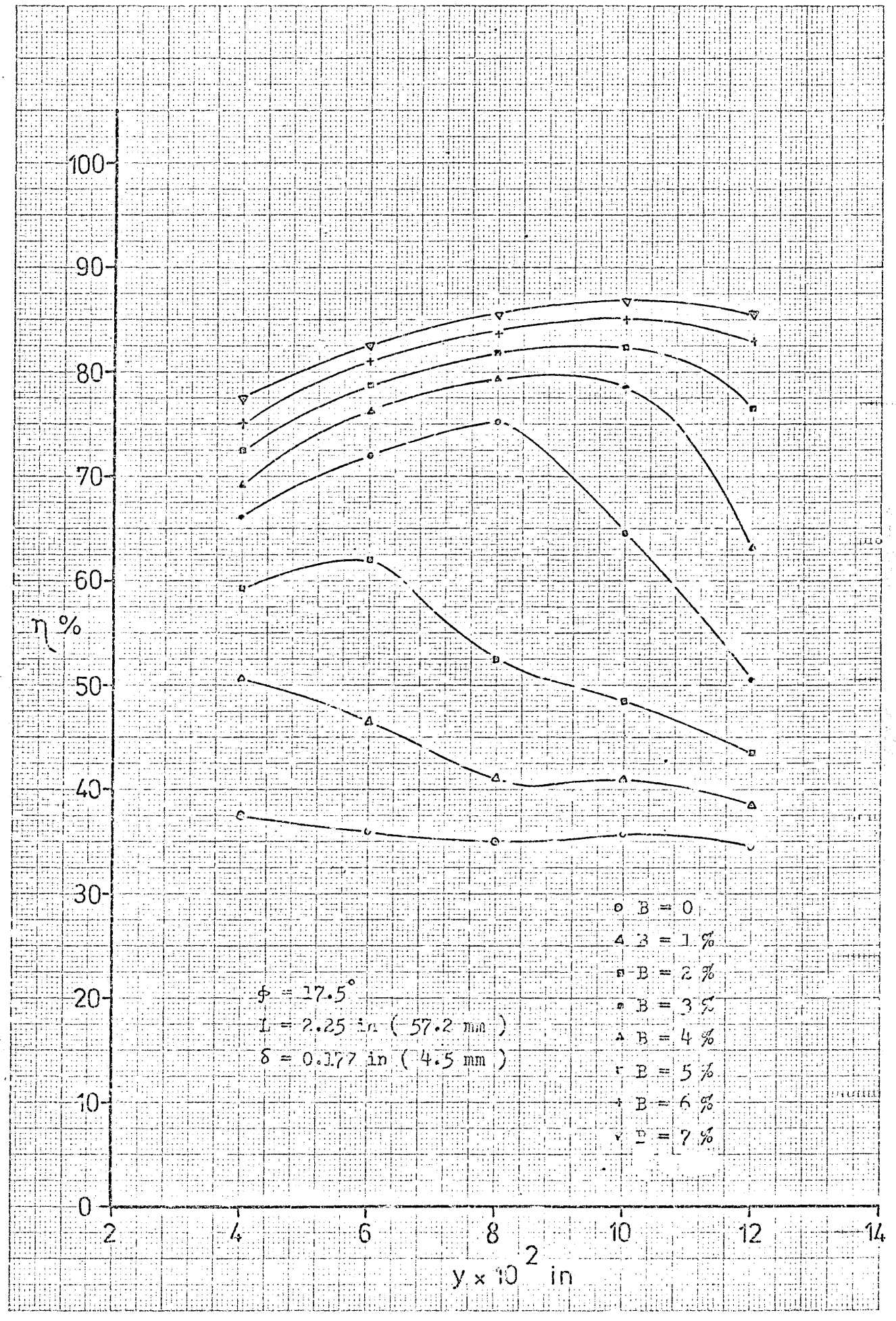

Fig.(c-3): The effect of y on η for different values of B%.

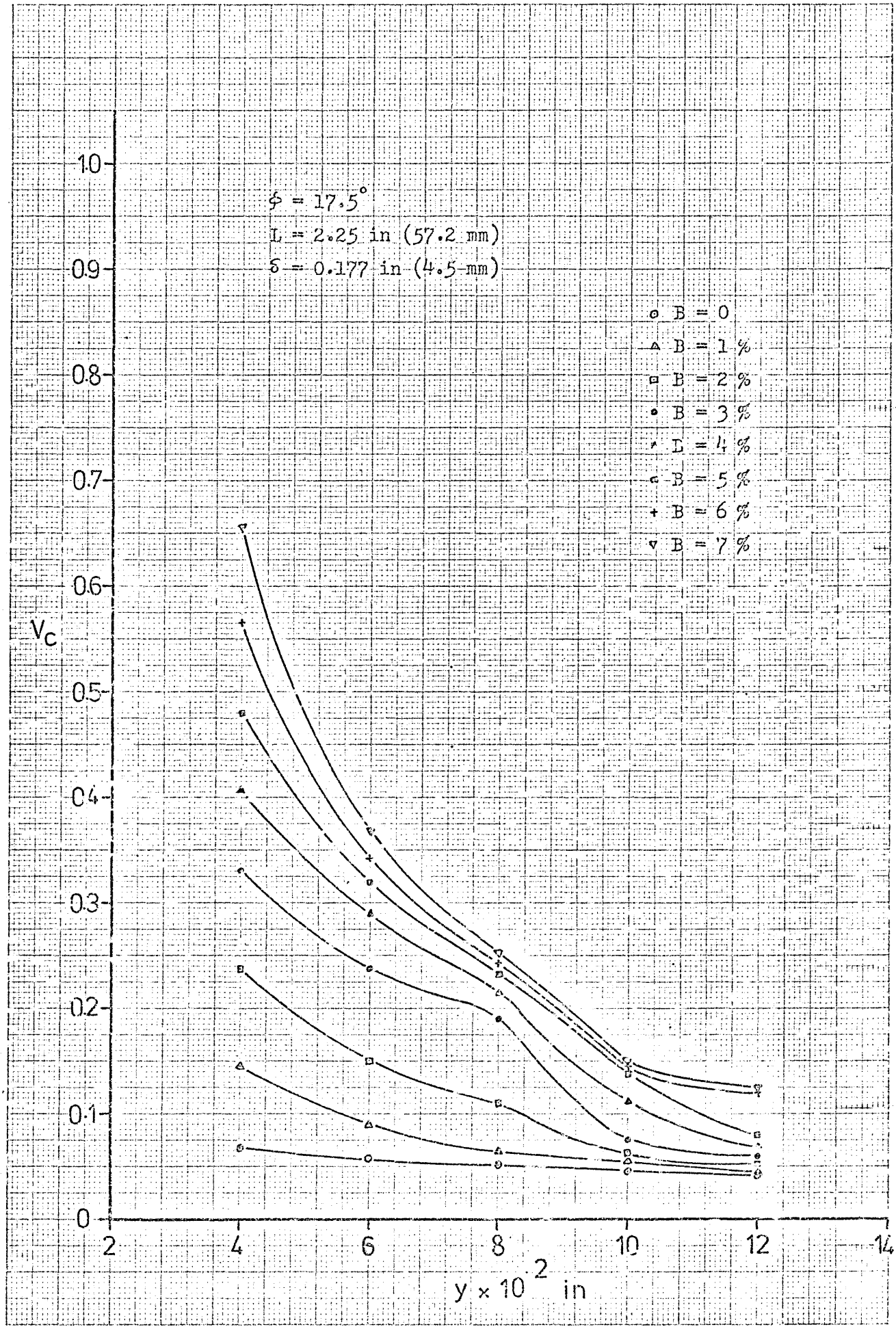

Fig.(c-4): The effect of y on V_c for different values of B%.

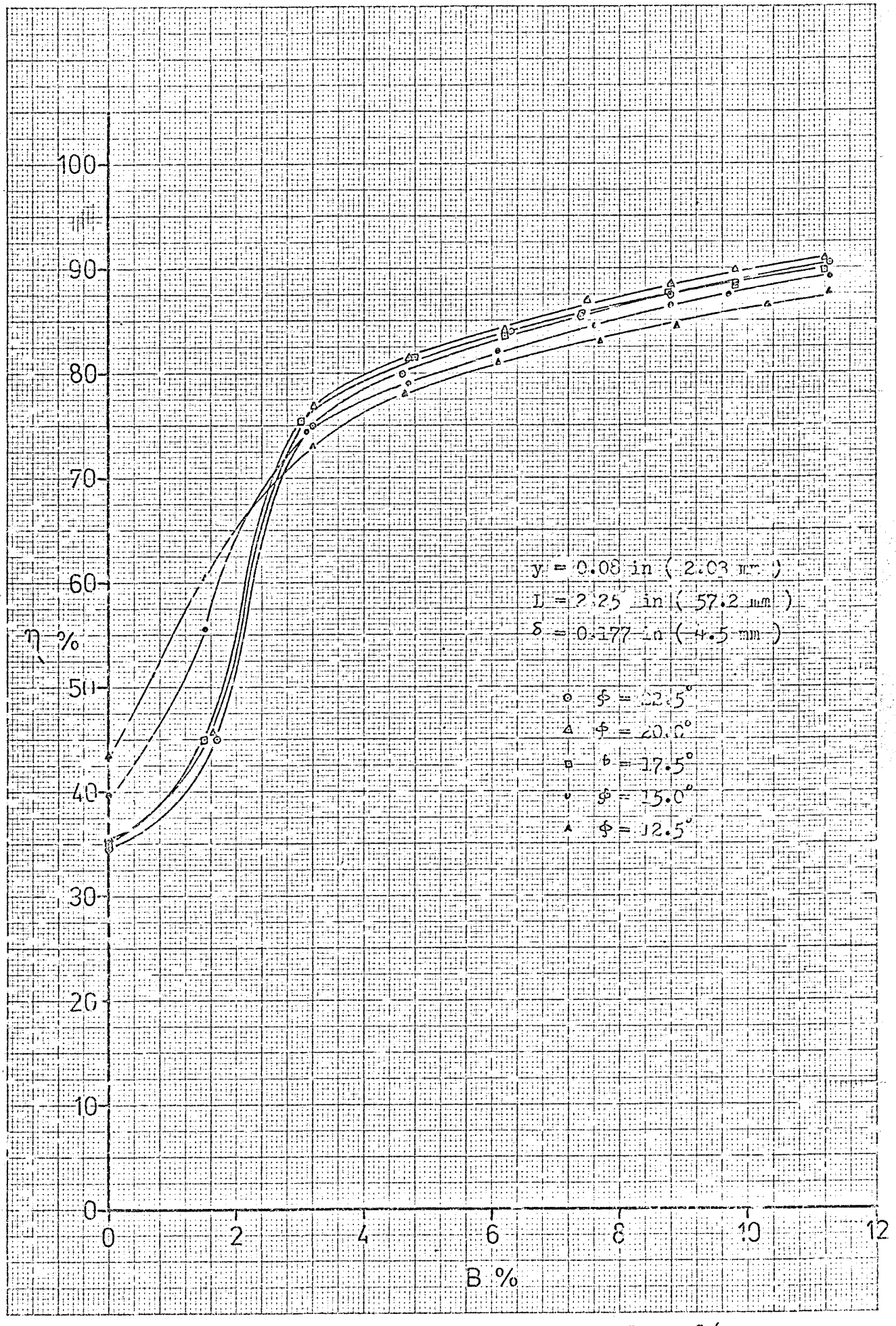

Fig.(c-5): The effect of B% on η for different values of φ.

Fig.(c-6): The effect of B% on V_c for different values of ϕ.

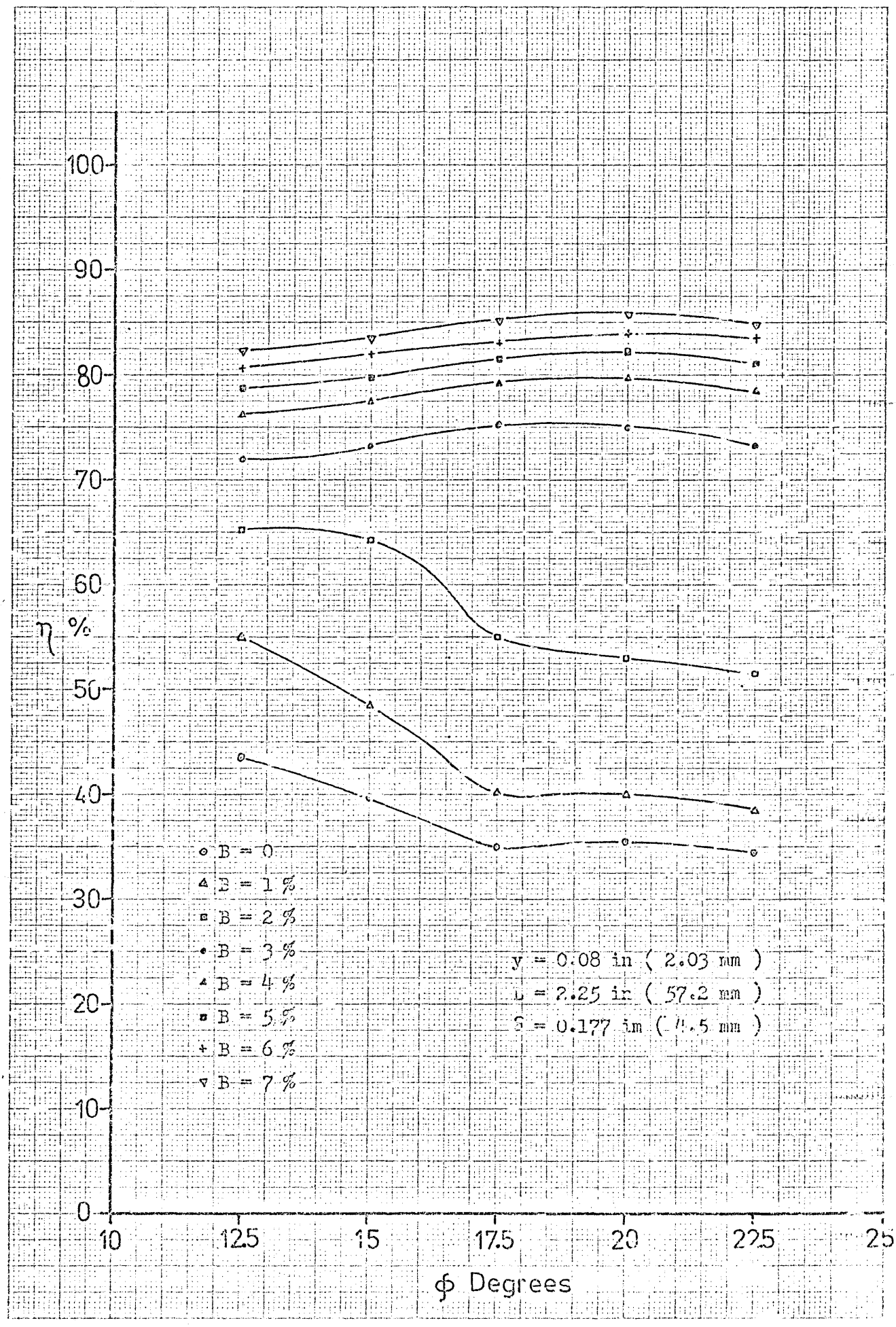

Fig.(c-7): The effect of ϕ on η for different values of B%.

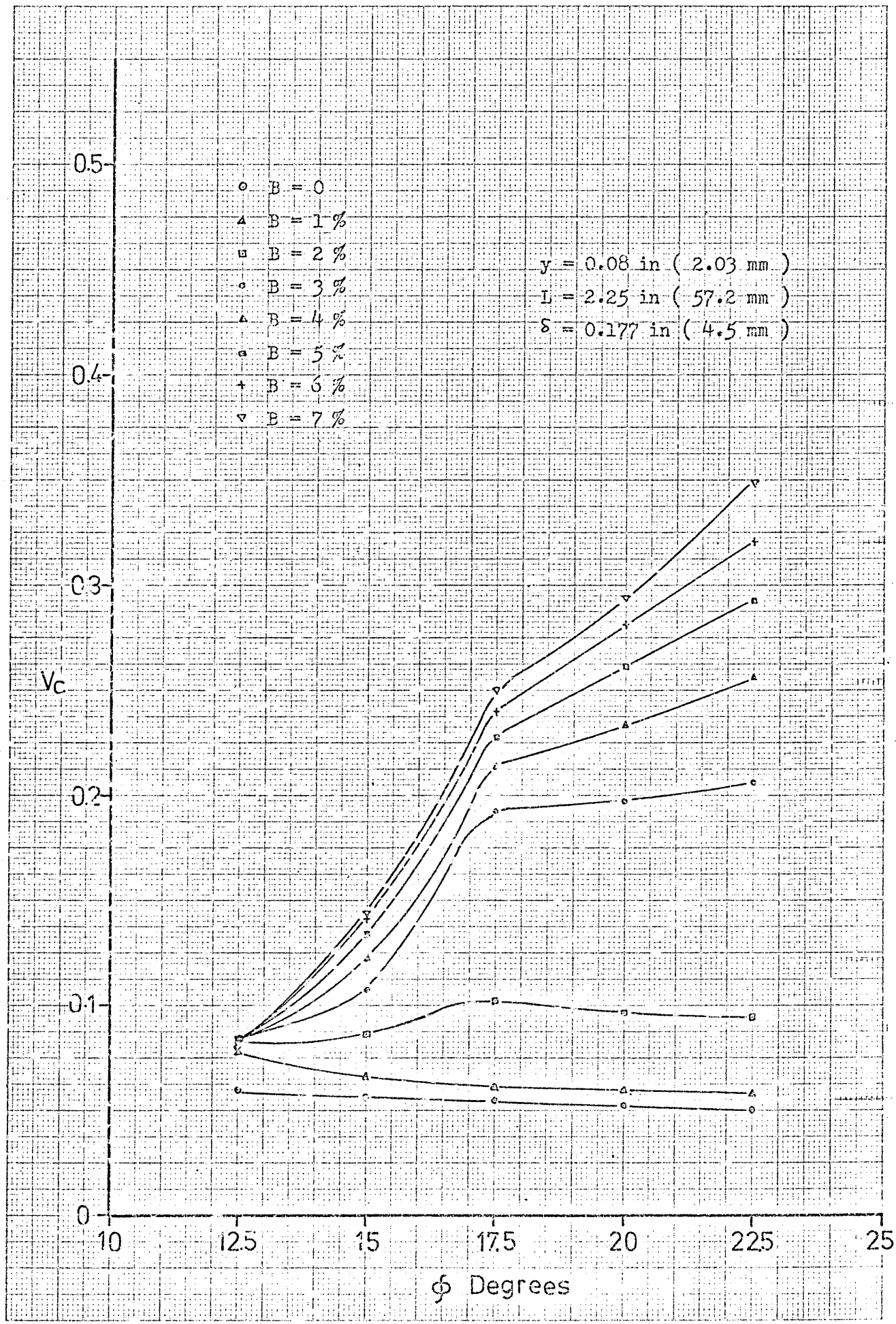

Fig.(c-8): The effect of ϕ on V_c for different values of B%.

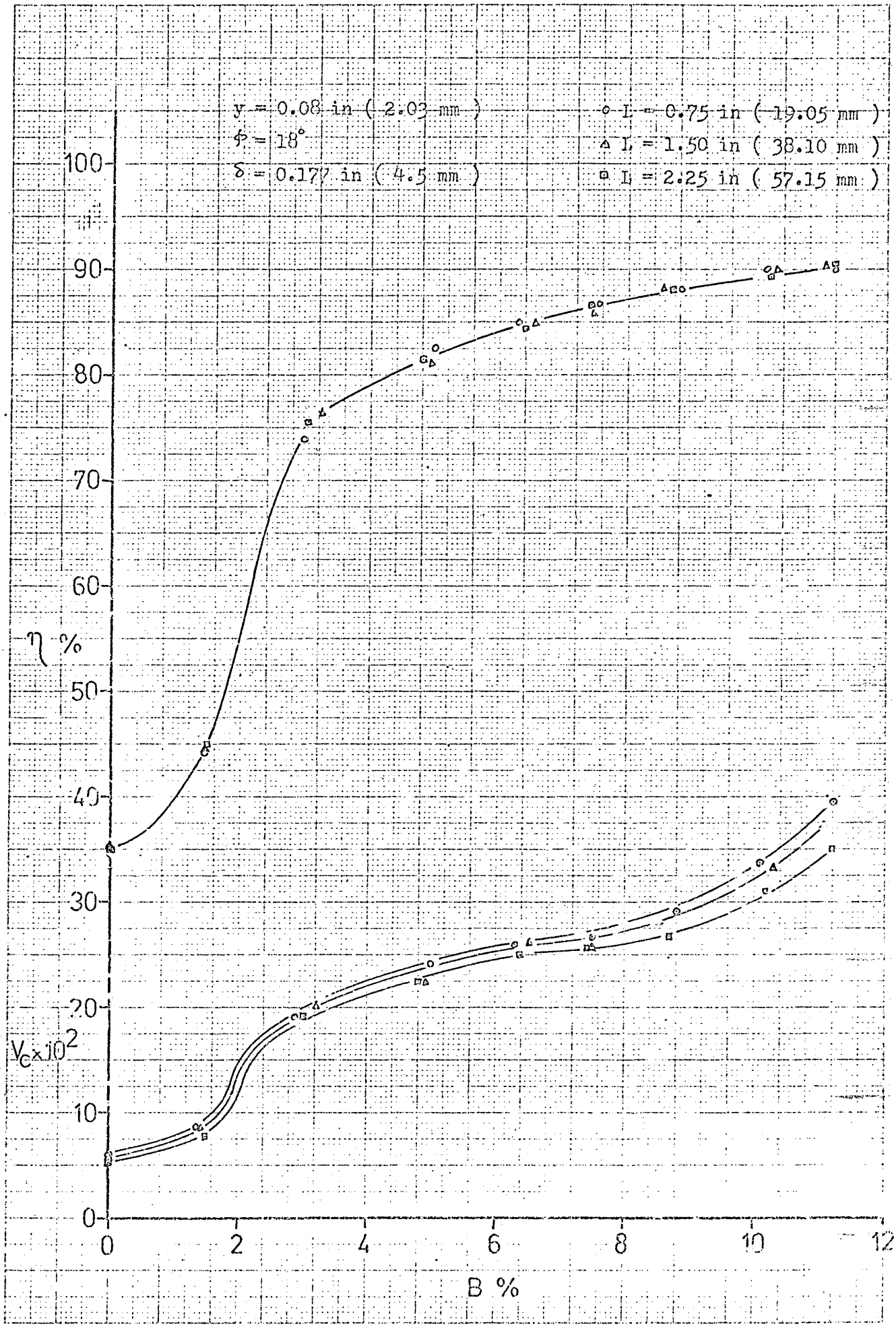

Fig.(c-9): The effect of B% on η and V_c for δ = 4.5 mm and different values of L.

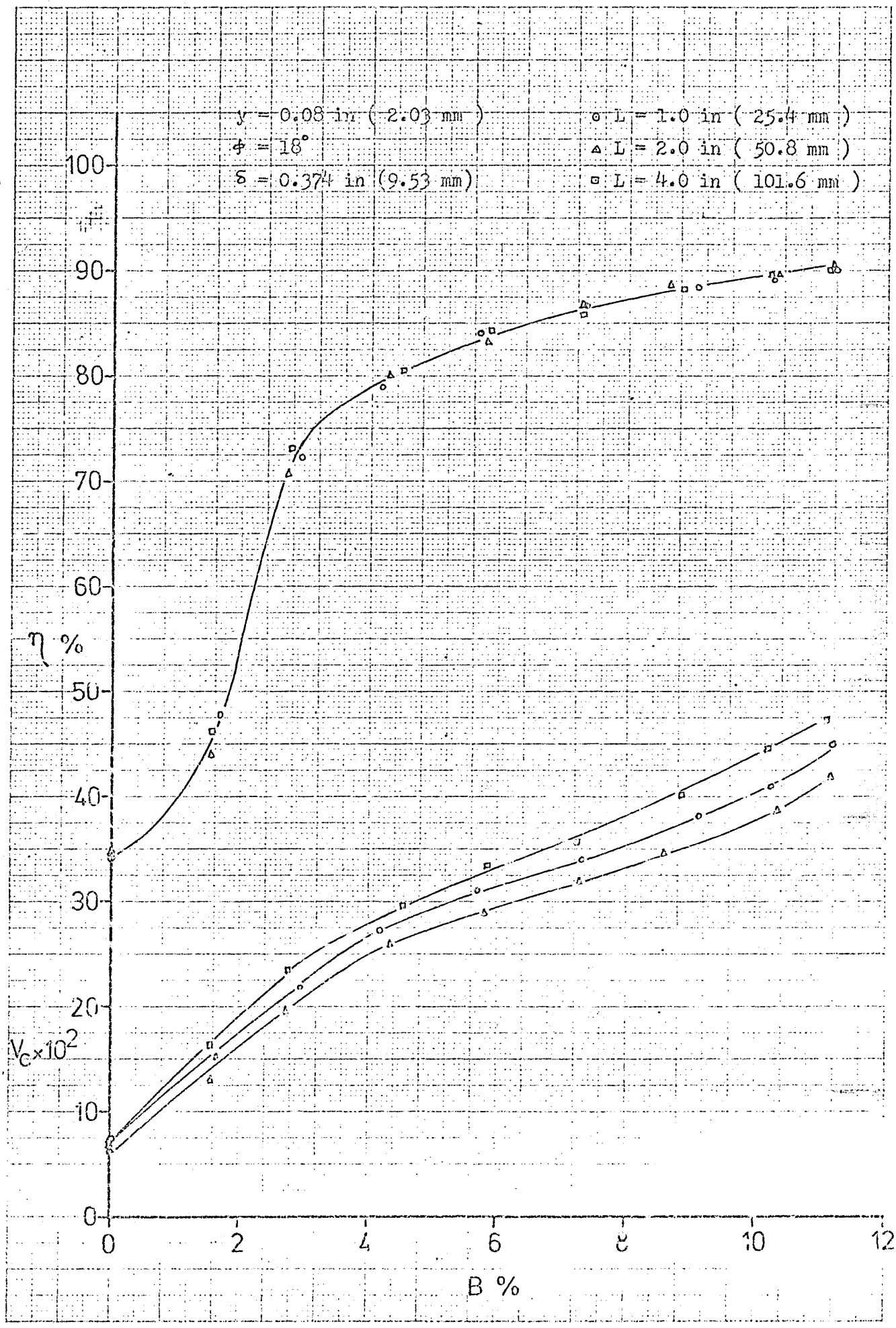

Fig.(c-10): The effect of B% on η and V_c for δ = 9.5 mm and different values of L.

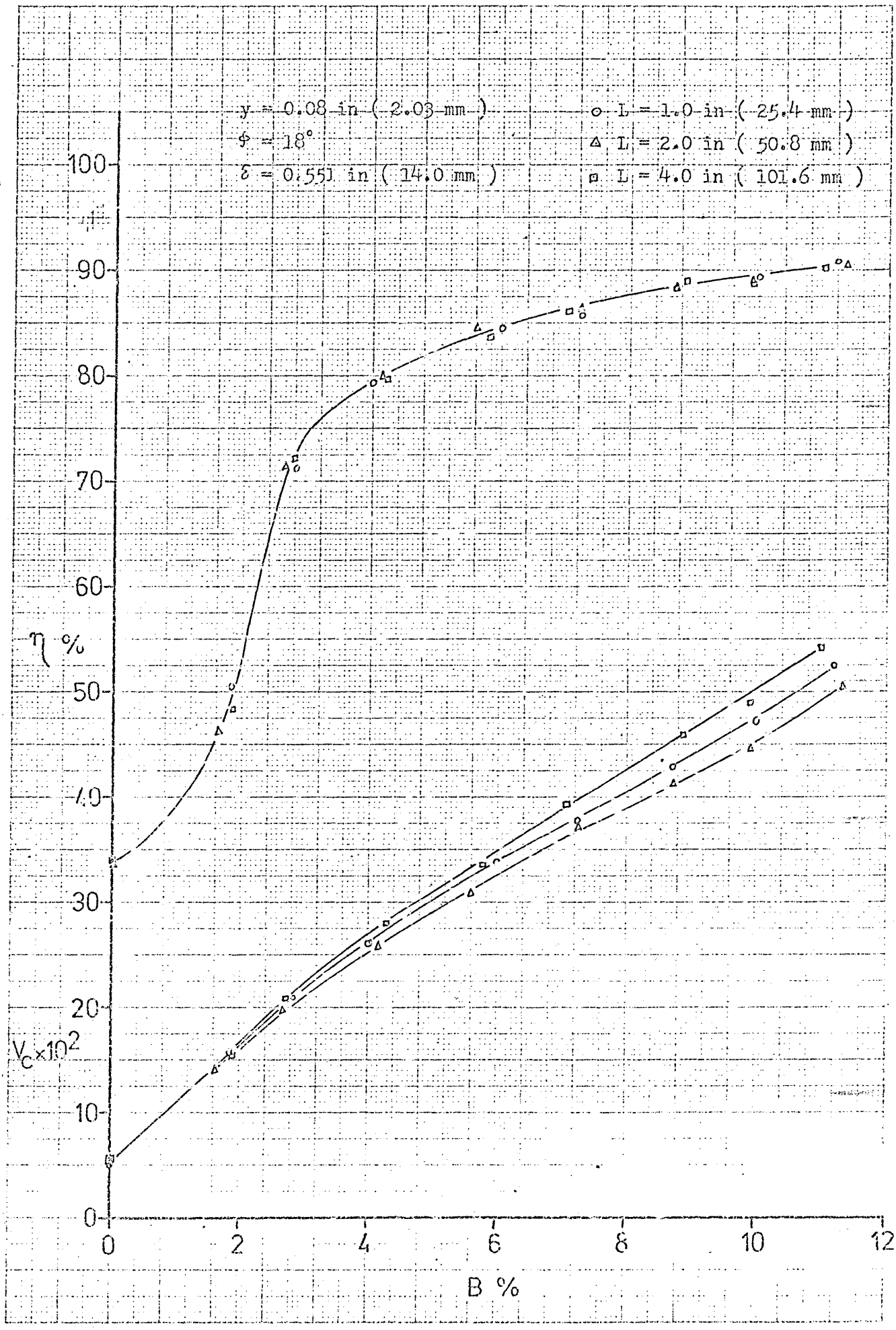

Fig.(c-11): The effect of B% on η and V_c for δ = 14 mm and different values of L.

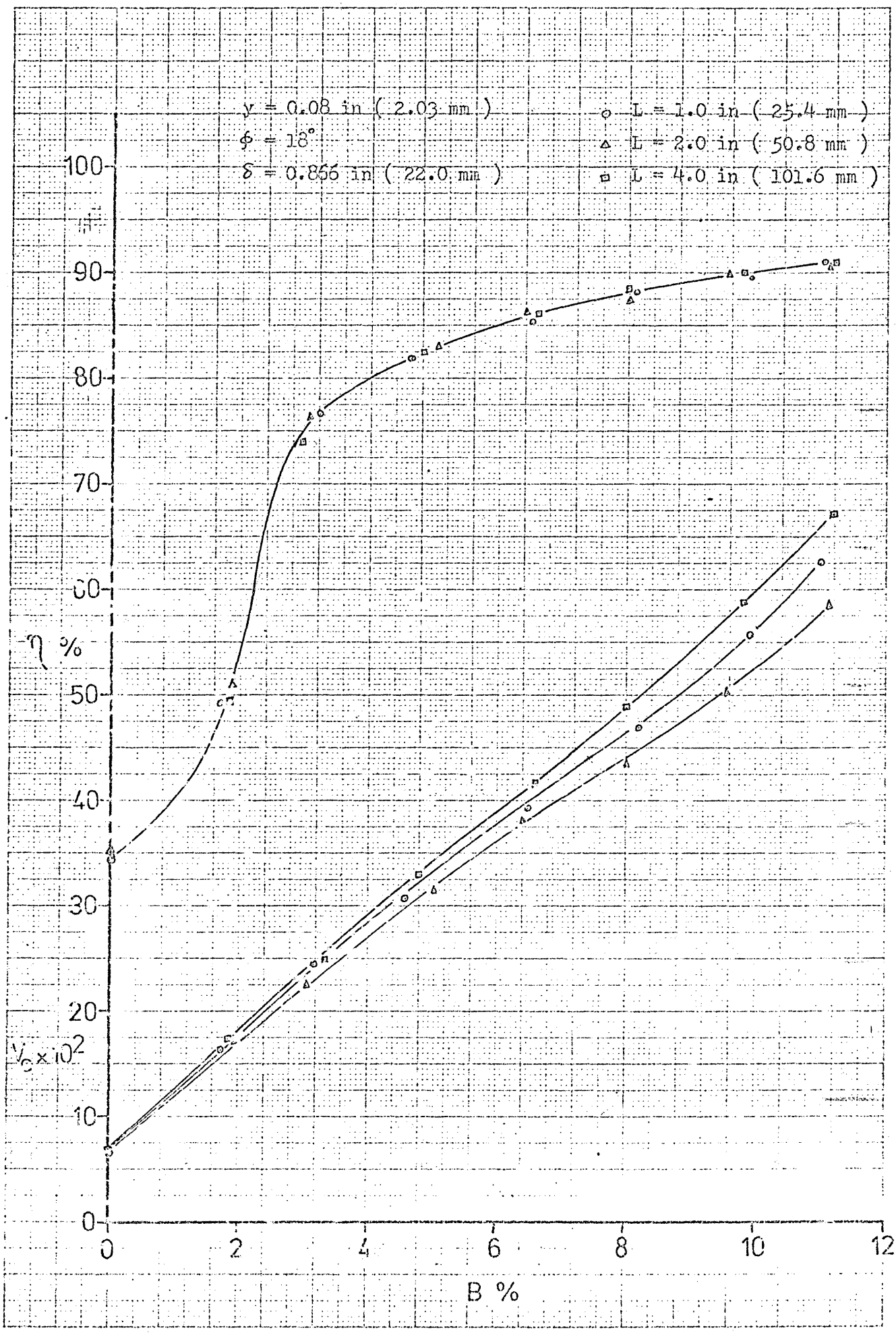

Fig.(c-12): The effect of B% on η and V_c for δ = 22 mm and different values of L.

ISSUE	MODIFICATION
A	—

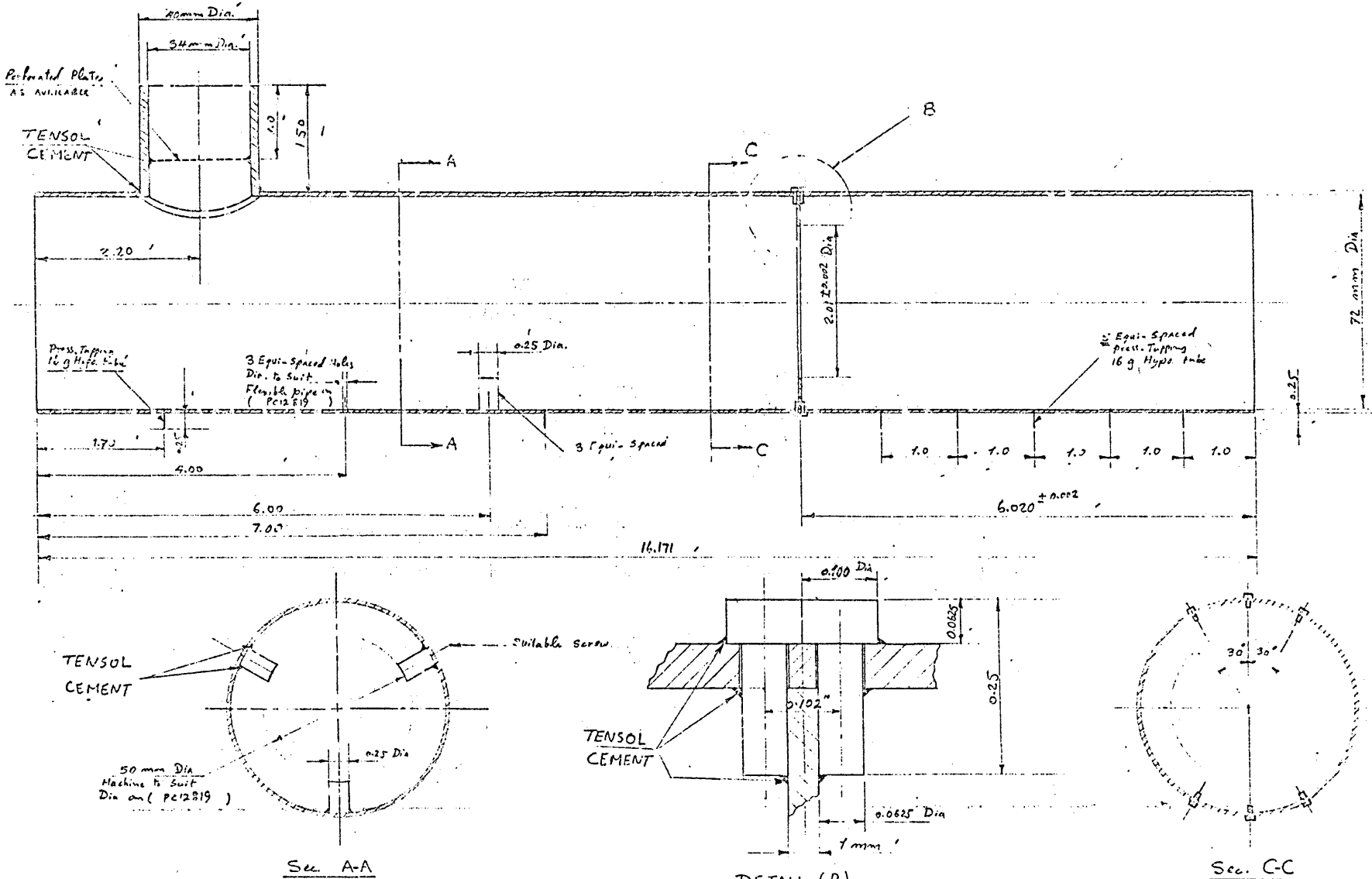

Sec. A-A

DETAIL (B)
Scale 10:1

Sec. C-C

Fig.(D-1): Details of the secondary and the vortex chamber ducts.

THIRD ANGLE PROJECTION			SHEET SIZE A 2	1		Secondary Duct	1	perspex		75 — 00 / 73 — 10		
				ITEM	PART No.	DESCRIPTION	No. OFF	MATL	SPEC.	REMARKS		
GENERAL TOLERANCE ON DIMENSIONS MACHINED ± .010" UNMACHINED OTHER DIMENSIONS AS STATED	JOB No.	No. OF SETS REQD 1	SCALE 1:1	DRAWN SAAD 3.9.79	CHK'D	APPV'D	STRESS APPVD.	TITLE:- SECONDARY DUCT				
WELD WHERE SHOWN THUS ~~~~			FINISH Self	ISSUED BY SME				DRAWING No. PC12820				
MACHINE WHERE SHOWN THUS ✓	USED ON DRG. PC12818.			CRANFIELD INSTITUTE OF TECHNOLOGY CRANFIELD.				SHT. 1 OF 1 SHEETS				

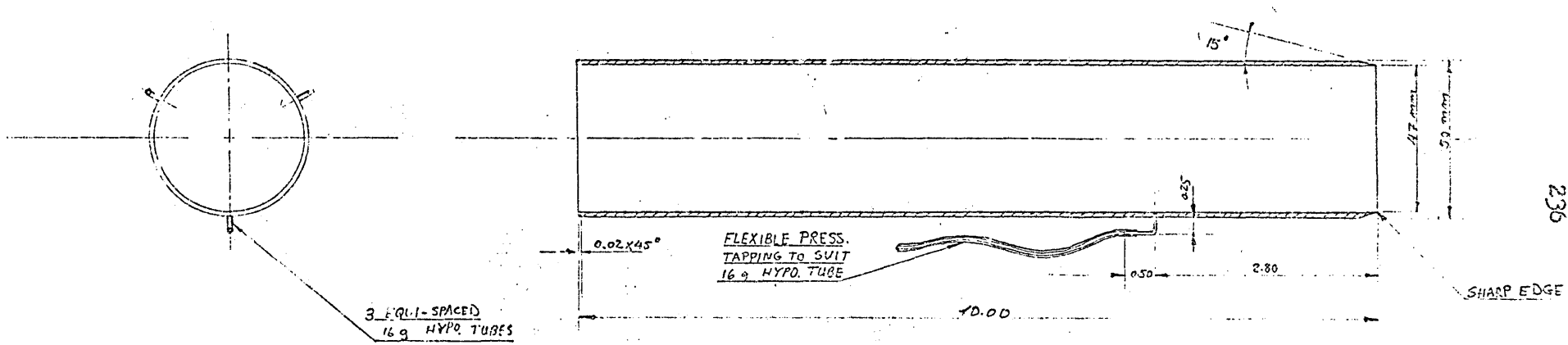

Fig.(D-2). Details of the primary duct.

				1		PRIMARY DUCT	1	Perspex		47.10 50.00	Lathe
				ITEM	PART No.	DESCRIPTION	No. OFF	MATL	SPEC.	REMARKS	

THIRD ANGLE PROJECTION

SHEET SIZE A2

GENERAL TOLERANCE ON DIMENSIONS
MACHINED ±·010
UNMACHINED
OTHER DIMENSIONS AS STATED
WELD WHERE SHOWN THUS ~~~
MACHINE WHERE SHOWN THUS ✓

JOB No.

No. OF SETS REQD 1

USED ON DRG. P.B.12818

SCALE 1:1

FINISH SELF

DRAWN	CHKD	APPVD	STRESS APPVD
SAAD 31.8.79			

TITLE:- PRIMARY DUCT

ISSUED BY SME

CRANFIELD INSTITUTE OF TECHNOLOGY
CRANFIELD.

DRAWING No. PC 12819

SHT. 1 OF 1 SHEETS

ISSUE	MODIFICATION
A	—

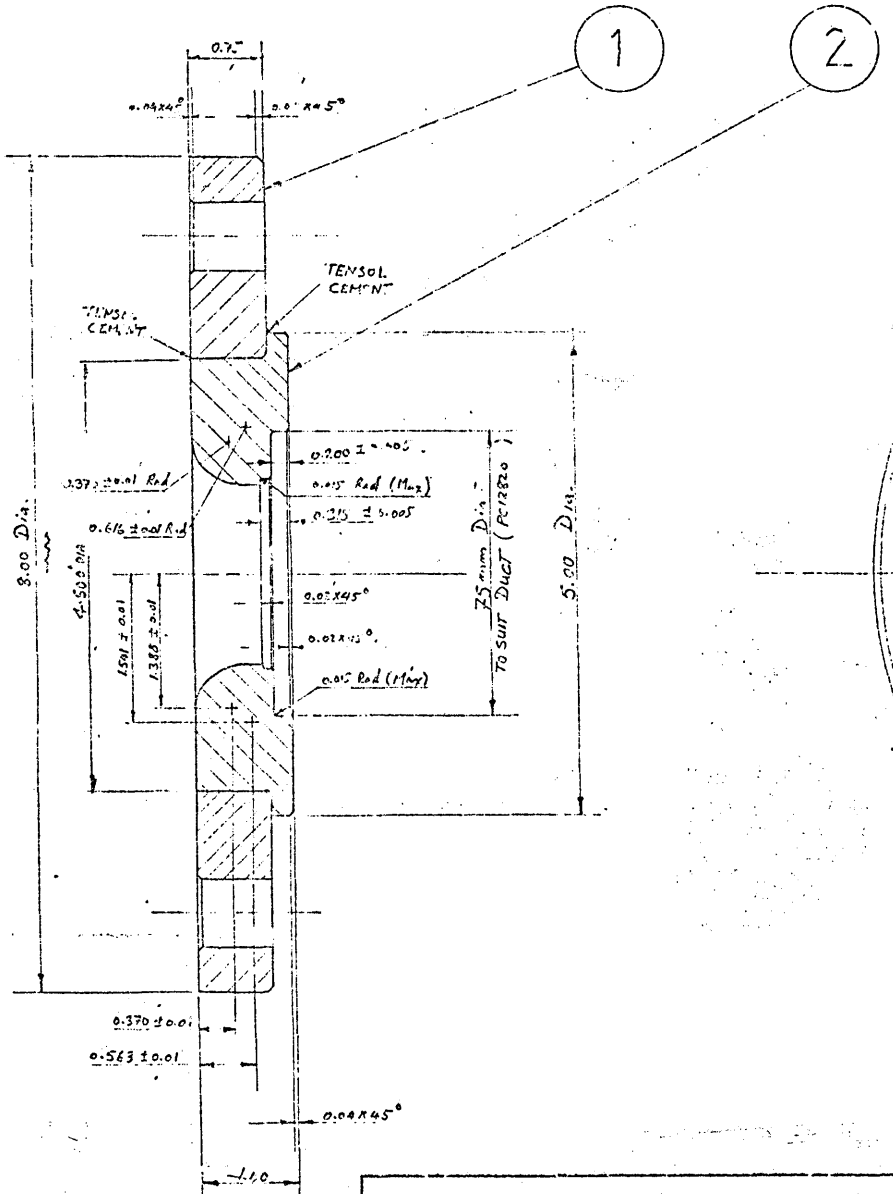

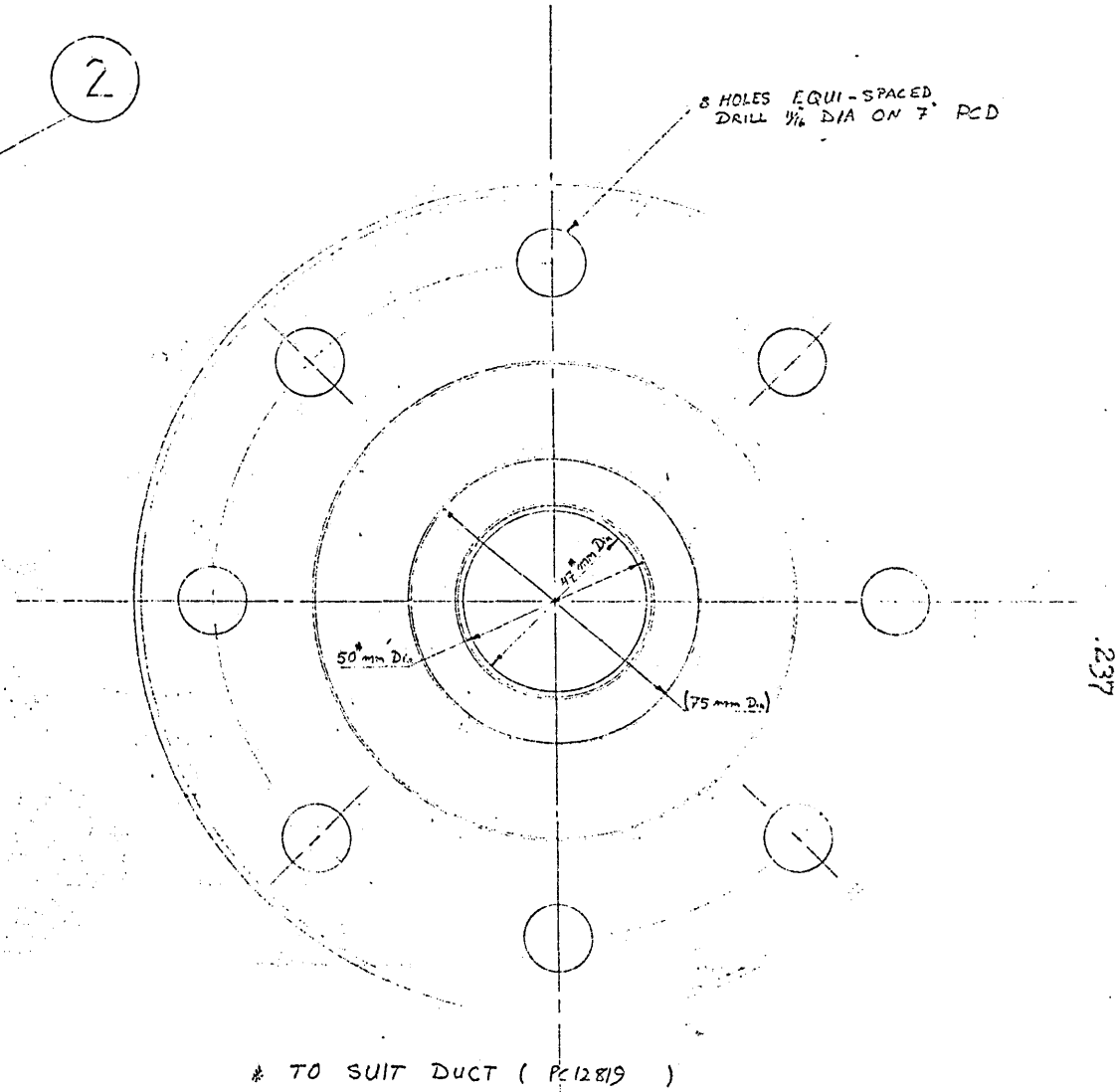

Fig.(D-3): Details of the inlet nozzle.

ITEM	PART No.	DESCRIPTION	No. OFF	MATL	SPEC.	REMARKS
2	—	NOZZLE	1	Perspex		1" BLANK
1	—	FLANGE	1	Perspex		3/4" BLANK

THIRD ANGLE PROJECTION

SHEET SIZE A2

GENERAL TOLERANCE ON DIMENSIONS
MACHINED ±.010
UNMACHINED
OTHER DIMENSIONS AS STATED
WELD WHERE SHOWN THUS
MACHINE WHERE SHOWN THUS

JOB No. | No. OF SETS REQ 1 | USED ON DRG. Pc12818

SCALE 1:1

FINISH SELF

DRAWN	CHK'D	APPV'D	STRESS APPV'D
S.A.A.D. 31/5/79			

TITLE:- NOZZEL ASS.

ISSUED BY SME

CRANFIELD INSTITUTE OF TECHNOLOGY
CRANFIELD.

DRAWING No. Pc/2827

SHT. 1 OF 1 SHEETS

APPENDIX E

Calculation of the components of the mean velocity and the Reynolds' Stresses:

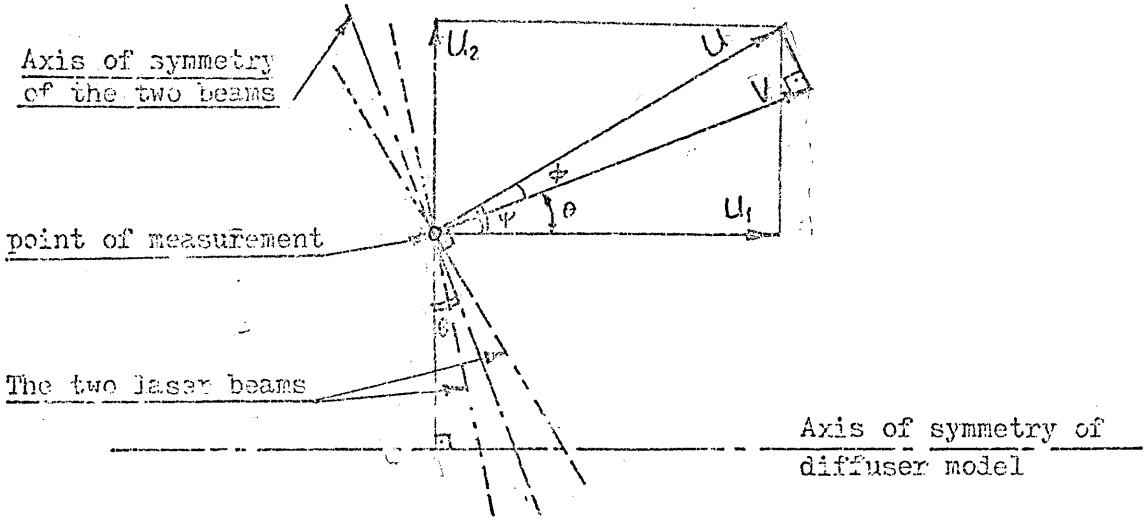

Fig.(E-1): The velocity diagram

The transmitting optics was set so that the axis of symmetry of the two beams was at an angle θ, to the perpendicular to the axis of symmetry of the diffuser model, Fig.(E-1). The measured instantaneous velocity, V can be related to the instantaneous axial and radial velocity, U_1 and U_2, as follows:

$$V = U \cos \phi$$

or,

$$V = U \cos (\psi - \theta)$$

hence,

$$V = U (\cos\psi \cos\theta + \sin\psi \sin\theta) \qquad (1)$$

But,

$$\cos\psi = \frac{U_1}{U}, \text{ and } \sin\psi = \frac{U_2}{U}$$

substituting in equation (1) and rearranging, we get:

$$V = U_1 \cos\theta + U_2 \sin\theta \qquad (2)$$

But,

$$V = \bar{V} + \acute{v}$$

$$U_1 = \bar{U}_1 + \acute{u}_1$$

$$U_2 = \bar{U}_2 + \acute{u}_2$$

Substituting in equation (2), we get:

$$\bar{V} + \acute{v} = (\bar{U}_1 + \acute{u}_1)\cos\theta + (\bar{U}_2 + \acute{u}_2)\sin\theta \qquad (3)$$

Time averaging, we get:

$$\bar{V} = \bar{U}_1 \cos\theta + \bar{U}_2 \sin\theta \qquad (4)$$

Squaring equation (3), time averaging, and rearranging we get:

$$\bar{V}^2 + \bar{v}^2 = (\bar{U}_1^2 + \bar{u}_1^2)\cos^2\theta + (\bar{U}_2^2 + \bar{u}_2^2)\sin^2\theta + 2(\bar{U}_1\bar{U}_2 + \overline{u_1 u_2})\cos\theta\sin\theta \qquad (5)$$

The mean velocity, $\bar{V}$ and the turbulence intencity, T were measured at three different angles θ_1, θ_2, θ_3. The results are $\bar{V}_1$, $\bar{V}_2$ & $\bar{V}_3$ and T_1, T_2 & T_3.

But,

$$\bar{v}^2 = \bar{V}^2 \cdot T^2 \qquad (6)$$

Hence,

$$\bar{v}_1^2 = \bar{V}_1^2 \cdot T_1^2 \qquad (6)\,a$$

$$\bar{v}_2^2 = \bar{V}_2^2 \cdot T_2^2 \qquad (6)\,b$$

$$\bar{v}_3^2 = \bar{V}_3^2 \cdot T_3^2 \qquad (6)\,c$$

Application of equation (4) twice gives:

$$\bar{V}_1 = \bar{U}_1 \cos\theta_1 + \bar{U}_2 \sin\theta_1 \qquad (7)\,a$$

$$\bar{V}_2 = \bar{U}_1 \cos\theta_2 + \bar{U}_2 \sin\theta_2 \qquad (7)\,b$$

Equations (7) were solved simultaneously to render the required mean velocity components $\bar{U}_1$ and $\bar{U}_2$.

Application of equation (5) three times gives:

$$\bar{V}_1^2 + \bar{v}_1^2 = (\bar{U}_1^2 + \bar{u}_1^2)\cos^2\theta_1 + (\bar{U}_2^2 + \bar{u}_2^2)\sin^2\theta_1 + 2(\bar{U}_1\bar{U}_2 + \overline{u_1 u_2})\cos\theta_1\sin\theta_1 \qquad (8)a$$

$$\bar{V}_2^2 + \bar{v}_2^2 = (\bar{U}_1^2 + \bar{u}_1^2)\cos^2\theta_2 + (\bar{U}_2^2 + \bar{u}_2^2)\sin^2\theta_2 + 2(\bar{U}_1\bar{U}_2 + \overline{u_1 u_2})\cos\theta_2\sin\theta_2 \qquad (8)b$$

$$\bar{V}_3^2 + \bar{v}_3^2 = (\bar{U}_1^2 + \bar{u}_1^2)\cos^2\theta_3 + (\bar{U}_2^2 + \bar{u}_2^2)\sin^2\theta_3 + 2(\bar{U}_1\bar{U}_2 + \overline{u_1 u_2})\cos\theta_3\sin\theta_3 \qquad (8)c$$

Where $\overline{v_1'^2}$, $\overline{v_2'^2}$, and $\overline{v_3'^2}$ were given by equations (6) a, b and c Equations (8) were solved simultaneously to render the required Reynolds' stresses $\overline{u_1'^2}$, $\overline{u_2'^2}$ and $\overline{u_1' u_2'}$.

For convenience $\overline{u_1'^2}$, $\overline{u_2'^2}$ and $\overline{u_1' u_2'}$ were denoted $\overline{u'^2}$, $\overline{v'^2}$, and $\overline{u'v'}$ respectively. Similarly; $\overline{U}_1$ and $\overline{U}_2$ were denoted $\overline{U}$ and $\overline{V}$ respectively.

Appendix F1: The static pressure distribution.

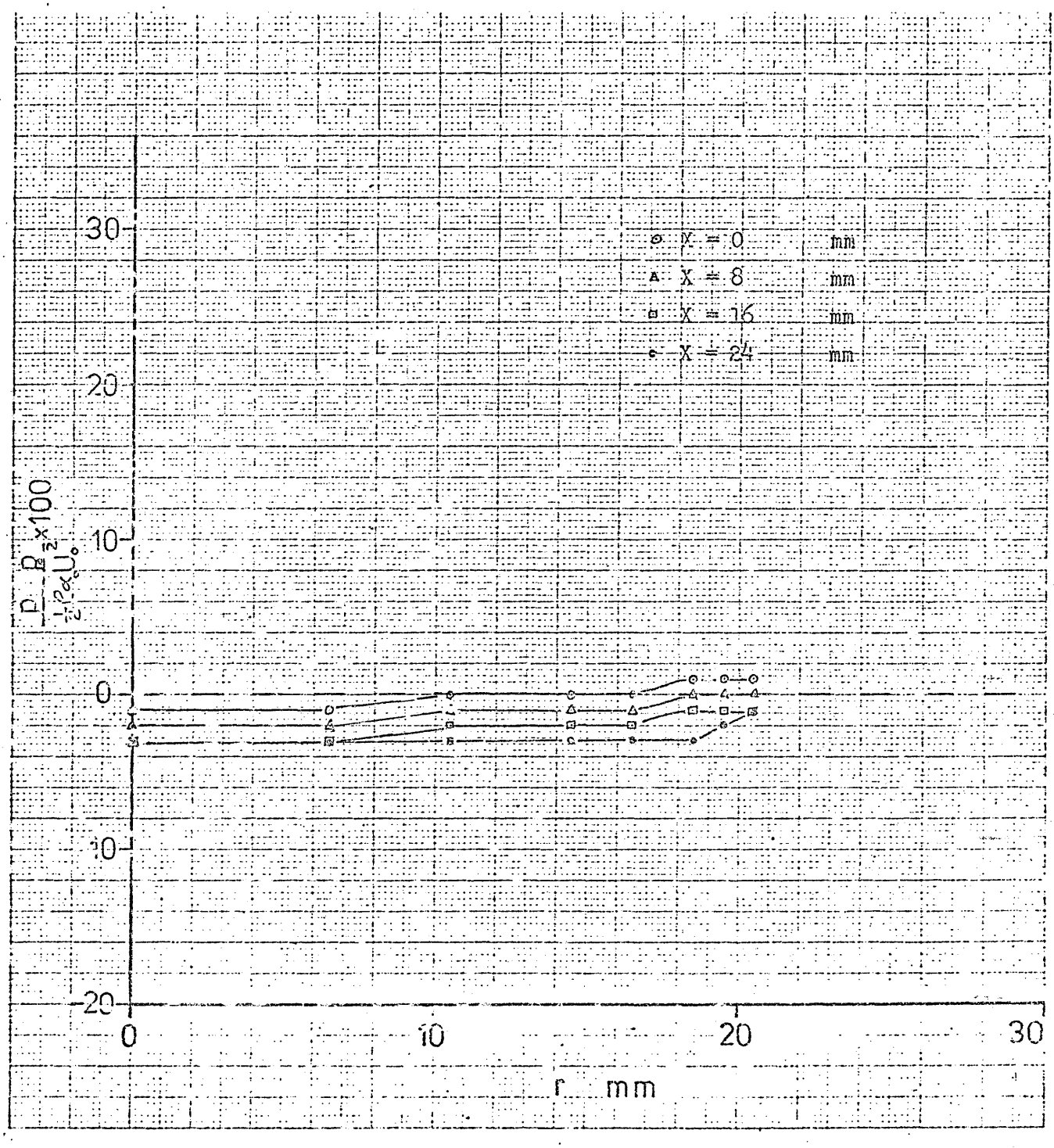

Fig.(F1-1): The static pressure distribution in region (1).

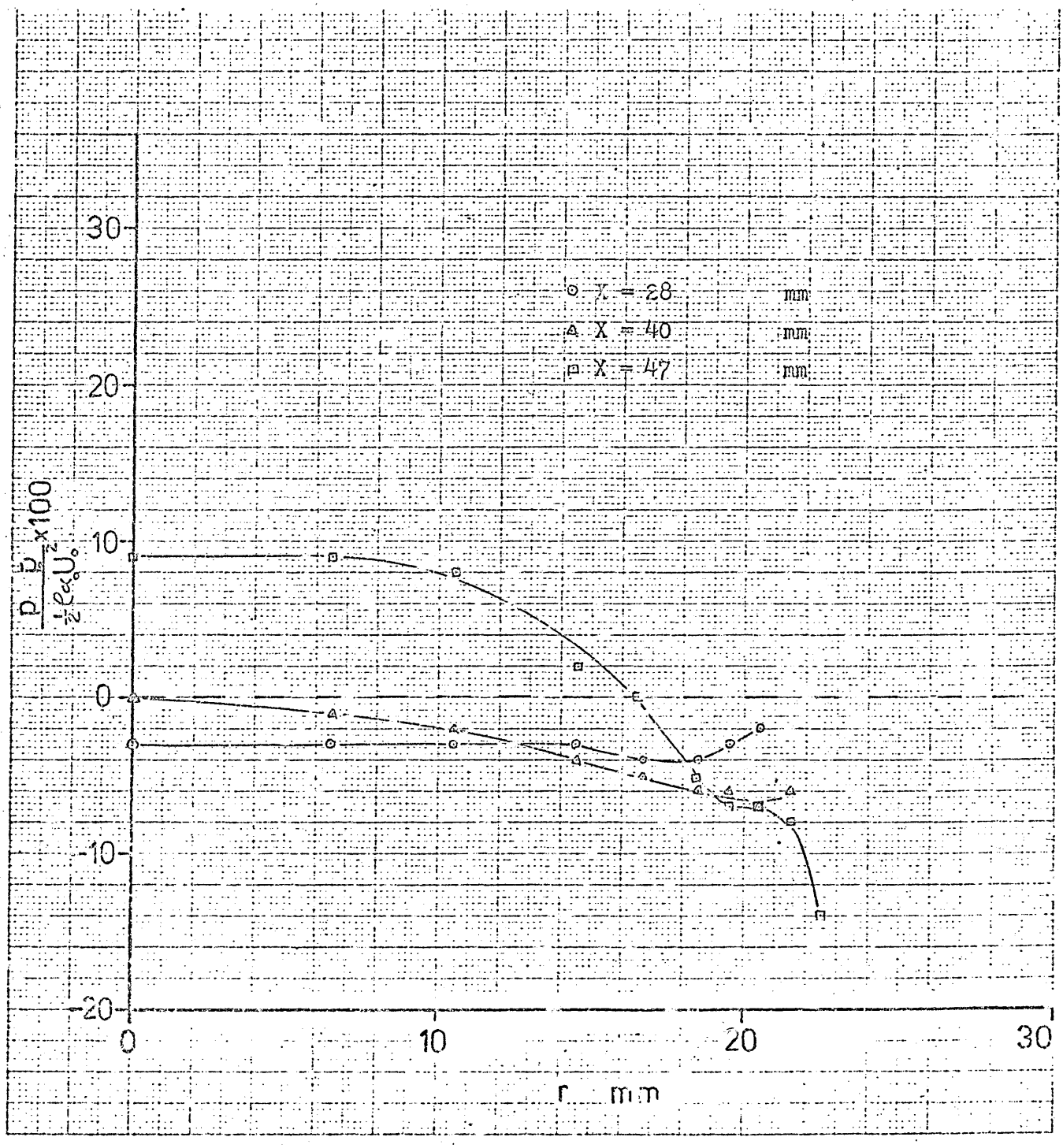

Fig.(F1-2): The static pressure distribution in region (2).

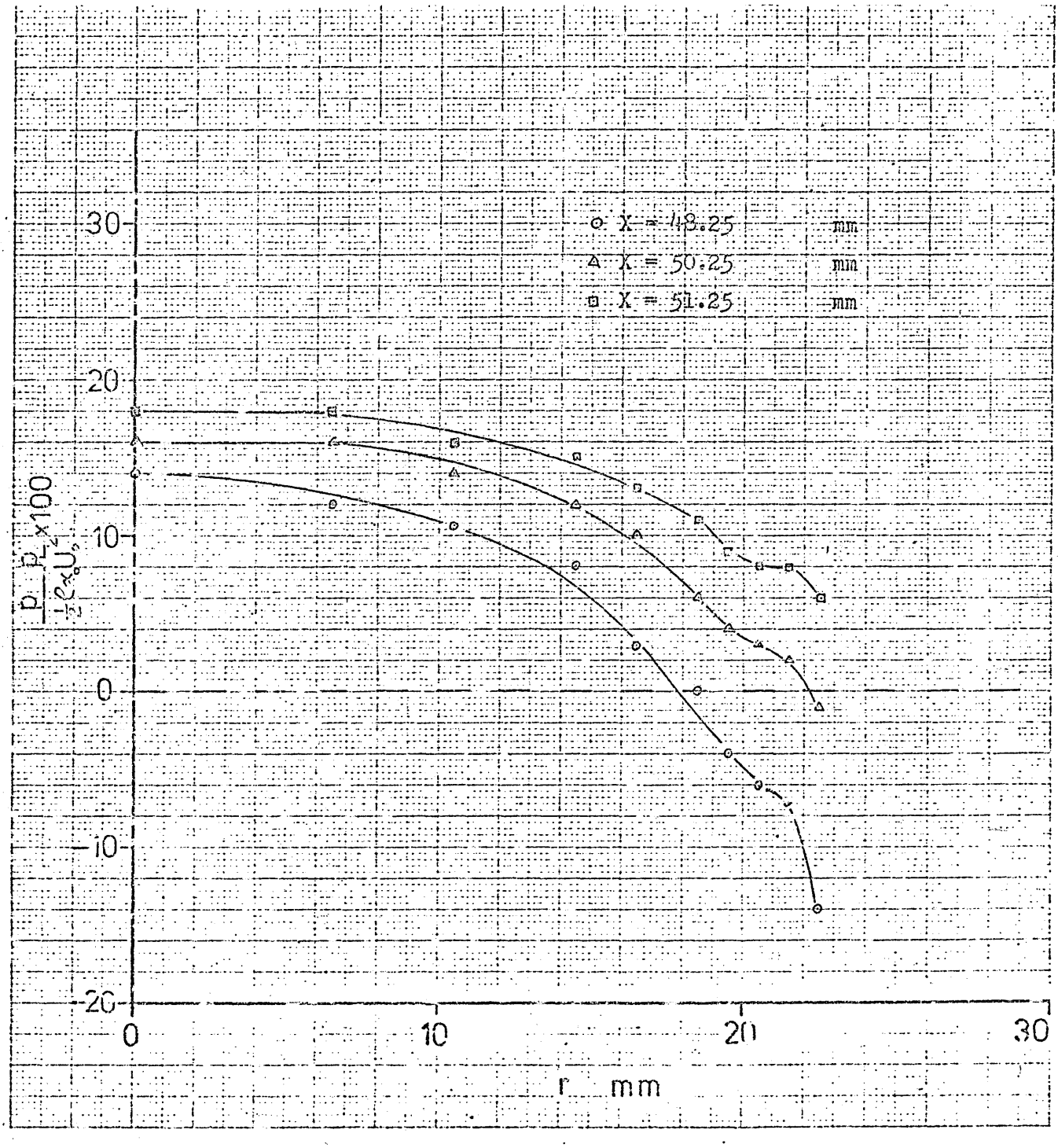

Fig.(F1-3): The static pressure distribution in region (3).

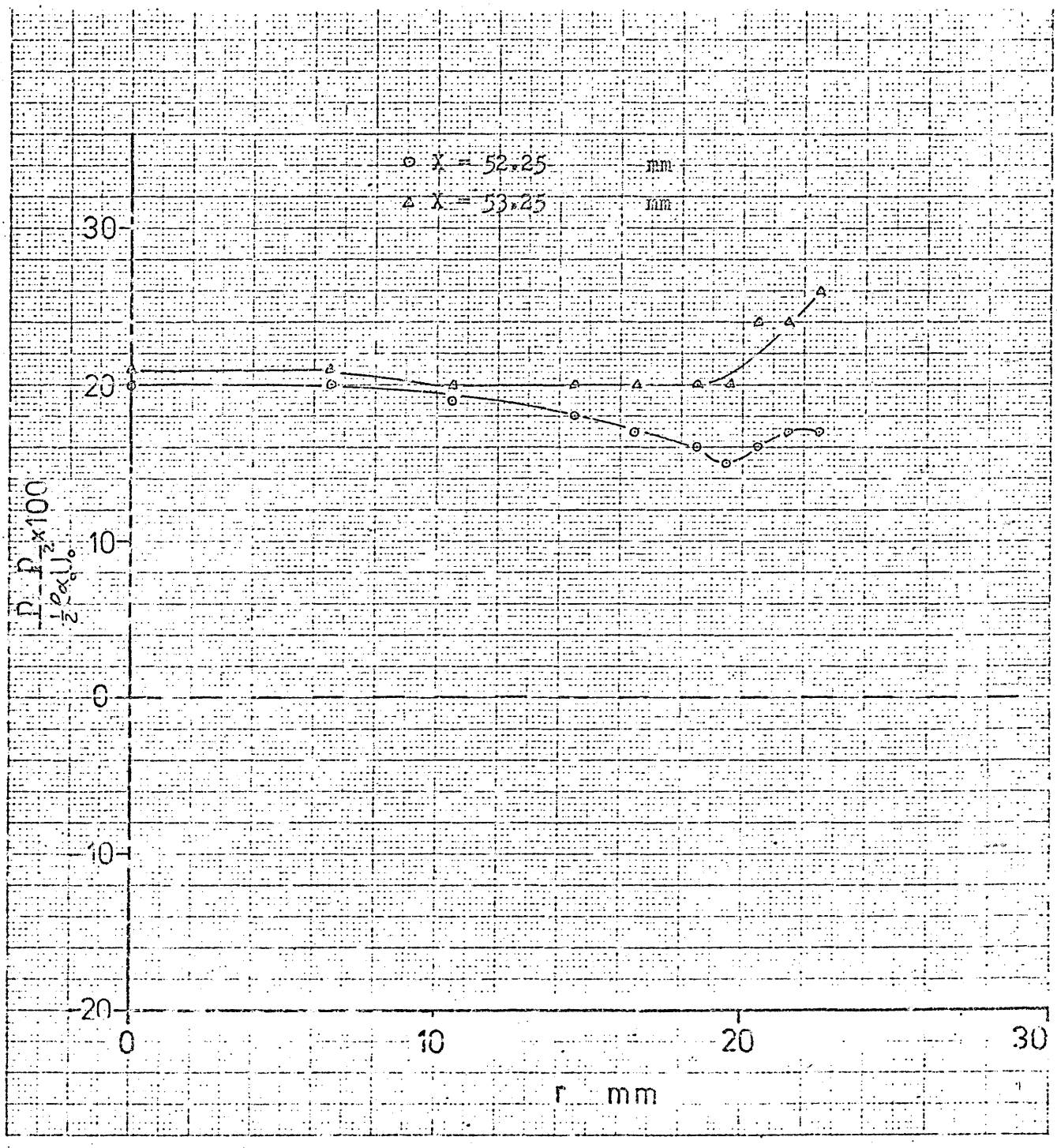

Fig.(F1-4): The static pressure distribution in region (4).

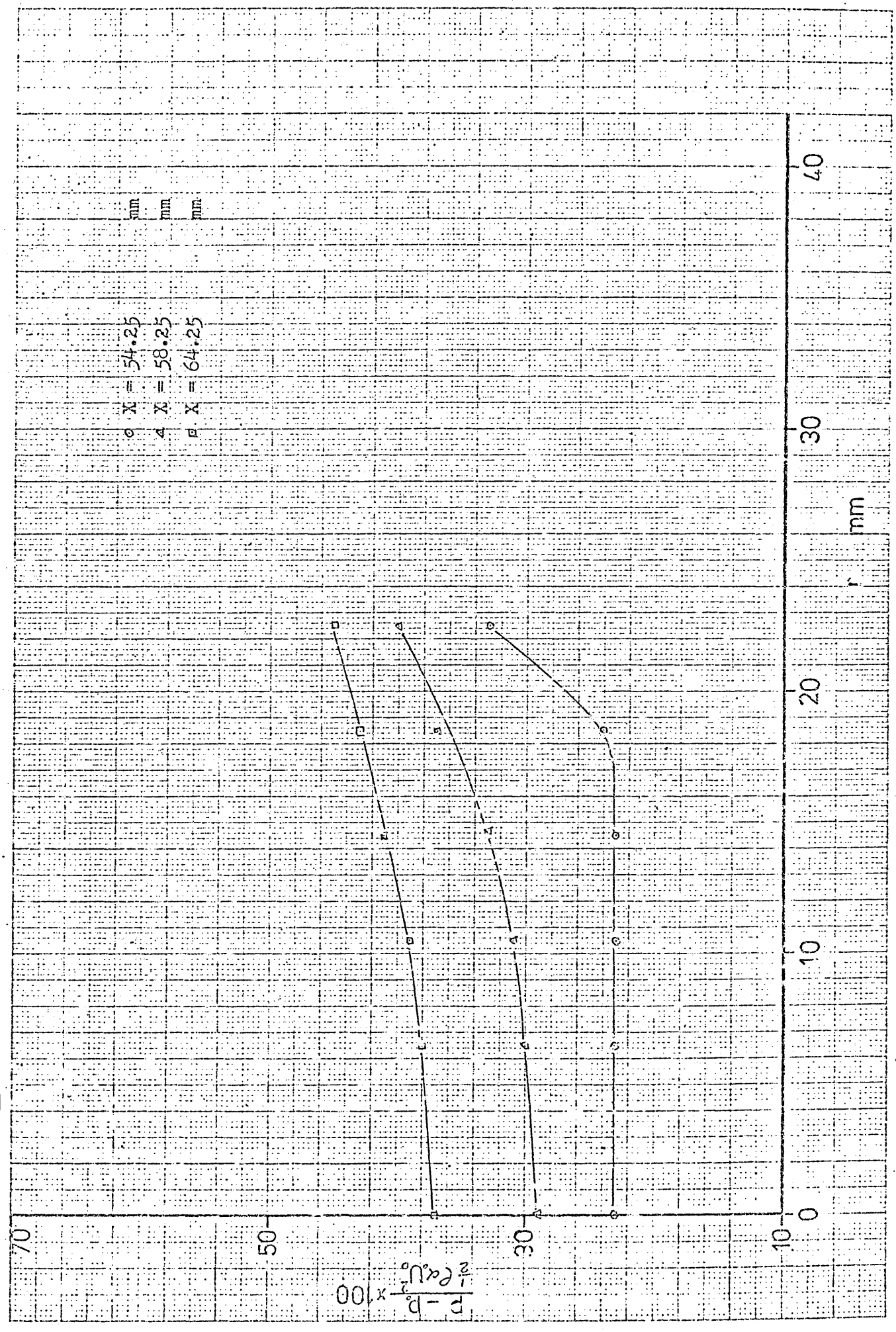

Fig.(F1-5): The static pressure distribution in region (5).

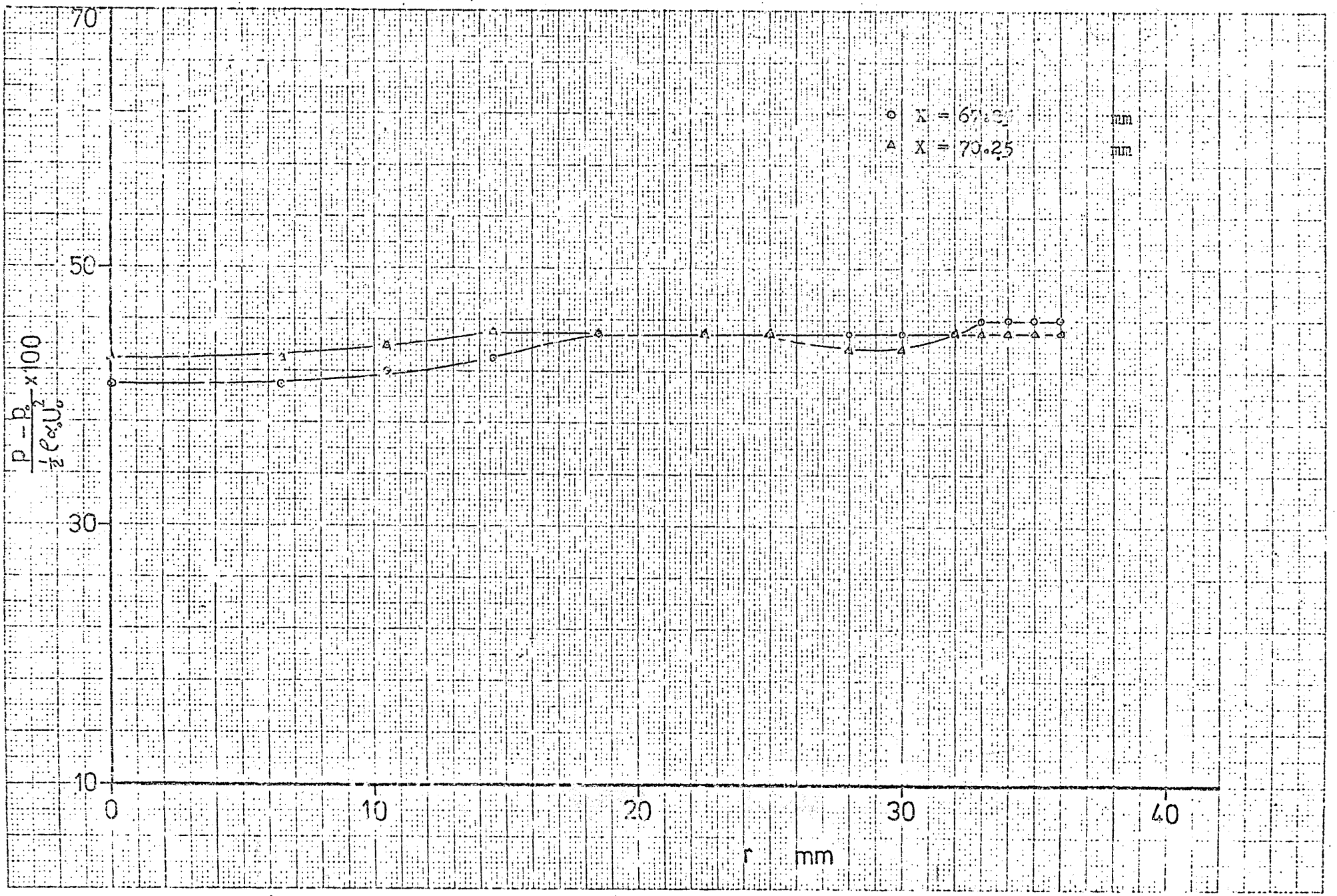

Fig.(F1-6): The static pressure distribution in region (6).

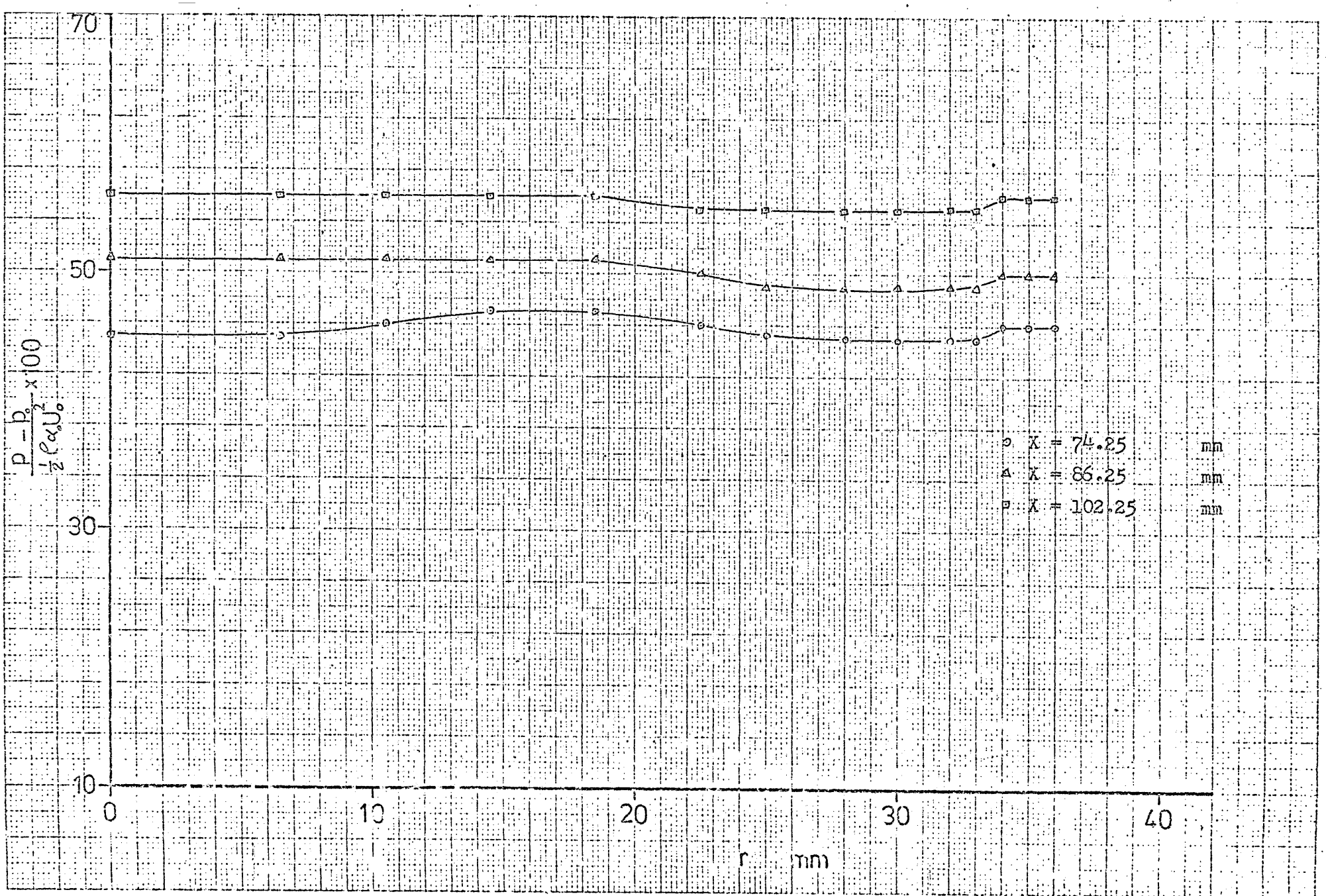

Fig.(F1-7): The static pressure distribution in region (7).

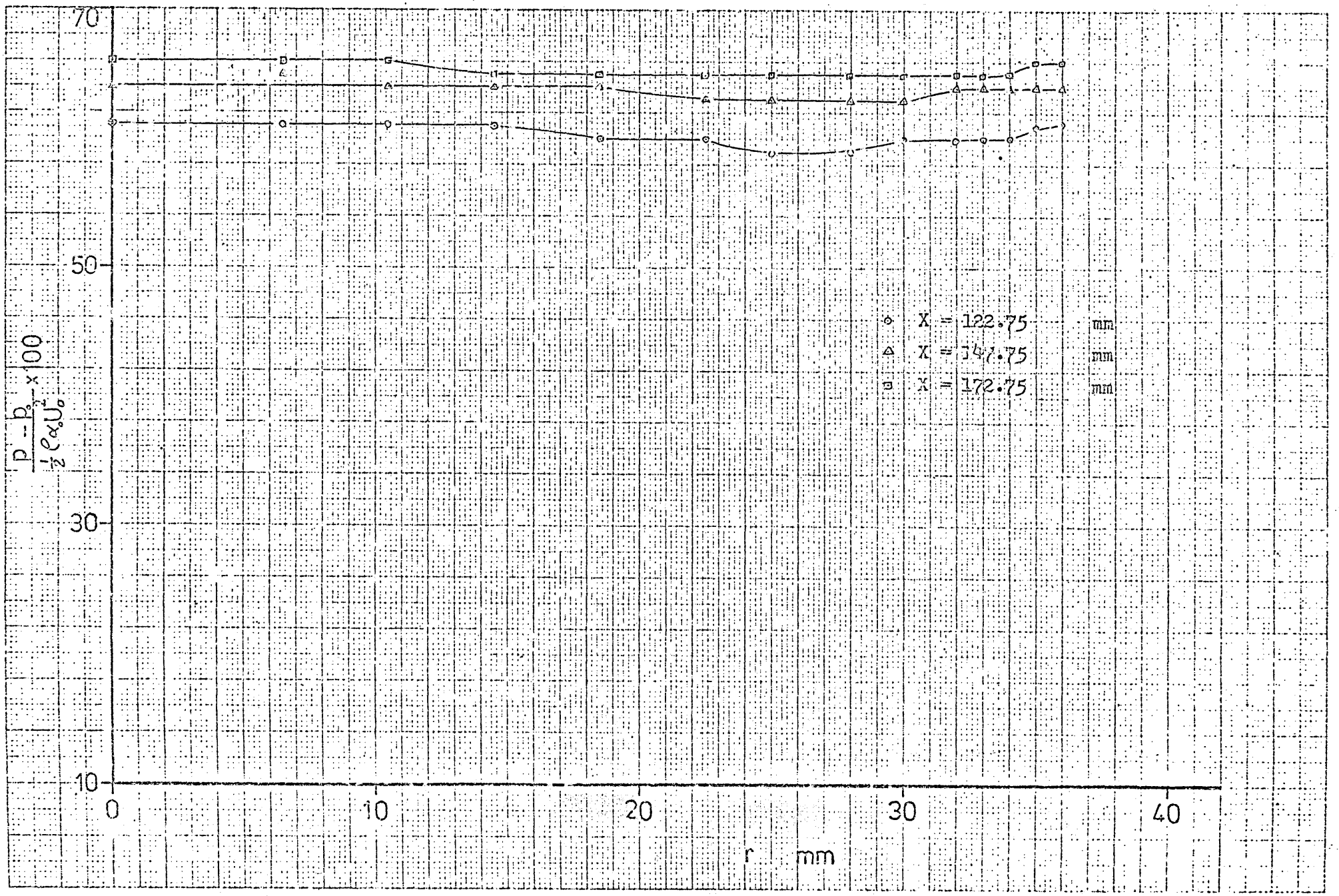

Fig.(F1-8): The static pressure distribution in region (8).

Appendix F2: The distribution of the axial component of the mean velocity.

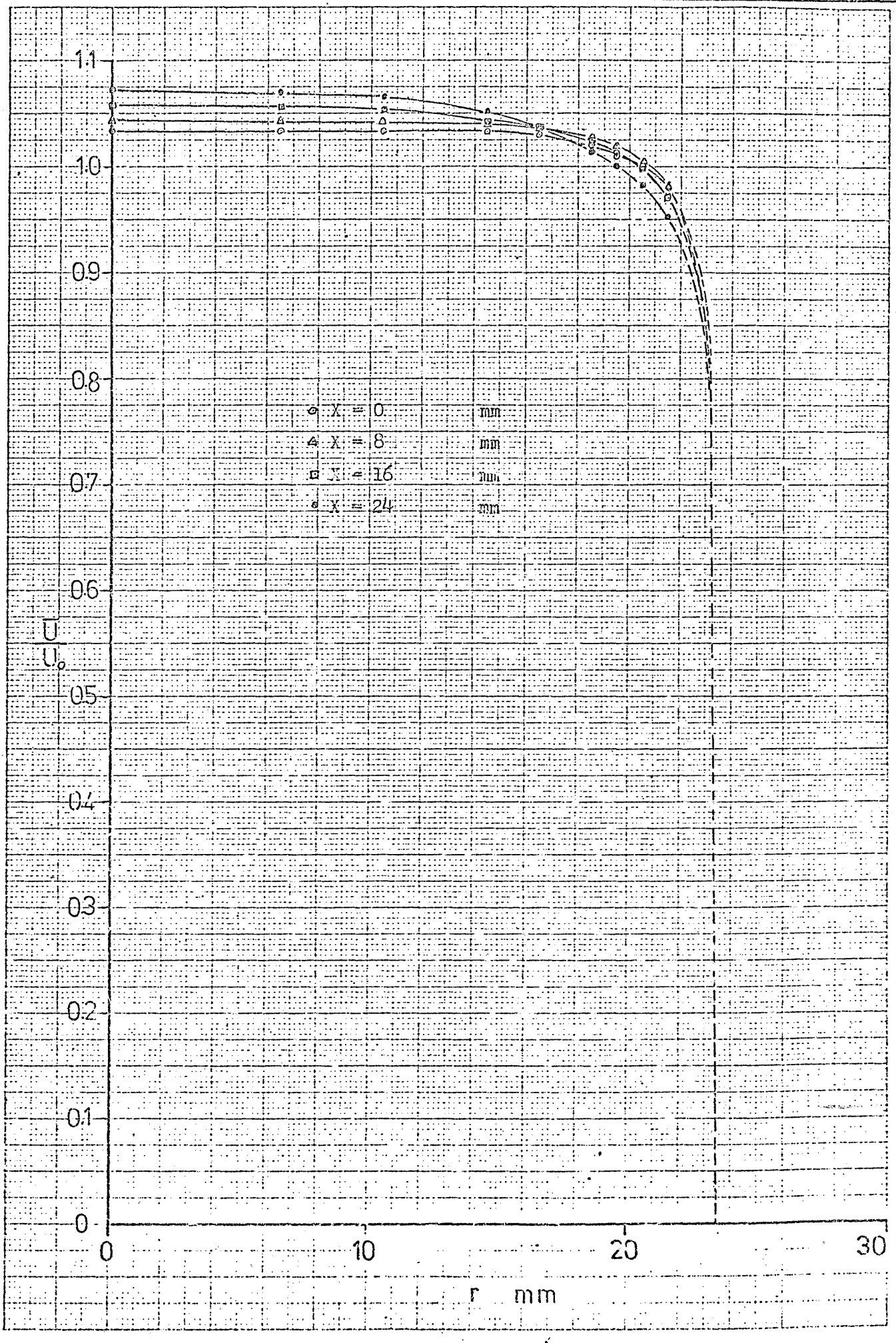

Fig.(F2-1): The distribution of $\bar{U}$ in region (1).

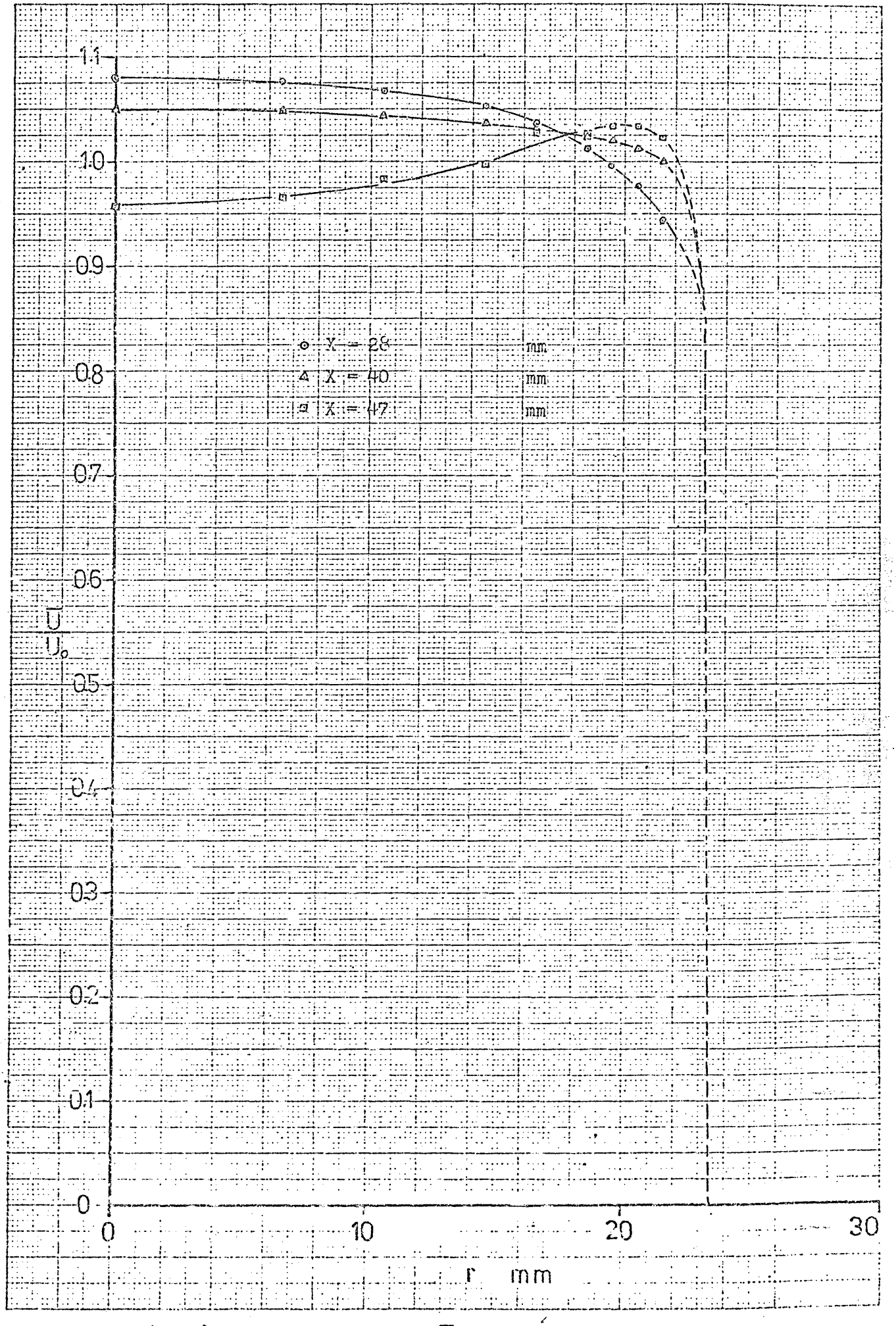

Fig.(F2-2): The distribution of $\bar{U}$ in region (2).

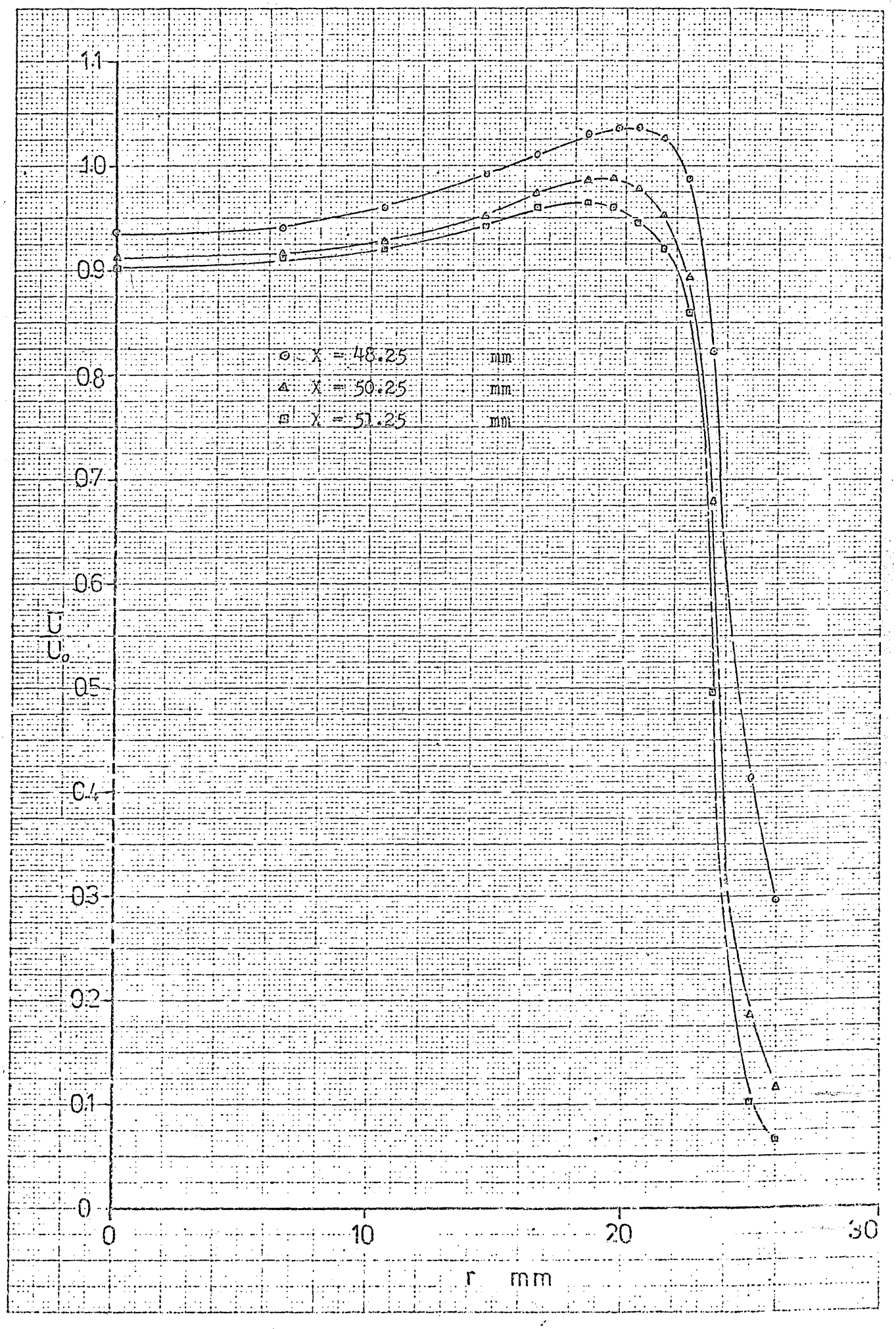

Fig.(F2-3): The distribution of $\bar{U}$ in region (3).

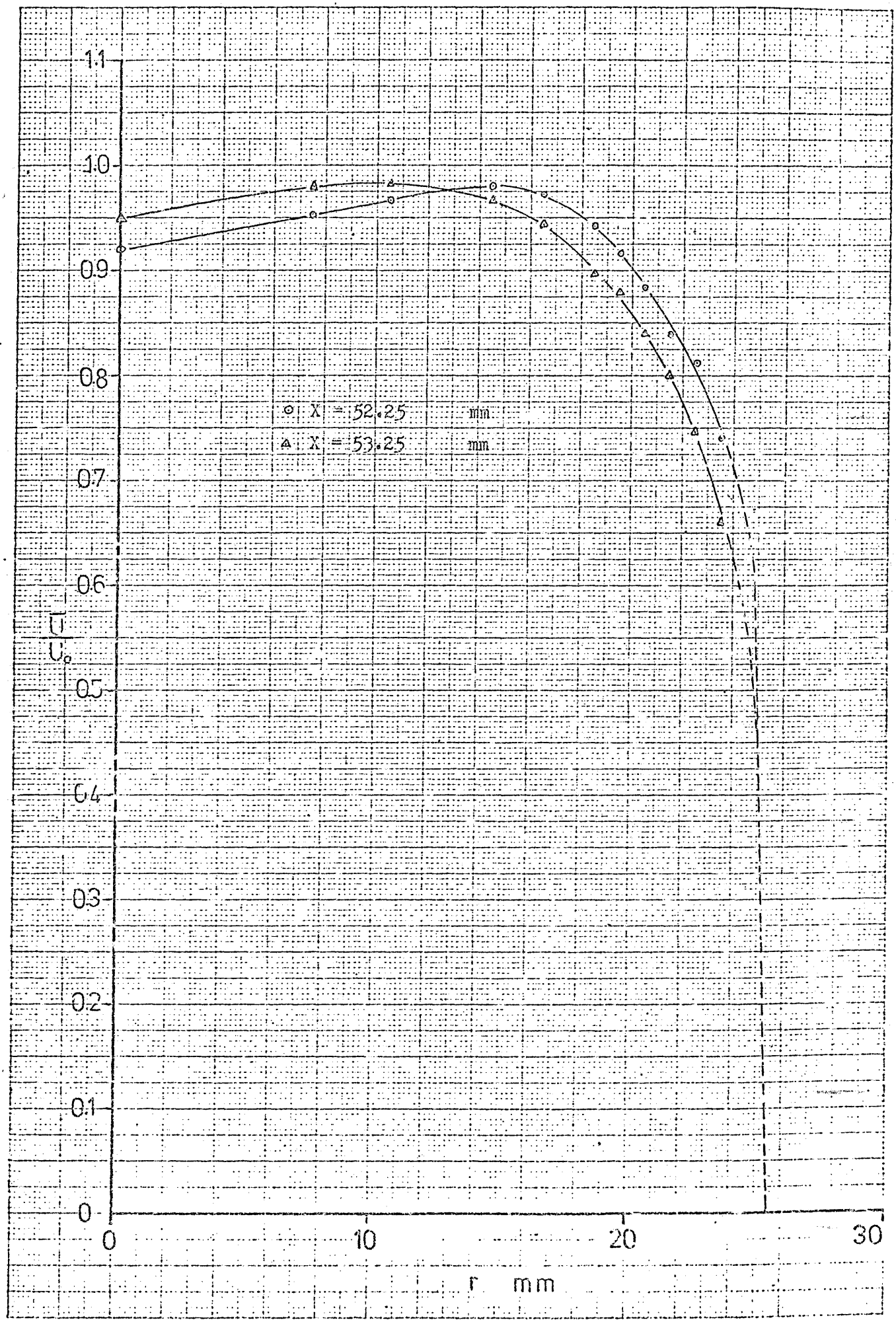

Fig.(F2-4): The distribution of $\bar{U}$ in region (4).

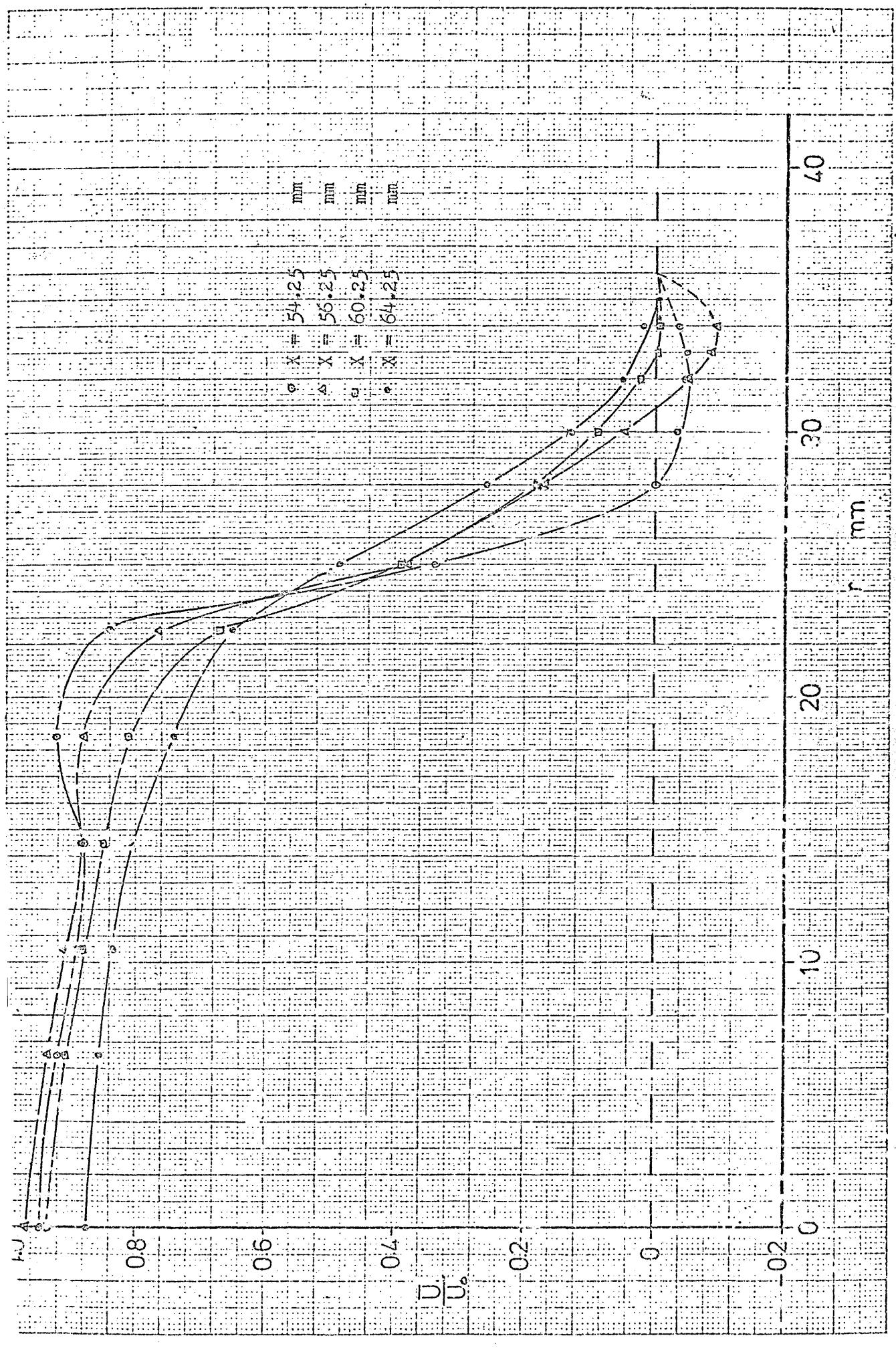

Fig.(F2-5): The distribution of $\bar{U}$ in region (5).

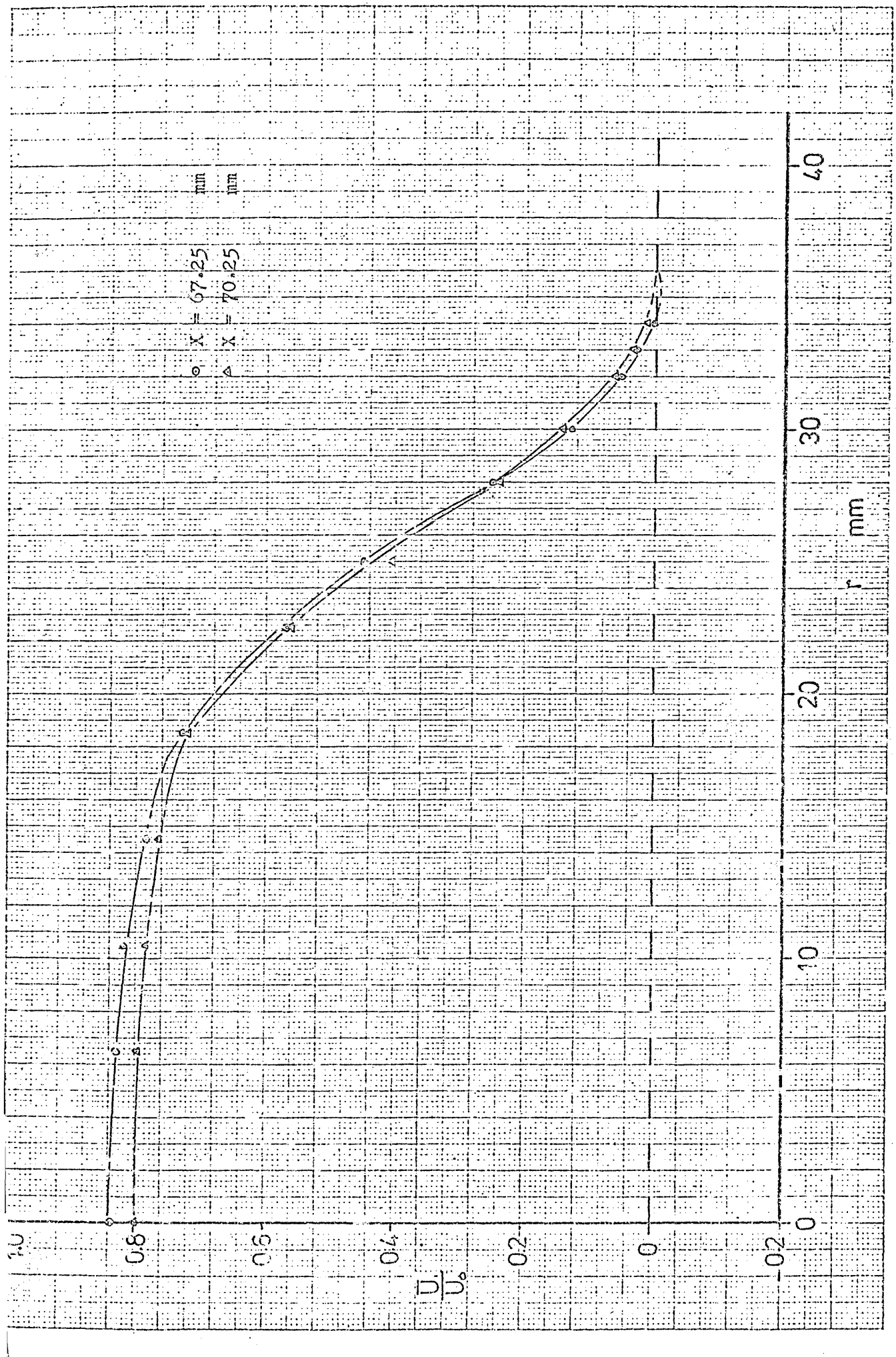

Fig.(F2-6): The distribution of $\bar{U}$ in region (6).

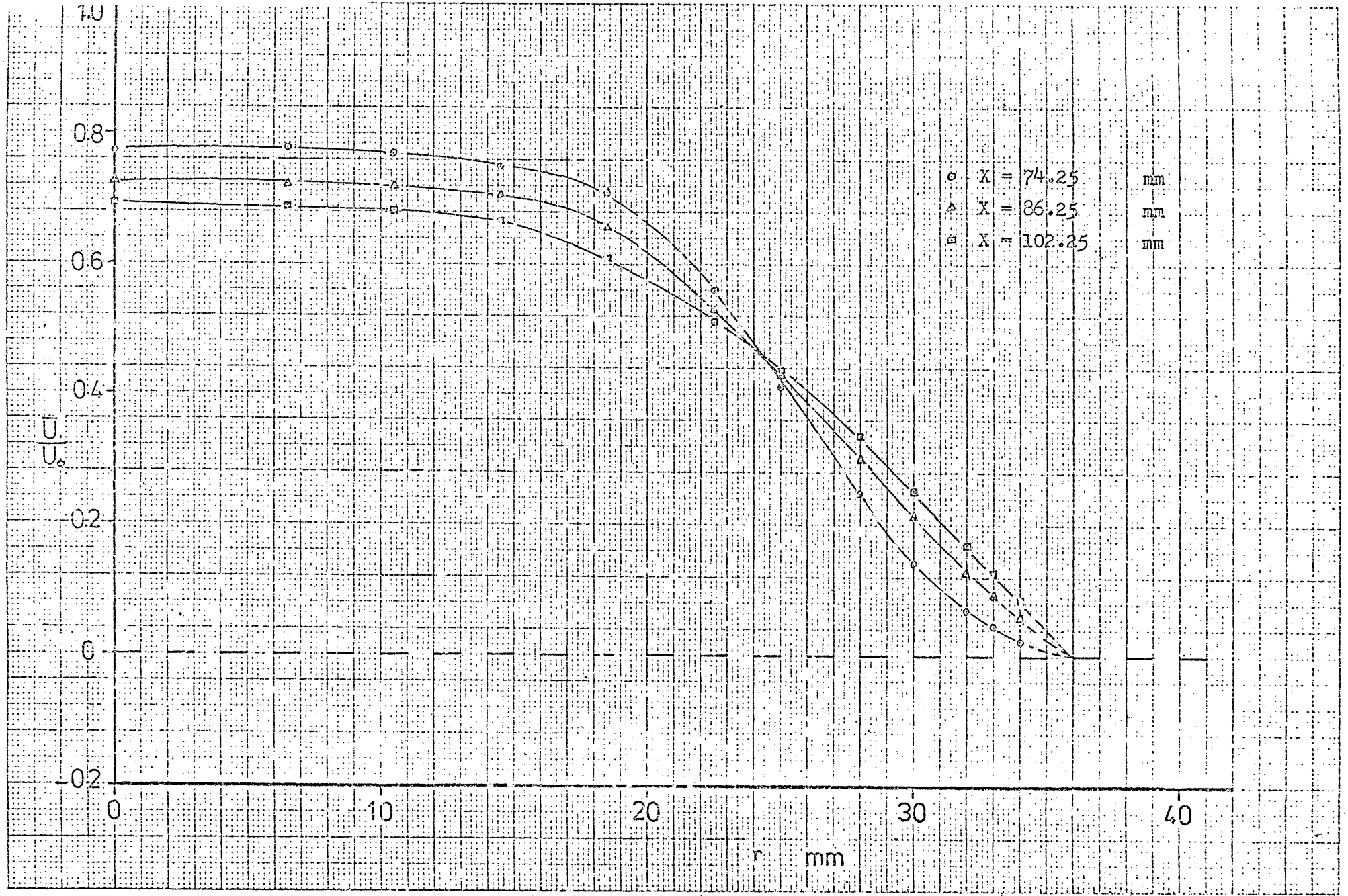

Fig.(F2-7): The distribution of $\bar{U}$ in region (7).

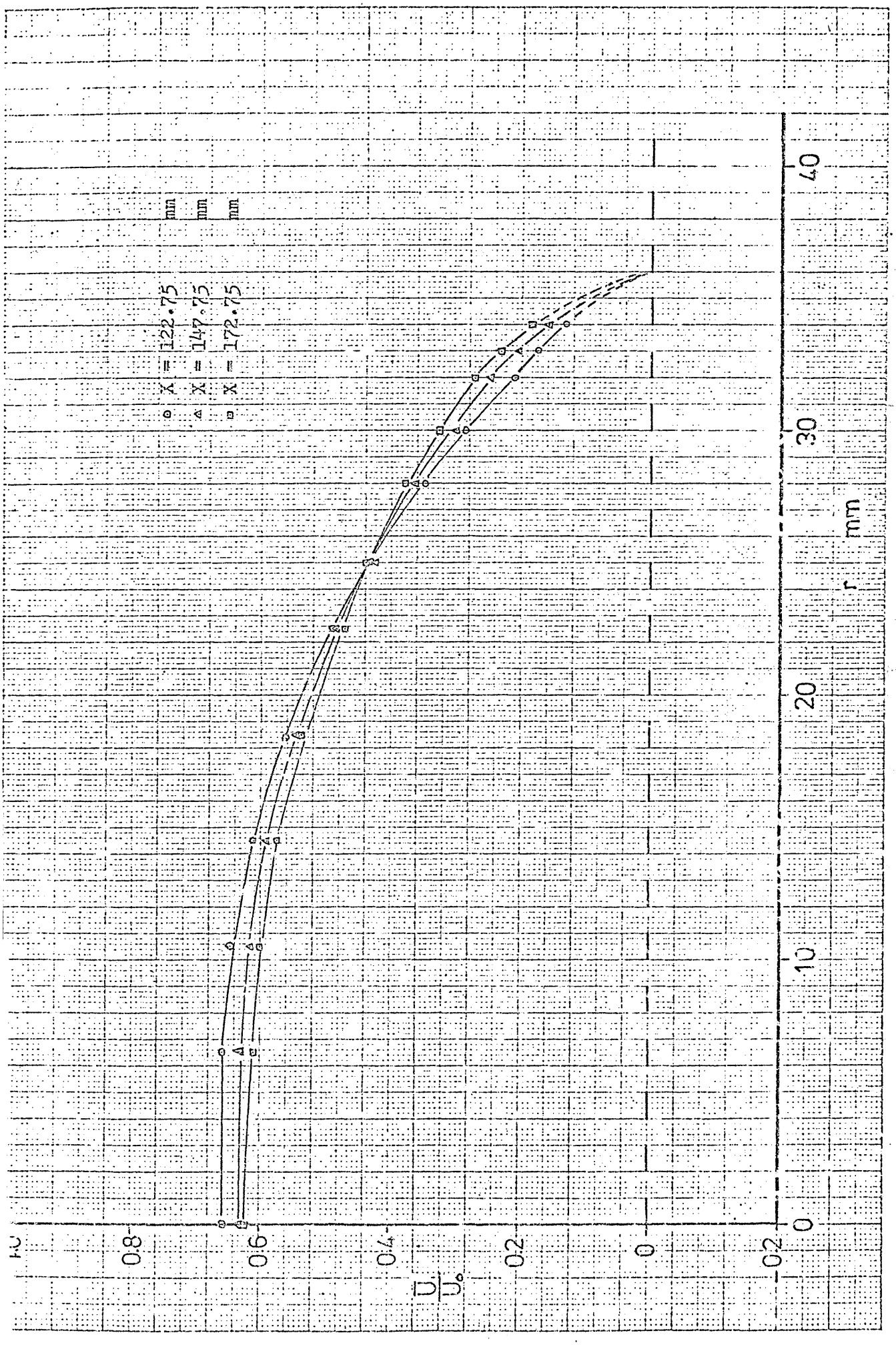

Fig.(F2-8): The distribution of $\overline{U}$ in region (8).

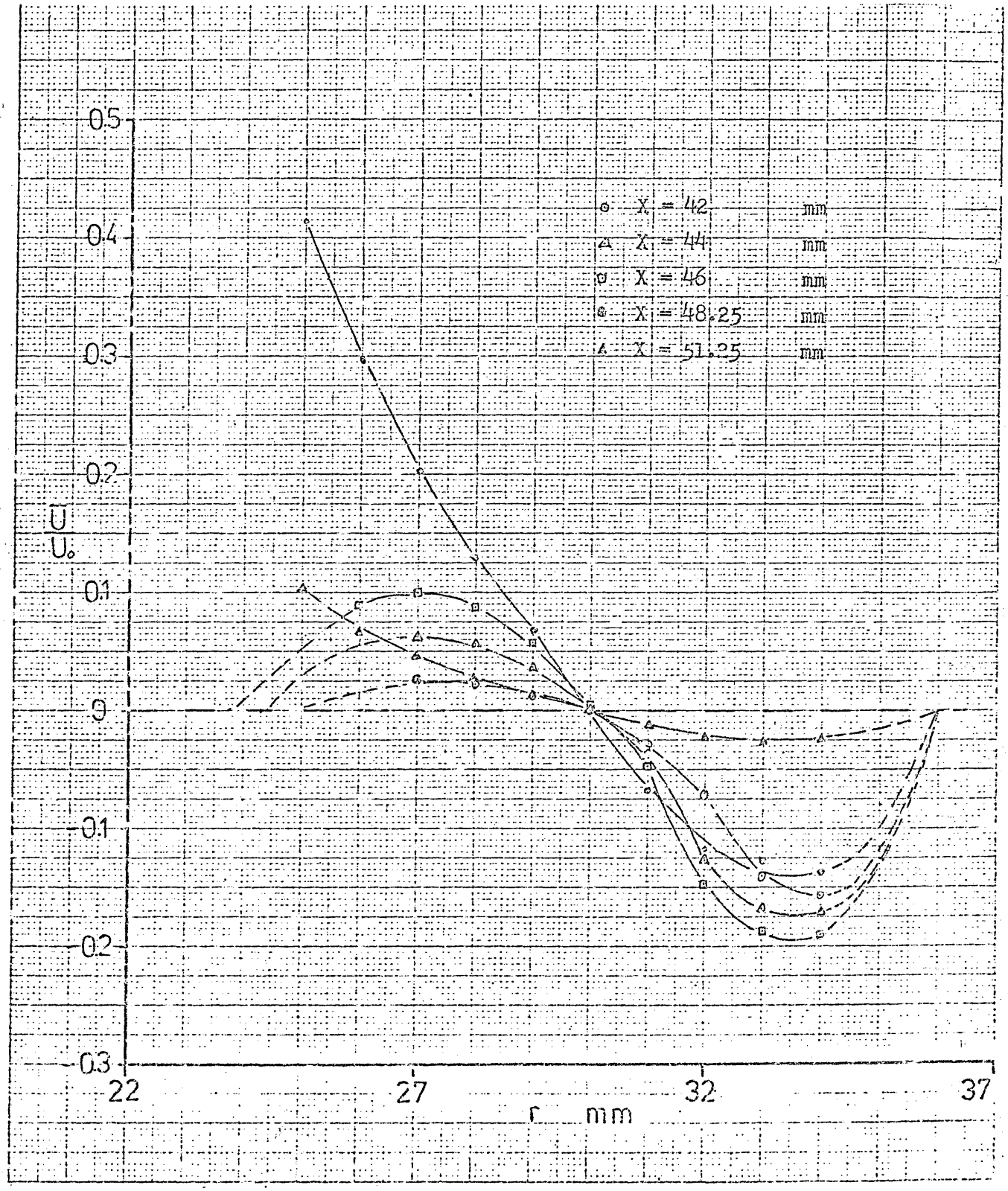

Fig.(F2-9): The distribution of $\bar{U}$ in region (9).

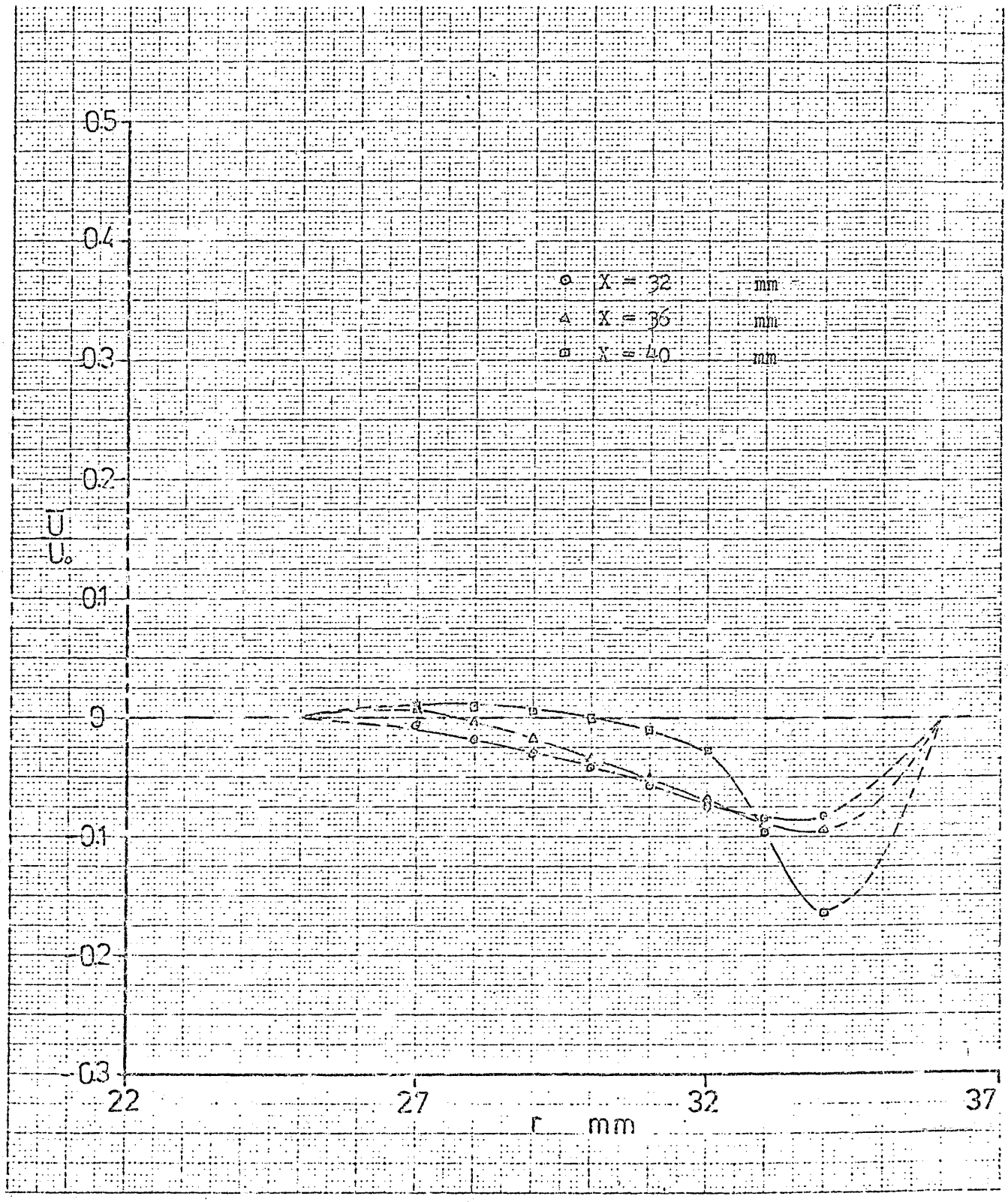

Fig.(F2-10): The distribution of $\bar{U}$ in region (10).

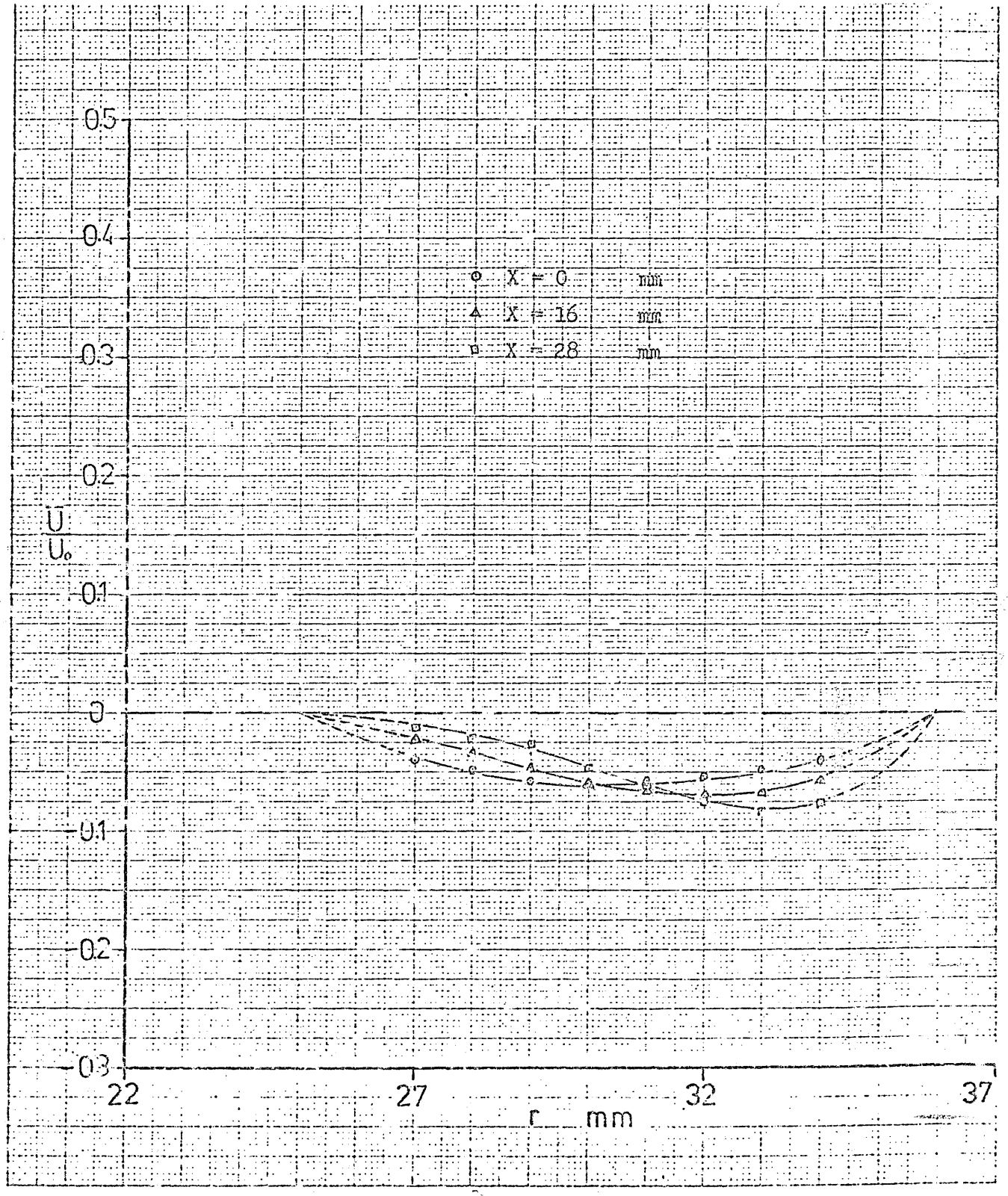

Fig.(F2-11): The distribution of $\bar{U}$ in region (11).

Appendix F3: The distribution of the radial component of the mean velocity.

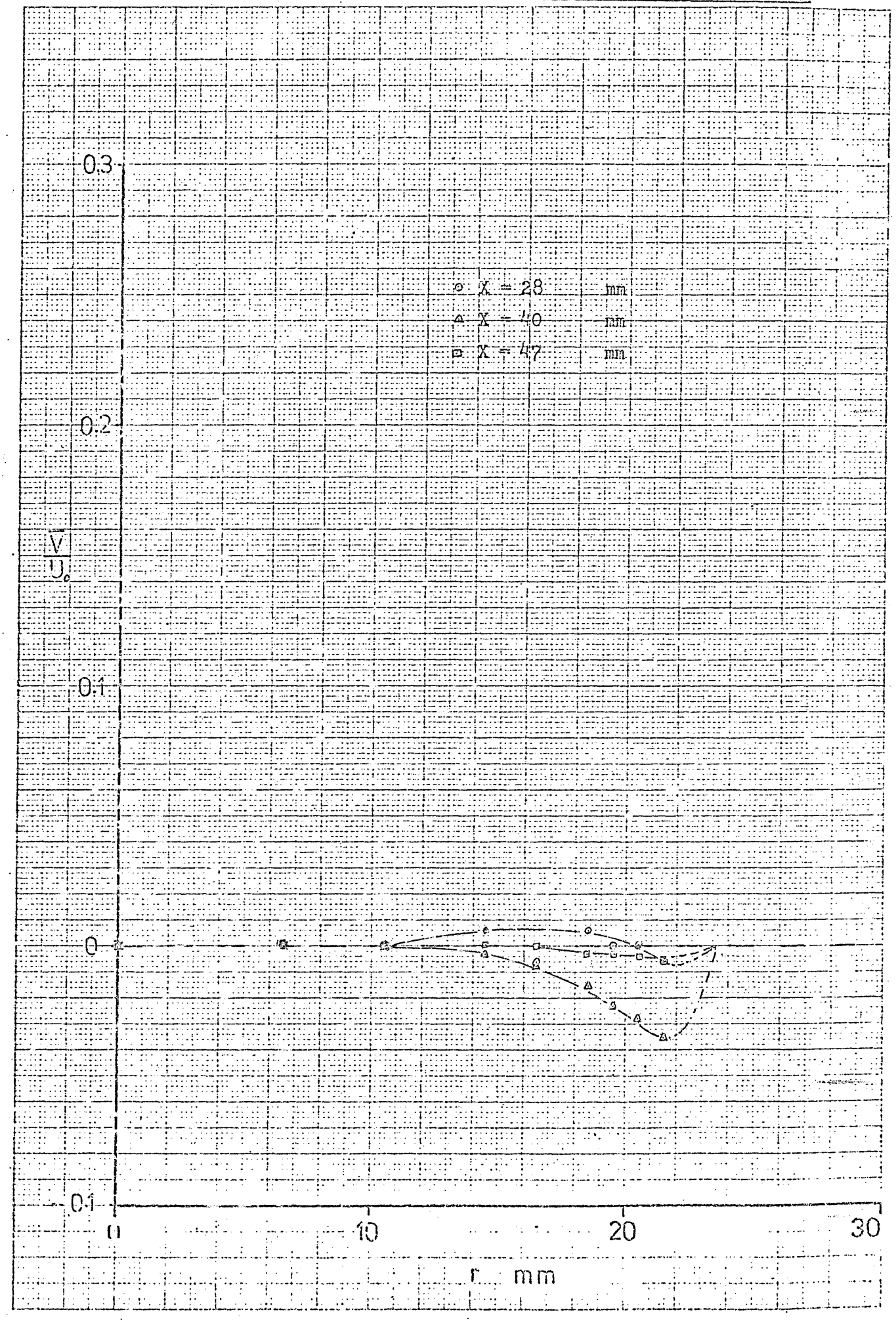

Fig.(F3-1): The distribution of $\bar{V}$ in region (2).

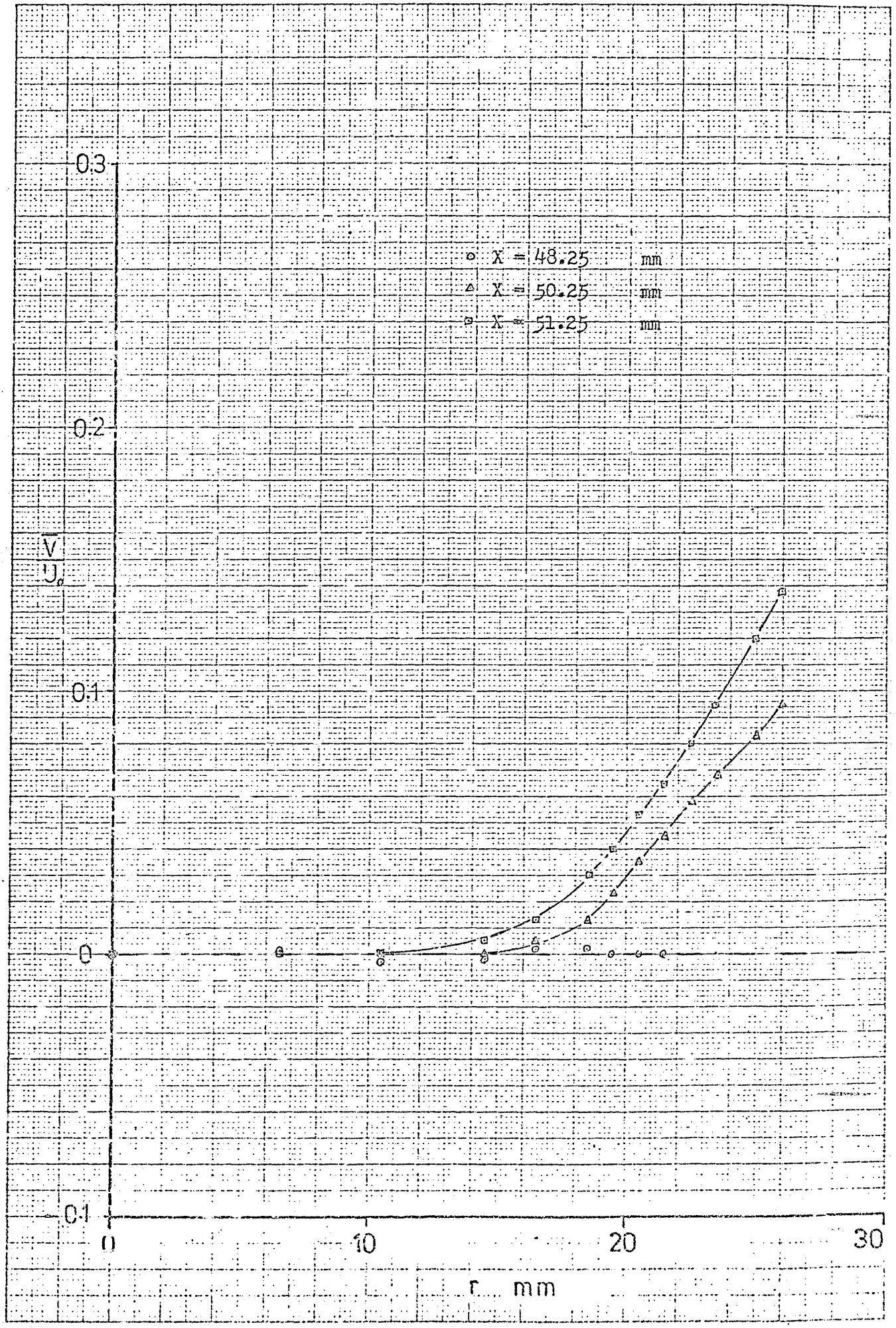

Fig.(F3-2): The distribution of $\bar{V}$ in region (3).

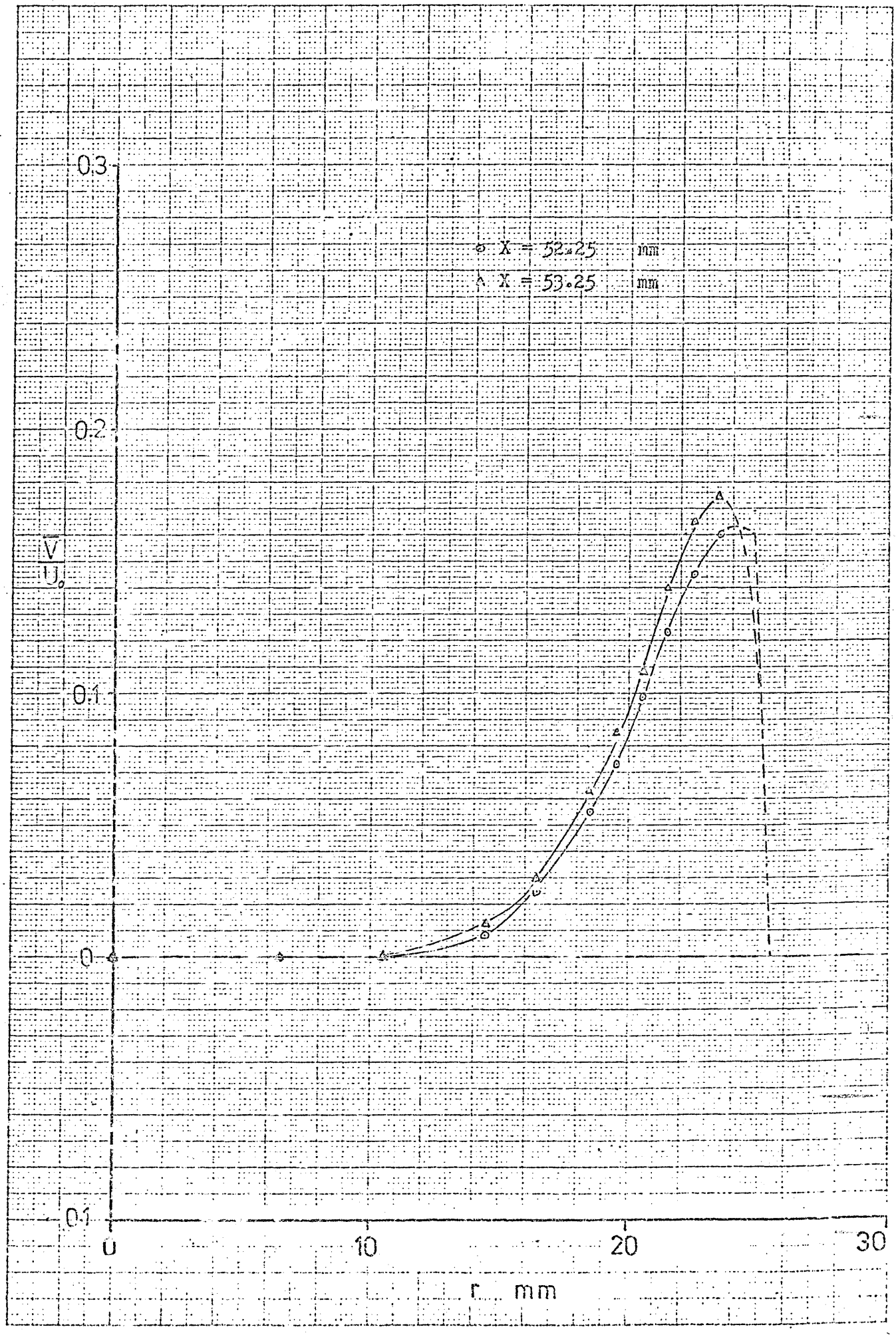

Fig.(P3-3): The distribution of $\bar{V}$ in region (4).

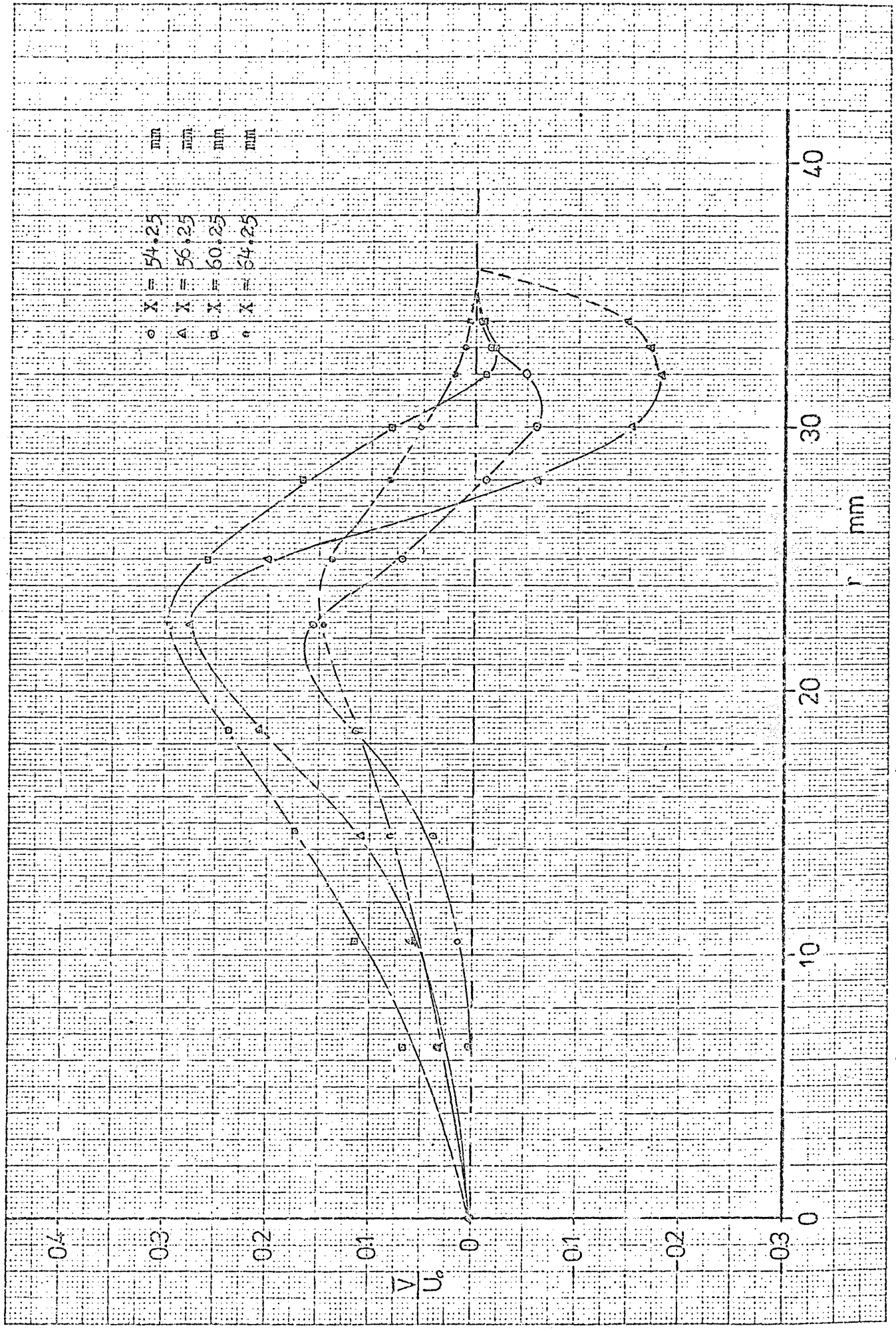

Fig.(F3-4): The distribution of $\overline{V}$ in region (5).

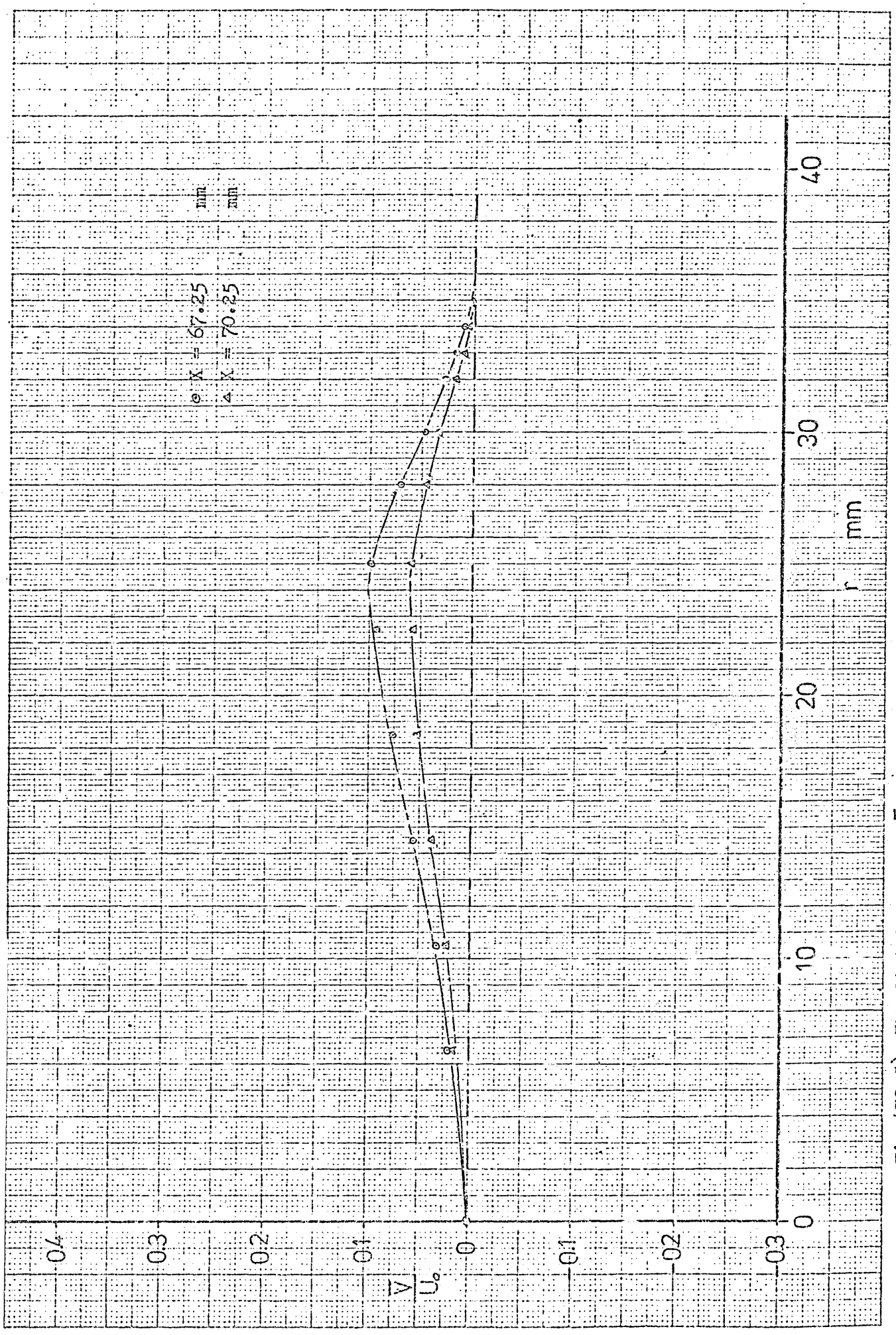

Fig.(F3-5): The distribution of $\overline{V}$ in region (6).

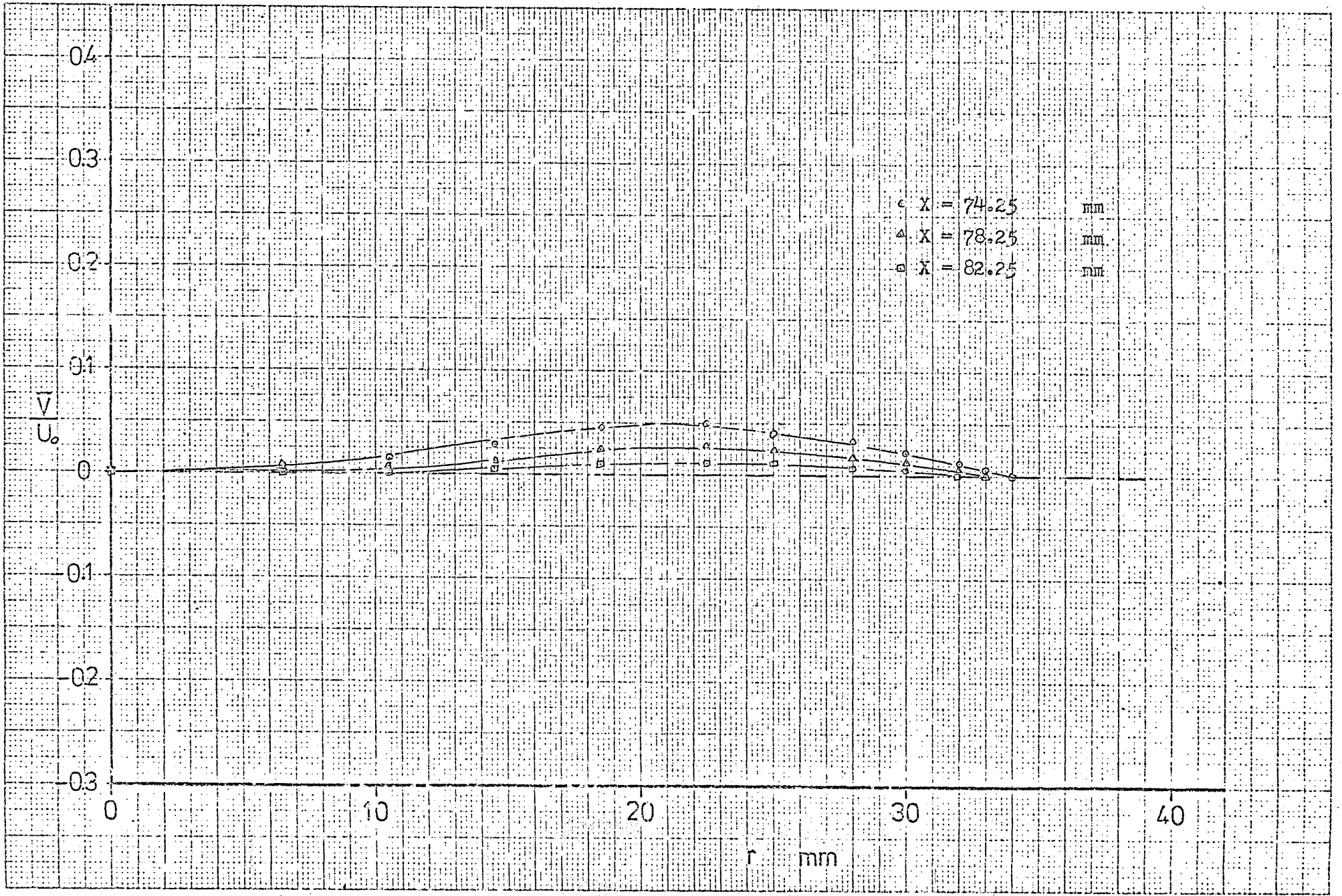

Fig.(F3-6): The distribution of $\overline{V}$ in region (7).

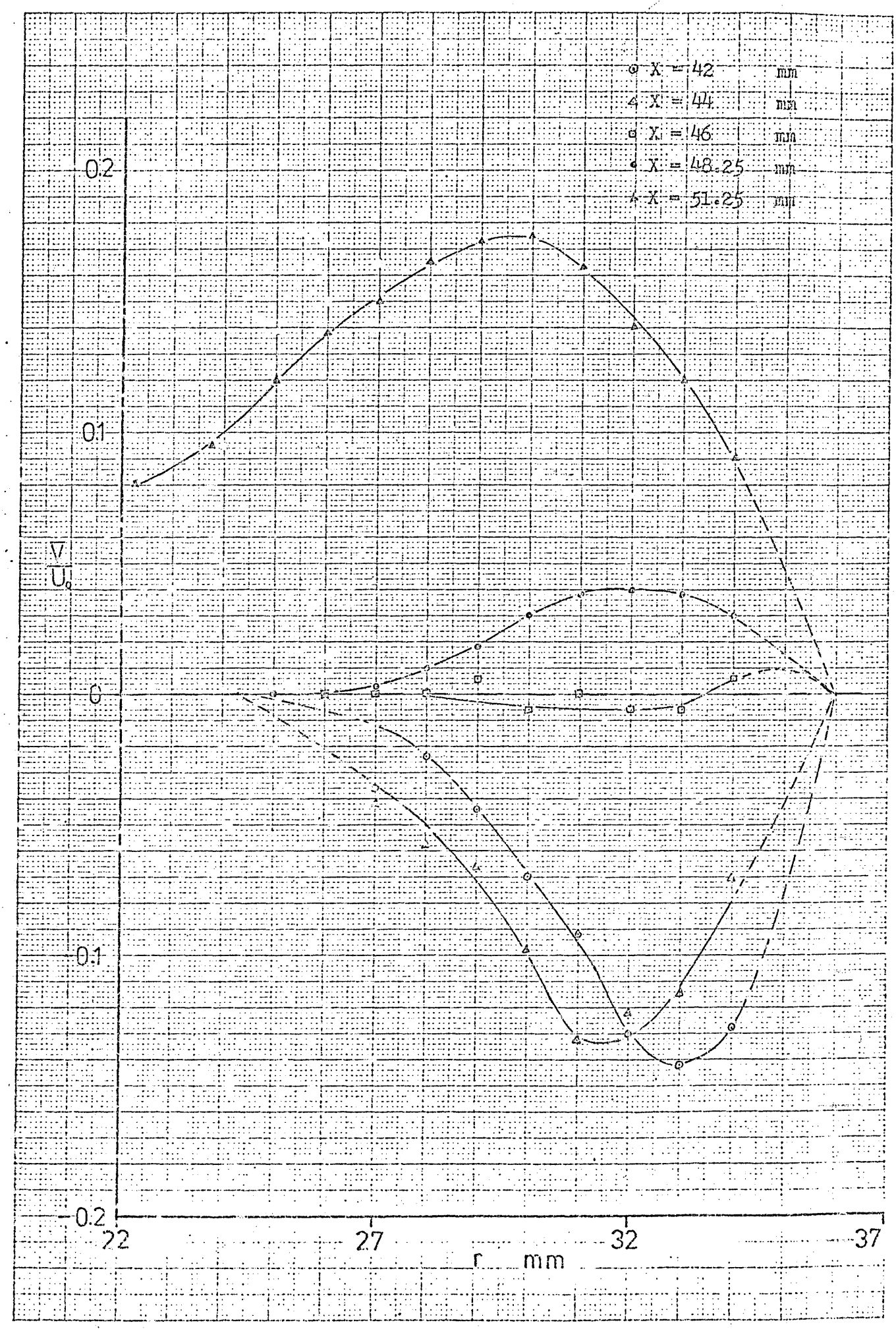

Fig.(F3-7): The distribution of $\bar{V}$ in region (9).

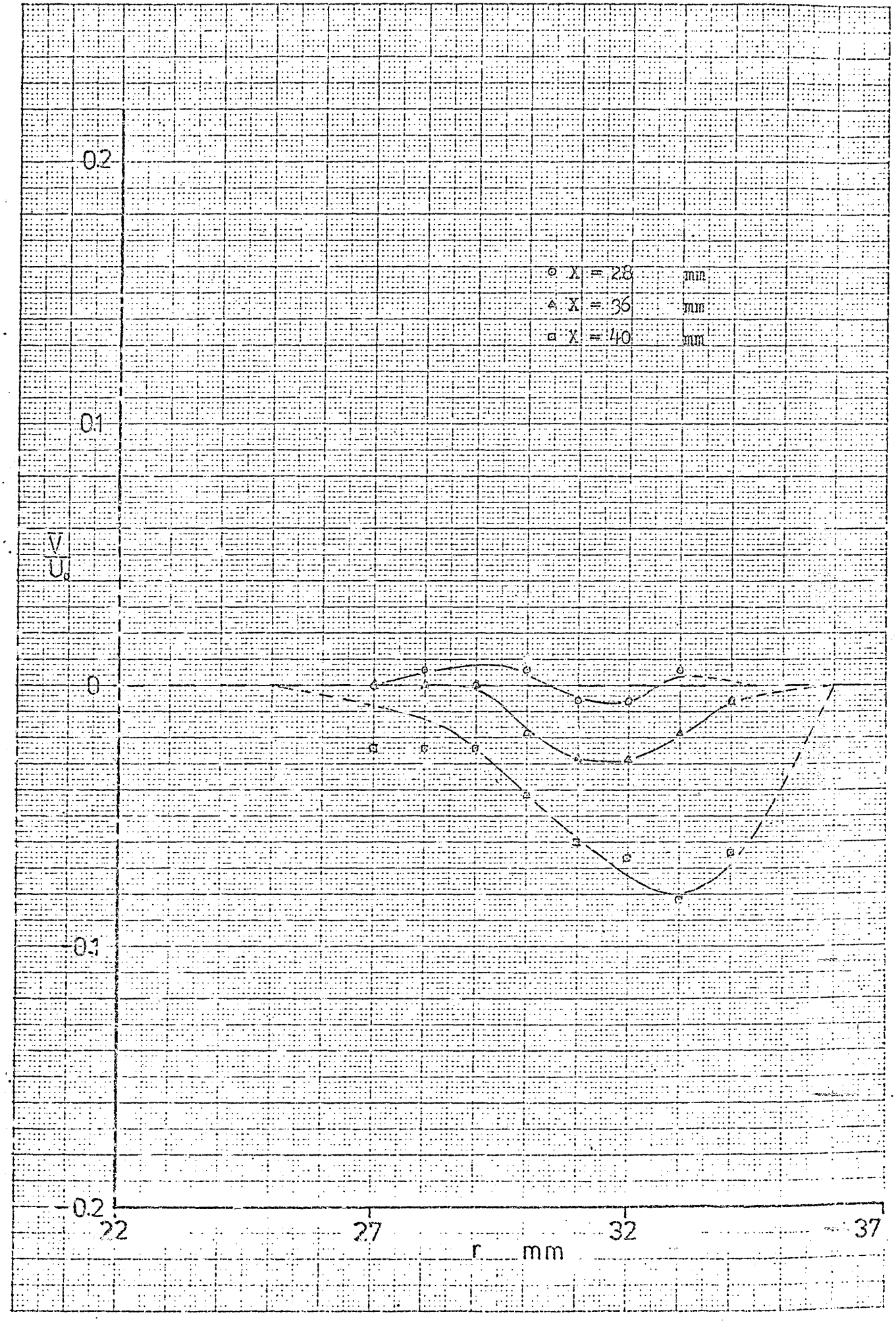

Fig.(F3-8): The distribution of $\bar{V}$ in region (10).

Appendix F4: The distribution of the axial normal Reynolds' stress

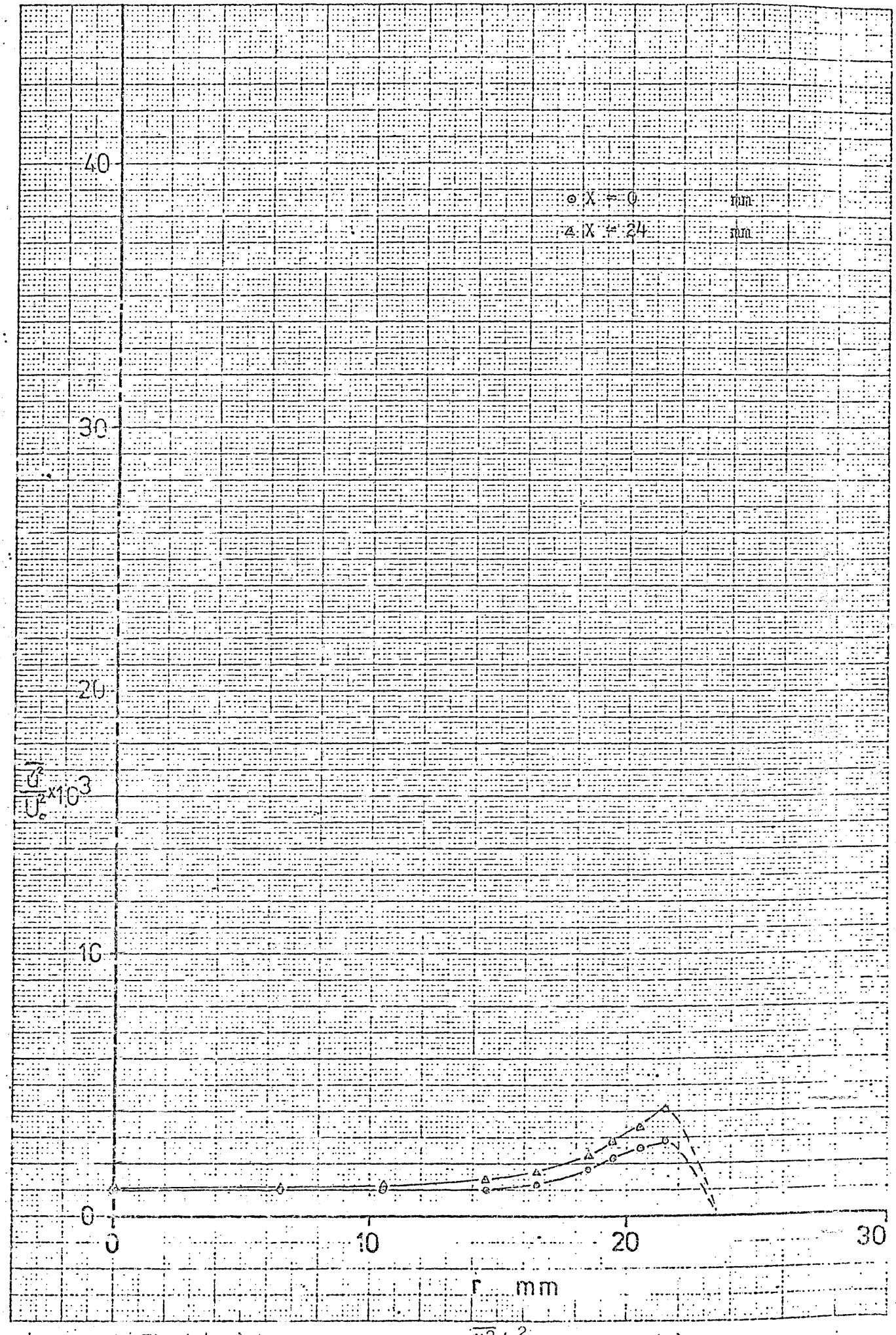

Fig.(F4-1): The distribution of $\overline{u^2}/U_o^2$ in region (1).

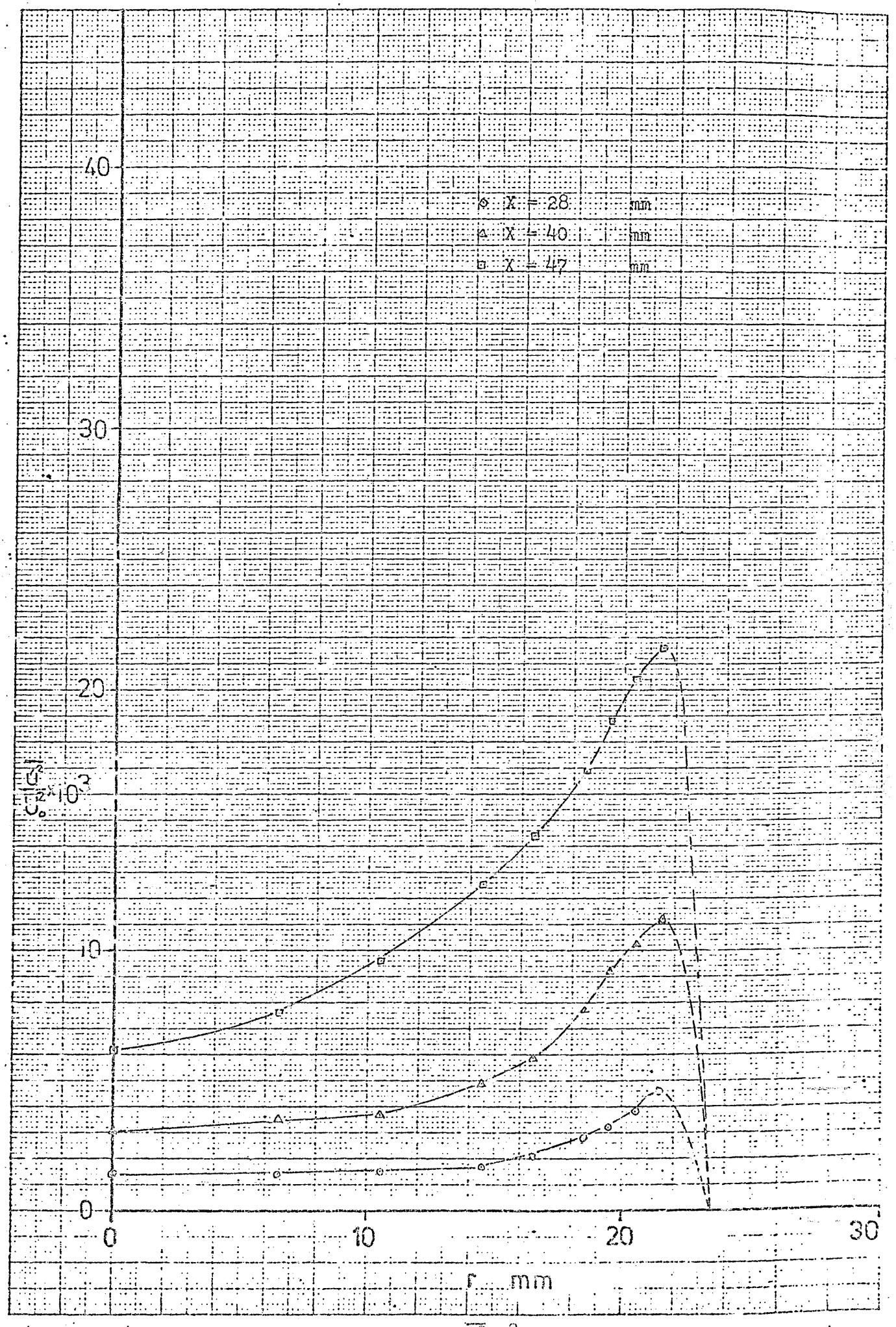

Fig.(F4-2): The distribution of $\overline{u^2}/U_o^2$ in region (2).

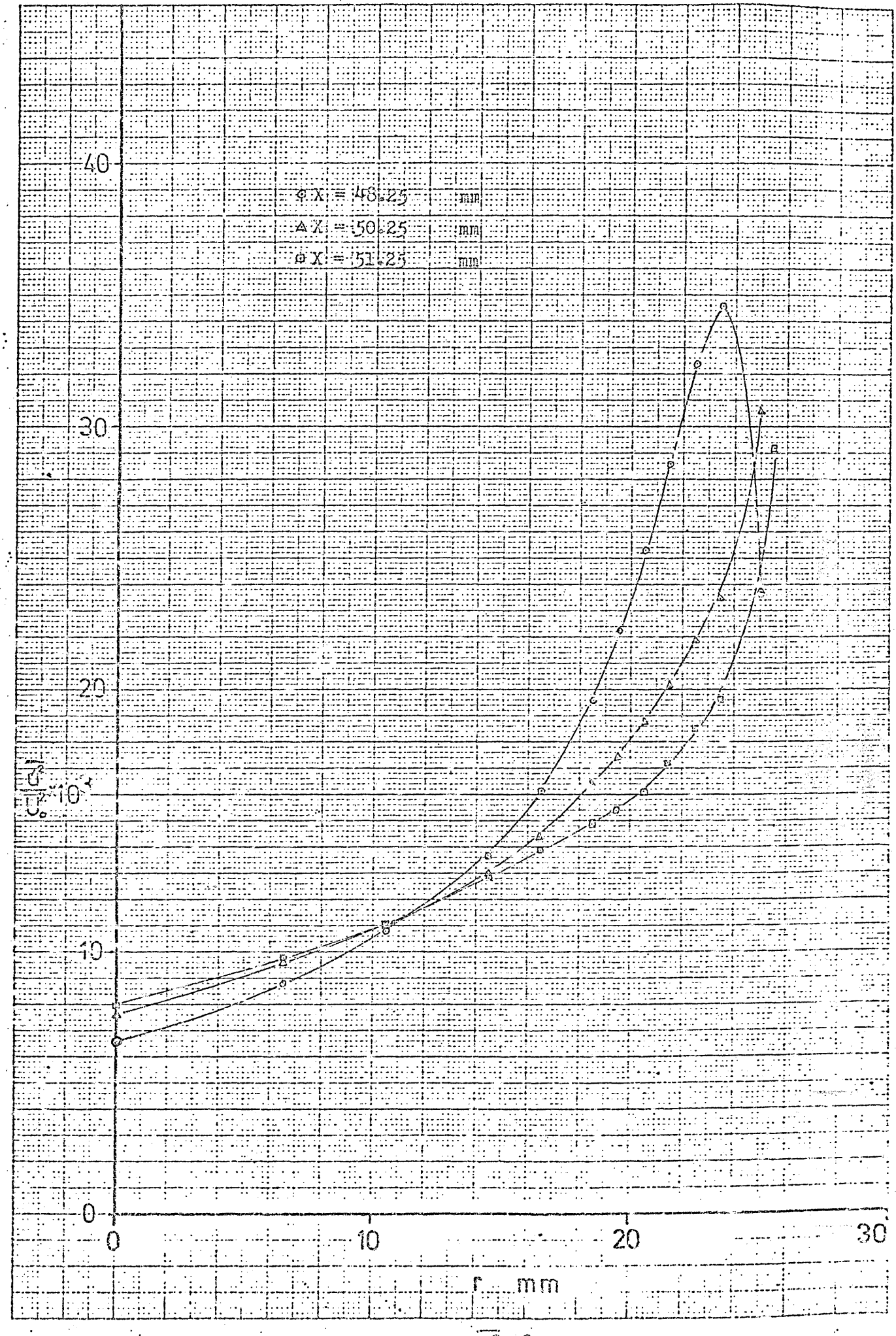

Fig.(F4-3): The distribution of $\overline{u^2}/U_o^2$ in region (3).

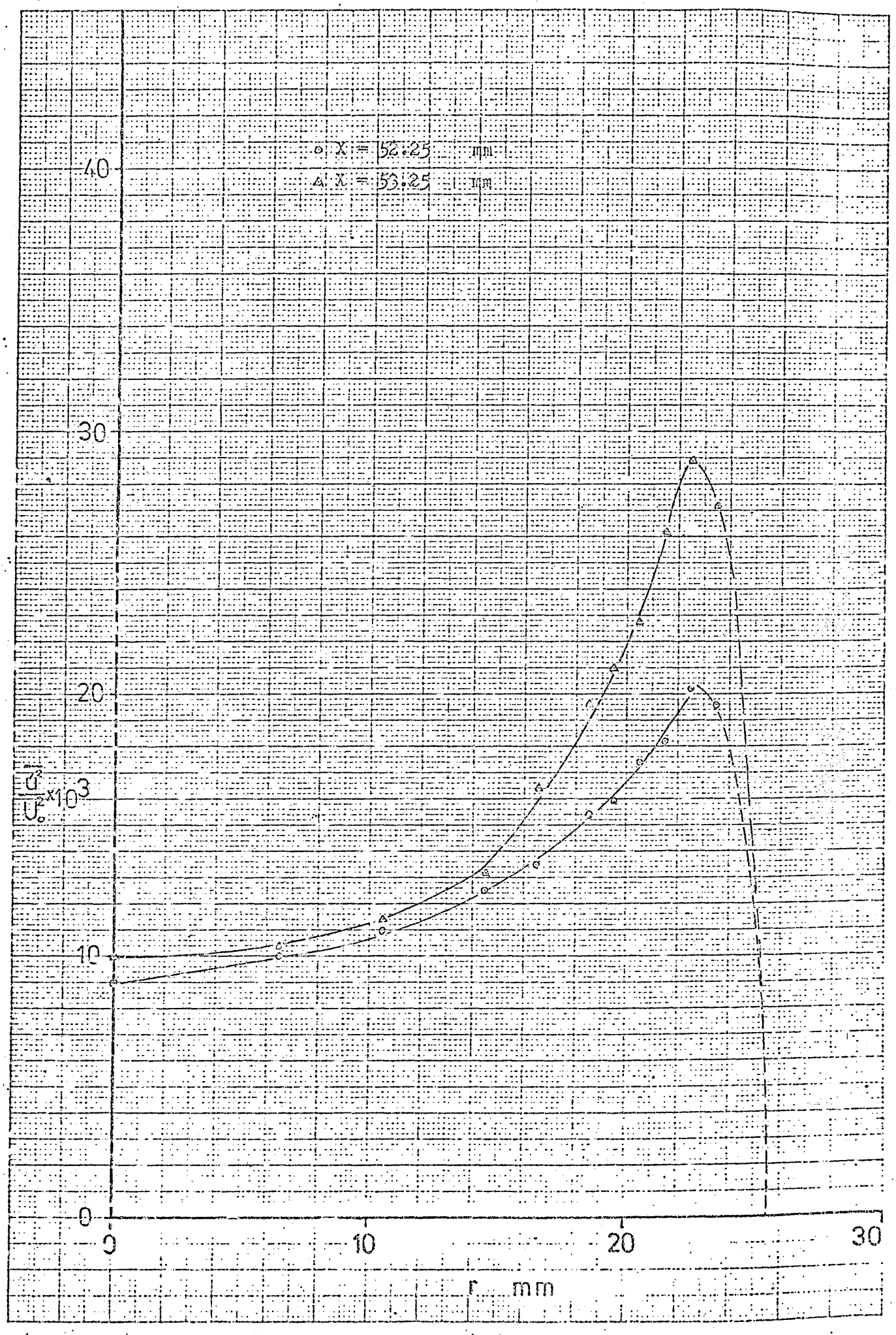

Fig.(F4-4): The distribution of $\overline{u^2}/U_o^2$ in region (4).

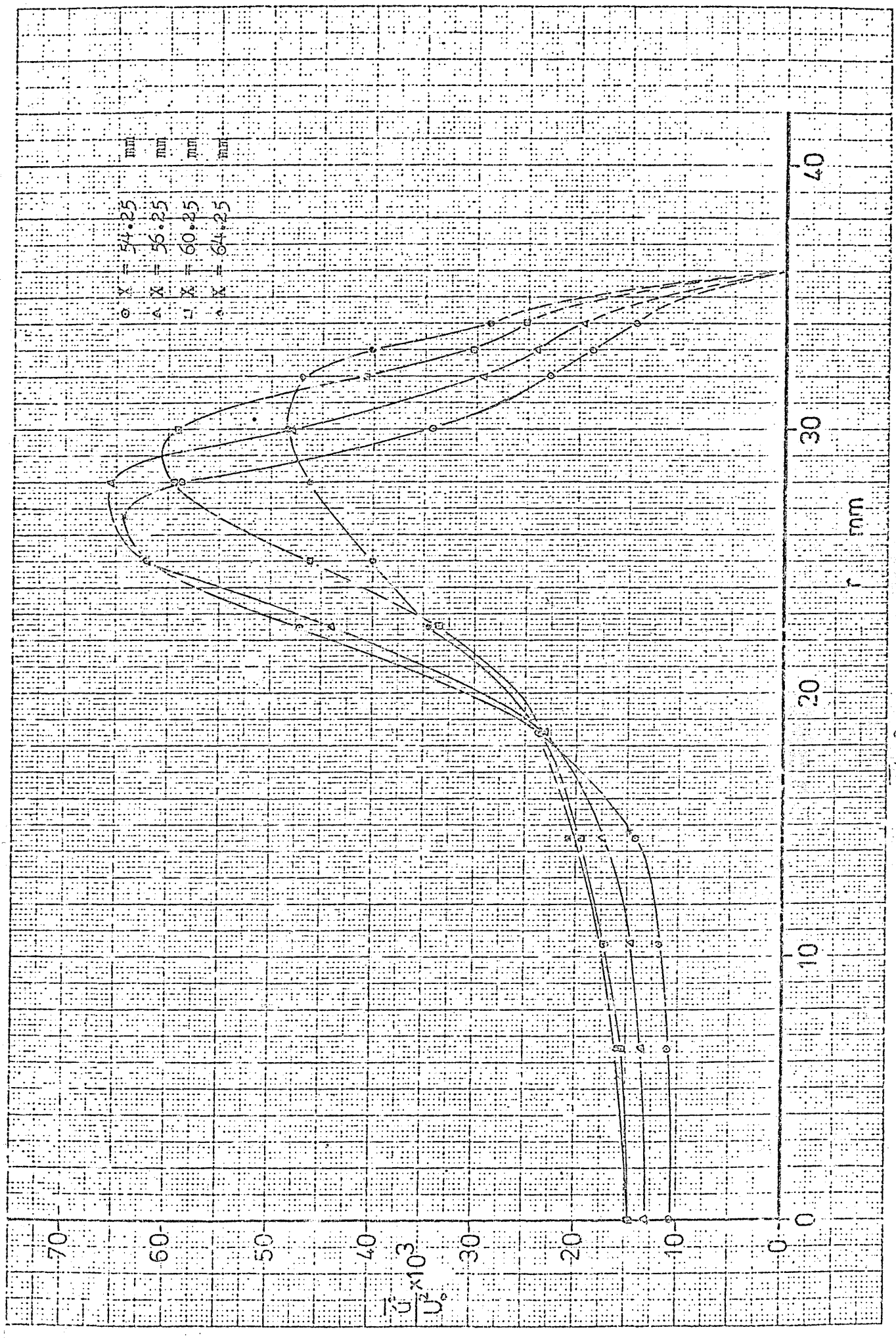

Fig.(F4-5): The distribution of $\overline{u^2}/U_o^2$ in region (5).

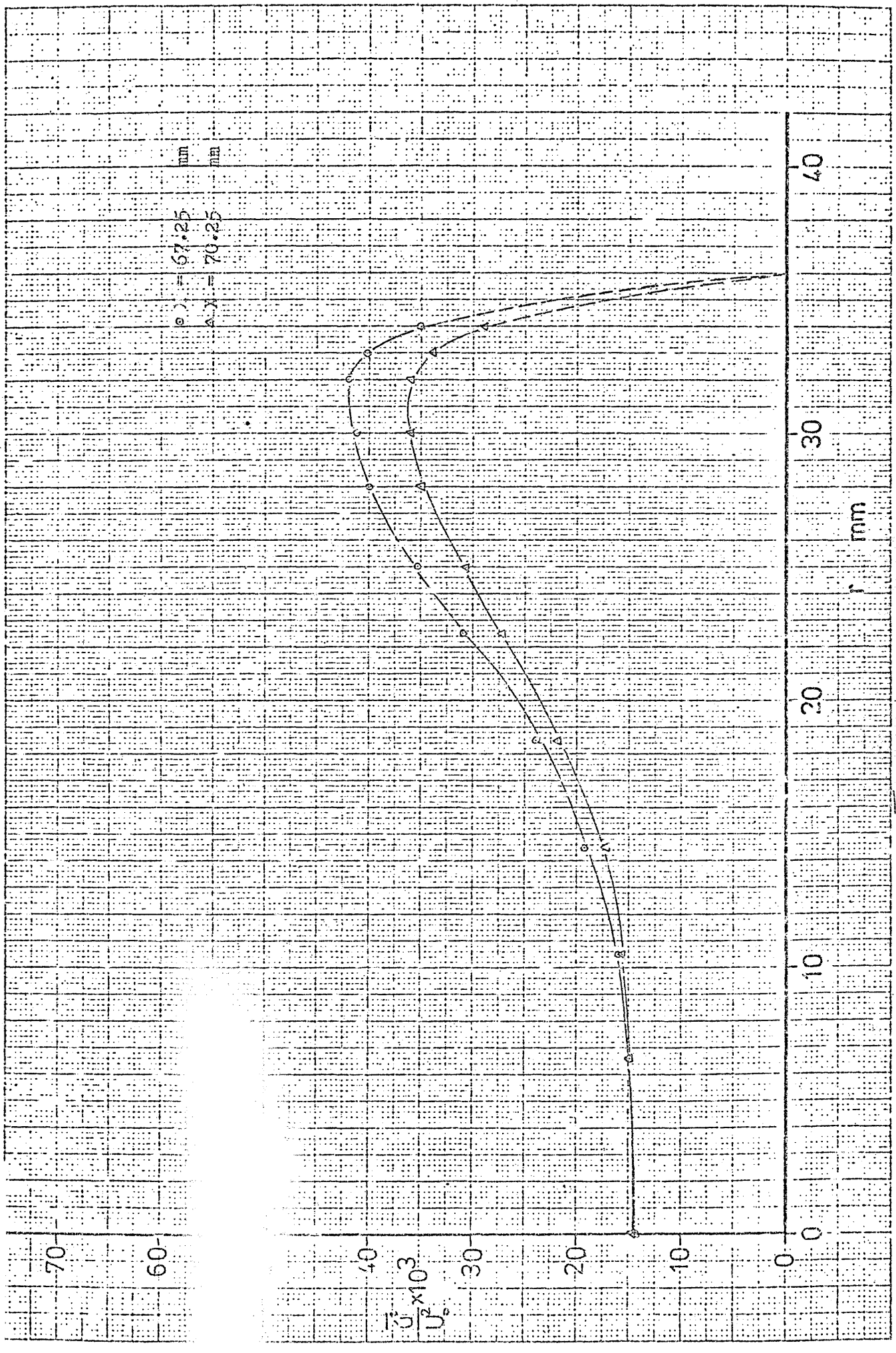

Fig. (F4-6): The distribution of $\overline{u^2}/U_o^2$ in region (6).

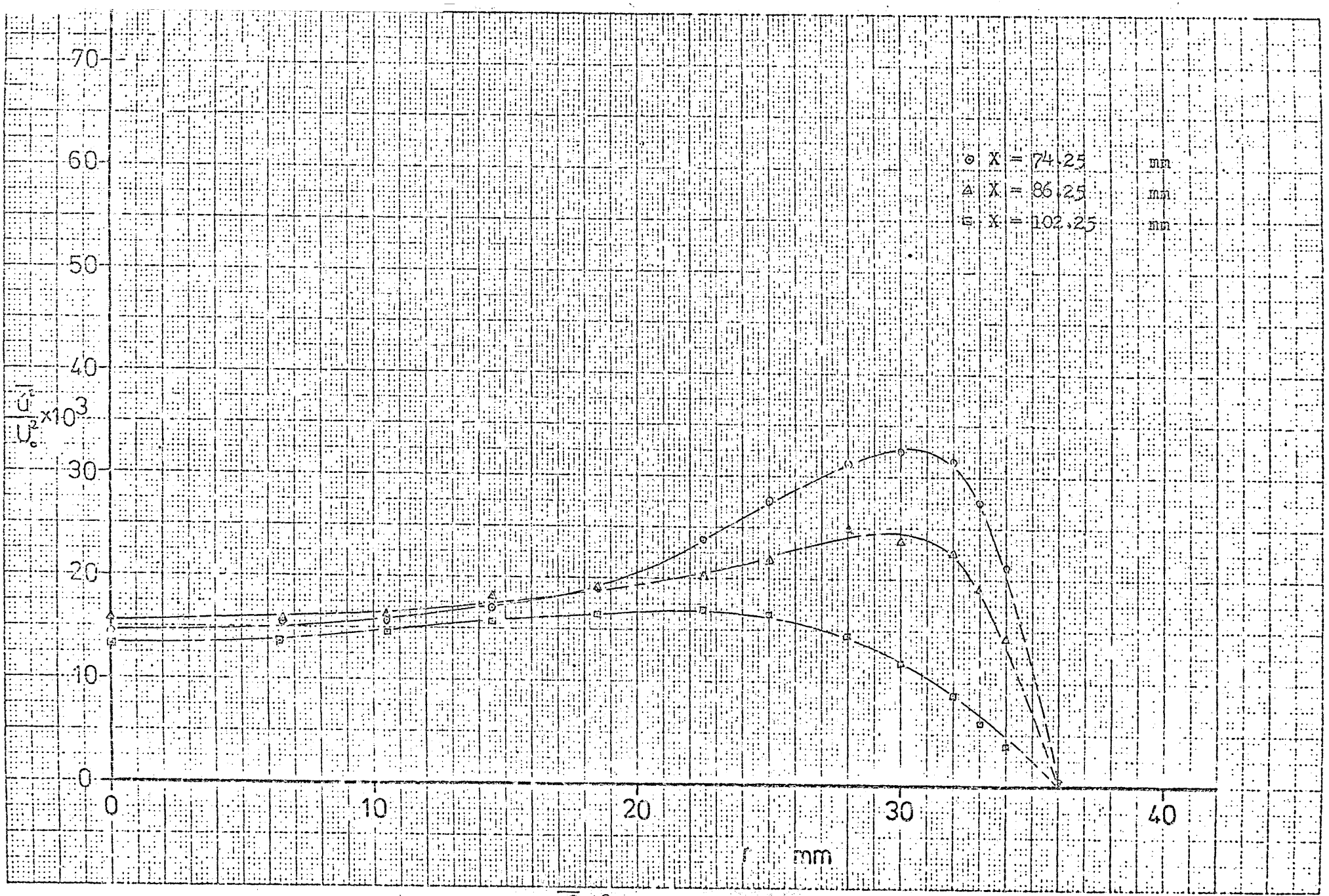

Fig.(F4-7): The distribution of $\overline{u^2}/U_o^2$ in region (7).

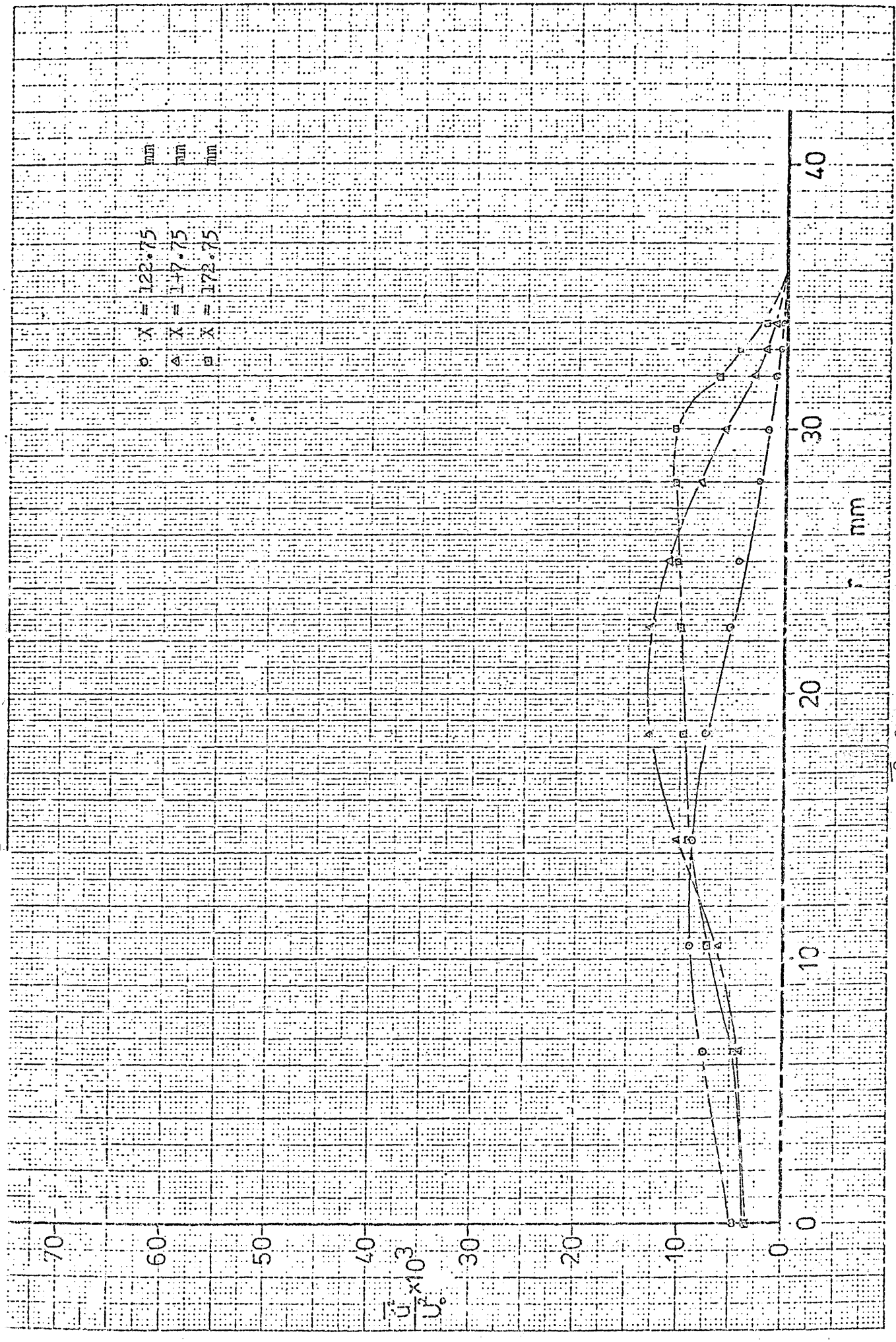

F'g.(F4-8): The distribution of $\overline{u^2}/U_o^2$ in region (8).

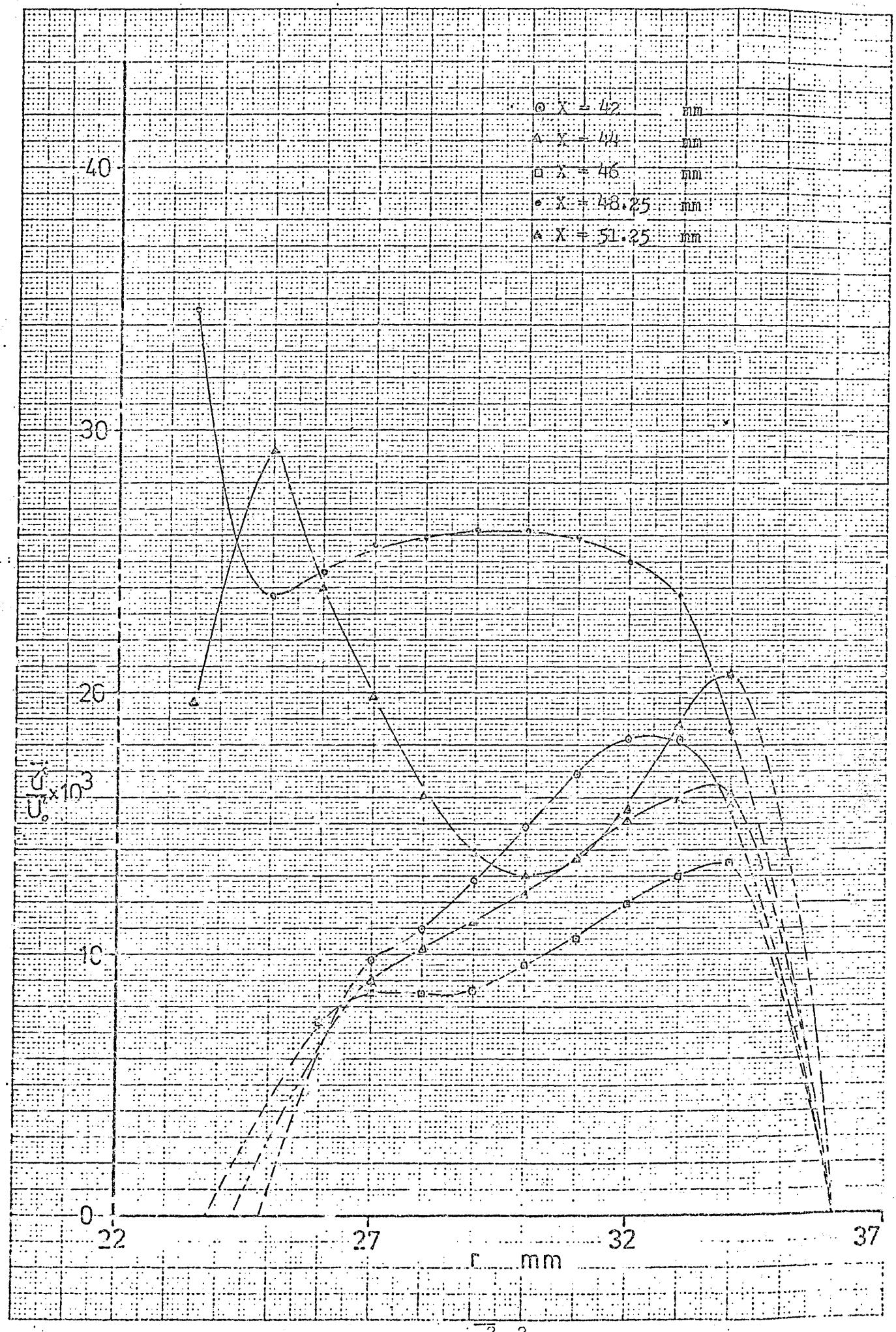

Fig.(F4-9): The distribution of $\overline{u^2}/U_o^2$ in region (9).

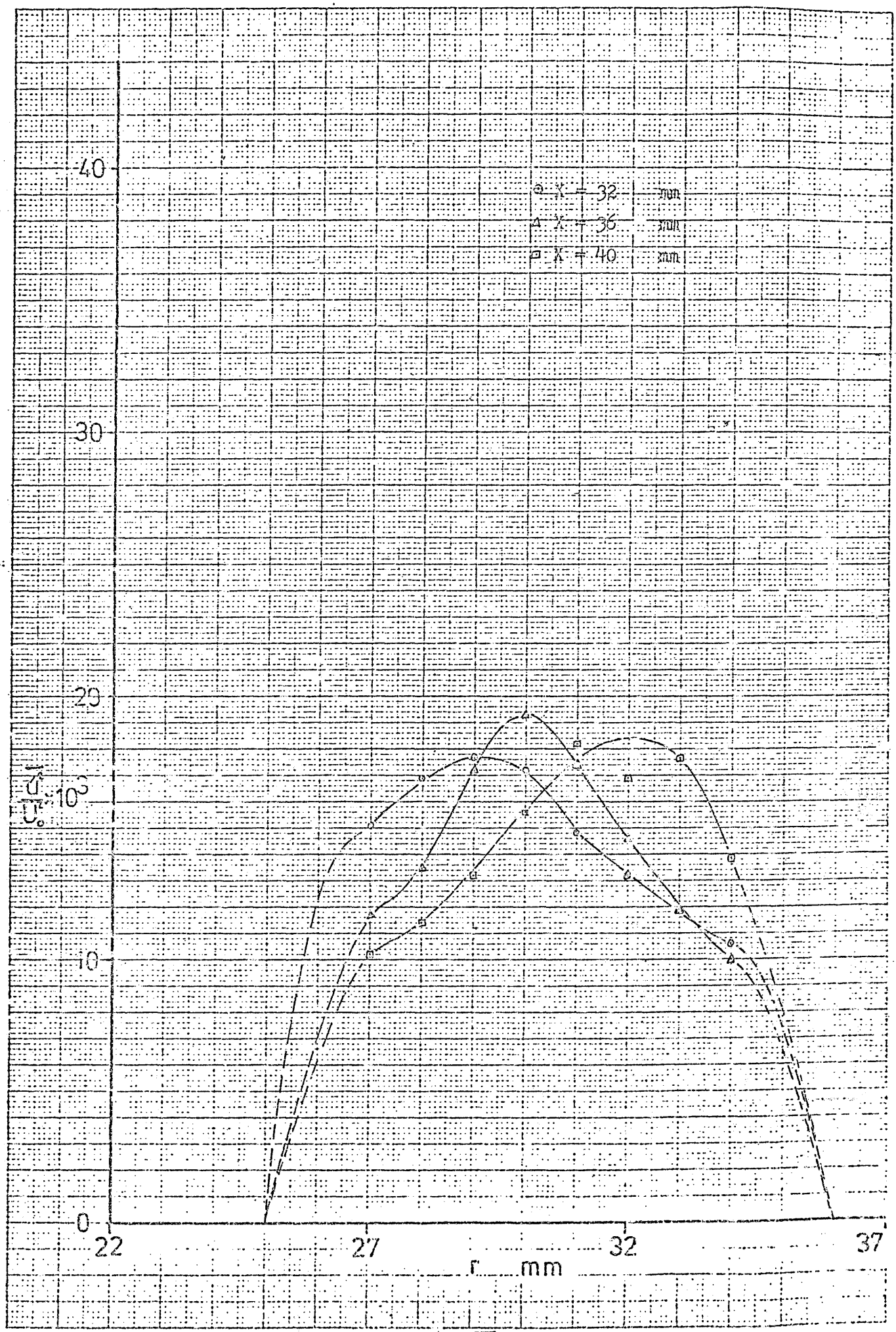

Fig.(F4-10): The distribution of $\overline{u^2}/U_o^2$ in region (10).

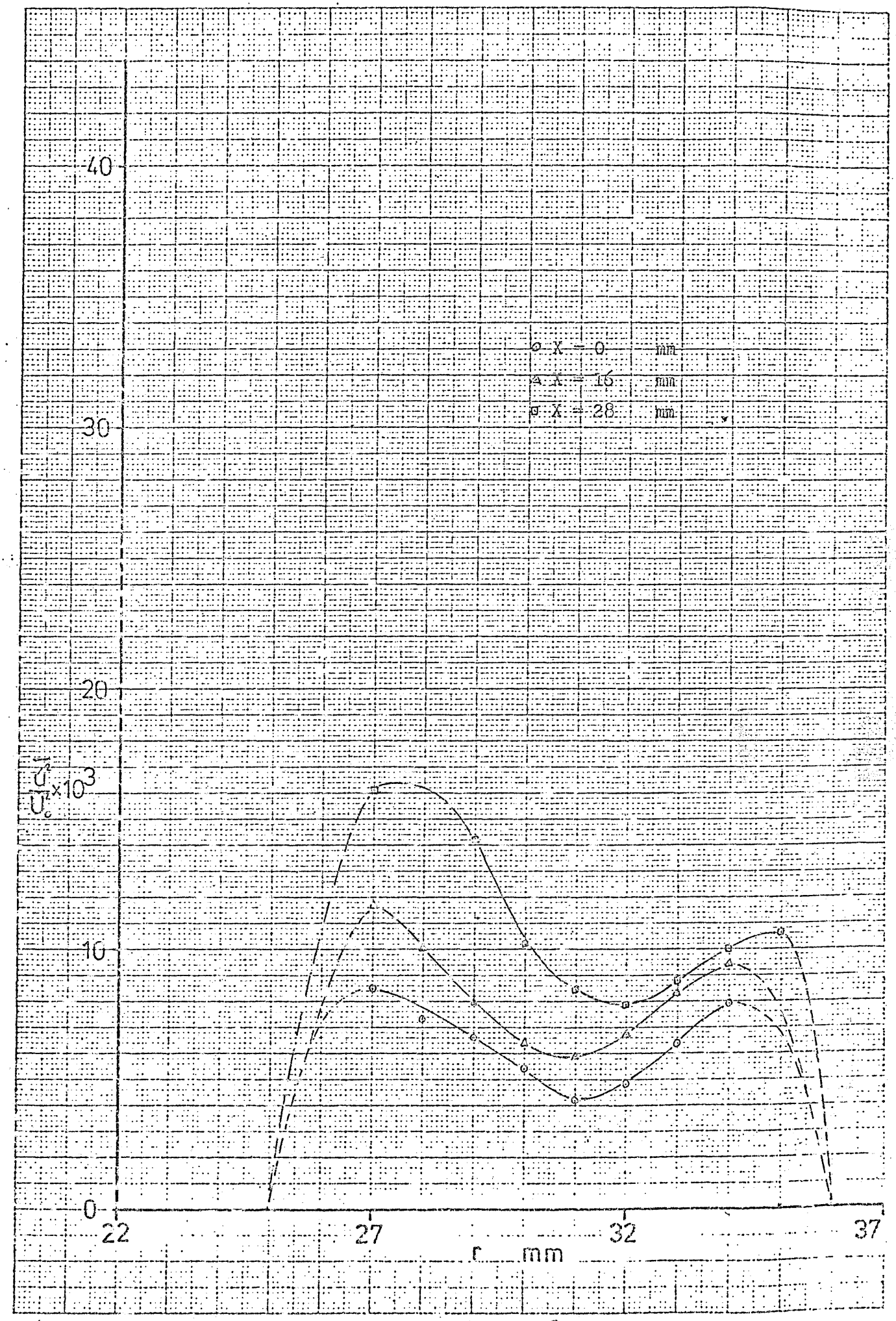

Fig.(F4-11): The distribution of $\overline{u^2}/U_o^2$ in region (11).

Appendix F5: The distribution of the radial normal Reynolds' stress

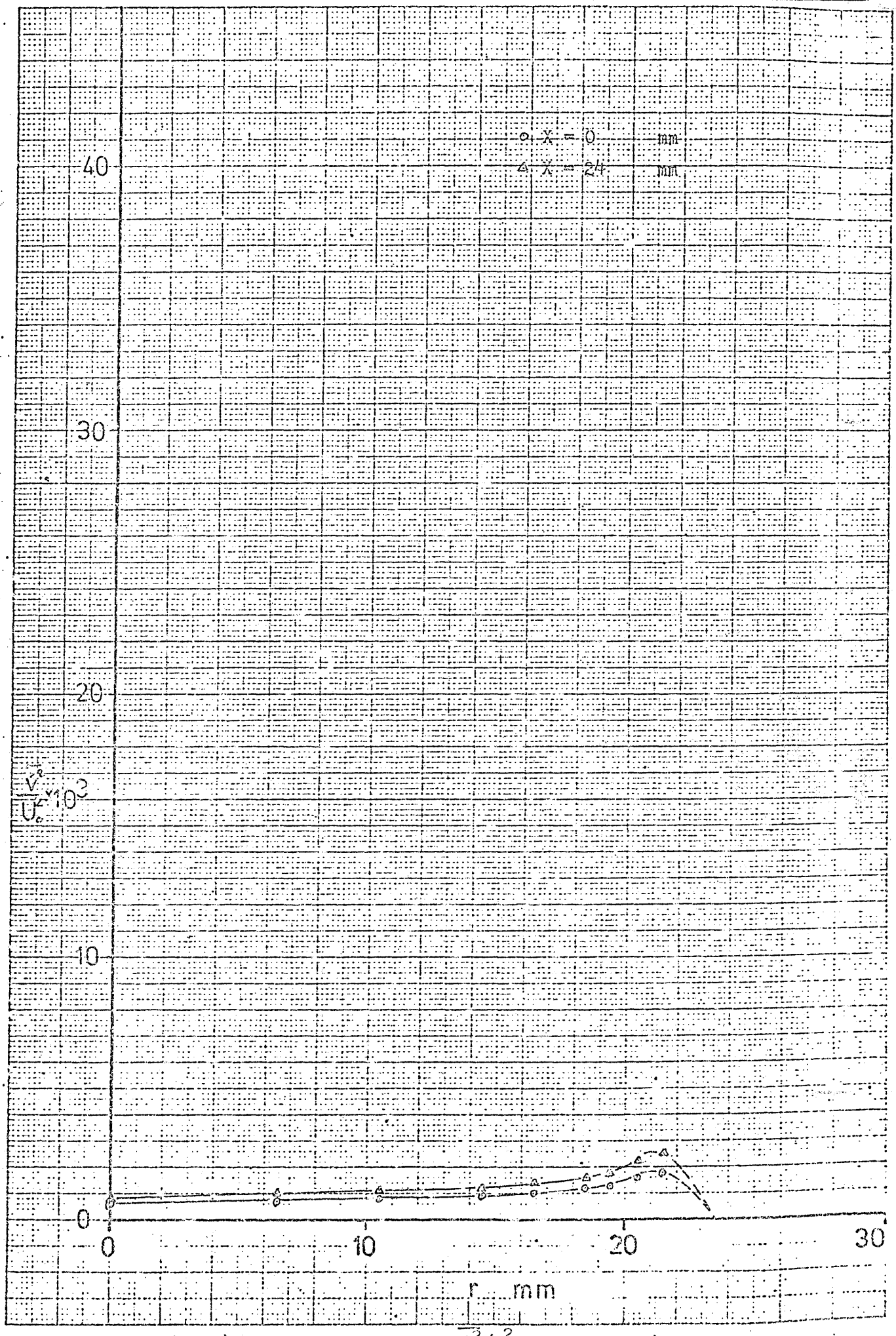

Fig.(F5-1): The distribution of $\overline{v^2}/U_o^2$ in region (1).

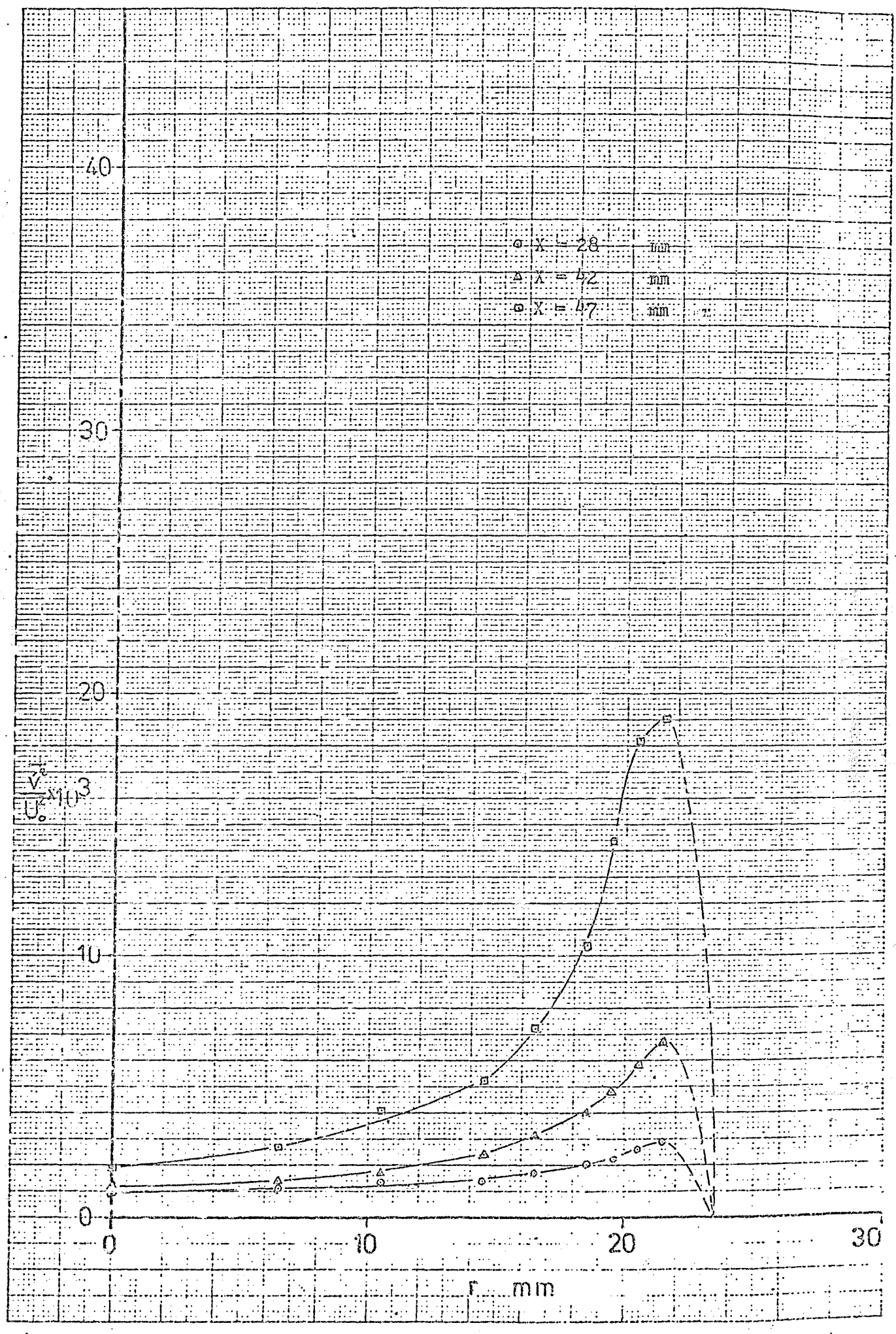

Fig.(F5-2): The distribution of $\overline{v^2}/U_o^2$ in region (2).

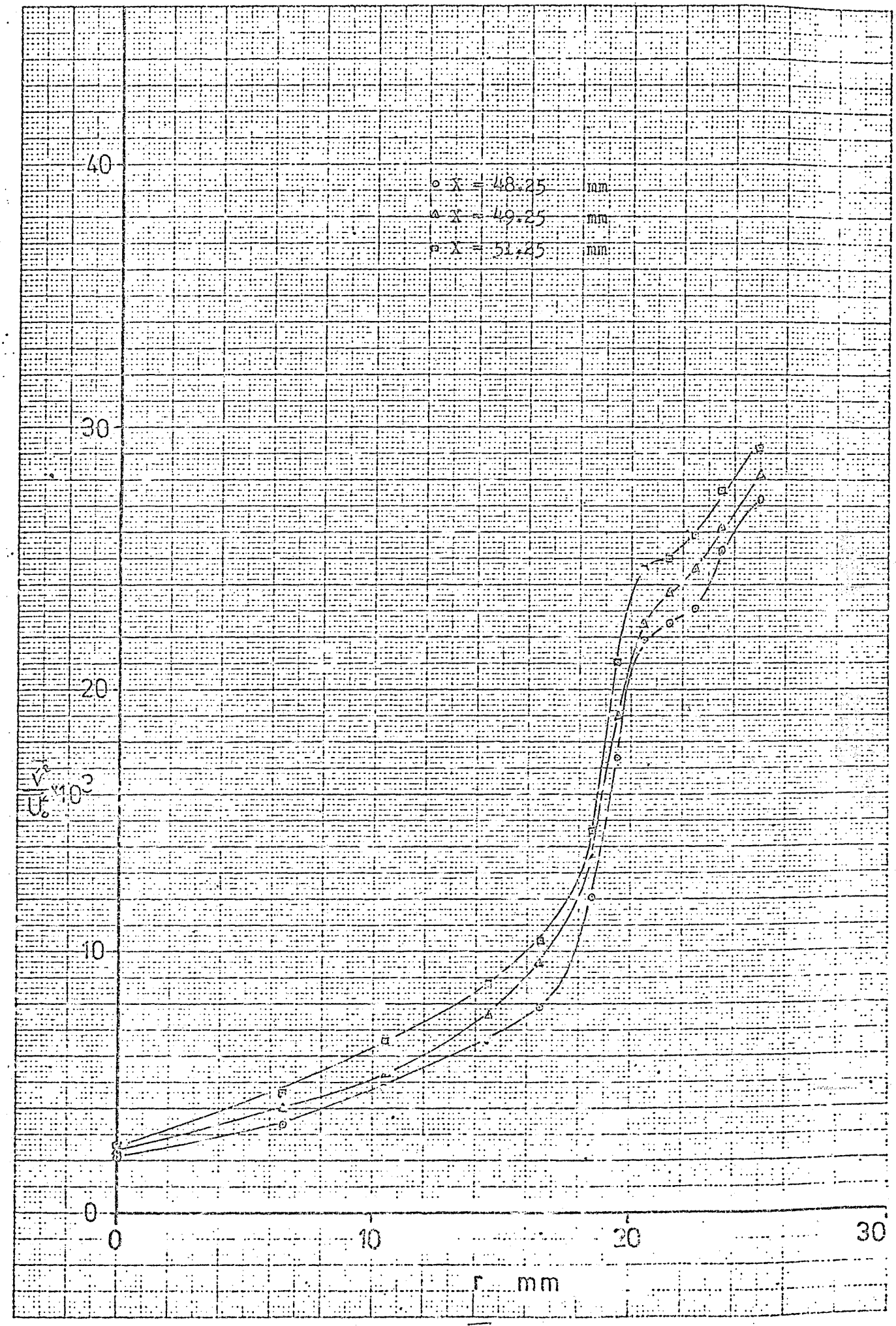

Fig.(F5-3): The distribution of $\overline{v^2}/U_o^2$ in region (3).

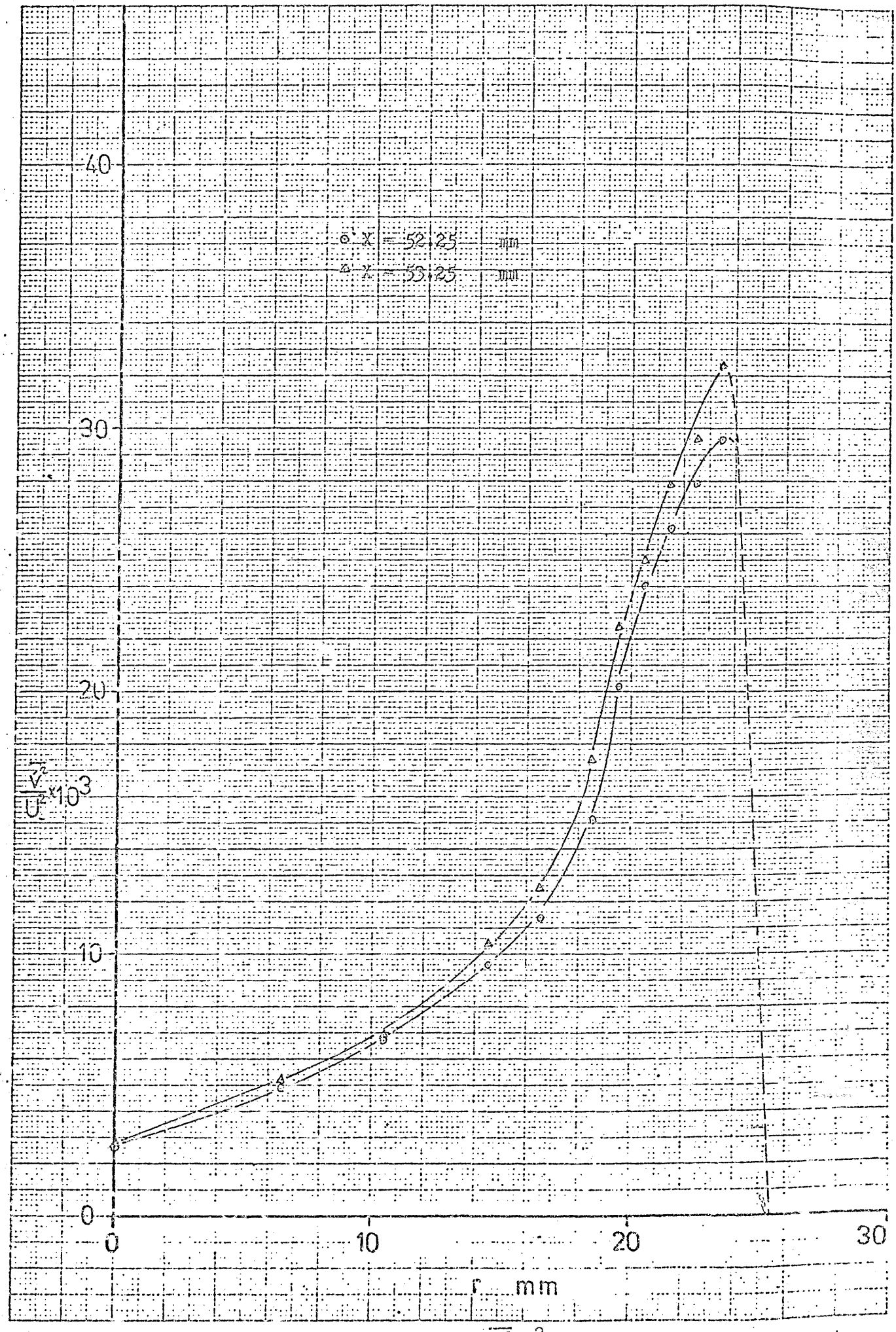

Fig.(F5-4): The distribution of $\overline{v^2}/U_o^2$ in region (4).

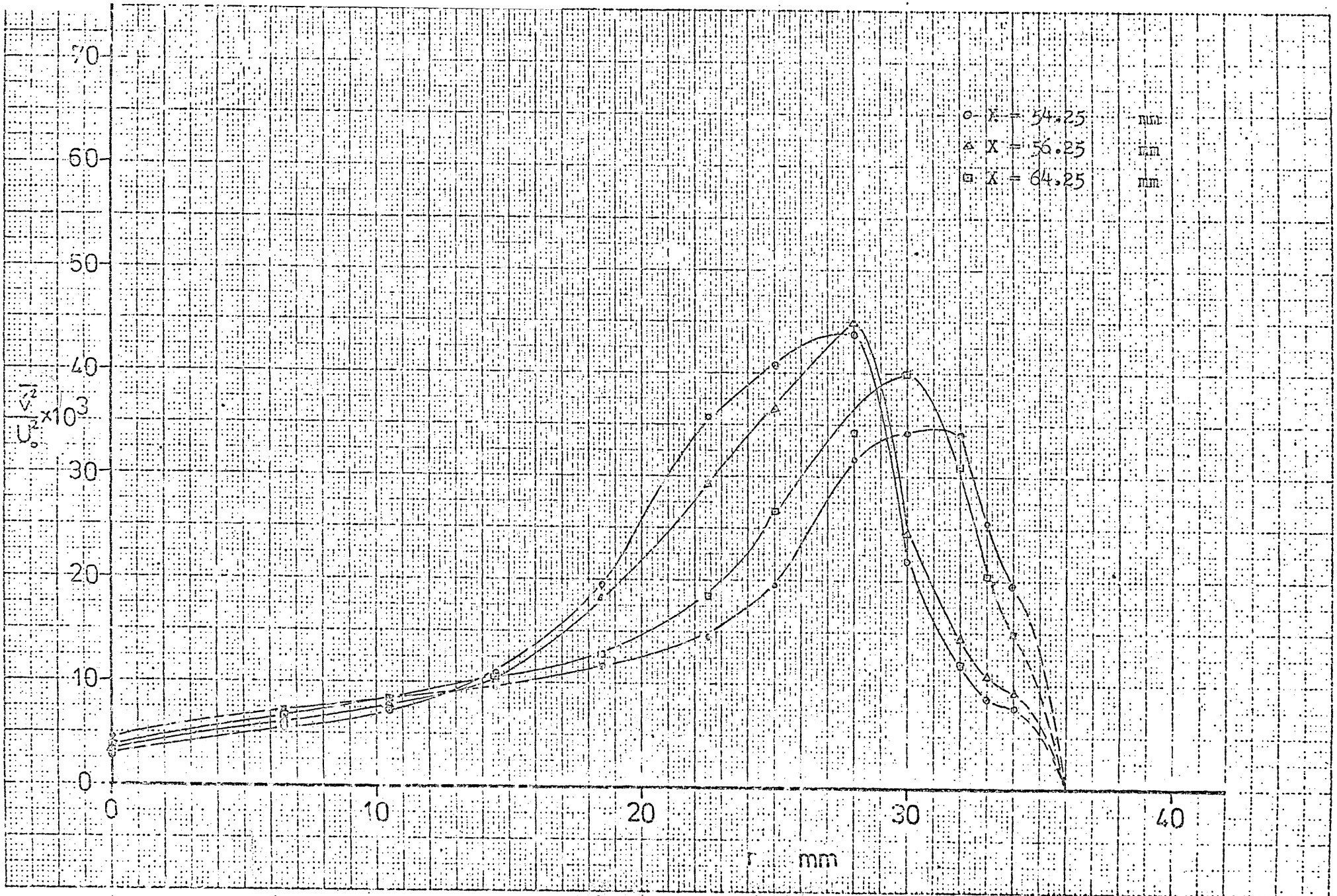

Fig.(5-5) : The distribution of $\overline{v^2}/U_o^2$ in region (5).

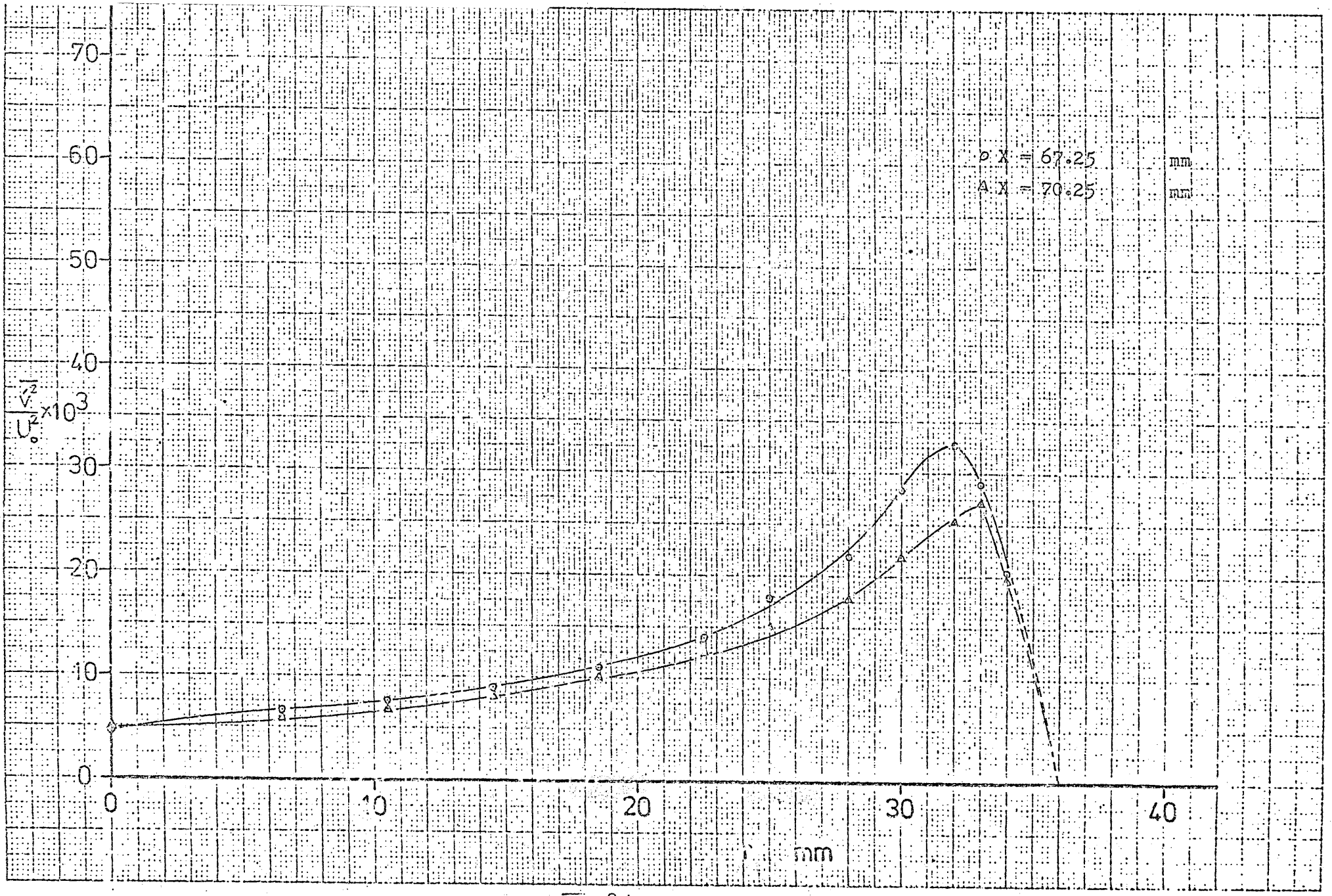

Fig.(F5-6): The distribution of $\overline{v^2}/U_o^2$ in region (6).

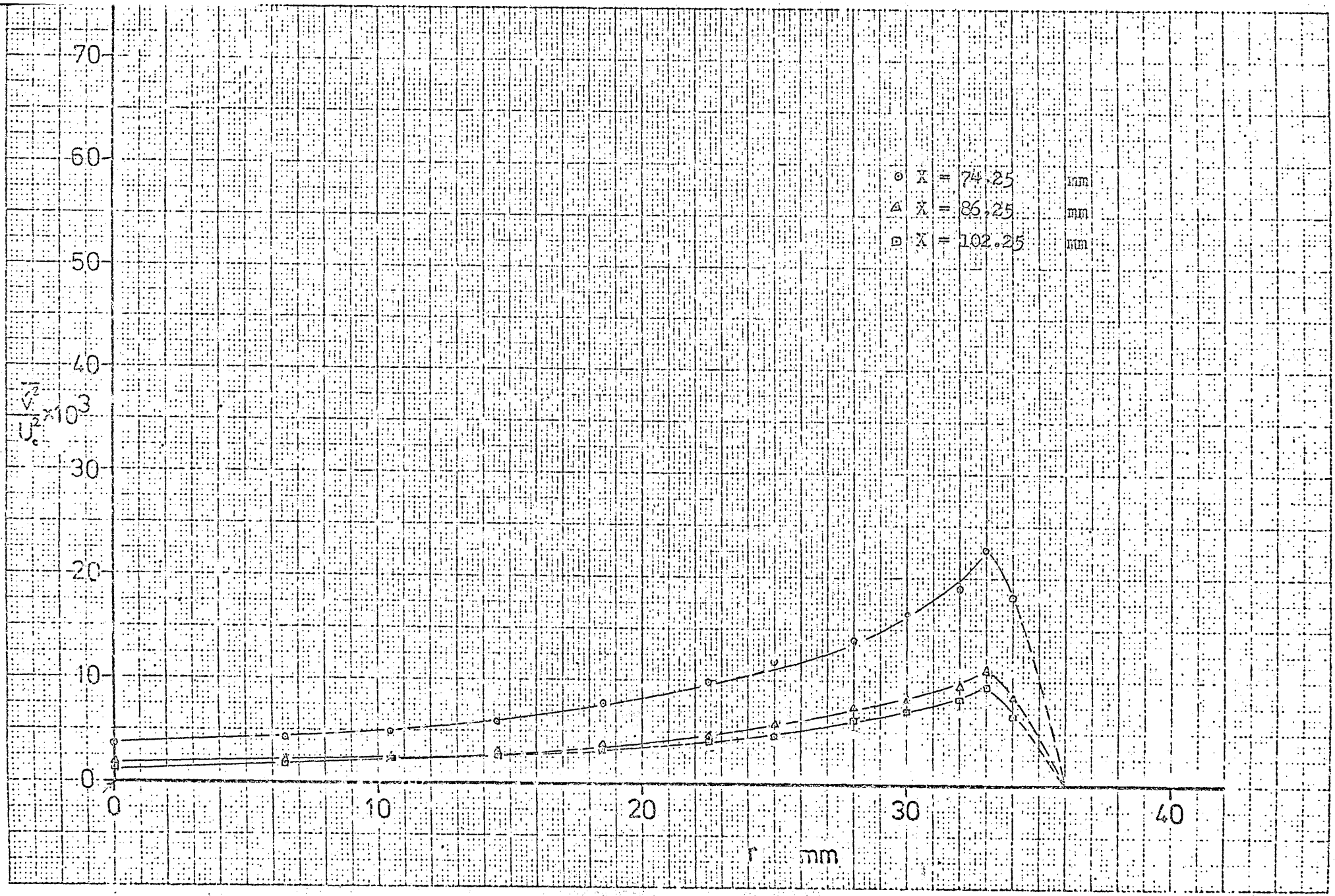

Fig. (F5-7): The distribution of $\overline{v^2}/U_c^2$ in region (7).

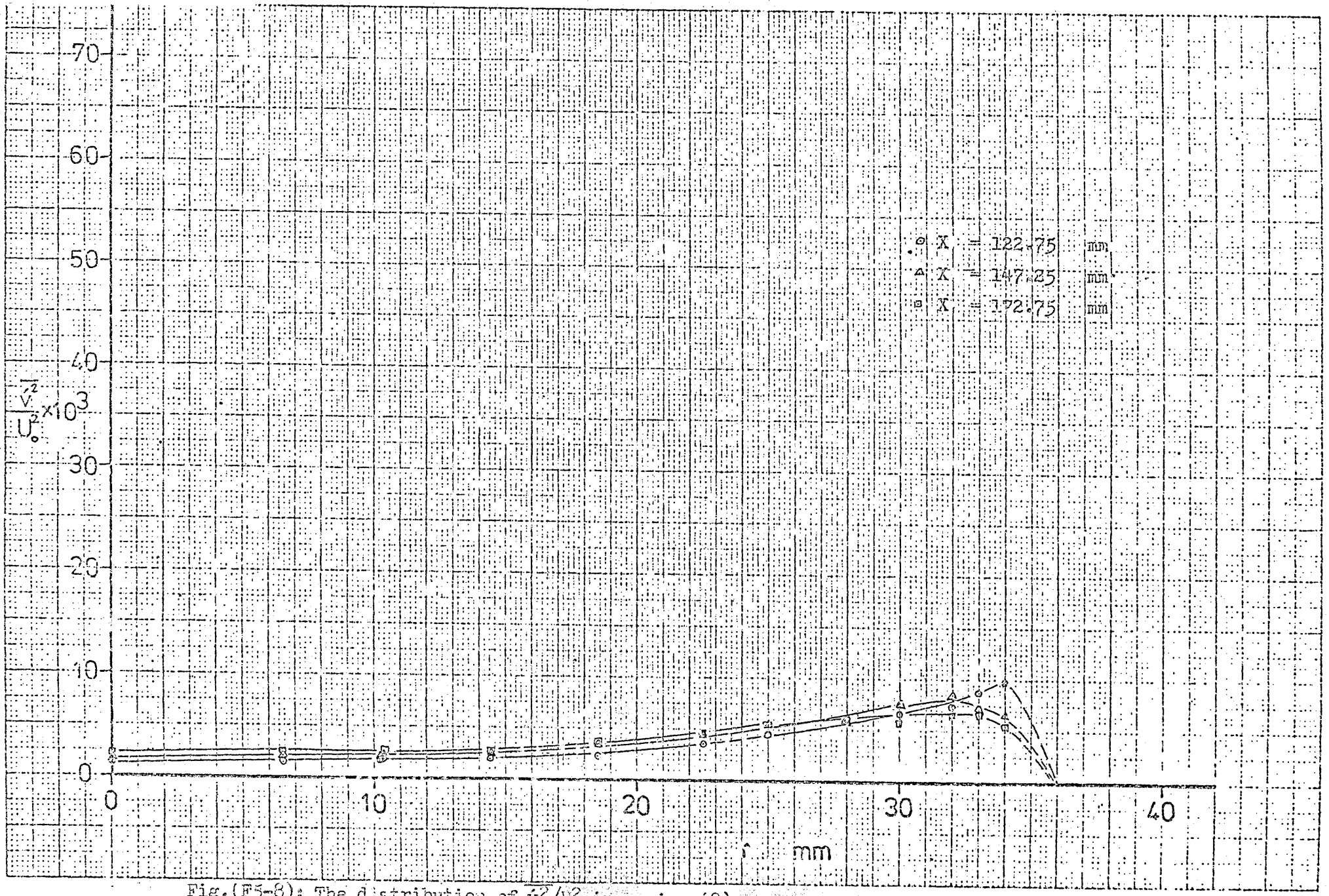

Fig.(F5-8): The distribution of $\overline{v^2}/U_o^2$ in region (8).

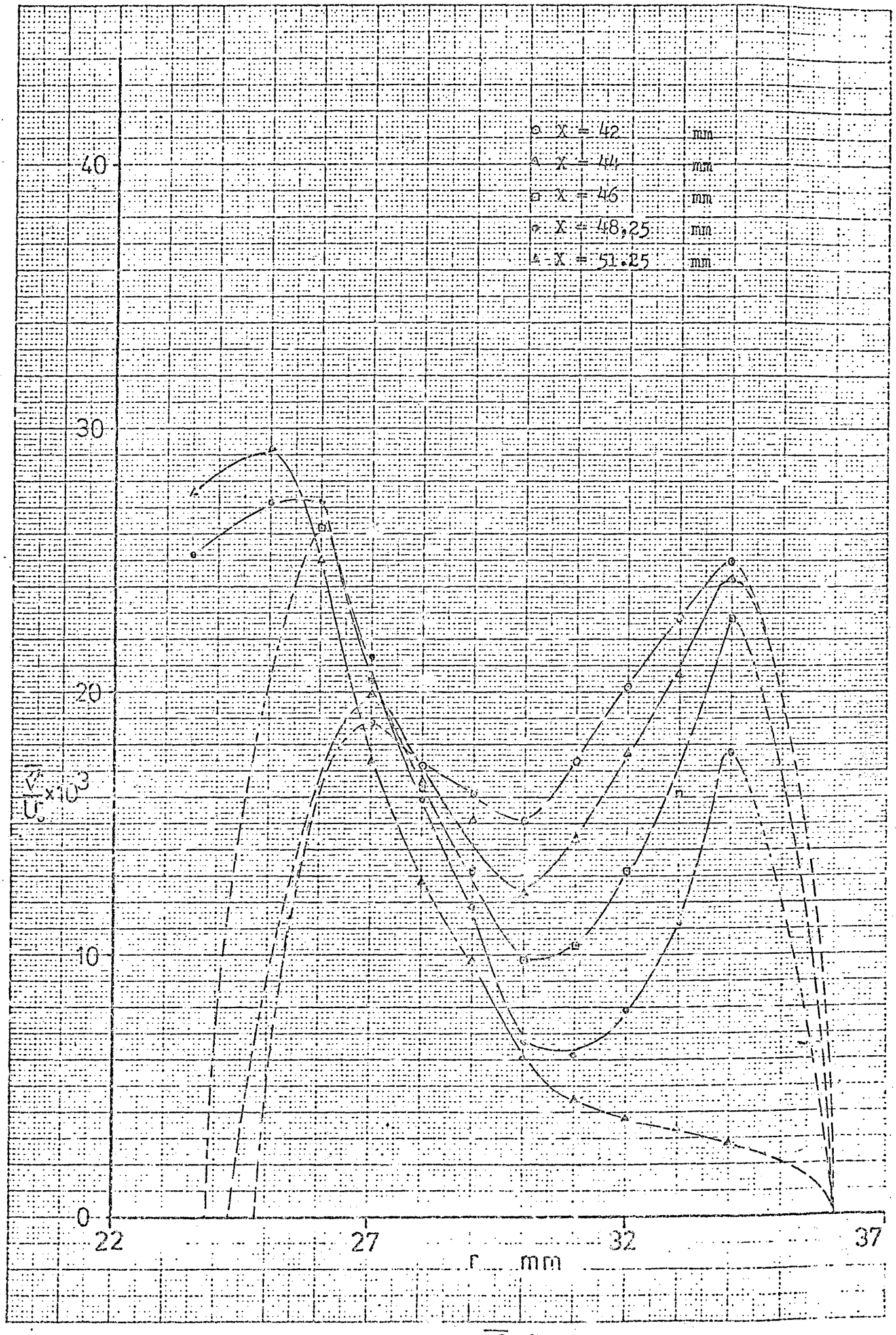

Fig.(F5-9): The distribution of $\overline{v^2}/U^2$ in region (9).

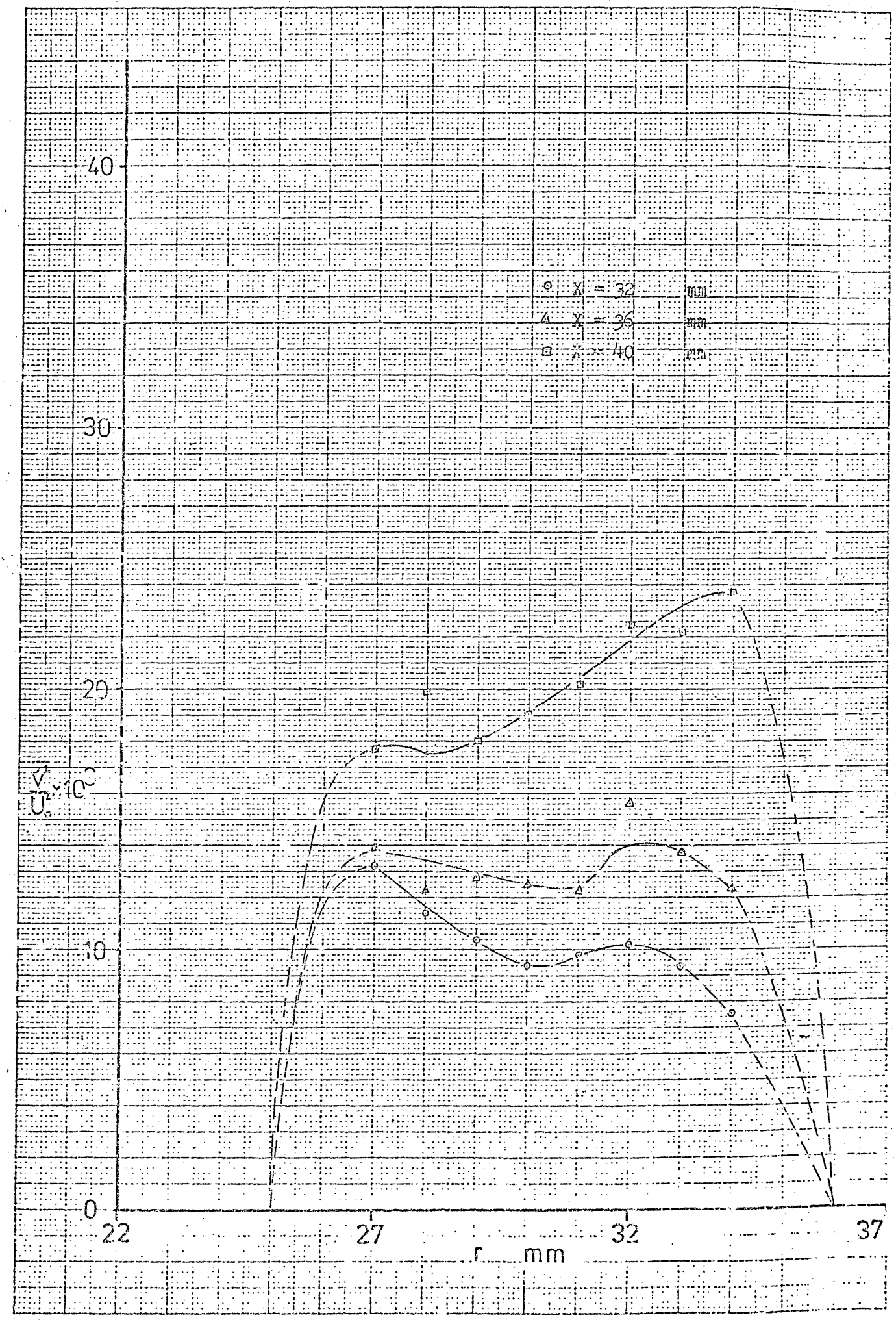

Fig.(F5-10): The distribution of $\overline{v^2}/U_o^2$ in region (10).

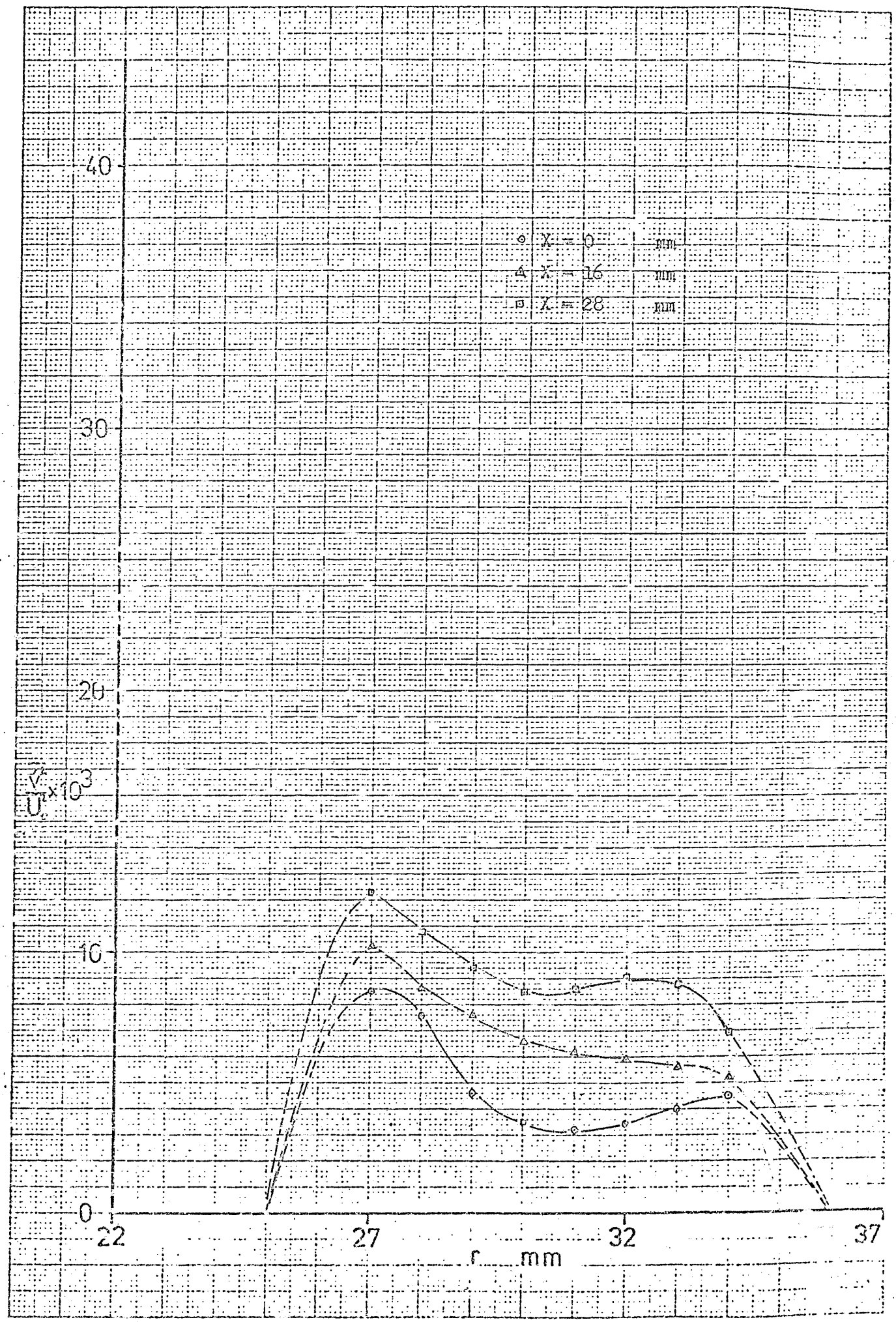

Fig.(F5-11): The distribution of $\overline{v^2}/U_o^2$ in region (11).

Appendix F6: The distribution of the Reynolds' shear stress.

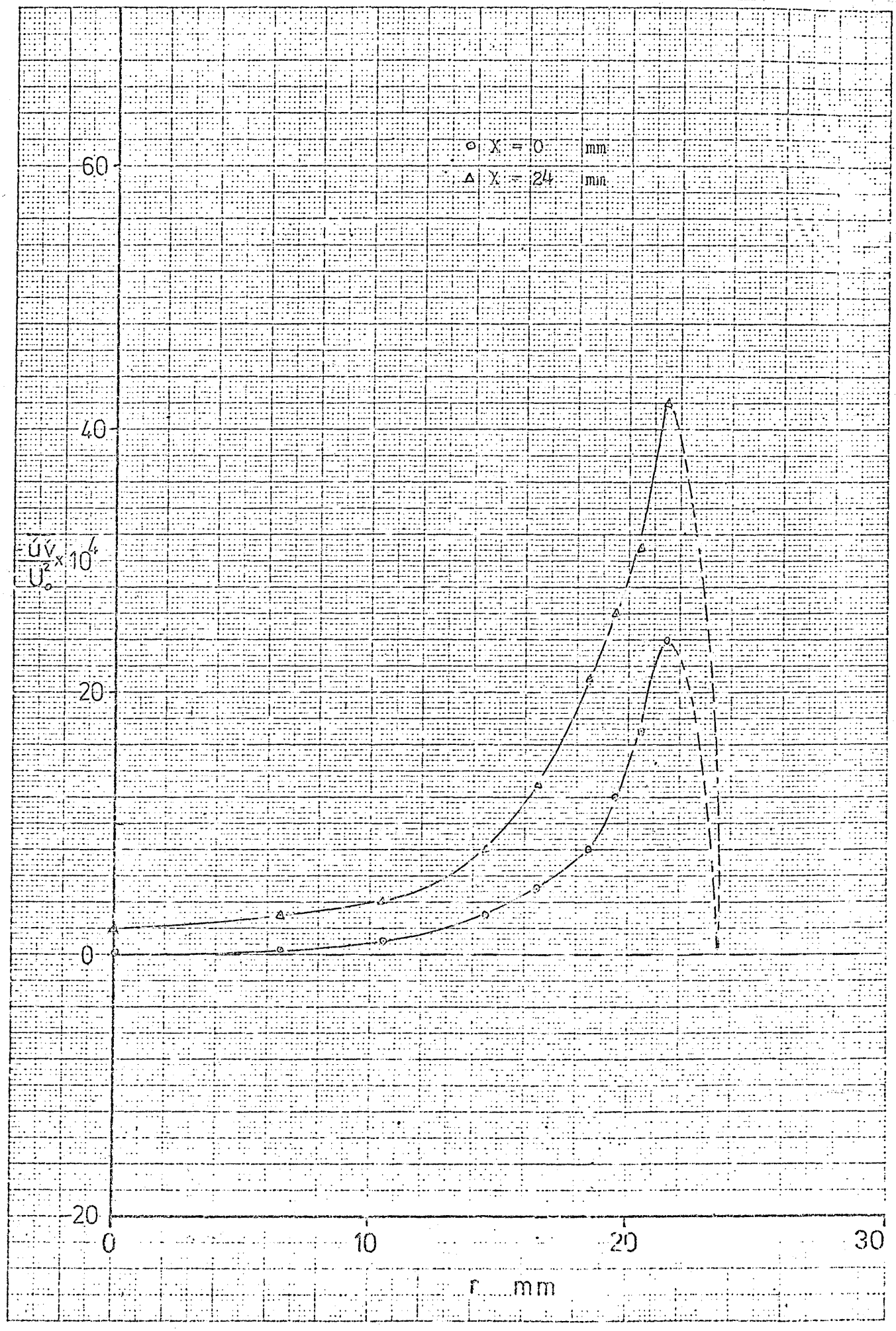

Fig.(F6-1): The distribution of $-\overline{uv}$ in region (1).

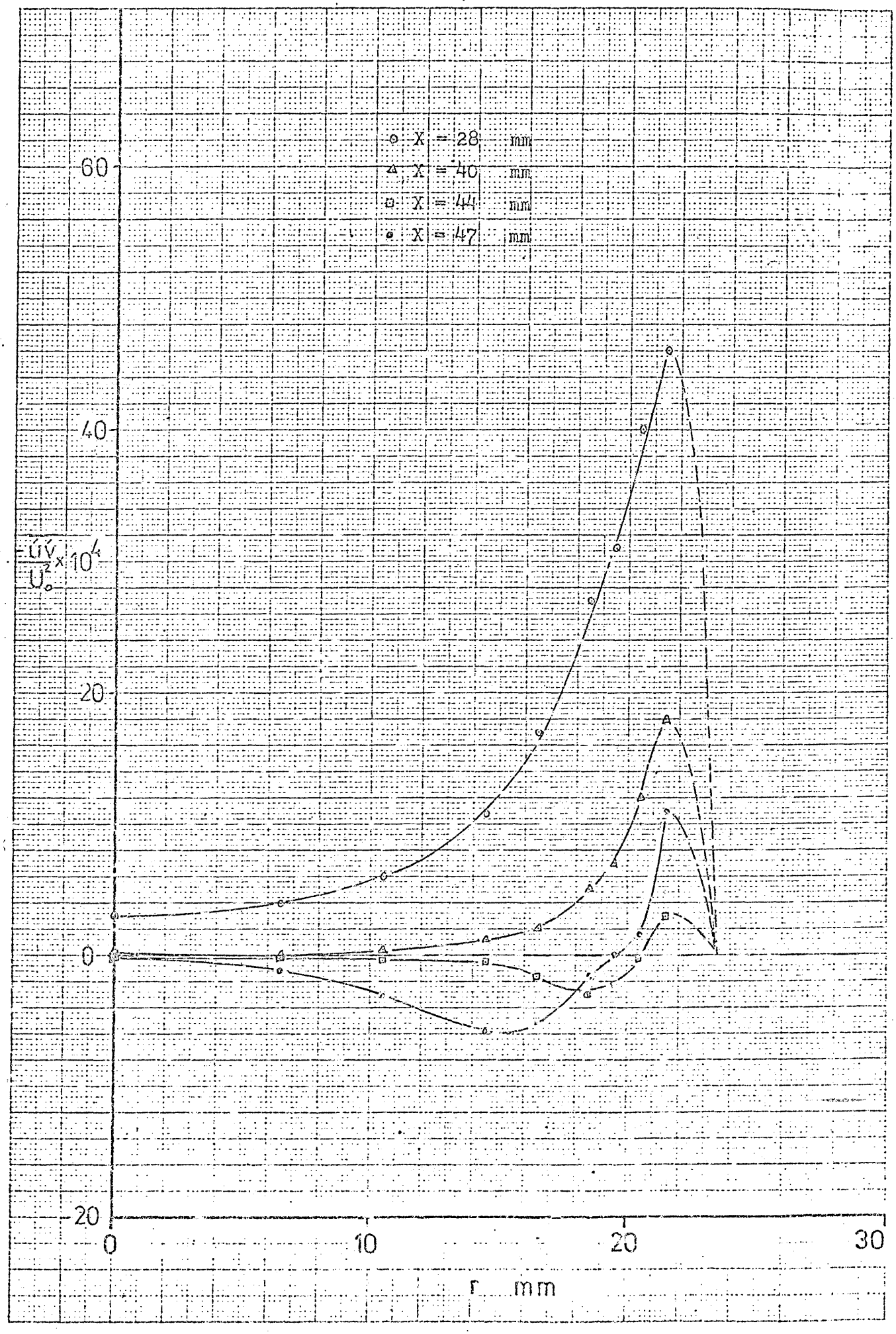

Fig.(F6-2): The distribution of $-\overline{uv}$ in region (2).

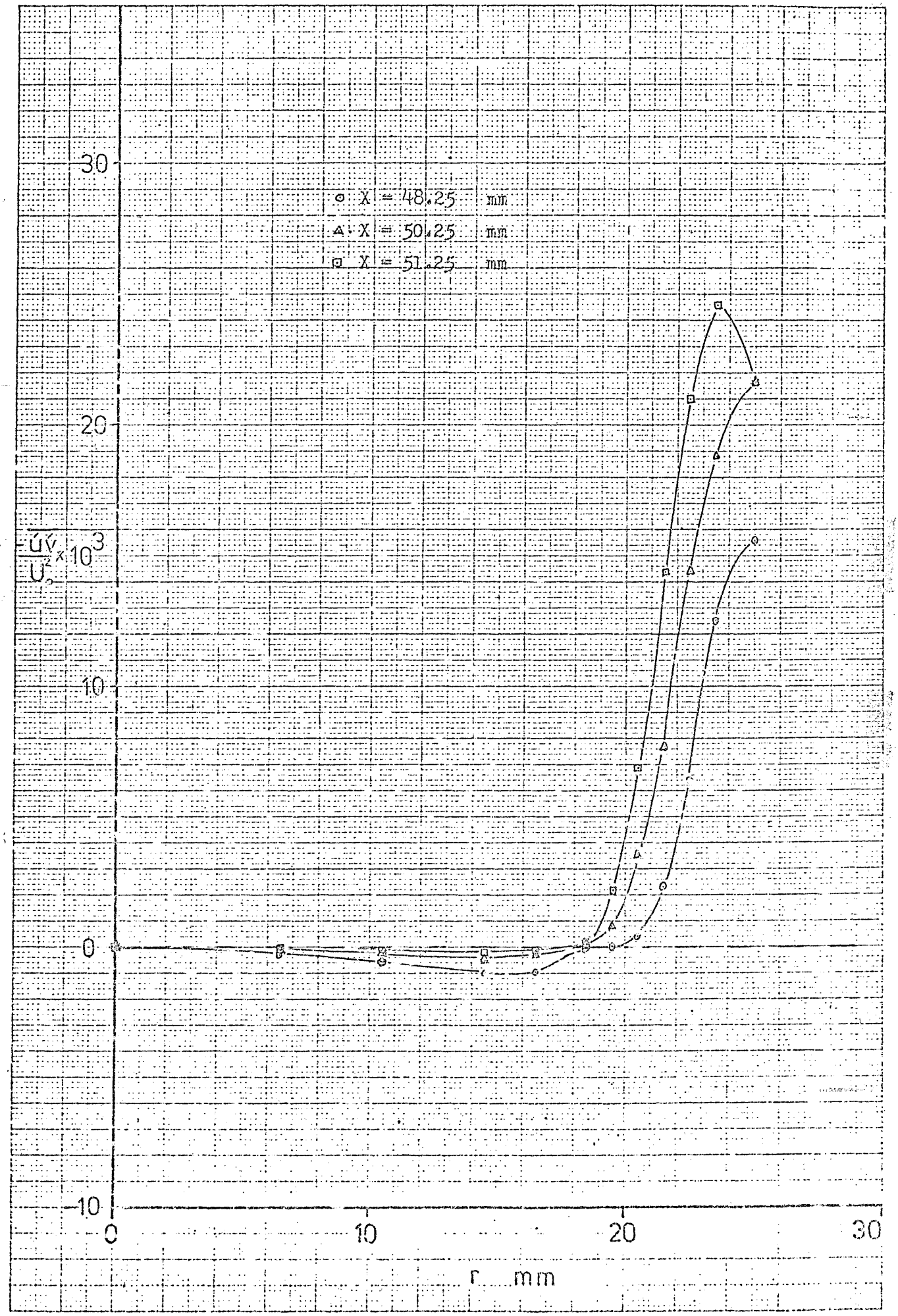

Fif.(F6-3): The distribution of $-\overline{uv}$ in region (3).

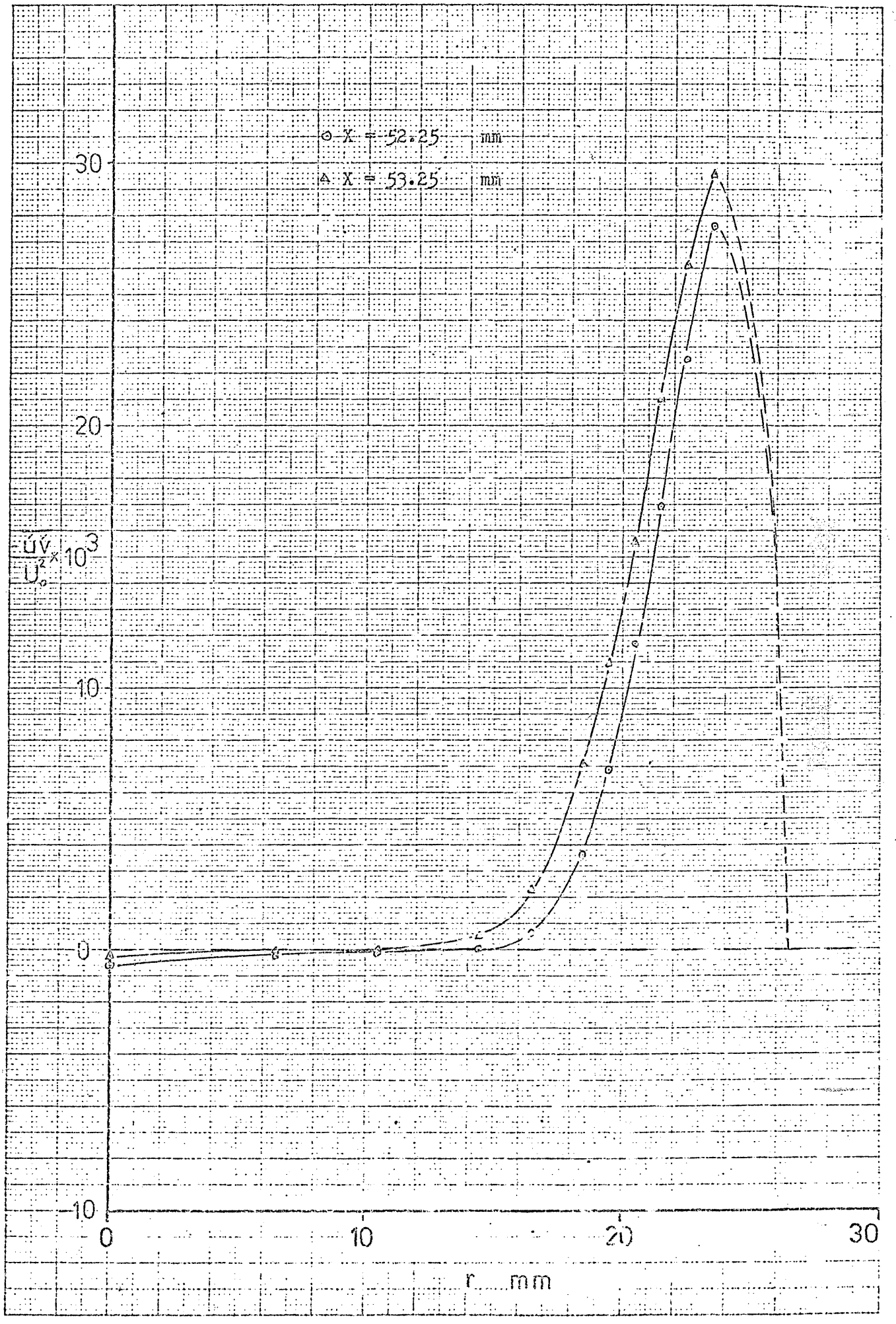

Fig.(F6-4): The distribution of $-\overline{u'v'}$ in region (4).

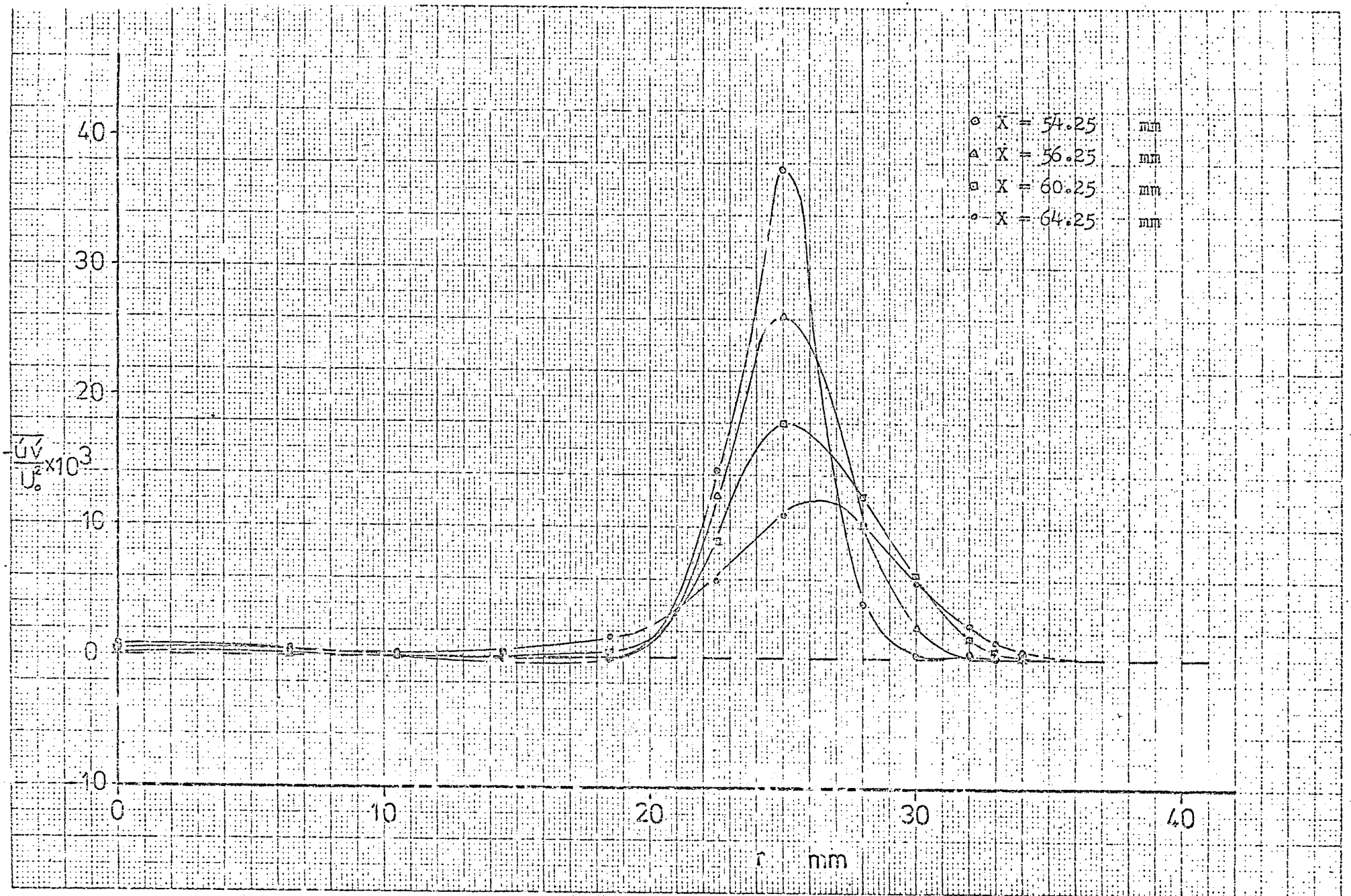

Fig.(F6.5): The distribution of $-\overline{u'v'}$ in region (5).

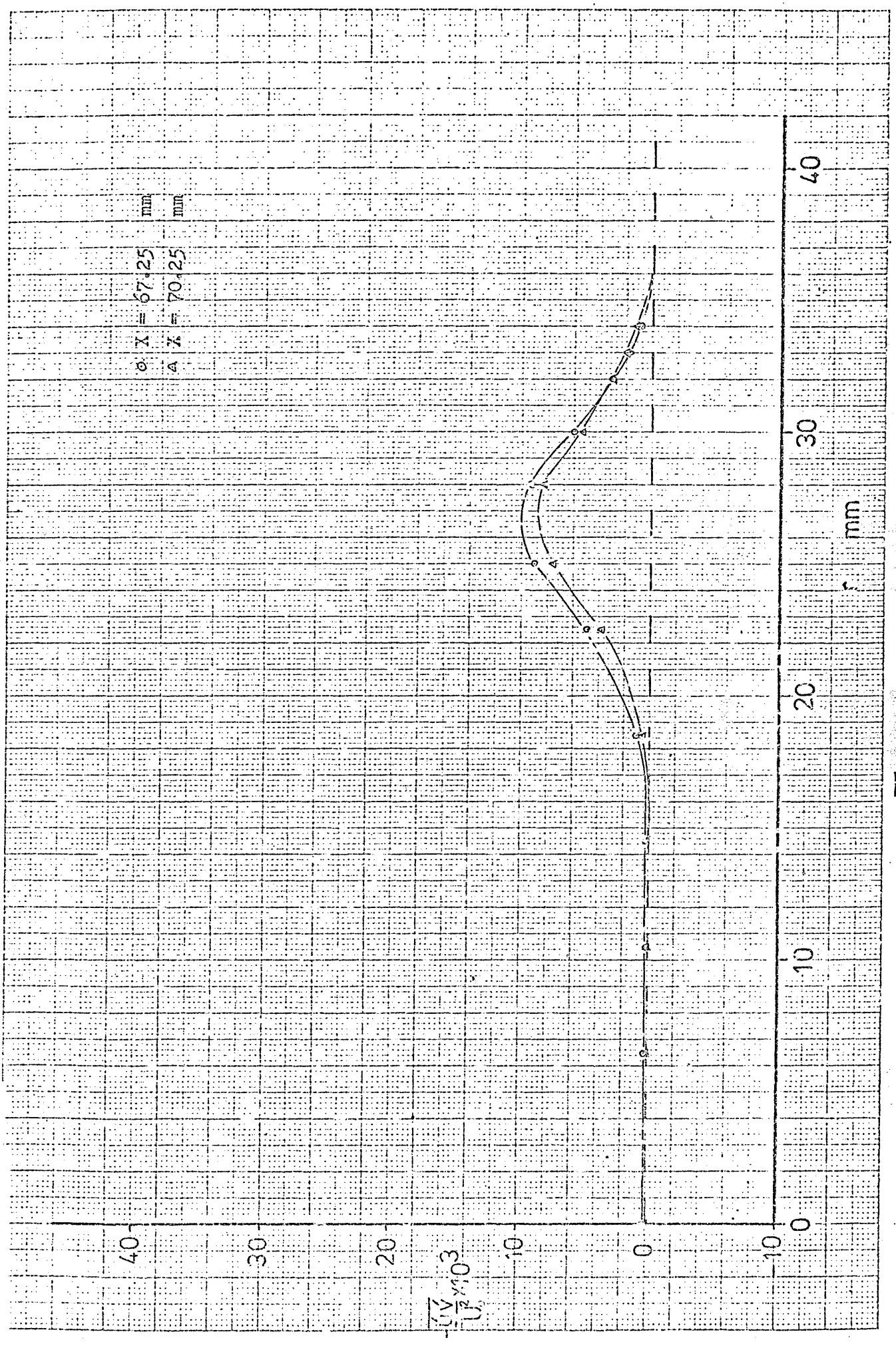

Fig.(F6-6): The distribution of $-\overline{uv}$ in region (6).

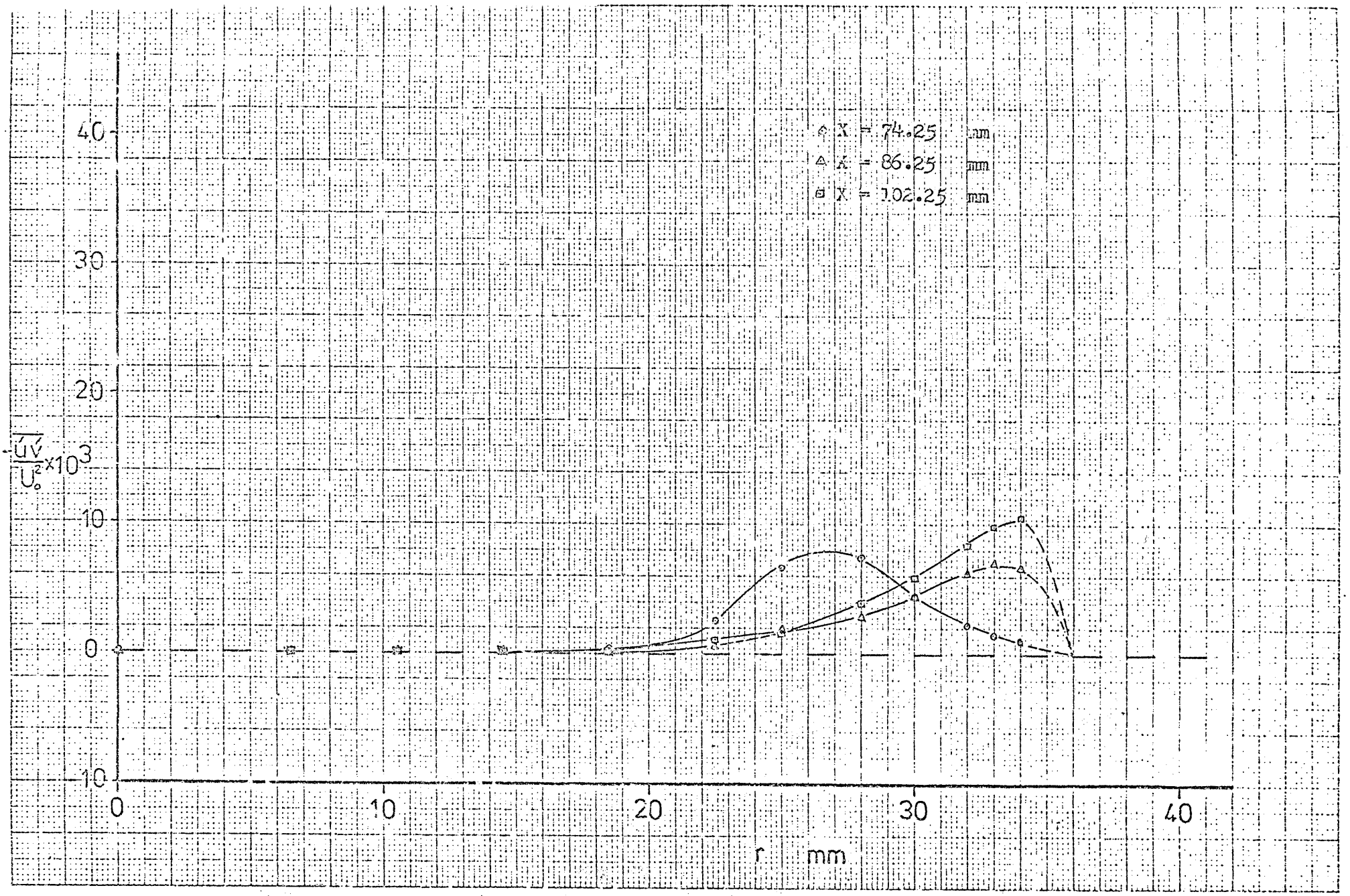

Fig.(P6-7): The distribution of $-\overline{u'v'}$ in region (7).

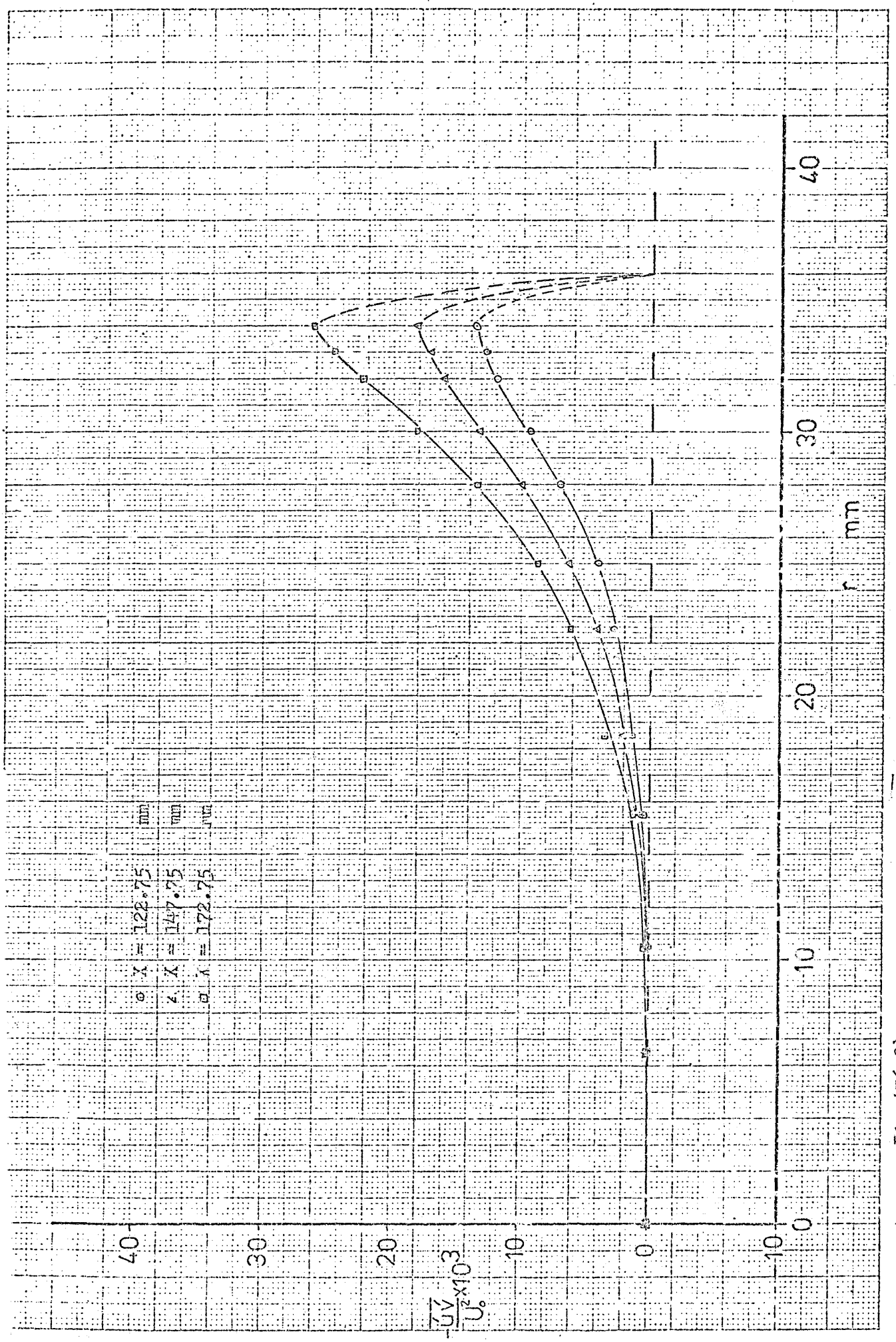

Fig.(F6-8): The distribution of $-\overline{uv}$ in region (3).

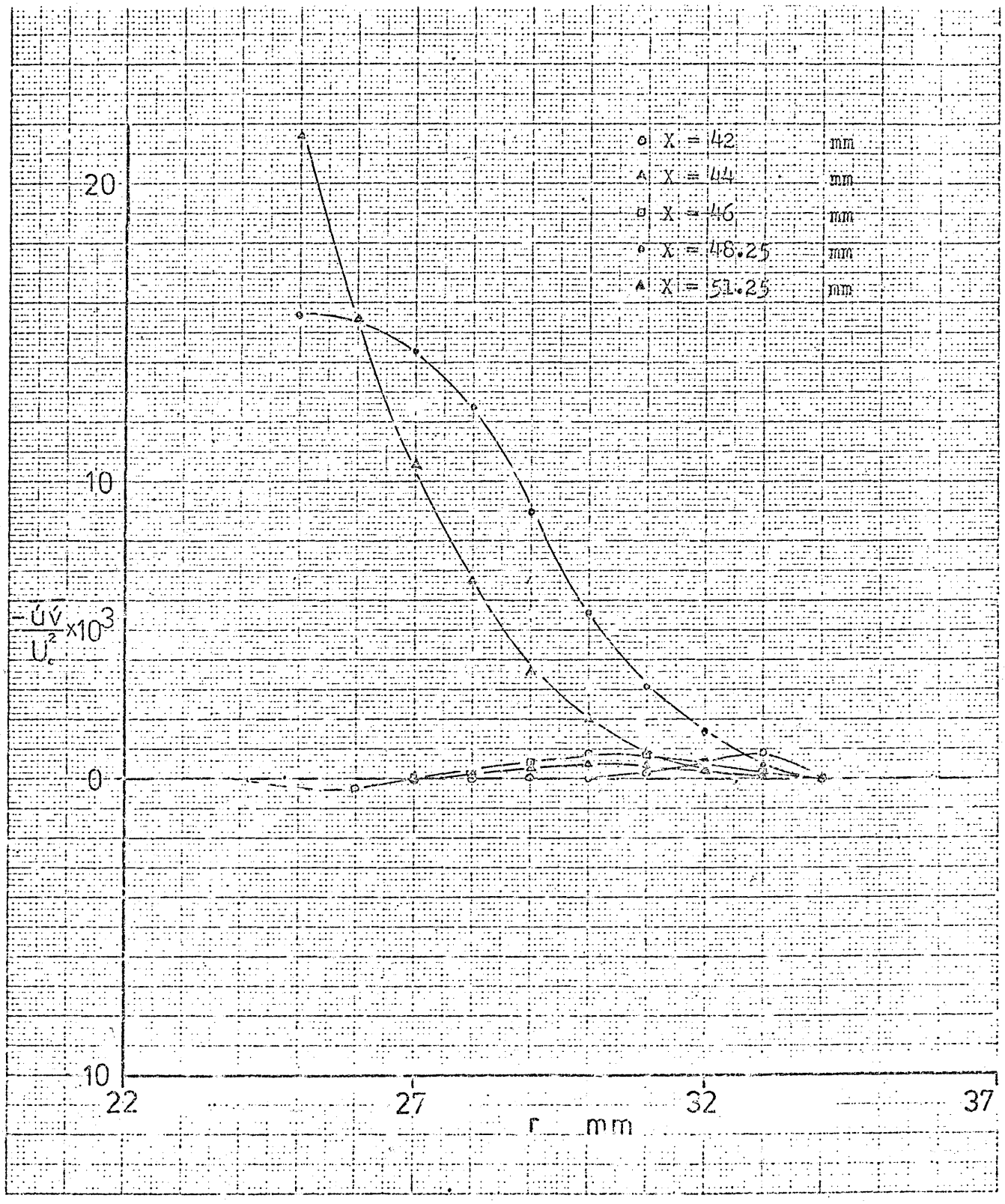

Fig.(FC-9): The distribution of $-\overline{u'v'}$ in region (9).

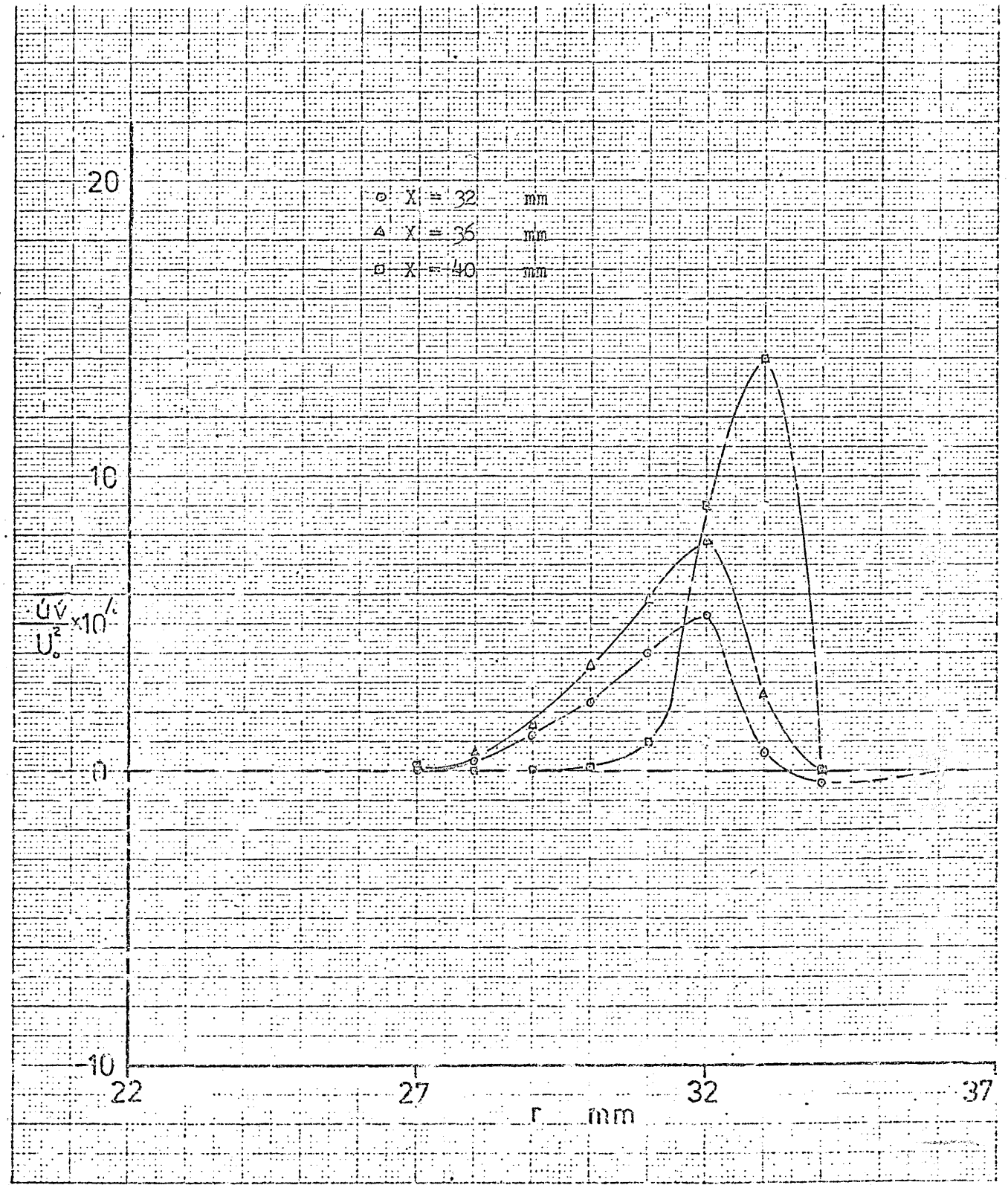

Fig.(F6-10): The distribution of $-\overline{u'v'}$ in region (10).

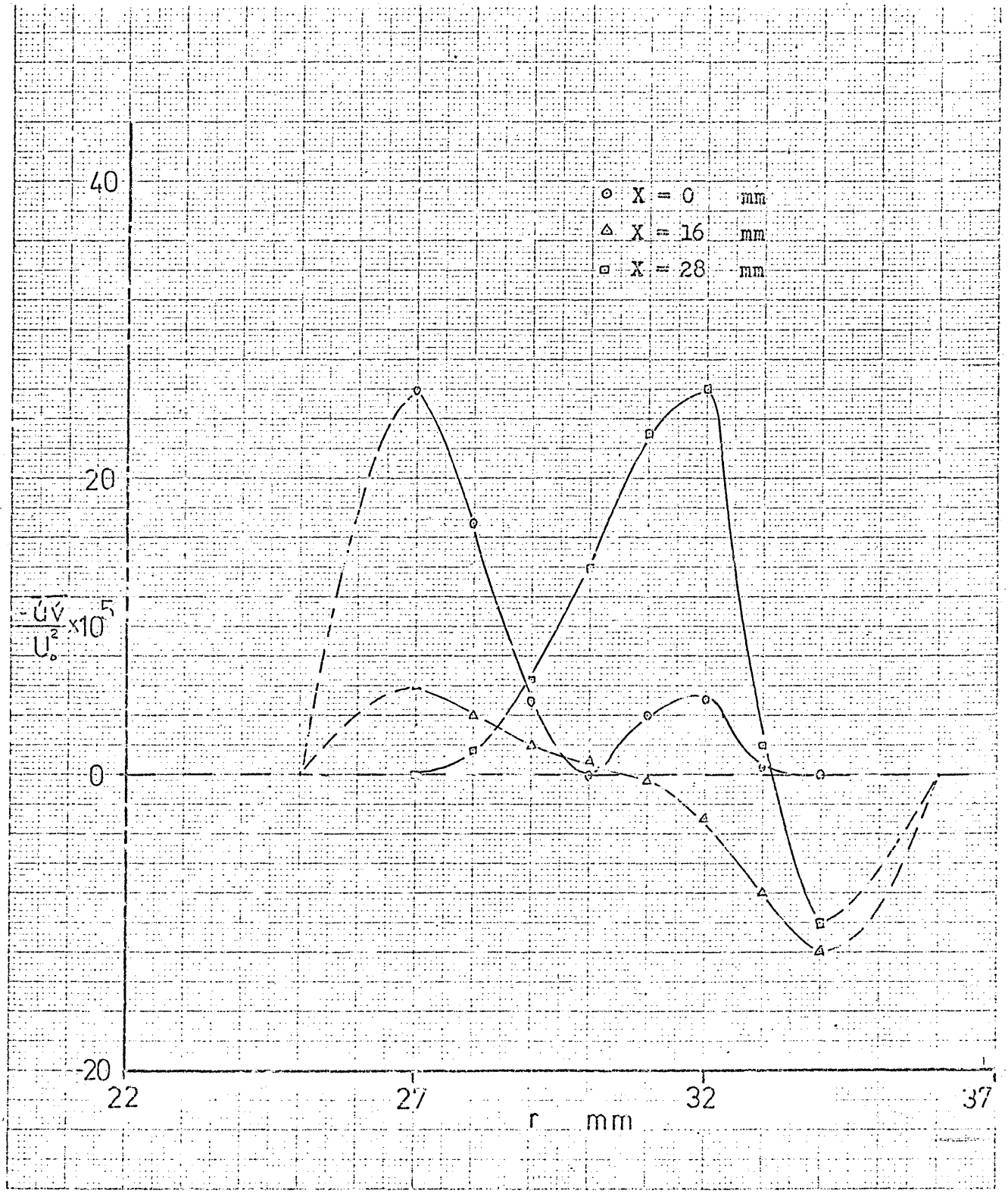

Fig.(F6-11): The distribution of $-\overline{uv}$ in region (11).

Appendix F7: The distribution of the tangential normal Reynolds' stress.

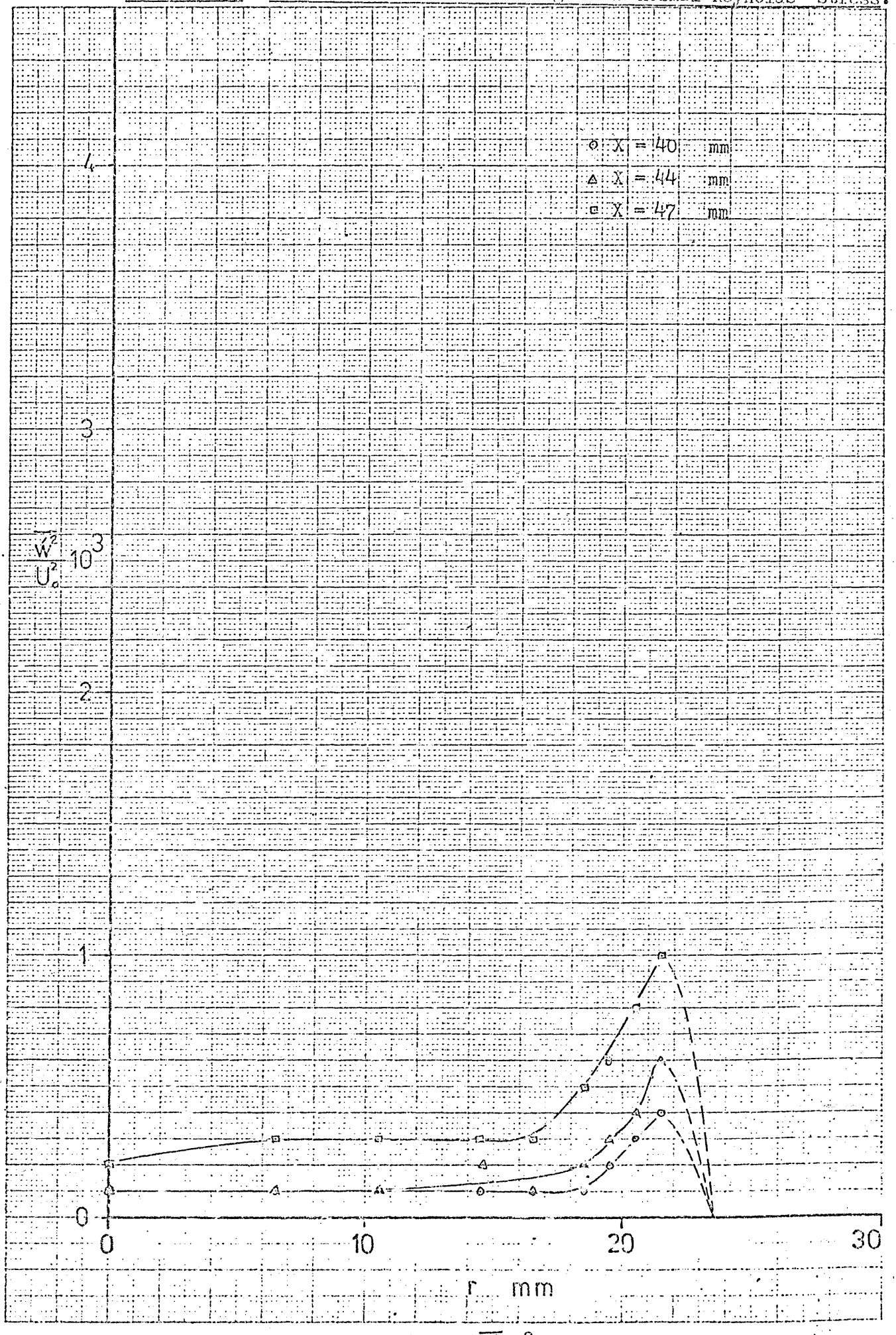

Fig.(F7-1): The distribution of $\overline{w^2}/U_o^2$ in region (2).

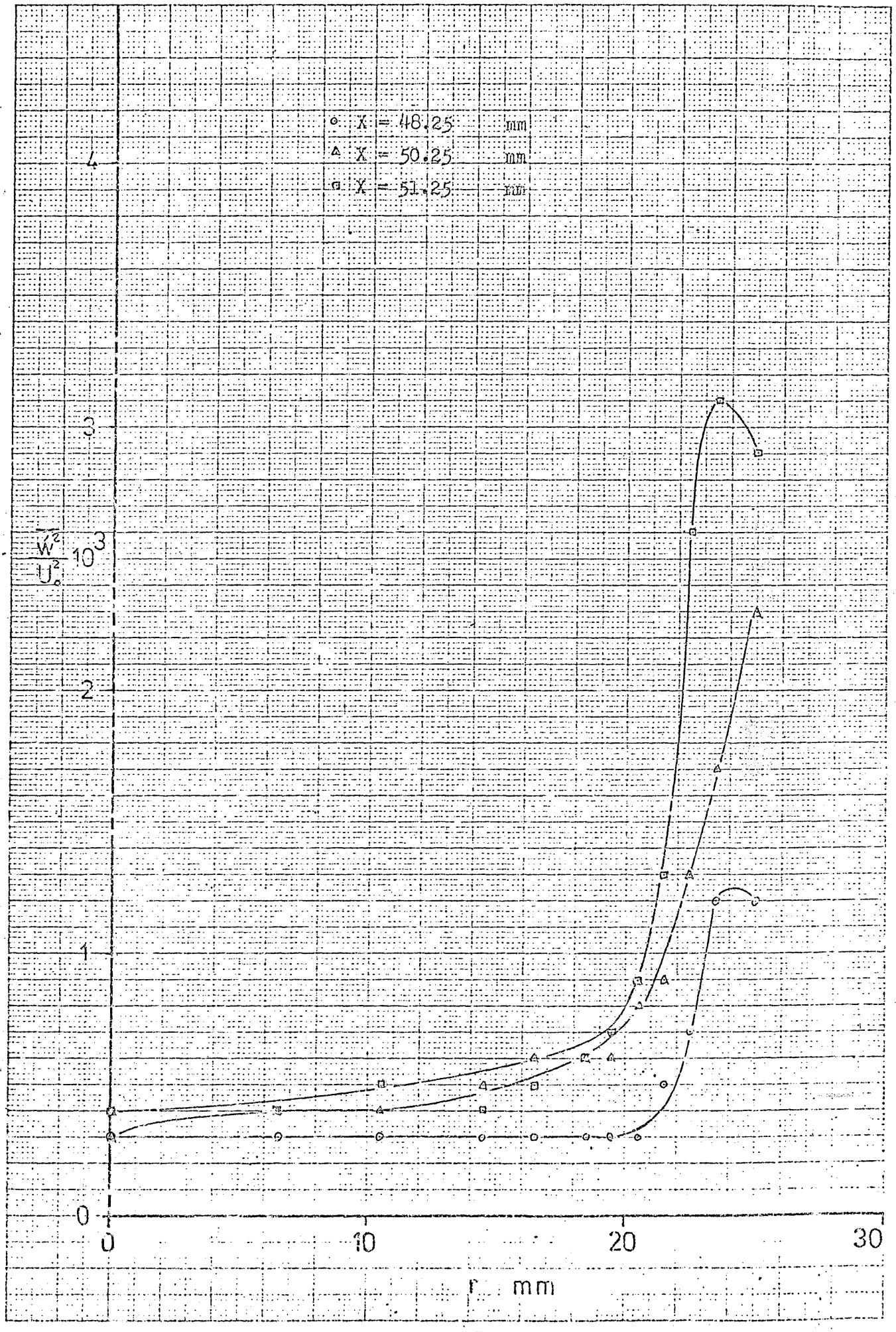

Fig.(F7-2): The distribution of $\overline{w^2}/U_o^2$ in region (3).

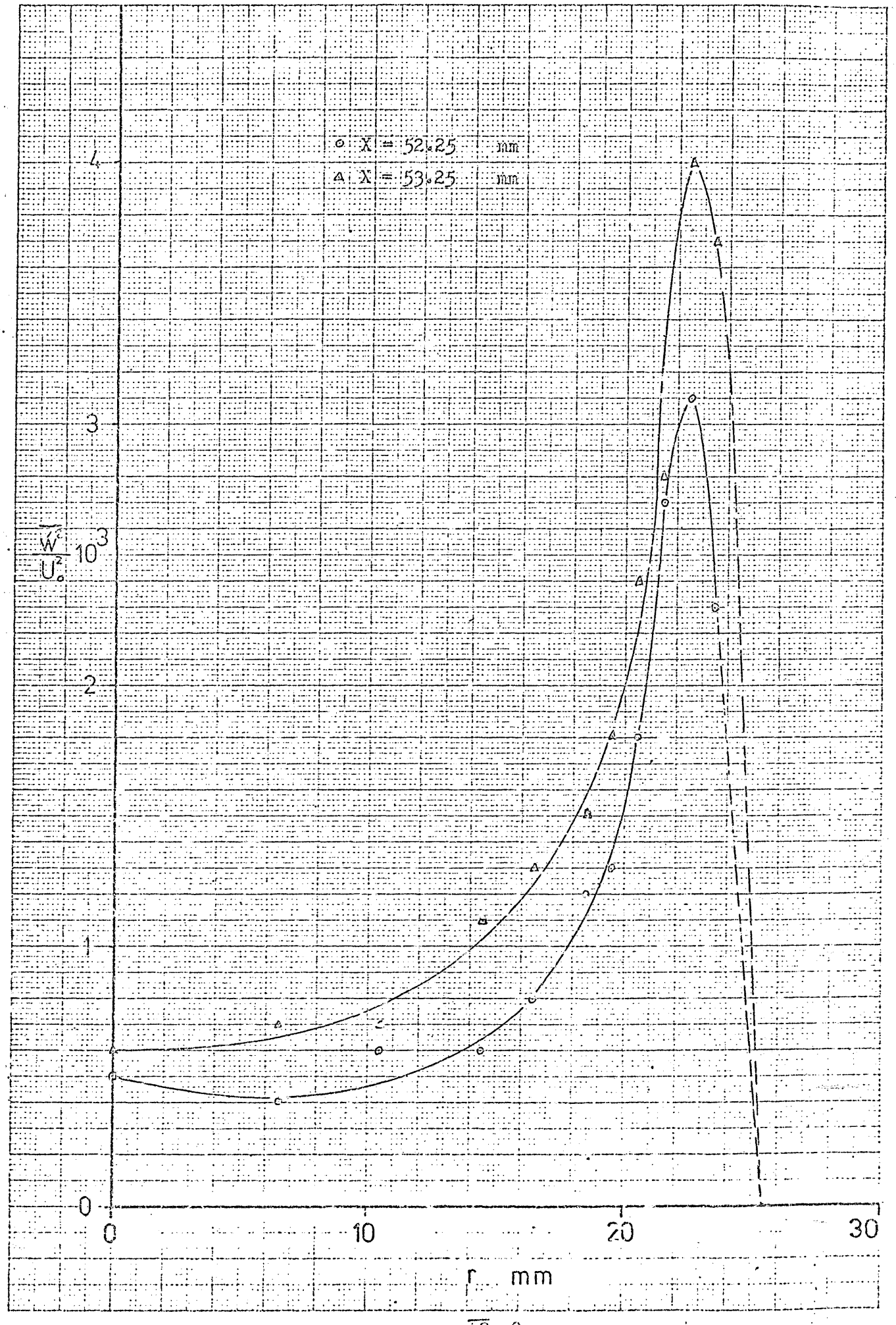

Fig.(F7-3): The distribution of $\overline{w^2}/U_o^2$ in region (4).

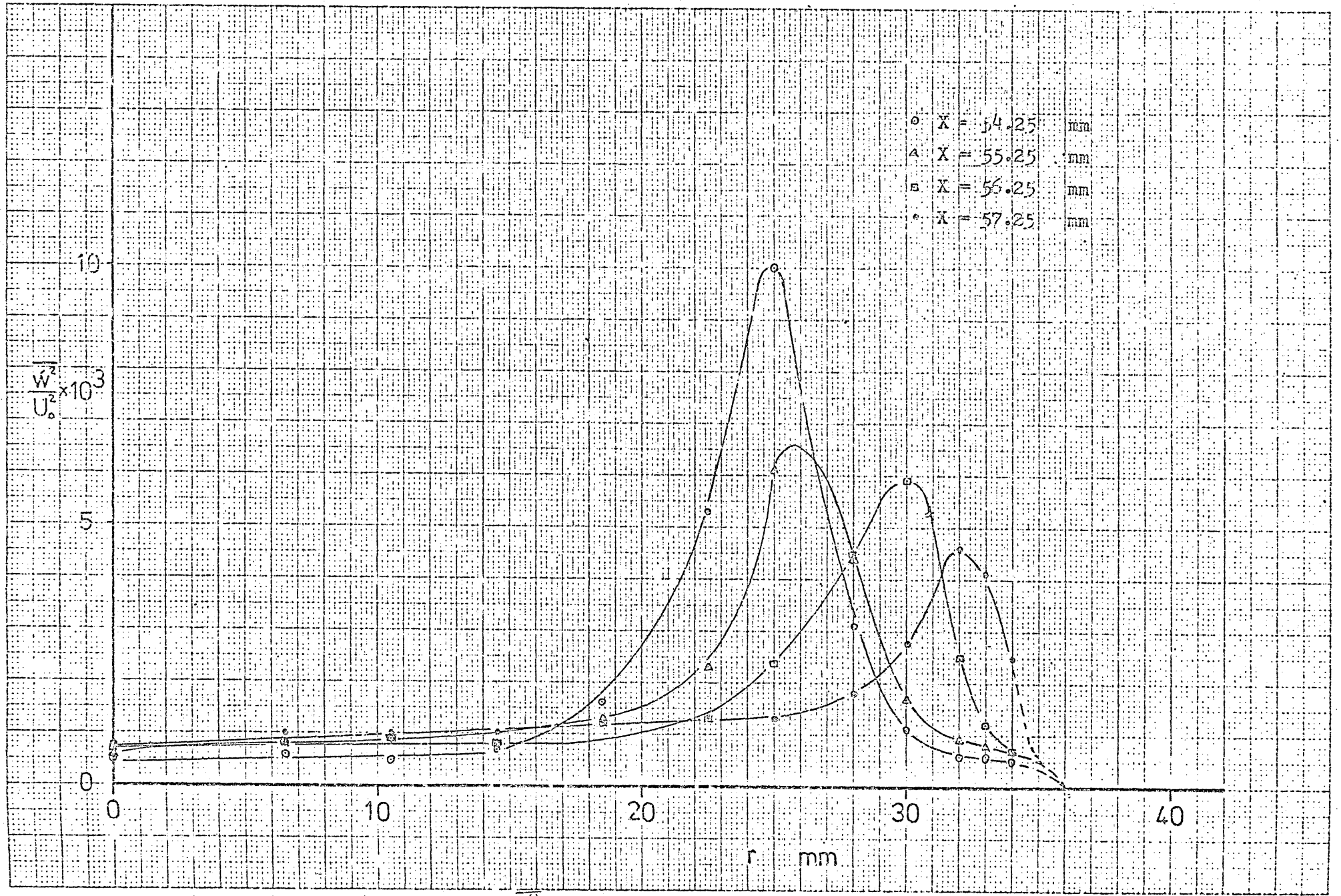

Fig.(F7-4): The distribution of $\overline{w^2}/U_o^2$ in region (5).

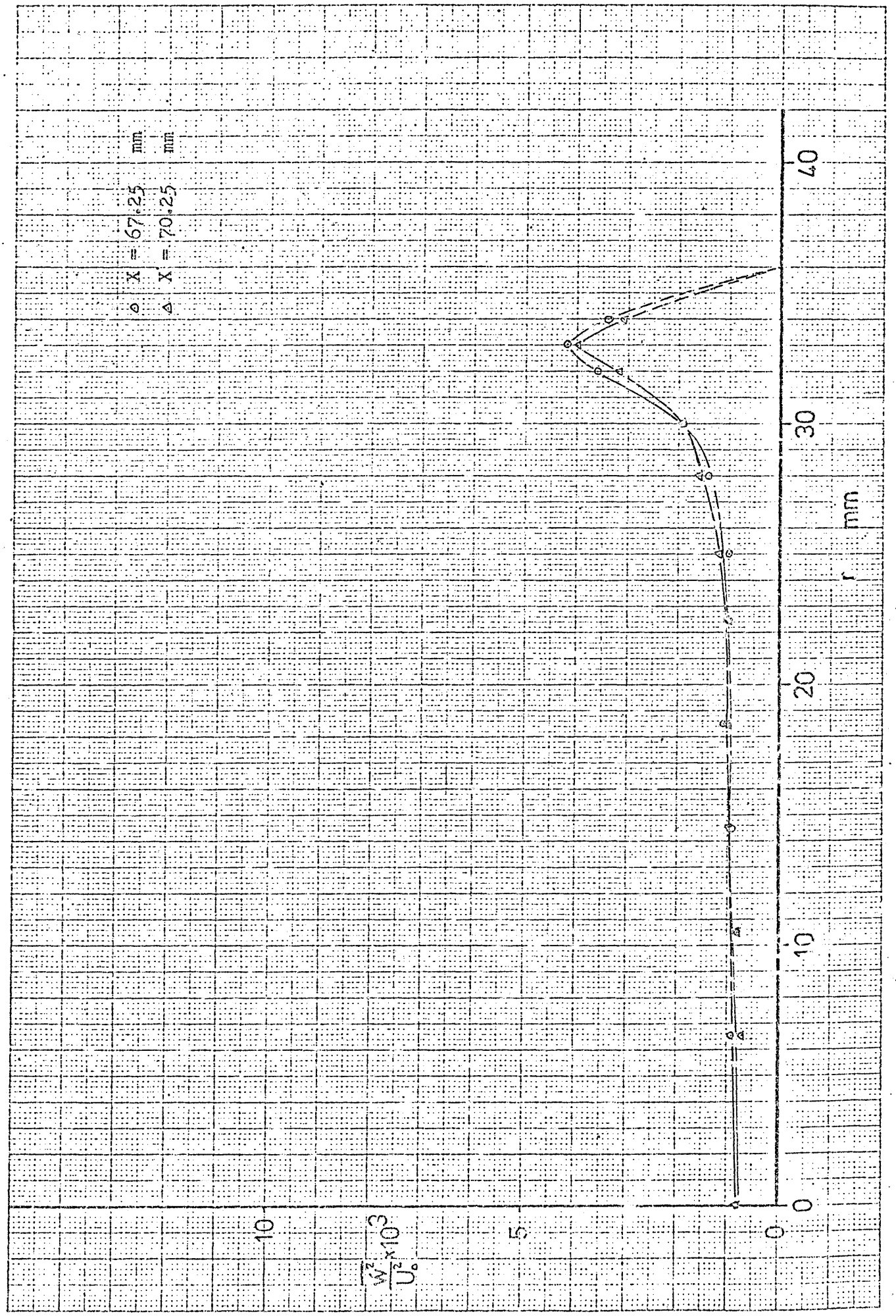

Fig.(F7-5): The distribution of $\overline{w^2}/U_o^2$ in region (6).

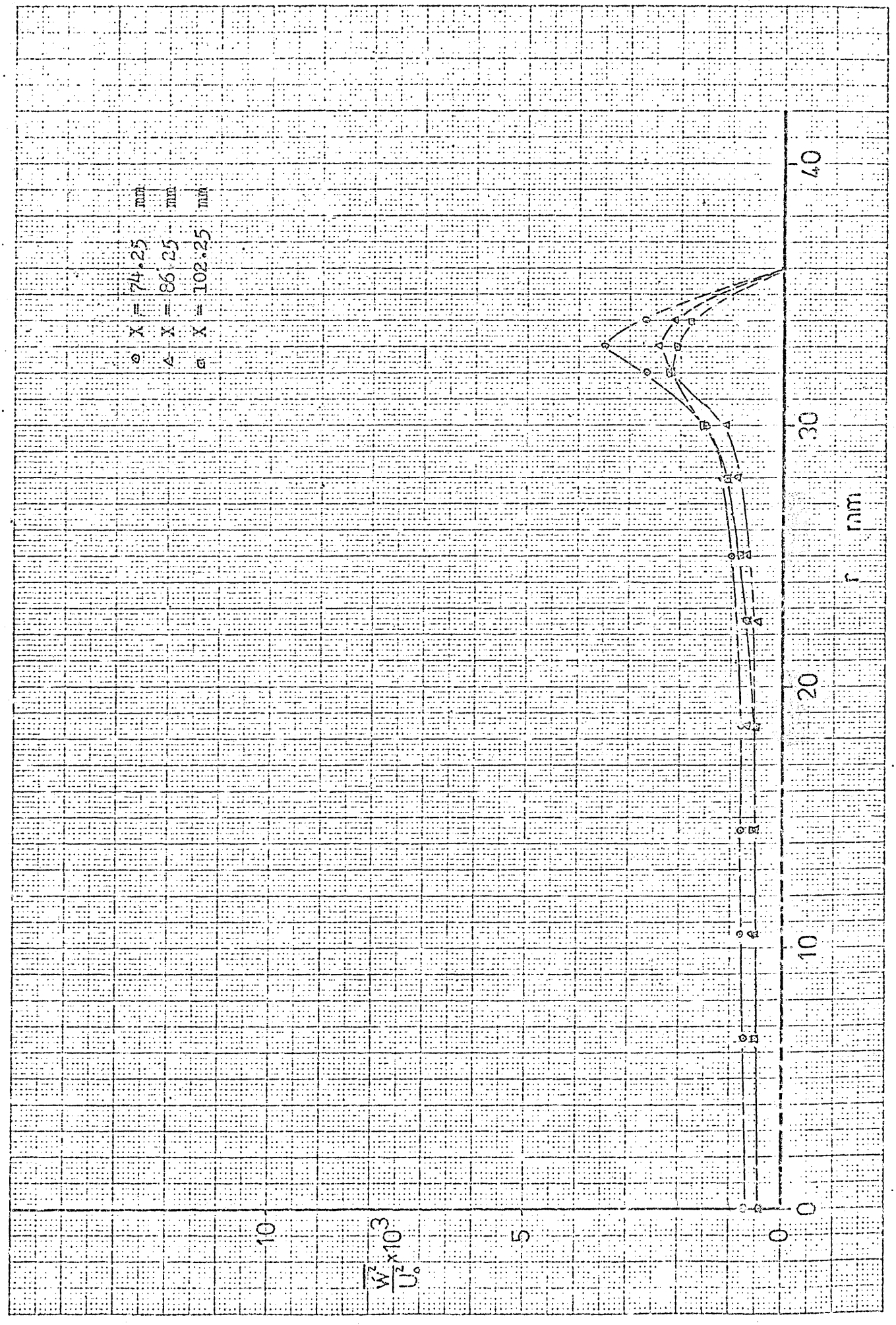

Fig.(F7-6): The distribution of $\overline{w^2}/U_o^2$ in region (7).

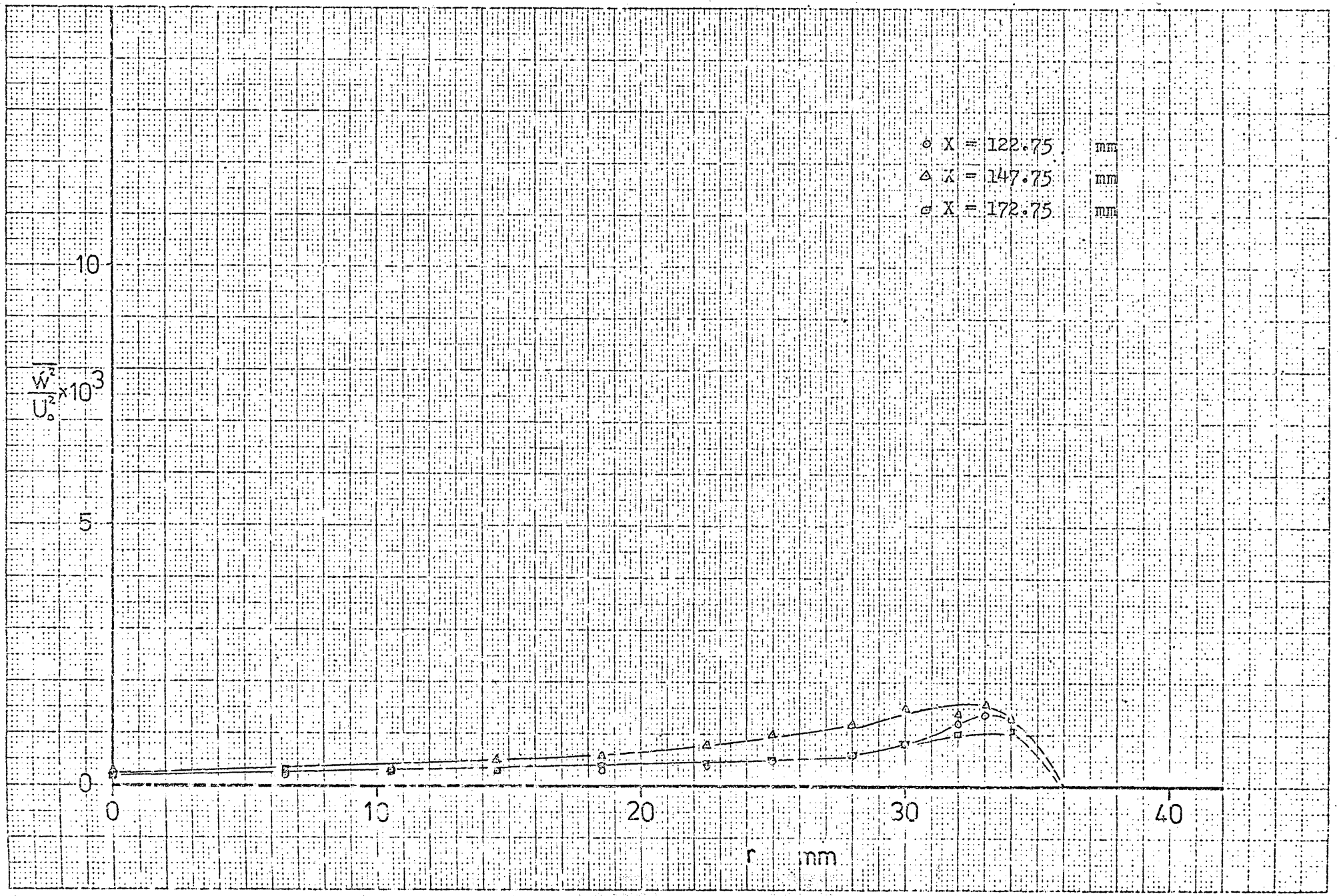

Fig.(F7-7): The distribution of $\overline{w^2}/U_o^2$ in region (8).

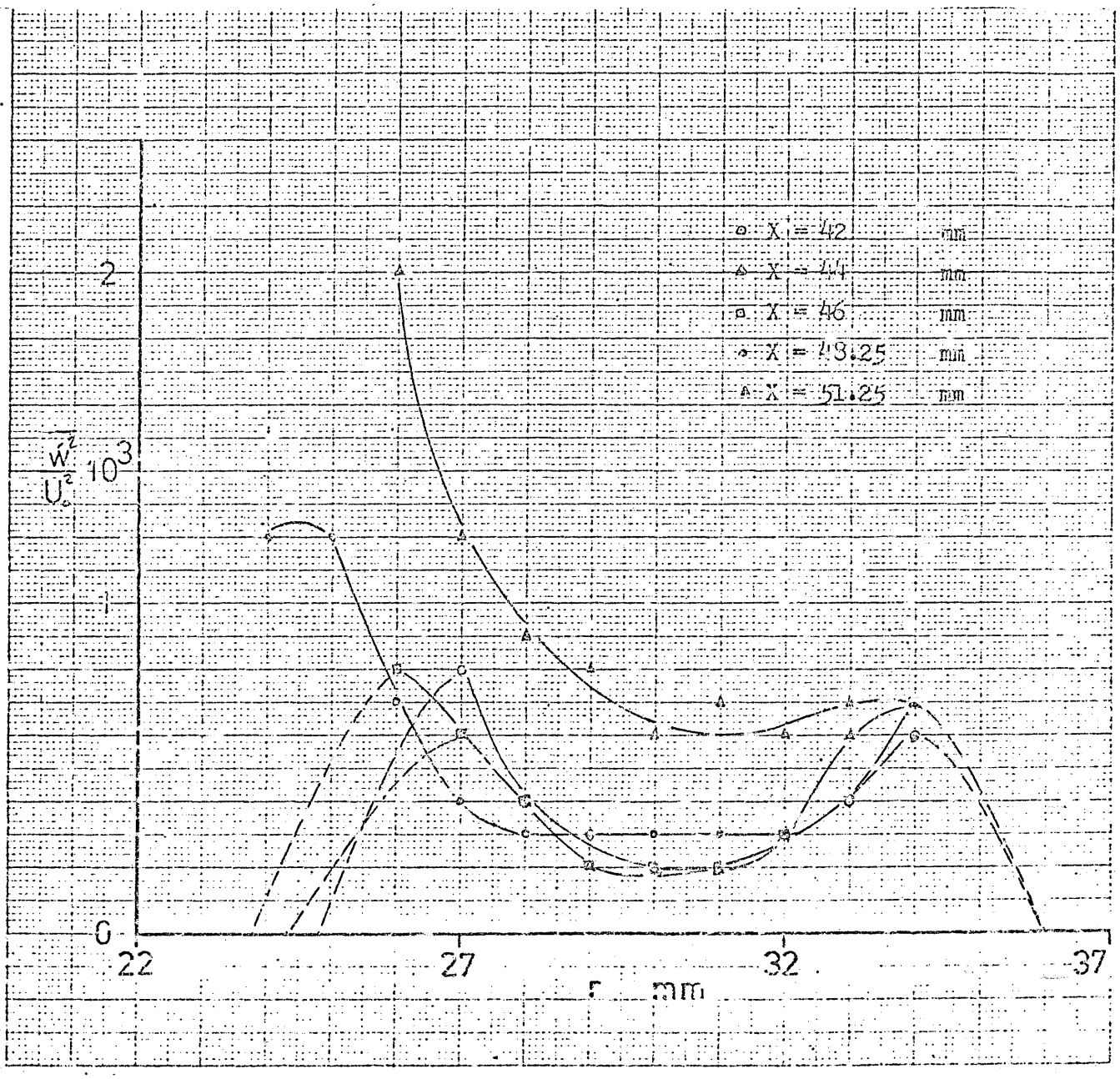

Fig.(F7-8): The distribution of $\overline{w^2}/u_o^2$ in region (9).

Appendix F8: The distribution of the kinetic energy of tubulence

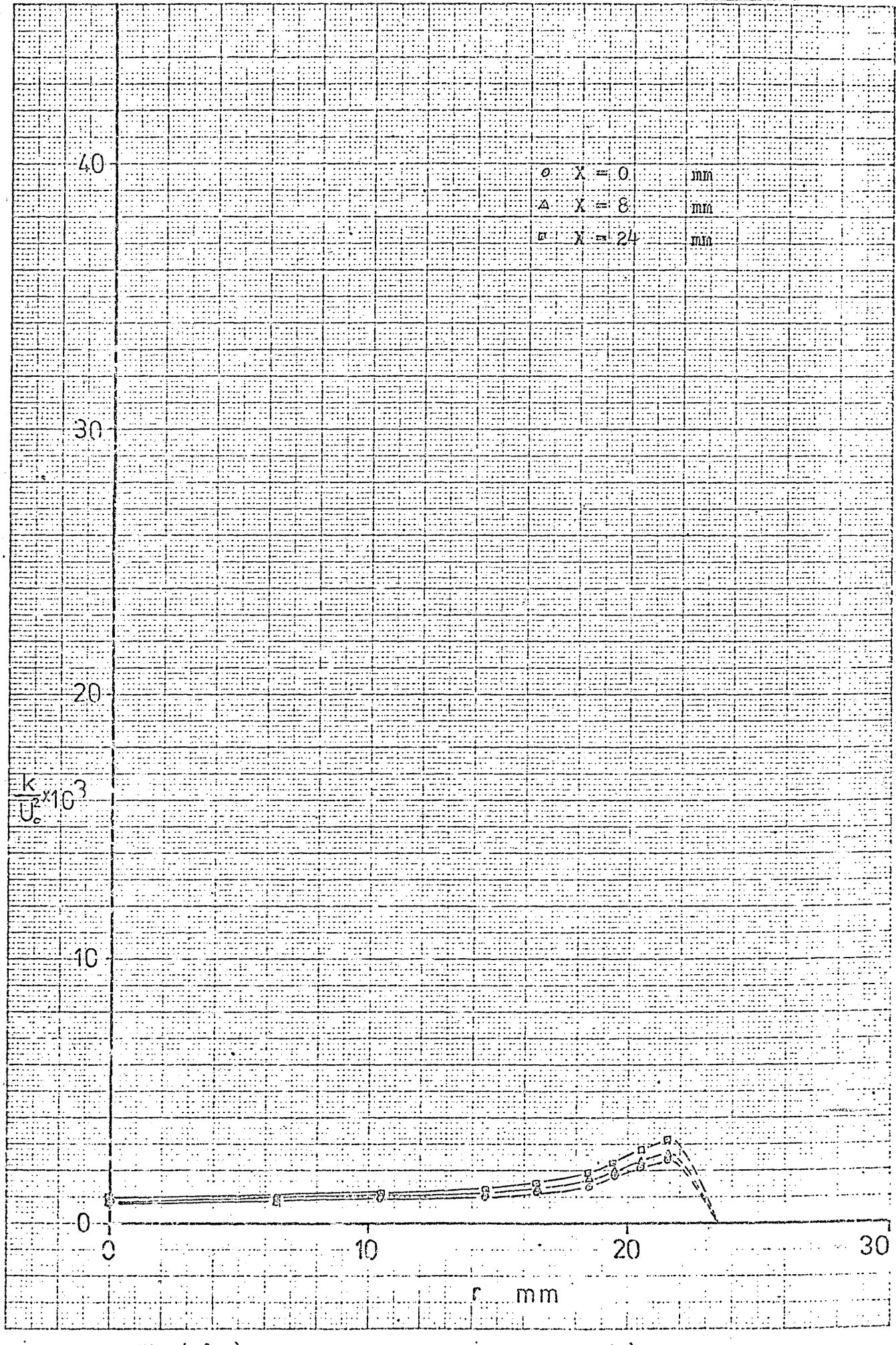

Fig.(F8-1): The distribution of k in region (1).

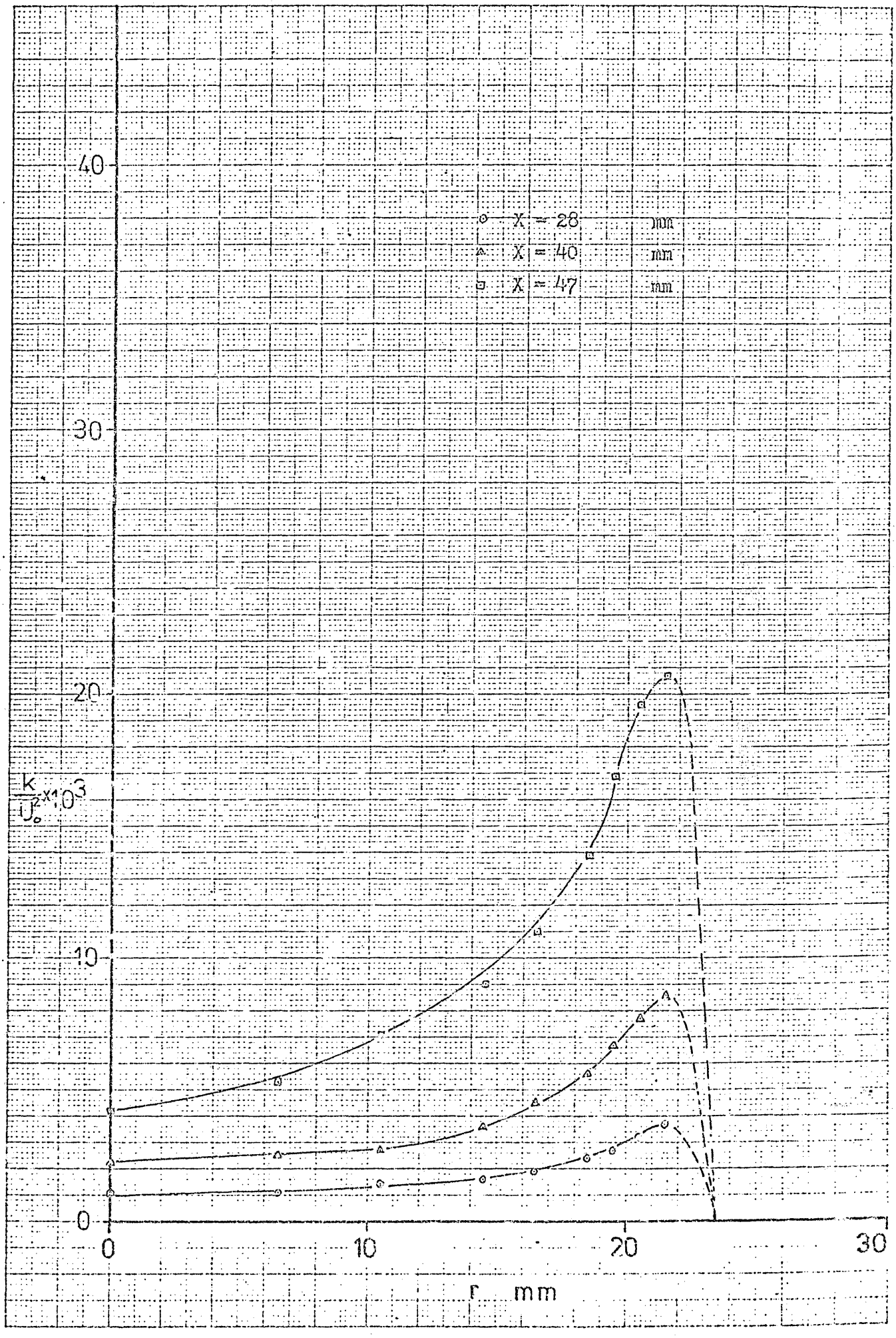

Fig.(F8-2): The distribution of k in region (2).

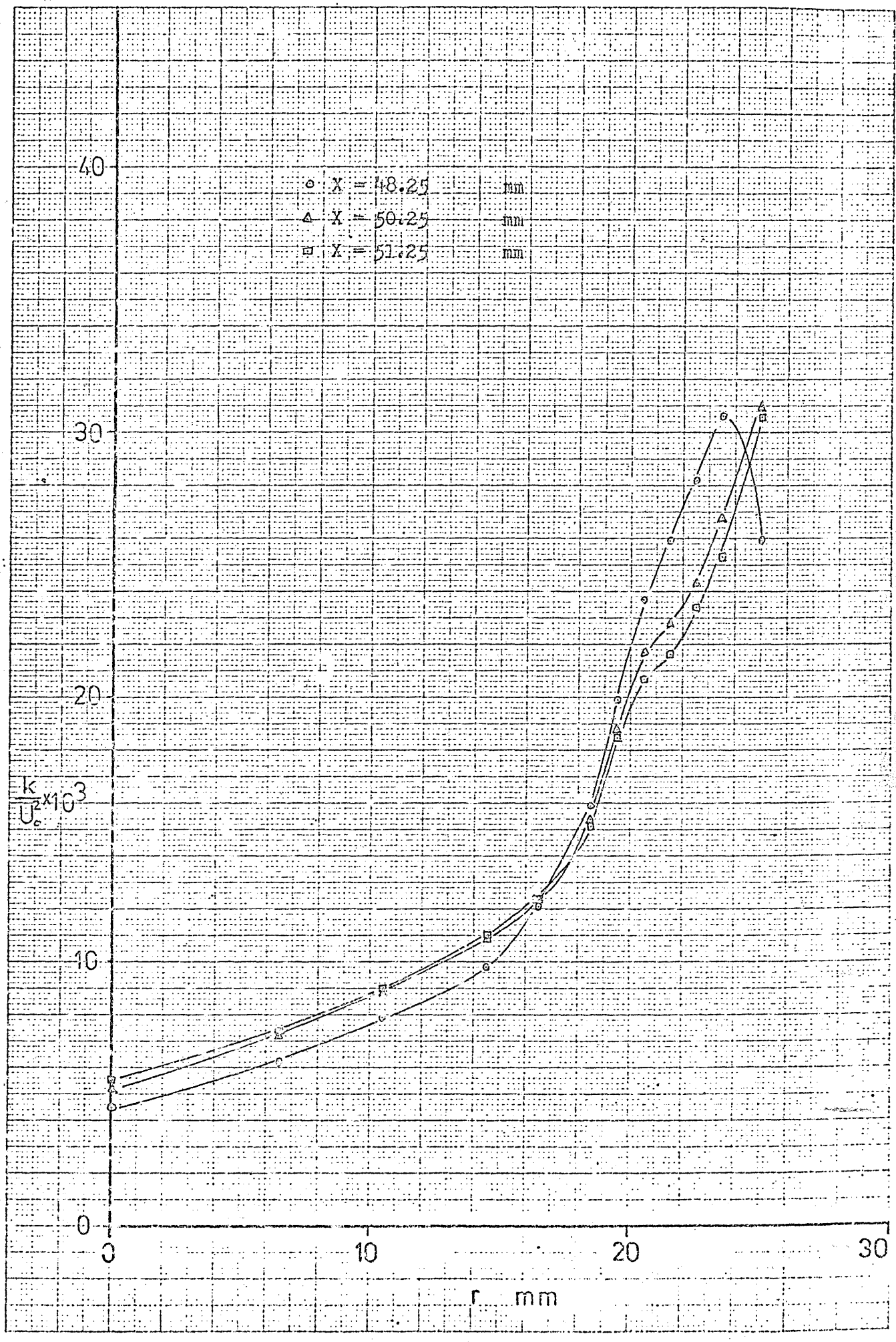

Fig.(F2-3): The distribution of k in region (3).

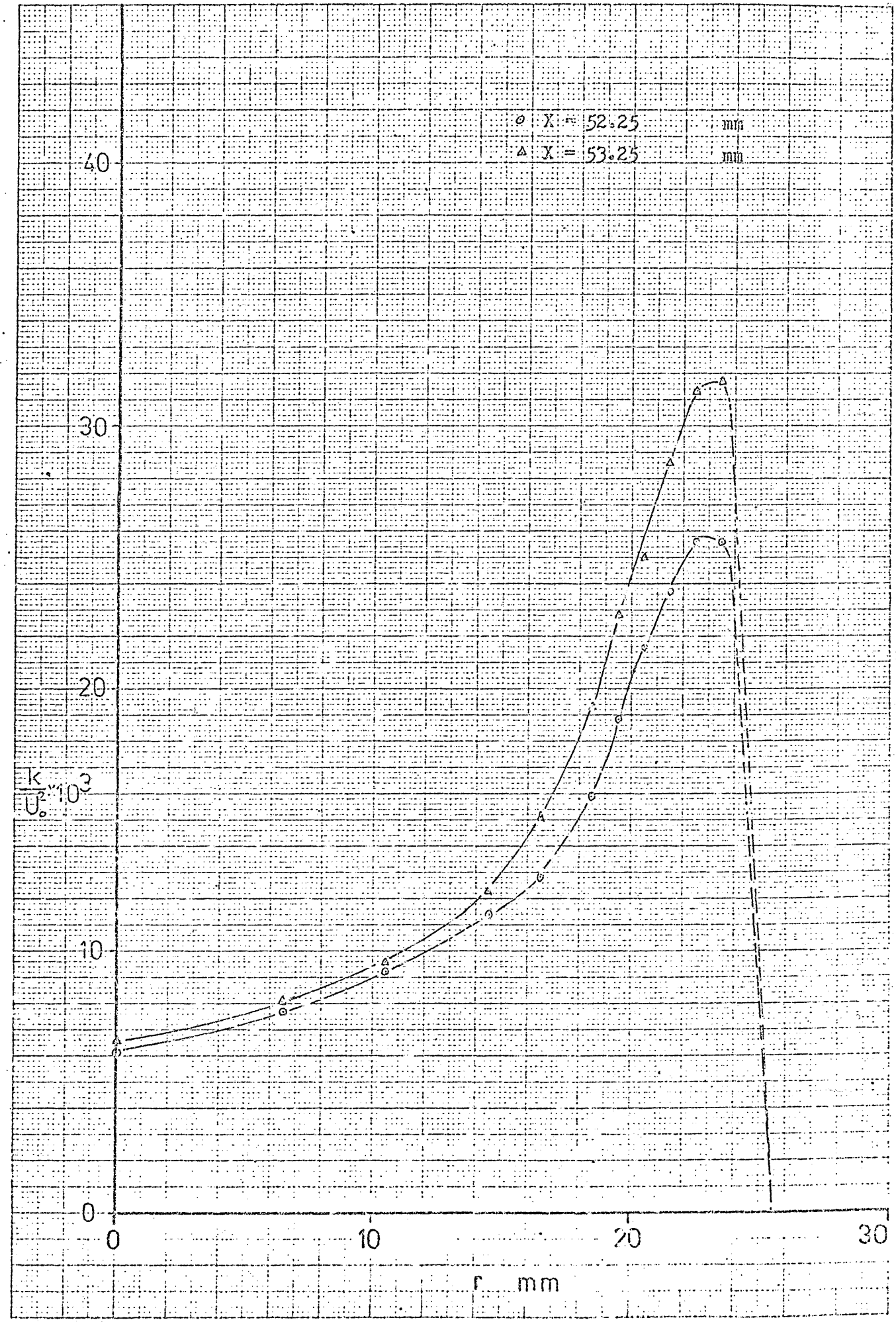

Fig. (F8-4): The distribution of k in region (4).

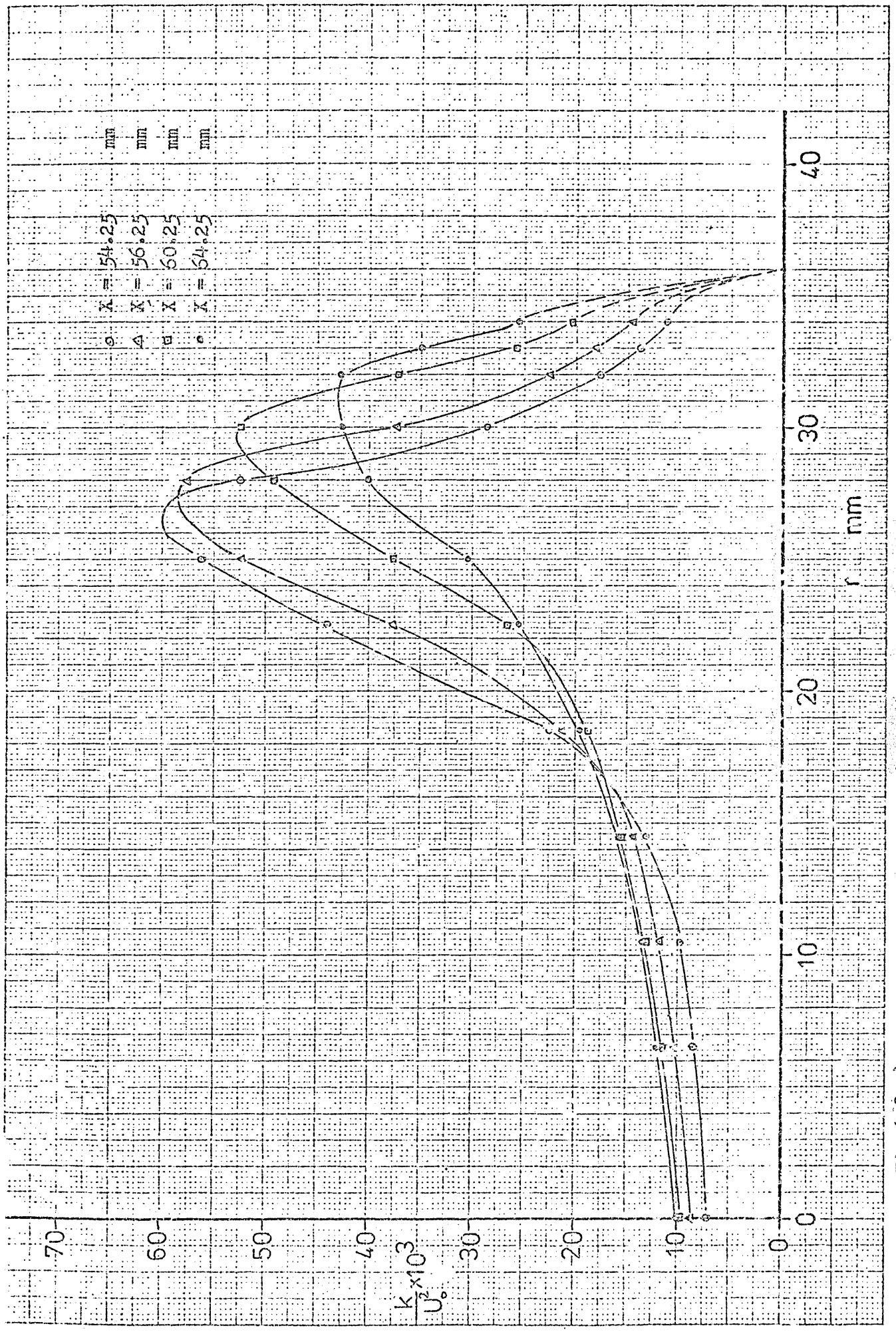

Fig.(F8-5): The distribution of k in region (C)

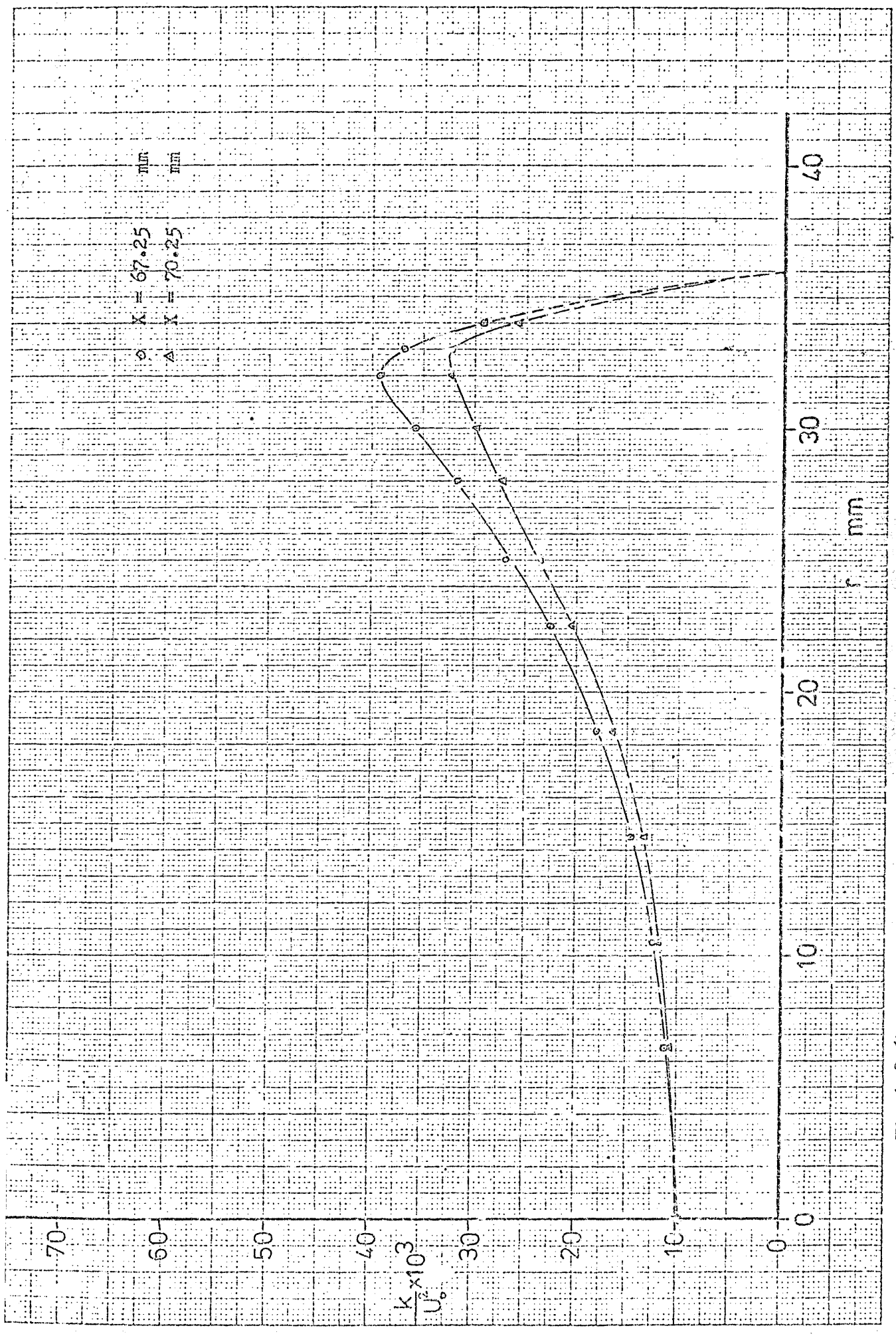

Fig.(F8-5): The distribution of k in region (6).

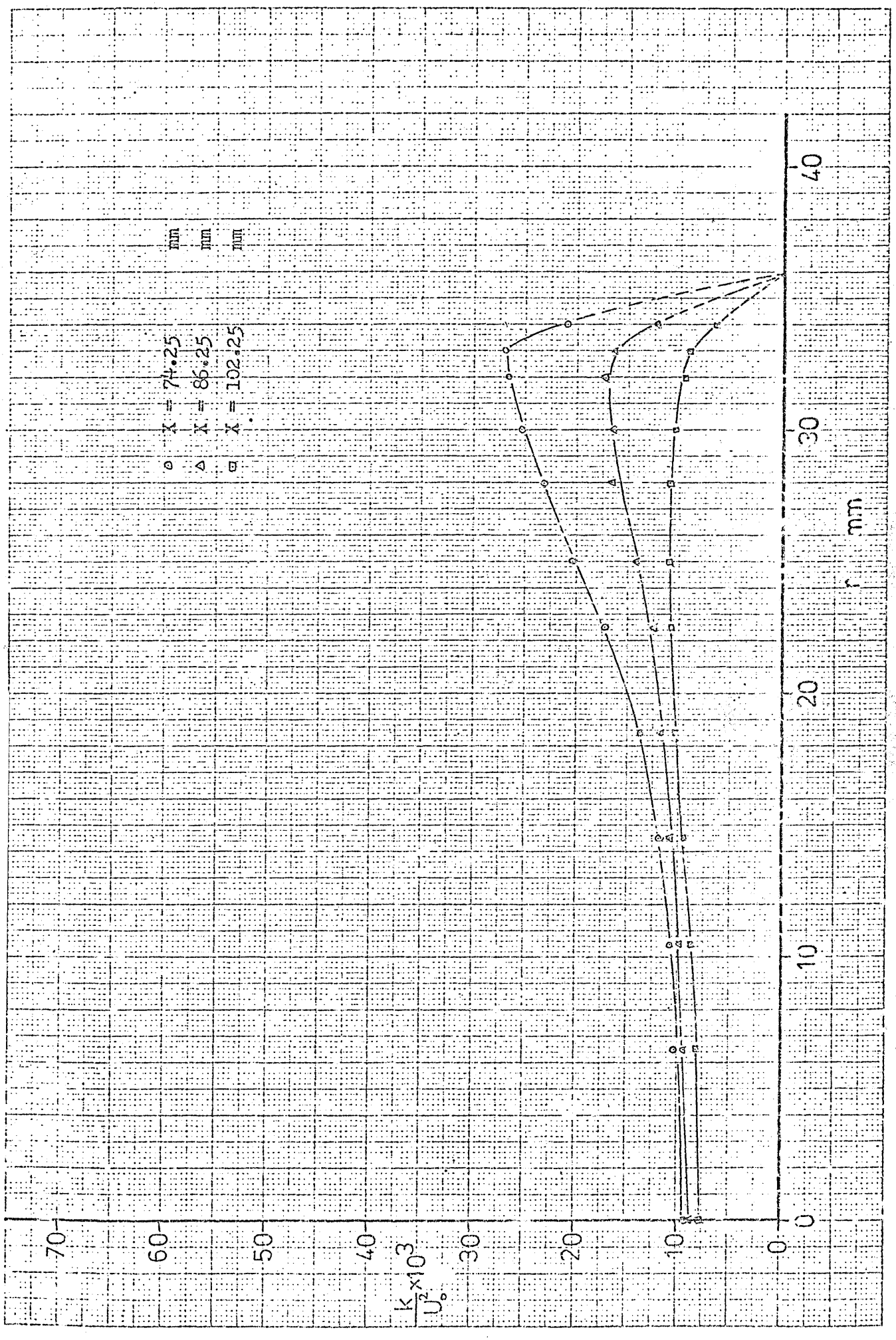

Fig.(FC-7): The distribution of K in region (7).

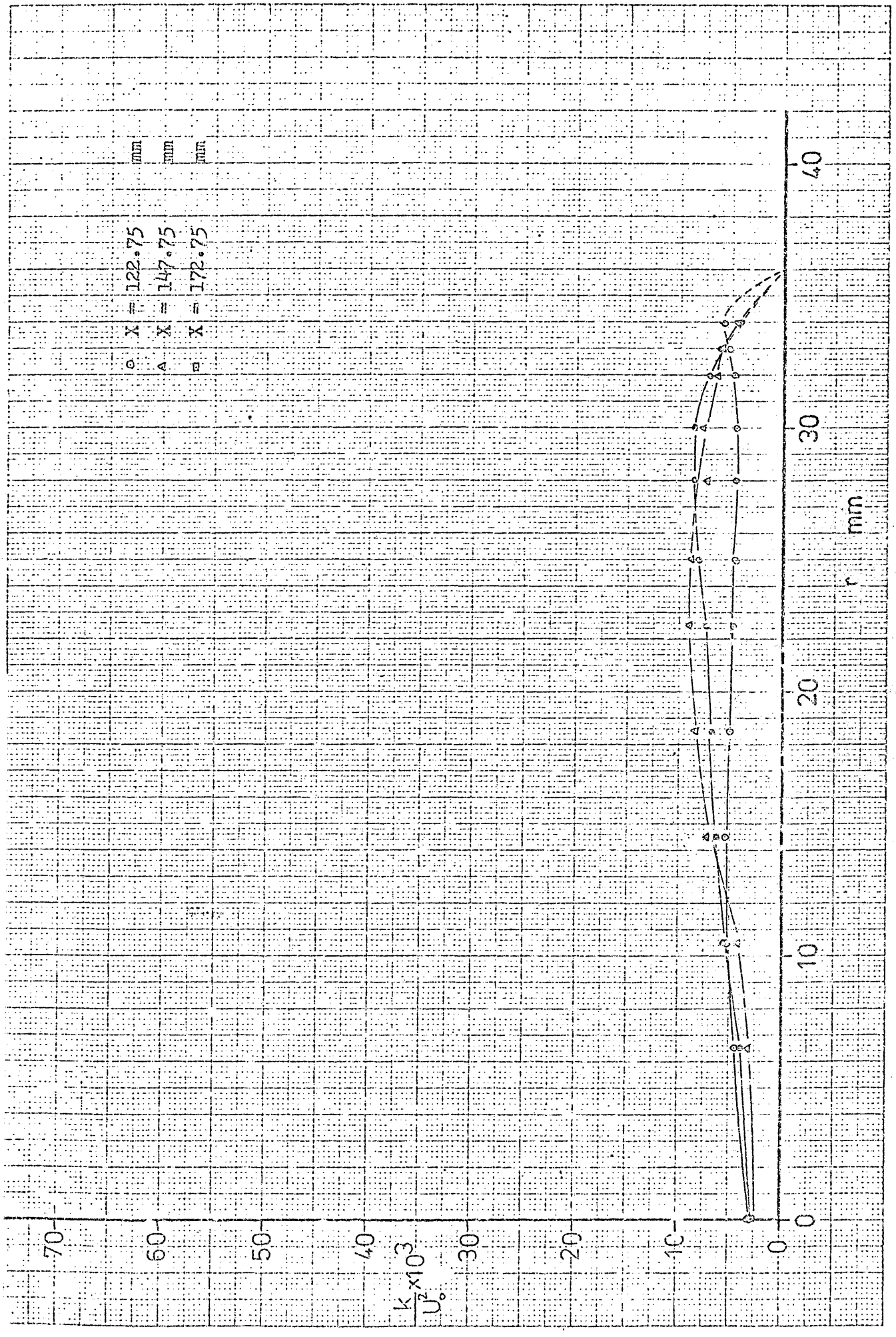

Fig. (F8-8): The distribution of k in region (8).

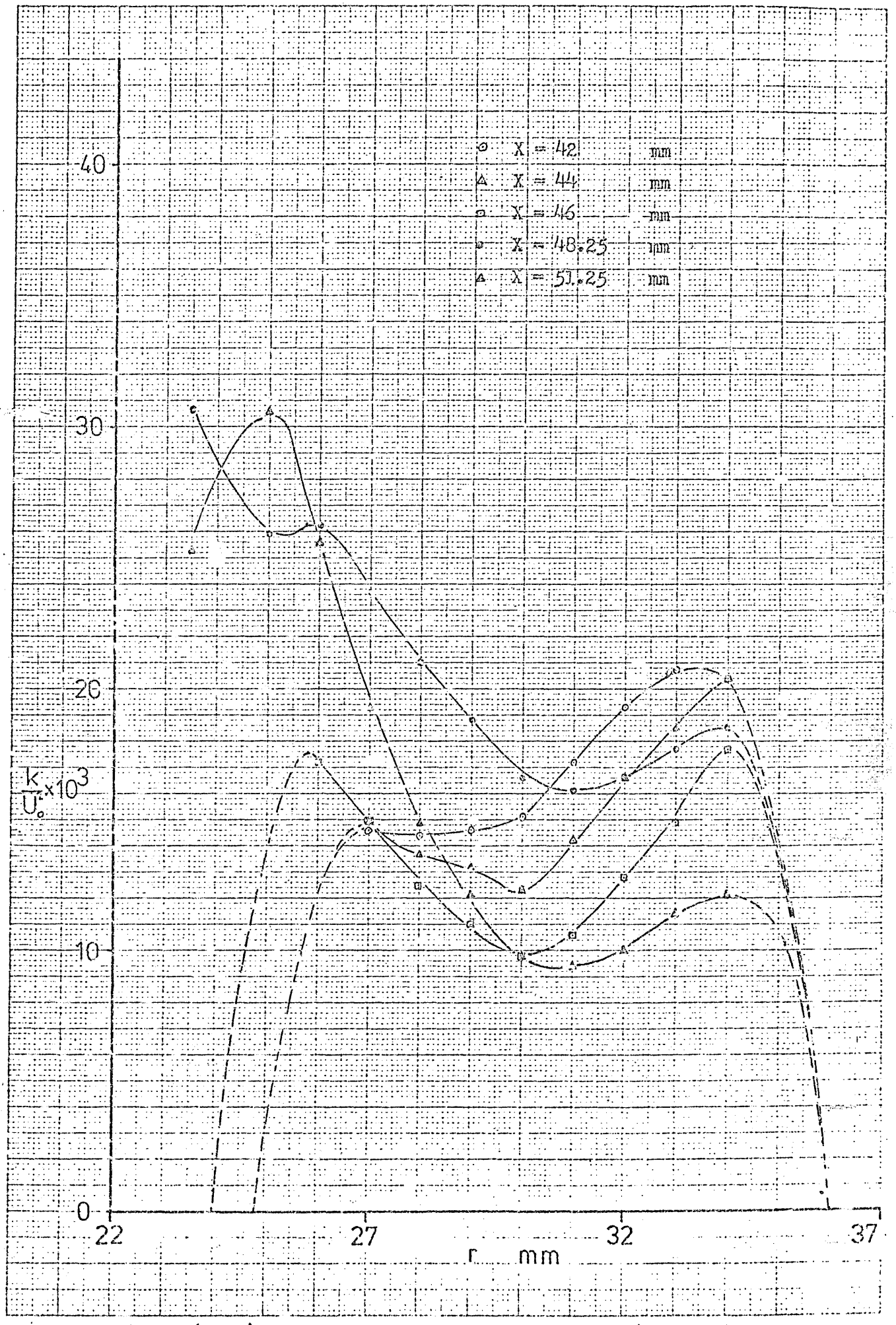

Fig.(F8-9): The distribution of k in region (9).

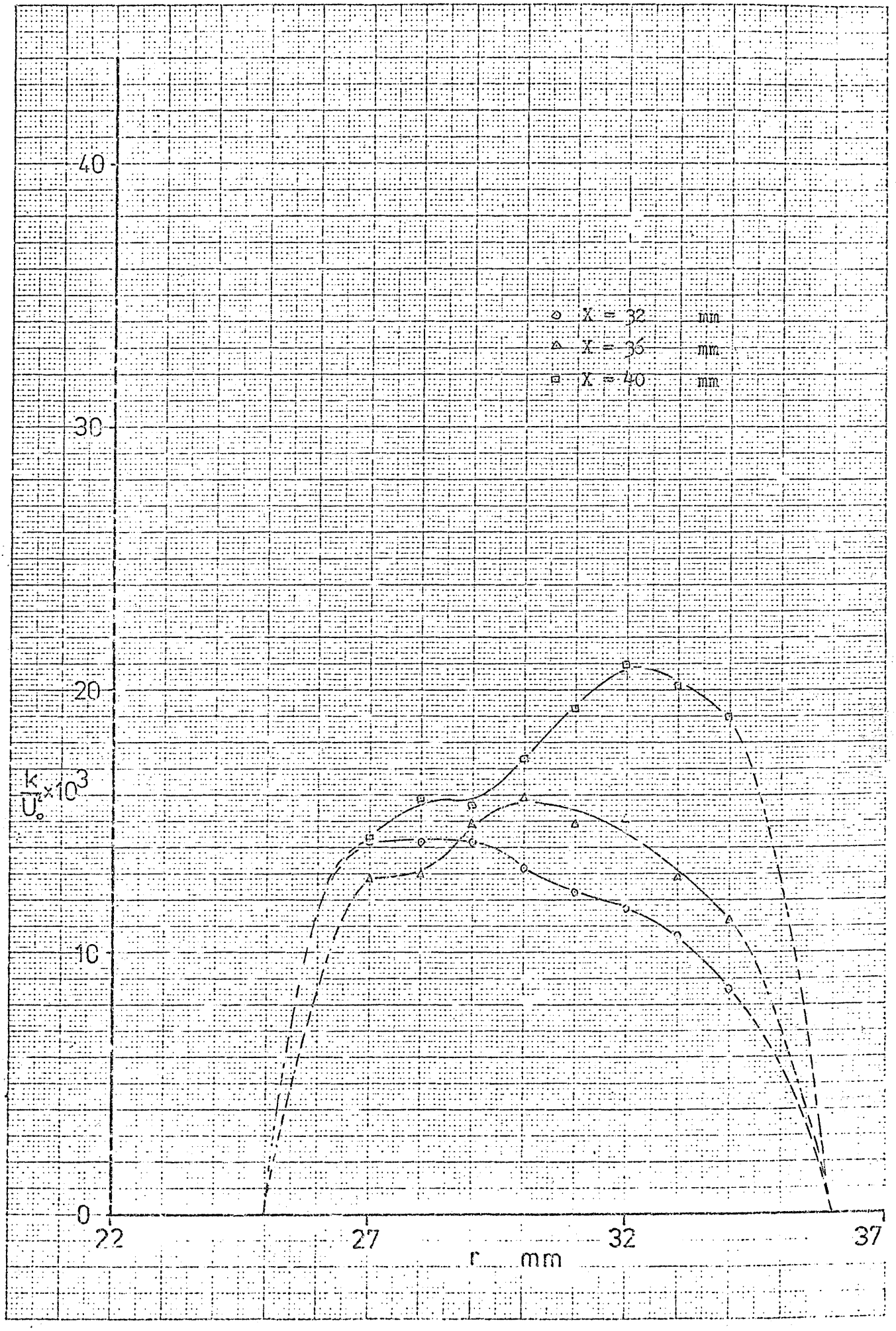

Fig.(F6-10): The distribution of k in region (10).

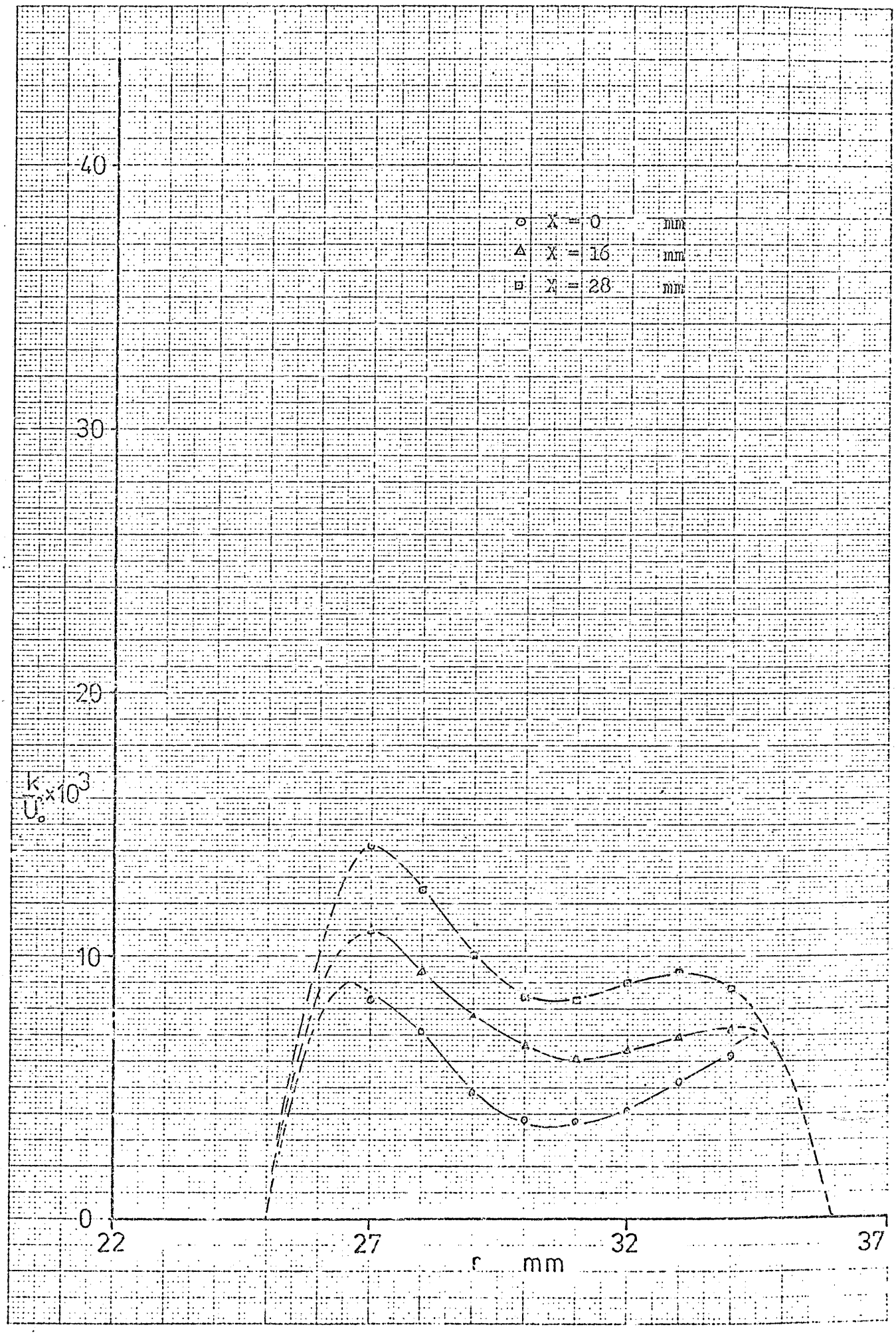

Fig.(F8-11): The distribution of k in region (11).

Appendix G: A print out of the computer programme.

```
      MASTER SAAD
      REAL MU
      COMMON/CGRID/R(26),X(37)
      COMMON/CVLO/UO(26,37),VO(26,37)
      COMMON/CKETO/TO(26,37)
      COMMON/CSP/SP(26,37)
      COMMON/CLCONS/CON,CTO,CTR,CFO,CFV,CSX
      COMMON/CDIMS/RP,RS,RPO,RF,RIC
      COMMON/CROH/ROH
      COMMON/CFMU/MU
      COMMON/CMUEF/CMU
      COMMON/CKEEG/CD,SEGK
      COMMON/CLSEG/CA,CB,SEGL
      COMMON/CLS/AL(26,37)
      COMMON/CSTFU/EPSI(26,37)
      COMMON/CVORFU/OMEGA(26,37)
      COMMON/CKET/T(26,37)
      COMMON/CEPSIR/EPSIR(26,37)
      COMMON/COMEGAR/OMEGAR(26,37)
      COMMON/CTR/TR(26,37)
      COMMON/CALR/ALR(26,37)
      COMMON/CFVL/U(26,37),V(26,37)
      COMMON/CCPCL/CP(26,37),CL(26,37)
      COMMON/COPER/SPOT,ALPHO,VOI,SPET,ALPHE,VE,CPT,CLT
      COMMON/CK/K
      COMMON/CM/MEPSI,NOMEC4,MT,MAL
      COMMON ZA(26,37),ZB(26,37),ZC(26,37),ZD(26,37),ZE(26,37)
     1,ZF(26,37),ZG(26,37),ZH(26,37),ZI(26,37),ZJ(26,37)
     2,ZK(26,37),ZL(26,37),ZM(26,37),ZN(26,37),ZO(26,37)
     3,ZP(26,37),ZQ(26,37),ZR(26,37),ZS(26,37),ZT(26,37),ZU(26,37)
C
C           ***********************************************
C           *                                             *
C           * THIS IS THE MAIN PROGRAMME USED FOR THE     *
C           *                                             *
C           * PREDICTION OF THE FLOW AND THE PERFORMANCE  *
C           *                                             *
C           * PARAMETERS OF THE CRANFIELD DIFFUSER        *
C           *                                             *
C           ***********************************************
C
      CALL HASSAN
      DO 10 J=1,25
      AL(J,37)=(RS*CON)-(CTO*R(J)*R(J)/RS)-(((CON-CTO)*(R(J)**4.0))/(RS**
     1*3.0))
   10 CONTINUE
      DO 11 J=1,10
      AL(J,1)=(RP*CTR)-(CFO*R(J)*R(J)/RP)-(((CTR-CFO)*(R(J)**4.0))/(RP**3
     1.0))
   11 CONTINUE
      DO 12 J=14,22
      DO 12 I=1,14
      AL(J,I)=((RIC-RPO)*CFV)-(CSX*((RIC-R(J))**2.0)/(RIC-RPO))-(((CFV-CS
     1X)*((RIC-R(J))**4.0)/((RIC-RPO)**3.0))
   12 CONTINUE
      DO 13 J=22,25
      DO 13 I=1,14
      AL(J,I)=((RS-RIC)*CFV)-((CSX*((R(J)-RIC)**2.0))/(RS-RIC))-(((CFV-C
     1SX)*((R(J)-RIC)**4.0))/((RS-RIC)**3.0))
   13 CONTINUE
      DO 14 I=2,36
      AL(1,I)=(RP*CTR)+(X(I)*(CS*CON-RP*CTR)/.07035)
   14 CONTINUE
      DO 15 I=1,37
      AL(26,I)=.0
   15 CONTINUE
      DO 16 I=1,14
      AL(11,I)=.0
      AL(13,I)=.0
   16 CONTINUE
      AL(12,14)=.0
      DO 17 J=14,25
      AL(J,19)=.0
      AL(J,20)=.0
   17 CONTINUE
```

```
      DO 18 J=2,25
      DO 18 I=15,18
      AL(J,I)=AL(1,I)-(CTO*R(J)*R(J)/RS)-(((CON-CTO)*(R(J)**4.0)/(RS**3.0
     1))
   18 CONTINUE
      DO 19 J=2,25
      DO 19 I=21,36
      AL(J,I)=AL(1,I)-(CTO*R(J)*R(J)/RS)-(((CON-CTO)*(R(J)**4.0)/(RS**3.0
     1))
   19 CONTINUE
      DO 20 J=2,13
      DO 20 I=19,20
      AL(J,I)=AL(1,I)-(CTO*R(J)*R(J)/RF)-(((CON-CTO)*(R(J)**4.0)/(RF**3.0
     1))
   20 CONTINUE
      DO 21 J=2,10
      DO 21 I=2,14
      AL(J,I)=AL(1,I)-(CTO*R(J)*R(J)/RP)-(((CON-CTO)*(R(J)**4.0)/(RP**3.0
     1))
   21 CONTINUE
      DO 25 J=22,25
      DO 25 I=15,36
      AL(J,I)=ABS(AL(J,I))
   25 CONTINUE
      DO 30 I=1,37
      EPSI(1,I)=0.0
   30 CONTINUE
      DO 31 J=2,26
      EPSI(J,37)=EPSI(J-1,37)+ROH*((UO(J-1,37)*R(J-1)+UO(J,37)*R(J))/2.0
     1)*(R(J)-R(J-1))
   31 CONTINUE
      DO 32 I=20,36
      EPSI(26,I)=EPSI(26,37)
   32 CONTINUE
      DO 33 J=14,25
      EPSI(J,20)=EPSI(26,37)
   33 CONTINUE
      DO 34 J=2,11
      EPSI(J,1)=EPSI(J-1,1)+ROH*((UO(J-1,1)*R(J-1)+UO(J,1)*R(J))/2.0)*(R
     1(J)-R(J-1))
   34 CONTINUE
      DO 35 I=2,14
      EPSI(11,I)=EPSI(11,1)
   35 CONTINUE
      DO 36 I=1,14
      EPSI(13,I)=EPSI(11,1)
   36 CONTINUE
      EPSI(12,14)=EPSI(11,1)
      DO 37 J=14,25
      EPSI(J,1)=EPSI(J-1,1)+ROH*((UO(J-1,1)*R(J-1)+UO(J,1)*R(J))/2.0)*(R
     1(J)-R(J-1))
   37 CONTINUE
      DO 38 I=2,19
      EPSI(26,I)=EPSI(26,1)
   38 CONTINUE
      DO 39 J=14,25
      EPSI(J,19)=EPSI(26,1)
   39 CONTINUE
      DO 40 J=2,10
      DO 40 I=2,36
      EPSI(J,I)=EPSI(J-1,I)+ROH*((UO(J-1,I)*R(J-1)+UO(J,I)*R(J))/2.0)*(R
     1(J)-R(J-1))
   40 CONTINUE
      DO 41 J=11,13
      DO 41 I=15,36
      EPSI(J,I)=EPSI(J-1,I)+ROH*((UO(J-1,I)*R(J-1)+UO(J,I)*R(J))/2.0)*(R
     1(J)-R(J-1))
   41 CONTINUE
      DO 42 J=14,25
      DO 42 I=2,18
      EPSI(J,I)=EPSI(J-1,I)+ROH*((UO(J-1,I)*R(J-1)+UO(J,I)*R(J))/2.0)*(R
     1(J)-R(J-1))
   42 CONTINUE
      DO 43 J=14,25
      DO 43 I=21,36
      EPSI(J,I)=EPSI(J-1,I)+ROH*((UO(J-1,I)*R(J-1)+UO(J,I)*R(J))/2.0)*(R
     1(J)-R(J-1))
   43 CONTINUE
      DO 50 J=2,25
      OMEGA(J,37)=(2.0/(ROH*R(J)*R(J)*(R(J-1)-R(J+1))))*((EPSI(J+1,37)-
     1EPSI(J,37))/(R(J+1)-R(J))-(EPSI(J,37)-EPSI(J-1,37))/(R(J)
     2-R(J-1)))
```

```
   50 CONTINUE
      DO 51 J=2,10
      OMEGA(J,1)=(2.0/(ROH*R(J)*R(J)*(R(J-1)-R(J+1))))*((EPSI(J+1,1)-
     1EPSI(J,1))/(R(J+1)-R(J))-(EPSI(J,1)-EPSI(J-1,1))/(R(J)-R(
     2J-1)))
   51 CONTINUE
      DO 52 J=14,25
      OMEGA(J,1)=(2.0/(ROH*R(J)*R(J)*(R(J-1)-R(J+1))))*((EPSI(J+1,1)-
     1EPSI(J,1))/(R(J+1)-R(J))-(EPSI(J,1)-EPSI(J-1,1))/(R(J)-R(
     2J-1)))
   52 CONTINUE
      DO 53 J=2,10
      DO 53 I=2,36
      OMEGA(J,I)=((VO(J,I+1)-VO(J,I-1))/(X(I+1)-X(I-1))-(UO(J+1,I)-UO(J-
     11,I))/(R(J+1)-R(J-1)))/R(J)
   53 CONTINUE
      DO 54 J=11,13
      DO 54 I=15,36
      OMEGA(J,I)=((VO(J,I+1)-VO(J,I-1))/(X(I+1)-X(I-1))-(UO(J+1,I)-UO(J-
     11,I))/(R(J+1)-R(J-1)))/R(J)
   54 CONTINUE
      DO 55 J=14,25
      DO 55 I=2,13
      OMEGA(J,I)=((VO(J,I+1)-VO(J,I-1))/(X(I+1)-X(I-1))-(UO(J+1,I)-UO(J-
     11,I))/(R(J+1)-R(J-1)))/R(J)
   55 CONTINUE
      DO 56 J=14,25
      DO 56 I=21,36
      OMEGA(J,I)=((VO(J,I+1)-VO(J,I-1))/(X(I+1)-X(I-1))-(UO(J+1,I)-UO(J-
     11,I))/(R(J+1)-R(J-1)))/R(J)
   56 CONTINUE
      DO 58 J=1,26
      DO 58 I=1,37
      T(J,I)=TO(J,I)
   58 CONTINUE
      CALL NAEL
      K=1
    7 CALL WAEL
      MEPSI=26*37
      DO 300 J=1,26
      DO 300 I=1,37
      IF(ABS(EPSIR(J,I)).LT.0.000005)GO TO 260
      IF((ABS(EPSIR(J,I)-EPSI(J,I))/ABS(EPSIR(J,I))).LT.0.005)
     1MEPSI=MEPSI-1
  260 IF(ABS(EPSIR(J,I)).LT.0.000005)MEPSI=MEPSI-1
      IF(ABS(EPSIR(J,I)).LT.0.000005)GO TO 270
      IF((ABS(EPSIR(J,I)-EPSI(J,I))/ABS(EPSIR(J,I))).GT.0.005)
     1EPSI(J,I)=EPSIR(J,I)
  270 IF(ABS(EPSIR(J,I)).LT.0.000005)EPSI(J,I)=EPSIR(J,I)
  300 CONTINUE
      CALL KOTKOT
      MOMEGA=26*37
      DO 400 J=1,26
      DO 400 I=1,37
      IF(ABS(OMEGAR(J,I)).LT.0.000005)GO TO 360
      IF((ABS(OMEGAR(J,I)-OMEGA(J,I))/ABS(OMEGAR(J,I))).LT.
     10.005)MOMEGA=MOMEGA-1
  360 IF(ABS(OMEGAR(J,I)).LT.0.000005)MOMEGA=MOMEGA-1
      IF(ABS(OMEGAR(J,I)).LT.0.000005)GO TO 370
      IF((ABS(OMEGAR(J,I)-OMEGA(J,I))/ABS(OMEGAR(J,I))).GT.
     10.005)OMEGA(J,I)=OMEGAR(J,I)
  370 IF(ABS(OMEGAR(J,I)).LT.0.000005)OMEGA(J,I)=OMEGAR(J,I)
  400 CONTINUE
      CALL CHAZO
      MT=26*37
      DO 500 J=1,26
      DO 500 I=1,37
      IF(ABS(TR(J,I)).LT.0.000005)GO TO 460
      IF((ABS(TR(J,I)-T(J,I))/ABS(TR(J,I))).LT.0.005)
     1MT=MT-1
  460 IF(ABS(TR(J,I)).LT.0.000005)MT=MT-1
      IF(ABS(TR(J,I)).LT.0.000005)GO TO 470
      IF((ABS(TR(J,I)-T(J,I))/ABS(TR(J,I))).GT.0.005)
     1T(J,I)=TR(J,I)
  470 IF(ABS(TR(J,I)).LT.0.000005)T(J,I)=TR(J,I)
  500 CONTINUE
      CALL ABCKHALIL
      MAL=26*37
      DO 600 J=1,26
      DO 600 I=1,37
      IF(ABS(ALR(J,I)).LT.0.000005)GO TO 560
```

```
      IF((ABS(ALR(J,I)-AL(J,I))/ABS(ALR(J,I))).LT.0.005)
     1MAL=MAL-1
  560 IF(ABS(ALR(J,I)).LT.0.000005)MAL=MAL-1
      IF(ABS(ALR(J,I)).LT.0.000005)GO TO 570
      IF((ABS(ALR(J,I)-AL(J,I))/ABS(ALR
     1(J,I))).GT.0.005)AL(J,I)=ALR(J,I)
  570 IF(ABS(ALR(J,I)).LT.0.000005)AL(J,I)=ALR(J,I)
  600 CONTINUE
      WRITE(6,700)MEPSI,MOMEGA,MT,MAL,K
      IF(MEPSI.EQ.0.AND.MOMEGA.EQ.0.AND.MT.EQ.0.AND.MAL.EQ.0)GO TO 110
      IF(K.GT.100)GO TO 1000
      K=K+1
      GO TO 7
  110 CALL SAID
      CALL SAWSAN
      CALL SALWA
      CALL KAFAL
      CALL AHMED
      GO TO 2000
  700 FORMAT(/,10X,5I6)
 1000 WRITE(6,700)MEPSI,MOMEGA,MT,MAL,K
 2000 STOP
      END
      SUBROUTINE HASSAN
      COMMON/CVLO/TS2(962),TS3(962)
      COMMON/CFVL/U(26,37),V(26,37)
      COMMON/CKETO/TS1(962)
      COMMON/CKET/T(26,37)
      K=0
      DO 1 I=1,26
      DO 1 J=1,37
      K=K+1
      T(I,J)=TS1(K)
      U(I,J)=TS2(K)
    1 V(I,J)=TS3(K)
      K=0
      DO 2 J=1,37
      DO 2 I=1,26
      K=K+1
      TS1(K)=T(I,J)
      TS2(K)=U(I,J)
    2 TS3(K)=V(I,J)
      RETURN
      END
      SUBROUTINE NAEL
      COMMON/CGRID/R(26),X(37)
      COMMON/CSTFU/EPSI(26,37)
      COMMON/CVORFU/OMEGA(26,37)
      COMMON/CROH/ROH
C
C         ***********************************************************
C         *                                                         *
C         * THIS SUBROUTINE CALCULATES THE FIRST VALUES OF          *
C         *                                                         *
C         * THE BOUNDARY CONDITIONS AT THE AXIS OF SYMMETRY         *
C         *                                                         *
C         * AND THE WALLS FOR THE VORTICITY FUNCTION                *
C         *                                                         *
C         ***********************************************************
C
      DO 60 I=1,37
      OMEGA(1,I)=(8.0*((EPSI(3,I)-EPSI(1,I))/(R(3)*R(3))-(EPSI(2,I)-
     1EPSI(1,I))/(R(2)*R(2))))/(ROH*(R(2)**2-R(3)*R(3)))
   60 CONTINUE
      DO 61 I=1,18
      OMEGA(26,I)=(24.0/(ROH*R(26)*(13.0*R(26)-5.0*R(25))))*(((EPSI(26,
     11)-EPSI(25,I))/((R(26)-R(25))**2.0))-((ROH/24.0)*(2.0*R(26)-R(25))
     2*(7.0*R(26)-3.0*R(25))*(OMEGA(25,I))))
   61 CONTINUE
      DO 62 I=21,37
      OMEGA(26,I)=(24.0/(ROH*R(26)*(13.0*R(26)-5.0*R(25))))*(((EPSI(26,
     11)-EPSI(25,I))/((R(26)-R(25))**2.0))-((ROH/24.0)*(2.0*R(26)-R(25))
     2*(7.0*R(26)-3.0*R(25))*(OMEGA(25,I))))
   62 CONTINUE
      DO 63 I=1,14
      OMEGA(11,I)=(24.0/(ROH*R(11)*(13.0*R(11)-5.0*R(10))))*(((EPSI(11,
     11)-EPSI(10,I))/((R(11)-R(10))**2.0))-((ROH/24.0)*(2.0*R(11)-R(10))
     2*(7.0*R(11)-3.0*R(10))*(OMEGA(10,I))))
      OMEGA(12,I)=(24.0/(ROH*R(12)*(13.0*R(12)-5.0*R(11))))*(((EPSI(12,
     11)-EPSI(11,I))/((R(11)-R(10))**2.0))-((ROH/24.0)*(2.0*R(12)-R(11))
     2*(7.0*R(12)-3.0*R(11))*(OMEGA(11,I))))
   63 CONTINUE
```

```
      OMEGA(12,14)=((3.0*(EPSI(12,14)-EPSI(12,15)))/(ROH*R(12)*R(12)*((X
     1(15)-X(14))**2.0)))-(.5*OMEGA(12,15))
      DO 64 J=14,26
      OMEGA(J,19)=((3.0*(EPSI(J,19)-EPSI(J,18)))/(ROH*R(J)*R(J)*((X(19)-
     1X(18))**2.0)))-(.5*OMEGA(J,18))
      OMEGA(J,20)=((3.0*(EPSI(J,20)-EPSI(J,21)))/(ROH*R(J)*R(J)*((X(21)-
     1)(20))**2.0)))-(.5*OMEGA(J,21))
   64 CONTINUE
      RETURN
      END
      SUBROUTINE WAEL
      COMMON/CEPSIR/EPSIR(26,37)
      COMMON/CSTFU/EPSI(26,37)
      COMMON/CGRID/R(26),X(37)
      COMMON/CROH/ROH
      COMMON/CVORFU/OMEGA(26,37)
      COMMON BE(26,37),BW(26,37),BS(26,37),BN(26,37)
     1, CE(26,37),CW(26,37),CS(26,37),CN(26,37),D(26,37)
C
C            ****************************************
C            *                                      *
C            * THIS SUBROUTINE CALCULATES THE NEW VALUES *
C            *                                      *
C            * OF THE STREAM FUNCTION AT ALL THE GRID    *
C            *                                      *
C            * NODES AS PART OF THE ITERATION PROCESS    *
C            *                                      *
C            ****************************************
C
      DO 70 J=1,26
      DO 70 I=1,37
      EPSIR(J,I)=EPSI(J,I)
   70 CONTINUE
      DO 78 N=1,4
      IF(N.GT.1)GO TO 74
      LJ=2
      MJ=10
      LI=2
      MI=36
      GO TO 77
   74 IF(N.GT.2)GO TO 75
      LJ=11
      MJ=13
      LI=15
      MI=36
      GO TO 77
   75 IF(N.GT.3)GO TO 76
      LJ=14
      MJ=25
      LI=2
      MI=18
      GO TO 77
   76 LJ=14
      MJ=25
      LI=21
      MI=36
   77 DO 78 J=LJ,MJ
      DO 78 I=LI,MI
      BE(J,I)=((R(J+1)-R(J-1))/(X(I+1)-X(I)))/(2.0*ROH*R(J))
      BW(J,I)=((R(J+1)-R(J-1))/(X(I)-X(I-1)))/(2.0*ROH*R(J))
      BN(J,I)=(X(I+1)-X(I-1))/(ROH*(R(J+1)*R(J))*(R(J+1)-R(J)))
      BS(J,I)=(X(I+1)-X(I-1))/(ROH*(R(J)+R(J-1))*(R(J)-R(J-1)))
      CE(J,I)=(BE(J,I))/(BE(J,I)+BW(J,I)+BN(J,I)+BS(J,I))
      CW(J,I)=CE(J,I)*BW(J,I)/BE(J,I)
      CN(J,I)=CE(J,I)*BN(J,I)/BE(J,I)
      CS(J,I)=CE(J,I)*BS(J,I)/BE(J,I)
      D(J,I)=OMEGA(J,I)*R(J)*(X(I+1)-X(I-1))*(R(J+1)-R(J-1))/(4.0*(BE(J
     1,I)+BW(J,I)+BN(J,I)+BS(J,I)))
      EPSIR(J,I)=(CE(J,I)*EPSIR(J,I+1))+(CW(J,I)*EPSIR(J,I-1))+(CN(J,I)*
     1EPSIR(J+1,I))+(CS(J,I)*EPSIR(J-1,I))+D(J,I)
   78 CONTINUE
      RETURN
      END
      SUBROUTINE KOTKOT
      COMMON/COMEGAR/OMEGAR(26,37)
      COMMON/CVORFU/OMEGA(26,37)
      COMMON/CGRID/R(26),X(37)
      COMMON/CSTFU/EPSI(26,37)
      COMMON/CROH/ROH
      COMMON/CKET/T(26,37)
      COMMON/CMUEF/CMU
```

```
      COMMON/CLS/AL(26,37)
      COMMON/CEPSIR/EPSIR(26,37)
      COMMON AE(26,37),AW(26,37),AN(26,37),AS(26,37),BE(26,37),BW(26
     1,37),BN(26,37),BS(26,37),SEGAB(26,37),CE(26,37),CW(26,37),CN(26,37
     2),CS(26,37),DON(26,37),DTO(26,37),DTR(26,37),EON(26,37),ETO(26,37)
     3,ETR(26,37),DOMEGA(26,37),D(26,37)
C
C            ******************************************
C            *                                        *
C            * THIS SUBROUTINE CALCULATES THE NEW VALUES *
C            *                                        *
C            * OF THE VORTICITY FUNCTION AT ALL THE GRID *
C            *                                        *
C            * NODES AS PART OF THE ITERATION  PROCESS  *
C            *                                        *
C            ******************************************
C
      DO 80 J=1,26
      DO 80 I=1,37
      OMEGAR(J,I)=OMEGA(J,I)
   80 CONTINUE
      DO 88 N=1,4
      IF(N.GT.1)GO TO 84
      LJ=2
      MJ=10
      LI=2
      MI=36
      GO TO 87
   84 IF(N.GT.2)GO TO 85
      LJ=11
      MJ=13
      LI=15
      MI=36
      GO TO 87
   85 IF(N.GT.3)GO TO 86
      LJ=14
      MJ=25
      LI=2
      MI=18
      GO TO 87
   86 LJ=14
      MJ=25
      LI=21
      MI=36
   87 DO 88 J=LJ,MJ
      DO 88 I=LI,MI
      AE(J,I)=((R(J)*R(J))/8.0)*((EPSI(J-1,I+1)+EPSI(J-1,I)-EPSI(J+1,I+1
     1)-EPSI(J+1,I))+ABS(EPSI(J-1,I+1)+EPSI(J-1,I)-EPSI(J+1,I+1)-EPSI(J+
     21,I)))
      AW(J,I)=((R(J)*R(J))/8.0)*((EPSI(J+1,I-1)+EPSI(J+1,I)-EPSI(J-1,I-1
     1)-EPSI(J-1,I))+ABS(EPSI(J+1,I-1)+EPSI(J+1,I)-EPSI(J-1,I-1)-EPSI(J-
     21,I)))
      AN(J,I)=((R(J)*R(J))/8.0)*((EPSI(J+1,I+1)+EPSI(J,I+1)-EPSI(J+1,I-1
     1)-EPSI(J,I-1))+ABS(EPSI(J+1,I+1)+EPSI(J,I+1)-EPSI(J+1,I-1)-EPSI(J,
     21-1)))
      AS(J,I)=((R(J)*R(J))/8.0)*((EPSI(J-1,I+1)+EPSI(J,I-1)-EPSI(J-1,I+1
     1)-EPSI(J,I+1))+ABS(EPSI(J-1,I-1)+EPSI(J,I-1)-EPSI(J-1,I+1)-EPSI(J,
     21+1)))
      BE(J,I)=((R(J)**2.0)/2.0)*((R(J+1)-R(J-1))/(X(I+1)-X(I)))
      BW(J,I)=((R(J)**2.0)/2.0)*((R(J+1)-R(J-1))/(X(I)-X(I-1)))
      BN(J,I)=(((R(J+1)**2.0)+(R(J)*R(J)))/8.0)*((X(I+1)-X(I-1))/(R(J+1)
     1-R(J)))*(R(J+1)+R(J))
      BS(J,I)=(((R(J-1)**2.0)+(R(J)*R(J)))/8.0)*((X(I+1)-X(I-1))/(R(J)-R
     1(J-1)))*(R(J-1)+R(J))
      SEGAB(J,I)=(AE(J,I)+AW(J,I)+AN(J,I)+AS(J,I))*ROH*SQRT(T(J,I))*AL(J
     1,I)*CMU*(BE(J,I)+BW(J,I)+BN(J,I)+BS(J,I))
      CE(J,I)=(AE(J,I)+BE(J,I)*ROH*SQRT(T(J,I+1))*AL(J,I+1)*CMU)/SEGAB(
     1J,I)
      CW(J,I)=(AW(J,I)+BW(J,I)*ROH*SQRT(T(J,I-1))*AL(J,I-1)*CMU)/SEGAB(
     1J,I)
      CN(J,I)=(AN(J,I)+BN(J,I)*ROH*SQRT(T(J+1,I))*AL(J+1,I)*CMU)/SEGAB(
     1J,I)
      CS(J,I)=(AS(J,I)+BS(J,I)*ROH*SQRT(T(J-1,I))*AL(J-1,I)*CMU)/SEGAB(
     1J,I)
      DON(J,I)=(2.0*ROH*CMU/(X(I+1)-X(I-1)))*((SQRT(T(J,I+1))*AL(J,I+1)
     1-SQRT(T(J,I))*AL(J,I))/(X(I+1)-X(I))-(SQRT(T(J,I))*AL(J,I)-SQRT(T(
     2J,I-1))*AL(J,I-1))/(X(I)-X(I-1)))
      DTO(J,I)=(2.0*ROH*CMU/(R(J+1)-R(J-1)))*((SQRT(T(J+1,I))*AL(J+1,I)
     1-SQRT(T(J,I))*AL(J,I))/(R(J+1)-R(J))-(SQRT(T(J,I))*AL(J,I)-SQRT(T(
     2J-1,I))*AL(J-1,I))/(R(J)-R(J-1)))
```

```
      DTR(J,I)=(ROH*CMU*(SQRT(T(J+1,I+1))*AL(J+1,I+1)+(SQRT(T(J-1,I-1))*
     1AL(J-1,I-1))-SQRT(T(J-1,I+1))*AL(J-1,I+1)-(SQRT(T(J+1,I-1))*AL(J+1
     2,I-1)))/((X(I+1)-X(I-1))*(R(J+1)-R(J-1)))
      EON(J,I)=((EPSI(J+1,I)-EPSI(J,I))/(R(J+1)-R(J))
     1-(EPSI(J,I)-EPSI(J-1,I))/(R(J)-R(J-1)))/(R(J+1)-R(J-1))
      ETO(J,I)=((EPSI(J,I+1)-EPSI(J,I))/(X(I+1)-X(I))
     1-(EPSI(J,I)-EPSI(J,I-1))/(X(I)-X(I-1)))/(X(I+1)-X(I-1))
      ETR(J,I)=(EPSI(J+1,I+1)-EPSI(J-1,I+1
     1)+EPSI(J-1,I-1)-EPSI(J+1,I-1))/((X(I+1)-X(I-1))*(R(J+1)-
     2R(J-1)))
      DOMEGA(J,I)=4.0*(DON(J,I)*EON(J,I)+DTO(J,I)*ETO(J,I)
     1-DTR(J,I)*ETR(J,I))/ROH
      D(J,I)=(((R(J)/4.0)*(X(I-1)-X(I+1))*(R(J+1)-R(J-1)))*(DOMEGA(J,I))
     2)/SEGAB(J,I)
   88 CONTINUE
      DO 110 N=1,4
      IF(N.GT.1)GO TO 100
      LJ=2
      MJ=9
      LI=2
      MI=36
      GO TO 108
  100 IF(N.GT.2)GO TO 102
      LJ=10
      MJ=12
      LI=16
      MI=36
      GO TO 108
  102 IF(N.GT.3)GO TO 104
      LJ=13
      MJ=24
      LI=22
      MI=36
      GO TO 108
  104 LJ=15
      MJ=24
      LI=2
      MI=17
  108 DO 110 J=LJ,MJ
      DO 110 I=LI,MI
      OMEGAR(J,I)=(CE(J,I)*OMEGAR(J,I+1))+(CW(J,I)*OMEGAR(J,I-1))+(CN(J,
     2I)*OMEGAR(J+1,I))+(CS(J,I)*OMEGAR(J-1,I))+D(J,I)
  110 CONTINUE
      OMEGAR(10,15)=CE(10,15)*OMEGAR(10,16)+CW(10,15)*OMEGAR(10,14)
     1+CN(10,15)*OMEGAR(11,15)+CS(10,15)*OMEGAR(9,15)+D(10,15)
      OMEGAR(13,21)=CE(13,21)*OMEGAR(13,22)+CW(13,21)*OMEGAR(13,20)
     1+CN(13,21)*OMEGAR(14,21)+CS(13,21)*OMEGAR(12,21)+D(13,21)
      OMEGAR(25,14)=CE(25,18)*OMEGAR(25,19)+CW(25,18)*OMEGAR(25,17)
     1+CN(25,18)*OMEGAR(26,18)+CS(25,18)*OMEGAR(24,18)+D(25,18)
      OMEGAR(25,21)=CE(25,21)*OMEGAR(25,22)+CW(25,21)*OMEGAR(25,20)
     1+CN(25,21)*OMEGAR(26,21)+CS(25,21)*OMEGAR(24,21)+D(25,21)
      DO 115 I=16,18
      OMEGAR(13,I)=CE(13,I)*OMEGAR(13,I+1)+CW(13,I)*OMEGAR(13,I-1)
     1+CN(13,I)*OMEGAR(14,I)+CS(13,I)*OMEGAR(12,I)+D(13,I)
  115 CONTINUE
      DO 117 I=15,17
      OMEGAR(14,I)=CE(14,I)*OMEGAR(14,I+1)+CW(14,I)*OMEGAR(14,I-1)
     1+CN(14,I)*OMEGAR(15,I)+CS(14,I)*OMEGAR(13,I)+D(14,I)
  117 CONTINUE
      DO 120 I=2,14
      OMEGAR(10,I)=(CE(10,I)*OMEGAR(10,I+1)+CW(10,I)*OMEGAR(10,I-1)
     1+CS(10,I)*OMEGAR(9,I)-3.0*CN(10,I)*(EPSI(10,I)-EPSI(11,I))/
     2(ROH*(((R(11)-R(10))*R(11))**2.0))+D(10,I))/(1.0+CN(10,I)/
     32.0)
      OMEGAR(14,I)=(CE(14,I)*OMEGAR(14,I+1)+CW(14,I)*OMEGAR(14,I-1)+C
     1N(14,I)*OMEGAR(15,I)-3.0*CS(14,I)*(EPSI(14,I)-EPSI(13,I))/(ROH
     2*(((R(14)-R(13))*R(13))**2.0))+D(14,I))/(1.0+CS(14,I)/2.0)
  120 CONTINUE
      DO 130 I=2,17
      OMEGAR(25,I)=(CE(25,I)*OMEGAR(25,I+1)+CW(25,I)*OMEGAR(25,I-1)+C
     1S(25,I)*OMEGAR(24,I)-3.0*CN(25,I)*(EPSI(25,I)-EPSI(26,I))/(ROH
     2*(((R(26)-R(25))*R(26))**2.0))+D(25,I))/(1.0+CN(25,I)/2.0)
  130 CONTINUE
      DO 140 I=21,36
      OMEGAR(25,I)=(CE(25,I)*OMEGAR(25,I+1)+CW(25,I)*OMEGAR(25,I-1)+C
     1S(25,I)*OMEGAR(24,I)-3.0*CN(25,I)*(EPSI(25,I)-EPSI(26,I))/(ROH
     2*(((R(26)-R(25))*R(26))**2.0))+D(25,I))/(1.0+CN(25,I)/2.0)
  140 CONTINUE
      DO 150 I=19,20
```

```
      OMEGAR(13,I)=(CE(13,I)*OMEGAR(13,I+1)+CW(13,I)*OMEGAR(13,I-1)+C
     1S(13,I)*OMEGAR(12,I)-3.0*CN(13,I)*(EPSI(13,I)-EPSI(14,I))/(ROH
     2*(((R(14)-R(13))*R(14))**2.0))+D(13,I))/(1.0+CN(13,I)/2.0)
  150 CONTINUE
      DO 160 J=11,13
      OMEGAR(J,15)=(CE(J,15)*OMEGAR(J,16)+CN(J,15)*OMEGAR(J+1,15)+CS
     1(J,15)*OMEGAR(J-1,15)-3.0*CW(J,15)*(EPSI(J,14)-EPSI(J,15))/(RO
     2H*(((X(15)-X(14))*R(J))**2.0))+D(J,15))/(1.0+CW(J,15)/2.0)
  160 CONTINUE
      DO 170 J=14,24
      OMEGAR(J,21)=(CE(J,21)*OMEGAR(J,22)+CN(J,21)*OMEGAR(J+1,21)+CS(
     1J,21)*OMEGAR(J-1,21)-3.0*CW(J,21)*(EPSI(J,20)-EPSI(J,21))/(ROH
     2*(((X(21)-X(20))*R(J))**2.0))+D(J,21))/(1.0+CW(J,21)/2.0)
  170 CONTINUE
      DO 180 J=14,24
      OMEGAR(J,18)=(CW(J,18)*OMEGAR(J,17)+CN(J,18)*OMEGAR(J+1,18)+CS(
     1J,18)*OMEGAR(J-1,18)-3.0*CE(J,18)*(EPSI(J,19)-EPSI(J,18))/(ROH
     2*(((X(19)-X(18))*R(J))**2.0))+D(J,18))/(1.0+CE(J,18)/2.0)
  180 CONTINUE
      DO 89 I=1,37
      OMEGAR(1,I)=(8.0*(((EPSI(3,I)-EPSI(1,I))/(R(3)*R(3))-(EPSI(2,I)-
     1EPSIR(1,I))/(R(2)*R(2))))/(ROH*(R(2)*R(2)-R(3)*R(3)))
   89 CONTINUE
      DO 90 I=1,18
      OMEGAR(26,I)=(24.0/(ROH*R(26)*(13.0*R(26)-5.0*R(25))))*(((EPSI(2
     16,I)-EPSI(25,I))/((R(26)-R(25))**2.0))-((ROH/24.0)*(2.0*R(26)-R(2
     25))*(7.0*R(26)-3.0*R(25))*(OMEGAR(25,I))))
   90 CONTINUE
      DO 91 I=21,37
      OMEGAR(26,I)=(24.0/(ROH*R(26)*(13.0*R(26)-5.0*R(25))))*(((EPSI(2
     16,I)-EPSI(25,I))/((R(26)-R(25))**2.0))-((ROH/24.0)*(2.0*R(26)-R(2
     25))*(7.0*R(26)-3.0*R(25))*(OMEGAR(25,I))))
   91 CONTINUE
      DO 92 I=1,14
      OMEGAR(11,I)=(24.0/(ROH*R(11)*(13.0*R(11)-5.0*R(10))))*(((EPSI(1
     11,I)-EPSI(10,I))/((R(11)-R(10))**2.0))-((ROH/24.0)*(2.0*R(11)-R(1
     20))*(7.0*R(11)-3.0*R(10))*(OMEGAR(10,I))))
      OMEGAR(13,I)=(24.0/(ROH*R(13)*(13.0*R(13)-5.0*R(14))))*(((EPSI(1
     13,I)-EPSI(14,I))/((R(14)-R(13))**2.0))-((ROH/24.0)*(2.0*R(13)-R(1
     24))*(7.0*R(13)-3.0*R(14))*(OMEGAR(14,I))))
   92 CONTINUE
      OMEGAR(12,14)=(((4.0*(EPSI(12,14)-EPSI(12,15)))/(ROH*R(12)*R(12)*
     1(X(15)-X(14))**2.0)))-(.5*OMEGAR(12,15))
      DO 93 J=14,26
      OMEGAR(J,19)=(((3.0*(EPSI(J,19)-EPSI(J,18)))/(ROH*R(J)*R(J)*((X(1
     19)-X(18))**2.0)))-(.5*OMEGAR(J,18))
      OMEGAR(J,20)=(((3.0*(EPSI(J,20)-EPSI(J,21)))/(ROH*R(J)*R(J)*((Y(2
     11)-X(20))**2.0)))-(.5*OMEGAR(J,21))
   93 CONTINUE
      RETURN
      END
      SUBROUTINE SAWSAN
      COMMON/CGRID/R(26),X(37)
      COMMON/CROH/ROH
      COMMON/CFVL/U(26,37),V(26,37)
      COMMON/CMUEF/CMU
      COMMON/CKET/T(26,37)
      COMMON/CLS/AL(26,37)
      COMMON/CSP/SP(26,37)
      COMMON DXUU(26,37),DRVV(26,37),DRUV(26,37),DXUV(26,37),DXU(26,3
     17),DRU(26,37),DXV(26,37),DRV(26,37),ADUV(26,37),RADUV(26,37),XADUV
     2(26,37),ADU(26,37),XADU(26,37),ADV(26,37),RADV(26,37),DXP(26,37),D
     3RP(26,37)
C
C            ************************************************
C            *                                              *
C            * THIS SUBROUTINE CALCULATES THE VALUES OF     *
C            *                                              *
C            * THE STATIC PRESSURE AT ALL THE GRID NODES    *
C            *                                              *
C            ************************************************
C
      DO 154 N=1,4
      IF(N.GT.1)GO TO 150
      LJ=2
      MJ=10
      LI=2
      MI=36
      GO TO 153
  150 IF(N.GT.2)GO TO 151
      LJ=11
      MJ=13
      LI=15
```

```
      MI=36
      GO TO 153
  151 IF(N.GT.3)GO TO 152
      LJ=14
      MJ=25
      LI=2
      MI=18
      GO TO 153
  152 LJ=4
      MJ=25
      LI=21
      MI=36
  153 DO 154 J=LJ,MJ
      DO 154 I=LI,MI
      DXUU(J,I)=(((((X(I+1)-X(I))**2.0)-((X(I)-X(I-1))**2.0))*U(J,I)*U(J
     1,I))+(ABS((X(I)-X(I-1))*U(J,I+1))**2.0)-(ABS((X(I+1)-X(I))*U(J,I-1
     2))**2.0))/((X(I+1)-X(I))*(X(I)-X(I-1))*(X(I+1)-X(I-1)))
      DRVV(J,I)=(((((R(J+1)-R(J))**2.0)-((R(J)-R(J-1))**2.0))*V(J,I)*V(J
     1,I))+(ABS((R(J)-R(J-1))*V(J+1,I))**2.0)-(ABS((R(J+1)-R(J))*V(J-1
     2,I))**2.0))/((R(J+1)-R(J))*(R(J)-R(J-1))*(R(J+1)-R(J-1)))
      DRUV(J,I)=(((((R(J+1)-R(J))**2.0)-((R(J)-R(J-1))**2.0))
     1*U(J,I)*V(J
     2,I))+(((R(J)-R(J-1))**2.0)*U(J+1,I)*V(J+1,I))-(((R(J+1)-R(J))**2.0
     3)*U(J-1,I)*V(J-1,I)))/((R(J+1)-R(J))*(R(J)-R(J-1))*(R(J+1)-R(J-1))
     4)
      DXUV(J,I)=(((((X(I+1)-X(I))**2.0)-((X(I)-X(I-1))**2.0))*U(J,I)*V(J
     1,I))+(((X(I)-X(I-1))**2.0)*U(J,I+1)*V(J,I+1))-(((X(I+1)-X(I))**2.0
     2)*U(J,I-1)*V(J,I-1)))/((X(I+1)-X(I))*(X(I)-X(I-1))*(X(I+1)-X(I-1))
     3)
      DXU(J,I)=(((((X(I+1)-X(I))**2.0)-((X(I)-X(I-1))**2.0))*U(J,I))+(((
     1X(I)-X(I-1))**2.0)*U(J,I+1))-(((X(I+1)-X(I))**2.0)*U(J,I-1)))/((X(
     2I+1)-X(I))*(X(I)-X(I-1))*(X(I+1)-X(I-1)))
      DRU(J,I)=(((((R(J+1)-R(J))**2.0)-((R(J)-R(J-1))**2.0))*U(J,I))+(((
     1R(J)-R(J-1))**2.0)*U(J+1,I))-(((R(J+1)-R(J))**2.0)*U(J-1,I)))/((R(
     2J+1)-R(J))*(R(J)-R(J-1))*(R(J+1)-R(J-1)))
      DXV(J,I)=(((((X(I+1)-X(I))**2.0)-((X(I)-X(I-1))**2.0))*V(J,I))+(((
     1X(I)-X(I-1))**2.0)*V(J,I+1))-(((X(I+1)-X(I))**2.0)*V(J,I-1)))/((X(
     2I+1)-X(I))*(X(I)-X(I-1))*(X(I+1)-X(I-1)))
      DRV(J,I)=(((((R(J+1)-R(J))**2.0)-((R(J)-R(J-1))**2.0))*V(J,I))+(((
     1R(J)-R(J-1))**2.0)*V(J+1,I))-(((R(J+1)-R(J))**2.0)*U(J-1,I)))/((R(
     2J+1)-R(J))*(R(J)-R(J-1))*(R(J+1)-R(J-1)))
      ADUV(J,I)=(ROH*SQRT(T(J,I)) *AL(J,I)*CMU)*(DRU(J,I)+DXV(J,I))
      ADU(J,I)=(2.0*ROH*SQRT(T(J,I)) *AL(J,I)*CMU)*DXU(J,I)
      ADV(J,I)=(ROH*SQRT(T(J,I)) *AL(J,I)*CMU)*2.0*DRV(J,I)
  154 CONTINUE
      DO 155 I=2,36
      ADUV(1,I)=ADUV(2,I)+(ADUV(2,I)-ADUV(3,I))*R(2)/(R(3)-R(2))
      ADU(1,I)=ADU(2,I)+(ADU(2,I)-ADU(3,I))*R(2)/(R(3)-R(2))
      ADV(1,I)=ADV(2,I)+(ADV(2,I)-ADV(3,I))*R(2)/(R(3)-R(2))
  155 CONTINUE
      DO 156 I=2,18
      ADUV(26,I)=ADUV(25,I)+(ADUV(25,I)-ADUV(24,I))*(R(26)-R(25))/(R(25)
     1-R(24))
      ADU(26,I)=ADU(25,I)+(ADU(25,I)-ADU(24,I))*(R(26)-R(25))/(R(25)-R(2
     14))
      ADV(26,I)=ADV(25,I)+(ADV(25,I)-ADV(24,I))*(R(26)-R(25))/(R(25)-R(2
     14))
  156 CONTINUE
      DO 157 I=21,36
      ADUV(26,I)=ADUV(25,I)+(ADUV(25,I)-ADUV(24,I))*(R(26)-R(25))/(R(25)
     1-R(24))
      ADU(26,I)=ADU(25,I)+(ADU(25,I)-ADU(24,I))*(R(26)-R(25))/(R(25)-R(2
     14))
      ADV(26,I)=ADV(25,I)+(ADV(25,I)-ADV(24,I))*(R(26)-R(25))/(R(25)-R(2
     14))
  157 CONTINUE
      DO 158 J=1,26
      ADUV(J,37)=ADUV(J,36)+(ADUV(J,36)-ADUV(J,35))*(X(37)-X(36))/(X(36)
     1-X(35))
      ADU(J,37)=ADU(J,36)+(ADU(J,36)-ADU(J,35))*(X(37)-X(36))/(X(36)-X(3
     15))
      ADV(J,37)=ADV(J,36)+(ADV(J,36)-ADV(J,35))*(X(37)-X(36))/(X(36)-X(3
     15))
  158 CONTINUE
      DO 159 J=14,26
      ADUV(J,20)=ADUV(J,21)+(ADUV(J,21)-ADUV(J,22))*(X(21)-X(20))/(X(22)
     1-X(21))
      ADUV(J,19)=ADUV(J,18)+(ADUV(J,18)-ADUV(J,17))*(X(19)-X(18))/(X(18)
     1-X(17))
```

```
      ADU(J,20)=ADU(J,21)+(ADU(J,21)-ADU(J,22))*(X(21)-X(20))/(X(22)-X(2
     11))
      ADU(J,19)=ADU(J,18)+(ADU(J,18)-ADU(J,17))*(X(19)-X(18))/(X(18)-X(1
     17))
      ADV(J,20)=ADV(J,21)+(ADV(J,21)-ADV(J,22))*(X(21)-X(20))/(X(22)-X(2
     11))
      ADV(J,19)=ADU(J,18)+(ADV(J,18)-ADV(J,17))*(X(19)-X(18))/(X(18)-X(1
     17))
  159 CONTINUE
      DO 160 I=2,14
      ADUV(11,I)=ADUV(10,I)+(ADUV(10,I)-ADUV(9,I))*(R(11)-R(10))/(R(10)-
     1R(9))
      ADU(11,I)=ADU(10,I)+(ADU(10,I)-ADU(9,I))*(R(11)-R(10))/(R(10)-R(9)
     1)
      ADV(11,I)=ADV(10,I)+(ADV(10,I)-ADV(9,I))*(R(11)-R(10))/(R(10)-R(9)
     1)
      ADUV(13,I)=ADUV(14,I)+(ADUV(14,I)-ADUV(15,I))*(R(14)-R(13))/(R(15)
     1-R(14))
      ADU(13,I)=ADU(14,I)+(ADU(14,I)-ADU(15,I))*(R(14)-R(13))/(R(15)-R(1
     14))
      ADV(13,I)=ADV(14,I)+(ADV(14,I)-ADV(15,I))*(R(14)-R(13))/(R(15)-R(1
     14))
  160 CONTINUE
      ADUV(12,14)=ADUV(12,15)+(ADUV(12,15)-ADUV(12,16))*(X(15)-X(14))/(X
     1(16)-X(15))
      ADU(12,14)=ADU(12,15)+(ADU(12,15)-ADU(12,16))*(X(15)-X(14))/(X(16)
     1-X(15))
      ADV(12,14)=ADV(12,15)+(ADV(12,15)-ADV(12,16))*(X(15)-X(14))/(X(16)
     1-X(15))
      DO 161 J=1,11
      ADUV(J,1)=ADUV(J,2)+(ADUV(J,2)-ADUV(J,3))*X(2)/(X(3)-X(2))
      ADU(J,1)=ADU(J,2)+(ADU(J,2)-ADU(J,3))*X(2)/(X(3)-X(2))
      ADV(J,1)=ADV(J,2)+(ADV(J,2)-ADV(J,3))*X(2)/(X(3)-X(2))
  161 CONTINUE
      DO 162 J=13,26
      ADUV(J,1)=ADUV(J,2)+(ADUV(J,2)-ADUV(J,3))*X(2)/(X(3)-X(2))
      ADU(J,1)=ADU(J,2)+(ADU(J,2)-ADU(J,3))*X(2)/(X(3)-X(2))
      ADV(J,1)=ADV(J,2)+(ADV(J,2)-ADV(J,3))*X(2)/(X(3)-X(2))
  162 CONTINUE
      DO 167 N=1,4
      IF(N.GT.1)GO TO 163
      LJ=2
      MJ=10
      LI=2
      MI=36
      GO TO 166
  163 IF(N.GT.2)GO TO 164
      LJ=11
      MJ=13
      LI=15
      MI=36
      GO TO 166
  164 IF(N.GT.3)GO TO 165
      LJ=14
      MJ=25
      LI=2
      MI=18
      GO TO 166
  165 LJ=14
      MJ=25
      LI=21
      MI=36
  166 DO 167 J=LJ,MJ
      DO 167 I=LI,MI
      PADUV(J,I)=((((R(J+1)-R(J))**2.0)-((R(J)-R(J-1))**2.0))*ADUV(J,I)
     1)+(((R(J)-R(J-1))**2.0)*ADUV(J+1,I))-(((R(J+1)-R(J))**2.0)*ADUV(J-
     21,I)))/((R(J+1)-R(J))*(R(J)-R(J-1))*(R(J+1)-R(J-1)))
      XADUV(J,I)=((((X(I+1)-X(I))**2.0)-((X(I)-X(I-1))**2.0))*ADUV(J,I)
     1)+(((X(I)-X(I-1))**2.0)*ADUV(J,I+1))-(((X(I+1)-X(I))**2.0)*ADUV(J,
     2I-1)))/((X(I+1)-X(I))*(X(I)-X(I-1))*(X(I+1)-X(I-1)))
      XADU(J,I)=((((X(I+1)-X(I))**2.0)-((X(I)-X(I-1))**2.0))*ADU(J,I))+
     1(((X(I)-X(I-1))**2.0)*ADU(J,I+1))-(((X(I+1)-X(I))**2.0)*ADU(J,I-1
     2)))/((X(I+1)-X(I))*(X(I)-X(I-1))*(X(I+1)-X(I-1)))
      RADV(J,I)=((((R(J+1)-R(J))**2.0)-((R(J)-R(J-1))**2.0))*ADV(J,I))+
     1(((R(J)-R(J-1))**2.0)*ADV(J+1,I))-(((R(J+1)-R(J))**2.0)*ADV(J-1,I)
     2))/((R(J+1)-R(J))*(R(J)-R(J-1))*(R(J+1)-R(J-1)))
      DXP(J,I)=RADUV(J,I)+(ADUV(J,I)/R(J))*XADU(J,I)-(ROH*DXUU(J,I))-(RO
     1H*V(J,I)*U(J,I)/R(J))-(ROH*DRUV(J,I))
      DRP(J,I)=RADV(J,I)+(ADV(J,I)/R(J))*XADUV(J,I)-(ROH*DRVV(J,I))-(ROH
     1*V(J,I)*V(J,I)/R(J))-ROH*DXUV(J,I)-(2.0*V(J,I)*ROH*SQRT(T(J,I)) *A
     2L(J,I)*CRU/(R(J)*R(J)))
```

```
  167 CONTINUE
      DO 168 I=2,36
      DXP(1,I)=DXP(2,I)+(DXP(2,I)-DXP(3,I))*R(2)/(R(3)-R(2))
      DRP(1,I)=DRP(2,I)+(DRP(2,I)-DRP(3,I))*R(2)/(R(3)-R(2))
  168 CONTINUE
      DO169 I=2,18
      DXP(26,I)=DXP(25,I)+(DXP(25,I)-DXP(24,I))*(R(26)-R(25))/(R(25)-R(2
     14))
      DRP(26,I)=DRP(25,I)+(DRP(25,I)-DRP(24,I))*(R(26)-R(25))/(R(25)-R(2
     14))
  169 CONTINUE
      DO 170 I=21,36
      DXP(26,I)=DXP(25,I)+(DXP(25,I)-DXP(24,I))*(R(26)-R(25))/(R(25)-R(2
     14))
      DRP(26,I)=DRP(25,I)+(DRP(25,I)-DRP(24,I))*(R(26)-R(25))/(R(25)-R(2
     14))
  170 CONTINUE
      DO 171 J=1,26
      DXP(J,37)=DXP(J,36)+(DXP(J,36)-DXP(J,35))*(X(37)-X(36))/(X(36)-X(3
     15))
      DRP(J,37)=DRP(J,36)+(DRP(J,36)-DRP(J,35))*(X(37)-X(36))/(X(36)-X(3
     15))
  171 CONTINUE
      DO 172 J=14,26
      DXP(J,20)=DXP(J,21)+(DXP(J,21)-DXP(J,22))*(X(21)-X(20))/(X(22)-X(2
     11))
      DRP(J,20)=DRP(J,21)+(DRP(J,21)-DRP(J,22))*(X(21)-X(20))/(X(22)-X(2
     11))
      DXP(J,19)=DXP(J,18)+(DXP(J,18)-DXP(J,17))*(X(19)-X(18))/(X(18)-X(1
     17))
      DRP(J,19)=DRP(J,18)+(DRP(J,18)-DRP(J,17))*(X(19)-X(18))/(X(18)-X(1
     17))
  172 CONTINUE
      DO 173 I=2,14
      DXP(11,I)=DXP(10,I)+(DXP(10,I)-DXP(9,I))*(R(11)-R(10))/(R(10)-R(9)
     1)
      DRP(11,I)=DRP(10,I)+(DRP(10,I)-DRP(9,I))*(R(11)-R(10))/(R(10)-R(9)
     1)
      DXP(13,I)=DXP(14,I)+(DXP(14,I)-DXP(15,I))*(R(14)-R(13))/(R(15)-R(1
     14))
      DRP(13,I)=DRP(14,I)+(DRP(14,I)-DRP(15,I))*(R(14)-R(13))/(R(15)-R(1
     14))
  173 CONTINUE
      DXP(12,14)=DXP(12,15)+(DXP(12,15)-DXP(12,16))*(X(15)-X(14))/(X(16)
     1-X(15))
      DRP(12,14)=DRP(12,15)+(DRP(12,15)-DRP(12,16))*(X(15)-X(14))/(X(16)
     1-X(15))
      DO 174 J=1,11
      DXP(J,1)=DXP(J,2)+(DXP(J,2)-DXP(J,3))*X(2)/(X(3)-X(2))
      DRP(J,1)=DRP(J,2)+(DRP(J,2)-DRP(J,3))*X(2)/(X(3)-X(2))
  174 CONTINUE
      DO 175 J=13,26
      DXP(J,1)=DXP(J,2)+(DXP(J,2)-DXP(J,3))*X(2)/(X(3)-X(2))
      DRP(J,1)=DRP(J,2)+(DRP(J,2)-DRP(J,3))*X(2)/(X(3)-X(2))
  175 CONTINUE
      DO 176 J=1,10
      DO 176 I=2,36
      SP(J,I)=SP(J,I-1)+.5*(DXP(J,I-1)+DXP(J,I+1))*(X(I+1)-X(I-1))
  176 CONTINUE
      DO 177 I=1,13
      SP(11,I)=SP(10,I)+(SP(10,I)-SP(9,I))*(R(11)-R(10))/(R(10)-R(9))
      SP(12,I)=.0
  177 CONTINUE
      DO 178 J=11,25
      DO 178 I=14,36
      SP(J,I)=SP(J-1,I)+.5*(DRP(J-1,I)+DRP(J-1,I))*(R(J+1)-R(J-1))
  178 CONTINUE
      DO 179 N=1,12
      SP(13,14-N)=SP(13,15-N)-.5*(DXP(13,13-N)+DXP(13,15-N))*(X(15-N)-X(
     113-N))
  179 CONTINUE
      DO 180 J=14,25
      DO 180 I=2,13
      SP(J,I)=SP(J-1,I)+.5*(DRP(J-1,I)+DRP(J+1,I))*(R(J+1)-R(J-1))
  180 CONTINUE
      DO 181 I=2,36
      SP(26,I)=SP(25,I)+(SP(25,I)-SP(24,I))*(R(26)-R(25))/(R(25)-R(24))
  181 CONTINUE
      DO 182 J=1,26
      SP(J,37)=SP(J,36)+(SP(J,36)-SP(J,35))*(X(37)-X(36))/(X(36)-X(35))
  182 CONTINUE
```

```
      DO 183 J=13,26
      SP(J,1)=SP(J,2)+(SP(J,2)-SP(J,3))*X(2)/(X(3)-X(2))
  183 CONTINUE
      RETURN
      END
      SUBROUTINE SALWA
      COMMON/CGRID/R(26),X(37)
      COMMON/CSP/SP(26,37)
      COMMON/CFVL/U(26,37),V(26,37)
      COMMON/CROH/ROH
      COMMON/CCPCL/CP(26,37),CL(26,37)
      COMMON/COPER/SPOT,ALPHO,VOI,SPET,ALPHE,VE,CPT,CLT
      DIMENSION A(11),B(11),C(11),AA(26),BB(26),CC(26)
C
C         ************************************************
C         *                                              *
C         * THIS SUBROUTINE CALCULATES THE STATIC PRESSURE *
C         *                                              *
C         * RISE COEFFICIENT AND THE TOTAL PRESSURE LOSS  *
C         *                                              *
C         * COEFFICIENT AT EACH NODE IT ALSO CALCULATES THE *
C         *                                              *
C         * OVERALL STATIC PRESSURE RISE COEFFICIENT AND  *
C         *                                              *
C         * THE OVERALL TOTAL PRESSURE LOSS COEFFICIENT   *
C         *                                              *
C         * ************************************************
C
      A(2)=((SP(1,1)+SP(2,1))/2.0)*R(2)*R(2)
      B(2)=((U(1,1)+U(2,1))/2.0)*R(2)*R(2)
      C(2)=(ABS((U(1,1)+U(2,1))/2.0)**3.0)*R(2)*R(2)
      DO 185 J=3,11
      A(J)=A(J-1)+((SP(J-1,1)+SP(J,1))/2.0)*(R(J)-R(J-1))*(R(J)+R(J-1))
      B(J)=B(J-1)+((U(J-1,1)+U(J,1))/2.0)*(R(J)-R(J-1))*(R(J)+R(J-1))
      C(J)=C(J-1)+(ABS((U(J-1,1)+U(J,1))/2.0)**3.0)*(R(J)-R(J-1))*(R(J)+
     1R(J-1))
  185 CONTINUE
      SPOT=A(11)/(R(11)*R(11))
      VOI=B(11)/(R(11)*R(11))
      ALPHO=C(11)/(R(11)*R(11)*(VOI**3.0))
      EDP=.5*ROH*ALPHO*VOI*VOI
      ETP=SPOT+EDP
      DO 186 J=1,26
      DO 186 I=1,37
      CP(J,I)=(SP(J,I)-SPOT)/EDP
      CL(J,I)=(ETP-(SP(J,I)+SQRT(U(J,I)*U(J,I)+V(J,I)*V(J,I))*ROH*.5))
     1/ETP
  186 CONTINUE
      AA(2)=((CP(1,37)+CP(2,37))/2.0)*R(2)*R(2)
      BB(2)=((U(1,37)+U(2,37))/2.0)*R(2)*R(2)
      CC(2)=((U(1,37)+U(2,37))/2.0)**3.0)*R(2)*R(2)
      DO 187 J=3,26
      AA(J)=AA(J-1)+((SP(J-1,37)+SP(J,37))/2.0)*(R(J)-R(J-1))*(R(J)+R(J-
     11))
      BB(J)=BB(J-1)+((U(J-1,37)+U(J,37))/2.0)*(R(J)-R(J-1))*(R(J)+R(J-1)
     1)
      CC(J)=CC(J-1)+(ABS((U(J-1,37)+U(J,37))/2.0)**3.0)*(R(J)-R(J-1))*(R
     1(J)*R(J-1))
  187 CONTINUE
      SPET=AA(26)/(R(26)*R(26))
      VE=BB(26)/(R(26)*R(26))
      ALPHE=CC(26)/(R(26)*R(26)*(VE**3.0))
      CPT=(SPET-SPOT)/EDP
      CLT=(ETP-(SPET+.5*ROH*ALPHE*VE*VE))/ETP
      RETURN
      END
      SUBROUTINE CHAZO
      REAL MU
      COMMON/CGRID/R(26),X(37)
      COMMON/CKET/T(26,37)
      COMMON/CTR/TR(26,37)
      COMMON/CSTFU/EPS1(26,37)
      COMMON/CROH/ROH
      COMMON/CLS/AL(26,37)
      COMMON/CMUEF/CMU
      COMMON/CFMU/MU
      COMMON/CKEEG/CD,SEGK
      COMMON FON(26,37),GON(26,37),GTO(26,37),HSKT(26,37),VPVSK(26,37),A
     1E(26,37),AW(26,37),AN(26,37),AS(26,37),BE(26,37),BW(26,37),BN(26,3
     27),BS(26,37),SEGAB(26,37),CE(26,37),CW(26,37),CN(26,37),CS(26,37),
     3DK(26,37)
```

```
C
C          ************************************************
C          *                                              *
C          * THIS SUBROUTINE CALCULATES THE NEW VALUES    *
C          *                                              *
C          * OF THE TURBULENT KINETIC ENERGY AT ALL THE   *
C          *                                              *
C          * GRID NODES AS PART OF THE ITERATION PROCESS  *
C          *                                              *
C          ************************************************
C
      DO 95 J=1,26
      DO 95 I=1,37
      TR(J,I)=T(J,I)
   95 CONTINUE
      DO 125 N=1,4
      IF(N.GT.1)GO TO 120
      LJ=2
      MJ=10
      LI=2
      MI=36
      GO TO 124
  120 IF(N.GT.2)GO TO 121
      LJ=11
      MJ=13
      LI=15
      MI=36
      GO TO 124
  121 IF(N.GT.3)GO TO 123
      LJ=14
      MJ=25
      LI=2
      MI=18
      GO TO 124
  123 LJ=14
      MJ=25
      LI=21
      MI=36
  124 DO 125 J=LJ,MJ
      DO 125 I=LI,MI
      FON(J,I)=(EPSI(J+1,I+1)+EPSI(J-1,I-1)-EPSI(J+1,I-1)-EPSI(J-1,I+1))
     1/(R(J)*(R(J+1)-R(J-1))*(X(I+1)-X(I-1)))
      GON(J,I)=((((EPSI(J+1,I)-EPSI(J,I))/(R(J+1)-R(J)))-((EPSI(J,I)-EPS
     1I(J-1,I))/(R(J)-R(J-1))))*2.0)/(R(J)*(R(J+1)-R(J-1)))
      GTO(J,I)=((((EPSI(J,I+1)-EPSI(J,I))/(X(I+1)-X(I)))-((EPSI(J,I)-EPS
     1I(J,I-1))/(X(I)-X(I-1))))*2.0)/(R(J)*(X(I+1)-X(I-1)))
      WSKT(J,I)=((ROH*SQRT(TR(J,I))*AL(J,I)*(MU-MU)/(ROH*ROH))*((4.0*(FO
     1N(J,I)*FON(J,I)))*(ABS(GON(J,I)-GTO(J,I))**2.0))
      DK(J,I)=((ROH*CD*(TR(J,I)**0.5))/AL(J,I))
      AE(J,I)=((EPSI(J-1,I+1)+EPSI(J-1,I)-EPSI(J+1,I+1)-EPSI(J+1,I))+(AB
     1S(EPSI(J-1,I+1)+EPSI(J-1,I)-EPSI(J+1,I+1)-EPSI(J+1,I))))/8.0
      AW(J,I)=((EPSI(J+1,I-1)+EPSI(J+1,I)-EPSI(J-1,I-1)-EPSI(J-1,I))+(AB
     1S(EPSI(J+1,I-1)+EPSI(J+1,I)-EPSI(J-1,I-1)-EPSI(J-1,I))))/8.0
      AN(J,I)=((EPSI(J+1,I+1)+EPSI(J,I+1)-EPSI(J+1,I-1)-EPSI(J,I-1))+(AB
     1S(EPSI(J+1,I+1)+EPSI(J,I+1)-EPSI(J+1,I-1)-EPSI(J,I-1))))/8.0
      AS(J,I)=((EPSI(J-1,I-1)+EPSI(J,I-1)-EPSI(J-1,I+1)-EPSI(J,I+1))+(AB
     1S(EPSI(J-1,I-1)+EPSI(J,I-1)-EPSI(J-1,I+1)-EPSI(J,I+1))))/8.0
      BE(J,I)=((ROH*CMU)/(8.0*SEGK))*(SQRT(TR(J,I+1))*AL(J,I+1)+SQRT(TR(
     1J,I))*AL(J,I))*((R(J+1)-R(J-1))/(X(I+1)-X(I)))*R(J)*2.0
      BW(J,I)=((ROH*CMU)/(8.0*SEGK))*(SQRT(TR(J,I-1))*AL(J,I-1)+SQRT(TR(
     1J,I))*AL(J,I))*((R(J+1)-R(J-1))/(X(I)-X(I-1)))*R(J)*2.0
      BN(J,I)=((ROH*CMU)/(8.0*SEGK))*(SQRT(TR(J+1,I))*AL(J+1,I)+SQRT(TR(
     1J,I))*AL(J,I))*((X(I+1)-X(I-1))/(R(J+1)-R(J)))*(R(J+1)*R(J))
      BS(J,I)=((ROH*CMU)/(8.0*SEGK))*(SQRT(TR(J-1,I))*AL(J-1,I)+SQRT(TR(
     1J,I))*AL(J,I))*((X(I+1)-X(I-1))/(R(J)-R(J-1)))*(R(J-1)*R(J))
      SEGAB(J,I)=AE(J,I)+AW(J,I)+AN(J,I)+AS(J,I)+BE(J,I)+BW(J,I)+BN(J,I)
     1+BS(J,I)
      CE(J,I)=(AE(J,I)+BE(J,I))/SEGAB(J,I)
      CW(J,I)=(AW(J,I)+BW(J,I))/SEGAB(J,I)
      CN(J,I)=(AN(J,I)+BN(J,I))/SEGAB(J,I)
      CS(J,I)=(AS(J,I)+BS(J,I))/SEGAB(J,I)
      VPWSK(J,I)=(WSKT(J,I)*R(J)/4.0)*(X(I+1)-X(I-1))*(R(J+1)-R(J-1
     1))
      TR(J,I)=(CE(J,I)*TR(J,I+1)+CW(J,I)*TR(J,I-1)+CN(J,I)*TR(J+1,I)+CS(
     1J,I)*TR(J-1,I)+VPWSK(J,I)/SEGAB(J,I))/(1.0+DK(J,I)*(R(J)/4.0)
     1*(X(I+1)-X(I-1))*(R(J+1)-R(J-1))/SEGAB(J,I))
      TR(J,I)=.5*TR(J,I)+.5*T(J,I)
  125 CONTINUE
      RETURN
      END
      SUBROUTINE ABOKHALIL
      REAL MU
      COMMON/CALP/ALP(26,37)
```

```
      COMMON/CLS/AL(26,37)
      COMMON/CSTFC/EPSI(26,37)
      COMMON/CGRID/R(26),X(37)
      COMMON/CROP/ROH
      COMMON/CKET/T(26,37)
      COMMON/CMUEF/CMU
      COMMON/CFMU/MU
      COMMON/CLSEG/CA,CB,SEGL
      COMMON  FON(26,37),GON(26,37),GTO(26,37),WSKT(26,37),DL(26,37),
     1AE(26,37),AW(26,37),AN(26,37),AS(26,37),BE(26,37),BW(26,37),BN(26,
     237),BS(26,37),SEGAB(26,37),CE(26,37),CW(26,37),CN(26,37),CS(26,37)
     3,D(26,37)
C
C           ********************************************
C           *                                          *
C           * THIS SUBROUTINE CALCULATES THE NEW VALUES *
C           *                                          *
C           * OF THE LENGTH SCALE AT ALL THE GRID NODES *
C           *                                          *
C           * AS PART OF THE ITERATION PROCESS         *
C           *                                          *
C           ********************************************
C
      DO 130 J=1,26
      DO 130 I=1,37
      ALR(J,I)=AL(J,I)
  130 CONTINUE
      DO 139 N=1,4
      IF(N.GT.1)GO TO 135
      LJ=2
      MJ=10
      LI=2
      MI=36
      GO TO 138
  135 IF(N.GT.2)GO TO 136
      LJ=11
      MJ=13
      LI=15
      MI=36
      GO TO 138
  136 IF(N.GT.3)GO TO 137
      LJ=14
      MJ=25
      LI=2
      MI=18
      GO TO 138
  137 LJ=14
      MJ=25
      LI=21
      MI=36
  138 DO 139 J=LJ,MJ
      DO 139 I=LI,MI
      FON(J,I)=(EPSI(J+1,I+1)+EPSI(J-1,I-1)-EPSI(J+1,I-1)-EPSI(J-1,I+1))
     1/(R(J)*(R(J+1)-R(J-1))*(X(I+1)-X(I-1)))
      GON(J,I)=((((EPSI(J+1,I)-EPSI(J,I))/(R(J+1)-R(J)))-((EPSI(J,I)-EPS
     1I(J-1,I))/(R(J)-R(J-1))))*2.0)/(R(J)*(R(J+1)-R(J-1)),
      GTO(J,I)=((((EPSI(J,I+1)-EPSI(J,I))/(X(I+1)-X(I)))-((EPSI(J,I)-EPS
     1I(J,I-1))/(X(I)-X(I-1))))*2.0)/(R(J)*(X(I+1)-X(I-1)))
      WSKT(J,I)=((ROH*SQRT(T(J,I))*ALR(J,I)*CMU-MU)/(ROH*ROH))*((4.0*(FO
     1N(J,I)*FON(J,I)))+(ABS(GON(J,I)-GTO(J,I))**2.0))
      DL(J,I)=(CB*ALR(J,I)/T(J,I))*WSKT(J,I)-(CA*ROH*SQRT(T(J,I)))
      AE(J,I)=((EPSI(J-1,I+1)+EPSI(J-1,I)-EPSI(J+1,I+1)-EPSI(J+1,I))+(AB
     1S(EPSI(J-1,I+1)+EPSI(J-1,I)-EPSI(J+1,I+1)-EPSI(J+1,I))))/8.0
      AW(J,I)=((EPSI(J+1,I-1)+EPSI(J+1,I)-EPSI(J-1,I-1)-EPSI(J-1,I))+(AB
     1S(EPSI(J+1,I-1)+EPSI(J+1,I)-EPSI(J-1,I-1)-EPSI(J-1,I))))/8.0
      AN(J,I)=((EPSI(J+1,I+1)+EPSI(J,I+1)-EPSI(J+1,I-1)-EPSI(J,I-1))+(AB
     1S(EPSI(J+1,I+1)+EPSI(J,I+1)-EPSI(J+1,I-1)-EPSI(J,I-1))))/8.0
      AS(J,I)=((EPSI(J-1,I-1)+EPSI(J,I-1)-EPSI(J-1,I+1)-EPSI(J,I+1))+(AB
     1S(EPSI(J-1,I-1)+EPSI(J,I-1)-EPSI(J-1,I+1)-EPSI(J,I+1))))/8.0
      BE(J,I)=((ROH*CMU)/(2.0*SEGL))*(SQRT(T(J,I+1))*ALR(J,I+1)+SQRT(T(
     1J,I))*ALR(J,I))*((R(J+1)-R(J-1))/(X(I+1)-X(I)))*R(J)*2.0
      BW(J,I)=((ROH*CMU)/(2.0*SEGL))*(SQRT(T(J,I-1))*ALR(J,I-1)+SQRT(T(
     1J,I))*ALR(J,I))*((R(J+1)-R(J-1))/(X(I)-X(I-1)))*R(J)*2.0
      BN(J,I)=((ROH*CMU)/(2.0*SEGL))*(SQRT(T(J+1,I))*ALR(J+1,I)+SQRT(T(
     1J,I))*ALR(J,I))*((X(I+1)-X(I-1))/(R(J+1)-R(J)))*(R(J+1)+R(J))
      BS(J,I)=((ROH*CMU)/(2.0*SEGL))*(SQRT(T(J-1,I))*ALR(J-1,I)+SQRT(T(
     1J,I))*ALR(J,I))*((X(I+1)-X(I-1))/(R(J)-R(J-1)))*(R(J-1)+R(J))
      SEGAB(J,I)=AE(J,I)+AW(J,I)+AN(J,I)+AS(J,I)+BE(J,I)+BW(J,I)+BN(J,I)
     1+BS(J,I)
```

```
      CE(J,I)=(AE(J,I)+BE(J,I))/SEGAB(J,I)
      CW(J,I)=(AW(J,I)+BW(J,I))/SEGAB(J,I)
      CN(J,I)=(AN(J,I)+BN(J,I))/SEGAB(J,I)
      CS(J,I)=(AS(J,I)+BS(J,I))/SEGAB(J,I)
      D(J,I)=(DL(J,I)/SEGAB(J,I))*(R(J)/4.0)*(X(I+1)-X(I-1))*(R(J+1)-R(J
     1-1))
      ALR(J,I)=CE(J,I)*ALR(J,I+1)+CW(J,I)*ALR(J,I-1)+CN(J,I)*ALR(J+1,I)+
     1CS(J,I)*ALR(J-1,I)-D(J,I)
      ALR(J,I)=.5*ALR(J,I)+.5*AL(J,I)
  139 CONTINUE
      RETURN
      END
      SUBROUTINE SAID
      COMMON/CVLO/UO(26,37),VO(26,37)
      COMMON/CGRID/R(26),X(37)
      COMMON/CROH/ROH
      COMMON/CSTFU/EPSI(26,37)
      COMMON/CFVL/U(26,37),V(26,37)
C
C     ***************************************************
C     *                                                 *
C     * THIS SUBROUTINE CALCULATES THE FINAL VALUES OF  *
C     *                                                 *
C     * THE MEAN VELOCITY COMPONENTS AT ALL THE GRID NODES *
C     *                                                 *
C     ***************************************************
C
      DO 140 I=1,37
      U(1,I)=UO(1,I)
      V(1,I)=VO(1,I)
      U(26,I)=UO(26,I)
      V(26,I)=VO(26,I)
  140 CONTINUE
      DO 141 J=14,25
      U(J,19)=UO(J,19)
      V(J,19)=VO(J,19)
      U(J,20)=UO(J,20)
      V(J,20)=VO(J,20)
  141 CONTINUE
      DO 142 J=11,13
      DO 142 I=1,14
      U(J,I)=UO(J,I)
      V(J,I)=VO(J,I)
  142 CONTINUE
      DO 143 J=2,25
      U(J,1)=UO(J,1)
      V(J,1)=VO(J,1)
      U(J,37)=UO(J,37)
      V(J,37)=VO(J,37)
  143 CONTINUE
      DO 144 I=1,14
      U(12,I)=.0
      V(12,I)=.0
  144 CONTINUE
      DO 149 N=1,4
      IF(N.GT.1)GO TO 145
      LJ=2
      MJ=10
      LI=2
      MI=36
      GO TO 148
  145 IF(N.GT.2)GO TO 146
      LJ=11
      MJ=13
      LI=15
      MI=36
      GO TO 148
  146 IF(N.GT.3)GO TO 147
      LJ=14
      MJ=25
      LI=2
      MI=18
      GO TO 148
  147 LJ=14
      MJ=25
      LI=21
      MI=36
  148 DO 149 J=LJ,MJ
      DO 149 I=LI,MI
      U(J,I)=(((((R(J+1)-R(J))**2.0)-((R(J)-R(J-1))**2.0))*EPSI(J,I))*((
     1(R(J)-R(J-1))**2.0)*EPSI(J+1,I))-(((R(J+1)-R(J))**2.0)*EPSI(J-1,I)
     2))/((R(J+1)-R(J))*(R(J)-R(J-1))*(R(J+1)-R(J-1))*R(J)*ROH)
```

```
      V(J,I)=(((((X(I+1)-X(I))**2.0)-((X(I)-X(I-1))**2.0))*EPSI(J,I))+((
     1(X(I)-X(I-1))**2.0)*EPSI(J,I+1))-(((X(I+1)-X(I))**2.0)*EPSI(J,I-1)
     2))/((X(I)-X(I+1))*(X(I)-X(I-1))*(X(I+1)-X(I-1))*R(J)*ROH)
  149 CONTINUE
      RETURN
      END
      SUBROUTINE KAMAL
C
C        ************************************************
C        *                                              *
C        * THIS SUBROUTINE PRINTS THE TITLE AND THE HEADING *
C        *                                              *
C        ************************************************
C
  200 FORMAT(////////////,20X,80HPREDICTION OF THE FLOW AND THE PERFORMAN
     1CE PARAMETERS OF THE CRANFIELD DIFFUSER////)
  201 FORMAT(50X,15HCONVERGENT CASE////)
      WRITE(6,200)
      WRITE(6,201)
      RETURN
      END
      SUBROUTINE AHMAD
      COMMON/CSTFU/EPSI(26,37)
      COMMON/CVORFU/OMEGA(26,37)
      COMMON/CKET/T(26,37)
      COMMON/CLS/AL(26,37)
      COMMON/CFVL/U(26,37),V(36,37)
      COMMON/CSP/SP(26,37)
      COMMON/CCPCL/CP(26,37),CL(26,37)
      COMMON/COPER/SPOT,ALPHO,VOI,SPET,ALPHE,VE,CPT,CLT
      COMMON/CK/K
C
C        ************************************
C        *                                  *
C        * THIS SUBROUTINE PRINTS THE RESULTS *
C        *                                  *
C        ************************************
C
  400 FORMAT (1H1,50X,7HRESULTS)
  401 FORMAT (///,2X,19HTHE STREAM FUNCTION)
  402 FORMAT (/,2X,10E12.4)
  403 FORMAT (1H1,2X,22HTHE VORTICITY FUNCTION)
  404 FORMAT (1H1,2X,18HTHE KINETIC ENERGY)
  406 FORMAT (1H1,2X,16HTHE LENGTH SCALE)
  407 FORMAT (1H1,2X,19HTHE AXIAL VELOCITY)
  408 FORMAT (1H1,2X,19HTHE RADIAL VELOCITY)
  410 FORMAT (1H1,2X,19HTHE STATIC PRESSURE)
  411 FORMAT (/,2X,10F11.1)
  412 FORMAT (1H1,2X,36HTHE STATIC PRESSURE RISE COEFFICIENT)
  413 FORMAT (/,2X,10F10.3)
  414 FORMAT (1H1,2X,35HTHE TOTAL PRESSURE LOSS COEFFICIENT)
  415 FORMAT (////,2X,20HDIFFUSER PERFORMANCE PARAMETERS)
  416 FORMAT (/,4X,4HSPOT,7X,4HSPET,11X,3HVOI,8X,2HVE,7X,3HCPT,8X,3HCLT,
     17X,5HALPHO,6X,5HALPHE)
  417 FORMAT (/,4F11.1,4F11.3)
  418 FORMAT (//////,2X,17HITERATION COUNTER)
  419 FORMAT (1H+,2X,I4)
  420 FORMAT (//////,14HEND OF RESULTS)
      WRITE(6,400)
      WRITE(6,401)
      DO 450 J=1,26
      WRITE(6,402)(EPSI(J,I),I=1,37)
  450 CONTINUE
      WRITE(6,403)
      DO 454 J=1,26
      WRITE(6,402)(OMEGA(J,I),I=1,37)
  454 CONTINUE
      WRITE(6,404)
      DO 458 J=1,26
      WRITE(6,402)(T(J,I),I=1,37)
  458 CONTINUE
      WRITE(6,406)
      DO 461 J=1,26
      WRITE(6,402)(AL(J,I),I=1,37)
  461 CONTINUE
      WRITE(6,407)
      DO 465 J=1,26
      WRITE(6,402)(U(J,I),I=1,37)
  465 CONTINUE
      WRITE(6,409)
      DO 467 J=1,26
      WRITE(6,402)(V(J,I),I=1,37)
```

```
  467 CONTINUE
      WRITE(6,410)
      DO 469 J=1,26
      WRITE(6,411)(SP(J,I),I=1,37)
  469 CONTINUE
      WRITE(6,412)
      DO 473 J=1,26
      WRITE(6,413)(CP(J,I),I=1,37)
  473 CONTINUE
      WRITE(6,414)
      DO 475 J=1,26
      WRITE(6,413)(CL(J,I),I=1,37)
  475 CONTINUE
      WRITE(6,415)
      WRITE(6,416)
      WRITE(6,417)SPOT,SPET,VOI,VE,CPT,CLT,ALPHO,ALPHE
      WRITE(6,418)
      WRITE(6,419)K
      WRITE(6,420)
      RETURN
      END
      BLOCK DATA
      REAL MU
      COMMON/CGRID/R(26),X(37)
      COMMON/CVLO/UOA(37),UOB(37),UOC(37),UOD(37),UOE(37),UOF(37),UOG(37
     1),UOH(37),UOI(37),UOJ(37),UOK(37),UOL(37),UOM(37),UON(37),UOO(37),
     2UOP(37),UOQ(37),UOR(37),UOS(37),UOT(37),UOU(37),UOV(37),UOW(37),UO
     3X(37),UOY(37),UOZ(37),VOA(37),VOB(37),VOC(37),VOD(37),VOE(37),VOF(
     437),VOG(37),VOH(37),VOI(37),VOJ(37),VOK(37),VOL(37),VOM(37),VON(37
     5),VOO(37),VOP(37),VOQ(37),VOR(37),VOS(37),VOT(37),VOU(37),VOV(37),
     6VOW(37),VOX(37),VOY(37),VOZ(37)
      COMMON/CKETO/TOA(37),TOB(37),TOC(37),TOD(37),TOE(37),TOF(37),TOG(3
     17),TOH(37),TOI(37),TOJ(37),TOK(37),TOL(37),TOM(37),TON(37),TOO(37)
     2,TOP(37),TOQ(37),TOR(37),TOS(37),TOT(37),TOU(37),TOV(37),TOW(37),T
     3OX(37),TOY(37),TOZ(37)
      COMMON/CSP/SP(26,37)
      COMMON/CLCONS/CON,CTO,CTR,CFO,CFV,CSX
      COMMON/CDIMS/RP,RS,RPO,RF,RIC
      COMMON/CROH/ROH
      COMMON/CFMU/MU
      COMMON/CMUEF/CMU
      COMMON/CKEFG/CD,SEGK
      COMMON/CLSEG/CA,CB,SEGL
C
C           * * * * * * * * * * * * * * * * * * * * * * * * * * **
C           *                                                     *
C           * THIS IS THE INPUT DATA REQUIRED TO PREDICT          *
C           *                                                     *
C           * THE PERFORMANCE OF THE CRANFIELD DIFFUSER           *
C           *                                                     *
C           ** * * * * * * * * * * * * * * * * * * * * * * * * * *
C
      DATA R/0.0    ,.00475,.00875,.012   ,.01475,.017   ,.01875,.02025,
     1.02115,.0225 ,.0235 ,.02435,.025   ,.0255 ,.02615,.027  ,.028  ,.
     2029  ,.03   ,.031  ,.032  ,.033   ,.034  ,.03485,.0355 ,.036  /
      DATA X/0.0    ,.004  ,.007  ,.0095 ,.012  ,.014  ,.0155 ,.01675,.0
     118  ,.019  ,.02   ,.021  ,.022  ,.023  ,.02425,.02525,.02625,.0272
     25,.02825,.02925,.03025,.03125,.03225,.03325,.03425,.0355 ,.03675,.
     303825,.04025,.04525,.04625,.05025,.05425,.05825,.06225,.06625,.070
     425/
      DATA UOA/52.6,54.0,53.8,53.7,53.6,53.0,52.7,52.3,51.8,51.0,50.6,49
     1.8,48.8,47.8,46.6,46.1,45.6,45.2,46.0,47.5,47.3,48.2,48.5,48.4,48.
     20,47.0,46.0,45.3,43.8,41.8,40.0,38.6,37.8,37.3,36.3,35.9,35.5/
      DATA UOB/55.6,53.9,53.8,53.6,53.5,53.0,52.6,52.2,51.8,51.3,50.6,49
     1.8,49.0,48.1,46.9,46.3,45.7,45.5,47.0,48.5,46.4,47.0,47.5,47.3,47.
     20,46.2,45.4,44.5,43.2,41.7,40.0,38.9,38.0,37.5,36.2,35.8,35.5/
      DATA UOC/53.4,53.6,53.4,53.3,53.2,52.6,52.4,52.0,51.7,51.3,50.6,49
     1.9,49.3,48.3,47.6,46.7,46.1,45.8,48.0,49.0,45.2,45.8,46.0,45.9,45.
     26,45.0,44.4,43.6,42.4,41.4,39.6,38.6,37.8,37.2,37.1,35.6,35.1/
      DATA UOD/53.0,53.1,52.9,52.8,52.7,52.4,52.1,51.8,51.6,51.3,50.7,50
     1.1,49.6,49.0,47.7,47.0,46.4,48.6,48.8,44.5,44.0,44.6,44.3,44.
     28,44.2,44.6,42.6,41.7,40.6,39.0,38.0,37.4,36.7,35.9,35.2,34.5/
      DATA UOE/52.6,52.4,52.5,52.4,52.3,52.1,51.9,51.7,51.5,51.2,50.7,50
     1.4,50.1,49.9,49.1,48.4,47.8,47.5,48.9,48.0,44.1,44.3,44.1,43.7,44.
     21,43.7,42.9,41.6,40.4,39.4,38.2,37.6,36.6,36.0,35.2,34.5,33.6/
      DATA UOF/51.9,51.5,51.5,51.5,51.5,51.4,51.4,51.4,51.4,51.2,51.0,51
     1.0,51.2,51.4,50.4,49.8,49.9,48.8,48.4,48.7,45.2,44.9,44.3,43.6,43.
     23,42.4,41.5,40.4,38.4,38.0,37.2,36.5,35.6,35.2,34.5,33.5,32.5/
      DATA UOG/50.7,5 .8,50.5,50.6,50.7,5 .9,51.0,51.1,51.2,51.1,51.1,51
     1.2,51.3,51.5,51.6,50.4,49.8,48.2,48.8,44.7,46.2,45.8,44.2,43.1,42.
     20,41.0,40.0,39.0,38.8,38.0,35.6,35.1,34.5,34.3,33.5,32.5,31.5/
```

```
 DATA UOH/49.1,49.1,49.3,49.5,49.7,50.3,50.5,50.7,50.9,51.1,51.3,51
1.4,51.5,51.7,51.9,50.8,49.5,47.3,44.6,43.5,45.5,44.1,42.7,41.7,40.
24,39.5,38.5,37.5,35.6,33.9,34.0,33.0,32.4,32.2,31.3,30.2,29.0/
 DATA UOI/47.6,47.8,48.2,48.5,48.9,49.7,50.0,50.2,50.4,50.9,51.1,50
1.9,51.2,51.4,51.4,50.2,48.2,46.5,43.3,40.6,44.8,43.0,41.3,40.2,38.
24,37.2,37.0,36.0,34.6,31.8,32.2,31.1,30.7,30.3,29.6,28.6,27.5/
 DATA UOJ/46.2,44.5,44.9,45.2,45.5,46.5,47.3,49.0,48.5,46.8,45.0,49
1.1,49.3,49.5,49.4,46.9,44.7,43.0,43.6,37.4,42.0,40.0,38.2,37.0,35.
20,30.5,34.0,33.5,32.4,33.5,28.0,28.0,27.5,27.5,26.5,25.7,25.3/
 DATA UOK/  .0,  .0,  .0,  .0,  .0,  .0,  .0,  .0,  .0,  .0,  .0,
1.0,  .0,  .0,41.1,37.7,34.0,24.2,37.0,33.0,36.0,35.0,32.5,31.2,31.
24,31.0,30.6,30.2,30.2,25.3,25.2,25.0,25.0,25.0,24.7,24.0,23.4/
 DATA UOL/99.9,99.9,99.9,99.9,99.9,99.9,99.9,99.9,99.9,99.9,99.9,99
1.9,99.9,  .0,26.0,20.0,15.0, 9.0,31.0,24.0,25.0,24.0,24.0,22.0,23.
25,24.0,25.0,26.0,27.0,22.6,22.2,22.9,22.7,22.5,22.3,22.0,21.7/
 DATA UOM/  .0,  .0,  .0,  .0,  .0,  .0,  .0,  .0,  .0,  .0,  .0,
1.0,  .0,  .0,20.7,15.6, 9.3, 5.2,20.0,15.0,17.0,18.5,19.0,17.2,18.
23,19.8,21.3,23.0,24.3,20.5,20.2,20.5,20.4,21.3,21.4,21.0,20.5/
 DATA UON/-0.2,-0.2,  .0,  .1,  .2,  .3,  .4,  .5,  .6, 1.0, 1.7, 4
1.0, 3.8, 3.4,17.5,13.1, 7.1, 4.0,  .0,  .0,13.2,16.2,17.0,14.6,16.
25,17.5,18.5,20.0,22.0,19.0,18.9,19.0,19.3,20.0,20.5,20.0,19.5/
 DATA UOO/-0.5,-0.4,-0.1,  .1,  .3,  .5,  .6,  .7,  .8, 1.3, 2.4, 4
1.9, 4.5, 4.2,13.5,10.0, 5.5, 3.0,  .0,  .0, 8.2,13.0,14.5,12.4,14.
20,15.0,16.0,17.0,19.1,17.1,16.7,17.0,17.6,18.5,19.0,18.8,18.5/
 DATA UOP/-0.9,-0.6,-0.2,  .2,  .4,  .9, 1.1, 1.2, 1.3, 1.8, 3.1, 5
1.4, 5.0, 4.5,10.1, 7.3, 4.0, 2.3,  .0,  .0, 3.1, 9.2,11.7,10.2,11.
21,11.9,12.7,13.6,16.0,14.9,14.3,14.7,15.3,16.6,17.3,17.0,16.8/
 DATA UOQ/-1.5,-1.1,-0.7,-0.4,-0.1,  .3,  .7,  .9, 1.1, 1.6, 2.8, 4
1.9, 4.4, 3.8, 6.4, 4.6, 2.6, 1.4,  .0,  .0,  .0, 8.0, 8.5, 7.7, 8.
23, 8.8, 9.4,10.0,13.0,12.5,12.0,12.4,13.0,14.5,15.0,15.0,15.0/
 DATA UOR/-2.1,-1.3,-1.1,-1.0,-0.9,-0.2,  .2,  .4,  .6,  .9, 1.8, 3
1.3, 2.9, 2.4, 3.4, 2.4, 1.3,  .6,  .0,  .0,-1.0, 2.5, 5.5, 5.4, 6.
20, 6.5, 7.0, 7.6, 9.4, 9.6, 9.3, 9.6,10.4,12.2,12.9,13.1,13.2/
 DATA UOS/-2.7,-2.4,-2.1,-1.9,-1.7,-1.1,-0.7,-0.2,  .0,  .0,  .0,
1.0,  .0,  .0,  .0,  .1,  .0,  .0,  .0,  .0,-1.5,-0.2, 2.5, 3.0, 3.
27, 4.2, 4.7, 5.3, 6.5, 6.5, 7.0, 7.2, 7.8,10.0,10.7,11.0,11.5/
 DATA UOT/-3.3,-3.0,-2.8,-2.6,-2.5,-2.4,-2.0,-1.7,-1.4,-1.8,-3.3,-4
1.6,-4.4,-4.2,-3.4,-2.3,-3.3,-0.6,  .0,  .0,-2.0,-1.8,-0.2, 1.1, 2.
20, 2.4, 2.8, 3.3, 4.4, 4.5, 5.0, 5.4, 6.2, 8.0, 8.6, 8.9, 9.4/
 DATA UOU/-3.7,-3.7,-3.6,-3.5,-3.4,-3.8,-3.7,-3.6,-3.5,-4.7,-6.5,-7
1.5,-7.3,-7.4,-5.9,-4.0,-2.4,-1.1,  .0,  .0,-2.2,-3.0,-2.5,-0.6,  .
27, 1.0, 1.4, 1.8, 2.5, 2.7, 3.0, 3.5, 4.5, 6.0, 6.5, 7.1, 7.5/
 DATA UOV/-3.9,-4.1,-4.3,-4.4,-4.5,-5.1,-5.3,-6.0,-7.0,-7.8,-8.4,-9
1.7,-9.4,-9.0,-7.7,-5.1,-2.9,-1.3,  .0,  .0,-2.2,-3.7,-4.3,-2.2,-1.
22,-0.7,-0.1,  .5, 1.0, 1.3, 1.7, 2.4, 3.0, 4.0, 4.7, 5.1, 5.3/
 DATA UOW/-3.5,-3.8,-4.1,-4.4,-4.7,-5.5,-5.4,-6.6,-7.8,-8.2,-8.5,-9
1.9,-9.5,-9.1,-8.4,-5.2,-3.0,-1.2,  .0,  .0,-1.8,-3.9,-4.7,-3.2,-1.
27,-1.4,-1.0,-0.5,-0.1,  .2,  .7, 1.2, 1.8, 2.4, 3.0, 3.6, 3.7/
 DATA UOX/-3.0,-2.5,-2.9,-3.3,-3.7,-4.6,-5.0,-5.0,-6.5,-7.5,-7.8,-8
1.3,-7.5,-7.0,-7.3,-4.5,-2.7,-1.1,  .0,  .0,-1.4,-2.9,-3.7,-4.2,-1.
29,-1.5,-1.1,-0.7,-0.4,-0.3,  .2,  .7, 1.0, 1.4, 1.8, 2.2, 2.5/
 DATA UOY/-1.0,-1.2,-1.5,-1.8,-2.0,-2.8,-3.2,-3.6,-4.0,-5.0,-5.2,-4
1.2,-4.0,-3.5,-4.2,-2.5,-2.0,-0.7,  .0,  .0,-0.8,-2.0,-2.5,-3.0,-1.
24,-1.1,-0.8,-0.4,-0.3,-0.2,  .0,  .3,  .6,  .7,  .8, 1.5, 2.1/
 DATA UOZ/  .0,  .0,  .0,  .0,  .0,  .0,  .0,  .0,  .0,  .0,  .0,  .0,
1.0,  .0,  .0,  .0,  .0,  .0,  .0,  .0,  .0,  .0,  .0,  .0,  .0,
20,  .0,  .0,  .0,  .0,  .0,  .0,  .0,  .0,  .0,  .0,  .0,  .0/
 DATA VOA/  .0,  .0,  .0,  .0,  .0,  .0,  .0,  .0,  .0,  .0,  .0,
1.0,  .0,  .0,  .0,  .0,  .0,  .0,  .0,  .0,  .0,  .0,  .0,  .0,
20,  .0,  .0,  .0,  .0,  .0,  .0,  .0,  .0,  .0,  .0,  .0,  .0/
 DATA VOB/  .0,  .3,  .2,  .1,  .1,  .0,  .0,  .0,  .0,  .0,  .2,
1.5,  .6,  .8,  .6,  .6, 1.0, 1.2,  .8, 1.2,  .1,  .4, 1.0, 1.6, 2.
22, 1.9, 1.6, 1.2, 1.1,  .6,  .4,  .2,  .1,  .0,  .0,  .0,  .0/
 DATA VOC/  .0,  .2,  .1,  .0,  .0,  .0,  .0,  .0,  .0,  .1,  .5, 1
1.0, 1.2, 1.5, 1.5, 1.5, 1.9, 2.4, 1.8, 2.3,  .4, 1.2, 2.3, 3.4, 4.
22, 3.7, 3.2, 2.7, 2.2, 1.2,  .9,  .8,  .5,  .1,  .0,  .0,  .0/
 DATA VOD/  .0,  .2,  .2,  .1,  .1,  .0,  .0,  .1,  .2,  .4, 1.0, 1
1.7, 2.0, 2.6, 2.5, 2.5, 3.2, 3.6, 3.0, 3.5, 1.0, 2.5, 3.8, 5.0, 6.
20, 5.5, 5.0, 4.4, 5.2, 2.0, 1.4, 1.0,  .4,  .2,  .0,  .0,  .0/
 DATA VOE/  .0,  .3,  .3,  .3,  .3,  .0,  .1,  .2,  .4,  .8, 1.9, 3
1.1, 3.8, 5.1, 5.5, 5.0, 5.2, 5.3, 4.3, 5.0, 2.1, 4.3, 5.8, 7.0, 8.
20, 7.4, 6.9, 6.1, 4.1, 2.8, 1.9, 1.4,  .7,  .3,  .1,  .0,  .0/
 DATA VOF/  .0,  .3,  .2,  .1,  .1,  .0,  .2,  .5,  .8, 1.1, 3.0, 4
1.8, 6.6, 8.1, 9.9, 8.9, 7.6, 6.8, 6.1, 6.7, 4.0, 7.0, 8.2, 9.4,10.
20, 9.5, 8.9, 8.4, 4.9, 3.5, 2.3, 1.5, 1.0,  .4,  .2,  .0,  .0/
 DATA VOG/  .0,  .3,  .2,  .2,  .2,  .4,  .6,  .9, 1.2, 1.8, 4.3, 6
1.6, 8.5,11.5,14.0,12.2, 9.9, 8.6, 8.0, 8.6, 5.6, 8.8,10.9,11.8,12.
20,11.6,11.0,10.3, 9.6, 3.9, 2.5, 1.7, 1.1,  .5,  .3,  .1,  .0/
 DATA VOH/  .0,  .2,  .2,  .2,  .2,  .7, 1.0, 1.4, 1.8, 2.6, 6.0, 9
1.0,11.3,14.2,16.0,15.0,12.0,10.4,10.0,10.6, 7.0,10.2,12.6,14.0,13.
27,13.0,12.2,11.4, 6.3, 4.2, 2.8, 2.0, 1.2,  .6,  .4,  .1,  .0/
 DATA VOI/  .0,  .1,  .2,  .2,  .3,  .6,  .9, 1.2, 1.6, 2.4, 5.4, 8
1.0,10.3,13.7,15.5,16.4,13.0,11.5,12.0,12.7, 7.5,10.8,13.4,15.1,14.
27,13.8,12.9,11.9, 6.8, 4.5, 3.0, 2.0, 1.2,  .6,  .4,  .1,  .0/
```

```
 DATA VOJ/ .0, .2, .2, .2, .2, .1, .2, .3, .5, 1.0, 2.5, 4
1.0, 5.3, 7.5,13.0,16.6,14.0,12.0,13.5,14.2, 7.8,11.1,13.8,15.9,15.
26,14.7,13.4,12.1, 7.3, 4.6, 2.8, 2.2, 1.4, .6,-0.3, .2, .0/
 DATA VOK/ .0, .0, .0, .0, .0, .0, .0, .0, .0, .0, .0,
1.0, .0, .0,11.5,15.5,13.7,12.5, 8.4, 3.5, 6.8,10.0,13.0,15.3,15.
20,14.0,12.9,11.6, 7.4, 4.7, 2.8, 2.1, 1.3, .6, .3, .1, .0/
 DATA VOL/99.9,99.9,99.9,99.9,99.9,99.9,99.9,99.9,99.9,99.9,99.9,99
1.9,99.9, .0,10.4,13.9,12.7,10.0, 3.0, 1.1, 4.8, 8.4,11.5,14.1,14.
20,13.0,12.0,11.2, 7.2, 4.8, 2.9, 2.1, 1.3, .6, .4, .3, .0/
 DATA VOM/ .0, .0, .0, .0, .0, .0, .0, .0, .0, .0, .0,
1.0, .0, .0, 9.6,12.4,11.5, 8.0, 1.1, .4, 3.5, 7.1,10.0,13.1,12.
28,12.1,11.5,10.0, 6.9, 4.9, 3.0, 2.0, 1.2, .6, .6, .5, .0/
 DATA VON/ .0, .0, .0, .0, .0, .0,-0.1,-0.2,-0.3,-0.5,-0.7,-0
1.8, .0, .6, 9.0,11.4,11.1, 7.3, .0, .0, 3.0, 5.6, 7.5,11.6,11.
28,11.2,10.6,10.0, 6.5, 4.6, 2.9, 1.9, 1.1, .5, .4, .3, .0/
 DATA VOO/ .0, .0, .0, .0, .0, .0,-0.2,-0.4,-0.7,-0.9,-1.1,-1
1.1, .0, .9, 8.5,10.5,10.4, 7.1, .0, .0, 1.9, 3.4, 4.1, 9.5,10.
25,11.0,10.0, 9.4, 5.8, 4.3, 2.8, 1.8, 1.0, .5, .3, .1, .0/
 DATA VOP/ .0, .0, .0, .0, .0,-0.1,-0.6,-1.2,-1.8,-1.6,-2.1,-1
1.7, .0, 1.4, 8.0,10.6,10.0, 7.5, .0, .0, .6,-0.5, 1.0, 6.0, 8.
20,10.0, 9.0, 8.0, 5.0, 4.1, 2.6, 1.7, .9, .4, .2, .0, .0/
 DATA VOQ/ .0, .3, .2, .1, .0,-0.3,-1.0,-1.7,-2.4,-2.4,-2.9,-2
1.6, .0, 2.0, 7.6,12.0,10.5, 8.2, .0, .0,-0.6,-4.1,-3.0, 2.1, 5.
29, 6.1, 6.4, 6.7, 4.2, 3.5, 2.3, 1.6, .9, .4,-0.3, .1, .0/
 DATA VOR/ .0, .0, .0, .0, .0,-0.5,-1.1,-1.7,-2.2,-2.7,-3.3,-3
1.2, .3, 2.3, 7.0,15.5,11.5, 8.0, .0, .0,-2.2,-6.9,-5.6,-1.7, 3.
26, 4.0, 4.5, 5.0, 3.4, 3.0, 2.0, 1.2, .7, .3, .1, .0, .0/
 DATA VOS/ .0, .3, .0,-0.4,-0.9,-1.0,-1.8,-2.6,-3.5,-4.2,-4.9,-4
1.0,-0.3, 3.5, 6.2,11.5,10.5, 7.2, .0, .0,-3.0,-9.4,-7.6,-3.9, 1.
28, 2.3, 2.9, 3.4, 2.6, 2.4, 1.7, 1.1, .6, .3, .0, .0, .0/
 DATA VOT/ .0,-0.3,-0.6,-1.0,-1.4,-1.5,-2.5,-3.5,-4.6,-5.5,-6.6,-4
1.6, .0, 4.3, 6.6, 8.5, 9.0, 7.0, .0, .0,-3.0,-9.0,-8.7,-4.8, .
23, .7, 1.2, 1.7, 1.7, 1.8, 1.2, .8, .4, .1, .1, .0, .0/
 DATA VOU/ .0,-0.3,-0.7,-1.1,-1.4,-1.2,-2.9,-4.7,-6.5,-7.0,-6.2,-3
1.7,-0.3, 3.4, 6.2, 6.5, 7.5, 6.2, .0, .0,-2.5,-9.9,-9.0,-5.1,-0.
29,-0.4, .1, .4, 1.0, 1.4, .9, .6, .3, .0, .3, .1, .0/
 DATA VOV/ .0, .3, .0,-0.4,-0.9,-1.5,-3.2,-5.1,-7.1,-7.8,-5.7,-3
1.2,-0.3, 3.2, 6.0, 5.0, 6.0, 5.4, .0, .0,-0.9,-9.3,-8.5,-4.9,-1.
26,-1.5,-0.6,-0.4, .5, .9, .5, .3, .0, .0, .0, .0, .0/
 DATA VOW/ .0,-0.3,-0.3,-0.3,-0.3,-0.8,-2.3,-3.6,-6.4,-6.5,-4.5,-2
1.6, .3, 2.3, 3.8, 4.0, 4.5, 3.6, .0, .0,-0.3,-8.6, 7.4,-4.1,-1.
25,-0.9,-0.3, .0, .3, .5, .3, .0, .0, .0, .3, .0, .0/
 DATA VOX/ .0, .0,-0.1,-0.2,-0.2,-0.2,-1.3,-2.6,-4.4,-4.8,-2.9,-1
1.6, .0, 1.5, 2.7, 2.7, 2.5, 2.5, .0, .0,-0.1,-5.4,-4.6,-3.0,-1.
24,-0.8,-0.3, .0, .1, .3, .1, .0, .0, .0, .0, .0, .0/
 DATA VOY/ .0, .0, .0, .0, .0,-0.1,-0.9,-1.7,-2.4,-2.6,-1.3,-0
1.8, .0, .7, 1.1, 1.1, 1.1, 1.1, .0, .0,-0.1,-2.4,-2.0,-1.6,-0.
20,-0.4,-0.2, .0, .1, .1, .0, .0, .0, .0, .0, .0, .0/
 DATA VOZ/ .0, .0, .0, .0, .0, .0, .0, .0, .0, .0, .0, .0,
1.0, .0, .0, .0, .0, .0, .0, .0, .0, .0, .0, .0, .0, .0, .
20, .0, .0, .0, .0, .0, .0, .0, .0, .0, .0, .0, .0, .0/
 DATA TOA/ 2.5, 3.8, 3.3, 3.5, 4.0, 4.5, 5.3, 5.8, 6.3, 7
1.3, 7.8, 8.8, 9.5, 10.5, 11.3, 12.0, 13.0, 13.8, 15.3, 16.5, 17
6.8, 19.5, 21.0, 22.0, 22.5, 23.0, 23.5, 24.5, 24.5, 24.3, 25.0, 23.
3.5, 23.5, 23.5, 23.0, 22.0, 21.3/
 DATA TOB/ 2.5, 2.8, 3.0, 3.5, 4.0, 5.0, 5.5, 6.0, 6.0, 7
1.8, 8.8, 10.0, 11.3, 12.5, 14.0, 15.0, 16.0, 17.3, 18.0, 19.0, 20
2.0, 22.0, 24.0, 25.3, 26.0, 26.3, 26.5, 27.0, 27.5, 27.0, 26.0, 25
3.0, 24.5, 23.8, 23.0, 22.5, 21.8/
 DATA TOC/ 2.8, 3.0, 3.5, 4.0, 4.5, 5.3, 6.0, 6.8, 7.8, 9
1.0, 10.8, 12.0, 14.0, 15.0, 17.5, 19.0, 20.0, 21.0, 21.5, 22.0, 23
2.0, 25.0, 27.5, 28.0, 29.8, 30.0, 30.5, 31.0, 32.0, 29.5, 28.0, 26
3.0, 25.0, 25.5, 23.5, 23.0, 22.5/
 DATA TOD/ 3.0, 3.5, 3.8, 4.3, 4.5, 6.0, 7.0, 8.3, 9.5, 11
1.0, 13.0, 15.0, 17.5, 19.0, 21.0, 23.0, 23.5, 24.5, 25.0, 26.5, 27
2.0, 29.0, 31.0, 32.0, 33.5, 33.8, 34.0, 34.5, 36.0, 33.0, 30.0, 27
3.5, 25.8, 27.5, 25.0, 24.3, 24.3/
 DATA TOE/ 3.3, 4.3, 4.8, 5.3, 6.0, 7.5, 9.0, 10.5, 12.0, 14
1.3, 16.5, 18.5, 22.0, 24.0, 25.0, 27.0, 27.0, 28.5, 29.0, 32.0, 34
2.0, 34.8, 37.0, 37.5, 38.0, 38.3, 38.5, 39.0, 39.5, 37.5, 32.5, 29
3.5, 28.5, 29.0, 26.5, 25.8, 25.5/
 DATA TOF/ 3.8, 5.3, 5.8, 6.5, 7.3, 9.3, 10.8, 12.5, 14.3, 18
1.0, 20.0, 23.8, 27.0, 29.0, 32.0, 33.5, 32.5, 32.5, 33.5, 40.0, 45
2.0, 45.0, 46.0, 43.5, 43.0, 43.3, 43.8, 44.5, 45.0, 41.5, 37.5, 32
3.0, 30.0, 30.5, 28.0, 27.3, 26.5/
 DATA TOG/ 4.8, 6.3, 7.3, 8.3, 9.5, 11.8, 13.5, 15.5, 17.5, 21
1.5, 24.3, 29.0, 33.0, 37.0, 40.5, 42.5, 42.5, 39.8, 42.5, 50.0, 58
2.5, 57.0, 57.5, 52.5, 49.5, 49.5, 49.8, 50.0, 49.5, 45.5, 41.0, 35
3.0, 32.0, 31.5, 29.0, 28.0, 27.0/
 DATA TOH/ 7.0, 7.5, 8.8, 10.0, 11.5, 15.0, 17.0, 19.0, 21.3, 26
1.0, 30.0, 35.0, 41.0, 47.5, 57.5, 53.5, 52.0, 50.0, 52.0, 62.0, 73
2.5, 70.0, 68.5, 62.5, 58.0, 57.5, 57.0, 56.5, 54.5, 49.5, 44.5, 37
3.5, 33.5, 32.5, 30.5, 29.3, 28.3/
```

```
 DATA TOI/  8.0,  9.0, 10.8, 12.5, 14.3, 17.0, 19.3, 21.8, 24.3, 30
1.0, 34.3, 39.0, 45.0, 51.0, 63.5, 54.0, 56.0, 53.0, 58.0, 70.0, 85
2.0, 81.0, 77.0, 71.0, 63.0, 62.3, 61.8, 61.0, 57.0, 52.0, 46.5, 39
3.5, 34.5, 33.0, 30.5, 29.8, 29.0/
 DATA TOJ/  5.5,  7.0,  8.0,  9.0, 10.0, 11.8, 14.0, 16.5, 19.0, 21
1.0, 23.0, 30.0, 35.0, 42.0, 70.5, 64.0, 60.8, 58.5, 64.0, 78.3,110
2.3,106.0, 94.0, 88.3, 75.8, 23.8, 71.8, 69.8, 63.3, 57.0, 51.0, 43
3.0, 36.5, 33.8, 31.3, 30.5, 29.8/
 DATA TOK/   .0,   .0,   .0,   .0,   .0,   .0,   .0,   .0,   .0,
1.0,   .0,   .0,   .0,   .0, 76.5, 70.5, 66.5, 63.3, 64.0, 79.3,126
2.0,122.0,110.0,103.0, 89.5, 83.3, 79.8, 76.5, 68.0, 60.0, 53.5, 46
3.0, 39.0, 35.5, 33.0, 32.0, 31.0/
 DATA TOL/999.9,999.9,999.9,999.9,999.9,999.9,999.9,999.9,999.9,999
1.9,999.9,999.9,999.9,   .0, 70.0, 72.0, 75.0, 71.0, 49.0, 69.0,137
2.0,133.5,123.0,115.5, 97.0, 92.5, 87.5, 83.0, 72.5, 63.5, 56.5, 48
3.5, 40.5, 37.0, 34.5, 33.3, 32.3/
 DATA TOM/   .0,   .0,   .0,   .0,   .0,   .0,   .0,   .0,   .0,
1.0,   .0,   .0,   .0,   .0, 64.8, 72.3, 77.5, 76.5, 30.0, 50.0,140
2.5,139.3,131.0,122.0,109.3,100.0, 93.8, 88.3, 75.0, 67.3, 58.5, 50
3.5, 42.3, 37.8, 35.5, 34.0, 33.3/
 DATA TON/ 17.0, 14.0, 14.3, 14.5, 14.8, 15.0, 16.0, 17.0, 18.0, 26
1.0, 30.0, 38.0, 40.0, 42.0, 65.0, 72.0, 73.0, 70.0,   .0,   .0,142
2.0,141.0,136.0,129.5,110.0,105.0, 97.5, 91.0, 80.0, 68.0, 60.0, 51
3.5, 43.0, 39.0, 36.0, 35.3, 34.8/
 DATA TOO/ 26.5, 25.0, 25.3, 25.5, 26.0, 28.0, 30.0, 32.0, 34.0, 35
1.0, 36.0, 41.0, 43.0, 44.5, 65.0, 70.5, 68.0, 60.0,   .0,   .0,143
2.0,143.0,141.0,136.0,118.0,110.0,103.5, 95.0, 84.5, 70.0, 62.0, 53
3.5, 44.5, 40.0, 37.0, 36.0, 35.0/
 DATA TOP/ 32.0, 35.5, 34.5, 33.3, 32.0, 32.5, 33.8, 35.0, 36.5, 36
1.5, 37.3, 36.5, 37.3, 38.5, 59.3, 60.8, 53.3, 48.3,   .0,   .0,143
2.0,144.0,146.5,142.5,133.5,122.5,112.5,103.0, 93.0, 74.5, 64.5, 55
3.5, 47.0, 41.5, 38.5, 37.5, 36.5/
 DATA TOQ/ 27.0, 31.3, 31.5, 32.0, 32.5, 37.3, 36.8, 36.3, 36.0, 34
1.8, 34.3, 32.5, 31.3, 32.5, 52.5, 46.3, 40.3, 37.3,   .0,   .0,131
2.0,138.0,144.0,146.5,142.8,135.0,127.5,118.3,100.0, 79.3, 68.0, 57
3.8, 49.0, 44.5, 41.5, 39.5, 37.8/
 DATA TOR/ 22.0, 25.0, 29.0, 33.0, 37.3, 39.0, 38.3, 37.3, 36.5, 35
1.5, 33.0, 29.8, 27.5, 29.3, 47.0, 34.0, 32.0, 30.3,   .0,   .0, 98
2.0,105.0,117.0,130.0,141.0,132.5,127.5,120.0,104.5, 84.0, 71.5, 60
3.5, 51.0, 45.0, 41.0, 39.5, 38.0/
 DATA TOS/ 18.5, 21.5, 27.5, 33.3, 39.8, 41.0, 40.0, 38.8, 37.8, 35
1.5, 30.8, 27.5, 24.5, 23.5, 41.5, 27.0, 25.5, 24.5,   .0,   .0, 71
2.5, 81.0, 93.0,103.0,122.0,123.0,124.3,125.5,107.0, 89.3, 74.8, 63
3.3, 53.3, 45.5, 41.0, 39.3, 37.8/
 DATA TOT/ 18.0, 20.8, 26.3, 31.8, 37.3, 47.0, 45.8, 45.5, 43.0, 41
1.0, 35.0, 30.8, 26.5, 23.5, 40.5, 26.5, 24.0, 23.5,   .0,   .0, 55
2.0, 63.5, 72.5, 82.5, 99.0,103.0,111.0,118.0,108.5, 94.5, 78.0, 65
3.0, 56.0, 47.0, 43.0, 40.5, 37.5/
 DATA TOU/ 19.0, 22.5, 27.5, 32.5, 37.5, 49.8, 49.3, 48.8, 48.3, 46
1.3, 41.5, 35.5, 32.0, 28.5, 41.5, 29.8, 26.5, 25.0,   .0,   .0, 44
2.3, 50.5, 56.3, 65.5, 80.0, 87.5, 93.8,100.0,107.0, 98.3, 81.0, 66
3.5, 57.8, 47.5, 43.0, 39.8, 36.5/
 DATA TOV/ 19.8, 23.5, 25.5, 27.5, 32.0, 44.3, 46.8, 49.3, 51.8, 50
1.5, 46.3, 41.5, 37.3, 33.0, 44.5, 34.8, 30.3, 28.5,   .0,   .0, 34
2.8, 39.0, 45.0, 51.0, 62.5, 66.0, 69.5, 73.0, 57.5, 99.3, 81.0, 67
3.3, 56.5, 46.3, 41.0, 37.5, 33.8/
 DATA TOW/ 19.8, 22.0, 24.0, 26.0, 28.0, 39.0, 43.0, 47.0, 51.0, 52
1.5, 51.0, 51.0, 44.3, 43.0, 46.3, 39.8, 34.3, 30.3,   .0,   .0, 28
2.0, 32.0, 36.5, 39.8, 49.0, 52.3, 55.5, 58.5, 64.0, 73.0, 64.8, 52
3.5, 40.3, 34.3, 30.8, 26.5, 26.0/
 DATA TOX/ 14.5, 16.0, 17.0, 18.0, 19.5, 29.3, 33.5, 37.8, 42.0, 47
1.0, 45.0, 46.0, 35.0, 30.0, 38.0, 32.0, 27.0, 22.5,   .0,   .0, 23
2.0, 26.0, 29.0, 30.5, 40.0, 41.0, 42.0, 43.0, 45.0, 53.0, 47.0, 35
3.0, 29.0, 23.0, 21.5, 18.8, 18.0/
 DATA TOY/  5.0,  8.0,  8.5,  8.5,  9.0, 13.0, 17.0, 21.5, 25.0, 30
1.0, 25.0, 30.0, 19.0, 17.0, 20.0, 15.0, 12.0, 10.0,   .0,   .0, 17
2.0, 17.5, 18.0, 18.5, 22.0, 22.0, 22.0, 22.0, 27.0, 25.0, 19
3.0, 14.5, 11.0, 11.0, 10.5,  9.0/
 DATA TOZ/   .0,   .0,   .0,   .0,   .0,   .0,   .0,   .0,   .0,
1.0,   .0,   .0,   .0,   .0,   .0,   .0,   .0,   .0,   .0,   .0,
2.0,   .0,   .0,   .0,   .0,   .0,   .0,   .0,   .0,   .0,   .0,
3.0,   .0,   .0,   .0,   .0,   .0/
 DATA SP(1,1)/101120.0/,SP(2,1)/101120.0/,SP(3,1)/101120.0/,SP(4,1)
1/101120.0/,SP(5,1)/101120.0/,SP(6,1)/101120.0/,SP(7,1)/101120.0/,
2SP(8,1)/101120.0/,SP(9,1)/101120.0/,SP(10,1)/101140.0/,SP(11,1)/10
31140.0/
 DATA CON,CTO,CTR,CFO,CFV,CSX/.14,.09,.14,.08,.14,.08/
 DATA RP,RS,RFO,RF,RIC/.0235,.036,.025,.0255,.033/
 DATA ROH,CD,SEGK,CA,CB,SEGL/1.18,.313,1.53,.5,.313,1.0/
 DATA CMU/.2/
 DATA MU/.000018/
 END
 FINISH
```

VIII PLATES

Plate (1): The laser Doppler velocimeter.

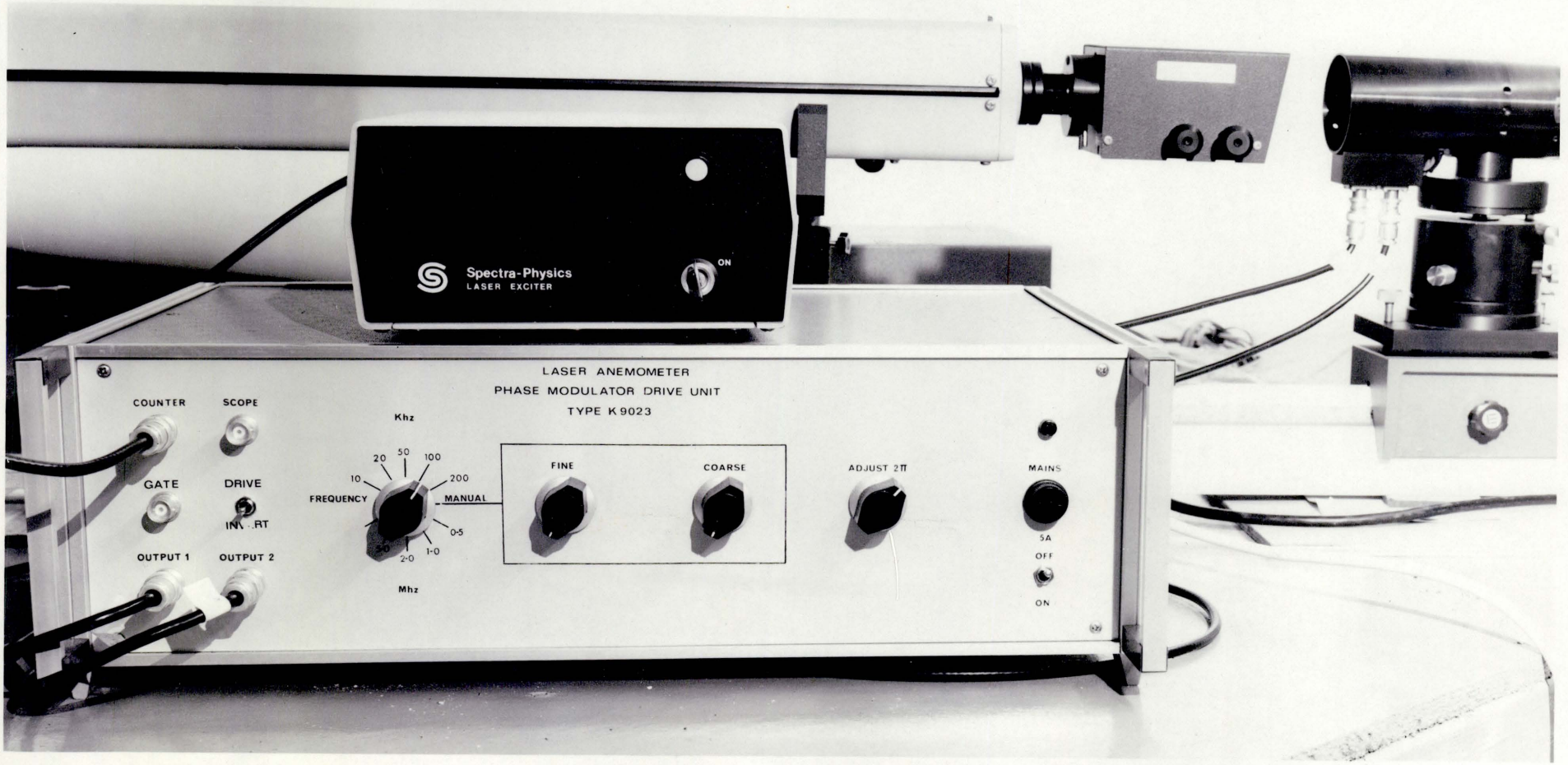

Plate (2): The transmitting optics.

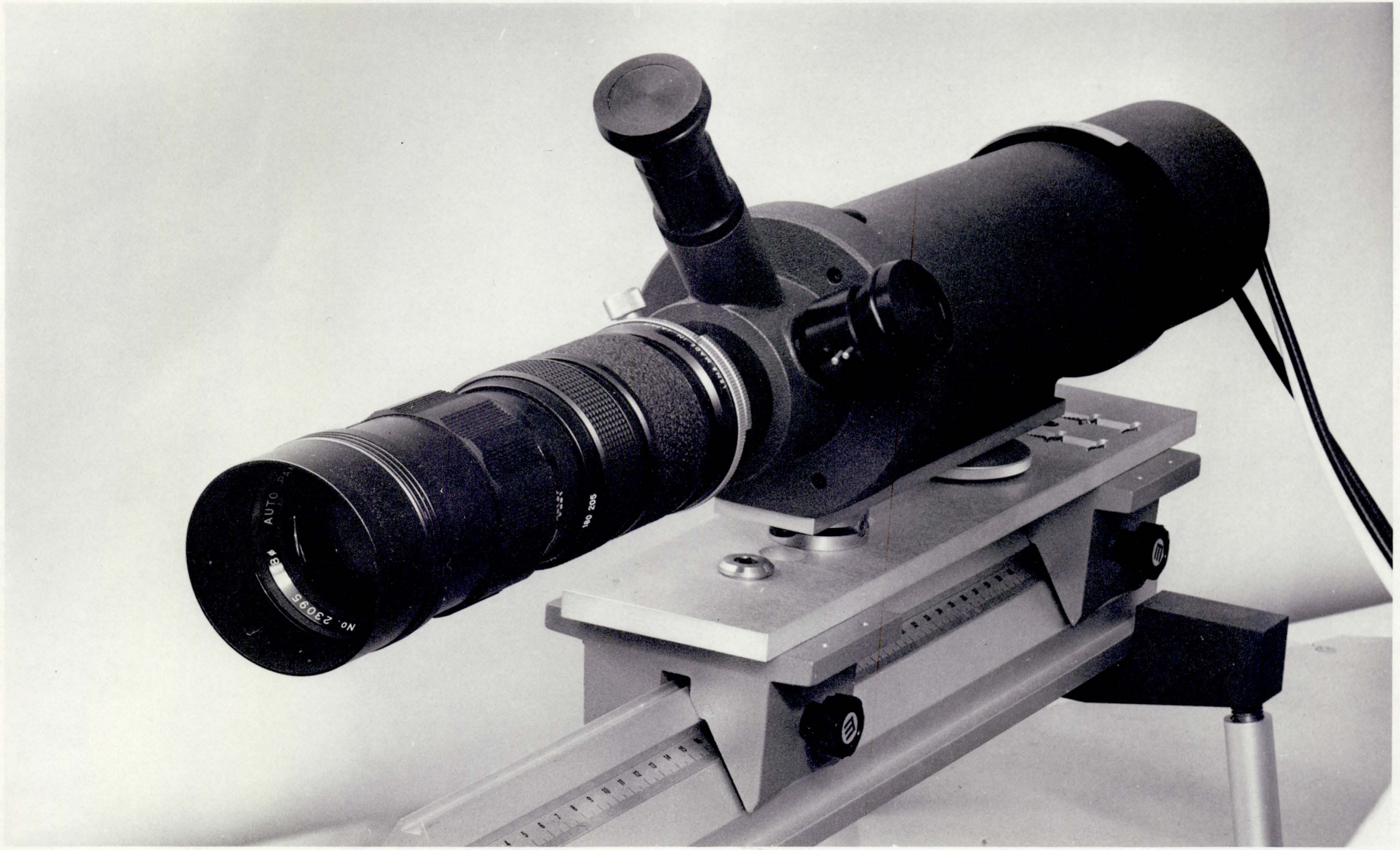

Plate (3): The receiving optics.

Plate (4): The signal and data processing system.

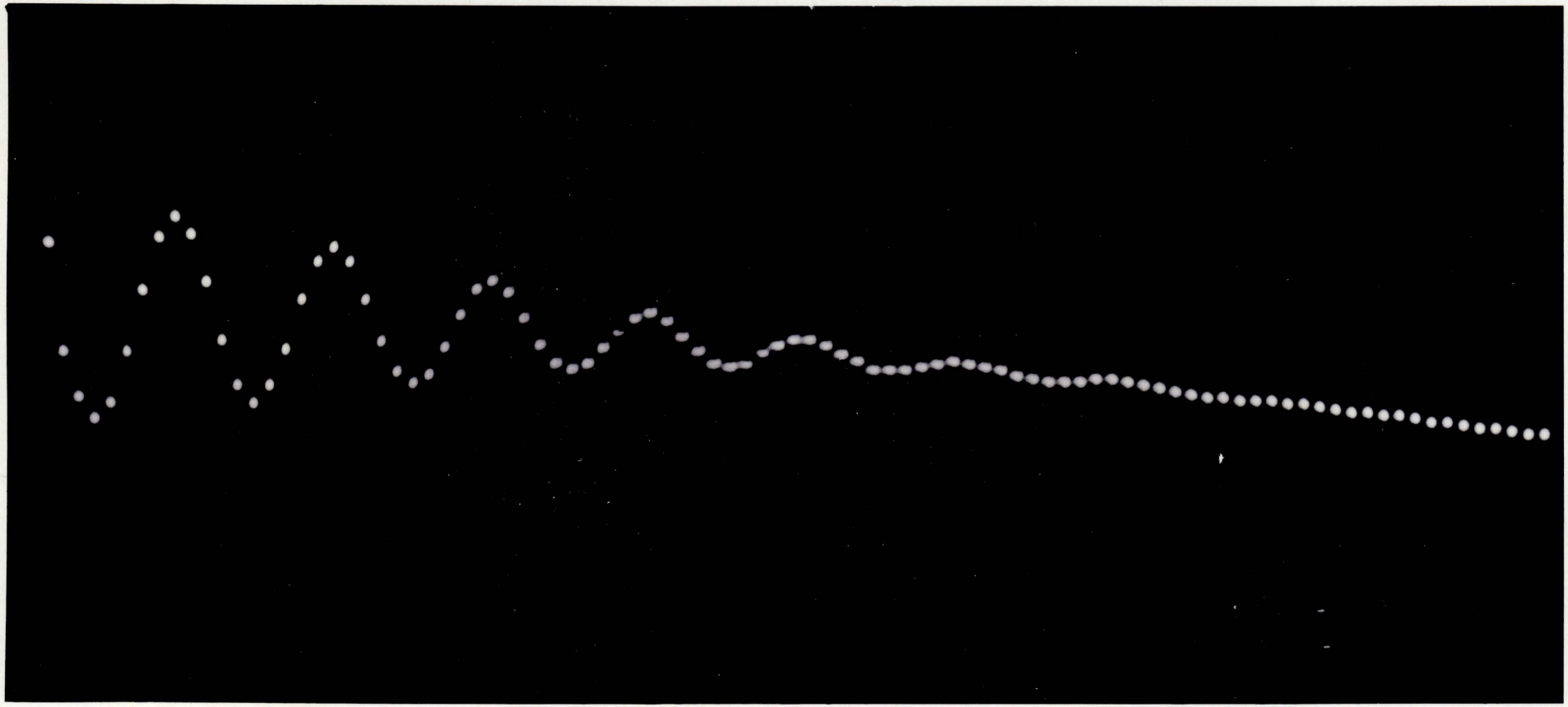

Plate (5): A typical correlogram.

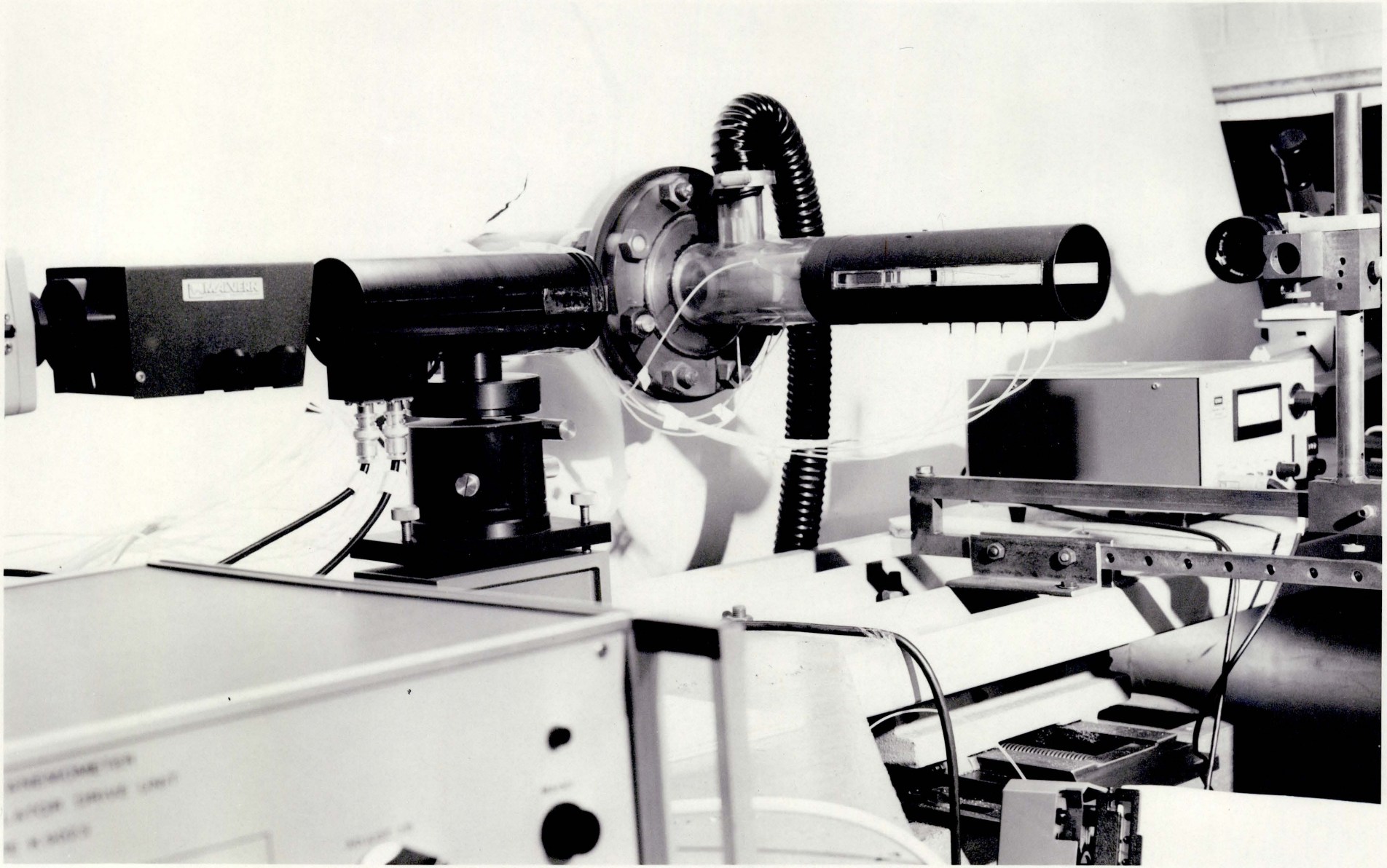

Plate (6): The test section.